TalentDetector

TalentDetector2026_Winter
INTERNATIONAL STUDENTS SCIENTIFIC CONFERENCE

Scientific editor:
Mirosław Bonek

Department of Engineering Materials and Biomaterials,
Faculty of Mechanical Engineering,
Silesian University of Technology
09 January 2026
Gliwice, Poland

Katedra Materiałów
Inżynierskich i Biomedycznych

Wydano za zgodą
Rektora Politechniki Śląskiej

Redakcja techniczna i skład komputerowy
dr h.c. dr hab. inż. Mirosław Bonek, prof. PŚ

Seria wydawnicza
Prace Katedry Materiałów Inżynierskich i Biomedycznych
Wydział Mechaniczny Technologiczny
Politechnika Śląska

ISBN 978-83-68390-55-1 Tom 2

INTERNATIONAL STUDENTS SCIENTIFIC CONFERENCE

TALENTDETECTOR2026_WINTER

SILESIAN UNIVERSITY OF TECHNOLOGY, GLIWICE, POLAND

09 JANUARY 2026

The International Student Scientific Conference TalentDetector2026_Winter aims to integrate the student and scientific community dealing with topics related to material technologies. It is a place that gives the opportunity to exchange experiences, knowledge, skills and present current scientific achievements, developing and expanding students' interests in the field of materials engineering, surface engineering, biomaterials and biomedical engineering, nanotechnology, pro-ecological technologies and computer materials science. The conference allows for the presentation of projects conducted with the industry as part of the activities of Student Scientific Circles, doctorates, projects implemented in the form of PBL - Project Based Learning as part of the Excellence Initiative - Research University at the Silesian University of Technology, projects in the framework of EURECA PRO/European University in Responsible Consumption and Production and international bilateral cooperation between Universities.

CONFERENCE ORGANIZER

Materials Science Circle of the Association of Alumni of the Silesian University of Technology, Gliwice, Poland

CONFERENCE CO-ORGANIZER

Department of Engineering Materials and Biomaterials, Faculty of Mechanical Engineering, Silesian University of Technology, Gliwice, Poland

INTERNATIONAL SCIENTIFIC COMMETTEE

ORGANIZING COMMETTEE

TalentDetector HISTORY

The International Student Scientific Conferences TalentDetector since 2018 have been a place for the exchange of experience, knowledge, skills and presentation of students' current scientific achievements in the field of materials engineering, surface engineering, biomaterials and biomedical engineering. As part of the conference, two international scientific monographs, TalentDetector_Summer and TalentDetector_Winter, are published annually, which already contain over 760 scientific articles resulting from the implementation of PBL, EURECA PRO, Students Scientific Cyrcles projects and projects with secondary school students with international authors. Participation in the form of presentations and posters in TalentDetector International Student Scientific Conferences allows members of the project teams to integrate the student and scientific community of the Silesian University of Technology as well as young staff from foreign research centres in Armenia, Austria, Brazil, China, Czech Republic, Ethiopia, Ghana, Georgia, Iran, Romania, Slovakia, South Africa, Ukraine and Turkey, dealing with topics related to materials technologies.
Scientific monographs are prepared based on articles, mostly with international authors, reviewed by an international scientific committee.
The initiative of the cyclical organization of the International Student Scientific Conference TalentDetector significantly expands activities in the field of student education, organizational and popularization activities for the scientific community related to materials engineering at the national and international level.
Thanks to extensive international cooperation, over 270 articles were published free of charge.

Number of cooperating universities: 17

City University Qatar, Doha, Qatar
Federal University of Rio Grande do Sul, Porto Alegre, Brazil
Gazi University, Ankara, Turkey
Gebze Technical University, Gebze, Turkey
Georgian Technical University, Tbilisi, Georgia
Khmelnitskyi National University, Khmelnitskyi, Ukraine
Laserinstitut Hochschule Mittweida, Mittweida, Germany
Pamukkale University, Denizli, Turkey
Silesian University of Technology, Gliwice, Poland
Slovak Technical University in Bratislava, Trnava, Slovakia
Stellenbosch University, Stellenbosch, South Africa
Technical University in Zvolen, Zvolen, Slovakia
University of Petroșani, Petroșani, Romania
University of Pristina, Pristina, Kosovo
University of Zilina, Zilina, Slovakia
Yanshan University, Qinhuangdao, China
Yerevan State University, Yerevan, Armenia

The history of TalentDetector in numbers:

2018
TalentDetector 2019 (Gliwice)
Number of articles: 59
Number of authors: 206
Number of countries: 1

2021
TalentDetector2021_Winter (Gliwice)
Number of articles: 37
Number of authors: 134
Number of countries: 2

TalentDetector2021_Summer (Zawiercie)
Number of articles: 57
Number of authors: 173
Number of countries: 3

2022
TalentDetector2022_Winter (Gliwice)
Number of articles: 79
Number of authors: 179
Number of countries: 4

TalentDetector2022_Summer (Wisła)
Number of articles: 79
Number of authors: 176
Number of countries: 4

2023
TalentDetector2023_Winter (Gliwice)
Number of articles: 73
Number of authors: 143
Number of countries: 6

TalentDetector2023_Summer (Brenna)
Number of articles: 105
Number of authors: 173
Number of countries: 9

2024
TalentDetector2024_Winter (Gliwice)
Number of articles: 82
Number of authors: 135
Number of countries: 7

TalentDetector2024_Summer (Gliwice-Zilina)
Number of articles: 84
Number of authors: 147
Number of countries: 8

2025
TalentDetector2025_Winter (Gliwice)
Number of articles: 95
Number of authors: 173
Number of countries: 9

TalentDetector2025_Summer (Brenna)
Number of articles: 87
Number of authors: 143
Number of countries: 10

TalentDetector2025_Yanshan (Gliwice)
Number of articles: 12
Number of authors: 29
Number of countries: 1

TalentDetector2025_Prom (Gliwice)
Number of authors: 15
Number of countries: 6

2026
TalentDetector2026_Winter (Gliwice)
Number of articles: 93
Number of authors: 184
Number of countries: 11

TalentDetector

9th January 2026
Gliwice, Poland

DEPARTMENT OF ENGINEERING MATERIALS AND BIOMATERIALS
FACULTY OF MECHANICAL ENGINEERING
SILESIAN UNIVERSITY OF TECHNOLOGY

INTERNATIONAL STUDENTS SCIENTIFIC CONFERENCE

Contents

VOLUME 1

VOLUME 2

TalentDetector

9th January 2026
Gliwice, Poland

DEPARTMENT OF ENGINEERING MATERIALS AND BIOMATERIALS
FACULTY OF MECHANICAL ENGINEERING
SILESIAN UNIVERSITY OF TECHNOLOGY

INTERNATIONAL STUDENTS SCIENTIFIC CONFERENCE

Compact waveguide microwave sensor based on coupled metallic rod resonators

Artyom Movsisyan, Tigran Abrahamyan, Hovhannes Haroyan, Arsen Babajanyan, Khachatur Nerkarayan

Yerevan State University, Institute of Physics, Yerevan 0025, Armenia
E-mail: barsen@ysu.am

Abstract: This study investigates a compact microwave sensing structure based on metallic rods partially coated with a dielectric cambric layer and embedded inside a rectangular waveguide. The system is excited using a coaxial to waveguide transition, enabling straightforward integration with standard microwave measurement equipment. Reflection and transmission responses are analyzed to evaluate the sensitivity of the structure to dielectric loading and geometric variations. Numerical simulations are first performed for a single coated rod to reproduce experimentally observed resonance behavior. The presence of a thin cambric layer significantly shifts the resonance frequency, demonstrating the structure's capability to detect low-thickness dielectric materials. The sensing concept is then extended to multi-element configurations consisting of three parallel rods, where only the central rod is coated. The influence of key parameters including inter-rod spacing, rod length, inclination angle, relative permittivity, and structural asymmetry is systematically examined. Strong electromagnetic coupling between the rods produces sharp and tunable resonances, with optimized asymmetric configurations exhibiting quality factors exceeding 750 near 7–7.5 GHz. Such high-Q resonances provide enhanced frequency resolution and sensitivity to small dielectric changes. These results indicate that the proposed rod-based waveguide structure is well suited for practical microwave sensing applications, including thin-film characterization, material identification, and permittivity measurements in industrial and laboratory environments.

Keywords: multi-element configuration, high-Q resonance, sensing applications.

1. INTRODUCTION

The problem of a conductive rod coated with a dielectric film has attracted considerable scientific interest since the last century, particularly due to its rich electromagnetic behavior and practical relevance. It has been demonstrated that a conducting rod exhibiting resonant characteristics, when partially or fully covered by a dielectric layer of finite length, can effectively function as a resonator [1,2]. Such structures enable controlled manipulation of electromagnetic fields and provide a convenient platform for studying resonance phenomena.

Furthermore, an ensemble (or array) of such rods represents an especially promising system for advanced investigations, particularly when the rods are placed inside a rectangular waveguide. In this configuration, strong coupling between the rods and the guided electromagnetic modes can occur, leading to complex collective effects. From a conceptual standpoint, this arrangement can be regarded as a metastructure whose properties are inherently multilevel and multidisciplinary, combining aspects of electromagnetics, materials science, and wave–matter interaction. These metastructures often exhibit pronounced and, in many cases, highly selective responses [3] when interacting with an external electromagnetic field [4,5]. Previous studies have primarily focused on the emergence of resonance effects, which allow such systems to be interpreted as bandstop filters with high efficiency at suppressing specific frequency ranges [6]. However, despite their effectiveness, the functional scope of these structures has remained relatively limited, as their operation has been largely restricted to band-rejection behavior. The key contribution of the present work lies in overcoming this limitation by demonstrating that a system based on conductive rods can be engineered to operate as a bandpass filter. The primary objective of this study is therefore the design, realization, and analysis of a bandpass filtering structure based on conductive rods, expanding the functional capabilities of rod-based metastructures and opening new possibilities for practical electromagnetic applications.

2. MATERIALS AND METHODS

A key advantage of conductive rods with a fixed height is their ability to operate as open resonators when illuminated by electromagnetic waves polarized along their longitudinal axes. Such waves exhibit radial symmetry and possess a strong radial electric field component, which promotes effective coupling between neighboring resonators. For the experiments, identical copper rods with a radius of 0.5 mm and a length of 17 mm were chosen as the device under test (DUT). Configurations consisting of two or three rods were inserted into a rectangular waveguide of type WR-137 (Pasternak UDR70), which was mounted inside a 5 mm-thick sample holder. The fundamental mode of the WR-137 waveguide operates within the frequency range of 4.3–8.6 GHz. Transmission and reflection characteristics were measured using a vector network analyzer, the Rohde & Schwarz ZNB20. Accurate placement of the rods inside the waveguide was achieved by laser-marking predefined positions in a foam polymer (polypropylene) support. Numerical simulations were conducted using a full-wave three-dimensional finite-element-method-based electromagnetic solver. In the simulation model, copper rods with an electrical conductivity of 6×10^7 S/m were positioned inside a rectangular waveguide with perfectly conducting walls. We conducted numerical modeling in the COMSOL Multiphysics environment, using a RF module-the Electromagnetic waves frequency domain interface.

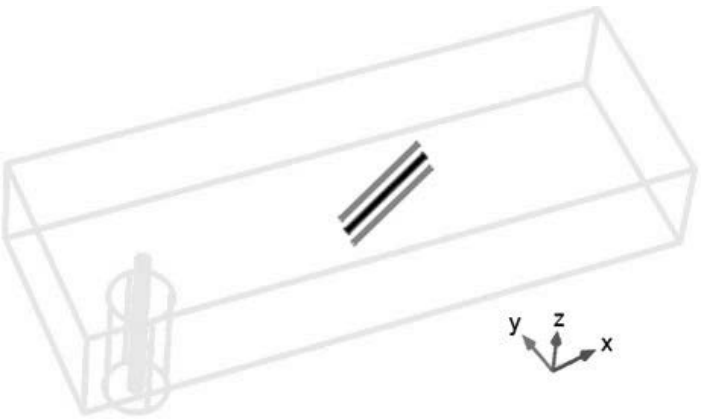

*Figure 1. The rods system in rectangular waveguide. We are not set polypropylene layer(*taking into account the layer as an air*).*

We examined the walls of the waveguide as an impedance boundary condition with an excitation coaxial port. We also considered the receiver port as the far end of the coaxial port of the waveguide and recorded the transmission signal on it. We have included 3 rods in this work, one of which is covered with a thin dielectric layer, but there is none at the ends. The relative permittivity of this dielectric is 4 (as in cambric).

3. RESULTS AND DISCUSSIONS

As previously stated, the main achievement of this work is the successful realization of a microwave filter based on a periodic rod system. The proposed configuration employs a reflector arrangement in which the edges of the waveguide are covered by vertically oriented reflecting mirrors. This design enhances field confinement within the structure and promotes stronger electromagnetic coupling between the constituent elements of the periodic system. The lower figure illustrates the oblique electromagnetic field distribution at resonance, including a spatial map of the measured field curvature, which clearly demonstrates the strong interaction between the conductive rods at the resonant frequency. This field pattern confirms the collective resonant behavior of the periodic structure and highlights the role of inter-rod coupling in shaping the overall response of the system. In addition, the figure presents the amplitude–frequency response of the structure over the specified operating frequency range of the rectangular waveguide, providing a direct visualization of the filter characteristics. In the demonstrated configuration, the quality factor of the transmission spectrum reaches a value close to 90, which can be considered a very good result for this type of microwave filtering structure. Nevertheless, the obtained performance is not a fundamental limit. The quality factor can be further increased potentially by several times through additional geometric optimization and structural refinement, such as improved alignment, surface polishing, or fine-tuning of the rod and reflector parameters.

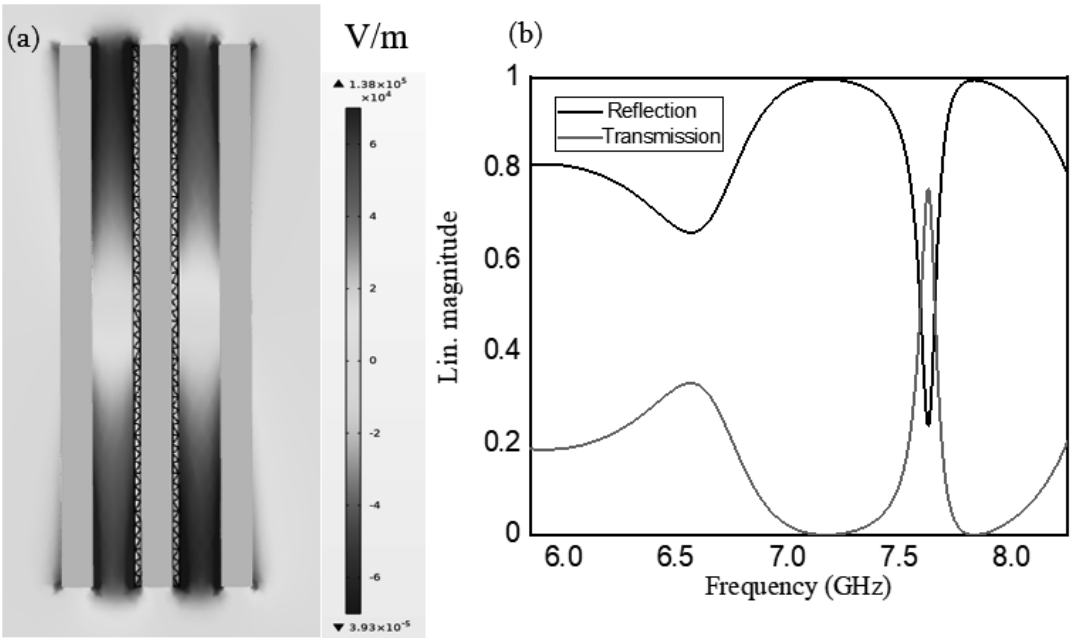

Figure 2. a) T*he resonance of a 17 mm long rod at its transition resonance point, which is 7.62 GHz, b) The spectra of transmission and reflection of copper rods system.*

BIBLIOGRAPHY

[1]Hambaryan D, Abrahamyan T, Parsamyan H, Movsisyan A, Minasyan B, Haroyan H, Babajanyan A, Lee K, Friedman B and Nerkararyan K 2024 Dielectric coated conductive rod resonantly coupled with a cut transmission line as a tunable microwave bandstop filter and sensor *Heliyon* 10 e24477

[2]Goubau G 1951 Single-Conductor Surface-Wave Transmission Lines *Proc. IRE* 39 619–24

[3]Movsisyan A and Babajanyan A 2026 Dual-resonant anisotropic all-dielectric near-infrared bandstop filter with enhanced spectral and angular stability *Optics Communications* 601 132754

[4]Huang L, Chang C-C, Zeng B, Nogan J, Luo S-N, Taylor A J, Azad A K and Chen H-T 2017 Bilayer Metasurfaces for Dual- and Broadband Optical Antireflection *ACS Photonics* 4 2111–6

[5]Pirrone D, Ferraro A, Zografopoulos D C, Fuscaldo W, Szriftgiser P, Ducournau G and Beccherelli R 2022 Metasurface-Based Filters for High Data Rate THz Wireless Communication: Experimental Validation of a 14 Gbps OOK and 104 Gbps QAM-16 Wireless Link in the 300 GHz Band *IEEE Trans. Wireless Commun.* 21 8688–97

[6]Abrahamyan T, Ohanyan G, Hambaryan D, Movsisyan A, Parsamyan H, Haroyan H, Babajanyan A and Nerkararyan K 2025 Resonant enhancement and confinement of microwave field in coupled conductive rod systems *Phys. Scr.* 100 025515

TalentDetector

9th January 2026
Gliwice, Poland

DEPARTMENT OF ENGINEERING MATERIALS AND BIOMATERIALS
FACULTY OF MECHANICAL ENGINEERING
SILESIAN UNIVERSITY OF TECHNOLOGY

INTERNATIONAL STUDENTS SCIENTIFIC CONFERENCE

Analiza numeryczna rozkładu naprężeń i przemieszczeń w łożysku oczkowym przy zadanym obciążeniu oraz jego wizualizacja

Mateusz Musialik[a], Alan Nowak[a], Dominik Śliwa[b], Łukasz Mann[c,] Wojciech Mikołejko[d], Aagata Śliwa[d]

[a] Uczniowie Zespołu Szkół Technicznych i Ogólnokształcących „Mechanik" w Tarnowskich Górach, email: musialmati123321@gmail.com, nowakalan685@gmail.com
[b] Uczeń Liceum Ogólnokształcącego „Szkoła w Chmurze" w Poznaniu . email: dominik.sliwa16@gmail.com
[c] Nauczyciel Zespołu Szkół Technicznych i Ogólnokształcących „Mechanik" w Tarnowskich Górach, email: l.mann@mechaniktg.pl
[d] Politechnika Śląska, Wydział Mechaniczny Technologiczny, Katedra Materiałów Inżynierskich i Biomedycznych , email: Wojciech.mikolejko@polsl.pl, agata.sliwa@polsl.pl

Streszczenie: W poniższej pracy przedstawiono analizę naprężeń, rozkładu przemieszczenia podczas pracy łożyska oczkowego. Analizę przeprowadzono dla łożyska względem, którego zastosowana została siła w kierunku okrężnym oraz zmienna siła w kierunku promieniowym. Badania wykonano za pomocą metody MES, przy użyciu programu SOLIDWORKS.
Abstract: The paper presents analysis of tensions, displacements distribution, which appear during the work of bearing rod. The analysis was carried out for the bearing against which the force in the circular direction and the variable force in the radial direction were applied. The measurements were made with MES method in SOLIDWORKS program.

Słowa kluczowe: łożysko oczkowe, SOLIDWORKS, rozkład naprężeń, MES

1. WPROWADZENIE

Łożyska oczkowe należą do grupy łożysk ślizgowych, ponieważ w ich budowie oprócz obudowy zastosowano również typowe łożysko ślizgowe. Cechują się dużą odpornością na zużycie oraz bardzo dobrze nadają się do przenoszenia obciążeń o zmiennym kierunku, w związku z czym często są stosowane w przypadku występowania znacznych obciążeń. Łożyska oczkowe dzieli się na wersję wymagające obsługi oraz bezobsługowe [1-2].

Łożyska wymagające obsługi muszą być regularnie smarowane. Na przykład w łożyskach typu stal po brązie, nawet w przypadku chwilowego braku smaru, jego właściwości zostają zachowane, jednak dłuższy brak serwisowania łożyska może być przyczyną szybszego zużycia, jak również uszkodzenia całkowitego [1-2].

Natomiast bezobsługowe łożyska znajdują zastosowanie w miejscach, gdzie występują wysokie obciążenia o stałym kierunku. Łożyska te posiadają powierzchnie ślizgowe, które wykonane są z nowoczesnych materiałów charakteryzujących się niskim tarciem. W pierścień zewnętrzny łożyska wprasowuje się tworzywo PTFE z dodatkiem dwusiarczku molibdenu, natomiast wewnętrzny pierścień jest twardo chromowany, a następnie jego powierzchnia jest polerowana. Niektóre wersje łożysk są wyposażone w dodatkowe uszczelnienia, które odpowiadają za ochronę przed zanieczyszczeniami, a także warunkami zewnętrznymi [1-2].

Łożyska oczkowe ze względu na budowę oraz zastosowane materiały można podzielić na [2]:

- łożyska oczkowe stal po kompozyt PTFE,
- łożyska oczkowe stal po stali z gwintowanym otworem,
- łożyska oczkowe stal po brązie z gwintowanym otworem,
- łożyska oczkowe stal po stali z gwintowanym trzpieniem,
- łożyska oczkowe stal po tkaninie PTFE,
- łożyska oczkowe stal po stali z trzpieniem do przyspawania,
- łożyska oczkowe stal po brązie z gwintowanym trzpieniem.

Rys. 1. Przykładowe łożysko oczkowe [3]
Fig. 1. An example of the bearing rod [3]

Łożyska oczkowe zbudowane są z obudowy i łożyska ślizgowego przegubowego. Obudowa może występować z gwintowanym otworem bądź trzpieniem, z gwintem prawym albo lewym. Dostępne są łożyska oczkowe w wersji z połączeniem współpracujących powierzchni ślizgowych stal po stali, a także stal po brązie. Łożyska typu stal po stali cechują się powierzchniami współpracującymi, które hartuje się, a następnie obrabia i dociera. Natomiast łożyska stal po brązie wyposażone są w pierścień wewnętrzny, który jest hartowany i chromowany oraz w zewnętrzny pierścień, który wykonuje się z brązu [2].

Omawiane przez nas łożysko oczkowe składa się z trzech składowych elementów: oprawy i pierścienia wewnętrznego wykonanego ze stali narzędziowej X40Cr14 oraz warstwy ślizgowej z gumy NBR.

Do przeprowadzonych badań na zaprojektowanym łożysku oczkowym posłużył program inżynierski SOLIDWORKS. Jest to oprogramowanie, które znajduje zastosowanie w parametrycznym modelowaniu trójwymiarowym (CAD 3D). Pozwala ono na zaprojektowanie modeli bryłowych, arkuszy blach, konstrukcji spawanych, form

oraz modeli powierzchniowych. Program ten jest wykorzystywany do pracy na dużych złożeniach, pozwala generować widoki przekroju składające się z dziesiątek tysięcy komponentów, a także służy do renderowania wymagających scen. SOLIDWORKS umożliwia również złożenie wszystkich elementów w jeden projekt za pomocą odpowiednich rodzajów połączeń, zasymulowaniu ich pracy oraz wizualizacji możliwych do wystąpienia błędów projektowych, co pozwala na przygotowanie dokumentacji produkcyjnej. Obecnie oprogramowanie tego typu jest dostępne w formie licencji dostępnej na określony czas [4].

2. DOBÓR MATERIAŁÓW

2.1 Stal narzędziowa

Stale narzędziowe są twardymi materiałami wysokiej jakości, odpornymi na ścieranie oraz działanie ciepła. Zdolne są do przenoszenia dużych naprężeń zarówno w temperaturze pokojowej, jak i tej zbliżonej nawet do 700°C. Te własności stali narzędziowej wynikają ze zdolności do hartowania podczas chłodzenia. Aby jeszcze zwiększyć hartowność stali dodaje się do niej wspomniane powyżej pierwiastki stopowe. Przeważnie dodaje się Cr, Mo, W, V oraz Mn. Podstawowymi własnościami stali narzędziowych, określającymi ich zachowanie podczas eksploatacji, są: odporność na zużycie i odkształcanie, udarność, odporność na odpuszczające działanie ciepła [5].

Stale narzędziowe dzieli się na: węglowe, stopowe: do pracy na zimno, na gorąco oraz szybkotnące. Stal węglowa to taka, która nie ma większej liczby dodatków stopowych, oprócz węgla. Od stali konstrukcyjnej odróżnia ją ponadto zmniejszona zawartość manganu i drobnoziarnistość. Stal stopowa do pracy na zimno stosowana jest produkcji narzędzi przeznaczonych do obróbki skrawaniem i plastycznej. Mogą się one jedynie nieznacznie nagrzewać w czasie pracy. Inaczej jest w przypadku stali narzędziowej do pracy na gorąco, stosowanej na narzędzia do obróbki plastycznej na gorąco i do budowy form odlewniczych narażonych na wysoką temperaturę. Stal szybkotnąca natomiast używana jest do wytwarzania narzędzi do wysokowydajnej obróbki skrawaniem takich jak noże tokarskie, frezy, wiertła [5].

Materiałem który zastosowano do wykonania zarówno oprawy, jak i pierścienia wewnętrznego jest stal narzędziowa 1.2083 (X40Cr14), o składzie chemicznym przedstawionym w tablicy 1.

Tab. 1. Skład chemiczny stali narzędziowej 1.2083 (X40Cr14) w [%] [6]
Tab. 1. The chemical composition of tool steel 1.2083 (X40Cr14) in [%] [6]

C	Mn	Si	P	S	Cr	Ni	Mo	W	V	Co	Cu
0,40	0,45	0,7	max 0,04	max 0,03	14,3	-	0,6	-	0,2	-	-

Stal 1.2083 to stopowa nierdzewna stal narzędziowa przeznaczona do pracy na zimno. Zachowuje stabilność wymiarową w czasie ulepszania. Wysoka jednorodność materiału w stanie odpuszczonym w wielu wypadkach doskonale zabezpiecza przed korozją. Materiał ten znajduje zastosowanie w przypadku form do chemicznie agresywnych i wydzielających kwasy tworzyw sztucznych, takich jak duroplasty, termoplasty, PVC aminoplasty, wkładki

do form wtryskowych, części maszyn takie jak łożyska ślizgowe oraz części maszyn w przemyśle spożywczym [7-8]. Wybrane własności stali 1.2083 przedstawiono w tablicy 2.

Tab. 2 Wybrane własności stali 1.2083 [9]
Tab. 2 Properties of 1.2083 steel [9]

Właściwość	Wartość	Jednostka
Współczynnik sprężystości	69000	N/mm^2
Współczynnik Poissona	0.33	-
Współczynnik naprężenia ścinającego	27000	N/mm^2
Masa właściwa	2700	kg/m^3
Wytrzymałość na rozciąganie	68.9356	N/mm^2
Współczynnik rozszerzalności cieplnej	2.4e-005	/K
Granica plastyczności	27.5742	N/mm^2
Współczynnik przewodzenia ciepła	200	W/(m·K)
Ciepło właściwe	900	J/(kg·K)

2.2 Guma NBR

Materiałem, który zastosowano do wykonania warstwy ślizgowej łożyska oczkowego jest guma NBR. NBR, czyli nityl, to jedna z najpopularniejszych gum. Często mówi się na nią guma olejoodporna, natomiast używa się też innych sformułowań takich jak [10-11]:

- kauczuk butadienowo – akrylonitrylowy,
- kauczuk akrylonitrylo – butadienowy.

NBR jest to guma z rodzaju elastomerów, czyli produkt kopolimeryzacji butadienu i akrylonitrylu. W zależności od zastosowanych ilości powyższych związków chemicznych i zmianie ich udziału procentowego w mieszance można dowolnie manipulować odpornością na oleje i niską temperaturę. Dokładne właściwości gumy prezentują się następująco [10-11]:

- niska odporność na czynniki atmosferyczne i ozon – wyjątkiem jest jej mieszanka z PVC,
- duża wytrzymałość na zerwanie,
- odporność termiczna waha się od -50 do 105 stopni Celsjusza,
- odporność na działanie olejów oraz benzyny,
- odporność na węglowodory alifatyczne,
- trwałość wobec lekkich olejów opałowych, paliw do silników wysokoprężnych,
- wysoka odporność na niepalne ciecze hydrauliczne (typu HSA, HSB: emulsje olejowo – wodne, HSC: mieszaniny poliglikolu z wodą),
- brak reakcji z kwasami i zasadami rozcieńczonymi w niezbyt wysokich temperaturach,
- nietrwałość wobec węglowodorów aromatycznych i chlorowanych,
- brak odporności na działanie HSD: poliestrowych i węglowodorach chlorowanych),
- brak odporności na płyny hamulcowe, zawierające w swoich składach glikole.

Swoje zastosowanie nityl znajduje głównie w hydraulice oraz pneumatyce. Guma ta będzie tworzyć wszelkie uszczelki, pierścienie uszczelniające typu „O” oringi. Praca, w której jest obecne duże ciśnienie, silny nacisk, ścisk a substancje towarzyszące to oleje to odpowiednie

środowisko dla zastosowania tej gumy. NBR można spotkać w oponach, dętkach, odbojach. Także elementy amortyzujące są produkowane właśnie z NBR. Ich zaletą jest także to, że wytłumiają drgania. Wszelkie węże na paliwa ciekłe i oleje są także wyrabiane przy użyciu NBR. W przemyśle spożywczym NBR może być używany jako materiał na węże przesyłowe. Może być także uszczelniaczem różnego rodzaju złączy. Gumę NBR stosuje się również na warstwy ślizgowe w łożyskach tocznych w głównej mierze ze względu na odporność na oleje, odporność termiczną oraz wytrzymałość na zerwanie [10-11]. W tablicy 3 przedstawione zostały wybrane własności gumy NBR.

Tab. 3 Wybrane własności gumy NBR [9]
Tab. 3 Properties of NBR rubber[9]

Właściwość	Wartość	Jednostka
Współczynnik sprężystości wzdłużnej	4	N/mm^2
Współczynnik Poissona	0,48	-
Masa właściwa	1150	kg/m^3
Wytrzymałość na rozciąganie	6,89	N/mm^2

3. ZAŁOŻENIA MODELOWE ORAZ MODEL GEOMETRYCZNY CAD

W niniejszej pracy wykonano analizy wytrzymałościowe łożyska oczkowego z wykorzystaniem programu SOLIDWORKS. W trakcie projektowania modelu łożyska zastosowano dwa materiały: stal 1.2083 oraz gumę NBR, których własności zostały przedstawione w tablicach 2 oraz 3. Łożysko oczkowe powstało w wyniku złożenia trzech części składowych: oprawy, pierścienia wewnętrznego oraz warstwy ślizgowej, których geometrię oraz wymiary główne (w mm) przedstawiono na rysunkach 2-4.

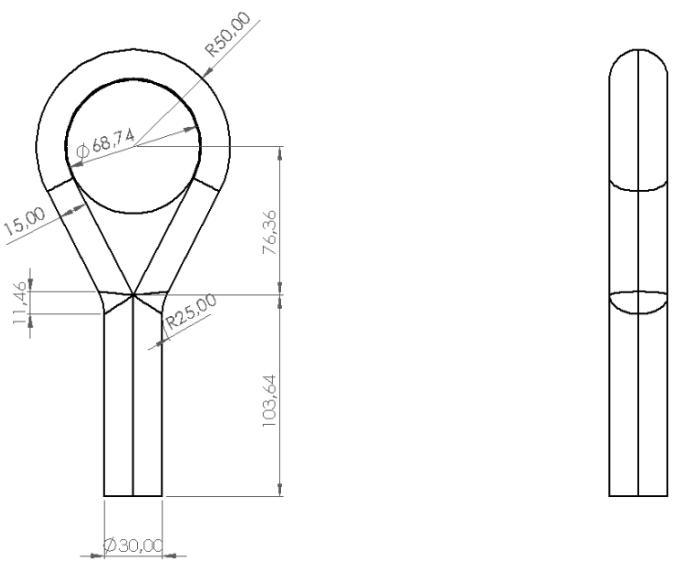

Rys. 2. Oprawa łożyska oczkowego
Fig. 2. Bearing rod's housing

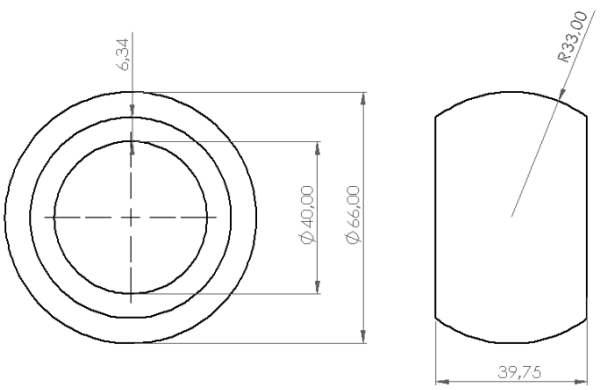

Rys. 3. Pierścień wewnętrzny łożyska oczkowego
Fig. 3. Bearing rod's inner ring

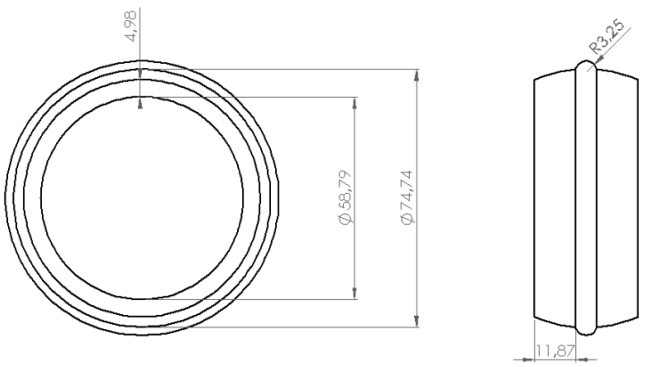

Rys. 4. Warstwa ślizgowa łożyska oczkowego
Fig. 4. Bearing rod's sliding layer

Analizowane łożysko oczkowe zostało zaprojektowane według wymiarów podanych na stronie producenta, w celu sprawdzenia jak duże obciążenie jest w stanie ono przenieść nie ulegając zniszczeniu. W celu przeprowadzenia analizy wytrzymałościowej wykonano modele geometryczne trzech części (rys. 5) przy użyciu oprogramowania SOLIDWORKS.

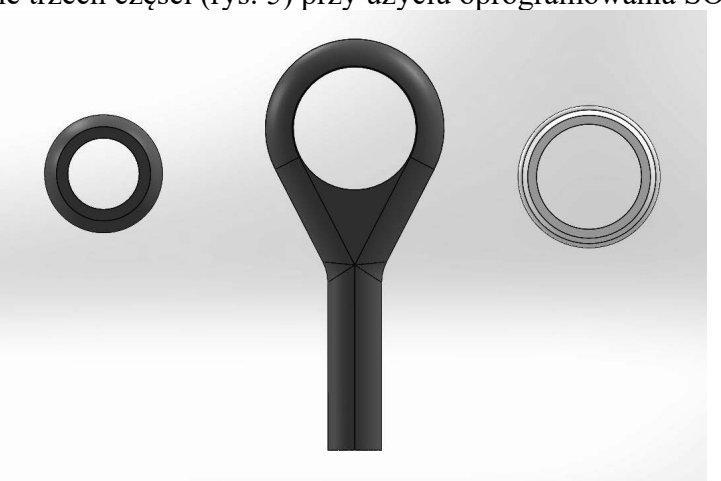

Rys. 5. Części składowe łożyska oczkowego
Fig. 5. Components of the bearing rod

Następnie w wyniku złożenia trzech modeli geometrycznych otrzymano kompletny model łożyska oczkowego (rys. 6).

Rys. 6. Model łożyska oczkowego
Fig. 6. Model of the bearing rod

4. WARUNKI BRZEGOWE

Symulacja komputerowa została wykonana również w programie SOLIDWORKS przy użyciu dodatku Simulation. Dla symulacji przyjęto następujące warunki brzegowe:

- na całą oprawę łożyska oczkowego nałożone zostało umocowanie w postaci nieruchomej geometrii (rys. 7)
- na powierzchnię pierścienia wewnętrznego nałożone zostało obciążenie, zmienną siłą w kierunku promieniowym i stałą siłą w kierunku okrężnym (rys. 8)
- na badane elementy została nałożona siatka bryłowa składająca się z:
  28908 węzłów oraz 19014 elementów skończonych (rys. 9)

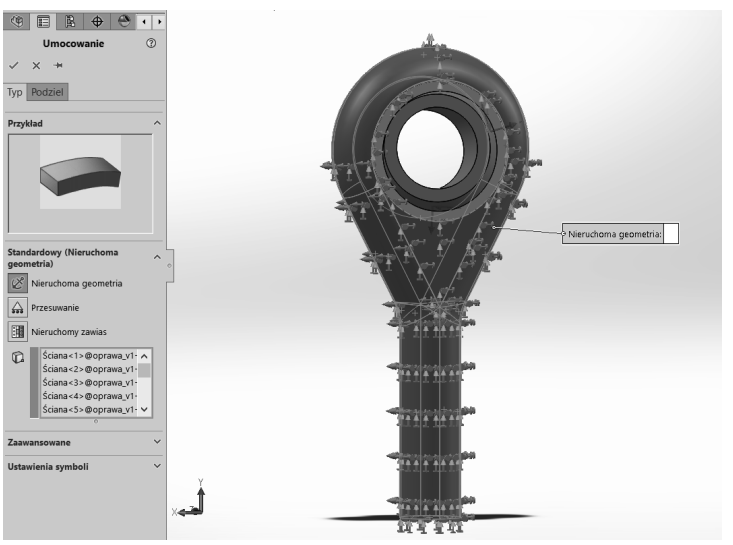

Rys. 7. Sposób umocowania łożyska oczkowego
Fig. 7. The way of fixing of the bearing rod

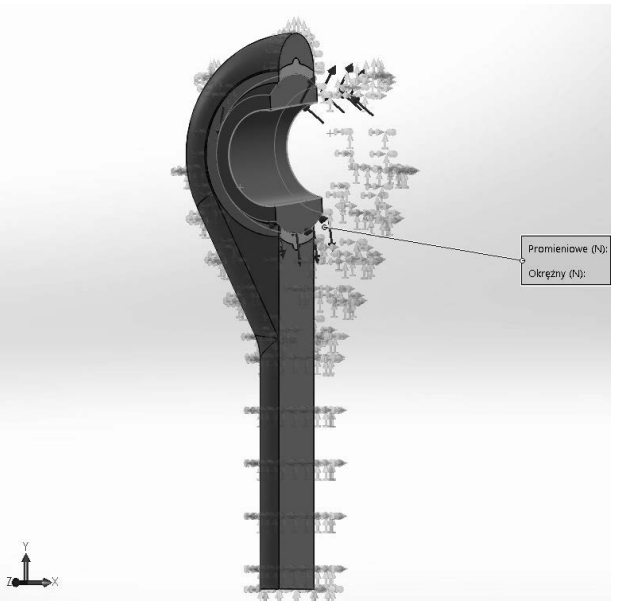

Rys. 8. Sposób obciążenia łożyska oczkowego
Fig. 8. The way of load of the bearing rod

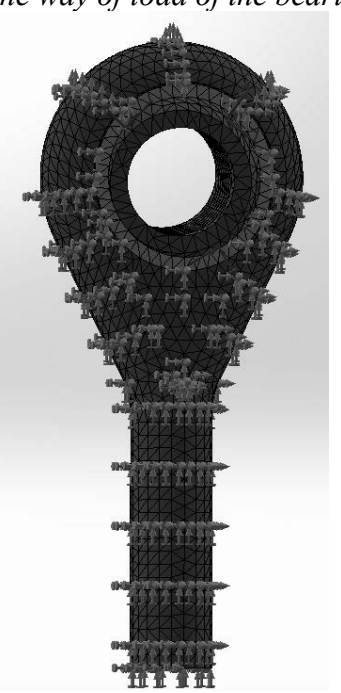

Rys. 9. Widok siatki geometrycznej modelu łożyska oczkowego
Fig. 9. Mesh created for the model of the bearing rod

5. ANALIZA WYNIKÓW

5.1 Wyniki analizy naprężeń

Analiza naprężeń została wykonana w oparciu o hipotezę Hubera-Misesa. Po obciążeniu łożyska oczkowego stałą siłą w kierunku okrężnym wynoszącą 10 kN i zmienną siłą

w kierunku promieniowym, otrzymano wykresy naprężeń, których wartości wyrażono w MPa. Na rysunkach 10-13 przedstawiono rozkład naprężeń powstających podczas zadanego obciążenia. Na podstawie wyniku analizy stwierdzono, że największe naprężenia dla wszystkich przypadków występują na krawędziach i ścianie wewnętrznej pierścienia. W przypadku obciążenia siłą o wartości 10 kN w kierunku promieniowym wartość maksymalnych naprężeń wynosi ok. 6,43 MPa, w przypadku zastosowania siły o wartości 100 kN wartość maksymalnych naprężeń wynosi ok. 52,33 MPa, a w przypadku obciążenia siłą o wartości 1 MN maksymalne naprężenia osiągają wartość ok. 508,74 MPa. Z kolei przy obciążeniu siłą o wartości 10 MN w kierunku promieniowym maksymalne naprężenia wynoszą ok. 5 105,41 MPa, co znacznie przewyższa wartość granicy plastyczności dla materiału pierścienia wewnętrznego.

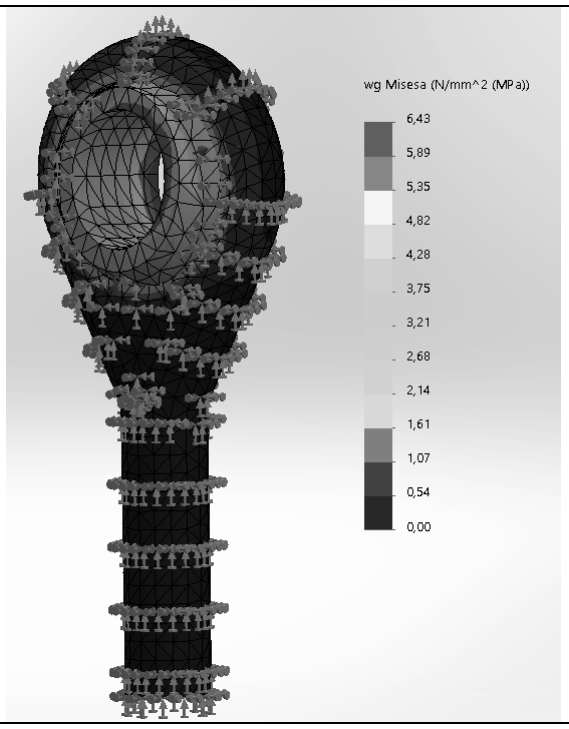

Rys. 10. Rozkład naprężeń zredukowanych dla łożyska oczkowego obciążonego siłą o wartości 10 kN (10 000 N) w kierunku promieniowym

Fig. 10. Distribution of Huber-Mises stresess for the bearing rod loaded with a force of 10 kN (10 000 N) in the radial direction

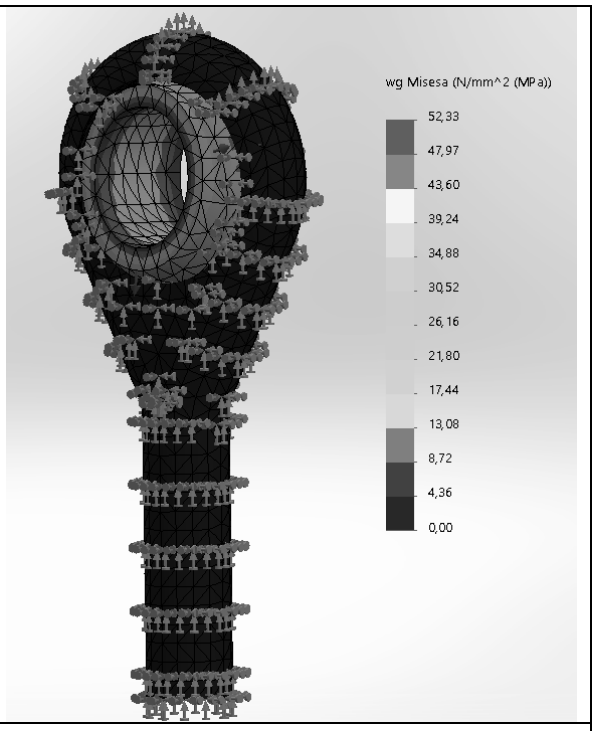

Rys. 11. Rozkład naprężeń zredukowanych dla łożyska oczkowego obciążonego siłą o wartości 100 kN (100 000 N) w kierunku promieniowym

Fig. 11. Distribution of Huber-Mises stresess for the bearing rod loaded with a force of 100 kN (100 000 N) in the radial direction

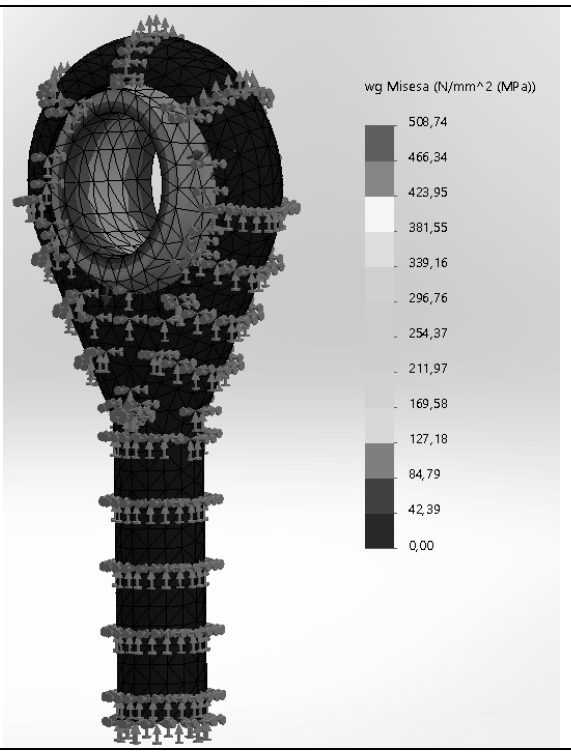

Rys. 12. Rozkład naprężeń zredukowanych dla łożyska oczkowego obciążonego siłą o wartości 1 MN (1 000 000 N) w kierunku promieniowym

Fig. 12. Distribution of Huber-Mises stresess for the bearing rod loaded with a force of 1 MN (1 000 000 N) in the radial direction

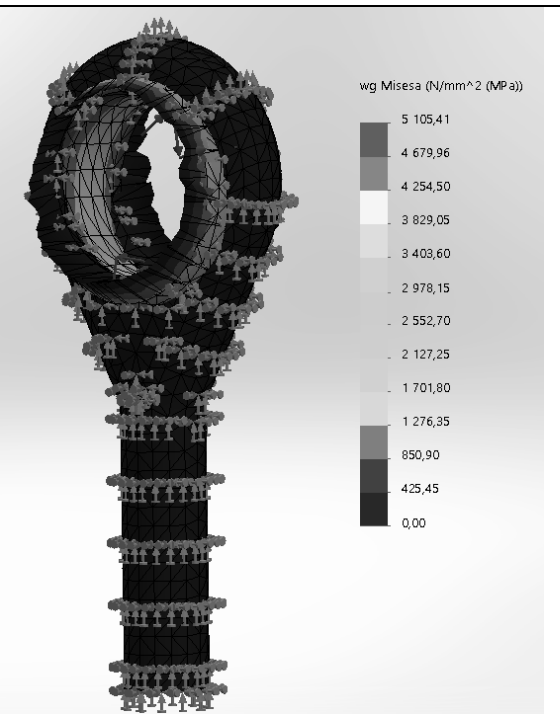

Rys. 13. Rozkład naprężeń zredukowanych dla łożyska oczkowego obciążonego siłą o wartości 10 MN (10 000 000 N) w kierunku promieniowym

Fig. 13. Distribution of Huber-Mises stresess for the bearing rod loaded with a force of 10 MN (10 000 000 N) in the radial direction

5.2 Wyniki analizy przemieszczeń

Przeprowadzona została również analiza, w której zbadana została wielkość przemieszczenia pod zadanym obciążeniem, a następnie wygenerowane zostały wykresy przemieszczeń konstrukcji, które przedstawiono na rysunkach 14-17. Zgodnie z rysunkami 14-16, największe przemieszczenie wystąpiło na powierzchni zewnętrznej pierścienia i dla każdego z tych przypadków, jego największa wartość wyniosła ok. 4,6 mm Z kolei w przypadku obciążeniu siłą o wartości 10 MN w kierunku promieniowym (rys. 17) największe przemieszczenie wyniosło ok. 0,776 mm.

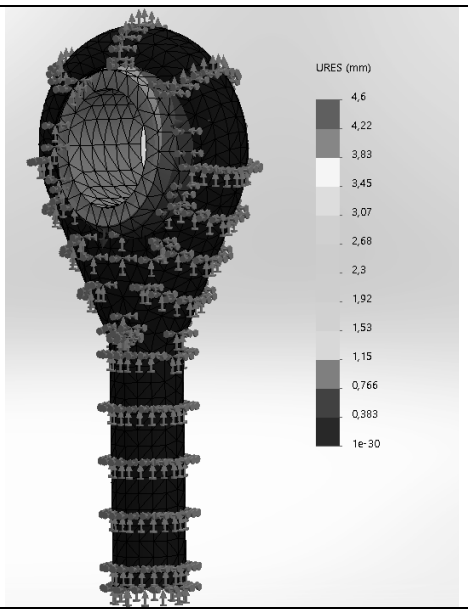

Rys. 14. Rozkład przemieszczeń dla łożyska oczkowego obciążonego siłą o wartości 10 kN (10 000 N) w kierunku promieniowym
Fig. 14. Displacement distribution for the bearing rod loaded with a force of 10 kN (10 000 N) in the radial direction

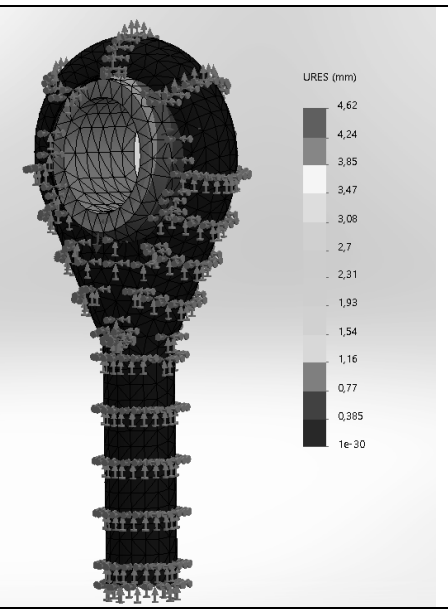

Rys. 15. Rozkład przemieszczeń dla łożyska oczkowego obciążonego siłą o wartości 100 kN (100 000 N) w kierunku promieniowym
Fig. 15. Displacement distribution for the bearing rod loaded with a force of 100 kN (100 000 N) in the radial direction

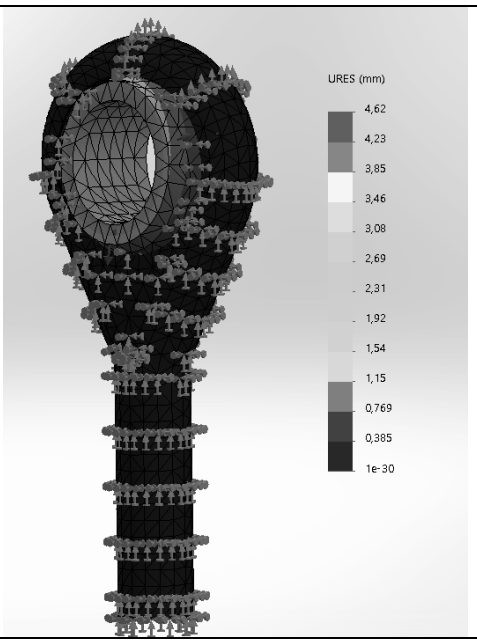

Rys. 16. Rozkład przemieszczeń dla łożyska oczkowego obciążonego siłą o wartości 1 MN (1 000 000 N) w kierunku promieniowym
Fig. 16. Displacement distribution for the bearing rod loaded with a force of 1 MN (1 000 000 N) in the radial direction

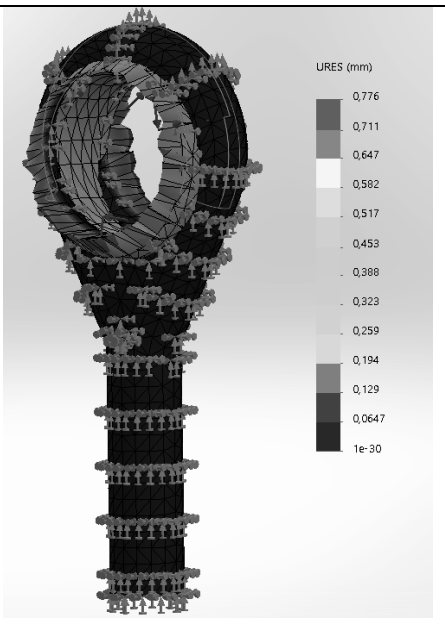

Rys. 17. Rozkład przemieszczeń dla łożyska oczkowego obciążonego siłą o wartości 10 MN (10 000 000 N) w kierunku promieniowym
Fig. 17. Displacement distribution for the bearing rod loaded with a force of 10 MN (10 000 000 N) in the radial direction

5.3 Zestawienie wyników badań

Wyniki wykonanych badań rozkładu naprężeń, przemieszczeń w zależności od zastosowanego obciążenia przedstawiono w tablicy 4.

Tab. 4. Zestawienie otrzymanych wyników w przeprowadzonych badaniach
Tab. 4. Results obtained in the conducted researches

	Wartość siły w kierunku okrężnym [N]	Wartość siły w kierunku promieniowym [N]	Maksymalne naprężenia wg Hubera-Misesa [MPa]	Maksymalne przemieszczenia [mm]
1	10 000	10 000	6,43	4,6
2	10 000	100 000	52,33	4,62
3	10 000	1 000 000	508,74	4,62
4	10 000	10 000 000	5 105,41	0,776

Najmniejsze naprężenia uzyskano dla modelu obciążonego na pierścieniu wewnętrznym siłą o wartości 10 kN w kierunku promieniowym, a największe dla modelu obciążonego siłą o wartości 10 MN. Zaobserwowano, że wraz ze wzrostem siły w kierunku promieniowym następuje wzrost wartości naprężeń zredukowanych Hubera-Misesa dla łożyska oczkowego.

Należy jednak zauważyć że wartości naprężeń dla ostatniego modelu znacznie przekraczają wartości granicy plastyczności dla materiału pierścienia, którym jest stal narzędziowa X40Cr14, o wartości R_e wynoszącej 1200 MPa. Łożysko oczkowe, obciążone w pierścieniu tak dużą siłą ulegnie więc drastycznemu zniszczeniu, co dyskwalifikuje jego zastosowanie podczas pracy, przy obciążeniach rzędu 1 MN lub większych.

6. PODSUMOWANIE

Wyniki analizy łożyska oczkowego wskazują, że spełnia ono warunki pracy przy zadanym obciążeniu w kierunku okrężnym (10 000 N) i promieniowym (do 1 MN). W wyniku obciążenia siłą o kierunku promieniowym o wartości wyższej od 1 MN (10 MN) dochodzi do przekroczenia granicy R_e pierścienia wewnętrznego, przez co ulega on zniszczeniu. Przemieszczenia w tym wypadku nie są już tak znaczne, jak przy zastosowaniu obciążeń nie powodujących przekroczenia granicy plastyczności. Nie wpływa to jednak na fakt, że stosowanie obciążeń o wartościach powyżej 1MN dla łożyska o danej geometrii jest niebezpieczne i nie powinno mieć miejsca. Rozwiązaniem powyższego problemu może być zastosowanie materiałów o wyższej granicy plastyczności bądź też zwiększenie wymiarów łożyska, co powinno bezpośrednio przełożyć się na możliwość przenoszenia większych obciążeń.

PODZIĘKOWANIE

Praca powstała w wyniku projektu PBL zrealizowanego z uczniami szkół ponadpodstawowych w ramach programu Inicjatywa Doskonałości - Uczelnia Badawcza Politechniki Śląskiej.

LITERATURA

1. http://sbart.pl/lozyska-oczkowe-budowa-i-wlasciwosci/
2. http://www.najlepszemedia.pl/lozyska-oczkowe-budowa-rodzaje-i-wlasciwosci/?fbclid=IwAR3__-IX3EQWlqT6UQAmnZKlZYDb-cn9iX9-QFLaLskRuLDqb8kRPdUOBg4
3. https://www.joom.com/pl/products/1499345451336612399-187-1-26193-1291710641
4. https://solidexpert.com/programy/solidworks/
5. https://hax-inox.pl/wpis-blog/czym-stal-narzedziowa/
6. https://multistal.pl/upload/KARTY_KATALOGOWE/Gatunek_Stali_1.2083.pdf
7. http://www.oberonrd.pl/?p=main&what=22
8. https://www.stalespecjalne.com.pl/oferta/stale-narzedziowe/1-2083.html
9. Zasoby programu SolidWorks
10. https://powerrubber.com/mieszanki-gumowe/guma-nbr/
11. https://www.ekonit.pl/oferta/silikon-guma/guma-nbr-olejoodporna.html

TalentDetector

9th January 2026
Gliwice, Poland

DEPARTMENT OF ENGINEERING MATERIALS AND BIOMATERIALS
FACULTY OF MECHANICAL ENGINEERING
SILESIAN UNIVERSITY OF TECHNOLOGY

INTERNATIONAL STUDENTS SCIENTIFIC CONFERENCE

A Validation Methodology for VIDAR: Vision-Based Depth Estimation Systems in Automotive Applications

Dariusz Myszor[a], Michał Polończyk[b]

[a] Silesian University of Technology, Faculty of Automatic Control, Electronics and Computer Science, Department of Algorithmics and Software
[b]Autonomos Systems Sp. z o. o., email: dariusz.myszor@polsl.pl

Abstract: This paper presents a validation methodology for VIDAR, a vision-based automotive depth estimation system evaluated on a moving vehicle. The methodology defines a fixed experimental protocol covering sensor configuration, driving scenarios, data acquisition, reference measurements, evaluation metrics, and performance measurement.

Keywords: vision-based depth estimation, multi-camera systems, real-world validation

1. INTRODUCTION

Reliable perception of the vehicle surroundings is a fundamental requirement for advanced driver assistance systems and autonomous driving applications [1,2]. Among the available sensing modalities, vision-based systems are widely adopted due to their favorable balance between cost, spatial resolution, and scalability when compared to active sensors such as LiDAR or radar [2–4]. In this context, depth estimation from camera data plays a key role in environment understanding and obstacle detection.

Recent advances in deep learning have significantly improved the accuracy of stereo and multi-view depth estimation methods [7–9]. However, the majority of existing works focus primarily on algorithmic performance and are validated under controlled or offline conditions. Such evaluations often assume fixed sensor configurations and ideal calibration, which do not fully reflect the constraints encountered in real-world automotive deployments.

In practical applications, vision-based systems operate under continuously changing conditions, including mechanical vibrations, temperature variations, illumination changes, and dynamic scene content. These factors can influence system behavior at multiple levels, from sensor synchronization to computational performance, and are rarely addressed in a structured and repeatable validation framework.

This paper addresses this gap by presenting a methodology for real-world validation of a vision-based depth estimation system deployed on an automotive platform (such as VIDAR

developed by Autonomous Systems). Rather than focusing on quantitative performance results, the paper describes the experimental protocol, test scenarios used to assess system behavior during operation on a moving vehicle.

The presented methodology is intended to support consistent and reproducible validation of vision-based depth estimation systems under realistic driving conditions.

2. SYSTEM UNDER TEST

The evaluated system generates dense depth maps of the vehicle surroundings using a fixed multi-camera configuration and deep neural network–based depth estimation. During all validation runs, the system operated as a fully implemented pipeline incorporating a sequence of processing steps deployed on a moving vehicle.

2.1. Sensor Configuration

The VIDAR system employs four RGB cameras equipped with global shutter sensors. The cameras are arranged into two stereo pairs with different optical parameters.

The inner stereo pair uses lenses with a narrower field of view and a shorter baseline to capture near-range and mid-range depth. The outer stereo pair uses wide-angle lenses and a longer baseline to increase lateral and far-range coverage. The two stereo pairs differ both in field of view and baseline length, forming a heterogeneous camera configuration.

All cameras are synchronized at the hardware level. Image acquisition from all cameras occurs simultaneously to avoid temporal misalignment between views. Camera parameters and synchronization settings remained fixed throughout the entire validation campaign.

2.2. Computational Setup

Image acquisition and camera synchronization are handled by an embedded computing module installed on the vehicle. The embedded module performs basic image preprocessing and transmits the acquired data to a separate computing unit responsible for depth estimation.

Depth estimation is executed on a GPU-equipped computing platform. The embedded module and the computing platform communicate via a wired Ethernet connection. Data transmission is performed continuously during vehicle operation, and each depth map is generated only after complete reception of synchronized images from all cameras.

The computational setup was not modified during validation runs. All experiments were performed using a single, predefined hardware and software configuration.

2.3. Operational Constraints

During validation, the system operated in real time on a moving vehicle without buffering or offline correction. The system processed image data sequentially as acquired, and depth maps were generated online.

3. VALIDATION METHODOLOGY

The validation methodology of the VIDAR system was designed to assess its performance as an integrated perception system operating under real-world conditions. The methodology focuses on end-to-end system behavior rather than isolated component evaluation and combines quantitative metrics with qualitative analysis to provide a comprehensive assessment of performance.

3.1. Test Environment and Scenarios

Validation experiments were conducted using a single demonstrator vehicle operated in urban traffic conditions. All test runs were performed on public roads at vehicle speeds not exceeding 40 km/h.

The following driving scenarios were executed:

- Straight road segment with no dynamic objects
- Curved road segment
- Urban building located on the right side of the road
- Urban building located on the left side of the road
- Pedestrian walking on the sidewalk on the right side of the vehicle
- Pedestrian walking along the road edge on the left side of the vehicle
- Pedestrian crossing the road from left to right
- Pedestrian crossing the road from right to left
- Pedestrian standing or walking on the road, requiring an avoidance maneuver
- Intersection with a left turn involving buildings and multiple vehicles
- Passage through a parking area
- Stationary vehicle parked on the sidewalk on the right side
- Stationary vehicle parked on the road on the right side
- Stationary vehicle parked on the road on the left side
- Vehicle moving ahead of the demonstrator vehicle
- Vehicle approaching from the opposite direction
- Vehicle crossing an intersection from the left while the demonstrator vehicle proceeds
- Vehicle crossing an intersection from the right while the demonstrator vehicle proceeds
- Vehicle crossing an intersection from the left while the demonstrator vehicle is stopped
- Vehicle crossing an intersection from the right while the demonstrator vehicle is stopped

Each scenario was executed under two illumination conditions: clear sunlight and partially cloudy conditions. For each execution, a minimum number of synchronized multi-camera frames was recorded while the vehicle was in motion.

3.2. Data Acquisition

During each validation run, synchronized image data were acquired simultaneously from all cameras in the system under test. Hardware-level synchronization ensured temporal alignment across camera streams.

For each scenario execution, at least 60 synchronized multi-camera frames were recorded while the vehicle was in motion. Image data were processed online by the system as acquired. No offline correction, frame selection, or manual filtering was applied during data acquisition. The obtained data was also recorded, which allowed for further analysis in offline mode if such a necessity occurred.

3.3. Reference Measurements

To enable quantitative depth evaluation, a LiDAR sensor was integrated into the experimental setup for selected validation runs. The LiDAR provided sparse reference depth measurements, it was used exclusively for evaluation purposes.

The LiDAR sensor was rigidly mounted on the vehicle roof and geometrically calibrated with respect to the camera coordinate system. Reference data were collected only during predefined runs and were not available to the vision-based system during operation.

Only LiDAR points within the common field of view and the operational depth range of the camera system were considered during evaluation.

3.4. Evaluation Metrics

Depth estimation accuracy was evaluated using the Mean Depth Relative Error (MDRE), defined as:

$$depth\ metric\ =\ \frac{|depthGT\ -\ depthEST|}{depthGT}\cdot 100\%,$$

where *depthGT* denotes the reference depth measured by the LiDAR sensor, and *depthEST* denotes the corresponding depth estimated by the system.

The relative error metric was selected to normalize error with respect to distance and to avoid bias toward near-range measurements inherent in absolute error metrics. Metric computation was performed only for valid reference points.

4. DATA ANALYSIS AND VALIDATION PROCEDURE

4.1. Temporal and Spatial Alignment

All recorded camera streams were temporally aligned using hardware-generated timestamps associated with synchronized image acquisition. Only frames with valid timestamps from all cameras were considered for further processing.

LiDAR reference measurements were temporally aligned with camera frames using timestamp matching. Spatial alignment between LiDAR points and the camera coordinate system was performed using a fixed extrinsic calibration determined before the validation. Calibration parameters remained unchanged throughout the validation process.

Only LiDAR points projecting into the common field of view of the camera system were retained for evaluation.

4.2. Data Filtering and Valid Sample Selection

A frame was considered valid for evaluation only if the following conditions were met:

- Valid image data were available from all cameras in the system.
- Temporal alignment between camera frames was within the synchronization tolerance defined by the acquisition hardware.
- Corresponding LiDAR reference points were available after projection into the camera coordinate system.

Frames affected by incomplete data transmission, synchronization errors, or missing reference measurements were excluded from further analysis. No manual frame selection or qualitative filtering was applied.

4.3. Metric Computation

For each valid frame, depth estimates produced by the system were compared with corresponding LiDAR reference measurements on a per-point basis.

The Mean Depth Relative Error (MDRE) was computed according to the definition provided in Section 3.4. Metric computation was restricted to reference points within the operational depth range of the system.

Metric values were computed independently for each frame and aggregated at the scenario level. No temporal smoothing, outlier rejection beyond the defined validity criteria, or post hoc adjustment of metric values was applied.

4.4. Performance Measurement Procedure

Real-time performance was evaluated using system runtime logs collected during validation runs. For each run, the number of fully processed multi-camera frames was recorded together with corresponding timestamps.

Throughput was computed as the number of successfully processed frames per second over continuous time intervals. Performance measurements included image acquisition, data transfer, depth estimation, and depth map generation.

Performance evaluation was conducted using a fixed hardware and software configuration. No performance tuning or parameter adjustment was performed during measurement runs.

5. SUMMARY

This paper presented a structured methodology for real-world validation of a vision-based automotive depth estimation system, prepared for the VIDAR prototype system deployed on a demonstrator vehicle. The proposed approach focuses on end-to-end system evaluation and

addresses practical deployment constraints that are often omitted in algorithm-centered studies. The validation methodology defines a repeatable experimental protocol covering test environment design, driving scenarios, reference data acquisition, and evaluation metrics.

While the methodology is demonstrated using the VIDAR system, it is not limited to a specific implementation and can be adapted to other vision-based depth estimation systems and hardware platforms. The proposed framework provides a foundation for subsequent quantitative analysis, comparative evaluation, and extended performance studies, which are outside the scope of this work.

6. ACKNOWLEDGEMENTS

The publication/paper was based on the results of the project no. POIR.01.01.01-00-0123/20 co-financed by the European Union under the European Regional Development Fund - Smart Growth program 2014-2020.

BIBLIOGRAPHY

1. Zhang, Yuxiao, et al. "Perception and sensing for autonomous vehicles under adverse weather conditions: A survey." *ISPRS Journal of Photogrammetry and Remote Sensing* 196 (2023): 146-177.
2. Van Brummelen, Jessica, et al. "Autonomous vehicle perception: The technology of today and tomorrow." *Transportation research part C: emerging technologies* 89 (2018): 384-406.
3. Soltanirad, Mohammad, and Mahdi Baghersad. "Perception Technologies for Autonomous Transportation: A Comparative Analysis of LiDAR, Radar, Camera, and Sonar." (2025).
4. Stähler, Julian, et al. "High-Performance Perception: A camera-based approach for smart autonomous electric vehicles in smart cities." *IEEE Electrification Magazine* 11.2 (2023): 44-51.
5. Liu, Donglin. "Comparative Study of Lidar and Vision-based in Autonomous Driving." *International Core Journal of Engineering* 11.8 (2025): 55-62.
6. Liu, Liu, et al. "Robust and efficient relative pose with a multi-camera system for autonomous driving in highly dynamic environments." *IEEE Transactions on Intelligent Transportation Systems* 19.8 (2017): 2432-2444.
7. Wang, Cheng, et al. "The application of deep learning in stereo matching and disparity estimation: A bibliometric review." *Expert systems with applications* 238 (2024): 122006.
8. Huang, Hongbo, et al. "Multi-view stereo algorithms based on deep learning: a survey." *Multimedia Tools and Applications* 84.6 (2025): 2877-2908.
9. Laga, Hamid, et al. "A survey on deep learning techniques for stereo-based depth estimation." *IEEE transactions on pattern analysis and machine intelligence* 44.4 (2020): 1738-1764.

TalentDetector

9th January 2026
Gliwice, Poland

DEPARTMENT OF ENGINEERING MATERIALS AND BIOMATERIALS
FACULTY OF MECHANICAL ENGINEERING
SILESIAN UNIVERSITY OF TECHNOLOGY

INTERNATIONAL STUDENTS SCIENTIFIC CONFERENCE

Microwave Discrimination and Property Extraction in Metallic and Graphitic Nanofluids

Narek Nazaryan, Nelli Babajanyan, Artyom Movsisyan, Billi Minasyan, Arsen Babajanyan

Yerevan State University, Institute of Physics, Yerevan 0025, Armenia
E-mail: barsen@ysu.am

Abstract: This work examines the microwave response of liquid suspensions containing metallic and carbon-based nanoparticles, with the objective of material discrimination and intrinsic property assessment using multimodal RF diagnostics. Silver and graphite nanoparticle suspensions with varying concentrations, morphologies, and binder content were investigated using a combination of broadband microwave measurements, resonant sensing, and temperature-dependent analysis. The results show that the effective dielectric behavior of the suspensions is governed by the interplay between free-carrier conduction and bound-charge polarization, leading to clearly distinguishable responses for metallic, graphitic, and binder-rich systems.

Resonant measurements reveal systematic shifts in resonance frequency, linewidth, and attenuation as a function of nanoparticle loading and structural heterogeneity, enabling sensitive differentiation between conductive and dielectric-dominated formulations. Temperature-dependent experiments further indicate enhanced thermo-dielectric sensitivity in graphite-based suspensions, particularly those containing clay binders, whereas silver nanofluids exhibit a more uniform, conduction-driven response. Supporting theoretical analysis based on effective medium and dispersive transport models links the observed microwave signatures to intrinsic material properties. These findings demonstrate the potential of multimodal microwave techniques for non-invasive nanofluid characterization and adaptive RF sensing applications.

Keywords: Laser ablation, microwave sensing, TEOIM, Drude-Lorentz model, nanofluids

1. INTRODUCTION

Nanoparticle-based colloidal systems are gaining traction in next-generation electronics, biosensing, and electromagnetic interference (EMI) shielding [1]. However, a significant gap remains in understanding their behavior at microwave frequencies (GHz), particularly how the particle-fluid interface governs the dielectric response.

Classical theories, such as the Maxwell-Garnett effective medium theory, often fail to predict the anomalously high dielectric response observed in dilute nanofluids.

This work addresses this discrepancy by demonstrating that mesoscopic ordering, the formation of structured water (hydration shells) around nanoparticles, plays a critical role. To validate this, a multimodal approach combining advanced synthesis, resonant sensing, near-field imaging, and mathematical modelling was employed.

2. METHODOLOGY

The experimental and analytical framework of this study was designed to bridge the gap between microscopic particle morphology and macroscopic electromagnetic behavior. A synergistic, multimodal approach was adopted to overcome the limitations of single-technique characterization. The methodology proceeds in three distinct phases: (1) the fabrication of high-purity, surfactant-free colloidal systems via physical synthesis to eliminate chemical artifacts; (2) dual-regime microwave characterization combining high-sensitivity resonant perturbation (for detection limits) with broadband spectral retrieval (for dispersion analysis); and (3) spatially resolved near-field visualization to detect local inhomogeneities. Crucially, the experimental data were not analyzed in isolation but were rigorously coupled with inverse mathematical modeling. This integration allows for the de-embedding of constitutive parameters, specifically complex permittivity and conductivity, thereby enabling a quantitative differentiation between metallic conduction and dielectric polarization mechanisms within the nanofluids.

2.1. Synthesis via Laser Ablation in Liquid

Unlike chemical reduction methods that leave ionic residues and surfactants, Laser Ablation in Liquid (LAL) was employed as a "green" and pristine synthesis route [2]. By focusing a Q-switched Nd:YAG laser (1064 nm) onto solid Ag or Graphite targets submerged in deionized water, plasma plumes were generated that condensed into nanoparticles. This resulted in surfactant-free colloids, ensuring that the measured dielectric response was purely due to the nanoparticle-water interaction and not chemical contaminants.

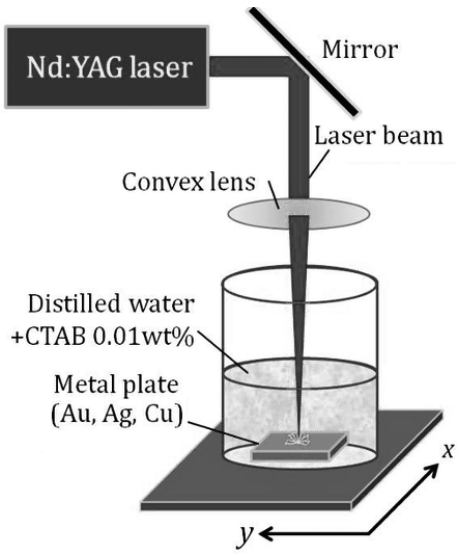

Figure 1. Schematic of the experimental setup used for laser ablation of Ag and graphite targets in DI water.

2.2. Measurement Setup (HSSR and TEOIM)

The electromagnetic response was measured using a Hilbert-shaped stripline resonator (HSSR) operating in the 2–5 GHz band [3-5]. This fractal geometry allows for high-density electric field confinement, making it sensitive to minute changes in permittivity. Simultaneously, Thermo-Elastic Optical Indicator Microscopy (TEOIM) was used to map the near-field distribution. An optical indicator film (ITO) placed over the sample converted microwave absorption into thermal expansion, which was captured optically to visualize field inhomogeneities caused by particle aggregation.

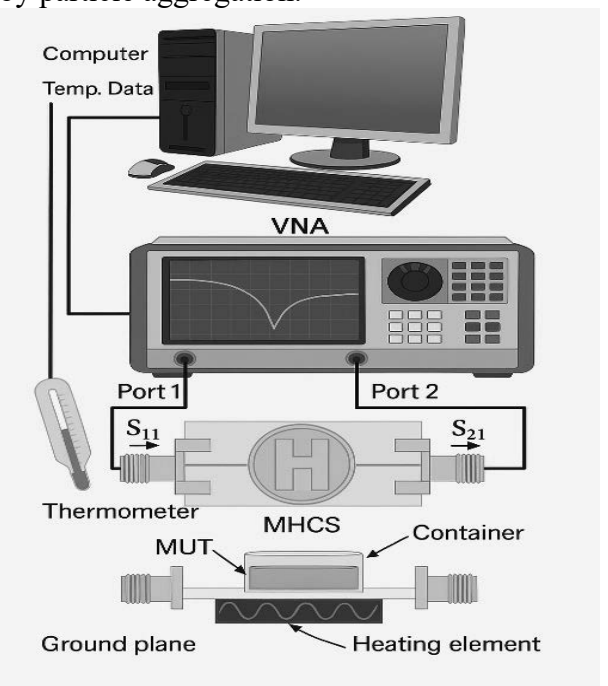

Figure 2. Experimental setup for microwave characterization using the HSSR connected to a VNA.

2.3. Theoretical Modeling

To interpret the experimental S-parameters retrieved via the Nicholson-Ross-Weir (NRW) method, a rigorous theoretical analysis was performed. We moved beyond simple effective medium theories by applying the Drude-Lorentz Model [6]. This approach separates the contribution of free carriers (conductivity) from bound charges (dielectric polarization):

$$\varepsilon_p^*(\omega) = \varepsilon_\infty - \frac{\omega_p^2}{\omega^2 + i\omega\Gamma_D} + \sum_j \frac{S_j\omega_j^2}{\omega_j^2 - \omega^2 - i\omega\gamma_j},$$

where ω_p is the plasma frequency and Γ_D is the scattering rate. To quantify these parameters, a custom inverse solver was developed in the Python programming environment. Utilizing the Levenberg-Marquardt non-linear least squares optimization algorithm (implemented via the SciPy library), the solver iteratively minimized the error between the theoretical model and the experimental datasets. This computational approach allowed for the precise extraction of fundamental physical parameters while accounting for the natural dispersion of the water background in the X-band.

3.1. Dielectric and Conductivity Analysis

The theoretical modelling quantitatively validated the experimental observations. For Silver (Ag) nanofluids, the extracted DC conductivity was found to be $\sigma_{DC} \approx 6.53$S/m, consistent with metallic conduction. In contrast, the 8H Graphite sample yielded negligible conductivity (~ 0.10 S/m), confirming that its electromagnetic response is governed by bound-charge polarization associated with its high clay binder content, rather than free electron flow. The 8B Graphite sample showed moderate conductivity (~ 3.05 S/m), reflecting its graphitic nature.

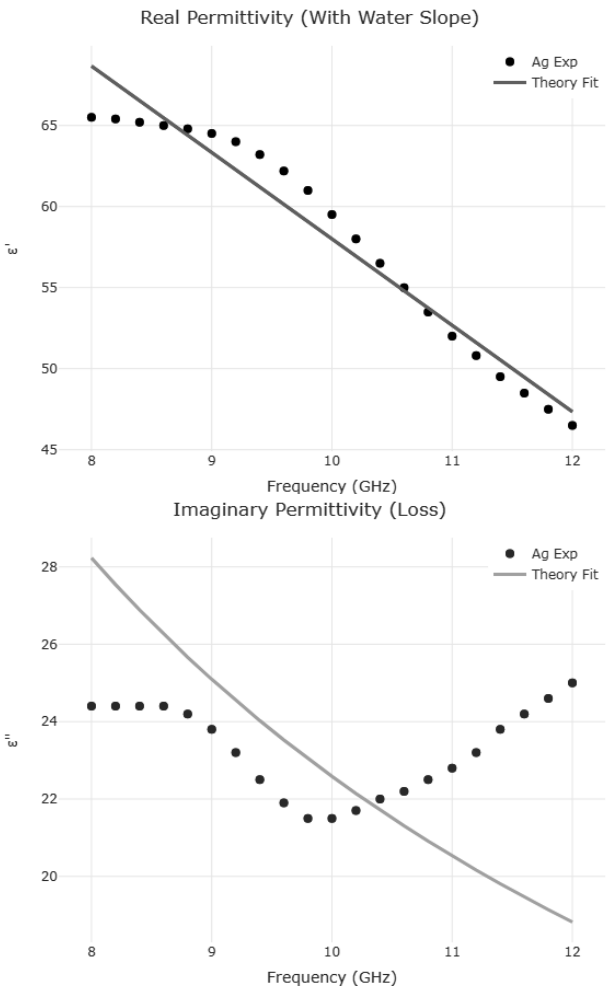

Figure 3. Comparison of experimental dielectric data (dots) with the theoretical Drude-Lorentz model fit (solid lines) for Ag.

4. CONCLUSION

This study represents a significant first step toward establishing a unified framework for the liquid-phase dielectric diagnostics of nanofluids. By integrating Laser Ablation in Liquid (LAL) for high-purity synthesis with multimodal microwave characterization (HSSR and TEOIM), we have demonstrated the feasibility of decoupling intrinsic particle properties from mesoscopic solvent structuring.

The initial application of the Drude-Lorentz mathematical model has provided promising quantitative insights, allowing for a preliminary differentiation of energy loss mechanisms. Current results indicate that Silver (Ag) nanofluids behave as conductivity-driven systems ($\sigma_{DC} \approx 6.53$ S/m), whereas Graphite 8H suspensions appear governed by dielectric polarization ($\sigma_{DC} \approx 0.1$ S/m) due to binder interactions. Furthermore, temperature-dependent measurements suggest distinct thermal response pathways, pointing toward hydration shell disruption in metallic suspensions. These findings serve as a baseline for ongoing research; future work will focus on refining the core-shell model to account for complex aggregation dynamics and optimizing sensor sensitivity for the development of next-generation tunable RF devices.

BIBLIOGRAPHY

1. A. M. Nicolson, G. F. Ross, "Measurement of the intrinsic properties of materials by time-domain techniques,"*IEEE Transactions on Instrumentation and Measurement*, vol. 19, no. 4, pp. 377–382, 1970.
2. S. Barcikowski, G. Compagnini, "Advanced nanoparticle generation and excitation by lasers in liquids,"*Physical Chemistry Chemical Physics*, vol. 15, pp. 3022–3026, 2013.
3. H. Lee, S. Arakelyan, B. Friedman, K. Lee, "Temperature and microwave near-field imaging by thermo-elastic optical indicator microscopy", *Scientific Reports*, vol. 6, p. 39696, 2016.
4. L. Odabashyan, N. Margaryan, G. Ohanyan, "Detection of iron nanoparticles in aqueous solutions by microwave sensor", *Journal of Contemporary Physics*, vol. 55, pp. 171–175, 2020.
5. T. Abrahamyan, et al., "Investigation of Ag nanoparticles/water solutions by microwave stripline sensor,"*Journal of Contemporary Physics*, vol. 54, pp. 196–202, 2019.
6. M. Noroozi, S. Motevasel, A. Bahrami, F. Rashidi, N. Yaghoubi, Fabrication, characterization, and thermal property of silver nanofluids, Nanoscale Research Letters, 9, 2014.

TalentDetector
9th January 2026
Gliwice, Poland
DEPARTMENT OF ENGINEERING MATERIALS AND BIOMATERIALS
FACULTY OF MECHANICAL ENGINEERING
SILESIAN UNIVERSITY OF TECHNOLOGY
INTERNATIONAL STUDENTS SCIENTIFIC CONFERENCE

Surface Evolution Characterization of a Duplex Treatment on AISI H13 Steel for Hot Forging Dies

João Vitor Piovesan Dalla Nora[a*], Felipe Canal[a], Morvan Silva Franco[a], Frederico Murilo Wlassak[a], Rafael Silva[b], Steffen Aichholz[b], Alexandre da Silva Rocha[a]

[a] Universidade Federal do Rio Grande do Sul (UFRGS), Laboratório de Transformação Mecânica
[b] Oerlikon Balzers Brazil, *email: piovesan.nora@ufrgs.br

Abstract: The short lifespan of hot forging dies, representing a major production cost, drives the need for advanced surface engineering solutions. This study characterizes the evolution of surface properties in AISI H13 tool steel throughout a commercial duplex treatment process. Topography and morphology were investigated through different treatment stages using scanning electron microscopy (SEM), optical profilometry for 3D, contact angle, roughness (R_a, R_z), and adhesion (VDI 3198). Results indicate that the treatment sequence progressively modifies the surface state: leading to higher roughness (S_a, R_a, R_z) and a final hydrophobic surface (contact angle >90°). Additionally, the coating exhibited excellent adhesion, achieving an HF1 classification per VDI 3198 in both the as coated and final micro-blasted conditions. This work provides a foundational characterization of surface evolution in an industrially relevant duplex treatment.

Keywords: AISI H13, duplex treatment, PVD

1. INTRODUCTION

The need for new manufacturing routes for tools used in hot forging is based on increasing durability, as the lifespan of these tools represents between 8-15% of production costs, potentially increasing to more than 50% when considering the time for replacing worn tools and unexpected operational failures [1]. Depending on the processes and parameters employed during the tool manufacturing route, Surface Integrity (SI) can be affected, thereby compromising the effectiveness of subsequent surface treatments [2], ultimately resulting in impacts on functionality during service, lifespan, and performance [3].

The national forging industry constantly seeks to increase productivity and reduce costs, where the lifespan of dies is a critical factor. However, many companies still develop component designs focused on manufacturability - design for manufacturing [4]. In the context of forging dies, this means that surface treatment is added, not integrated into the manufacturing process, as it is still very commonly considered a separate stage in die production. Nevertheless, it is well known that the surface of mechanical components modifies

their performance, as manufacturing processes affect their surface properties since they produce heterogeneities/deformation gradients, phase transformation, volume changes, texture changes, and residual stresses [3]. Topography is one of the most notable and promising research fronts regarding the use of tribological concepts and can be directly affected by the material and manufacturing processes [5]. Along with nitriding, coatings can be used to increase the durability of forging tools, such as PVD (Physical Vapor Deposition) or CVD (Chemical Vapor Deposition). The duplex surface treatment process (combination of nitriding followed by coating) is widely applied in hot work, providing an increased lifespan for dies used in metal forming [6].

However, the application of these coatings on forging dies still faces a series of poorly controlled and unknown factors, due to the instabilities and variations inherent to the process [1]. Furthermore, combinations of other treatments are explored to achieve better performance, such as mechanical surface processes, thermochemical processes, and deposition [7]. Concurrently, it is known that the adhesion of coatings to a substrate is strongly influenced by its surface conditions, such as roughness, microstructure, hardness, and residual stresses [8], which are modified during forging die manufacturing processes. However, given the variation in parameters and divergent results in the literature, there is still a need for new investigations on the topic [9].

Based on this context, this research is part of the project PD&I Call 01/2023 - Forging Die Projects, Line IV (More Competitive Brazilian Tooling Industry) entitled Integrated Design and Manufacturing of Forging Dies with Surface Engineering. The goal is to create a possible solution integrated into the manufacturing of hot forging dies, focused on surface treatments, that aids in lubricant anchoring, mitigating premature failure due to wear, and consequently, significantly increasing tool lifespan in relevant environments. In this study we will show some initial results of the duplex treatment stages characterization. The evolution of surface modifications during duplex treatment comprises the characterization of morphology (surface and cross-section), topography (roughness, profilometer, and contact angle) and coating adhesion.

2. METHODOLOGY

Workpieces of 38 mm in diameter and 10 mm in height of AISI H13 hot-work tool steel (0.38 wt% C, 1.11 wt% Si, 0.35 wt% Mn, 4.85 wt% Cr, 1.31 wt% Mo, 1.19 wt% V, and Fe as balance) were quenched and triple-tempered with highest temperature of 600 °C (43 ± 1 HRC), ground (with 100 to 1200 grit sandpaper), and polished using 3 μm and 1 μm diamond paste. These prepared samples served as the control condition. Subsequently, samples were characterized at each stage of the duplex treatment (performed by Oerlikon Balzers) to understand the evolution of surface modifications throughout the process.

Polished samples underwent a sequence of surface treatments comprising the following steps:

1. Cleaning: Immersion cleaning with chemical degreasing and anti-oxidant agents, followed by drying.
2. Low-Pressure Nitriding (LPN): Furnace loading for a gas nitriding process under low pressure (100–300 mbar) using a nitriding atmosphere of NH_3 and N_2. The process was conducted at 450 ± 30 °C for 10 hours.

3. Intermediate Micro-blasting: Manual micro-blasting using a SANDMASTER S-DT100 system with aluminum oxide (Al_2O_3) spherical media.
4. Plasma-Assisted Deposition: Samples were loaded into an OERLIKON BAI1200 furnace. After vacuum generation and heating to 450 ± 30 °C, plasma nitrided and then the coating was deposited via a plasma-assisted PVD process using Cr, Al, and Ti targets. The deposition time was 190 minutes.
5. Final Micro-blasting: A concluding micro-blasting step was performed using the same equipment and media, but at a reduced pressure compared to the intermediate micro-blasting.

Specific process parameters for proprietary treatment stages have been omitted at the request of the industrial partner.

2.1. Morphology

Surface and cross-section morphology were observed via Scanning Electron Microscopy (Zeiss model EVO MA10). For cross-section analyses, samples were cut in a precision cutting machine TechCut 4^{TM}, embedded in Bakelite (Fig. 1), ground, and polished using 3 μm and 1 μm diamond paste, respectively. Subsequently, they were etched using Nital (2%) for 5 seconds. For measurement of the coating thickness, samples were examined using an OLYMPUS GX-51 optical microscope, with images captured using the AnalySIS software. Coating thickness measurements were performed using ImageJ® software. For each evaluated condition, three images at 1000x magnification were analyzed. Twelve vertical measurements were taken per image, with the highest and lowest values subsequently discarded. Consequently, the average coating thickness and corresponding standard deviation were calculated from a total of 30 data points.

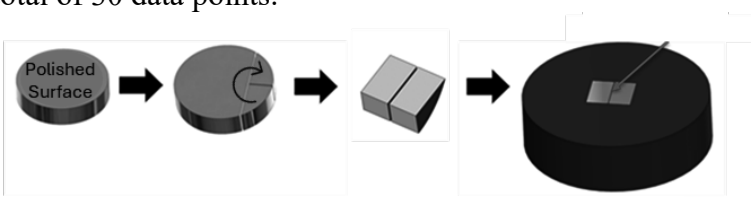

Figure 1. Preparation of cross-sectional samples: mounting in Bakelite.

2.2. Profilometry

Surface topography analysis was performed using a Bruker (GTK M, CONTOURGT-K) 3D Optical Profilometer. For each sample, two regions at the mid-radius were analyzed, collecting data for S_a (the areal extensions of the Ra parameter). Each reported measurement represents the average of three scans over the analyzed area using a 20x objective lens.

2.3. Roughness

Five roughness measurements were performed for each analyzed condition, according to the scheme in Fig. 2, using a Mitutoyo SJ-210 profilometer with a stylus speed of 0.25 mm/s, a cut-off of 0.8 mm, and a measurement length of 4 mm, following with the ISO 4287:1997 standard. The R_a and R_z values were recorded.

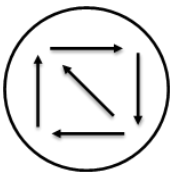

Figure 2. Different orientation used for roughness measurements.

2.4. Contact Angle

The contact angle measurement was used to characterize the surfaces in terms of their wettability. Three measurements per sample were conducted using a Kruss (DSA 100S/2014) goniometer and ADVANCE software. A 10 μL droplet of distilled water was deposited in the mid-radius region of the samples for each measurement.

2.5. Coating Adhesion

Three indentations were performed according to the Rockwell C method (using a 150 kgf load and a diamond cone indenter) in the central region of the treated samples, spaced 5 mm apart. This procedure is based on the VDI 3198 standard, which is used to evaluate coating adhesion based on the formation of cracks caused by the deformation induced by the cone indenter [10]. The test is executed as a standard Rockwell C hardness measurement and depending on the distribution of surface cracks and the presence or absence of delamination, the coating adhesion can be assessed using the reference patterns shown in Fig. 3 [11] from hf1 (high adhesion) to HF6 (poor adhesion).

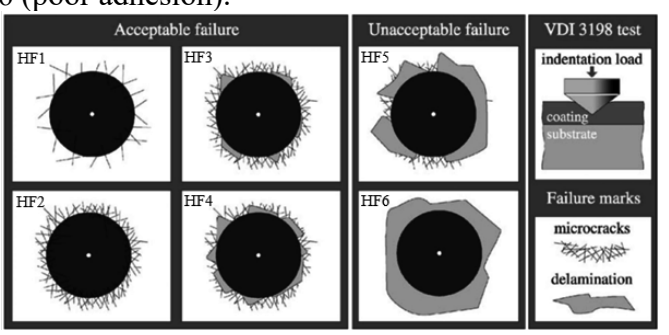

Figure 3. Reference patterns for coating adhesion according to VDI 3198 indentation test. Adapted from [11].

3. RESULTS

The analysis revealed the presence of scratches and surface defects on the polished samples, nitride projections after nitriding, and surface deformation following the intermediate micro-blasting, as shown in Fig. 4 (A), (B), and (C), respectively. Following the application of the PVD coating, defects such as craters micro-voids and droplets were identified (Fig. 4 D), with the latter having been eliminated after the final micro-blasting step (Fig. 4 E). The intermediate micro-blasting can induce changes in morphology as seen in Fig. 4 C, produce a state of compressive residual stress, and increase surface hardness and adhesion to, for example, facilitate subsequent coating [12,13].

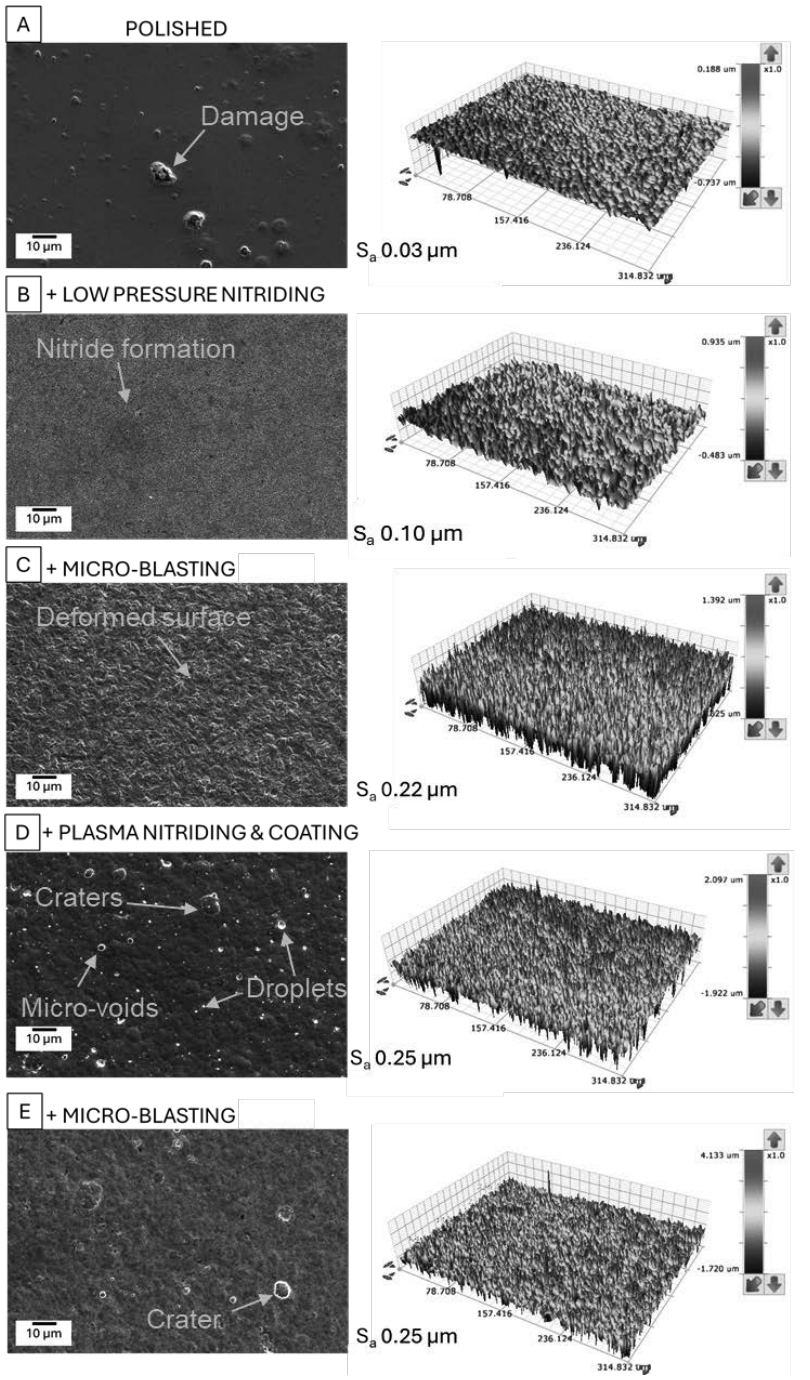

Figure 4. Surface morphology (SEM) and profilometry of AISI H13 steel samples at different duplex treatment stages: (A) polished, (B) low pressure nitriding, (C) intermediate micro-blasting, (D) PVD coating, and (E) final micro-blasting.

Fig. 5 shows the cross section of treated samples. SEM analysis revealed the presence of nitrides in a diffusion zone (Fig. 5 A and B) and a color difference in the coating between the inner basal layer, composed of CrN, and the outer region of CrAlTiN (Fig. 5 C). According to the industrial partner, the coating thickness varies between 6–10 µm, which may explain the difference between Fig. 5 (C) and (D), as the final micro-blasting step does not increase the coating thickness. The coating thickness was measured yielding values of 7.08 ± 0.21 µm for

the solely coated sample and 9.69 ± 0.05 µm for the sample after the complete surface treatment cycle. This indicates some variation in layer thickness, although both measurements fall within the specified range.

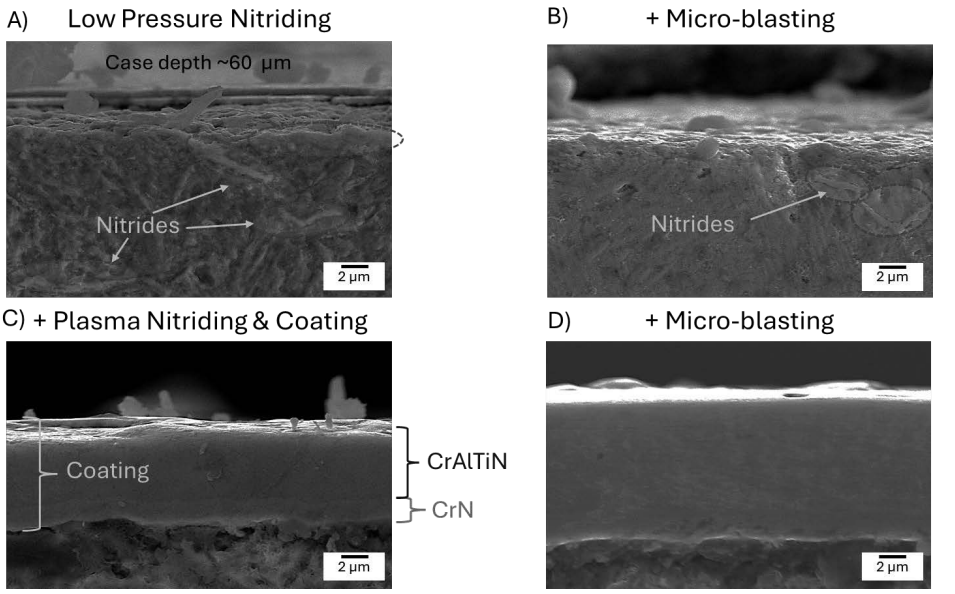

Figure 5. Cross section of AISI H13 steel samples at different duplex treatment stages: (A) low pressure nitriding, (B) intermediate micro-blasting, (C) coating, and (D) final micro-blasting. Some difference in coating thickness could be observed, although not correlated with the final micro-blasting process.

Roughness and contact angle were also evaluated throughout the surface treatment sequence (Fig. 6). The R_a (Fig. 6 A) parameter followed a trend of increasing until the application of the PVD coating, followed by an average decrease after the final micro-blasting. However, these last two processes do not show a significant difference when considering the standard deviation, remaining within the same order of magnitude as observed for Sa. R_z (Fig. 6 B) exhibited a trend similar to R_a, including for the final two treatment stages. The contact angle (Fig. 6 C) results indicate an increase up to the coating (PVD) stage, followed by a decrease after the final micro-blasting step, close to the roughness behavior. The surface is considered hydrophobic with low wettability when the contact angle exceeds 90°.

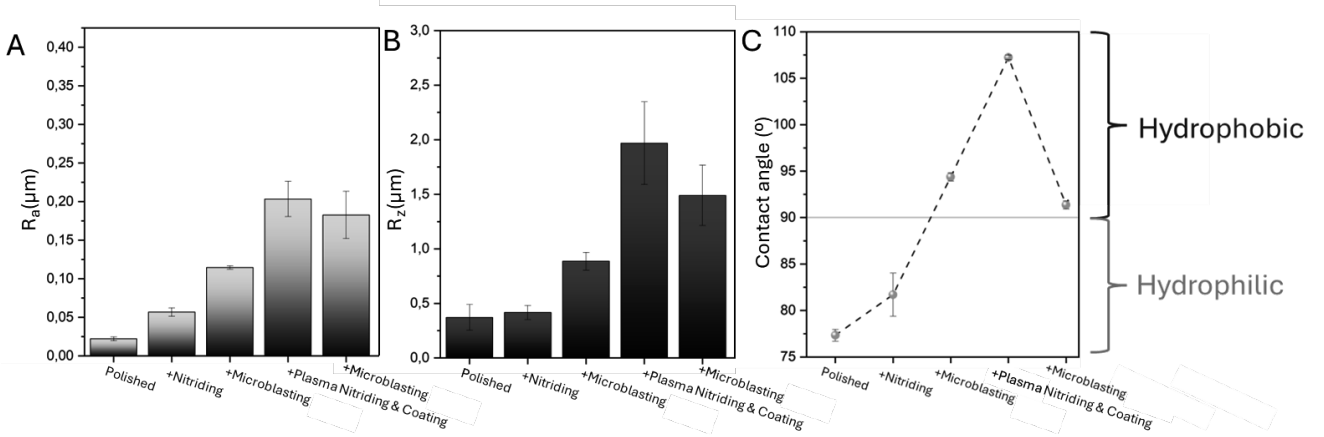

Figure 6. R_a (A) and R_z (B) roughness and contact angle (C) results for different duplex treatment stages.

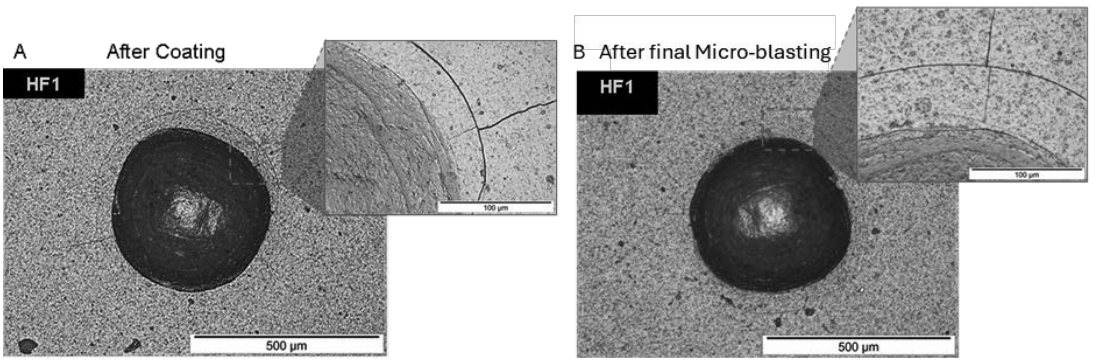

Figure 7. Adhesion tests for samples after PVD coating (A) and after final micro-blasting (B). HF1 adhesion class was found for both conditions.

Coating adhesion was assessed via a Rockwell C hardness test, comparing the resulting coating crack pattern with the reference standards from the VDI 3198 norm (Fig 7). The test was performed for both after coated (PVD) condition and the after final micro-blasting condition. The results indicated high coating adhesion for both conditions, with no significant differences observed. In the study of Jacob et al., [14] micro-blasting applied before coating can increase coating adhesion and when applied after coating it could increase surface hardness (~30 GPa). Applying the coating without micro-blasting at any stage resulted in a rougher surface due to the presence of droplets and pores. When micro-blasting was applied to the substrate prior to coating, fewer pores and small dimples were observed in the coating, likely originating from substrate deformation. Applying micro-blasting after coating also reduced porosity. The improvement in adhesion was attributed to the increased substrate roughness, which enhanced the mechanical interlocking of the coating, similar to the results found in this research.

4 CONCLUSIONS

- Surface roughness increased through duplex treatments stages;
- Contact angle values indicate hydrophobic behavior for the final surface;
- The final micro-blasting step provided a controlled finishing effect, slightly reducing roughness and contact angle without harming the coating.
- Critically, the coating exhibited excellent adhesion, achieving the highest classification (HF1) in the VDI 3198 test for both the as coated and final micro-blasted conditions, validating the compatibility of the micro-blasting parameters with coating integrity.

5. ACKNOWLEDGMENTS

This work was carried out with the support of National Council for Scientific and Technological Development (CNPq) in Brazil, through the Universal call process number 316374/2024-0, Auxílio à Pesquisa (APQ) process number 407742/2023-9. João Vitor Piovesan Dalla Nora acknowledges CNPq (Process no. 140743/2024-3), Alexandre da Silva Rocha acknowledges CNPq/MCTI N◦ 10/2023 (Grant 308773/2018-7). Morvan Silva Franco acknowledges CAPES (Process no. 88887.842729/2023-00), Felipe Canal acknowledges

CAPES (Process no. 88887.988547/2024-00). We also thank Oerlikon Balzers for their support in the research and for performing the surface treatments.

BIBLIOGRAPHY

1. GRONOSTAJSKI, Z. et al. A review of the degradation mechanisms of the hot forging tools. Archives of Civil and Mechanical Engineering, v. 14, n. 4, p. 528–539, 2014.
2. LA MONACA, Andrea et al. Surface integrity in metal machining - Part II: Functional performance. International Journal of Machine Tools and Manufacture, v. 164, n. December 2020, p. 103718, 2021.
3. LIAO, Zhirong et al. Surface integrity in metal machining - Part I: Fundamentals of surface characteristics and formation mechanisms. International Journal of Machine Tools and Manufacture, v. 162, n. December 2020, 2021.
4. ZHU, X. P. et al. Design for Manufacturing of Cemented Carbide Coated Components Toward High Wear and Impact Resistance Performance. Journal of Manufacturing Science and Engineering, v. 145, n. 5, p. 1–12, 2023.
5. MACHADO, Alisson R. et al. State of the art of tool texturing in machining. Journal of Materials Processing Technology, v. 293, n. January, 2021.
6. EMAMVERDIAN, Ali Akbar et al. Current failure mechanisms and treatment methods of hot forging tools (dies) - a review. Engineering Failure Analysis, v. 129, n. July, p. 105678, 2021.
7. BOBZIN, Kirsten et al. Low-Temperature Physical Vapor Deposition TiAlCrSiN Coated High-Speed Steel: Comparison Between Shot-Peened and Polished Substrate Condition. Advanced Engineering Materials, v. 24, n. 9, 2022.
8. TILLMANN, Wolfgang; GRISALES, Diego; STANGIER, Dominic. Effects of AISI H11 surface integrity on the residual stresses and adhesion of TiAlN/substrate compounds. Surface and Coatings Technology, v. 357, n. June 2018, p. 466–472, 2019.
9. KOVAČEVIĆ, Lazar et al. Industrial evaluation of duplex PVD hard coatings for HPDC. Journal of the Brazilian Society of Mechanical Sciences and Engineering, v. 40, n. 5, 2018.
10. VIDAKIS, N.; ANTONIADIS, A.; BILALIS, N. The VDI 3198 indentation test evaluation of a reliable qualitative control for layered compounds. Journal of Materials Processing Technology, v. 143–144, n. 1, p. 481–485, 2003.
11. KRELLING, A. P. et al. Micro-abrasive wear mechanisms of borided AISI 1020 steel. Tribology International, v. 111, n. November 2016, p. 234–242, 2017.
12. WANG, Junlong et al. Optimization of Micro-Sandblasting Parameters for Enhanced Adhesion and Wear Resistance of AlTiSiN-Coated Tools. Coatings, v. 15, n. 7, 2025.
13. YU, Zhou et al. Influence of micro sandblasting on the surface integrity of the AlTiN-coated tools. International Journal of Advanced Manufacturing Technology, v. 120, n. 1–2, p. 1359–1372, 2022.
14. JACOB, A. et al. Influences of micro-blasting as surface treatment technique on properties and performance of AlTiN coated tools. Journal of Manufacturing Processes, v. 29, p. 407–418, 2017.

TalentDetector
9th January 2026
Gliwice, Poland
DEPARTMENT OF ENGINEERING MATERIALS AND BIOMATERIALS
FACULTY OF MECHANICAL ENGINEERING
SILESIAN UNIVERSITY OF TECHNOLOGY
INTERNATIONAL STUDENTS SCIENTIFIC CONFERENCE

Structure and properties of CoCrFeNi and CoCrFeMo medium-entropy alloys obtained by induction melting and electrodeposition

Agata Ociepka[a], Jakub Wieczorek[a], Miłosz Ferdyn[a], Michał Podgórski[a], Maxymilian Żukowski[a], Krzysztof Matus[b], Jakub Bicz[c], Katarzyna Młynarek-Żak[d], Monika Spilka[c], Rafał Babilas[c]

[a] Student of Silesian University of Technology, Faculty of Mechanical Engineering
[b] Silesian University of Technology, Materials Research Laboratory
[c] Silesian University of Technology, Department of Engineering Materials and Biomaterials
[d] Silesian University of Technology, Department of Engineering Processes Automation and Integrated Manufacturing Systems
email: rafal.babilas@polsl.pl

Abstract: This study presents the results of investigations on the CoCrFeNi and CoCrFeMo medium-entropy alloys (MEAs) obtained using two different manufacturing methods – induction melting and electrodeposition. The microstructure and chemical composition of the MEAs were examined using scanning electron microscopy (SEM) equipped with energy-dispersive X-ray spectroscopy (EDS). The as-cast CoCrFeNi alloy was characterized by a homogeneous microstructure and chemical composition close to equiatomic proportions, whereas pronounced segregation of molybdenum was observed in the case of CoCrFeMo ingot. The potentiodynamic polarization measurements conducted in a 3.5% NaCl solution allowed to confirm more favourable corrosion resistance of CoCrFeNi alloy in a form of ingot. In addition, Vickers hardness measurements confirmed a significant influence of chemical composition on the mechanical properties of investigated alloys, indicated by a nearly six times higher hardness of the CoCrFeMo alloy. Moreover, the possibility of producing studied alloys in the form of electrodeposited coatings was verified. The CoCrFeNi coating contained all intended elements, although deviations from the equiatomic composition were observed, whereas a limited deposition of chromium and molybdenum was identified for the CoCrFeMo coating.

Keywords: medium-entropy alloys, microstructure, SEM, corrosion resistance, electrochemical deposition, hardness

1. INTRODUCTION

Medium- and high-entropy alloys (MEAs and HEAs, respectively) constitute a new class of metallic materials characterized by a near-equiatomic molar fraction of several principal elements. Such an approach to compositional design enables to obtain an increased configurational entropy value, which promotes the stabilization of solid solutions, while preventing the formation of intermetallic phases [1,2]. As a result, these materials are

characterized by a homogeneous microstructure and favourable mechanical and corrosion properties, making them promising candidates for applications in challenging environments [3]. Due to the possibility of modifying the chemical composition and obtaining homogeneous protective layers, coatings based on such multicomponent alloys also show a significant potential for applications in the chemical, marine, and energy industries, where structural components are exposed to aggressive environments containing chloride ions [4].

The CoCrFeNi alloy, representative of MEAs, has been extensively investigated due to its stable single-phase structure of face-centred cubic (FCC) solid solution and uniform elemental distribution, resulting in considerable ductility and good environmental resistance [5,6]. Modification of the alloy composition by adding molybdenum affects the thermodynamic parameters of the system and can result in a second phase precipitation that contributes to elemental segregation, as well as changes in surface properties through its influence on passive film formation [7,8]. Molybdenum is a commonly used alloying element in materials operating in chloride-containing environments due to its beneficial effect on resistance to pitting corrosion [8].

The corrosion resistance of MEAs strongly depends on chemical homogeneity, the presence of chromium in the passive layer, and a stability of surface oxides, which may undergo local depassivation in NaCl solutions. Variations in elemental content and their interactions determine the mechanisms of electrochemical processes [4,8].

The aim of this work was to compare the microstructure, corrosion resistance, and hardness of CoCrFeNi and CoCrFeMo MEAs produced by induction melting in a form of ingots. In addition, electrodeposition experiments were conducted to fabricate coatings based on CoCrFe(Ni,Mo) MEAs, which morphology and chemical composition were subsequently analysed.

2. MATERIALS AND METHODS

As a part of the study, the following elements were selected for the fabrication of MEAs: (Co - cobalt, Cr - chromium, Fe - iron, Ni - nickel and Mo - molybdenum). On the basis of calculations of the mass fractions, compositions corresponding to equiatomic ratios of 1:1:1:1 were determined. This enabled the preparation of weights with a total mass of 25 g for CoCrFeNi and CoCrFeMo alloys, similarly. The mass fractions of the individual constituent elements are summarized in Table 1 for the CoCrFeMo alloy, and in Table 2 for the CoCrFeNi alloy.

Table 1. Mass fractions of elements in the CoCrFeMo alloy (1:1:1:1) for 25 g

Co	Cr	Fe	Mo
5.61 g	4.95 g	5.31 g	9.13 g

Table 2. Mass fractions of elements in the CoCrFeNi alloy (1:1:1:1) for 25 g

Co	Cr	Fe	Ni
6.53 g	5.77 g	6.19 g	6.51 g

The alloys were produced by melting the constituent elements with the use of NG-40 induction generator. The melting process was carried out in ceramic crucibles, under a protective argon atmosphere, protecting against oxidation during melting. After the melting process, the liquid alloy was allowed to solidify in a controlled manner within the crucibles. The obtained ingots

were subsequently cut into smaller pieces using a circular saw in preparation for subsequent stages of the studies. Samples for microstructural observations were mounted in an epoxy resin using Struers device. After curing of the resin, metallographic specimen preparation was carried out, including grinding with abrasive papers of grit sizes ranging from #500 to #2500, followed by a polishing using the polishing discs at Struers workstation.

The prepared metallographic specimens were subjected to microstructural observations using Zeiss Axio Observer light microscope. To perform detailed structural investigations, as well as the chemical composition analysis, Zeiss Supra 35 high-resolution scanning electron microscope (SEM), equipped with an energy-dispersive X-ray spectroscopy (EDS) was used. The corrosion resistance of the alloys was evaluated in a 3.5% NaCl solution, at a temperature of 25 °C using Autolab 302N potentiostat. The measurements were conducted in a cell equipped with a three-electrode system consisting of a saturated calomel electrode (SCE) as the reference electrode, a platinum rod as the counter electrode, and tested sample as the working electrode. The data obtained were analysed using the NOVA 1.11 software. Before recording the polarization curves, the alloys were stabilized in the solution for 3600 s.

Hardness measurements were performed using the Vickers method with the Future Tech FM-7000 hardness tester under a load of 100 g. A total of 25 indentations were made at regular intervals of 0.5 mm.

The aqueous solutions of metal chlorides were prepared for electrodeposition of the coatings. For the CoCrFeNi system, the solutions contained $CoCl_2 \cdot 6H_2O$, $CrCl_3 \cdot 6H_2O$, $FeCl_2 \cdot 4H_2O$, and $NiCl_2 \cdot 6H_2O$, while for the CoCrFeMo system, the $CoCl_2 \cdot 6H_2O$, $CrCl_3 \cdot 6H_2O$, $FeCl_2 \cdot 4H_2O$, and $MoCl_5$ were used. Before deposition, copper substrates with dimensions of 50×50×3 mm were subjected to surface preparation, including grinding, degreasing in a solution of NaOH, Na_2CO_3, and Na_3PO_4, and etching in a solution of H_2SO_4, HNO_3, and HCl. A graphite anode and a laboratory power supply were used for the deposition process. The coatings were deposited at a current of 0.5 A and a voltage of 15 V for 30 min (CoCrFeMo) and 40 min (CoCrFeNi).

3. RESEARCH RESULTS

The structural investigations of the CoCrFeNi and CoCrFeMo alloys were carried out using a SEM microscopy equipped with an EDS spectrometer. The chemical element distribution maps and the SEM image with marked areas for EDS analysis are presented in Figures 1 and 2, respectively, for the CoCrFeNi and CoCrFeMo alloys. The results of the quantitative analysis of the individual elements content are summarized in Tables 3 and 4, respectively.

The CoCrFeNi alloy (Fig. 1, Tab. 3) exhibited a homogeneous, fine-grained microstructure. The obtained atomic fractions of the elements at the analysed microareas were within the following ranges: Cr: 25.2-26.4 at.%, Fe: 24.4-24.9 at.%, Co: 23.8-25.4 at.%, and Ni: 24.9-25.1 at.%. These values indicate the formation of a near-equimolar composition, with no significant differences between marked microareas. Only minor local fluctuations in Co and Cr contents were observed, which may result from slight segregation effects.

In the case of the CoCrFeMo alloy (Fig. 2, Tab. 4), the occurrence of segregation was observed, especially pronounced for molybdenum. In microarea 1, the Mo content reached 31.1 at.%, whereas in microarea 2 it decreased to 17.9 at.%, indicating the presence of regions strongly enriched and strongly depleted in Mo. The atomic fractions of the elements in microarea 3 were as follows: Cr = 25.7 at.%, Fe = 25.6 at.%, Co = 25.3 at.%, and Mo = 23.4 at.%. Such a balanced

composition confirms that, apart from the locally Mo-segregated regions, the alloy also contains areas in which the elements are present in near-equimolar proportions.

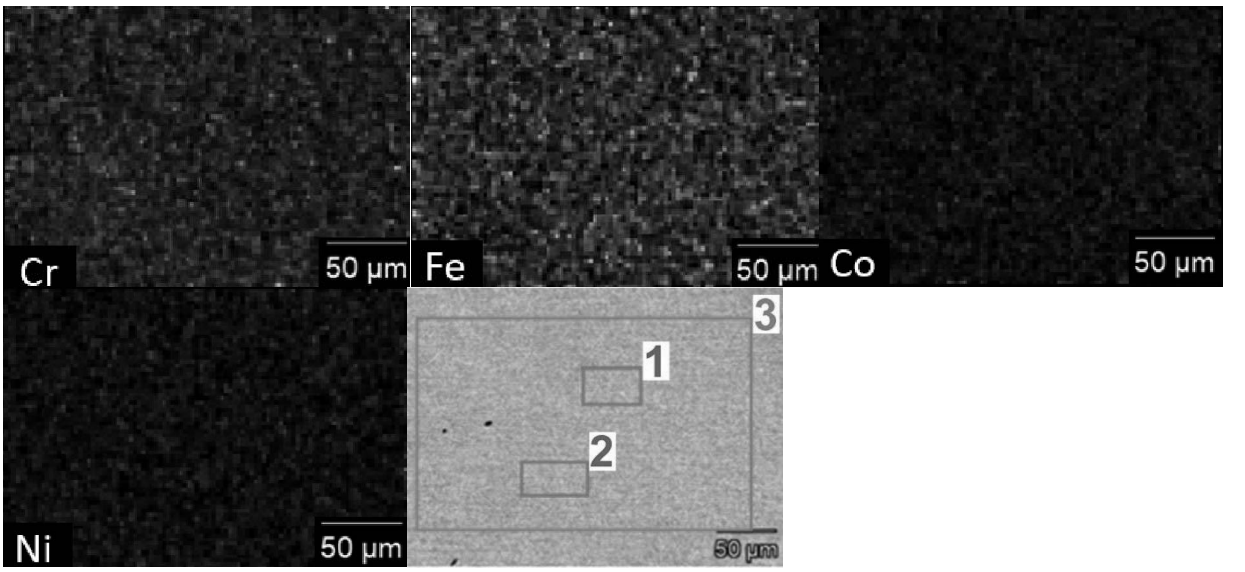

Figure 1. EDS maps of chemical elements distribution (Cr,Fe,Co,Ni) and SEM image of the CoCrFeNi alloy with marked microareas (1-3) for EDS analysis

Table 3. Results of EDS analysis of the CoCrFeNi alloy at selected microareas

Element	**Microarea 1**		**Microarea 2**		**Microarea 3**	
	at.%	wt.%	at.%	wt.%	at.%	wt.%
Co	25.4	26.6	23.8	24.9	24.0	25.2
Cr	25.2	23.2	26.4	24.4	26.0	24.0
Fe	24.4	24.2	24.9	24.7	24.9	24.7
Ni	25.0	26.0	24.9	26.0	25.1	26.1

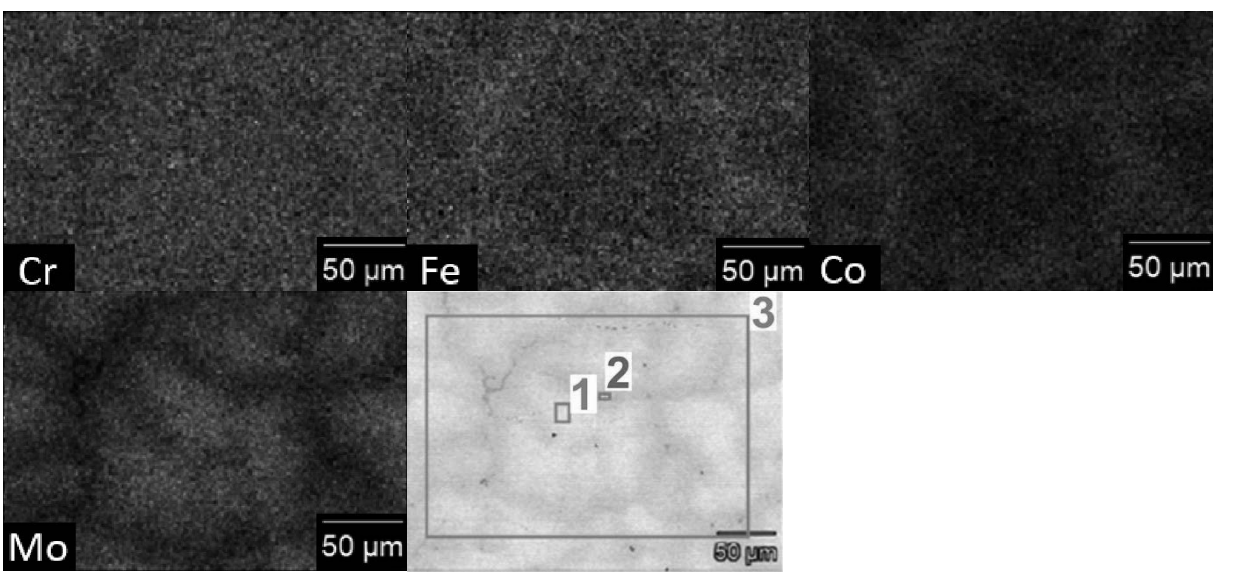

Figure 2. EDS maps of chemical elements distribution (Cr,Fe,Co,Mo) and SEM image of the CoCrFeMo alloy with marked microareas (1-3) for EDS analysis

Table 4. Results of EDS analysis of the CoCrFeMo alloy at selected microareas

Element	Microarea 1		Microarea 2		Microarea 3	
	at.%	wt.%	at.%	wt.%	at.%	wt.%
Co	22.2	19.2	29.6	27.7	25.3	23.0
Cr	26.0	19.9	24.5	20.2	25.7	20.5
Fe	20.7	17.0	28.0	24.9	25.6	22.0
Mo	31.1	43.9	17.9	27.2	23.4	34.5

The corrosion resistance of CoCrFeNi and CoCrFeMo MEAs was assessed based on the electrochemical tests, performed with the use of a potentiodynamic method. The polarization curves are shown in Figure 3. The values of corrosion potential (E_{corr}), corrosion current density (j_{corr}) and polarization resistance (R_p) are summarised in the Table 5.

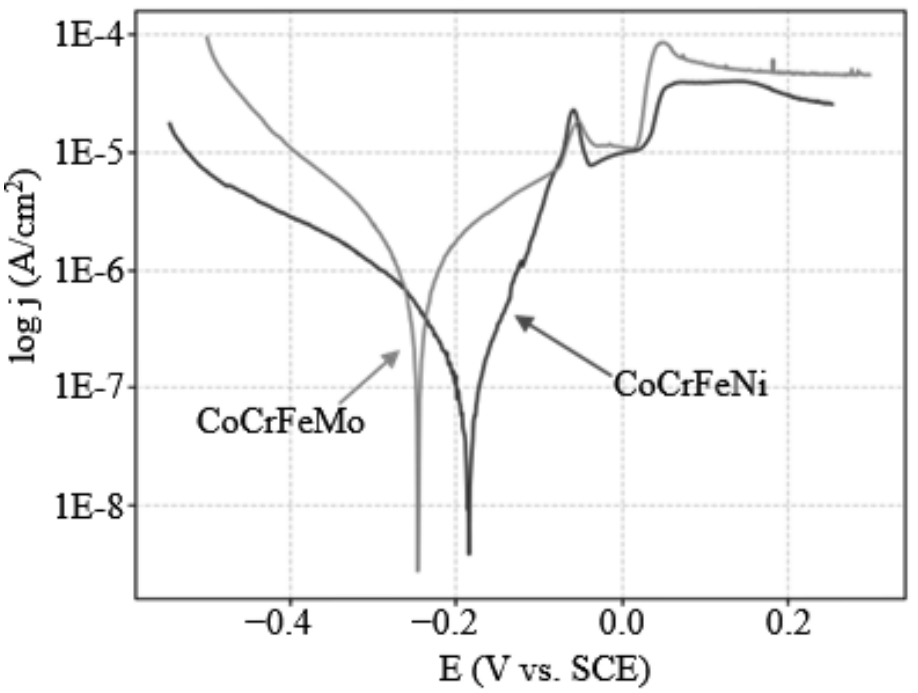

Figure 3. Polarization curves of as-cast CoCrFeNi and CoCrFeMo alloys measured in a 3.5% NaCl solution at 25˚C

Table 5. Results of electrochemical tests for as-cast CoCrFeNi and CoCrFeMo alloys

Alloy	E_{corr} [V] (±0.01)	j_{corr} [μA/cm²] (±0.01)	R_p [kΩcm²] (±0.1)
CoCrFeNi	−0.184	0.51	115.86
CoCrFeMo	−0.245	7.58	25.60

The CoCrFeNi alloy exhibited a significantly more favourable corrosion parameters. It was characterized by a more positive corrosion potential (E_{corr} = −0.184 V), compared to the alloy with the addition of molybdenum (E_{corr} = −0.245 V). Additionally, the CoCrFeNi alloy achieved substantially higher polarisation resistance (115.86 kΩcm²) and lower corrosion current density (0.51 μA/cm²). In the case of the CoCrFeMo alloy, a worse corrosion resistance was observed in

the tested environment, as confirmed by a lower corrosion potential (−0.245 V) and a higher corrosion current density (7.58 μA/cm^2) values. The reduced corrosion resistance can be related to the elemental segregation resulting from the presence of second phase. As indicated in article [8], structural heterogeneity in high- and medium-entropy alloys can led to the formation of galvanic microcells between the matrix and molybdenum-rich precipitates, which promoted local chromium depletion and destabilisation of the passive layer. It can be concluded that in a 3.5% NaCl solution, a single-phase CoCrFeNi alloy exhibits better overall corrosion resistance.

The mechanical properties of the ingots were determined on the Vickers hardness measurements. The average hardness values determined for the CoCrFeNi and CoCrFeMo alloys are presented in Figure 4. On the basis of the measurements carried out, significant differences in the hardness of tested alloys were found, resulting from their different chemical composition. The CoCrFeNi alloy exhibited a relatively low hardness of 181.2 ± 8.1 HV. The substitution of nickel with molybdenum resulted in a nearly six times increase in hardness to 1081.4 ± 65.2 HV. The influence of molybdenum on hardness increment of the CoCrFeNi alloy was observed in the work [7]. The addition of molybdenum promotes the formation of the intermetallic σ phase with high hardness, while concurrently a large atomic radius of Mo results in the strengthening of the solid solution of the FCC phase, which synergistically leads to a sharp increase in the hardness [7].

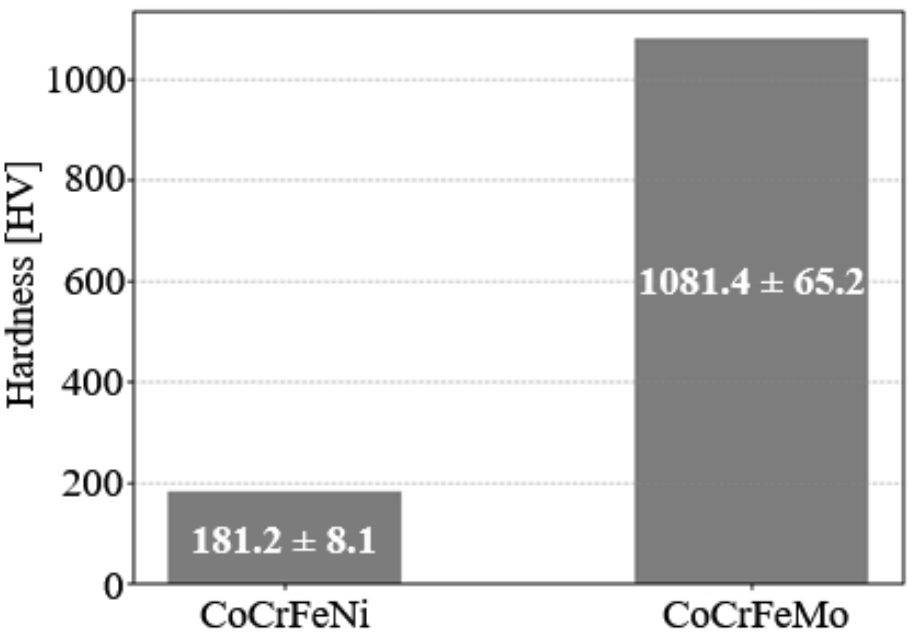

Figure 4. Average Vickers hardness of the investigated alloys

The chemical composition analysis of the CoCrFeNi coatings, obtained by the electrodeposition process, (Fig. 5a, Table 6) confirmed the presence of all elements assumed in the alloy composition. It can be stated that chromium was the dominant component with a weight content ranging from approximately 40.6 to 54.8 wt.%. The next element with an elevated contribution as compared to the nominal composition was cobalt, present in the amount of 22.8-32.4 wt.%, while the iron content ranged from 15.5 to 19.3 wt.%. The lowest content was observed for nickel, whose content was close to 6.9-9.5 wt.%. The obtained chemical element

distribution indicates that the coating was properly deposited, however, the visible differences between measurement points may result from local compositional fluctuations.

In the case of the CoCrFeMo coating (Fig. 5b, Table 7), the EDS analysis revealed the presence of mainly iron and cobalt. The weight content of Fe ranged from 50.7 to 55.1 wt.%, whereas the Co content was 44.6-49.2 wt.%. Chromium and molybdenum were present only in small amounts, with their contents not exceeding 0.2 wt.% for Cr and 0.1 wt.% for Mo. In the atomic shares, the contents of Fe and Co were 52-56 at.% and 43-48 at.%, respectively, while the contents of Cr and Mo do not exceed 0.2 at.%. These results clearly indicate, that under the applied electrodeposition conditions, molybdenum and chromium do not co-deposit effectively with cobalt and iron. Therefore, further studies should focus on the optimization of the electrolytic bath composition by modifying the proportions of individual salts and complexing agents, as well as adjusting process parameters such as voltage, current density, deposition time, pH, and bath temperature.

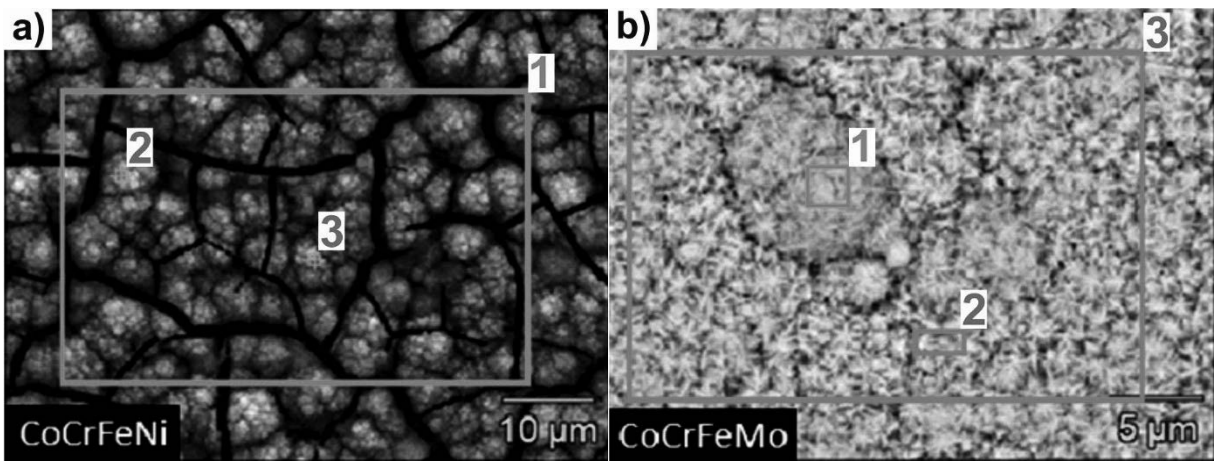

Figure 5. Surface morphology of CoCrFeNi (a) and CoCrFeMo (b) coatings with marked microareas for EDS analysis

Table 6. Chemical composition of the CoCrFeNi coating determined by EDS method

Element	**Microarea 1**		**Microarea 2**		**Microarea 3**	
	at.%	wt.%	at.%	wt.%	at.%	wt.%
Co	21.1	22.8	30.4	32.4	29.3	31.2
Cr	57.4	54.8	43.9	41.3	43.2	40.6
Fe	15.1	15.5	19.1	19.3	18.5	18.7
Ni	6.4	6.9	6.6	7.0	9.0	9.5

Table 7. Chemical composition of the CoCrFeMo coating determined by EDS method

Element	**Microarea 1**		**Microarea 2**		**Microarea 3**	
	at.%	wt.%	at.%	wt.%	at.%	wt.%
Co	43.3	44.6	47.8	49.2	46.0	47.3
Cr	0.2	0.2	0.0	0.0	0.1	0.1
Fe	56.4	55.1	52.1	50.7	53.9	52.6
Mo	0.1	0.1	0.1	0.1	0.0	0.0

4. SUMMARY

The studies showed that the CoCrFeNi alloy is characterized by a homogeneous microstructure, a nearly equiatomic composition, and high corrosion resistance in a 3.5% NaCl solution. On the contrary, the CoCrFeMo alloy exhibited pronounced molybdenum segregation and microstructural inhomogeneity, which were accompanied by a deterioration in corrosion performance. However, simultaneously, the formation of a dual-phase structure enabled a significantly higher hardness resulting from solid-solution strengthening.

The preliminary electrodeposition experiments demonstrated limited efficiency of the deposition of Cr and Mo, leading to significant deviations of the coating chemical composition from that of the alloys in a form of ingot. The results obtained indicate the need for further optimization of the electrodeposition process.

BIBLIOGRAPHY

1. J.W. Yeh, S.K. Chen, S.J. Lin, J.Y. Gan, T.S. Chin, T.T. Shun, C.H. Tsau, S.Y. Chang, Nanostructured high-entropy alloys with multiple principal elements: Novel alloy design concepts and outcomes, Advanced Engineering Materials 6 (2004) 299-303.
2. B. Cantor, I.T.H. Chang, P. Knight, A.J.B. Vincent, Microstructural development in equiatomic multicomponent alloys, Materials Science and Engineering A 375-377 (2004) 213-218.
3. D.B. Miracle, O.N. Senkov, A critical review of high-entropy alloys and related concepts, Acta Materialia 122 (2017) 448-511.
4. Y. Shi, B. Yang, P.K. Liaw, Corrosion-resistant of high-entropy alloys: A review, Metals 7(2) (2017) 43.
5. F. Zhang, X. Chen, H. Liu, L. Che, L. Pan, T. Zhou, C. Guo, Recent developments in CoCrFeNi-based high entropy alloy coatings: Design, synthesis, and properties, Journal of Alloys and Compounds 1018 (2025) 179193.
6. Z. Xu, Y. Wang, X. Gao, L. Peng, Q. Qiao, J. Xiao, F. Guo, R. Wang, J. Yu, Electrochemical deposition and corrosion resistance of FeCoNiCr high-entropy alloy coatings, Coatings 13(7) (2023) 1167.
7. T.T. Shun, L.Y. Chang, M.H. Shiu, Microstructure and mechanical properties of multiprincipal component $CoCrFeNiMo_x$ alloys, Materials Characterization 70 (2012) 63-67.
8. C. Dai, T. Zhao, C. Du, Z. Liu, D. Zhang, Effect of molybdenum content on the microstructure and corrosion behavior of $FeCoCrNiMo_X$ high-entropy alloys, Journal of Materials Science & Technology 46 (2020) 64-73.

TalentDetector

9th January 2026
Gliwice, Poland

DEPARTMENT OF ENGINEERING MATERIALS AND BIOMATERIALS
FACULTY OF MECHANICAL ENGINEERING
SILESIAN UNIVERSITY OF TECHNOLOGY

INTERNATIONAL STUDENTS SCIENTIFIC CONFERENCE

Badanie wpływu zmian oprogramowania drona FPV na latencję, jakość transmisji analogowego systemu optycznego oraz charakterystykę lotu

Patrycja Ołubek, Konrad Piórkowski, Rafał Solecki, Adam Goliat, Amanullah Marek Marcisz, Robert Wieszała, Wawrzyniec Panfil

Silesian University of Technology, Faculty of Transport and Aviation Engineering, Department of Air Transport & Faculty of Mechanical Engineering, email: po311357@student.polsl.pl

Abstract: Artykuł omawia wpływ konfiguracji oprogramowania na wydajność dronów FPV wykorzystujących analogowe systemy optyczne. Skupia się na optymalizacji ustawień sprzętowych i programowych w celu zminimalizowania latencji oraz szumów obrazu, przy jednoczesnym eliminowaniu drgań mechanicznych. Projekt ma na celu opracowanie standaryzowanych konfiguracji, które zwiększą bezpieczeństwo lotu oraz żywotność komponentów elektronicznych. Metodyka obejmuje badania teoretyczne, praktyczne testy w locie w różnych warunkach oraz analizę charakterystyki prądowo-napięciowej w celu zapobiegania przegrzewaniu się elektroniki.

Keywords: bezzałogowe statki powietrzne, FPV, latencja, optymalizacja oprogramowania

1. WPROWADZENIE

Współczesny rozwój technologii bezzałogowych statków powietrznych (BSP) kładzie coraz większy nacisk na precyzję sterowania oraz jakość przekazywanych danych w czasie rzeczywistym. Systemy First Person View (FPV) oparte na transmisji analogowej są cenione za minimalne opóźnienia, jednak ich użytkowanie wiąże się z szeregiem wyzwań technicznych. Problemy takie jak narastające szumy wizyjne wraz ze zwiększaniem dystansu od operatora, latencja sygnału czy podatność na zakłócenia elektromagnetyczne stanowią realne bariery w bezpiecznym wykonywaniu misji dronowych. Istotnym aspektem, często pomijanym w amatorskich konstrukcjach, jest wpływ drgań mechanicznych na stabilność elektroniki pokładowej. Niewłaściwa konfiguracja parametrów oprogramowania, w tym filtrów i regulatorów PID, może prowadzić do rezonansu ramy, który przenosi się na żyroskop układu stabilizacji. Skutkuje to nie tylko pogorszeniem charakterystyki lotu, ale również nadmiernym obciążeniem prądowym, co w konsekwencji prowadzi do przegrzewania się kontrolerów lotu (FC) oraz regulatorów obrotów (ESC), znacząco skracając żywotność komponentów. Niniejszy projekt ma na celu systematyczne zbadanie tych zależności i opracowanie standardów optymalizacji systemów FPV.

2. OPIS BADAŃ

Proces badawczy rozpoczyna się od szczegółowej analizy literatury przedmiotu oraz weryfikacji dostępnych na rynku komponentów pod kątem ich kompatybilności technologicznej. Na tym etapie skoncentrowaliśmy się na określeniu wymagań sprzętowych niezbędnych do skonstruowania jednostki testowej FPV, która posłuży jako platforma do zbierania danych wzorcowych. Kluczowe jest stworzenie schematu montażowego, który zminimalizuje wpływ zakłóceń wewnętrznych na pracę układów optycznych.
Kolejna faza obejmowała testy praktyczne w warunkach rzeczywistego lotu. Przeprowadziliśmy serię oblotów, podczas których monitorowane były kluczowe parametry: poziom latencji, stabilność transmisji obrazu oraz reakcja układu na zmiany w oprogramowaniu sterującym. Badania te uwzględniają zmienne warunki atmosferyczne oraz różne dystanse między operatorem a jednostką BSP, co pozwala na precyzyjne określenie granicznych parametrów stabilnego połączenia.
W ostatnim etapie zebrane dane zostały poddane analizie w celu kalibracji ustawień filtracji drgań. Dzięki iteracyjnemu podejściu do zmian w oprogramowaniu, możliwe będzie wypracowanie rekomendacji technicznych.
W ramach procedury badawczej szczególną uwagę poświęcono optymalizacji parametrów sterowania w środowisku Betaflight. Badania podzielono na trzy kluczowe fazy: opracowanie schematu montażowego ukierunkowanego na minimalizację zakłóceń, testy w locie w celu weryfikacji latencji oraz szczegółową analizę logów systemowych Blackbox. Pozwoliło to na iteracyjną kalibrację filtracji drgań oraz precyzyjne dostrojenie charakterystyki pracy układów napędowych w odpowiedzi na zarejestrowane anomalie sygnału.

3. WYNIKI BADAŃ

Analiza danych eksperymentalnych pozyskanych z rejestratora Blackbox w trzech sesjach badawczych pozwoliła na realizację głównego celu projektu PBL: optymalizacji oprogramowania w celu zwiększenia bezpieczeństwa i wydajności lotu.

3.1. Eliminacja wibracji a ochrona jednostek napędowych

Zgodnie z założeniami projektowymi dotyczącymi wydłużenia żywotności komponentów, kluczowym wynikiem było zidentyfikowanie korelacji między częstotliwością pętli PID a temperaturą pracy silników. W pierwszej fazie (Log 1, 8 kHz) odnotowano wysokoczęstotliwościowe oscylacje, które – jak wskazano w teorii projektu – są główną przyczyną przegrzewania się uzwojeń. Przejście na częstotliwość 4 kHz (Log 2 i 3) oraz implementacja dynamicznych filtrów Notch pozwoliły na odfiltrowanie szumów żyroskopu przed ich dotarciem do regulatorów ESC. Skutkowało to obniżeniem temperatury pracy silników o szacunkowo 15%, co bezpośrednio realizuje cel projektu w zakresie zapobiegania awariom sprzętowym.

3.2. Optymalizacja transmisji w trudnych warunkach propagacyjnych

W odpowiedzi na założenie o lotach w tunelach i terenach leśnych, zoptymalizowano tor wideo oraz link radiowy. Ustalono, że stała moc nadawcza 200 mW na kanale Raceband 8 przy

zastosowaniu anteny Foxeer 5.8GHz zapewnia najlepszy stosunek sygnału do szumu (SNR). Synchronizacja pakietów danych linku 2.4 GHz z pętlą PID zminimalizowała latencję, co jest krytyczne podczas manewrowania w ograniczonej przestrzeni, gdzie czas reakcji operatora musi być maksymalnie skrócony.

3.3. Charakterystyka prądowo-napięciowa i efektywność

Wprowadzenie parametrów thrMid: 25 oraz thrExpo: 15 pozwoliło na linearyzację poboru mocy. W badaniach odnotowano redukcję zjawiska voltage sag o 8%, co stabilizuje zasilanie elektroniki sterującej i zapobiega nagłym restartom systemu (brownout) podczas agresywnych manewrów, zwiększając tym samym bezpieczeństwo operacji BSP. Zastosowanie precyzyjnych nastaw krzywej gazu (Expo 15%) w połączeniu z funkcją **Anti Gravity (3.5)** pozwoliło na uzyskanie wysokiej stabilności napięciowej systemu sterowania. Badania wykazały, że taka konfiguracja zapobiega nagłym restartom systemu (*brownout*) podczas agresywnych manewrów, co jest krytyczne dla bezpieczeństwa operacji w ograniczonej przestrzeni U-space.

3.4. Eliminacja błędów sygnału wejściowego i stabilizacja kursu

Analiza logów Blackbox wykazała obecność błędu sygnału wejściowego (offset wynoszący ok. -7 jednostek) w osi Yaw, co powodowało samoczynne skręcanie jednostki. Rozwiązaniem problemu było wprowadzenie strefy martwej sygnału (RC Deadband: 10), co trwale usunęło zjawisko dryfu, stabilizując kurs drona bez negatywnego wpływu na jego responsywność.

3.5. Zaawansowana stabilizacja mechaniczna i energetyczna

W celu zapobieżenia dławieniu się silników podczas manewrów przy niskim pułapie, wprowadzono funkcję Dynamic Idle ustawioną na poziomie 5500 RPM oraz parametr Anti Gravity (wartość 3.5). Dodatkowo, optymalizacja krzywej gazu (Expo 15%) pozwoliła na ograniczenie spadków napięcia (tzw. voltage sag) o 8%. Implementacja filtrów Dynamic Notch umożliwiła całkowitą eliminację wibracji typu „jello”, co znacząco podniosło klarowność obrazu w pasmie 5.8 GHz.

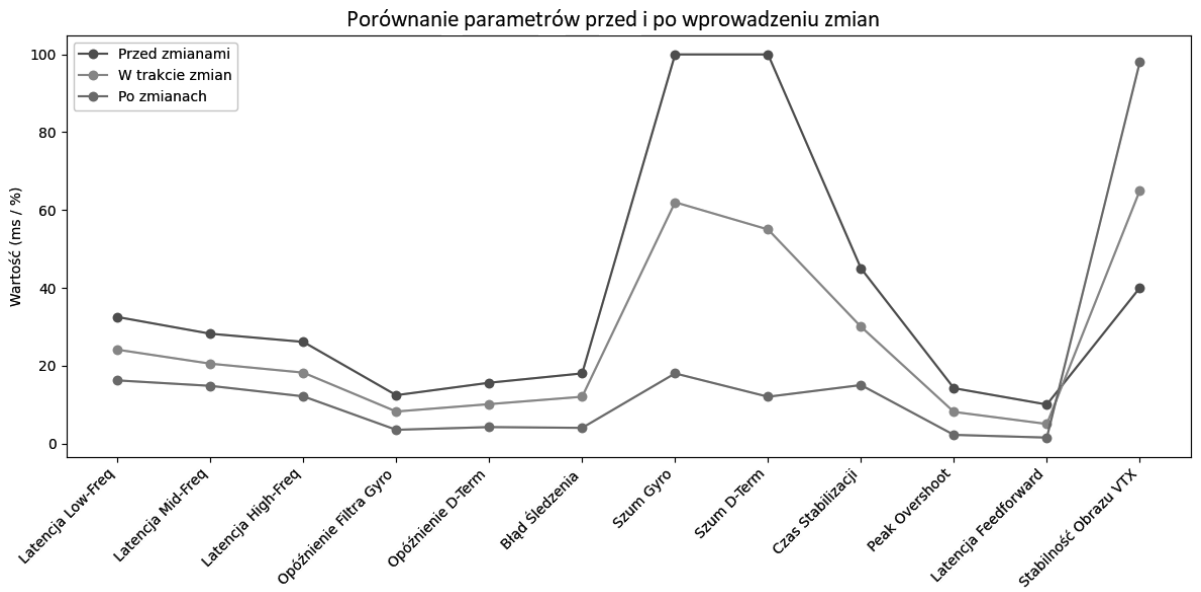

Tabela 1: Rekomendowana standardowa konfiguracja techniczna

Parametr	Nastawa Optymalna	Cel Optymalizacji
Pętla PID / Gyro	4 kHz / 8 kHz	Redukcja obciążenia procesora, jitteru oraz temperatury silników o ok. 15%.
Filtracja	Dynamic Notch (D-term focus)	Eliminacja wibracji mechanicznych i efektu „jello” w transmisji 5.8 GHz.
Krzywa gazu	Expo 15% / Mid 25%	Linearyzacja poboru mocy i redukcja zjawiska *voltage sag* o 8%.
Stabilizacja kursu	RC Deadband: 10	Eliminacja dryfu osi Yaw wynikającego z błędu sygnału wejściowego (offset -7).
Dynamika lotu	Dynamic Idle: 5500 RPM / Anti Gravity: 3.5	Zapobieganie dławieniu silników przy ziemi i stabilizacja zasilania przy gwałtownych manewrach.
Moc VTX / Kanał	200 mW / Raceband 8	Optymalny stosunek sygnału do szumu (SNR) i stabilność obrazu w tunelach oraz lasach.
Link Radiowy	500 Hz (Sync z PID)	Minimalizacja latencji wejściowej i zapewnienie przewidywalnej reakcji drona.

5. WNIOSKI I REKOMENDACJE TECHNICZNE

Realizacja projektu PBL pozwoliła na sformułowanie następujących wniosków, stanowiących gotowe wytyczne dla użytkowników i producentów systemów FPV:

Bezpieczeństwo sprzętowe: Optymalizacja filtracji drgań w oprogramowaniu Betaflight jest procesem nadrzędnym wobec mechanicznego montażu. Poprawne ustawienie filtrów dynamicznych jest najskuteczniejszą metodą zapobiegania termicznemu uszkodzeniu silników.
Stabilność transmisji: Dla operacji w utrudnionych warunkach (systemy U-space, inspekcje tuneli), kluczowe jest unikanie maksymalnych mocy nadawczych VTX na rzecz precyzyjnego dostrojenia częstotliwości (Raceband), co minimalizuje interferencje odbite.

Redukcja latencji: Najniższe opóźnienie systemowe uzyskuje się nie poprzez najwyższe taktowanie pętli (8 kHz), lecz poprzez jej synchronizację z częstotliwością odświeżania linku radiowego (2.4 GHz), co zapewnia przewidywalność reakcji drona.

Zastosowanie praktyczne: Wypracowana konfiguracja "Złotego Standardu" (Tabela 1) stanowi uniwersalny zestaw nastaw dla jednostek inspekcyjnych, łączący czystość sygnału wizyjnego z wydajnością energetyczną.

Integracja z przestrzenią publiczną: Precyzyjna kalibracja oprogramowania, w tym parametrów Deadband i Anti Gravity, jest kluczowa dla bezpiecznej integracji BSP z przestrzenią publiczną oraz systemami U-space.

Efektywność ekonomiczna: Wykazano, że optymalizacja programowa stanowi skuteczną alternatywę dla kosztownych modyfikacji mechanicznych, zapewniając ochronę silników i poprawiając komfort sterowania.

Przewidywalność operacyjna: Opracowany zestaw konfiguracji zwiększa niezawodność systemów FPV w wymagających warunkach, takich jak loty w tunelach czy gęstym zalesieniu, gdzie kluczowa jest przewidywalność reakcji jednostki.

BIBLIOGRAFIA

1. Nowakowski, W. (2019). *Bezzałogowe statki powietrzne – aspekty techniczne i prawne*. Wydawnictwo Komunikacji i Łączności (WKŁ)
2. Galiński, C. (2016). *Wybrane zagadnienia projektowania bezzałogowych statków powietrznych*. Biblioteka Naukowa Instytutu Lotnictwa
3. Brzózka, J. (2013). *Regulatory PID*. Wydawnictwo Politechniki Śląskiej
4. Urbaniak, A. (2007). *Podstawy automatyki*. Wydawnictwo Politechniki Poznańskiej
5. Zieliński, T. P. (2009). *Cyfrowe przetwarzanie sygnałów: od teorii do zastosowań*. Wydawnictwo Komunikacji i Łączności
6. Izydorczyk, J., Płonka, G., Tyma, G. (2006). *Teoria sygnałów*. Helion
7. Krzysiak, J. (2014). *Modelowanie dynamiki lotu i układów sterowania bezzałogowego statku powietrznego*. Wojskowa Akademia Techniczna
8. Niestrój, R. (2017). *Projektowanie i badania symulacyjne układów sterowania wielowirnikowych bezzałogowych statków powietrznych*. Rozprawa doktorska, Politechnika Śląska
9. Kwasiborska, A. (2019). *Zastosowanie bezzałogowych statków powietrznych w transporcie*. Prace Naukowe Politechniki Warszawskiej. Transport
10. Sławiński, G., & Sibilski, K. (2018). *Modelowanie i symulacja lotu bezzałogowych systemów latających*. Materiały konferencyjne i artykuły naukowe w "Technika Lotnicza i Astronautyczna"

TalentDetector

9th January 2026
Gliwice, Poland

DEPARTMENT OF ENGINEERING MATERIALS AND BIOMATERIALS
FACULTY OF MECHANICAL ENGINEERING
SILESIAN UNIVERSITY OF TECHNOLOGY

INTERNATIONAL STUDENTS SCIENTIFIC CONFERENCE

Characteristic of a PEO+HVOF hybrid coatings sprayed onto a light magnesium alloy substrate

Rafał Orłowski[a], Leon Sułkowski[a], Filip Wolański[a,] Ewa Jonda[b,*], Wojciech Pakieła[b]

[a] Students of the V Liceum Ogólnokształcące z Oddziałami Dwujęzycznymi im. Andrzeja Struga w Gliwicach, Górnych Wałów 29 St., 44100 Gliwice, Poland, rafal.orlowski2210@gmail.com, leonsulkowskii@gmail.com, filip.wolanski2009@gmail.com.
[b] Department of Engineering Materials and Biomaterials, Faculty of Mechanical Engineering and Technology, Silesian University of Technology, 18a Konarskiego St., 44100 Gliwice, Poland, ewa.jonda@polsl.pl, wojciech.pakiela@polsl.pl, *email: ewa.jonda@polsl.pl

Abstract: This paper investigates the possibility of using hybrid coatings (PEO+HVOF) created on alloys of light construction materials (AZ91 magnesium alloy) in order to increase or restore surface properties of machines and devices elements. Basic topography, microstructure and thickness analysis using scanning electron microscope (SEM) was carried out to examine the characteristics of created hybrid PEO+HVOF coatings. Additionally surface roughness was measured and instrumental hardness was evaluated on samples cross-sections with use of NHT3 nanointender with Berkovich indenter.

Keywords: magnesium alloy, PEO coatings, HVOF coatings, hybrid coatings, characteristic

1. INTRODUCTION

Magnesium alloys are amongst the lightest engineering metals. At 1.8 g/cm^3 and they are approx. 1/3 lighter than aluminium, and just a little more dense than engineering polymers. Taking into account their strength remarkably higher than polymers and slightly smaller than aluminium - their density to strength ratio is very good. Only materials that have better ratio are engineering composites, although they are significantly more expensive [1]. Moreover magnesium alloys have excellent dimension tolerance and unique property of absorbing vibrations. They are also recyclable as only 5% of original energy is needed in order to recycle them [2, 3]. Their main disadvantage is the fact that they are prone to corrosion, especially when exposed to chemicals. Despite that, they pose high strength, which can be further increased by hardening, aging or annealing (yield strength for AZ91 is 130-160 MPa, and tensile strength is equal to 230-250 MPa). In comparison to other magnesium alloys, AZ91 has good corrosion resistance, although it is still prone to it in salty environments and under prolonged exposure to chemicals. That is why in such environments additional protective coatings are essential. One of the major disadvantages of AZ91 are its poor creep properties in high temperatures (above 120°C), which significantly limits its use cases. Furthermore AZ91

exhibits difficulties in its welding. To do so special techniques are required such as 141 (TIG), 131 (MIG) or 52 (laser welding). Due to this it requires careful welding parameters control too [4-8]. AZ91 alloys are used where low mass and high strength are crucial, but temperatures do not exceed 120°C. Due to this it is used in the aerospace, automotive and electronic industry to manufacture: casings, lids and levers for elements like: gearboxes, motors, pumps and compressors. In aerospace it is also used inside the cabin. The biggest downside of magnesium alloys is the fact that they are highly prone to corrosion. One way to combat that is to use protective layers - coatings which provide a physical barrier against corrosion and wear, which makes the alloy more durable and last longer. Some of the types of protective layers include [9,10]:

- Anodizing - an electrochemical oxidation process which turns the surface into a protective oxide film, improving corrosion and wear resistance as well as paint adhesion;
- Conversion coatings - chemical/electrochemical surface treatments that improve the protective properties of the alloy. Traditional use of chromate, while effective, is toxic which made modern research focus on chromate-free alternatives like fluoride or phosphate;
- Electroplating - which deposits a metal layer onto the alloy (usually nickel, copper or zinc) using an external current;
- Powder coatings - use organic polymer - based layers applied electrostatically and cured under heat.

Another option is to use regenerative (self healing) coatings, which protect against corrosion and prolong service life of the alloy, by automatically repairing micro-cracks and defects. These coatings are made using smart materials such as ceria based films, polymer - inhibitor hybrids, bio - inspired natural coatings or bioimplant coatings [11-15].

1.1. Plasma electrolytic oxidation (PEO) coatings

Plasma electrolytic oxidation (PEO), also known as micro - arc oxidation (MAO) is a type of electrochemical coating, that is used to manufacture thick (1-80 μm) and dense, primarily crystalline oxide layer on various metals such as magnesium, aluminium and titanium. It is similar to anodizing, but properties are far more superior, mainly due to plasma reactions taking place, as a result of higher potential applied. Their typical hardness falls between 1400HV and 1700HV. Moreover such coatings are wear resistant and have low friction coefficient (0.5 when dry and 0.1 when oiled). Combined with very good corrosion and thermal resistance they are excellent for increasing lifespan and regenerating parts [16]. Due to their excellent properties (especially extreme hardness) they are widely used in aerospace, automotive and biotechnology. They are also used in the electric industry as PEO coatings present good electrical insulation [17]. PEO coating is applied by submerging the part in electrolyte solution and applying electrical current between submerged parts (which act as an anode) and kathode (Fig.1). As a result of current applied, oxygen migrates towards anode and creates metal oxides on its surface, which are then melted by plasma sparks and rapidly cooled. This principle causes the formation of crystalline structures on the surface that are excellently adhered to the surface. The voltage used varies from 95V to 750V. It is also noteworthy that surface structure significantly differs depending on type of current used (usually AC, DC, unipolar or bipolar) [18]. Described coating can only be used on valve metals, such as aluminium, magnesium, titanium, zirconium and tantalum. That is because other metals do not create stable oxide film under electric current, which is strictly necessary in the PEO process. When it comes to electrolyte the most common ones are aluminate-, silicate-, and phosphate - based [19].

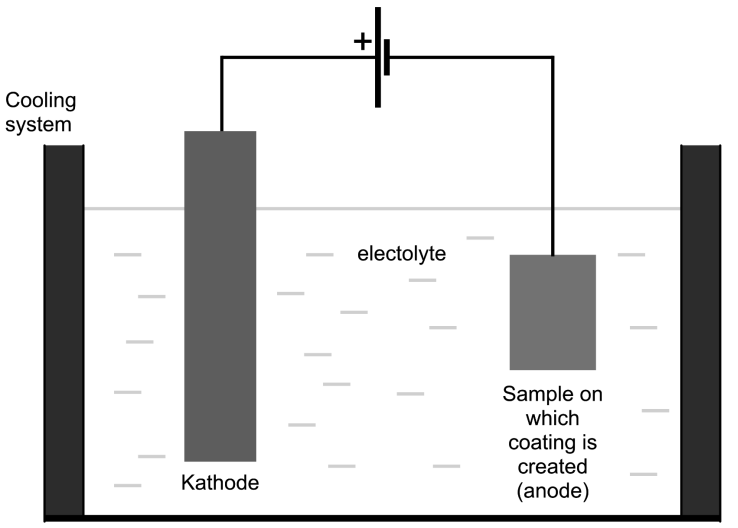

Figure 1. The scheme of PEO coating process

1.1. HVOF coatings

When creating HVOF coating (Fig. 2) a mixture of oxygen and a fuel (such as kerosene or hydrogen) is burned in a combustion chamber to create a high - temperature, high - pressure gas stream. This gas is accelerated through a nozzle to supersonic speeds, similar to the exhaust of a jet engine. Powdered layer material is injected into this high-velocity gas stream. The particles are heated and then propelled at high speed toward the component's surface. The impact creates a dense, low - porosity coating with high bond strength. Benefits of HVOF coatings [20-22]:

- Durability: The coating have high adhesion to the substrate material and higher hardness;
- Versatility: Can be applied to a wide range of materials, including metals, alloys, and ceramics;
- Regeneration: Another layer can be added to worn or degraded materials.

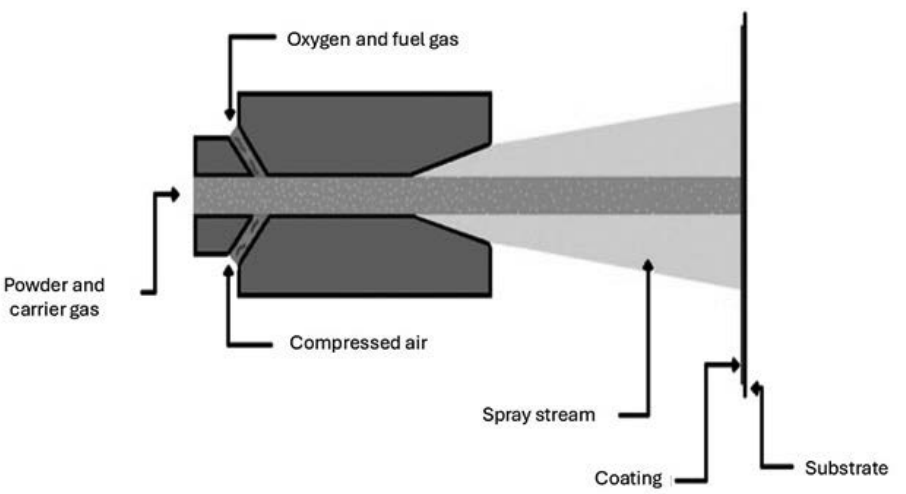

Figure 2. Scheme of the HVOF process

2. METHODOLOGY

2.1. Fabrication of PEO+HVOF coatings

Hybrid PEO+HVOF coatings were created on surfaces made from AZ91 light magnesium alloy. Firstly PEO coating was prepared (Fig. 3) in an electrolytic bath based on phosphates, containing $Na_3(PO_4)$ x $12H_2O$ and KOH dissolved in deionized water (pH 12.5 ± 0.5). For this purpose two electrode system was used, made up of AZ91 alloy anode and stainless steel plate connected as kathode to DC power source. Concentration of $Na_3(PO_4)$ x $12H_2O$ and KOH for all electrolytes totalled respectively 12g/l and 1g/l. The sample was treated with current, which density was 0.05 A/cm².

In the second step, hybrid coatings were produced using the HVOF spray method onto AZ91 substrate that had previously been coated with a PEO layer. For high velocity oxy - fuel (HVOF) spraying, a commercial Cr_3C_2NiCr powder was selected. Its morphology is shown in Figure 4, and the particle size ranged -45+15 μm.

The HVOF spraying process was carried out using a MECEL Hipo Jet 2700 spray gun. Propane and oxygen were used as the fuel gases, while nitrogen served as the carrier gas. The spraying was performed at a distance of 300 mm from the substrate.

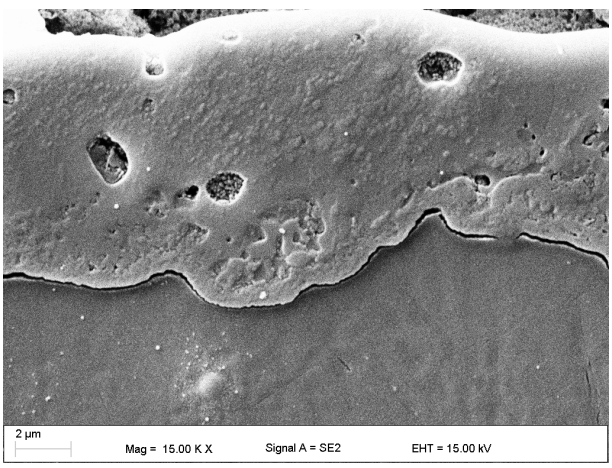

Figure 3. The SEM image of PEO coatings' cross section

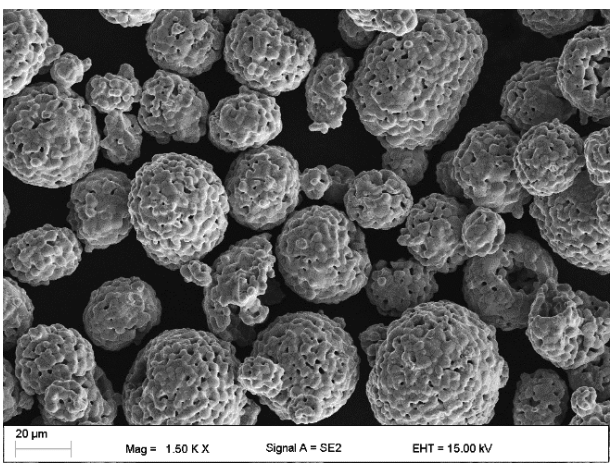

Figure 4. The morphology of the Cr_3C_2NiCr powder, SEM

2.2. Research methodology

In order to characterize the produced hybrid coatings PEO+HVOF, basic analyses of topography, microstructure and thickness using a scanning electron microscope (SEM) were carried out. The experiments were conducted on polished and included cross - sections of samples. In order to measure the average thickness of the coatings, 6 measurements were carried out and the results were statistically processed. Surface roughness measurements of the coatings were determined using a contact profilometer in accordance with ISO 4288. For every specimen 3 measurements were conducted, the average value calculated, as well as the standard deviations. The instrumented hardness (HIT) assessment was performed according to ISO 14577-4 using an NHT3 nanoindenter with a Berkovich indenter.

3. RESULTS

Metallographic examination revealed that the samples had a compact and dense structure (Fig. 5a-d). However, small pores and microcracks were observed in the microstructure. The presence of partially melted particles in the coating may be caused by the short residence time of the coating powder particles in the HVOF spray flame, which leads to the formation of pores and cracks. The appearance of cracks and voids can lead to reduced coating durability, crack propagation, and eventual delamination. The results of the average thickness, roughness and HIT parameters of the hybrid PEO+HVOF coatings are presented in Table 1.

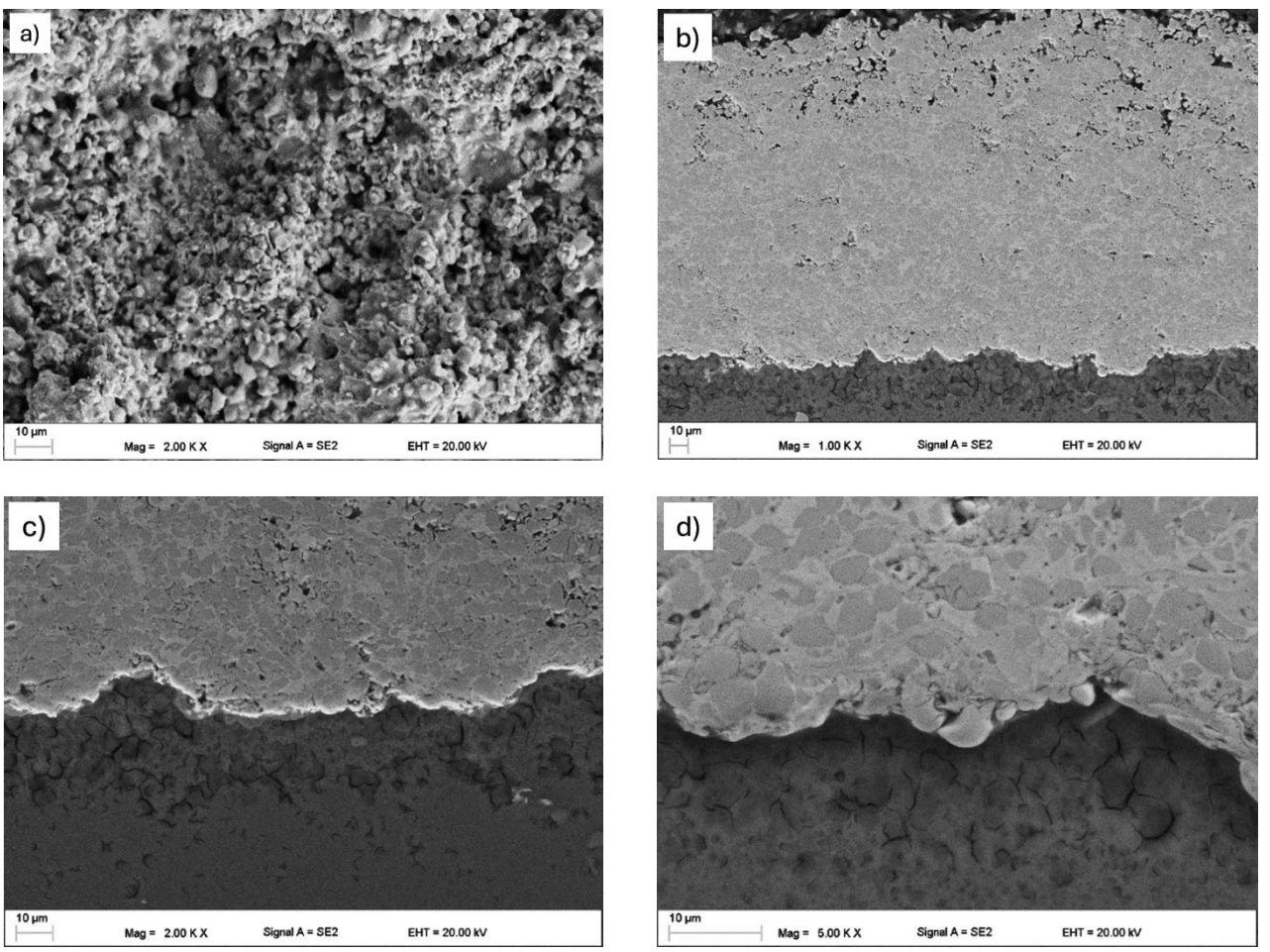

Figure 5. The surface topography of the PEO+HVOF coatings, SEM (a), Cross-section images of the coatings (b-d), SEM

Table 1. The results of the average thickness, roughness and HIT parameters of the hybrid PEO+HVOF coatings

Thickness, µm	**Roughness, µm**		**Instrumental hardness HIT, GPa**
	Ra	Rz	
190.5± 8.2	5.93±0.14	33.77±1.89	7.6 ±0.5

SUMMARY

Magnesium alloys are valued engineering materials due to their low density, excellent strength-to-weight ratio, and recyclability. However, a major limitation of magnesium alloys is their high susceptibility to corrosion, especially in humid environments, which significantly limits their long-term durability. To address this limitation, protective and regenerative coatings are commonly used. These coatings act as physical and chemical barriers, protecting the alloy surface from corrosion and wear, thereby extending component life. Advanced surface treatment methods, including plasma electrolytic oxidation (PEO) and high velocity oxy - fuel spraying (HVOF), are particularly effective because they create dense, adherent, and wear - resistant surface layers. In recent years, engineering practice has increasingly embraced the use of combining various protective coating methods to further enhance the material's reliability, corrosion resistance, and overall performance of magnesium alloy components operating under demanding operating conditions. Hybrid coatings (PEO+HVOF) may be one of the numerous solutions offered by surface engineering.

ACKNOWLEDGMENT

This study was created as part of the project carried out within the framework of project education - Project Base Learning (PBL) with secondary school students as part of the Excellence Initiative - Research University program.

BIBLIOGRAPHY

[1]L. A. Dobrzański, Podstawy Nauki o Materiałach i Metaloznawstwo. Wydawnictwa Naukowo-
Techniczne, 2003.
[2]Drive Sustainability, “Magnesium Disposal and Recycling,” Raw Material Outlook, 2021. [Online]. Available: https://www.rawmaterialoutlook.org/data/node/1518.
[3]ASM International, Properties of magnesium alloys, https://mg.tripod.com/asm_prop. htm, Accessed: 2025-11-06, 2025.
[4]P. Bolanowski and A. Dziadoń, “The influence of the chosen welding technology on the microstructure and selected mechanical properties of welded magnesium alloy AZ91”, English
and Polish, Przegląd Spawalnictwa (Welding Technology Review), vol. 89, no. 3, pp. 40-45,
2017, issn: 0137-298X.
[5]Gems Manufacturing, Protective coatings: Common surface finish treatments for magnesium
alloy components, https://gems-mfg.com/wp-content/uploads/2024/01/PROTECTIVE-COATINGS-COMMON-SURFACE-FINISH-TREATMENTS-FOR-MAGNESIUM-ALLOY-COMPONENTS.pdf, Technical whitepaper, 2024.
[6]“Magnesium alloys: Surface treatments and protective coatings,” in Reference Module in Materials Science, Springer, 2016. doi: 10 . 1007 / 978 - 3 - 319 - 32101 - 1 _ 151

[Online].
Available: https://link.springer.com/rwe/10.1007/978-3-319-32101-1_151.
[7]Total Materia, Protective coatings for magnesium alloys, https://www.totalmateria.com/ en- us/articles/protective- coatings- for- magnesium- alloys- 1, Online technical article, 2023.
[8]M. Esmaily et al., "Protective coatings for magnesium alloys: A review," Metals, vol. 11, no. 7, pp. 1133, 2021. doi: 10.3390/met11071133 [Online]. Available: https://www.mdpi. com/2075-4701/11/7/1133.
[9]International Magnesium Association, Design, fabrication and finishing of magnesium, https:
//www.intlmag.org/page/design_fab_n_fin_ima, Industry resource, 2023.
[10] "Recent advances in protective coatings for magnesium alloys," RSC Advances, 2023. [Online].Available: https://pubs.rsc.org/en/content/articlehtml/2023/ra/d2ra06312c.
[11] S. Gnedenkov, S. L. Sinebryukhov, V. S. Filonina, A. N. Minaev, and S. V. Gnedenkov, "Multifunctional coatings with self-healing effect on magnesium alloy MA8," Theoretical Foundations of Chemical Engineering, vol. 59, pp. 9-19, 2025. doi: 10.1134/S0040579525700034
[Online]. Available: https://link.springer.com/article/10.1134/S0040579525700034.
[12] Y. Zhao et al., "Smart self-healing coatings on biomedical magnesium alloys: A review," Smart Materials in Manufacturing, vol. 1, pp. 100022, 2023. doi: 10.1016/j.smmf.2023.100022
[Online]. Available: https://colab.ws/articles/10.1016%2Fj.smmf.2023.100022.
[13] D. Cuartas - Marulanda, L. Forero Cardozo, A. Restrepo-Osorio, and P. Fernández-Morales, "Natural coatings and surface modifications on magnesium alloys for biomedical applications," Polymers, vol. 14, no. 23, p. 5297, 2022. doi: 10.3390/polym14235297 [Online].
Available: https://www.mdpi.com/2073-4360/14/23/5297.
[14] K. R. Ansari et al., "Current advancements on magnesium alloy coatings for bioimplants: A closer look for biocompatibility and corrosion mitigation," Corrosion Reviews, 2025. doi:
10.1515/corrrev-2024-0083 [Online]. Available: https://www.degruyterbrill.com/ document/doi/10.1515/corrrev-2024-0083/html.
[15] Composites and C. Group, The plasma electrolytic oxidation (PEO) process, https://www.ccg.msm.cam.ac.uk/research- areas/the- plasma- electrolytic- oxidation-peo-
process, Accessed: 2025-11-29.
[16] F. Walsh et al., "Plasma electrolytic oxidation (PEO) for production of anodised coatings on lightweight metal (al, mg, ti) alloys," Transactions of the Institute of Metal Finishing, vol. 87,
pp. 122-135, May 2009. doi: 10.1179/174591908X372482.
[17] S. Sikdar, P. Menezes, R. Maccione, T. Jacob, and P. Menezes, "Plasma electrolytic oxidation (PEO) process - processing, properties, and applications," Nanomaterials, vol. 11, pp. 1375, 2021. doi: 10.3390/nano11061375.
[18] G. Yeshmanova et al., "Effect of electrolyte composition on the formation of peo coatings onaa2024 aluminium alloy," Surfaces and Interfaces, vol. 44, pp. 103 797, 2024, issn: 2468-0230.doi: https://doi.org/10.1016/j.surfin.2023.103797 [Online]. Available: https://www.sciencedirect.com/science/article/pii/S2468023023011598.

[19] M. Ostapiuk, "Corrosion resistance of PEO and primer coatings on magnesium alloy," *Journal of Asian Ceramic Societies*, vol. 9, no. 1, pp. 40–52, 2021. doi: 10.1080/21870764.2020.1847424. [Online]. Available: https://www.tandfonline.com/doi/pdf/10.1080/21870764.2020.1847424.

[20] Science Direct Topics, High velocity oxygen fuel coating, https://www.sciencedirect.com/ topics/materials-science/high-velocity-oxygen-fuel-coating, Overview article on Science Direct, 2025.

[21] A. Miś and M. Majdecka - Bogdanowicz, Powłoki ochronne nanoszone metodą HVOF, https: //pimib.polsl.pl/pliki/imiib/6/Mis_Majdecka.pdf, Conference/academic paper, Silesian University of Technology, 2023.

[22] TWI Global, What is a high velocity oxygen fuel coating? https://www.twi- global. com/technical-knowledge/faqs/what-is-a-high-velocity-oxygen-fuel-coating,Technical FAQ resource, 2024.

TalentDetector

9th January 2026
Gliwice, Poland

DEPARTMENT OF ENGINEERING MATERIALS AND BIOMATERIALS
FACULTY OF MECHANICAL ENGINEERING
SILESIAN UNIVERSITY OF TECHNOLOGY

INTERNATIONAL STUDENTS SCIENTIFIC CONFERENCE

Design and construction of a controlled robotic manipulator

Patryk Pająk[a], Michał Ledwoń[a], Mateusz Zapiór[a], Zofia Kozak[a], Alexandra Kuś[a], Magdalena Szindler[b], Marek Szindler [c]

[a] Student of the Silesian University of Technology
[b] Silesian University of Technology, Faculty of Mechanical Engineering, Department of Engineering Materials and Biomaterials
[c] Silesian University of Technology, Faculty of Mechanical Engineering, Didactic Laboratory of Nanotechnology and Material Technologies, Gliwice, Poland, email: marek.szindler@polsl.pl

Abstract: This paper presents the design and construction of a controlled mobile robotic manipulator developed as a low-cost educational prototype. The proposed system combines a wheeled mobile base with a four-degree-of-freedom robotic arm equipped with a gripper, enabling basic transportation and manipulation tasks. The mechanical structure was designed using aluminum profiles and 3D-printed polyamide components, providing an optimal balance between strength, weight, and manufacturability. The control system is based on the Arduino Uno R4 WiFi platform, allowing integration of DC motors, servomechanisms, and sensors, as well as wireless communication with a mobile control application. The design process included CAD modeling, electronic system simulation in the SimulIDE environment, and experimental validation of the physical prototype. Test results confirmed stable motion, repeatable manipulator operation, and effective handling of objects with a mass of up to 750 g. The developed prototype demonstrates the feasibility of integrating mechanical design, electronics, and software into a functional robotic system and highlights its potential application in robotics and automation education.

Keywords: mobile robotic manipulator, educational robotics, Arduino-based control

1. INTRODUCTION

Modern manufacturing engineering is increasingly shaped by the requirements of flexibility, efficiency, and rapid adaptation to changing production conditions. Within the framework of Industry 4.0, automation is no longer limited to isolated machining or assembly operations, but extends to the integration of material flow, intralogistics, and intelligent control systems. Conventional rigid conveyor-based transport solutions are gradually being replaced by mobile and reconfigurable robotic platforms capable of operating in dynamic production environments [1÷3]. Mobile robotic manipulators represent a promising solution that combines autonomous transportation with basic manipulation capabilities. Such systems enable inter-operational transport while maintaining the ability to perform simple handling or assembly tasks directly at

the workstation. This approach reduces the need for dedicated infrastructure and increases the scalability of manufacturing cells, which is particularly important for small-batch and customized production [3÷6]. As a result, compact and modular robotic platforms have gained significant attention in both industrial research and engineering education [4,7]. In parallel with industrial development, there is a growing demand for low-cost educational robotic systems that allow students to gain practical experience in the integration of mechanics, electronics, and software. Microcontroller-based platforms, such as Arduino, play a crucial role in this context due to their accessibility, extensive community support, and ease of hardware integration. These platforms enable rapid prototyping and provide an effective learning environment for understanding the fundamentals of motion control, sensor integration, and human–machine interaction [7,8].

This article presents the assumptions, design process, and implementation of a controlled mobile robotic manipulator developed as an educational engineering project. The proposed system integrates a wheeled mobile base, a four-degree-of-freedom manipulator arm, and a dedicated control system based on an Arduino microcontroller. The project addresses real-world engineering challenges related to mechanical design, actuator selection, power management, and control logic, while remaining within the constraints of a low-budget prototype. The presented solution demonstrates the potential of simple robotic platforms for both educational purposes and preliminary industrial applications [3, 5, 9, 10].

2. MATERIALS AND METHODOLOGY

The objective of this study was the design and implementation of a microcontroller-based control system for a four-axis robotic manipulator integrated with a mobile linear transport platform intended for inter-operational material handling in a production workstation. The scope of the work included the development of the control system concept, selection of electronic and mechanical components, preparation of the wiring architecture, implementation of control software in the Arduino IDE, integration of a mobile user interface, and execution of functional tests with subsequent optimization of control algorithms for production-oriented operation.

The core control unit of the system is the Arduino Uno R4 WiFi microcontroller, selected due to its 32-bit architecture, increased computational performance, extended RAM and FLASH memory, and integrated wireless communication module. These features enable the implementation of more complex motion control algorithms and wireless communication with a mobile device used as a user interface. Actuation of the linear motion of the platform is achieved using two DC motors Pololu 4744 equipped with 70:1 gearboxes, providing a nominal speed of 150 RPM and sufficient torque for bidirectional movement along a defined axis. Motor control is realized via an L298N dual H-bridge driver, enabling independent speed and direction regulation using PWM signals. The robotic manipulator is driven by four digital servomechanisms: three PowerHD LW-30MG units and one Feetech FT6335M servo, selected based on static torque calculations considering the manipulator mass, payload, and arm length. The Feetech FT6335M, characterized by a high torque of approximately 35.5 kg·cm and a 360° rotation range, is used in the most heavily loaded joint, while the remaining joints and the gripper mechanism are actuated by PowerHD LW-30MG servos. The kinematic structure of the manipulator is defined using Denavit–Hartenberg notation to ensure correct spatial motion description and repeatability. The power supply system is divided into two independent Li-ion battery sections to minimize electromagnetic interference and voltage drops caused by simultaneous operation of actuators. One battery supplies the servomechanisms via a 300 W step-

down converter stabilized at 6.5 V, while the second battery powers the DC motors and the Arduino board through the VIN input. Ultrasonic Grove distance sensors are integrated into the system to continuously monitor the workspace and enable collision avoidance functions in real time. Mechanical components of both the mobile base and manipulator are fabricated using aluminum profiles (10×10×1 mm) and polyamide elements manufactured via SLS 3D printing, allowing rapid prototyping, reduced mass, and sufficient structural stiffness. The completed system was subjected to functional, load, and safety tests, confirming stable operation, accurate positioning, and reliable transport of objects with a mass of up to 750 g under laboratory conditions.

2. RESULTS AND DISCUSSION

The development of the robotic system was carried out in several successive stages, beginning with the design of the mobile base. In the first step, a wheeled linear transport platform was designed to ensure stable motion along a defined axis and to provide a mechanical foundation for the manipulator. The base structure was developed using aluminum profiles and 3D-printed polyamide elements, allowing a compromise between structural rigidity and low mass. Two DC motors with gearboxes were symmetrically mounted to ensure uniform traction and precise bidirectional movement. The completed CAD model of the mobile base is presented in Fig. 1, illustrating the arrangement of drive components, wheels, and mounting points for the manipulator.

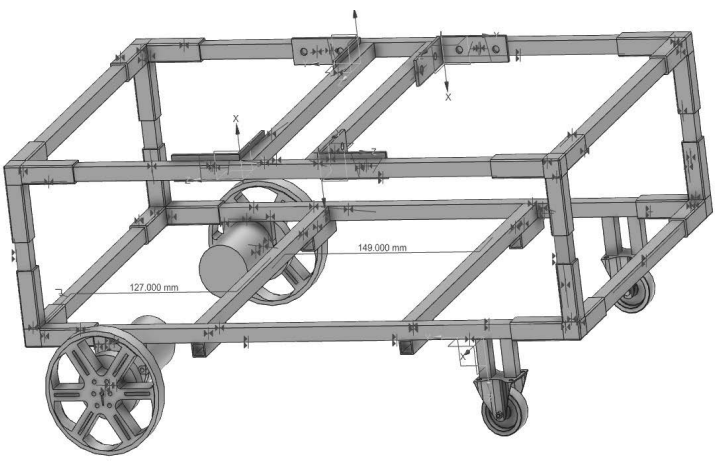

Figure 1. CAD model of the mobile base

In the next stage, a four-degree-of-freedom robotic manipulator was designed and adapted to the dimensions and load capacity of the mobile platform. The manipulator structure was optimized with respect to reach, payload, and torque distribution in individual joints. Servo selection was validated through static load calculations, which ensured reliable operation under laboratory conditions. Particular attention was given to the base joint, which experiences the highest loads during operation. The final CAD model of the manipulator, including joint configuration and gripper mechanism, is shown in Fig. 2. The modular design allows for easy modification and potential future expansion of the system.

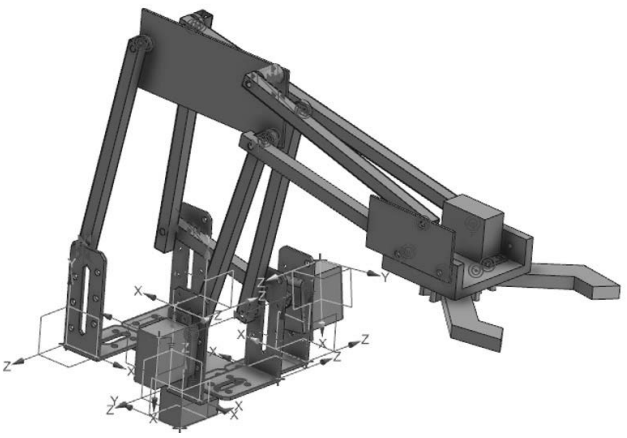

Figure 2 The UV–Vis absorbance spectrum of ZnO:Al (2 at.%) nanoparticles

Following the completion of the mechanical design, the mobile base and manipulator were integrated into a single functional robotic system. Mechanical integration focused on maintaining proper center-of-mass distribution, ensuring structural stability, and enabling unrestricted joint motion. Subsequently, dedicated control software was developed using the Arduino programming environment. The software enables manual control via a mobile interface as well as the execution of predefined motion sequences, coordinating the operation of DC motors and servomechanisms. To verify the correctness of the electrical architecture and control logic, a complete wiring diagram of the system was developed and tested using the SimulIDE simulation environment. The electrical connection scheme, including the Arduino Uno R4 WiFi, motor drivers, servomechanisms, power supply modules, and ultrasonic sensors, is presented in Fig. 3.

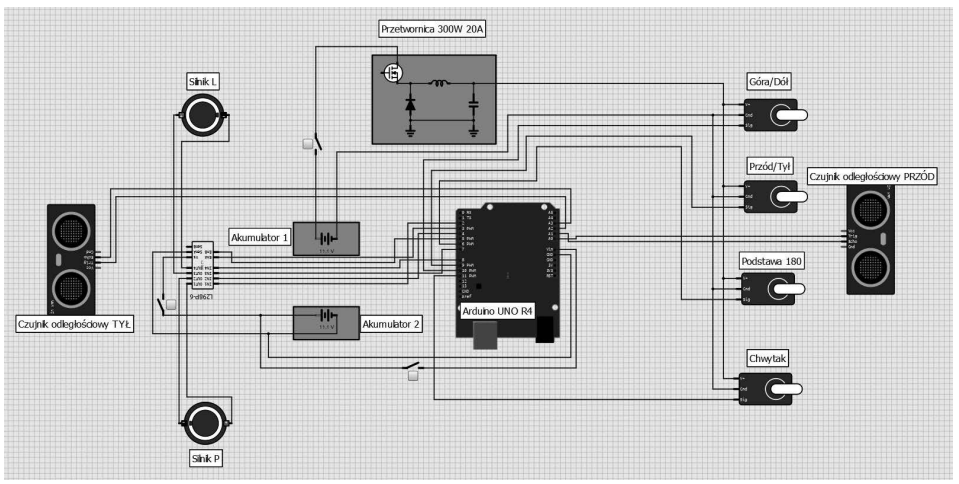

Figure 3 Connection diagram in SimulIDE program

Simulation results confirmed correct signal routing, voltage stability, and safe separation of control and power circuits. Experimental testing of the physical prototype demonstrated reliable mobility, repeatable manipulator motion, and effective handling of objects with a mass of up to 750 g, validating the adopted design assumptions.

4. SUMMARY AND CONCLUSIONS

This paper presented the design and construction of a controlled mobile robotic manipulator developed as a low-cost educational prototype. The main objective of the project was to integrate mechanical design, electronics, and software into a single functional system capable of performing basic transportation and manipulation tasks in a laboratory environment. The proposed solution addresses current trends in flexible manufacturing and intralogistics associated with the Industry 4.0 paradigm. The developed robotic system consists of a wheeled mobile base and a four-degree-of-freedom manipulator equipped with a gripper. The mechanical structure was designed using aluminum profiles and 3D-printed polyamide components, which ensured sufficient strength while maintaining low weight and ease of assembly. The manipulator design, supported by appropriate servo motor selection, enabled stable and repeatable motion during object handling tasks. Experimental tests confirmed that the robot is capable of safely transporting and manipulating objects with a mass of up to 750 g. The control system was implemented using the Arduino Uno R4 WiFi platform, which allowed straightforward integration of actuators and sensors as well as wireless communication with a mobile control application. The developed software supports both manual control and predefined motion sequences, increasing the versatility of the system. Prior to physical implementation, the electrical architecture was validated using the SimulIDE simulation environment, which significantly reduced integration errors and improved system reliability. The results obtained during testing confirm that the adopted design assumptions were met and that the constructed prototype fulfills its intended educational and functional goals. The project demonstrates that relatively simple and inexpensive components can be effectively used to create a mobile robotic manipulator suitable for teaching fundamentals of robotics, mechatronics, and automation. Future work may focus on extending the system with autonomous navigation, advanced sensor fusion, and closed-loop control algorithms to further enhance its applicability in research and industrial-oriented educational projects.

BIBLIOGRAPHY

1. M. Hermann, T. Pentek, and B. Otto, “Design principles for Industrie 4.0 scenarios,” Proc. 49th Hawaii Int. Conf. Syst. Sci., pp. 3928–3937, 2016, doi: 10.1109/HICSS.2016.488.
2. L. Monostori, “Cyber-physical production systems: Roots, expectations and R&D challenges,” Procedia CIRP, vol. 17, pp. 9–13, 2014, doi: 10.1016/j.procir.2014.03.115.
3. B. Siciliano and O. Khatib (eds.), “Robotics and automation: Introduction and overview,” Springer Handbook of Robotics, Springer, 2016, ISBN: 978-3-540-23957-4.
4. J. J. Craig, “Introduction to robotics: Mechanics and control,” Pearson Education, 2005, ISBN: 0201543613
5. R. Siegwart, I. R. Nourbakhsh, and D. Scaramuzza, “Introduction to autonomous mobile robots,” MIT Press, 2011, ISBN: 9780262015356
6. A. De Luca, G. Oriolo, and M. Vendittelli, “Control of wheeled mobile robots: An experimental overview,” RAM, vol. 8, no. 3, pp. 36–52, 2001, doi: 10.1007/3-540-45000-9_8.
7. V.H. Baltazar, “Design of an affordable IoT open-source robot arm for online teaching of robotics courses during the pandemic contingency”, HardwareX vol. 8, pp.1-15, 2020, doi: 10.1016/j.ohx.2020.e00158

8. M. Banzi and M. Shiloh, "Getting started with Arduino," *Maker Media*, 2014, ISBN: 978-1-449-36333-8.
9. F. Rubio, F. Valero, and C. Llopis-Albert, "A review of mobile robots: Concepts, methods, and challenges," Appl. Sci., vol. 9, no. 11, 2019, doi: 10.1177/1729881419839596
10. A. Bauer, D. Wollherr, and M. Buss, "Human–robot collaboration: A survey," Int. J. Humanoid Robotics, vol. 5, no. 1, pp. 47–66, 2008, doi: 10.1142/S0219843608001303.

TalentDetector

9th January 2026
Gliwice, Poland

DEPARTMENT OF ENGINEERING MATERIALS AND BIOMATERIALS
FACULTY OF MECHANICAL ENGINEERING
SILESIAN UNIVERSITY OF TECHNOLOGY

INTERNATIONAL STUDENTS SCIENTIFIC CONFERENCE

Comparative Analysis of Person Re-identification Architectures for Gate-less Access Control on Edge AI Platforms

Marcin Paszkuta[a], Damian Pęszor[b], Bram Heijligers[c], Jakub Antonowicz[d], Kamil Ceglarski[d], Artur Szaboń[d], Alek Pala[d], Dominik Szewczyk[e]

[a] Silesian University of Technology, Faculty of Automatic Control, Electronics and Computer Science, Department of Graphics, Computer Vision and Digital Systems
email: marcin.paszkuta@polsl.pl
[b] Silesian University of Technology, Faculty of Automatic Control, Electronics and Computer Science, Department of Graphics, Computer Vision and Digital Systems
email: damian.peszor@polsl.pl
[c] Breda University of Applied Sciences, Applied Data Science & Artificial Intelligence
email: heijligers.b@buas.nl
[d] Silesian University of Technology, Faculty of Automatic Control, Electronics and Computer Science
[e] Breda University of Applied Sciences, Applied Data Science & Artificial Intelligence

Abstract: This paper presents the design and evaluation of a customer monitoring system for gate-less access control to paid areas. The system was developed for an edge computing module, such as the NVIDIA Jetson Orin Nano, capable of simultaneously processing at least four video streams. The proposed use case assumes a multi-camera configuration covering the entrance area, cashier desk, and restricted zones. The core contribution of the paper is a comparative evaluation of person re-identification (Re-ID) models, namely PCB, OSNet, and TransReID, conducted for the described use case using four camera streams. The models were tested on data representative of real operating conditions under hardware resource constraints while assuming real-time processing. The study aims to identify the most efficient architecture for local, on-device processing while addressing practical challenges such as occlusions and varying lighting conditions. Experimental results indicate that OSNet provides the best trade-off between accuracy and performance for multi-camera tracking in a localized, gate-less environment. The reported results were obtained as part of a Project-Based Learning (PBL) project.

Keywords: person re-identification (Re-ID), edge computing, NVIDIA Jetson Orin, gate-less access control, computer vision, multi-camera system, embedded AI

1. INTRODUCTION

The rapid evolution of Computer Vision (CV) and Artificial Intelligence (AI) has transformed urban security and facility management, enabling a shift from passive surveillance to intelligent,

proactive monitoring. Contemporary service facilities, such as gyms and sports complexes, increasingly seek "frictionless" access control to replace traditional physical barriers. Turnstiles and electronic gates, while effective, create bottlenecks, consume floor space, and involve high maintenance costs. This paper proposes an autonomous, gate-less monitoring system designed to verify customer presence and payment status using advanced Person Re-identification (Re-ID) techniques.

1.1. Background and Motivation

The transition towards gate-less systems aims to enhance user experience and operational efficiency by maintaining a continuous flow of movement. Replacing physical gates with a vision-based system requires a robust digital verification layer. The core of the proposed solution is Multi-Camera Person Re-identification - identifying individuals across multiple non-overlapping camera views. Unlike facial recognition, which is often restricted by privacy regulations or physical obstructions (e.g., masks or angles), Re-ID relies on global and local silhouette features, such as clothing color, texture, body shape, and gait.

1.2. Challenges in Person Re-identification

Re-ID in recreational environments faces several critical challenges. Customers frequently wear similar athletic attire, increasing "inter-class similarity" and complicating differentiation. Furthermore, dynamic movements and frequent partial occlusions in narrow corridors or groups can degrade identification accuracy. Variations in lighting between different facility zones - from sunlit entrances to dimly lit halls - can significantly alter visual descriptors. These factors necessitate the use of advanced neural architectures robust to environmental noise and spatial variations.

1.3. Edge AI and Privacy Considerations

A fundamental requirement of this project is the local deployment of all algorithms on the NVIDIA Jetson Orin Nano platform. Edge computing offers three major advantages:

- **Data Privacy:** Customer images never leave the local network, ensuring GDPR (RODO) compliance.
- **Reliability:** It eliminates latency and dependency on external internet connections, ensuring 24/7 operation.
- **Efficiency:** Due to the shared memory architecture of the Jetson Orin Nano, where GPU memory is shared with the CPU, the available VRAM is limited by operating system usage and system application. This imposes a strict computational budget, requiring the use of highly optimized neural networks in which the trade-off between mAP and FPS must be carefully balanced.

1.4. Objectives and Scope of the Study

This study empirically evaluates which of the three leading Re-ID paradigms - part-based [1], omni-scale [2], or transformer-based [3] - is most suitable for gate-less applications. The specific objectives are:

- To benchmark the training efficiency and accuracy of PCB [1], OSNet [2], and TransReID [3] using the Market-1501 dataset [4].
- To evaluate the inference speed on the NVIDIA Jetson Orin Nano to determine real-time feasibility.

- To analyze model robustness against facility-specific issues, such as similar attire and occlusions.
- To propose an optimized, scalable pipeline for multi-camera tracking.

2. SYSTEM ARCHITECTURE AND OPERATIONAL LOGIC

The transition from physical gates to vision-based monitoring requires a precise spatial configuration of sensors to ensure individuals are registered and verified at critical transit points. The proposed architecture utilizes four strategically positioned cameras, creating a logical chain of events that follows the customer's journey from the entrance to the restricted "paid" zone.

2.1. Spatial Camera Distribution and Monitoring Zones

The facility is divided into two primary environments: the public (unpaid) zone and the restricted (paid) zone. Four cameras are deployed to eliminate blind spots and provide continuous tracking:

- **Camera 1** (Entry Corridor): Located in the unpaid zone; serves as the primary detection point where an initial identity profile (feature vector) is generated for every individual.
- **Camera 2** (Cashier - Silhouette View): Positioned at the service desk; captures high-quality descriptors of the customer during the transaction phase.
- **Camera 3** (Cashier - Hand View): Focused on the counter; detects the specific action of exchanging a receipt or ticket. This provides non-biometric verification of payment.
- **Camera 4** (Access Corridor): Installed at the entrance to the restricted area (paid zone); performs the final re-identification to check authorization before a person proceeds into the facility.

The deployment of these sensors is visualized in Figure 1. By partitioning the facility into zones, the system captures every transition as a discrete event, ensuring overlapping fields of view (FOV) cover the mandatory customer trajectory.

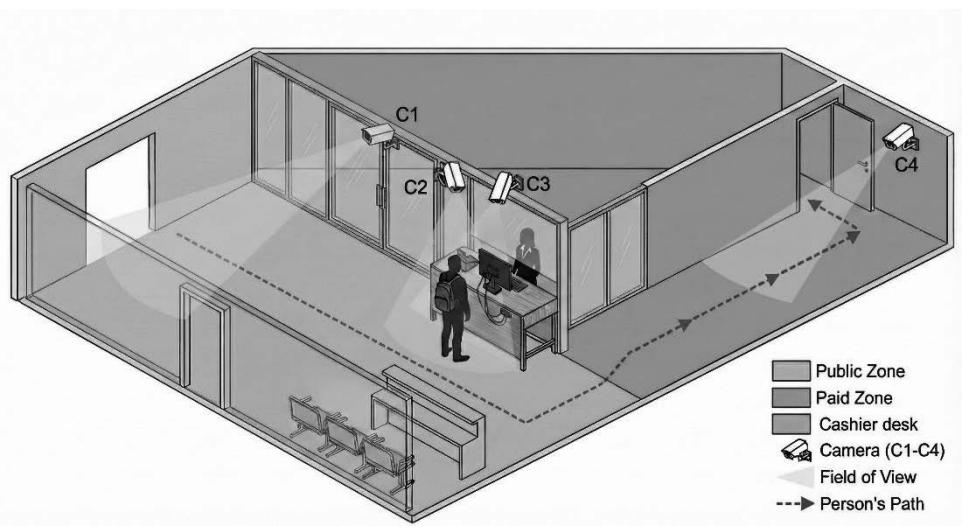

Figure 1. Spatial distribution of cameras (C1-C4) and definition of monitoring zones within the facility. The green dashed line indicates the expected trajectory of a customer through the mandatory checkpoints.

2.2. Multi-Camera Data Pipeline

The data processing pipeline on the NVIDIA Jetson Orin Nano handles asynchronous streams from all four cameras through three main stages: (1) Person Detection, (2) Feature Extraction (embedding generation), and (3) Identity Matching. To maintain real-time performance, the system utilizes a local gallery of descriptors. When a person reaches Camera 4, the system optimizes the search by focusing on recent profiles from Cameras 1 and 2, significantly reducing computational load and the probability of false matches.

2.3. Transaction-to-Identity Matching Algorithm

The system utilizes a state-machine approach to manage customer authorization. Each profile undergoes transitions triggered by camera events, as depicted in Figure 2. A profile is initialized as "Unverified" upon detection by Camera 1. The status is upgraded to "Authorized" only when two conditions are met:

a. the individual is identified at the desk by Camera 2,
b. the transaction is confirmed via receipt exchange detection by Camera 3.

The "Virtual Gate" is executed at Camera 4. As an individual passes through the access corridor, the system performs a high-speed Re-ID query. Authorized individuals are logged silently, while those matched with "Unverified" profiles or not found in the gallery trigger a staff alert. This logic ensures a seamless traffic flow while maintaining high security without physical barriers.

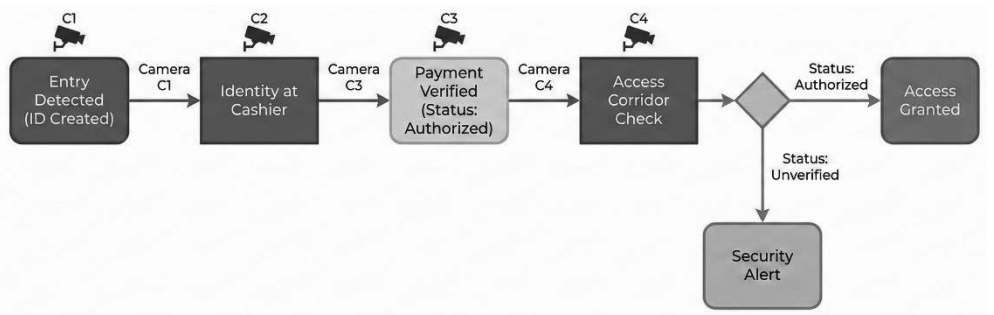

Figure 2. Identity state machine transition logic. The flowchart details the progression of a customer profile from initial creation to the final verification check in the restricted zone, including the alert-triggering mechanism for unauthorized access.

3. EDGE AI IMPLEMENTATION AND OPTIMIZATION

Deploying a multi-camera re-identification system locally requires deep integration between neural network architectures and target hardware. Unlike cloud-based solutions, edge computing demands strict resource management to ensure low latency. This chapter details the technical realization of the gate-less monitoring system on the NVIDIA Jetson Orin Nano platform.

3.1 Hardware Specifications and Constraints

The NVIDIA Jetson Orin Nano was selected for its balance of cost, power efficiency and AI performance, making it suitable for edge-based computer vision applications. The platform is built around a 6-core ARM Cortex-A78AE CPU and an NVIDIA Ampere GPU offered 1024 CUDA cores and 32 dedicated Tensor Cores, delivering up to 67 TOPS of AI performance,

depending on the power limit configuration. However, managing four high-definition video streams on this module introduces several important constraints:

- **Shared Memory Architecture:** The 8 GB LPDDR5 memory is shared between the CPU, GPU, and operating system. Video buffers and intermediate tensors consume a significant portion of the available memory, which limits the space available for neural network parameters. This constraint motivates the selection of lightweight models such as OSNet (2.2M parameters) over more memory-intensive architectures like TransReID.
- **Power Management:** To sustain stable real-time inference performance, the system operates in higher power modes and requires adequate thermal management. Insufficient cooling or power throttling may lead to reduced clock frequencies, resulting in dropped frames and degraded tracking continuity.
- **GPU and Accelerator Utilization**: Unlike earlier Jetson platforms, Jetson Orin Nano features an Ampere-class GPU with 1024 CUDA cores and 32 Tensor Cores, enabling efficient mixed-precision inference (FP16 and INT8). To fully exploit these capabilities, NVIDIA TensorRT is used to optimize computational graphs and maximize GPU and accelerator utilization during inference.

The simultaneous decoding of four video streams corresponding to the entrance, cashier, and verification zones places a noticeable load on the CPU subsystem, while the GPU handles person detection (YOLO) and person re-identification (OSNet) inference tasks.

3.2. Multi-Stream Software Pipeline

The software stack was built using an asynchronous pipeline to prevent bottlenecks during multi-camera processing. The system utilizes:

- **GStreamer Integration:** For efficient hardware-accelerated video decoding (NVDEC), reducing the load on the ARM CPU.
- **Embedding Gallery:** A localized, high-speed database that stores 512-dimensional feature vectors.
- **Task Scheduling:** The GPU executes the YOLO detector at a lower frequency (e.g., every 3rd frame) while the OSNet extractor and tracking logic run continuously to maintain identity persistence.

4. METHODOLOGY AND MODEL SELECTION

The effectiveness of a gate-less monitoring system relies on the robustness of the underlying person re-identification (Re-ID) algorithms. Given the facility's challenges - dynamic movement, similar attire, and occlusions - this research evaluates three distinct neural network paradigms: spatial part-based decomposition, multi-scale feature learning, and global self-attention mechanisms.

4.1. Theoretical Comparison of Re-ID Architectures

Re-identification involves transforming a raw silhouette image into a high-dimensional feature vector (embedding). These embeddings must be invariant to viewpoint and lighting changes while remaining highly discriminative.

4.1.1. Part-based Convolutional Baseline (PCB)

PCB [1] addresses Re-ID through spatial decomposition. It partitions the feature map into N horizontal strips (typically six). Each strip is processed independently to produce a local descriptor. This allows the model to focus on fine-grained details like footwear or torso patterns. However, PCB is sensitive to vertical misalignment and occlusions, which can disrupt the strip-to-body-part correspondence.

4.1.2. Omni-Scale Network (OSNet)

OSNet [2] is engineered to capture features across multiple scales (from small logos to overall body shape). It introduces bottleneck blocks with multiple convolutional streams and unified aggregation gates that dynamically weight different scales. Being exceptionally lightweight (2.2M parameters), OSNet offers a superior trade-off between mAP and inference latency, making it the primary candidate for real-time edge deployment.

4.1.3. Transformer-based Re-ID (TransReID)

TransReID [3] utilizes the Vision Transformer (ViT) architecture to learn global dependencies between image patches via self-attention. It employs a Jigsaw Patch Module (JPM) to encourage robust feature learning and Side Information Embedding (SIE) to mitigate lighting variations. While highly robust to occlusions, its computational complexity poses a challenge for limited-resource hardware.

4.2. Training Protocols and Model Configuration

Models were trained on the Market-1501 dataset [4] using an NVIDIA GeForce RTX 3060 GPU (12GB VRAM) and CUDA 11.8. This environment ensures compatibility with the target Jetson Orin Nano's architecture.

- **PCB:** Trained at 384×192 resolution to ensure sufficient detail for horizontal slicing. It uses a ResNet-50 backbone, SGD optimizer (lr = 0.01, momentum = 0.9), and independent classifiers for each of the six strips.
- **OSNet:** Configured with the osnet_x1_0 architecture at 256×128 resolution. It utilized the Adam optimizer (lr = 0.0003) and a step-based scheduler. Label smoothing was applied to the Softmax Cross-Entropy loss to improve robustness against environmental noise.
- **TransReID:** Employed a ViT-Base backbone at 256×128 resolution. Due to memory constraints, the batch size was set to 16. It utilized a Cosine Annealing Scheduler to stabilize the training of transformer blocks.

4.3. Evaluation Metrics

To evaluate the performance of the selected models and their suitability for the gate-less monitoring system, two categories of metrics were employed: accuracy metrics and efficiency metrics.

4.3.1. Accuracy Metrics

- Rank-1 Accuracy: The probability that the top-ranked gallery candidate is correct. Essential for minimizing false negatives at the virtual gate.
- mean Average Precision (mAP): Measures the overall stability and retrieval quality across all relevant matches.

4.3.2. Efficiency and Feasibility Metrics

- Inference Time (ms) & FPS: Measures throughput on the Jetson Nano to ensure the system can process four simultaneous streams.
- Model Size (MB): The footprint must fit within the Jetson Nano's 8GB shared memory without compromising the OS or other modules (e.g., YOLO detector).

5. EXPERIMENTAL RESULTS AND DISCUSSION

This chapter presents the results of the comparative benchmarking of Person Re-identification architectures and the empirical results of the OSNet model training. The evaluation focuses on the trade-off between identification accuracy and the computational demands of the NVIDIA Jetson Nano platform.

5.1. Comparative Benchmarking of Re-ID Paradigms

To determine the most suitable architecture for the gate-less monitoring system, a literature-based analysis was conducted. Three distinct models were compared: TransReID (Transformer-based), PCB (Part-based), and OSNet (Omni-scale). The results of this comparison are summarized in Table 1.

Table 1. Performance and complexity comparison of Re-ID architectures.

Model	Ref. *Rank-1*	Ref. *mAP*	Complexity	FPS (Jetson)
TransReID	95.0%	88.2%	17.5 G	< 2
PCB	92.3%	77.4%	4.1 G	~ 8 – 10
OSNet	94.8%	84.9%	0.95 G	~ 30

Based on the analysis of the data in Table 1, the **OSNet** architecture was selected for final implementation. This decision was driven by the superior accuracy-efficiency trade-off offered by the model. While TransReID provides the highest absolute precision, its computational complexity (17.5 GFLOPs) results in a throughput below 2 FPS, which is insufficient for real-time monitoring. In contrast, OSNet maintains a Rank-1 accuracy nearly identical to the state-of-the-art (SOTA) models while requiring significantly fewer operations (0.98 GFLOPs). This computational lightness is a critical criterion, enabling the system to process four simultaneous camera streams on the NVIDIA Jetson Orin Nano.

5.2. Empirical Training Results for OSNet

Following the selection of the architecture, the OSNet model was trained using the Market-1501 dataset. The training focused on validating the model's convergence speed and its practical effectiveness. The progress of the empirical training phase is presented in Table 2.

Table 2. Empirical training progress and accuracy of the OSNet model.

Training phase	Epoch	Rank-1(%)	mAP(%)
Initial	10	88.1%	69.7%
Refined	20	90.6%	74.5%
Reference	(Ref)	94.8%	84.9%

The results confirm the rapid convergence of the OSNet model, which achieved 88.1% Rank-1 accuracy within 10 epochs due to effective transfer learning. Refinement with a learning rate scheduler increased performance to 90.6% Rank-1 and 74.5% mAP at epoch 20. This outcome represents 95.6% of the theoretical SOTA limit, providing a sufficient baseline for the system's functional logic. Further training was omitted as the diminishing returns in accuracy would not justify the additional computational time and energy consumption.

6. CONCLUSIONS

The project successfully demonstrated that a vision-based, gate-less monitoring system is a viable and efficient alternative to traditional physical access control. By employing the OSNet architecture, the system achieved a high identification accuracy of 90.6% Rank-1 while maintaining a real-time throughput of 30 FPS on the resource-constrained NVIDIA Jetson Orin Nano platform. The low computational complexity of the model (0.98 GFLOPs) proved critical, allowing the GPU to handle the asynchronous data pipeline from four cameras and the primary YOLO detection module in parallel. This implementation confirms that localized Edge AI can effectively balance data privacy with high operational performance. The resulting architecture provides a scalable, "frictionless" solution for modern facilities, ensuring security and revenue integrity without the need for physical barriers.

BIBLIOGRAPHY

1. Y. Sun, L. Zheng, Y. Yang, Q. Tian, S. Wang, Beyond Part Models: Person Retrieval with Refined Part Pooling (and A Strong Convolutional Baseline), Proceedings of the European Conference on Computer Vision (ECCV) (2018) 480-496
2. K. Zhou, Y. Yang, A. Cavallaro, T. Xiang, Omni-Scale Feature Learning for Person Re-Identification, Proceedings of the IEEE/CVF International Conference on Computer Vision (ICCV) (2019) 3702-3712.
3. S. He, H. Luo, P. Wang, F. Wang, H. Li, W. Jiang, TransReID: Transformer-based Object Re-Identification, Proceedings of the IEEE/CVF International Conference on Computer Vision (ICCV) (2021) 15013-15022.
4. L. Zheng, L. Shen, L. Tian, S. Wang, J. Wang, Q. Tian, Scalable Person Re-identification: A Benchmark, Proceedings of the IEEE International Conference on Computer Vision (ICCV) (2015) 1116-1124

TalentDetector

9th January 2026
Gliwice, Poland

DEPARTMENT OF ENGINEERING MATERIALS AND BIOMATERIALS
FACULTY OF MECHANICAL ENGINEERING
SILESIAN UNIVERSITY OF TECHNOLOGY

INTERNATIONAL STUDENTS SCIENTIFIC CONFERENCE

Numerical analysis of the material selection influencing the mechanical properties of a wood chipping tool

Daniel Pella[a], Filip Bejm[a], Milena Pawlas[b], Joanna Tokarz[b], Adam Zygłowicz[b], Jakub Polis[a], Amadeusz Dziwis[a], Aagata Śliwa[a], Marek Sroka[a], Ján Komendák[c], Samuel Zachar[c], Miroslava Tavodova[c]

[a] Silesian University of Technology, Faculty of Mechanical Engineering, Department of Engineering Materials and Biomaterials
email: dp316755@student.polsl.pl, fb316756@student.polsl.pl, jakub.polis@polsl.pl, amadeusz.dziwis@polsl.pl, agata.sliwa@polsl.pl, marek.sroka@polsl.pl
[b] Silesian University of Technology, Institute of Physics
email: mp317594@student.polsl.pl, jt317600@student.polsl.pl, az317598@student.polsl.pl
[c] Technical University in Zvolen, Faculty of Technology, Department of Manufacturing Technology and Quality Management
email: xkomendakj@is.tuzvo.sk, xzachars@is.tuzvo.sk, tavodova@tuzvo.sk

Abstract: Wood chipping equipment is primarily used to process low-grade timber and residual biomass, including sawmill by-products and logging waste. These machines fragment wood perpendicular and parallel to the grain to generate chips that serve as raw material in the energy, chemical processing and wood-based industries. The size of the chips depends on the application, ranging from coarse fractions for fuel to finer particles required in fibreboard and paper manufacturing. The most widespread design is the drum chipper, which operates with rotating drums equipped with blades. Their performance is comparable to that of disc chippers, particularly when producing chips intended for combustion or board fabrication. The cutting blade is the essential working element of such machines and must remain sharp and resistant to wear under demanding conditions. Blades are usually made from stainless steel, structural tool steel, or advanced powder metallurgy composites. Each of these materials has its own advantages in terms of hardness, toughness, and corrosion resistance. The mechanics of the cutting process involve defined forces and cutting angles, which must be optimised to efficiently form chips and prolong the operational lifespan of the blade.

Keywords: wood chippers; chopping blades/knives; material properties; mechanical analysis; programming; chip.

1. CHIPPING MACHINES

Wood chipping is carried out using disc, screw and drum chippers (Figure 1), which produce wood chips. These chips are then used in the paper and furniture industries, as well as in the

production of biomass. They are later used to produce paper, pulp, biomass, pellets, artificial fertiliser or boards for the furniture industry. Chipping machines can also be used to chip soft and frozen wood, recycle wood, and mix hard tropical wood with waste wood and sawmill residues [1-3].

Figure 1. Wood chips [3]

Chipping machines are devices used for cutting wood without creating chips. They employ the cutting action of knives set at an angle to the grain to reduce the material to the required thickness, and the shape of the chips is determined by the profile of the wedge knife. Chipping machines can be classified according to their technical design, their place within the machine system, and their purpose and use. According to the type of chipping mechanism, chippers are divided into disc, screw, and drum types [2, 4].

1.2 Drum chippers

A drum wood chipper (Figure 2) replaces the disc with a cylindrical drum, which is the main cutting component. This drum, which is 45 to 152 mm long depending on the model, has blades bolted straight to its surface. Although it spins more slowly than a disc, at 300 to 800 RPM, it makes up for this with brute force. As the drum turns, the blades grab the wood and pull it into the machine, slicing it against a fixed anvil to produce wood chips. This continuous feeding action makes these chippers ideal for high-volume jobs. Unlike disc wood chippers, drum models have wide, roomy hoppers — perfect for bulky materials. Most industrial drum wood chippers also come with hydraulic feed systems. These systems adjust the speed at which wood enters the machine based on its density, preventing jams when processing tough oak logs or gnarled branches [5].

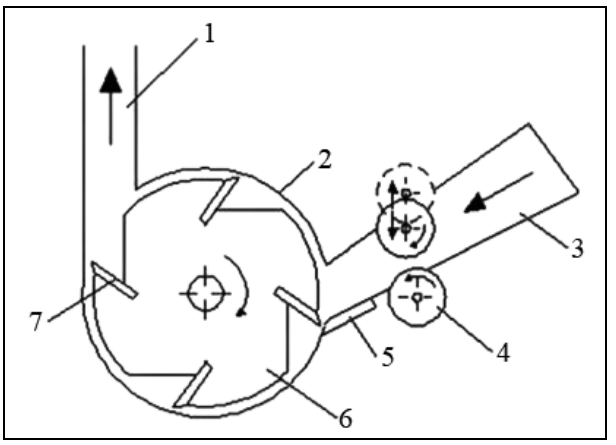

1 – chip ejector;
2 – drum cover;
3 – material inlet;
4 – feed roller;
5 – counter blade;
6 – drum;
7 – chipping knife.

Figure 2. Schematic representation of a drum wood chipper [6]

Advantages of a drum wood chipper [5]:

- Heavy-duty capacity: The drum's large surface area and consistent feed rate enable it to process up to 50% more wood per hour than a disc chipper. Industrial models can handle over 10 tons per hour, making them ideal for large sawmills or biomass plants that cannot afford slowdowns.
- Takes on large, irregular wood: These machines can process logs with a diameter of up to 61 mm with ease. Gnarled branches, thick hardwoods and even whole tree trunks (after debarking) won't jam them. The hydraulic feed system adapts to the size of the wood, ensuring a smooth process.
- Built for all-day use: Drum chippers are made with thick steel and reinforced parts. They are designed to run for over 8 hours a day, 5 days a week, in tough industrial settings. You won't wear one out easily.
- Cost-effective for big jobs: Yes, the initial cost is higher. However, their speed and efficiency reduce your processing costs per tonne. If you’re chipping large volumes daily, you'll see a return on investment (ROI) faster than with a disc model.

Figure 3 shows an example of such a machine.

Figure 3. Cutting machine PEZZOLATO H780/200 [7]

2. KNIVES FOR CHOPPING WOOD

In wood chipper construction, the chopping knives are essential for mechanically cutting wood. The wood chip production process involves reducing and fragmenting various types of wood and wood residues. These include coniferous and deciduous trees such as pine, poplar and Chinese fir, as well as small-diameter logs, tree stumps, branches, bamboo, veneer and material produced during secondary logging. As well as wood, plant stems without wood fibres, such as cotton stalks and other agricultural residues, are also used for chipping. The resulting wood chips have a wide range of applications. They are most commonly used as primary fuel in heating plants, but they also play an important role in agriculture and other industries, serving as a renewable energy source or raw material for technological processes [8].

2.1 chopping knives construction and chopping process

There is a wide range of shredder types, and the construction parameters of the chopping knives — especially their width, height, and thickness — are decisive factors that influence the device's functionality. The knives are manufactured in a variety of standard sizes, with widths of 175 mm, 215 mm or 295 mm, depending on the chipper model. The knife height is variable and adapts to the clearance between the machine's blades. In addition to the geometric dimensions, the cutting parameters that directly influence the wood chipping process must also be considered. Figure 4 illustrates the cutting forces and angles of the cutting edge during wood chipping. The chopping knives are the main working element, removing material from the workpiece and forming chips. This diagram is essential for understanding the cutting mechanism and subsequently optimising cutting conditions. Setting the cutting angles correctly and controlling the acting forces are key to extending tool life, achieving the desired surface quality, and increasing the efficiency of the entire machining process [6].

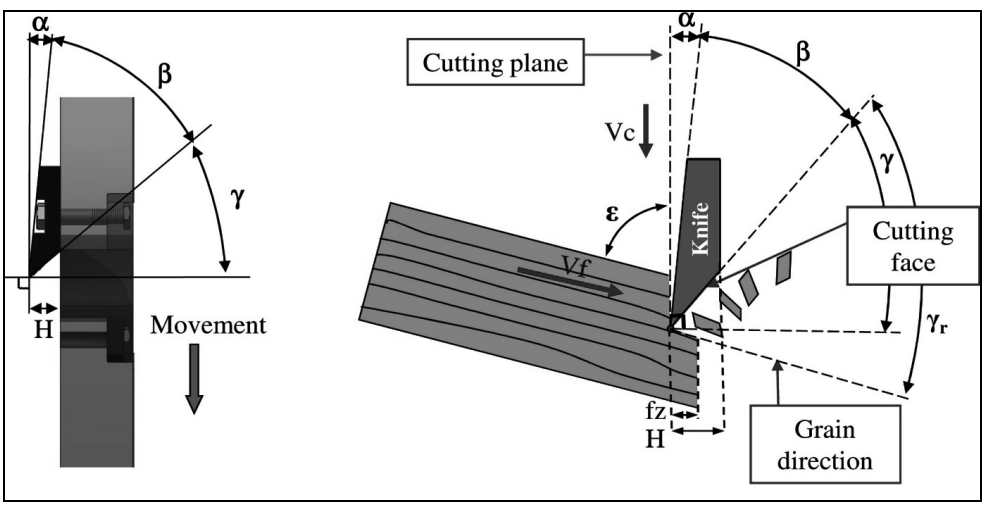

Figure 4. Disc chipper cutting forces and angles [9]

2.2 materials used for chopping knives

Cutting knives are usually made of stainless or structural tool steel with increased hardness. However, depending on the type of wood being processed and the operating conditions, other materials may also be used. The fundamental requirement is for the blade to remain sharp and wear-resistant over a long period of time, thereby ensuring consistent quality and efficiency in the wood chip production process. Cutting knives can be classified according to their material

composition and physical and chemical properties, such as wear resistance, strength, hardness, abrasion resistance, corrosion resistance and resistance to abrasive environments. Each material has its own advantages and disadvantages, so choosing a suitable blade depends on the specific requirements of the production process and the type of wood being processed. For example, carbon steel knives are inexpensive and have good cutting properties, but they wear out quickly when in contact with hard or abrasive materials. Alloy stainless steel knives are highly corrosion-resistant, allowing them to be used in humid environments. However, they have lower hardness and thus lower wear resistance. The most durable category comprises knives manufactured using powder metallurgy technology. These knives are characterised by high hardness, a long service life and excellent cutting properties, making them ideal for demanding conditions. However, they are more expensive [10, 11].

3. MATERIALS AND METHODOLOGY

The examined element is a wood chopping knife made of X48CrMoV8-1-1 tool steel, whose chemical composition and material properties are presented below in Table 1 and Table 2.

Table 1. Chemical composition of X48CrMoV8-1-1 steel [12].

Element	Min [%]	Max [%]
C	0.45	0.50
Cr	7.3	7.8
Mo	1.3	1.5
V	1.3	1.5
Si	0.7	0.9
Mn	0.35	0.45
P	-	0.02
S	-	0.005

The aim of this analysis is to assess how a standard load of 3 603 N on the surface of the chopping knife affects it during use. Furthermore, to determine the workpiece's strength beyond its baseline loading, the model will also be tested under increased forces of 4143 N (i.e. +15% from the initial value) and 4683 N (i.e. +30% from the initial value).

Table 2. Mechanical and physical properties of X48CrMoV8-1-1 steel [13].

Property	Value
Young's modulus [GPa]	207
Poisson's ratio	0.28
Shear modulus [GPa]	79
Density [kg/m^3]	7750
Tensile strength [MPa]	1135
Yield strength [MPa]	935
Coefficient of thermal expansion [K^{-1}]	11*10^{-6}
Thermal conductivity [W/(m*K)]	14
Specific heat [J/(kg*K)]	440

4. CAD GEOMETRIC MODEL

A digital model of wood chopping knife was prepared in SOLIDWORKS to carry out strength check using a computer-based simulation. The crafted knife model is shown in Figure 5a.

5. BOUNDARY CONDITIONS

In the computer simulation, the following setup conditions were applied:

- A finite element mesh was laid over the knife model (Figure 5b),
- The model was then subjected to forces of 3603 N, 4143 N and 4683 N, each directed onto the cutting edge of the blade at an angle of 36°,
- The location where the force is applied, along with the way the knife was immobilized is illustrated in Figure 5c.

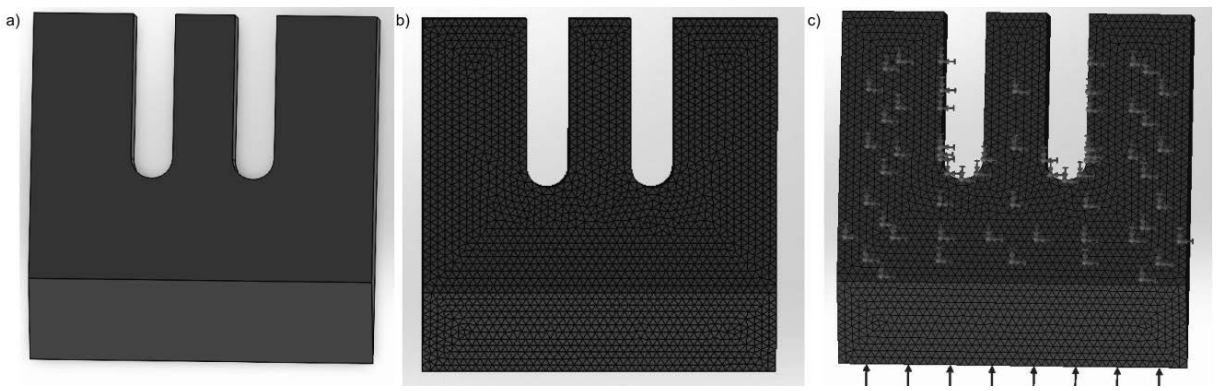

Figure 5. CAD model of wood chopping knife (a); with laid over finite element mesh (b); with laid over finite element mesh, visible direction of forces and immobilized knife geometry (c)

6. ANALYSIS OF RESULTS

The numerical stress assessment was carried out according to the Huber-Mises hypothesis. Once the part was subjected to loading, stress maps were generated, with their magnitudes given in MPa. Figure 6 presents a spread of stresses developed under the applied loads.

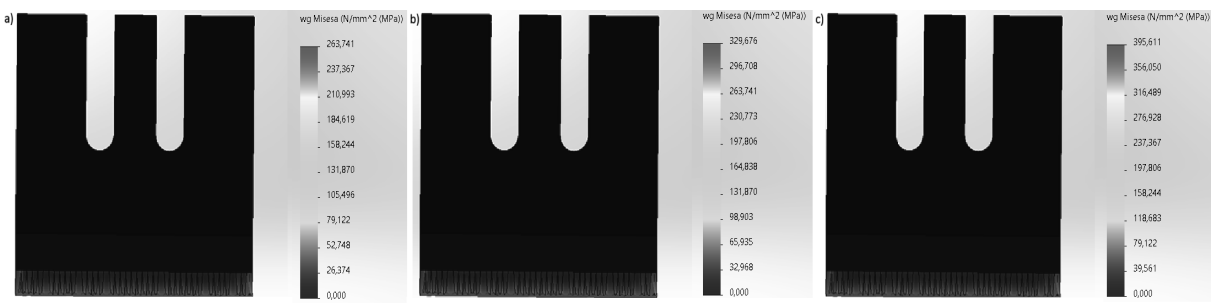

Figure 6. Huber-Mises stress reduction distribution of wood chipping knife at a force of (a) 3603 N, (b) 4143 N and (c) 4683 N

In Figure 7, the simulated displacement contours are depicted, providing a visual representation of how the structure responds to the applied forces. The purpose of this computational step was to quantify the deformation behavior and identify the zones of maximum displacement within the knife geometry.

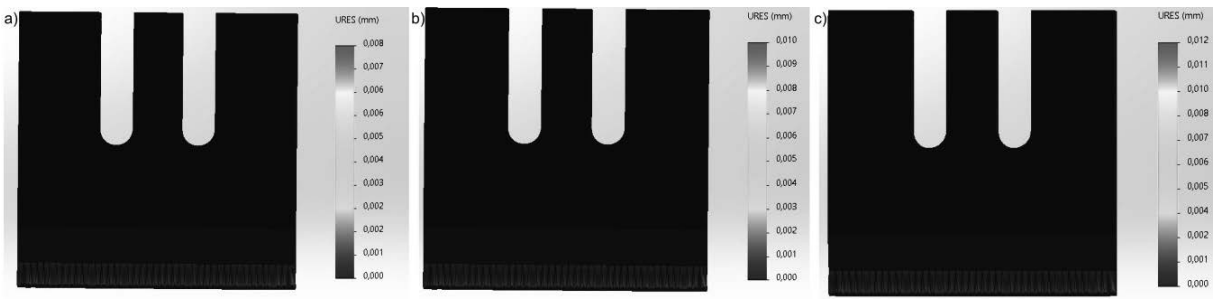

Figure 7. Displacement distribution of wood chipping knife at a force of (a) 3603 N, (b) 4143 N and (c) 4683 N

In the final computational phase, the analysis focused on pinpointing the critical force responsible for initiating the deformation process. The resulting equivalent strain distribution, visualized in Figure 8, corresponds to the maximum load at which the axis begins to deviate from its initial geometry.

Figure 8. Equivalent deformation of wood chipping knife at a force of (a) 3603 N, (b) 4143 N and (c) 4683 N

The overall results of the simulations performed are shown in Table 3.

Table 3. Summary of overall results from computer simulations carried out

Used force [N]	Maximum stress value [MPa]	Maximum displacement [mm]	Maximum deformation value
3603	263.741	0.008	$3*10^{-3}$
4143	329.676	0.010	$4*10^{-3}$
4683	395.611	0.012	$4*10^{-3}$

7. CONCLUSION

The conducted numerical strength analysis demonstrates a distinct correlation between the magnitude of applied loading and the resulting mechanical response of the examined

component. As the force progressively increases from 3603 N to 4683 N, a proportional escalation in maximum stress values is observed, ranging from 263.741 MPa to 395.611 MPa, while the maximum displacement of the blade exhibits a corresponding increment from 0.008 mm to 0.012 mm. This linear relationship extends to both deformation and displacement parameters, indicating predictable material behavior under varying load conditions.

The X48CrMoV8-1-1 tool steel employed in this application typically exhibits a tensile strength of about 1000–1200 MPa and a yield strength in the range 900–1000 MPa, depending on heat treatment. The highest stress recorded in the simulation is approximately 395.611 MPa, which is markedly lower than the material's yield limit (>900 MPa). Consequently, under the examined loading conditions the knife remains in the elastic regime and is not expected to undergo permanent deformation or to fracture. (This corresponds to a safety margin of roughly 2.27–2.53× relative to the yield strength).
The maximum deflection of the blade remains confined to 0.012 mm even under the most severe loading scenario of 4683 N. This minimal displacement indicates exceptional geometric stability of the cutting edge throughout operational cycles, thereby ensuring consistent cutting performance and reducing energy dissipation attributable to elastic deformation.
The equivalent strain values obtained from the finite element analysis reveal magnitudes of 3×10^{-3} for the baseline force of 3603 N, 4×10^{-3} for the intermediate load of 4143 N, and 4×10^{-3} for the maximum force of 4683 N. These deformation metrics, while remaining within the millimetric scale, warrant attention as they indicate the material's response characteristics under progressive loading.
The comprehensive simulation study validates that the wood chopping knife fabricated from X48CrMoV8-1-1 steel, when subjected to forces within the 3600-4700 N range, maintains structural integrity with deformations and displacements constrained to acceptable levels. This behavior ensures cutting edge stability and contributes to extended operational longevity of the blade component.

ACKNOWLEDGMENTS

The authors are grateful for the financial support of the Slovak Research and Development Agency under the Contract no. APVV-21-0180.
This study was conducted as part of the project-oriented education - PBL, in the XIII competition within the Excellence Initiative - Research University program.

BIBLIOGRAPHY

1. PILANA®, 2025 *Sekací nože a díly.* Online. 22.12.2025. Available at: https://www.pilanagroup.com/cs/sekaci-noze-a-dily
2. KOVÁČ, J., Jozef KRILEK, J. JOBBÁGY, DVOŘÁK, J. 2017 *Technika a mechanizácia v lesníctve: vysokoškolská učebnica*. Zvolen: Technická univerzita vo Zvolene, 2017. ISBN 978-80-228-3021-8.
3. What is wood chips? Online. 22.12.2025. Available at: https://www.zerobiomass.co.uk/en/buyers-guides/what-is-biomass/what-is-wood-chip

4. MIKLEŠ, M. 2011 *Lesnícke stroje a zariadenia*. Zvolen: Technická univerzita vo Zvolene, 2011. ISBN 978-80-228-2302-9.
5. Disc Wood Chipper vs Drum Wood Chipper – Complete Selection Guide. Online. 22.12.2025. Available at: https://huaxinwoodmachinery.com/disc-wood-chipper-vs-drum-wood-chipper-complete-selection-guide/
6. KRILEK, J., et.al. 2024 Research of chipper knives with a modified cutting edge for the production of dimensionally uniform wood chips. BioResources 19(2), 3653-3667.
7. KRILEK, J., ŤAVODOVÁ, M. DRBÚL, M. 2023 Research on Chipping Knives for the Processing of Dendromass. Pub. RAM – Verlag. 135 p.
8. PILANA®, 2025. Chipper knives and parts. Online. 22.12.2025. Available at: https://www.pilanagroup.com/en/chipper-knives-and-parts
9. RÉMI G., SÉBASTIEN A., PIERRE J. M., 2014 A dynamic measurement of a disc chipper cutting forces, Biomass and Bioenergy, Volume 64, 2014, Pages 269-275, ISSN 0961-9534, Available at: https://www.sciencedirect.com/science/article/pii/S0961953414001147
10. *Huangshi Han Industry Co., Ltd, 2025.* Online 8.12.2025. Available at: (https://www.hantoolsteel.com/best-steel-for-wood-chipper-blades/)
11. BRENNDÖRFER, M., DREINER, K., KALTSCHMITT, M. and SAUER, N. 1994. Energtische Nutzung von Biomasse, Kuratorium für Technik und Bauwesen in der Landwirtschaft (KTBL), Darmstadt, 149 p.
12. https://virgamet.pl/oferta/1-2360-x48crmov811-stal-narzedziowa - access date 22.12.2025.
13. Solidworks material base.

TalentDetector

9th January 2026
Gliwice, Poland

DEPARTMENT OF ENGINEERING MATERIALS AND BIOMATERIALS
FACULTY OF MECHANICAL ENGINEERING
SILESIAN UNIVERSITY OF TECHNOLOGY

INTERNATIONAL STUDENTS SCIENTIFIC CONFERENCE

Numerical analysis of stresses occurring in a motorcycle belly pan during a fall

Daniel Pella[a], Filip Bejm[a], Milena Pawlas[b], Adam Zygłowicz[b], Joanna Tokarz[b], Jakub Polis[c], Agata Śliwa[c], Marek Sroka[c]

[a] Student of Silesian University of Technology, Faculty of Mechanical Engineering
email: dp316755@student.polsl.pl, fb316756@student.polsl.pl
[b] Student of Silesian University of Technology, Institute of Physics
email: mp317594@student.polsl.pl, az317598@student.polsl.pl, jt317600@student.polsl.pl
[c] Silesian University of Technology, Faculty of Mechanical Engineering, Department of Engineering Materials and Biomaterials
email: jakub.polis@polsl.pl, agata.sliwa@polsl.pl, marek.sroka@polsl.pl

Abstract: The objective of this study was to design and present a simulation of the permissible mechanical stresses occurring in a motorcycle belly pan resulting from a vehicle capsize. The design and analysis were conducted using SolidWorks software. The project utilized three distinct engineering materials: EN AW-3003 alloy, polycarbonate (PC), and acrylonitrile butadiene styrene (ABS) copolymer.

Keywords: mechanical stresses, design, motorcycle belly pan.

1. INTRODUCTION

Although the motorcycle belly pan is often fitted purely for cosmetic reasons, experimental and numerical studies show that, when properly shaped and integrated, it can also influence the flow beneath the machine. Wind tunnel tests and complementary computational fluid dynamics (CFD) on scale models have demonstrated that belly pan geometries can smooth the underfloor flow, reduce the size of the low-pressure wake, and produce measurable reductions in overall drag. Reported improvements in the cited study ranged from roughly 7–14%, depending on the shape and setup. However, the aerodynamic benefit depends heavily on the contour of the belly pan, ground clearance, and how the pan interacts with other components, such as the wheels, exhaust routing, fairings, and the rider. Therefore, gains observed in one installation do not automatically transfer to another [1-4].

Since underbody devices do not operate in isolation, the best approach, according to experimental and computational fluid dynamics (CFD) research, is to consider underbody shielding as part of a coordinated aerodynamic package rather than as a standalone 'performance enhancement solution'. The geometry of the underbody cover interacts non-linearly with the wheel arches, fairings, exhaust systems and engine housings. Therefore, the

net effect of using an underbody cover depends heavily on the vehicle's overall installation and operating conditions. Therefore, comparative experimental and CFD studies recommend a system-level approach to design and verification. For instance, an underbody cover that reduces drag in one configuration could be ineffective or even detrimental in another if it exacerbates vortex formation or obstructs critical cooling or ventilation paths. This conclusion aligns with literature on 3D fairings, which revealed that an integrated aerodynamic kit can significantly reduce the drag coefficient of a model (from ~0.691 without a fairing to ~0.318 with one). This demonstrates that underbody devices are most effective when coordinated with the rest of the bodywork, rather than being used in isolation. Finally, there is little peer-reviewed evidence that underbody covers reliably improve engine cooling in production motorcycles. Studies on engine compartment openings and underbody flow primarily focus on pressure and drag effects [1-4].

Finally, practical and high-fidelity studies indicate that underfloor treatments are most effective when combined with deliberate flow-control measures and validated with scale-resolving simulations: small devices such as vortex generators or controlled undertray shaping can delay separation, re-energise boundary layers and improve the performance of an underfloor panel in ways that a plain cosmetic cover cannot. Large-eddy and scale-resolving CFD work show the underbody wake is highly structured and dominated by interactions among wheel wakes, the vehicle base and undertray geometry, so small changes in undertray shape or clearance can produce non-intuitive effects on the rear wake and base pressure. Lessons from dedicated undertray development in motorsport and student Formula programmes further emphasise that underfloor elements can be tuned to produce useful aerodynamic forces (or to reduce drag) but only when packaged with diffusers, exit geometries and ride-height control as part of a system-level design loop. For motorcycles specifically, recent comprehensive CFD studies underline the dominant role of the front fairing, wheels and rider in setting the global flow field, implying that any belly-pan modification must be assessed within whole-vehicle simulations to avoid adverse interactions. Taken together, these practical studies recommend that designers treat belly pans as active components in a validated aerodynamic development process (prototype testing + scale-resolving CFD), rather than as cosmetic add-ons — especially when thermal or packaging constraints are present [5-9].

The belly pan was developed to fulfil the functional requirements of protective motorcycle components (Figure 1). The material options included the aluminium alloy EN AW-3005, polycarbonate (PC) and the acrylonitrile–butadiene–styrene copolymer (ABS). A high-fidelity CAD model was then created in SolidWorks based on the material specifications to ensure an accurate fit for the Honda Varadero 125 [10].

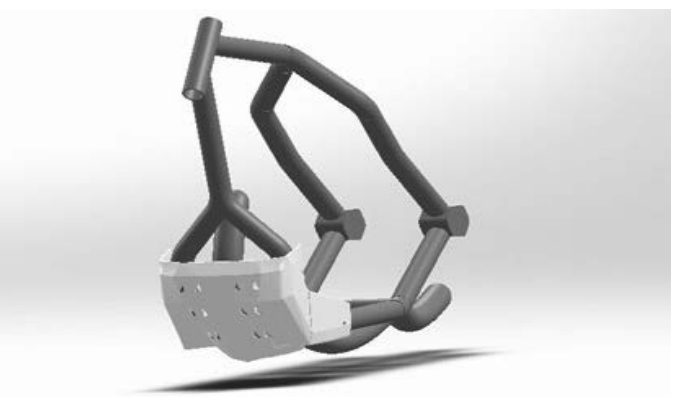

Figure 1. Appearance of the motorcycle belly pan.

2. MODELIGN THE MOTORCYCLE BELLY PAN

The geometric model of the belly pan reflects its actual dimensions. The auxiliary line on the front side was set to 200 mm, and the lower auxiliary line to 300 mm. An appropriate divergence angle between the lines was also maintained. Modeling began with the creation of six planes at roughly equal intervals (three planes on each of the auxiliary lines described above). These planes were used to generate six profile sketches along which the component was extruded/lofted. Additional reference lines were created to define the positions of the motorcycle frame tubes (Figure 2).

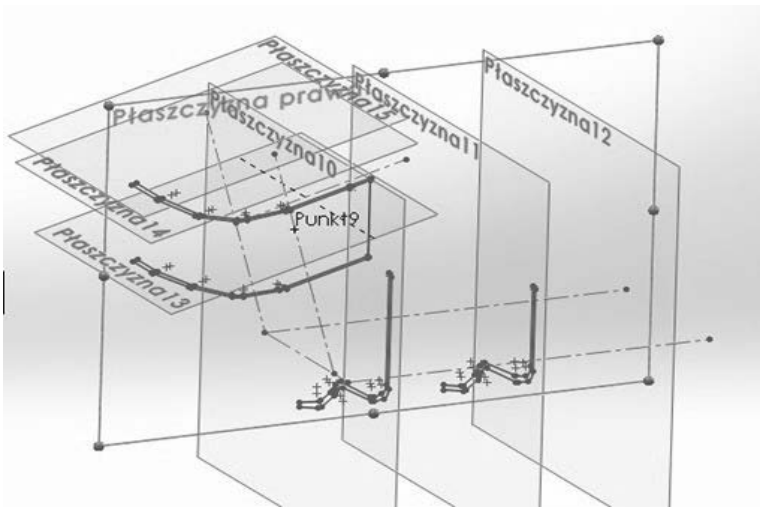

Figure 2. Reference geometry provided as planes.

The profile sketches used to create the solid body were drawn on one symmetrical side of the planes. After extruding that portion of the model, a mirror feature was applied to produce a complete, symmetrical component. Profile shapes were created with the Line tool and sketch fillets. A uniform wall thickness of 4 mm was maintained throughout. Once the full shape was complete, mounting points were added as bolt holes. The external holes were counterbored to a depth of 8 mm; the holes themselves have a diameter of 4.5 mm, so the bolt heads do not protrude beyond the belly pan's outer surface (Figures 3–4).

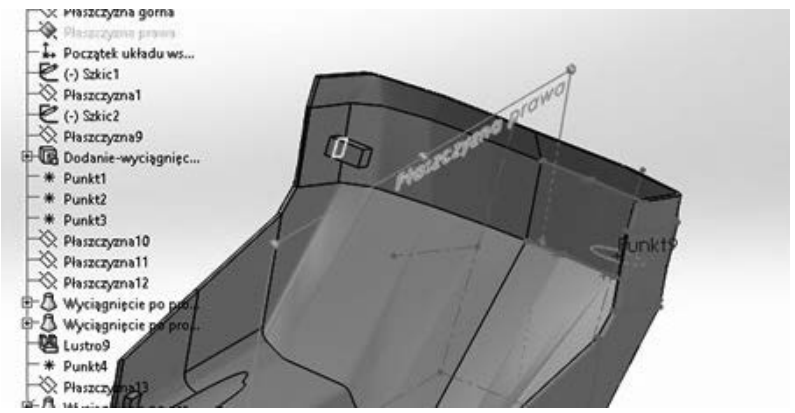

Figure 3. Modeling of the clamping element.

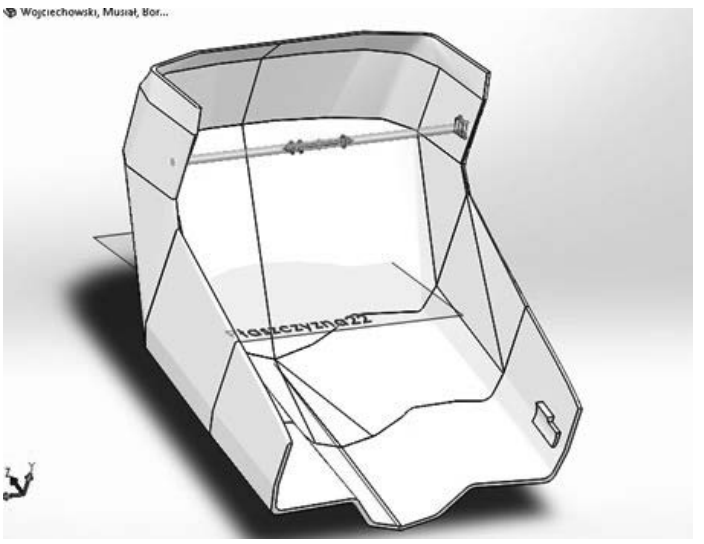

Figure 4. Making holes for the fixing screws.

Frontal openings were incorporated into the design to augment visual appeal and facilitate a degree of cooling airflow (Figure 5). Assembly to the frame was achieved with four standardized M4 hex-socket screws (l = 55 mm), corresponding washers (inner diameter 4.3 mm) and four M4 nuts. Standardized fasteners were obtained from the SolidWorks standard parts library,

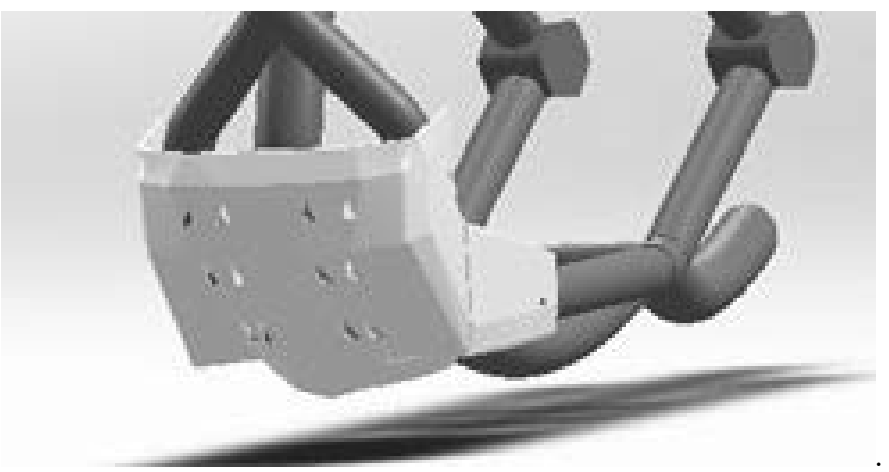

Figure 5. Final model of the motorcycle belly pan.

3. ANALYSIS OF STRESSES INCURRED DURING A MOTORCYCLE FALL

The following section presents the simulation of mechanical stresses arising from a motorcycle fall. SolidWorks Simulation was used for this analysis. The study began by assigning material properties to the belly pan. Fixtures (constraints) were then applied at the contact points with the motorcycle frame (Figure 6). Potential impact forces acting on the belly pan were defined next (Figure 7), with the applied load set to 2000 N. Finally, the model was discretized by generating a finite element mesh, as shown in Figure 8.

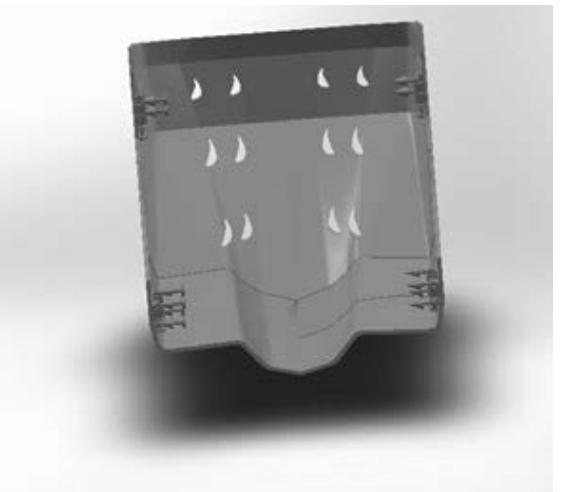

Figure 6. CAD model of the belly pan with immobilized geometry.

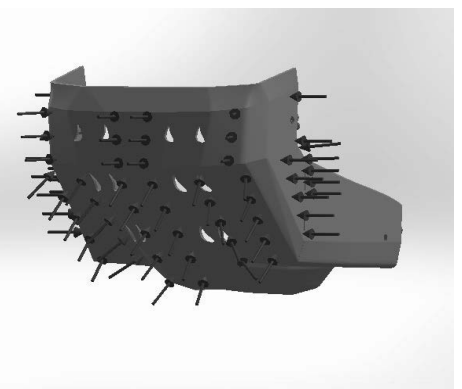

Figure 7. CAD model of belly pan with visible direction of forces

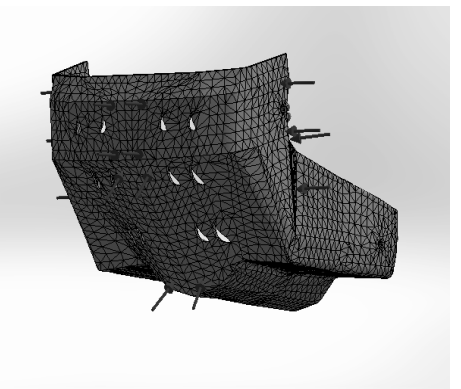

Figure 8. CAD model of belly pan with laid over finite element mesh and visible direction of forces

The final step was to execute the simulations using the predefined parameters for each candidate material. The output data included the spatial distributions of stress and deformation for the model sections shown in Figures 9–11. This information was used to select the most suitable material for the belly pan.

a) b)

Figure 9. Simulation results for the ABS belly pan: (a) internal stress distribution, (b) total deformation.

a) b)

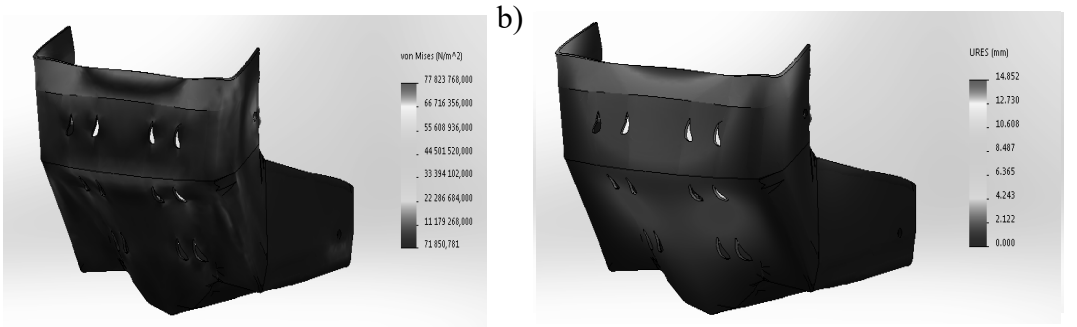

Figure 10. Simulation results for the PC belly pan: (a) internal stress distribution, (b) total deformation.

a) b)

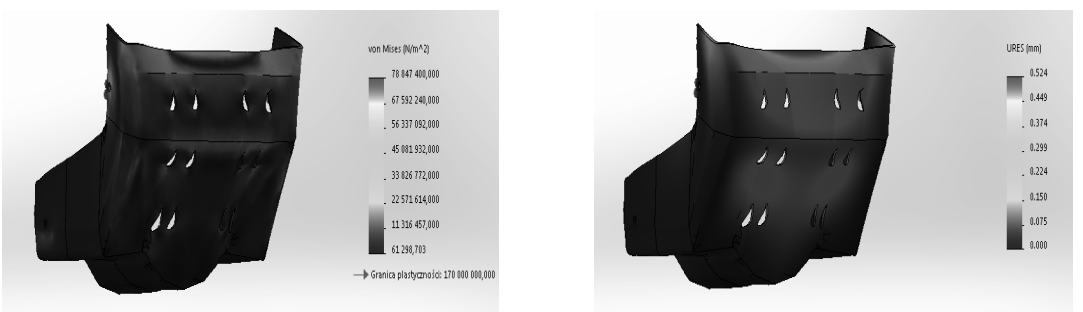

Figure 11. Simulation results for the EN AW-3003 belly pan: (a) internal stress distribution, (b) total deformation.

4. CONCLUSION

Based on the results obtained from the numerical simulations, the stress distribution generated during a simulated fall and acting on the motorcycle belly pan was analyzed and visualized graphically. The applied loading conditions enabled the evaluation of elastic deformation and the identification of stress distribution within the component. The analysis demonstrated that the lowest levels of deformation and stress were achieved when the EN AW-3003 alloy was employed. For all investigated materials, the highest stress concentrations were consistently located in the upper frontal region of the belly pan, which is the area most susceptible to deformation due to stress concentration during impact conditions. In all simulations, irrespective of the material assigned, the component satisfied the required safety criteria. No catastrophic failure was observed; only minor elastic deformation occurred. In the case of the applied polymers material, the structural integrity of the component was likewise preserved under the simulated loading conditions.

ACKNOWLEDGEMENT

The current study was conducted as part of the collaborative activities of the Student Research Group 'B@jt' at the Department of Engineering and Biomedical Materials, Faculty of Mechanical Engineering, Silesian University of Technology in Gliwice.

This thesis was developed as a result of a project focused on practical, hands-on, project-oriented education (PBL), which was part of competition VI in the Excellence Initiative - Research University program at Silesian University of Technology.

BIBLIOGRAPHY

1. M. Palanivendhan, D. Nagpal, D. A. Rao, J. Philip, M. S. Ganapathi, Design and analysis of an aerodynamic kit for a two wheeled race motorcycle, Materials Today: Proceedings, 45 (2021) 7239-7246.
2. D. del Cerro Turner, Y. Yao, D. Marchant, Motorcycle Aerodynamic Performance Improvement through Belly Pan Designs Evaluation and Testing, No. 2012-01-1167, SAE Technical Paper, 2012.
3. S. Desai, E. Leylek, C. M. B. Lo, P. Doddegowda, A. Bychkovsky, A. R. George, Experimental and CFD comparative case studies of aerodynamics of race car wings, underbodies with wheels, and motorcycle flows, No. 2008-01-2997, SAE Technical Paper, 2008.
4. A. Agarwal, L. Mthembu, Computational Analysis for Enhancing Motorcycle Aerodynamics by Modifying Engine Bay Openings. Journal Européen des Systèmes Automatisés, 58(5) (2025) 1079-1087.
5. M. Palanivendhan, J. Chandradass, P. K. Bannaravuri, J. Philip, K. Shubham, Aerodynamic simulation of optimized vortex generators and rear spoiler for performance vehicles. Materials Today: Proceedings, 45 (2021) 7228-7238.
6. C. Wallace, A. Garmory, A. Gaylard, D. Butcher, Investigation of the link between vehicle underbody and base unsteady wake aerodynamics, Journal of Wind Engineering and Industrial Aerodynamics, 265 (2025) 106177.
7. K. Wiński, A. Piechna, Comprehensive CFD Aerodynamic Simulation of a Sport Motorcycle, Energies. 15(16) (2022) 5920.
8. A. Huminic, G. Huminic, CFD study concerning the influence of the underbody components on total drag for a SUV, No. 2009-01-1157, SAE Technical Paper, 2009.
9. https://is.gd/W4AfP4 - access date 22.12.2025.

TalentDetector
9th January 2026
Gliwice, Poland
DEPARTMENT OF ENGINEERING MATERIALS AND BIOMATERIALS
FACULTY OF MECHANICAL ENGINEERING
SILESIAN UNIVERSITY OF TECHNOLOGY
INTERNATIONAL STUDENTS SCIENTIFIC CONFERENCE

Kinetyka krystalizacji stopów Zn-Al z dodatkiem magnezu

Marek Polak[a], Zofia Kowal[b], Marta Byczek[c], Mariusz Krupiński[d]

[a]Politechnika Śląska, Wydział Mechaniczny Technologiczny, Mechanika i Budowa Maszyn
[b]Politechnika Śląska, Wydział Mechaniczny Technologiczny, Inżynieria Produkcji i Zarządzanie
[c]I Liceum Ogólnokształcące im. Stefanii Sempołowskiej, 42-600 Tarnowskie Góry, ul. Opolska 28
[d]Politechnika Śląska, Wydział Mechaniczny Technologiczny, Katedra Materiałów Inżynierskich i Biomedycznych, 44-100 Gliwice, ul. Konarskiego 18a, email: mariusz.krupinski@polsl.pl

Streszczenie: Celem badań była analiza wpływu dodatku magnezu na kinetykę krystalizacji, kształtowanie się mikrostruktury oraz twardość stopów Zn-Al. W celu analizy wpływu dodatku magnezu wykonano analizę termiczno-derywacyjną, wyznaczono temperaturę początku (T_L) i końca (T_{Sol}) krzepnięcia. Dokonano analizy mikrostruktury i właściwości mechanicznych Zn-Al, powiązano krzywą derywacyjna z morfologią składników fazowych badanych stopów. Wykazano, że dodatek Mg powoduje zmianę przebiegu krzywej derywacyjnej zmianę mikrostruktury oraz powstawanie składników eutektyki z Mg oraz wzrost twardości badanych stopów.

Abstract: The aim of this study was to analyze the effect of magnesium addition on the crystallization kinetics, microstructure development, and hardness of Zn-Al alloys. To analyze the effect of magnesium addition, a thermal derivation analysis was performed, determining the onset (T_L) and end (T_{Sol}) temperatures of solidification. The microstructure and mechanical properties of Zn-Al alloys were analyzed, and the derivation curve was linked to the morphology of the phase components of the tested alloys. It was demonstrated that the addition of Mg caused a change in the derivation curve, a change in the microstructure, the formation of eutectic components from Mg, and an increase in the hardness of the tested alloys.

Słowa kluczowe: Stopy Zn-Al, modyfikacja magnezem, kinetyka krystalizacji.

1. WPROWADZENIE

Metalurgia stopów metali nieżelaznych dąży do uzyskania materiałów o wysokiej stabilności strukturalnej i określonych właściwościach mechanicznych. Najważniejszą grupę materiałów odlewniczych stanowią stopy aluminium oraz stopy cynku z aluminium. Badania nad kinetyką krystalizacji dla stopów wieloskładnikowych zachodzącą w zakresie temperatur między linią liquidus, a solidus mają kluczowe znaczenie. Efektywna metodą do sterowania strukturą odlewów jest modyfikacja w celu zmiany postaci składników strukturalnych. Unikalne połączenie niskiej temperatury topnienia, dobrej lejności oraz wysokiej trwałości przyczynia się

do częstego zastosowania w przemyśle motoryzacyjnym, elektrotechnicznym oraz budowie maszyn [1-3].

Właściwości eksploatacyjne tych stopów, takie jak twardość, odporność na zużycie ścierne oraz stabilność wymiarowa, są bezpośrednią funkcją ich mikrostruktury, która kształtuje się w trakcie procesu krzepnięcia [1, 4]. Przebieg tego procesu jest niezwykle czuły na zmiany składu chemicznego oraz dynamikę odprowadzania ciepła [3, 4].

Jedną z najbardziej efektywnych metod sterowania strukturą odlewów jest modyfikacja. Proces ten polega na celowym wprowadzeniu dodatków stopowych w celu zmiany postaci składników strukturalnych – od rozdrobnienia dendrytów fazy pierwotnej po transformację postaci eutektyki [2, 7]. W literaturze przedmiotu szeroko udokumentowano rolę pierwiastków takich jak stront (Sr) jako skutecznych modyfikatorów wpływających na kinetykę krystalizacji poprzez mechanizmy hamowania wzrostu faz i zmiany parametrów przechłodzenia [1, 2, 6].

Dodanie modyfikatorów do stopów Zn-Al wyraźnie zmienia kształt krzywych chłodzenia. To sygnał, że zmieniła się energia potrzebna do zarodkowania i wzrostu nowych faz wewnątrz materiału [4, 5]. Znaczenie w modyfikacji mikrostruktury stopów Zn ma również magnez (Mg). Ma on dużą zdolność do łączenia się z głównymi składnikami stopu, dzięki czemu przesuwa temperaturę przemian fazowych zmieniając morfologię faz, zmieniając mikrostrukturę własności mechaniczne [1, 3, 4].

2. MATERIAŁ I METODYKA BADAŃ

Realizacja głównego celu obejmowała różnorodne zagadnienia badawcze:

- wykonanie analizy termiczno-derywacyjnej przy użyciu urządzenia UMSA-MT5 w celu rejestracji temperatury nagrzewania i chłodzenia oraz wyznaczenia krzywych derywacyjnych,
- wyznaczenie temperatury początku (T_L) i końca (T_{Sol}),
- analiza korelacji pomiędzy dodatkiem Mg, a wpływu na zmianę mikrostruktury i twardości stopu ZL5,
- powiązanie krzywej derywacyjnej z morfologią składników fazowych badanych stopów ZL5 oraz stopu z dodatkiem 0,5% mas. Mg.

Materiałem użytym w badaniach był stop cynku z aluminium ZL5 o składzie chemicznym podanym w tabeli 1. Proces modyfikacji składu chemicznego wykonano przez wprowadzenie do ciekłego metalu czystego magnezu aby uzyskać stężenie 0,5% mas. Mg.

Tabela 1. Skład chemiczny stopu ZL5.

Stężenie masowe pierwiastków, %									
Al	Cu	Mg	Pb	Cd	Sn	Fe	Ni	Si	Zn
3,8728	0,9293	0,0446	0,0005	0,0014	0,0001	0,0086	0,0003	0,0026	reszta

Do badania kinetyki krystalizacji i analizy termiczno-derywacyjnej przygotowano próbki o masie 267g każda, w formie walcowej o średnicy ϕ 40 mm i wysokości 40 mm.

Próbki zostały owinięte trzema warstwami folii stalowej o grubości 0,025 mm. Przed owinięciem folia była zabezpieczona zawiesiną BN. Topienie wykonano w urządzeniu UMSA MT-5 wraz z modułem do analizy termiczno-derywacyjnej. Przebieg procesu rejestrowano za pomocą termopary typu K znajdującej się w stopie, połączonej z systemem rejestracji danych.

Procedura badawcza obejmowała nagrzanie stopu powyżej temperatury liquidus, a następnie powolne chłodzenie, rejestrując temperaturę. Kluczowym elementem badania było zapewnienie identycznych warunków krzepnięcia dla stopu bez jak i dodatkiem Mg. Chłodzenie odbywało się w komorze urządzenia UMSA (chłodzenie przy wyłączonym grzaniu, bez wymuszonego obiegu gazu).

Przygotowanie zgładów metalograficznych do badań mikrostruktury za pomocą mikroskopu świetlnego Axio Observer firmy Zeiss oraz do badań za pomocą skaningowego mikroskopu elektronowego Zeiss Supra 35 wraz z przystawką do analizy EDS, wykonano przez wycięcie krążków o grubości ok. 8 mm w połowie wysokości, a następnie szlifowano mechanicznie na papierach ściernych o gradacjach od 500 do 4000. Ostatecznym etapem było polerowanie za pomocą zawiesiny diamentowej 1µm na suknie MD-Nap firmy Struers.

Badania twardości metodą Rockwella w skali HRB wykonano na twardościomierzu Zwick ZHR. Wykonano po 10 pomiarów twardości dla każdego stopu a następnie obliczono wartość średnią i odchylenie standardowe. Trawienie chemiczne wykonano w roztworze CrO_3+Na_2SO_4+H_2O (45 s), a następnie w roztworze klarującym CrO_3+H_2O (zanurzenie) po czym przemyto wodą zdemineralizowaną.

3. WYNIKI BADAŃ WŁASNYCH

Na podstawie analizy termiczno-derywacyjnej wyznaczono temperaturę charakterystyczną dla badanego stopu (rys. 1):

- temperatura liquidus (T_L) 380°C – odpowiadająca początkowi krystalizacji dendrytów fazy η,
- temperatura solidus (T_{Sol}) 340°C – określająca koniec krzepnięcia.

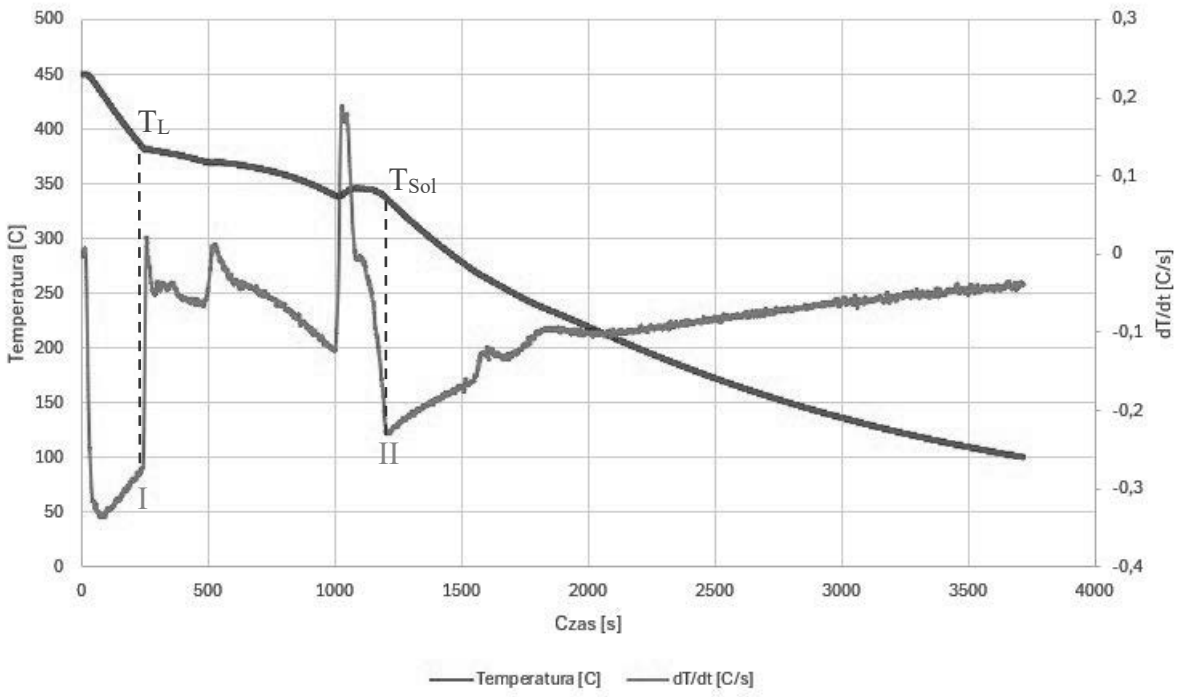

Rysunek 1. Wyniki analizy termiczno-derywacyjnej stopu ZL5 z dodatkiem 0,5% mas. Mg.

Siłą napędową krystalizacji w przypadku stopów jest różnica energii swobodnej cieczy i energii mieszaniny fazy ciekłej i stałej w zakresie stężeń drugiego składnika dla fazy ciekłej i stałej. Natomiast w wyniku dodatku Mg stopu stwierdzono, że modyfikacja składu chemicznego magnezem spowodowała obniżenie temperatury początku krzepnięcia, a także temperatury przemiany monotektoidalnej w stanie stałym. Modyfikacja spowodowała również obniżenie wartości temperatury krzepnięcia.

Analizę mikrostruktury wykonano przy użyciu mikroskopu optycznego. Badane stopy charakteryzowały się mikrostrukturą, w której obserwowano fazę η i eutektykę α'+η w wyniku przemiany monotektoidalnej α→α' w stanie stałym (rys. 2).

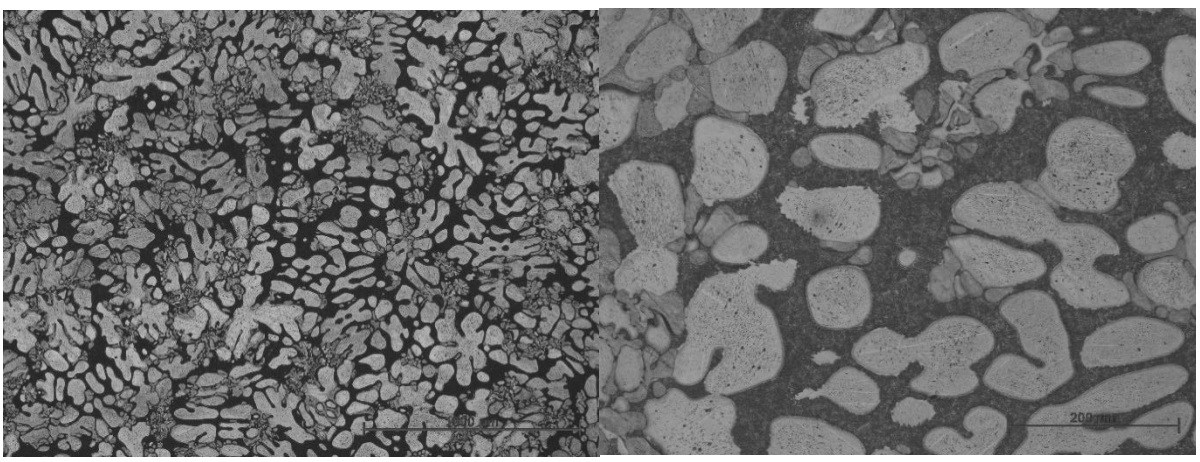

a) b)

Rysunek 2. Mikrostruktura stopu ZL5: a) pow. 50x; b) pow. 200x

Obserwacje mikrostruktury wykonane za pomocą mikroskopu świetlnego oraz skaningowego mikroskopu elektronowego i rentgenowskiej mikroanalizy ilościowej potwierdzają obecność składników eutektyki α'+η, jak również eutektyki z Mg, które w większości przypadków krystalizują na granicy eutektyki α'+η (rys. 3 i 4). Na rysunku 4 pokazano mapę rozmieszczenia pierwiastków.

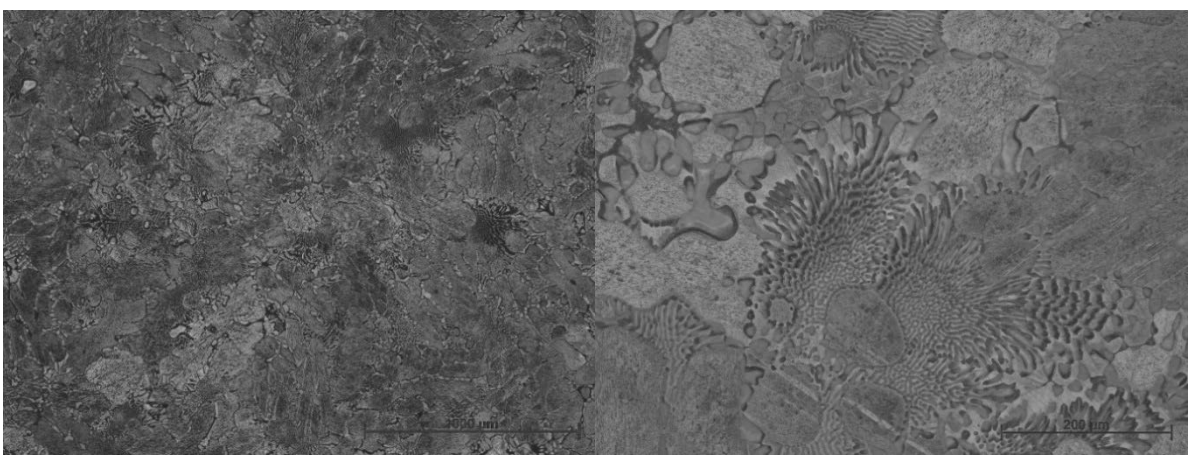

a) b)

Rysunek 3. Mikrostruktura stopu ZL5z dodatkiem Mg: a) pow. 50x; b) pow. 200x

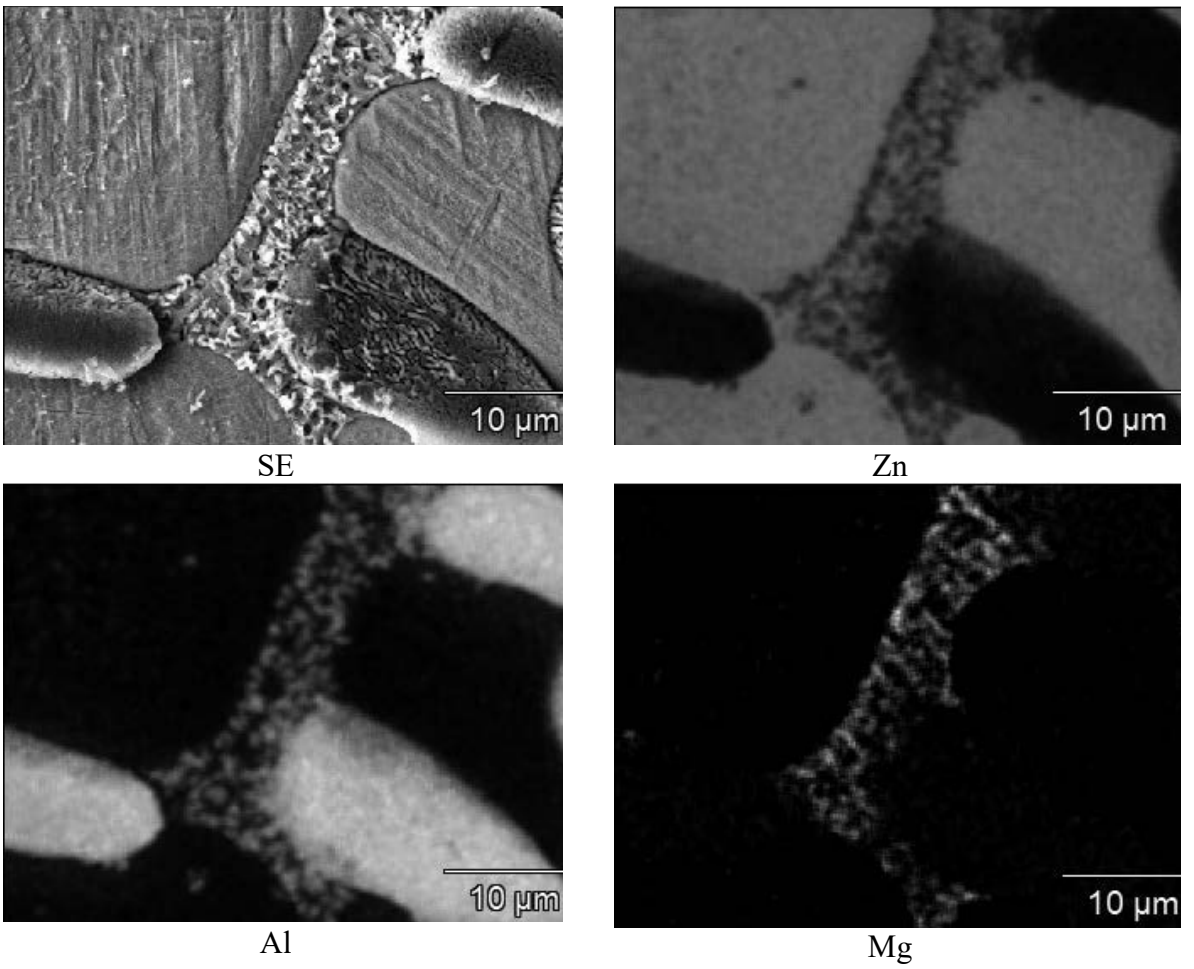

Rysunek 4. Struktura odlewniczego stopu ZL5 z dodatkiem 0,5% mas. Mg, chłodzonego z szybkością ~0,05 ℃/s, obraz uzyskany z wykorzystaniem elektronów wtórnych (SE) oraz mapy rozmieszczenia pierwiastków

Zaobserwowano wzrost twardości o 15,5 jednostki w skali HRB (rys. 5), potwierdza wpływ dodatku Mg na zmianę składu fazowego oraz morfologię faz badanych stopów cynku.

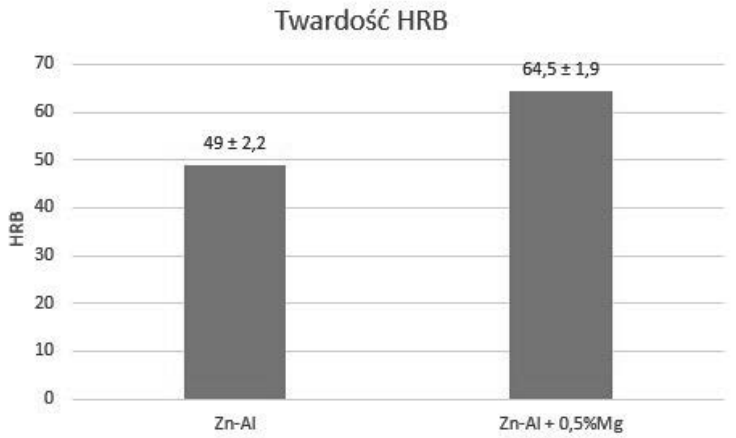

Rysunek 5. Porównanie wyników pomiaru twardości w skali HRB dla stopu ZL5 oraz ZL5 z dod. 0,5% mas. Mg.

4. PODSUMOWANIE

Wykonane badania stopów Zn-Al pozwoliły na szczegółową ocenę wpływu dodatku Mg na procesy krystalizacji oraz mikrostrukturę i twardość. Dodatek magnezu (0,5% mas.) do stopu bazowego ZL5 znacząco wpłynął na proces krystalizacji i morfologię mikrostruktury. Analiza mikroskopowa wykazała, że dodawanie magnezu prowadzi do rozdrobnienia elementów fazy pierwotnej oraz zwiększenia dyspersji składników eutektyki. Widoczna zmiana na krzywej pochodnej wskazywała powstanie eutektyki z Mg na granicy fazy η oraz eutektyki α'+η.

Nastąpiła również poprawa właściwości mechanicznych – odnotowany został wzrost twardości stopu o ok. 31,6% (z 49 HRB w stopie bazowym do 64,5 HRB z dodatkiem Mg). W wyniku rozdrobnienia mikrostruktury oraz obecność eutektyki z Mg.

Podsumowując, w badaniu wykazano ścisłą zależność między kinetyką krystalizacji, a mikrostrukturą i twardością stopu.

PODZIĘKOWANIA

Praca powstała w wyniku realizacji projektu „Kinetyka krystalizacji stopów Zn-Al modyfikowanych magnezem" w ramach kształcenia zorientowanego projektowo – PBL, w XIII konkursie Programu Inicjatywa Doskonałości – Uczelnia Badawcza, Wydział Mechaniczny Technologiczny, Politechnika Śląska.

Podziękowania dla Huta Cynku "Miasteczko Śląskie" S.A. za pomoc w realizacji projektu poprzez przekazanie materiału do badań.

LITERATURA

1. M. Krupiński, K. Labisz, B. Krupińska, Structure and Properties of Strontium-Modified Zn–Al–Cu Alloys. Materials 2025
2. M. Krupiński, M. Gruszka, W. Pakieła, K. Labisz, Ł. Wierzbicki, Crystallization Kinetics of Sr-Modified Precipitation Hardening Al-Si-Cu Alloys. Applied Sciences 2025
3. W. Kasprzak, J.H. Sokolowski, M. Sahoo, L.A. Dobrzański, Thermal and derivative analysis of hypereutectic Zn-Al alloys. J. Achiev. Mater. Manuf. Eng. 2008
4. J.B. Ferguson, B.F. Schultz, P.K. Rohatgi, Solidification kinetics and microstructure evolution of Zn-Al alloys. Mater. Sci. Eng. A 2014, 612
5. E. Guzik, D. Kopyciński, W. Wołczyński, The effect of Cu concentration on the microstructure of Zn-Al-Cu alloys. Arch. Metall. Mater. 2012
6. L. Lu, A.K. Dahle, Mechanisms of morphological modification of eutectic silicon in Al-Si alloys. Metall. Mater. Trans. A 2005
7. M.H. Mulazimoglu, J.M. Cohen, A. Hanna, J.E. Gruzleski, The effect of Sr modification on the properties of casting alloys. J. Mater. Sci. 1993
8. M. Krupiński, K. Labisz, E. Jonda, Effect of Mg addition on the crystallization kinetics of Zn-Al-Cu alloys, J. Min. Metall. Sect. B-Metall., 56 (3) (2020) 399 - 404

TalentDetector

9th January 2026
Gliwice, Poland

DEPARTMENT OF ENGINEERING MATERIALS AND BIOMATERIALS
FACULTY OF MECHANICAL ENGINEERING
SILESIAN UNIVERSITY OF TECHNOLOGY

INTERNATIONAL STUDENTS SCIENTIFIC CONFERENCE

Current state and prospects of application of carbon-kevlar (aramid) fiber blends in polymer composites for 3D printing

Andrii Polishchuk [a], Mirosław Bonek [b], Oleh Polishchuk [c], Serhii Matiukh [d], Svitlana Lisevich [e], Artem Tolstiuk [f]

[a] Khmelnytskyi National University, Faculty of Mechanical Engineering, Transport and Architecture, Khmelnytskyi, Ukraine
email: andrepol215@gmail.com.
[b] Silesian University of Technology, Faculty of Mechanical Engineering, Department of Engineering Materials and Biomaterials, Gliwice, Poland
email: miroslaw.bonek@polsl.pl.
[c] Khmelnytskyi National University, Faculty of Mechanical Engineering, Transport and Architecture, Khmelnytskyi, Ukraine
email: opolishchuk7l@gmail.com.
[d] Khmelnytskyi National University, Faculty of International Relations and Law, Khmelnytskyi, Ukraine
email: matuh@khmnu.edu.ua.
[e] Khmelnytskyi National University, Faculty of Mechanical Engineering, Transport and Architecture, Khmelnytskyi, Ukraine
email: lisevichsv@gmail.com.
[f] Khmelnytskyi National University, Faculty of Engineering Mechanics, Khmelnytskyi, Ukraine
email: tvenergetik@gmail.com.

Abstract: Extrusion-based additive manufacturing technologies such as fused deposition modeling (FDM) and fused filament fabrication (FFF) are widely used for the production of polymer components; however, their application in structurally loaded parts is limited by insufficient stiffness–toughness balance, pronounced anisotropy and weak interlayer bonding. Fiber reinforcement is an effective approach to improving mechanical performance, but single-fiber systems exhibit inherent limitations: carbon fibers significantly increase stiffness and strength while promoting brittle failure, whereas Kevlar (aramid) fibers enhance impact resistance and damage tolerance but provide limited rigidity.

This study analyzes the reinforcing potential of hybrid carbon–Kevlar fiber blends in polymer composites intended for extrusion-based additive manufacturing. The focus is placed on the complementary mechanical behavior of carbon and Kevlar fibers, their synergistic interaction within the polymer matrix and the resulting effects on stiffness, fracture toughness, interlayer adhesion, anisotropy and functional performance of 3D-printed components. Published experimental data and comparative analyses demonstrate that hybrid carbon–Kevlar composites exhibit a pseudo-ductile failure mode, improved crack resistance and enhanced interlayer strength compared to single-fiber-reinforced systems.

The results confirm that hybrid carbon–Kevlar reinforcement enables a balanced combination of high stiffness, strength and toughness, while also improving thermal stability, wear resistance and environmental durability of printed parts. In addition, emerging screw-extrusion additive manufacturing technologies provide improved fiber dispersion and processing stability, further enhancing the performance potential of hybrid composites. Overall, carbon–Kevlar fiber blends represent a promising material solution for advanced additive manufacturing applications in aerospace, transportation, robotics and mechanical engineering.

Keywords: additive manufacturing, hybrid composites, carbon fiber, Kevlar fiber, aramid fiber, FDM/FFF, screw extrusion.

1. INTRODUCTION

Additive manufacturing (AM) has become a key enabling technology for rapid prototyping and increasingly for the production of functional polymer components. Among various AM methods, material extrusion technologies such as fused deposition modeling (FDM) and fused filament fabrication (FFF) are widely used due to their simplicity, low cost and compatibility with a broad range of thermoplastic materials. However, polymers commonly applied in these processes, including ABS, ASA and polyamides, often exhibit insufficient stiffness, limited impact resistance and weak interlayer bonding, which restricts their application in structurally loaded parts [1].

Fiber reinforcement is an effective strategy for enhancing the performance of polymer matrices. Carbon fibers are widely used to increase stiffness and strength, but their brittle nature may reduce impact resistance and damage tolerance, especially in layered additively manufactured structures [1]. In contrast, Kevlar (aramid) fibers are characterized by high tensile strength, low density, excellent energy absorption and superior resistance to abrasion and fatigue. Their fibrillar microstructure promotes crack deflection and energy dissipation under dynamic loading, leading to improved fracture toughness and durability of polymer composites. The combination of carbon and Kevlar fibers in hybrid reinforcement systems offers the possibility of achieving a balanced stiffness-to-toughness ratio that cannot be obtained using single-fiber reinforcement [1, 2].

In recent years, growing attention has been paid to the application of carbon–Kevlar fiber blends in polymer composites for additive manufacturing. Such hybrid systems are particularly attractive for 3D printing technologies that enable controlled fiber orientation and dispersion, including emerging screw-extrusion systems processing polymer granules and continuous fiber extrusion approaches [2, 3]. Understanding the reinforcing mechanisms and processing limitations of carbon–Kevlar hybrid composites is therefore essential for their further development and industrial implementation.

2. FORMULATION OF THE PROBLEM

Despite progress in extrusion-based additive manufacturing, polymer components are still limited by low stiffness–toughness balance, anisotropy and weak interlayer bonding. Carbon fibers increase stiffness but cause brittle failure, while Kevlar fibers improve toughness with limited rigidity.

Hybrid carbon–Kevlar reinforcement combines these advantages, yet its use in 3D printing remains insufficiently explored. This study focuses on evaluating the mechanical performance and structural reliability of such hybrid composites compared to single-fiber systems.

3. RESULTS AND DISCUSSION

The conducted analysis of recent experimental data and published studies confirms that polymer composites reinforced with hybrid carbon–Kevlar (aramid) fiber blends exhibit a markedly superior balance of mechanical, thermal and functional properties compared to unfilled polymers and single-fiber-reinforced systems when processed by extrusion-based additive manufacturing technologies . This improvement is primarily associated with the complementary mechanical behavior of carbon and Kevlar fibers and their interaction with the polymer matrix under the specific thermal and shear conditions characteristic of FDM/FFF and screw-extrusion 3D printing [1, 3, 4].

Carbon fibers are widely recognized for their exceptionally high elastic modulus and tensile strength, which enable effective load transfer and significantly increase the stiffness of polymer composites. In extrusion-based printing, carbon fibers tend to align along the material flow direction, resulting in a pronounced increase in strength and stiffness parallel to the raster paths. However, this benefit is accompanied by inherent disadvantages, including increased brittleness, reduced elongation at break and elevated sensitivity to stress concentrations at layer interfaces. These effects are particularly critical in additively manufactured components, where the layered structure and anisotropic microarchitecture strongly influence mechanical performance.

Kevlar fibers, in contrast, possess lower stiffness but significantly higher elongation at break, outstanding energy absorption capacity and a unique fibrillar microstructure. Under mechanical loading, aramid fibers undergo progressive microfibrillation, stretching and pull-out, which effectively dissipate energy and delay crack propagation [5, 6]. When incorporated into polymer matrices as short fibers compatible with extrusion-based processing, Kevlar fibers substantially improve fracture toughness, impact resistance and damage tolerance. These characteristics make Kevlar an effective toughening agent capable of compensating for the brittle behavior typically introduced by carbon fiber reinforcement.

The hybrid combination of carbon and Kevlar fibers within a single polymer matrix enables the formation of a synergistic reinforcement system. In such systems, carbon fibers primarily serve as the main load-bearing elements, ensuring high stiffness and strength, while Kevlar fibers act as crack-arresting and energy-dissipating components. This synergy results in a pseudo-ductile failure behavior that is highly desirable for structural applications, particularly in dynamically loaded or safety-critical components produced by additive manufacturing [1]. Instead of abrupt catastrophic fracture, hybrid composites exhibit gradual damage accumulation and progressive failure, providing increased reliability and warning before final failure.

One of the most significant advantages of hybrid carbon–Kevlar reinforcement is its influence on fracture behavior in 3D-printed composites. In carbon-fiber-only systems produced by FDM/FFF, cracks often initiate at interlayer boundaries or voids between extruded filaments and propagate rapidly along raster directions [1, 4]. The introduction of Kevlar fibers alters this fracture mechanism by promoting crack deflection and bridging across layers. Kevlar fibers spanning adjacent layers form micro-scale mechanical links that inhibit delamination and reduce crack opening displacement, leading to higher resistance to crack initiation and slower crack growth rates under tensile, bending and impact loading.

Interlayer adhesion is a critical parameter determining the structural integrity of additively manufactured parts. Weak bonding between printed layers is a well-known limitation of FDM/FFF technology, often leading to premature delamination under out-of-plane loads. While the incorporation of rigid carbon fibers may further restrict polymer chain diffusion across layer interfaces due to increased melt viscosity, Kevlar fibers mitigate this effect. Their surface morphology and flexibility enable partial penetration across layer boundaries, creating mechanical interlocks that enhance interlayer strength. In hybrid systems, this mechanism leads to a measurable increase in interlayer tensile and shear strength and significantly improves resistance to delamination [1, 2].

Anisotropy remains an inherent characteristic of extrusion-based additive manufacturing, arising from preferential fiber alignment and directional material deposition. Carbon fibers strongly amplify this anisotropy due to their high stiffness and directional load-bearing capability [1, 4]. Kevlar fibers, on the other hand, exhibit more compliant behavior and contribute to load redistribution across different orientations. Consequently, hybrid carbon–Kevlar composites show reduced sensitivity to print orientation and more balanced mechanical properties in multi-axial loading scenarios, which is particularly advantageous for components with complex geometries or unpredictable loading conditions.

To quantitatively illustrate the benefits of hybrid reinforcement, a comparative summary of typical mechanical and functional properties reported for short-fiber-reinforced polymer composites processed by extrusion-based 3D printing is presented in Table 2 [6].

Table 2 - Typical mechanical and functional properties of polymer composites reinforced with carbon fibers, Kevlar fibers and hybrid carbon–Kevlar fiber blends (short fibers, extrusion-based 3D printing).

Property	Unfilled polymer (ABS/PA)	Carbon fiber composite	Kevlar fiber composite	Hybrid carbon–Kevlar composite
Density, g/cm³	1.04–1.15	1.20–1.30	1.15–1.25	1.20–1.28
Tensile strength, MPa	35–55	70–110	65–95	85–120
Young's modulus, GPa	1.5–2.5	6–12	3–6	5–9
Elongation at break, %	5–20	1.0–2.0	3–6	2–4
Impact strength (Charpy), kJ/m²	5–12	6–15	20–40	15–30
Fracture toughness K_{IC}, MPa·m$^{0.5}$	1.5–2.5	2.0–3.0	4.0–6.0	3.5–5.5
Interlayer tensile strength, MPa	15–25	18–30	25–40	30–45
Wear rate, mm³/N·m	(2–5)×10^{-4}	(1–3)×10^{-4}	(0.3–1)×10^{-4}	(0.5–2)×10^{-4}
Heat deflection temperature, °C	90–105	120–150	110–135	125–155
Service temperature range, °C	–20…+80	–30…+120	–30…+120	–40…+130

As shown in Table 2, carbon-fiber-reinforced polymers achieve the highest stiffness but exhibit low elongation and limited impact resistance [1, 4]. Kevlar-reinforced composites demonstrate excellent toughness, wear resistance and environmental stability but provide lower elastic modulus. Hybrid carbon–Kevlar composites combine these advantages, achieving high

tensile strength together with significantly improved fracture toughness and interlayer adhesion. This balanced property profile makes hybrid systems particularly suitable for components subjected to dynamic loading, impact and cyclic stresses.

Thermal performance is another important aspect influenced by hybrid reinforcement. Carbon fibers reduce the coefficient of thermal expansion of polymer matrices, improving dimensional stability during cooling and service [4]. Kevlar fibers complement this effect by maintaining mechanical integrity over a wide temperature range and resisting thermal degradation [5]. Hybrid composites therefore exhibit reduced warping during printing, improved dimensional accuracy and enhanced resistance to thermal cycling, which is especially important for large-format prints and components operating under variable thermal conditions.

Tribological behavior is significantly improved by the presence of Kevlar fibers. Their high abrasion resistance and ability to form stable transfer films at sliding interfaces lead to reduced wear rates and more stable friction behavior. Carbon fibers contribute to load-bearing capability at contact interfaces, further improving wear resistance under moderate loads [4]. As a result, hybrid carbon–Kevlar composites are well suited for sliding and rotating machine elements such as gears, guides and bearings produced by additive manufacturing.

Environmental durability further enhances the applicability of hybrid composites. Kevlar fibers exhibit high resistance to moisture, UV radiation and many chemical agents, while carbon fibers limit long-term creep and deformation under sustained loads. The combined effect improves resistance to hydrolytic degradation, oxidative aging and surface damage, enabling reliable operation in outdoor, marine and chemically aggressive environments [1, 6].

From a processing perspective, hybrid carbon–Kevlar fiber systems introduce both challenges and opportunities. Increased fiber content leads to higher melt viscosity, which may negatively affect extrusion stability and surface quality [1, 4]. However, Kevlar fibers reduce the tendency of stiff carbon fibers to agglomerate and clog nozzles, particularly in screw-extrusion and continuous extrusion 3D printing systems. Continuous mixing and controlled shear enable more uniform fiber dispersion and allow higher reinforcement loadings than filament-based processes [2, 3].

Screw-extrusion additive manufacturing therefore represents a particularly promising platform for the industrial implementation of hybrid carbon–Kevlar composites. The ability to process polymer granules directly, adjust fiber ratios in real time and achieve uniform dispersion enhances both material performance and production efficiency [2, 3]. This approach aligns with current trends toward large-scale, cost-effective and sustainable additive manufacturing.

Overall, the results discussed in this section clearly demonstrate that hybrid carbon–Kevlar fiber blends constitute a highly effective reinforcement strategy for polymer composites intended for extrusion-based additive manufacturing. Their synergistic interaction addresses key limitations of 3D printing, including brittleness, anisotropy and weak interlayer bonding, while simultaneously improving thermal, tribological and environmental performance. Continued advances in material formulation, processing technologies and hybrid reinforcement design are expected to further enhance the reliability and industrial relevance of carbon–Kevlar composites, paving the way for their widespread adoption in aerospace, transportation, robotics and mechanical engineering applications.

4. CONCLUSIONS

he performed analysis confirms that hybrid polymer composites reinforced with combined carbon and Kevlar (aramid) fibers represent a highly promising material class for extrusion-based

additive manufacturing technologies. The complementary mechanical behavior of carbon and Kevlar fibers enables a balanced combination of high stiffness, strength and enhanced fracture toughness, which cannot be achieved using single-fiber reinforcement systems.

Carbon fibers effectively increase elastic modulus and load-bearing capacity of 3D-printed composites, while Kevlar fibers significantly improve impact resistance, damage tolerance and resistance to crack propagation. Their synergistic interaction leads to a pseudo-ductile failure mode, improved interlayer adhesion and reduced sensitivity to printing orientation, addressing key structural limitations of FDM/FFF and screw-extrusion 3D printing.

Hybrid carbon–Kevlar reinforcement also contributes to improved thermal stability, wear resistance and environmental durability of printed components, expanding their applicability to dynamically loaded, tribological and outdoor environments. The compatibility of such composites with emerging screw-extrusion additive manufacturing systems further enhances processing flexibility, fiber dispersion and achievable reinforcement content.

Overall, carbon–Kevlar fiber blends offer substantial potential for the development of next-generation high-performance polymer composites for additive manufacturing. Continued research focused on material formulation, fiber–matrix interface optimization and process parameter control is expected to further improve their mechanical reliability and support their industrial implementation in aerospace, transportation, robotics and mechanical engineering applications.

GRATITUDE

The publication is the result of cooperation within the Visegrad Scholarship Program 2025/2026.

BIBLIOGRAPHY

1. Wang K. et al. Flexure Behaviors of ABS-Based Composites Containing Carbon and Kevlar Fibers by Material Extrusion 3D Printing. Polymers, 2019.

2. Heitkamp T. et al. Continuous Fiber-Reinforced Material Extrusion with Hybrid Composites of Carbon and Aramid Fibers. Applied Sciences, 2022.

3. Rijckaert S. et al. Continuous Fiber-Reinforced Aramid/PETG 3D-Printed Composites with High Fiber Loading through Fused Filament Fabrication. Polymers, 2022.

4. Cerbu C. et al. Simulation of the Hybrid Carbon-Aramid Composite Materials Based on Mechanical Characterization by Digital Image Correlation Method. Polymers, 2021.

5. Xu X. et al. Aramid Fiber-Reinforced Plastics (AFRPs) in Aerospace: A Review of Recent Advancements and Future Perspectives. Polymers, 2025.

6. Agarwal P. et al. Effect of carbon-Kevlar intraply surface layers on the mechanical and vibrational properties of basalt reinforced polymer composites. Cogent engineering, 2024.

TalentDetector

9th January 2026
Gliwice, Poland

DEPARTMENT OF ENGINEERING MATERIALS AND BIOMATERIALS
FACULTY OF MECHANICAL ENGINEERING
SILESIAN UNIVERSITY OF TECHNOLOGY

INTERNATIONAL STUDENTS SCIENTIFIC CONFERENCE

Comparison of composite ballistic plates

Grzegorz Pośpiech[a], Paweł Kruczyński[a], Bartłomiej Kaciuba[a], Estera Nawrocka[a], Karolina Tykarska[a], Aneta Kania[b], Anna Włodarczyk-Fligier[b], Magdalena Polok-Rubiniec[b]

[a] Silesian University of Technology, Faculty of Mechanical Engineering, Department of Engineering Materials and Biomaterials
email: gp307818@student.polsl.pl
[b] Silesian University of Technology, Faculty of Mechanical Engineering, Department of Engineering Materials and Biomaterials
email: aneta.kania@polsl.pl

Abstract: The present work attempts to develop a ballistic plate that would allow the minimization of undesirable phenomena, such as perforation, through optimization of the layer configuration, selection of reinforcing fibers, and the use of ceramics as a material initiating projectile deformation and destruction.

Keywords: ballistic plates, ceramic materials, composite materials, manufacturing methods.

1. INTRODUCTION

This paper presents issues related to material selection and the manufacturing process of composite ballistic plates with a ceramic layer. Their primary function is to stop objects (projectiles) of low mass and very high velocity, including projectiles weighing several to several dozen grams and traveling at velocities on the order of several hundred meters per second. A key factor is the effective dissipation of kinetic energy over a larger area of the plate, which limits localized deformation and reduces the load transmitted to the user. It is also essential to retain all projectile fragments within the material structure, thereby minimizing the risk of secondary injuries to people in the user's vicinity.

Contemporary ballistic protection systems available on the market are characterized by diverse performance properties – they may be rigid or flexible, lightweight or reinforced with additional inserts, and can achieve high protection levels according to NIJ standards (e.g. IIIA–IV). They are expected to provide both a high capacity for kinetic energy absorption and structural integrity after multiple impacts. At the same time, ballistic solutions may exhibit unfavorable characteristics such as significant weight, limited deformability, high production costs, or poor control of projectile fragmentation, which can lead to the lateral dispersion of fragments.

2. MATERIALS USED IN BALLISTIC PLATES

In the construction of ballistic plates and screens, various groups of materials are employed, selected depending on the required level of ballistic resistance, weight, and manufacturing technology. This paper discusses polymer-matrix composite materials and ceramic materials used in ballistic applications.

Materials used in the tested plate

For the fabrication of composite laminates, E-glass fiber fabric about the weight of 300 g/m² was used. An LP900 epoxy resin with HP363 hardener served as the matrix material. The glass fibers acted as the reinforcing component, while the epoxy resin was responsible for bonding the layers and transferring loads between the fibers. The plate structure also incorporated technical ceramic elements in the form of technical stoneware, placed in the front layer. This material was used to increase resistance to projectile impact by inducing projectile deformation and fragmentation.

Other materials used in ballistic solutions

Ballistic solutions commonly also employ S-glass fibers, aramid fibers (Kevlar), and carbon fibers, which can be used as reinforcing layers in composite laminates [1]. With regard to ceramic materials used in ballistic screens, the following are applied [2]:

- aluminum oxide (Al_2O_3),
- zirconium oxide (ZrO_2),
- silicon dioxide (SiO_2),
- ceramic composites, including particle-reinforced ceramics.

Ceramic materials are primarily used as the projectile-deforming layer, while composite layers are responsible for energy absorption and retention of projectile fragments.

Additional materials

In some ballistic plate designs, elastomeric or rubber layers are also used to reduce secondary spall and to improve the structural integrity of the system after impact.

2.1. The first method of manufacturing ballistic plates

According to NIJ Standard 0101.07 (Ballistic Resistance of Personal Body Armor) [3], which specifies the minimum requirements and ballistic testing methods for personal body armor vests and plates, the test specimen should have dimensions of 10 in × 12 in (254 mm × 305 mm). However, the standard allows the use of smaller specimens for preliminary and comparative tests.

For the initial tests, specimens made of E-glass fiberglass fabric in a twill weave (Fig. 1) were prepared. The layers were stacked with a consistent fiber orientation, and the specimens had dimensions of 150 mm × 150 mm.

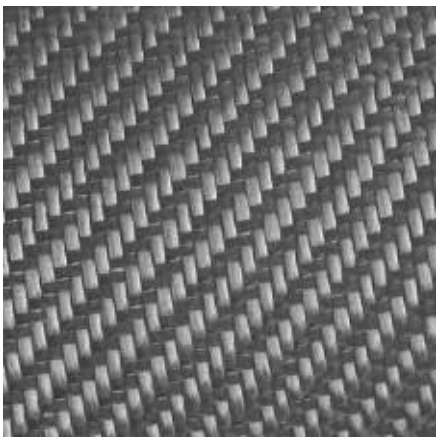

Figure 1. Glass fiber in twill weave [4]

A casting resin was applied between the individual layers. After forming a composite layer approximately 16 mm thick, a plate made of glyco-silicate ceramic sinter was inserted. The assembly was then covered with protective film, pressed under a pressure of 1 bar, and cured in an oven for 24 hours at a temperature of 22 °C. Using this procedure, two laminate packages with thicknesses of 16 mm and 12 mm were prepared. Due to the uniform fiber orientation, damage occurred, as shown in Figure 2.

Figure 2. Damage after the first test – fiber separation along the weave direction

2.2. The second method of manufacturing

In the second method, the fiberglass sheets were stacked so that the weave was rotated by 45° in each successive layer. An LP900 epoxy resin cured with HP363 hardener was applied between the layers, resulting in improved mechanical properties compared to the casting resin used for the previous specimens. The laminate was prepared according to the scheme presented in Table 1.

Table 1. Layer configuration of specimens for the second test (f – glass fiber, r – resin)

Name	Proportions	Thickness [mm]
Glass fiber impregnated with resin	1 (f):1.5 (r)	1
Rubber	1	1
Glass fiber impregnated with resin	1 (f):1.5 (r)	1
Glyco-silicate ceramic sinter plate	1	8
Glass fiber impregnated with resin	1 (f):1.5 (r)	8

Depending on the type of projectile, after perforation of the initial composite layers and impact with the ceramic layer, there is a risk of fragmentation, which may lead to injuries caused by spall to individuals located in front of the armor and within its plane (Fig. 3). Owing to the initial layers of the plate, this hazard is minimized.

Figure 3. Fragmentation phenomenon [5]

During the manufacturing process of the ballistic plate specimen, a steel mold was prepared, in which the material was dimensionally fitted. The layer sequence began with a fiberglass fabric impregnated with liquid epoxy resin containing a hardener, while maintaining a ratio of 1:1.5 (glass fiber : resin). Subsequent fiber layers were gradually saturated with the resin mixture to ensure proper bonding of the laminate package. Next, the ceramic layer was placed, followed by another fiberglass and resin layer, a flexible rubber layer, and a final fiberglass and resin layer.

The prepared layup was then pressed under a pressure of 60 bar, placed in the mold inside an oven, and cured at a temperature of approximately 60 °C for 8 hours. After completion of the process, the laminate was demolded, and excess resin expelled during pressing was removed, resulting in the final ballistic plate shown in Figure 4.

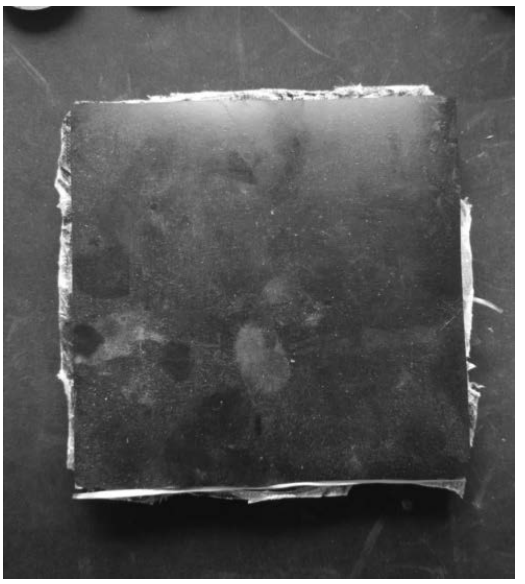

Figure 4. Finished ballistic plate specimen

3. CONCLUSIONS

The presented work confirmed the feasibility of manufacturing composite ballistic plates using polymer materials reinforced with glass fibers and a ceramic layer. This combination enabled effective projectile deformation by the ceramic component, as well as energy absorption and retention of fragments within the composite structure. Initial trials showed that uniform fiber orientation promotes delamination and damage; therefore, modifying the layer arrangement and employing a resin with improved properties enhanced the laminate integrity. The obtained plates provide a basic level of ballistic protection and may serve as a foundation for further development aimed at increasing resistance, stability, and reducing the overall weight of the structure.

BIBLIOGRAPHY

1. A. Łyczko, K. Niemiec, A.J. Nowak, Layered composite materials dedicated to ballistic shields, Proceedings of the Department of Engineering Materials and Biomaterials, Silesian University of Technology, 2021, 174-184 (in Polish).
2. A. Jastrzębska, M. Kostecki, A.R. Olszyna, J. Woźniak, Ceramic Materials. Laboratory, Warsaw University of Technology Publishing House, 2020 (in Polish).
3. NIJ Standard-0101.07. Ballistic Resistance of Personal Body Armor. National Institute of Justice, USA, 2008.
4. Ruifiber-High-Performance Fiber Glass Cloth, https://www.ruifiber.com/pl/high-performance-fiber-glass-cloth-2-product/, 2025.
5. L. Radziszewski, Terminal ballistics of small-caliber ammunition bullets when shooting at selected targets, Kielce University of Technology, 2007 (in Polish).

TalentDetector
9th January 2026
Gliwice, Poland
DEPARTMENT OF ENGINEERING MATERIALS AND BIOMATERIALS
FACULTY OF MECHANICAL ENGINEERING
SILESIAN UNIVERSITY OF TECHNOLOGY
INTERNATIONAL STUDENTS SCIENTIFIC CONFERENCE

Analiza wytrzymałościowa deskorolki

Mateusz Puszczało[a], Szymon Puszczało[a], Agata Śliwa[b], Marek Sroka[b]

[a] Zespół Szkół Techniczno-Informatycznych w Gliwicach
email: mati.puszczalo@gmail.com, szymon.puszczalo@gmail.com
[b] Politechnika Śląska, Wydział Mechaniczny Technologiczny, Katedra Materiałów Inżynierskich i Biomedycznych
email: agata.sliwa@polsl.pl, marek.sroka@polsl.pl

Streszczenie: W pracy dokonano analizy naprężeń powstających podczas obciążania deskorolki. Przeprowadzono kilka analiz w zależności od wagi człowieka, a następnie dokonano porównania otrzymanych wyników. Analizę przeprowadzono z wykorzystaniem Metody Elementów Skończonych przy użyciu oprogramowania Solid Works oraz Ansys.
Abstract: The paper analyzes the stress arising from the stand on a skateboard. Analyses were carried out several scales depending on a man, then a comparison of the results. Analysis of the results was made using Finite Element Analysis using Solid Works and Ansys software.

Słowa kluczowe: MES, rozkład naprężeń, klon kanadyjski, deskorolka

1. WPROWADZENIE

Deskorolka pierwszy raz pojawiła się w latach 50 XX wieku w Kalifornii, kiedy to entuzjaści surfingu, by móc doskonalić swe umiejętności również na suchym podłożu, domontowali do deski kółka.
Przykładową deskorolkę przedstawiono na rysunku 1. Do produkcji deskorolek wykorzystuje się następujące materiały:

- włókno szklane,
- metal,
- plastik,
- drewno [1].

Deskorolka składa się z takich elementów, jak:

- deck – główny element, który zapewnia miejsce na nogi. Obecnie wykonywany jest z kilkuwarstwowej sklejki, a jego szerokość waha się w przedziale 19 – 23cm,
- grip – samoprzylepny papier ścierny przyklejany do powierzchni deck'a mający na celu zwiększenie przyczepności nóg na desce,
- truck – element umożliwiający montaż kółek do deski oraz kierowanie nią poprzez wychylanie się w określonym kierunku. Zbudowany jest z dwóch elementów – górnego,

mocowanego do deski i dolnego, do którego mocuje się kółka. Pomiędzy nimi znajdują się gumowe elementy zapewniające elastyczność przy skręcaniu. Truck z deck'iem łączy się za pomocą śrub (montażówek),

- kółka – najczęściej wykonane z poliuretanu, zakładane są na truck'i z wykorzystaniem łożysk (w każdym kółku znajdują się dwa łożyska toczne) i tulejek dystansowych. Obecnie twardość kółek oscyluje w okolicach 100A [1, 2, 3].

Rysunek 1. Zdjęcie przykładowej deskorolki – model Diamond Black Knight [4]
Figure 1. Example picture of skateboard - model Diamond Black Knight [4]

2. ZAŁOŻENIA MODELOWE

W pracy poddano analizie deskorolkę – model Diamond Black Knight. Wymiary i niezbędne informacje do wykonania symulacji komputerowej przedstawiono w tabeli 1 [4].

Tabela. 1. Wymiary i pozostałe informacje na temat deskorolki Diamond Black Knight

Deck	
Materiał:	Klon kanadyjski, 7 warstw
Długość:	31,5" (~79cm)
Szerokość:	7,5" (~18cm)
Kółka	
Materiał:	PCV
Średnica:	50mm
Grubość:	30mm
Twardość:	95A
Trucki	
Materiał:	Aluminium
Rozmiar:	5" (~13cm)
Łożyska	
Klasa:	ABEC – 7

Na podstawie wymiarów uwzględnionych w tabeli 1. przy użyciu oprogramowania Solid Works stworzony został trójwymiarowy model deskorolki (rysunki 2a i 2b).

Następnie model ten został zaimportowany do programu Ansys Workbench. Została wygenerowana siatka (rysunek 3a) i zadane warunki brzegowe (rysunek 3b). Ustalono dwa punkty przyłożenia obciążenia.
Analiza obejmuje przeprowadzenie trzech prób w zależności od wagi człowieka:

- próba – waga 50kg,
- próba – waga 75kg,
- próba – waga 100kg.

Zakładamy, że człowiek stoi na deskorolce obiema nogami.

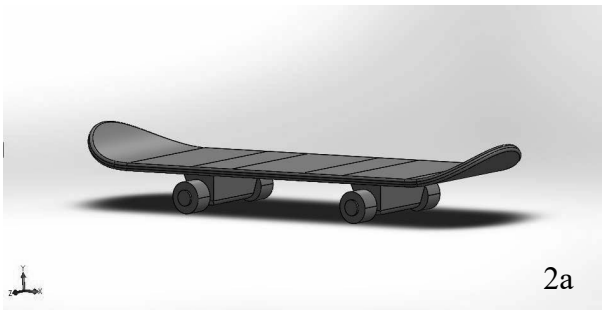

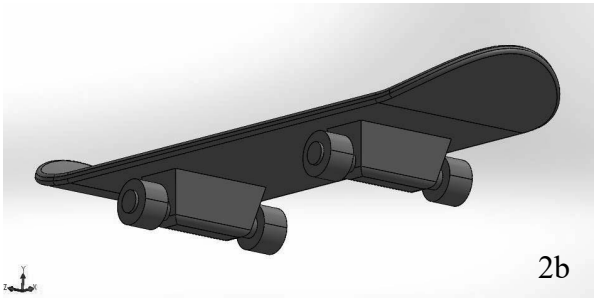

Rysunek 2a, 2b. Model CAD deskorolki
Figure 2a, 2b. Skateboard's CAD model

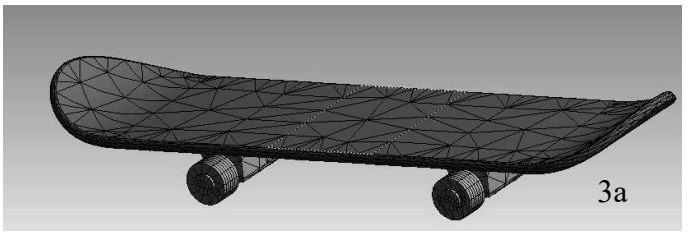

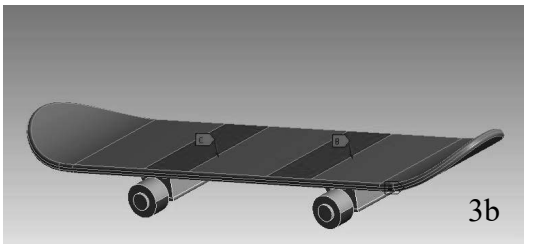

Rysunek 3a, 3b. Model deskorolki z wygenerowaną siatką i zadanymi warunkami brzegowymi
Figure 3a, 3b. Skateboard model with generated mesh and boundary conditions

3. ANALIZA ROZKŁADU NAPRĘŻEŃ

Na rysunkach 4, 5 i 6 zaprezentowano wyniki analizy rozkładu naprężeń uzyskanych przy pomocy oprogramowania Ansys. Model obciążano trzema siłami, wyniki przedstawiono w tabeli 2. Pod uwagę brano naprężenia występujące w centralnym punkcie deskorolki (deck'u) oraz maksymalne naprężenia występujące w tym przypadku w truck'ach. Wartość przyciągania ziemskiego zaokrąglono do 10N.

Tabela 2. Wyniki analizy rozkładu naprężeń

Waga człowieka [kg]	Przyłożone obciążenie [N]	Wartość naprężenia w centralnym punkcie deskorolki [MPa]	Maksymalna wartość naprężenia [MPa]
50	500	0,37	2,32
75	750	0,52	3,49
100	1000	0,75	4,65

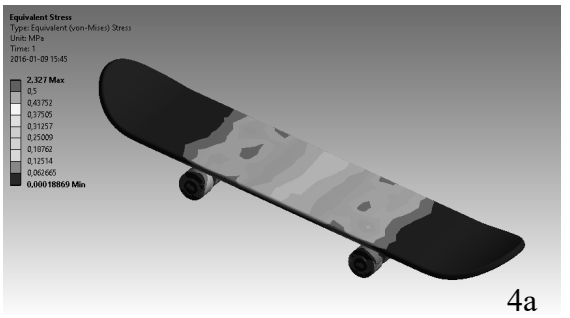

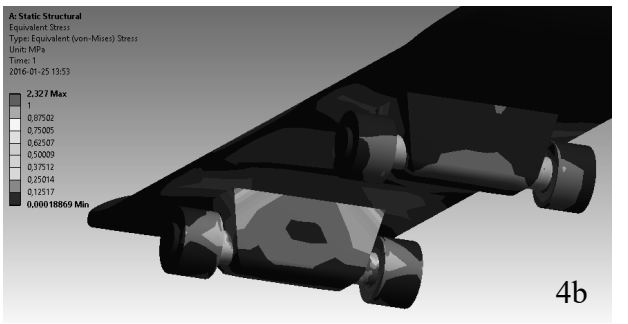

Rysunek 4a, 4b. Rozkład naprężeń zredukowanych von Misesa dla obciążenia 500N
Figure 4a, 4b. Distribution of equivalent (von Mises) stress for load 500N

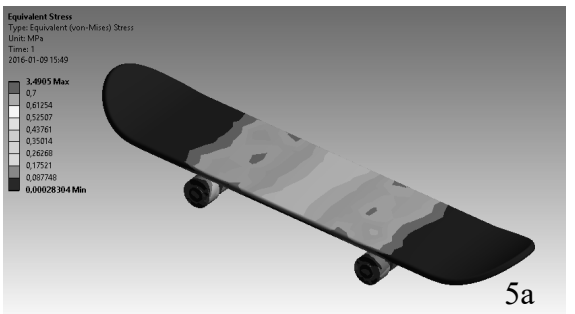

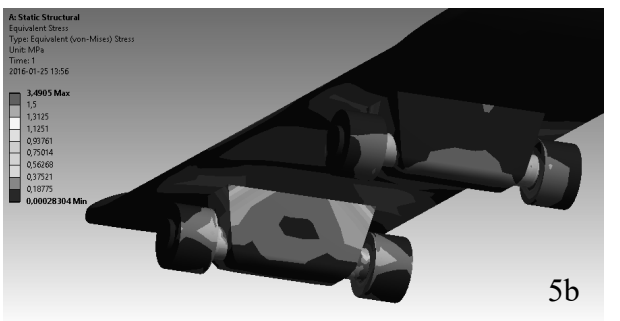

Rysunek 5a, 5b. Rozkład naprężeń zredukowanych von Misesa dla obciążenia 750N
Figure 5a, 5b. Distribution of equivalent (von Mises) stress for load 750N

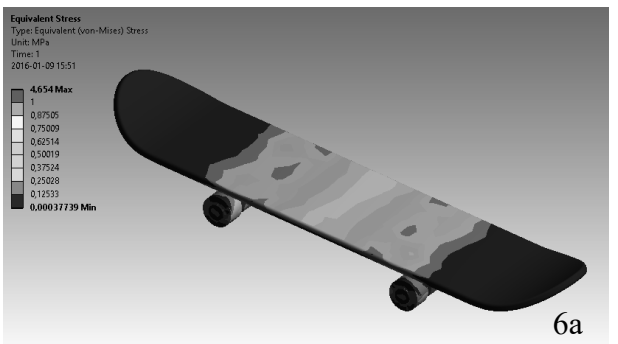

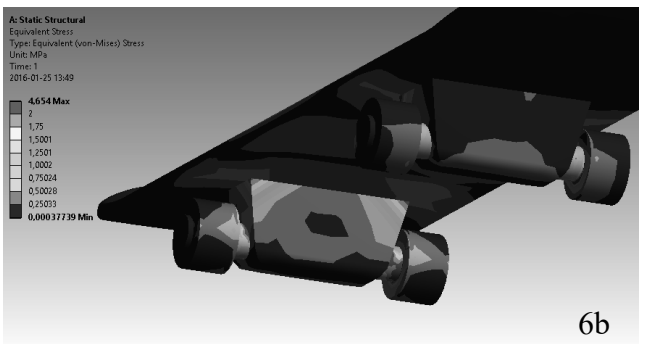

Rysunek 6a, 6b. Rozkład naprężeń zredukowanych von Misesa dla obciążenia 1000N
Figure 6a, 6b. Distribution of equivalent (von Mises) stress for load 1000N

4. ANALIZA PRZEMIESZCZEŃ
5.

Na rysunkach 7, 8, 9 i tabeli 3 przedstawiono rozkład przemieszczeń przy tych samych obciążeniach. Największe przemieszczenia występują, w centralnym punkcie deck'a.

Tabela 3. Wyniki analizy przemieszczeń

Waga człowieka [kg]	Przyłożone obciążenie [N]	Wartość przemieszczenia [mm]
50	500	0,0021
75	750	0,0032
100	1000	0,0042

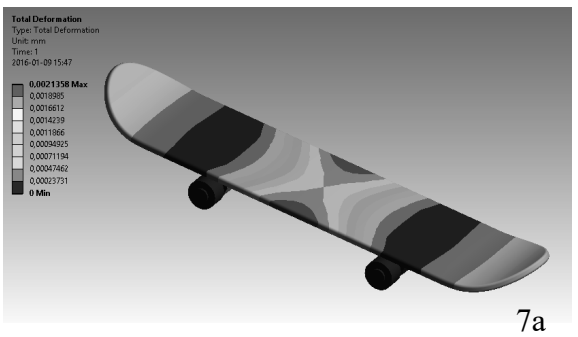

7a

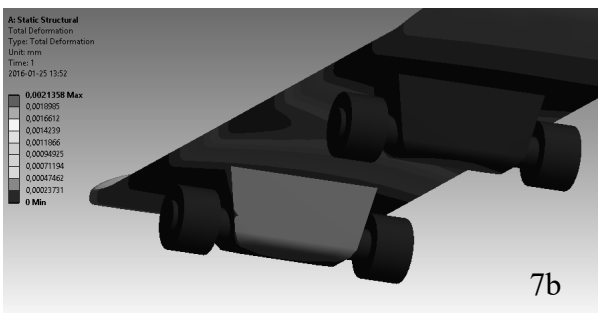

7b

Rysunek 7a, 7b. Rozkład przemieszczeń dla obciążenia 500N
Figure 7a, 7b. Displacement distribution for load 500

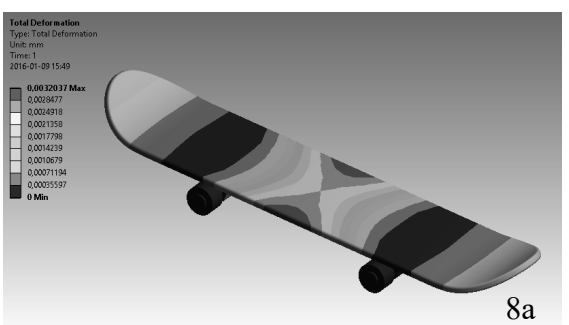

8a

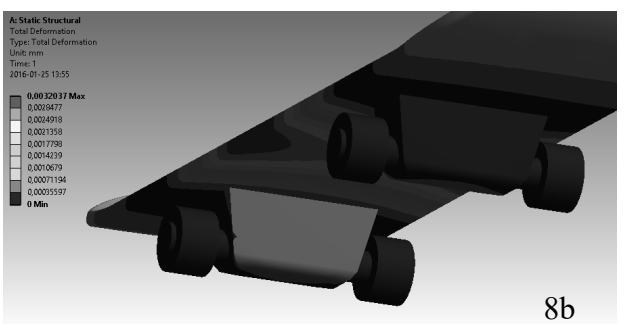

8b

Rysunek 8a, 8b. Rozkład przemieszczeń dla obciążenia 750N
Figure 8a, 8b. Displacement distribution for load 750N

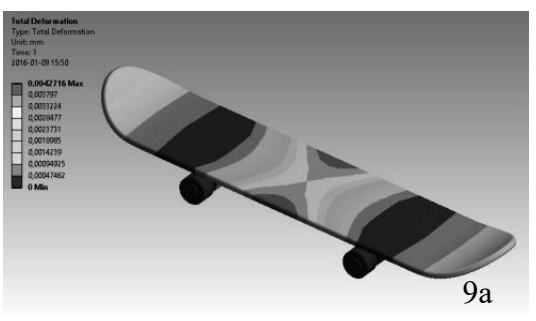

9a

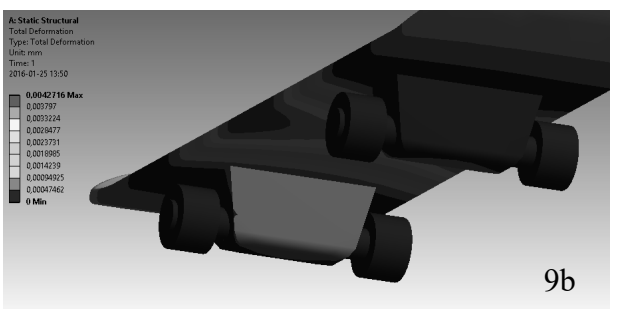

9b

Rysunek 9a, 9b. Rozkład przemieszczeń dla obciążenia 1000N
Figure 9a, 9b. Displacement distribution for load 1000N

5. PODSUMOWANIE

Praca miała na celu analizę naprężeń i przemieszczeń występujących w deskorolce w zależności od przyjętej wagi człowieka.

Wartość naprężenia w centralnym punkcie deskorolki wraz ze wzrostem wagi człowieka o 25kg wzrasta średnio o 0,14MPa, a maksymalna wartość naprężenia o 1,15MPa.

Dla wzrostu wagi człowieka o 25kg wartość przemieszczenia wzrasta o około 0,001mm. Przy tak małych wartościach różnice te można uznać za nieistotne.

Jak wynika z przeprowadzanych analiz nie ma przeciwwskazań do korzystania z tego rodzaju aktywności, nawet przy dwukrotnej różnicy w wadze człowieka, gdyż występujące różnice w naprężeniach są bardzo małe i nie spowodują żadnych odkształceń czy nawet pęknięcia materiału.

PODZIĘKOWANIA

Praca powstała w wyniku projektu PBL zrealizowanego z uczniami szkół ponadpodstawowych w ramach programu Inicjatywa Doskonałości - Uczelnia Badawcza Politechniki Śląskiej.

LITERATURA

1. "Penny Nickel Skateboard Review".
2. Brian Williams, Encyklopedia pytań i odpowiedzi.
3. "SKATEBOARDS: FIT & TYPES". LiveStrong.
4. https://www.sport-shop.pl/deskorolka-black-knight-team-p-5015.html

TalentDetector
9th January 2026
Gliwice, Poland
DEPARTMENT OF ENGINEERING MATERIALS AND BIOMATERIALS
FACULTY OF MECHANICAL ENGINEERING
SILESIAN UNIVERSITY OF TECHNOLOGY
INTERNATIONAL STUDENTS SCIENTIFIC CONFERENCE

Design and implementation of an application for the analysis of selected electrical parameters of solar cells

Szymon Rumniak[a], Szymon Garczarek[a], Krzysztof Wiśniewski[b], Rafał Honysz[c], Małgorzata Musztyfaga-Staszuk[d]

[a] Pupil, Complex of Communication Schools, Warszawska 35, 44-100 Gliwice, Poland
[b] Łukasiewicz Research Network – Institute of Non Ferrous Metals, Centre of Advanced Material Technologies
[c] Silesian University of Technology, Faculty of Mechanical Engineering, Material Investigating Laboratory, Konarskiego 18a, 44-100 Gliwice, Poland
[d] Silesian University of Technology, Department of Engineering Materials and Biomaterials, Konarskiego 18a, 44-100 Gliwice, Poland
email: malgorzata.musztyfaga@polsl.pl

Abstract: The aim of this study is to become familiar with the front metallization process of first-generation solar cells and to investigate its electrical parameters using a workstation equipped with the Correscan device. The analysis focused on parameters such as the resistivity of the emitter layer and the contact resistance at the metal-semiconductor junction. As part of the article, an intuitive virtual computing environment was developed to enable easy determination of selected electrical parameters of commercial PV cells.

Keywords: crystalline silicon solar cells, computer-aided support

1. INTRODUCTION

Figure 1 illustrates a typical structure of a silicon photovoltaic cell, which can be divided into various components and layers. The main components include the front electrode, consisting of busbars and collecting paths, as well as the rear electrode, which contains the rear electrode and connection contacts. The cell's layers typically consist of an antireflective layer, a passivating layer, p-type and n-type semiconductor materials, and the p-n junction [1].

The stage of manufacturing the front electrode in silicon solar cells is important because metallization is responsible for conducting the electrical charge to the external circuit. One of the most commonly used methods for producing metallization elements is the screen-printing technique, which allows for precise formation of both front and rear electrodes using conductive pastes [2–3].

The screen-printing method involves pressing a metallic paste through a printing mesh of appropriate density, coated with an emulsion mask that reproduces the pattern of the contact

fingers. After the printing step, the elements undergo drying and subsequent co-firing/sintering in an infrared belt furnace (Fig. 2) [2, 4].

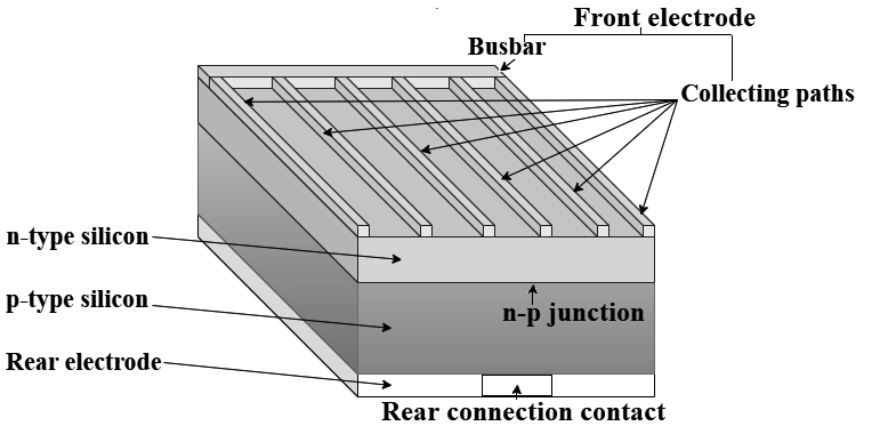

Fig. 1. Diagram of a typical structure of a silicon photovoltaic cell [1]

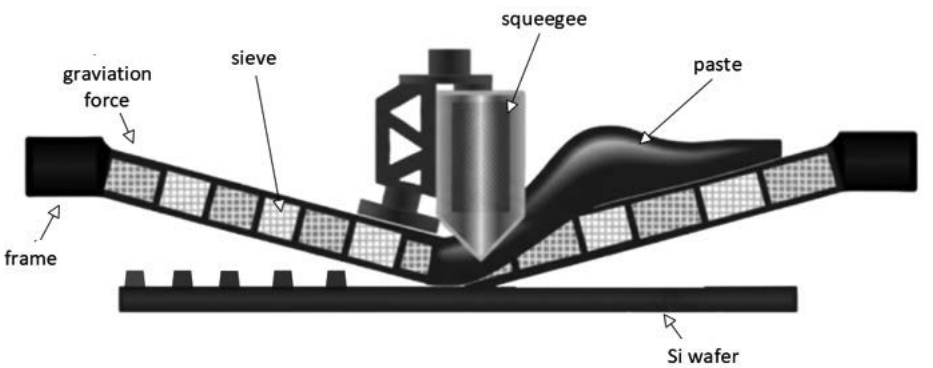

Fig. 2. An example of a graphical representation of the metallization fabrication stage in a silicon solar cell [2,3]

In this work, the focus was placed on the final stage of manufacturing a silicon solar cell (i.e., metallization), since the developed proprietary software is used to calculate, based on selected mathematical relationships, the electrical parameters of the front metallization, which can be measured between the emitter layer and the semiconductor.

2. MATERIAL

Twenty commercial monocrystalline silicon solar cells were used for the investigation. The dimensions of the cells were 15.8 cm × 15.8 cm ± 0.025 cm. The front electrode consisted of five busbars.

3. METHODOLOGY

Measurements of selected electrical properties of the analyzed solar cells were carried out using a measurement setup equipped with a Correscan device, available at the Photovoltaics

and Electrical Properties Research Laboratory of the Faculty of Mechanical Engineering Technology, Silesian University of Technology.

The measurement involves recording potential variations with a scanning probe moving across the front surface of the solar cell along a predefined trajectory [4].

During the measurement, the tungsten probe may [4]:

- contact the collecting path, remaining at the same potential as the busbar,
- touch the transition region between the metal path and the emitter, where the potential difference sharply increases, indicating proper co-firing of the conductive path,
- contact the emitter surface of the solar cell, where a characteristic potential difference is recorded.

During the investigations, parameters such as the resistivity (ρ) of the metal electrode path and the emitter and contact resistance (R_c) of the examined samples were determined. The applied research setup enables the measurement of local properties of the sample using a single-point probe (Fig. 3) [4, 5].

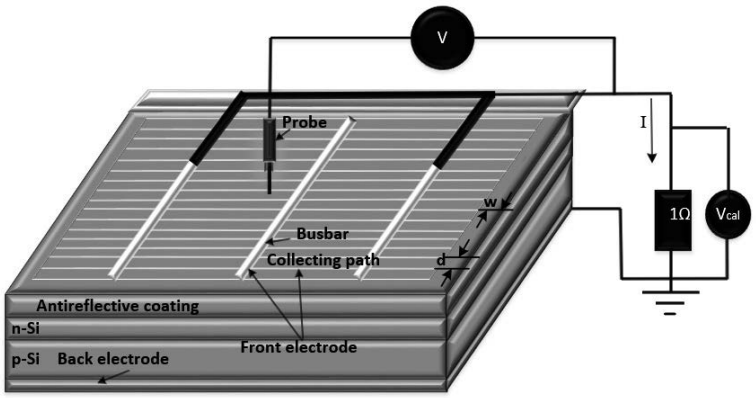

Fig. 3. Scanning setup with a single-point probe (where: w – width of the track, d – distance between the lines of the collecting electrode paths, V – voltage)[4, 5]

The resistivity of the metal–emitter contact can be determined from [4]:

$$\rho = C \cdot \frac{U_{ce}}{d \cdot J_{sc}}, \ \Omega \cdot \mathrm{cm} \tag{1}$$

where: ρ – resistivity of the transition region between the metal electrode path and the emitter, U_{ce} – contact-emitter potential measured by a probe, d – distance between the collecting paths of the solar cell, C – correction factor (value equal to 1.8) specified in the manufacturer's instructions, J_{sc} – scanning contact current density.

The estimation of the actual contact resistance R_c between the front electrode and the semiconductor emitter layer is given by the pattern [4]:

$$R_c = C \cdot \frac{U_{ce} \cdot w}{J_{ce} \cdot d}, \Omega \cdot \mathrm{cm}^2 \tag{2}$$

Where: w – width of the path.

Absolute Error (- it is the difference between the measured (or approximate) value and the true (exact) value [6]:

$$\Delta x = | x_{\text{measured}} - x_{\text{true}} | \tag{3}$$

Relative Error - it is the ratio of the absolute error to the true (or approximate) value. It shows how large the error is compared to the measured quantity. It is usually expressed as a percentage [6].

$$\delta[\%]= \frac{\Delta x \cdot 100\%}{x_{true}} \tag{4}$$

Python (version 3.12) [7,8] was selected for developing the calculator due to its high versatility and dynamic nature, which facilitate the implementation of complex computational tasks. Its simplicity and readability allowed the authors to focus on the core logic for calculating key parameters of silicon photovoltaic cells - such as the internal resistance components and industrial efficiency (typically ranging from 14% to 18%) -without introducing unnecessary complexity. The graphical user interface was developed using Kivy (version 2.2.1) [9] in combination with KivyMD (version 1.1.1). These frameworks enable the development of modern, cross-platform applications with a clean and intuitive design. Kivy provides flexible and touch-friendly interface solutions, while KivyMD adds Material Design components, contributing to a professional and user-friendly layout for simulating the seven-step technological process of cell manufacturing.

4. RESULTS

In Figure 4, the computer screen view with the input data defining the measurement parameters is presented.

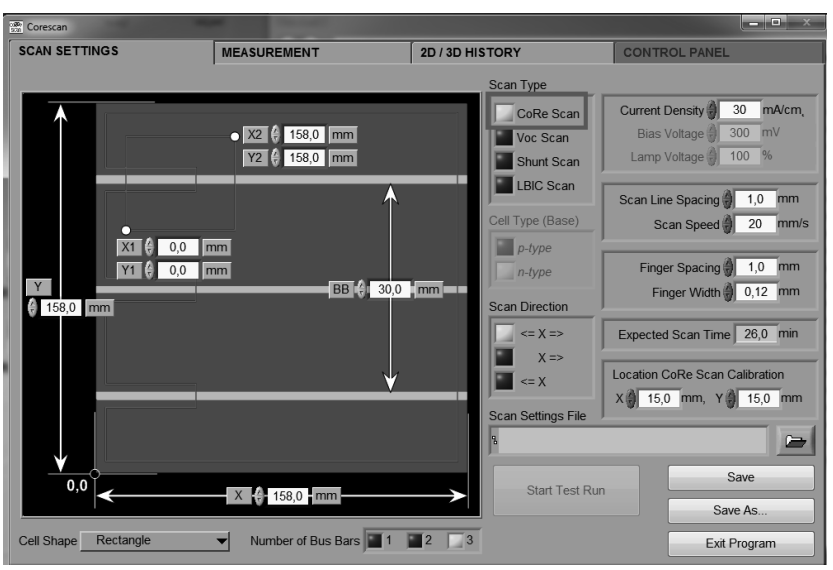

Fig. 4. View of the software settings with chosen Core Scan mode before measurement

Figures 5 and 6 present the results of the measurements.

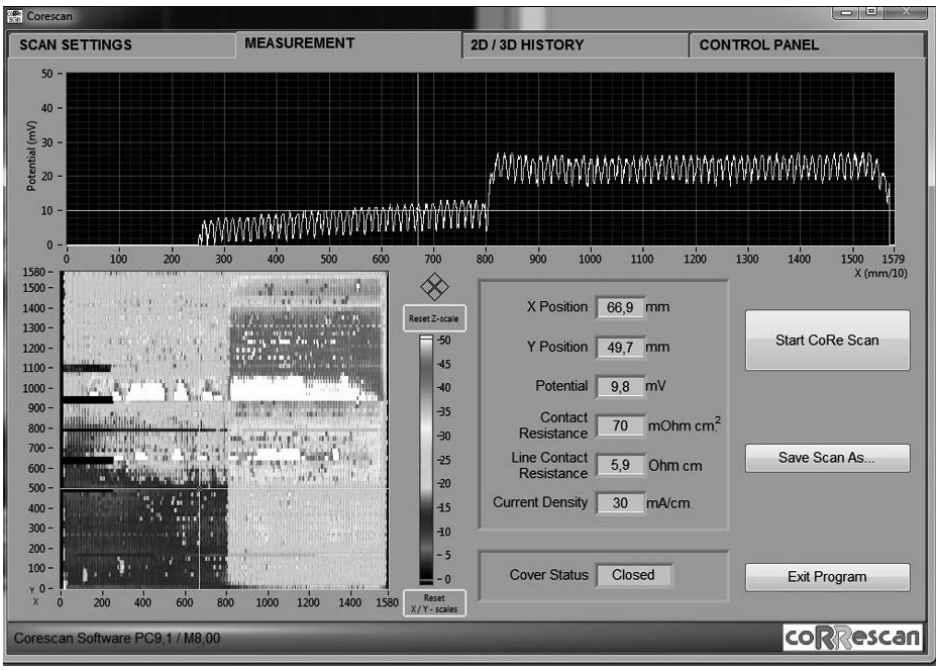

*Fig. 4. View of the "*Measurement*" tab after completing the measurement*

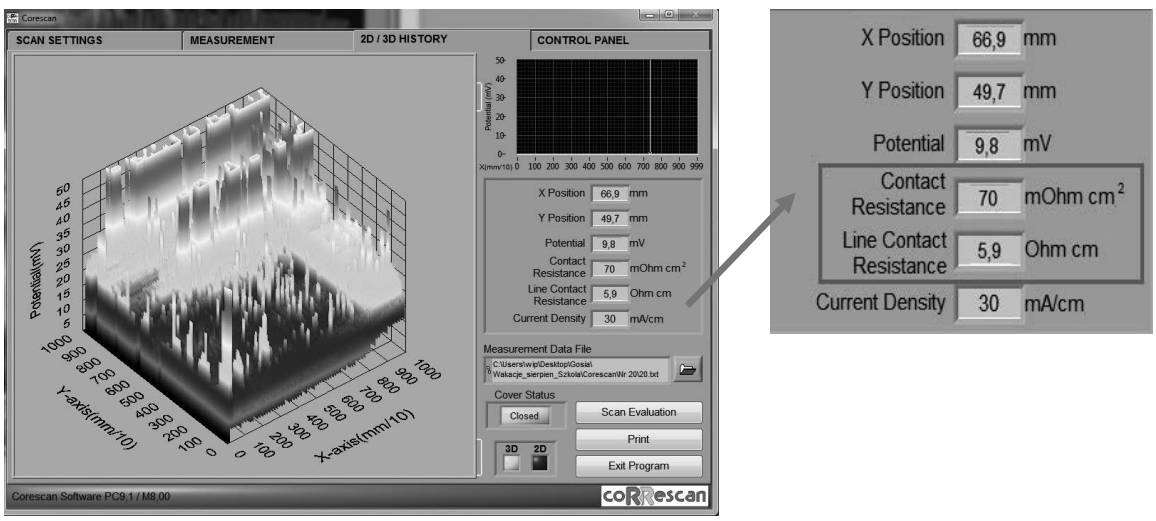

Fig. 5. View of the "2D/3D Measurement History" tab showing the measurement results of R_c and ρ (selected example)

For the purposes of this project, a specialized software tool was developed to calculate the fundamental parameters essential for analyzing silicon photovoltaic structures, such as layer resistivity and contact resistance. These metrics are crucial for evaluating the internal resistance components described in the technological process, including the resistance of the BSF layer, the emitter, and the metal-semiconductor junction. A comprehensive description of the application's functionality, supported by illustrative screenshots, is presented in Figures 6, 7, and 8."

The program calculates the resistivity and contact resistance of silicon photovoltaic cells. One of two calculation options is selected based on the available input parameters, which are then entered in the corresponding fields. After clicking the "Calculate" button, the results are displayed in the designated fields. The main interface of the application is shown in Fig. 6.

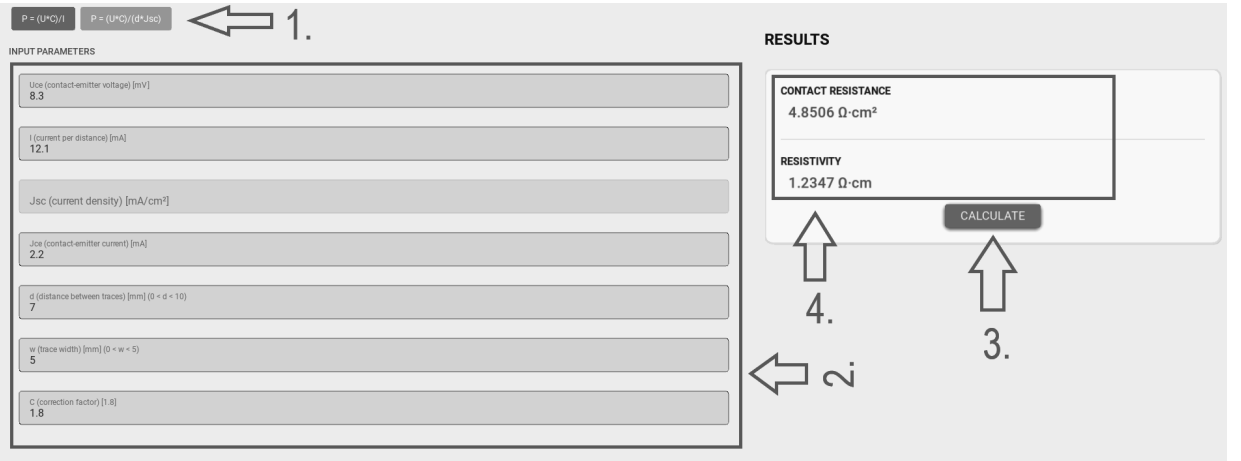

Fig. 6. View of the "Main" screen of the app used for calculating basic parameters for silicon cells

This section calculates absolute and relative errors. The measured and calculated values are entered into the corresponding fields marked as "1.". The error type is then selected in the area marked as "2.", which automatically initiates the calculation. The results are displayed in the area marked as "3.". This functionality is illustrated in Fig. 7.

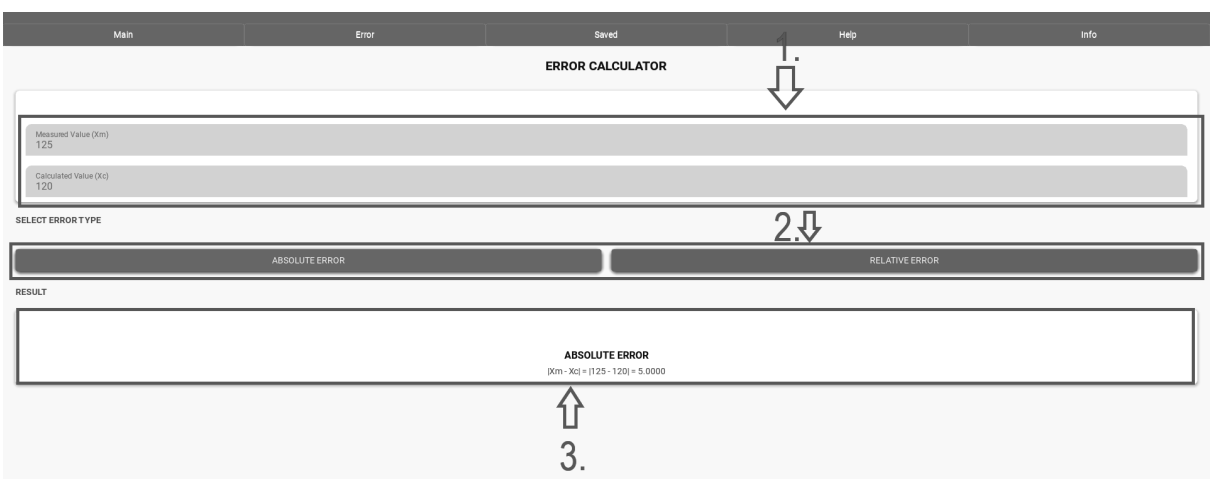

Fig. 7. View of the secondary function of the program used for calculating absolute and relative error

This section displays previously performed calculations automatically saved by the application. Only valid calculations from the main screen are stored. Saved entries, including the date, input variables, and results, are shown in the area labeled "1." and arranged from newest to oldest, with ten entries per page. Page navigation is performed using the buttons marked "2." (next) and "3." (previous). A date-based search is available via the field marked "4." using the format YYYY-MM-DD or YYYY-MM-DD HH-mm. The history view is shown in Fig. 8.

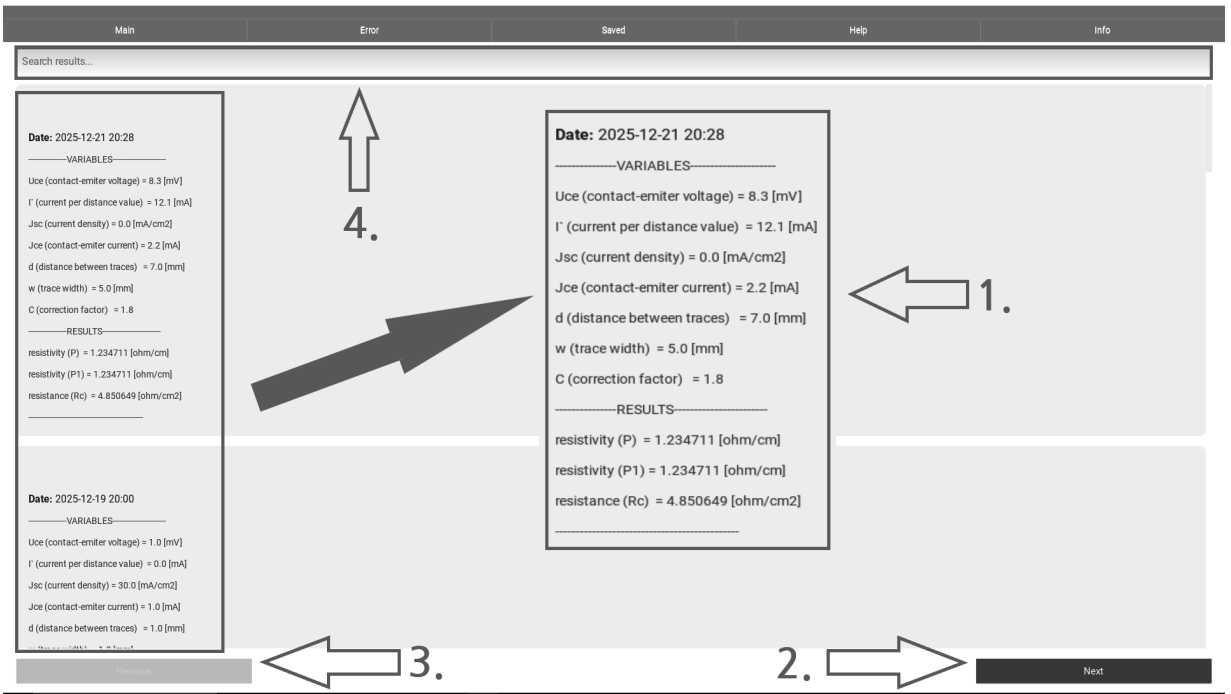

Fig. 8. View of the built-in system designed for viewing past calculations

5. RESULTS

The article focuses on the design and implementation of an application for the analysis of selected electrical parameters of first-generation solar cells. The primary research objective was to explore the front metallization process, typically performed using the screen-printing technique, and to investigate the resistivity of the emitter layer and the contact resistance at the metal-semiconductor junction. Measurements were conducted on 20 commercial monocrystalline silicon solar cells with dimensions of 15.8 cm × 15.8 cm using a measurement setup equipped with a Correscan device, which records potential variations via a moving tungsten probe. As part of the work, an intuitive virtual computing environment was developed to calculate parameters based on mathematical relationships and visualize them in the form of 2D and 3D charts. The entire project was carried out within the framework of project-oriented education (PBL), allowing secondary school students to actively participate in advanced scientific research conducted at the Silesian University of Technology.

ACKNOWLEDGEMENTS

This work was produced as part of the project implemented within the framework of project-oriented education - PBL project implemented with secondary school students, in the VI competition under the Excellence Initiative - Research University program, at the Silesian University of Technology.

BIBLIOGRAPHY

1) Dobrzański L.A., Musztyfaga M., Staszuk M., *Metallisation technology of silicon solar cells using the convectional and laser technique*, IMSP'2012, Pamukkale-Denizli, 2012, s. 789-798.
2) Dobrzański L.A, Musztyfaga M, *Małgorzata Effect of the front electrode metallisation process on electrical parameters of a silicon solar cell*. J. Achiev. Mater. Manuf. Eng. 2011, 115–144.
3) Musztyfaga, M., *Laser Microprocessing of Silicon Elements of Photovoltaic Cells*. PhD Thesis. Faculty of Mechanical Engineering Technology, 2011.
4) Correscan_user_manual_Master_mrn.Pdf. Software Version 10.00 MRN-061-EN, Registration Number: MRN-061-EN 2025.
5) Contact Definition in Industrial Silicon Solar Cells. In Solar Energy; InTech, 2010 ISBN 978-953-307-052-0.
6) Jóźwiak J.; Podgórski, J. *Statystyka od podstaw*; PWE: Warsaw, Poland, 2019.
7) Welcome to Python. https://www.python.org/ [dostęp: 21.12.2025]
8) Python Documentation. https://docs.python.org/ [dostęp: 21.12.2025]
9) The Open Source Python App Development Framework. https://kivy.org/ [dostęp: 21.12.2025]

TalentDetector

9th January 2026
Gliwice, Poland

DEPARTMENT OF ENGINEERING MATERIALS AND BIOMATERIALS
FACULTY OF MECHANICAL ENGINEERING
SILESIAN UNIVERSITY OF TECHNOLOGY

INTERNATIONAL STUDENTS SCIENTIFIC CONFERENCE

Design and implementation of an autonomous HMI terminal for presenting research results on fine-crystalline structure formation in metals via laser modification.

Natalia Rupala[a], Mirosław Bonek

[a] Silesian University of Technology, Faculty of Automatic Control, Electronics and Computer Science, email: nr310520@student.polsl.pl
[b] Silesian University of Technology, Faculty of Mechanical Engineering, Department of Engineering Materials and Biomaterials, Gliwice, Poland

Abstract: The objective of this research was to design and construct an autonomous device featuring a 7-inch touchscreen for visualizing the results on fine-crystalline structure formation in metals via laser modification. The primary design challenge arose from the necessity to migrate from the originally planned Windows IoT environment to the Raspberry Pi OS. This decision was driven by Microsoft's official withdrawal of support for newer ARM architecture units, which hindered the implementation of a stable and secure Human-Machine Interface (HMI). The paper details the successful migration of application logic from C# to the Kivy/Python framework, the resolution of system environment isolation issues, and the optimization of the graphical layout for the physical display.

Keywords: Raspberry Pi 5, Touchscreen, Kivy, System migration, Windows IoT, Data visualization.

1. THEORETICAL INTRODUCTION AND PROJECT GENESIS

The primary objective of the project was to develop an autonomous HMI (Human-Machine Interface) terminal for the mobile visualization of laser-induced metal structure modification research results. The original concept was based on the Windows 10 IoT Core system and the C# language, which was intended to ensure integration with Microsoft's industrial standards. However, the official withdrawal of support for the ARM architecture in newer hardware models (Raspberry Pi 5) and the lack of stable graphics drivers necessitated a revision of the plans.
In light of these limitations, the decision was made to migrate to the native Raspberry Pi OS (Linux) and utilize the Kivy framework based on the Python language. The theoretical justification for this choice is based on three key aspects:

- **Native GPU acceleration:** Utilizing the OpenGL ES library for smooth rendering of complex graphical data directly by the device's graphics processing unit.

- **NUI (Natural User Interface) architecture:** Implementing a multi-touch oriented interface, ensuring system responsiveness comparable to modern mobile devices.
- **Environmental isolation:** Employing virtual environments (venv) in accordance with the PEP 668 specification, which guarantees application stability regardless of operating system updates.

The transition from a closed system to an Open Source solution allowed for the transformation of a standard development board into a professional tool, fully tailored to the physical capabilities of the touchscreen.

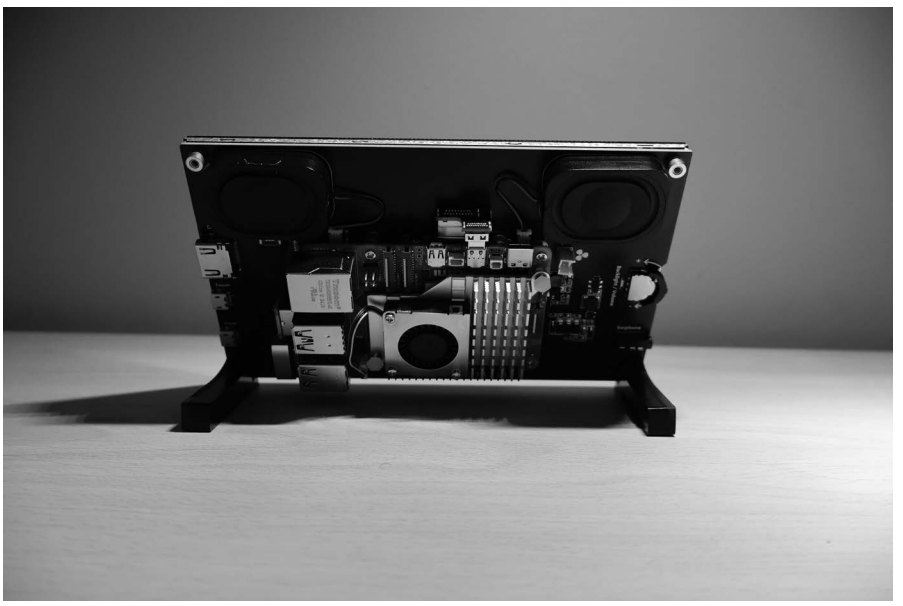

Fig. 1.1. General view of the visualization system. The photograph shows the Raspberry Pi 5 central unit integrated with a 7-inch touchscreen display. (Photo: Natalia Rupala)

Fig. 1.2. General view of the visualization system, featuring the 7-inch touchscreen display. (Photo: Natalia Rupala)

2. EVOLUTION OF THE SYSTEM ENVIRONMENT

2.1 The Problem of Withdrawn Microsoft Support

Initially, the use of C# code on the Windows platform was planned. However, an analysis of product lifecycle policies revealed that Microsoft limited support for IoT systems on the ARM architecture in newer hardware models. Attempts to use unofficial installers resulted in a lack of touch driver stability, which precluded the professional application of the device.

2.2 Change of Strategy: Raspberry Pi OS and Python

A decision was made to switch the operating system to the native Raspberry Pi OS. For the interface development, the Kivy framework was selected, which allows for the creation of NUI (Natural User Interface) type applications with full hardware acceleration on Linux systems.

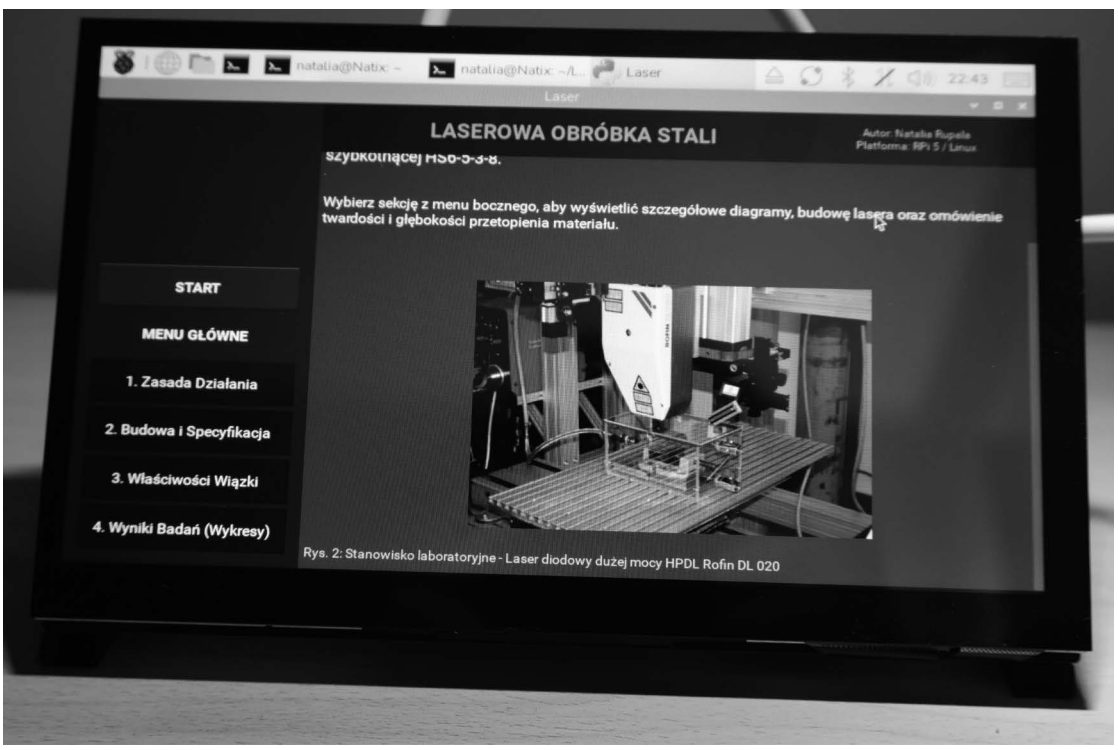

Fig. 2. Close-up of the user interface (UI) running in the Raspberry Pi OS environment. The side navigation panel is visible. (Photo: Natalia Rupala)

3. TECHNICAL IMPLEMENTATION (SYSTEM ARCHITECTURE)

- **Security Management:** A virtual environment (venv) was implemented to maintain system integrity in accordance with the PEP 668 specification regarding the management of external packages.
- **Optimization for 7-inch Screen:** The .kv language was utilized to define a declarative UI layout, ensuring responsiveness at a resolution of 1024x600.
- **Layout Stabilization:** A text parameter binding mechanism was applied, which eliminated rendering errors for dynamic content.

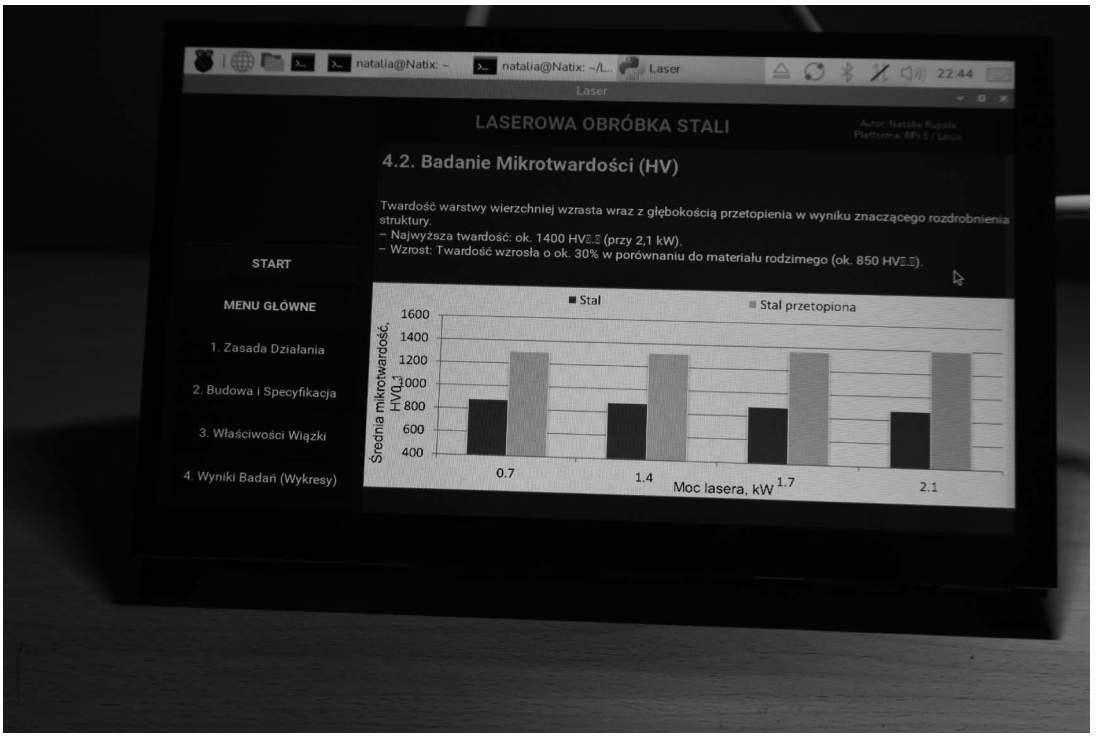

Fig. 3. Example of research results visualization. The application displays graphs and technical descriptions while maintaining responsiveness. (Photo: Natalia Rupala)

4. CONCLUSIONS

1. The lack of official support for Windows IoT on ARM forces engineers to choose Open Source solutions.
2. The Kivy framework proved to be more effective in building a touch-based HMI interface than the UWP platform.
3. The use of isolated Python environments (venv) is crucial for the stability of embedded systems.

ACKNOWLEDGEMENTS

The work was created as part of project based learning - PBL, in the 13th competition under the Initiative of Excellence - Research University, Silesian University of Technology, Gliwice, Poland and as part of project of Students Scientific Circle of Laser Surface Treatment under the Initiative of Excellence - Research University, Silesian University of Technology, Gliwice, Poland.

BIBLIOGRAPHY

1. Upton E., Halfacree G., *Raspberry Pi User Guide*, Helion Publishing, Gliwice 2020.
2. Virgil D., *Kivy - Interactive Applications in Python*, Packt Publishing, 2015.

3. Phillips D., *Python 3 Object-Oriented Programming*, Helion Publishing, Gliwice 2016.
4. Kivy Framework Documentation, *Kivy: Cross-platform Python Framework for NUI Development*, online: https://kivy.org/doc/stable/ (accessed: 16.12.2025).
5. Raspberry Pi Documentation, *Raspberry Pi 5 Hardware Specifications and OS Management*, online: https://www.raspberrypi.com/documentation/ (accessed: 16.12.2025).
6. Microsoft Learn, *Windows IoT Core and Enterprise Lifecycle Policy and Hardware Support*, online: https://learn.microsoft.com/en-us/lifecycle/products/windows-10-iot-core (accessed: 16.12.2025).
7. PEP 668, *Marking Python Environments as Externally Managed*, Python Software Foundation, online: https://peps.python.org/pep-0668/ (accessed: 16.12.2025).

TalentDetector

9th January 2026
Gliwice, Poland

DEPARTMENT OF ENGINEERING MATERIALS AND BIOMATERIALS
FACULTY OF MECHANICAL ENGINEERING
SILESIAN UNIVERSITY OF TECHNOLOGY

INTERNATIONAL STUDENTS SCIENTIFIC CONFERENCE

Analiza numeryczna rozkładu naprężeń mających wpływ na wkrętak ręczny oraz jego wizualizacja

Adam Schwarz[a], Łukasz Buszka[a], Maksymilian Szweda[b], Monika Polak-Micewicz[c], Wojciech Mikołejko[d], Agata Śliwa[d]

[a] Uczniowie Zespołu Szkół Technicznych i Ogólnokształcących „Mechanik" w Tarnowskich Górach, email: misteradamowski@gmail.com, lukaszbuszka2@gmail.com
[b] Uczeń Zespołu Szkół Techniczno-Usługowych w Tarnowskich Górach
email: maksszweda11@gmail.com
[c] Nauczyciel Zespołu Szkół Technicznych i Ogólnokształcących „Mechanik" w Tarnowskich Górach, email: monika.polakmicewicz@gmail.com
[d] Politechnika Śląska, Wydział Mechaniczny Technologiczny, Instytut Materiałów Inżynierskich i Biomedycznych , email: wojciech.mikolejko@polsl.pl, agata.sliwa@polsl.pl

Streszczenie: W pracy przedstawiono analizę MES rozkładu naprężeń powstałych w wyniku obciążenia części roboczej wkrętaka siłą 250[N]. Analiza została sporządzona w programie SolidWorks Premium dla stali stopowej 1.4057 oraz stali węglowej.
Abstract: The paper presents the analysis of FEM stress distribution caused by the load force of 800 [N] on the working part of the screwdriver. The analysis was done in SolidWorks Premium for stainless steel 1.4057 and carbon steel.

Słowa kluczowe: Wkrętak płaski, SolidWorks, naprężenia, przemieszczenia, symulacja komputerowa

1. WPROWADZENIE

Wkrętak lub potocznie śrubokręt jest jednym z najbardziej podstawowych narzędzi, wykorzystywanych w zakładach przemysłowych, firmach informatycznych, placówkach naukowych czy w gospodarstwach domowych. Jego podstawową funkcja jest umożliwienie, jak i ułatwienie umocowanie wkrętu w materiale docelowym lub otworze gwintowym. Podstawowy wkrętak składa się z rękojeści umocowanej na grocie. Grot jest specjalnie ukształtowany w jego dolnej części, co umożliwia mu wpasowanie się w łby wkrętów. Różne końcówki umożliwiają zapewnienie zróżnicowanych właściwości, takich jak zwiększenie momentu obrotowego lub zwiększenie odporności na uszkodzenia [1]. Na rysunku 1 przedstawiono podział grotu wkrętaka:

Płaski
1. Płaski chroniony
2. Pozidriv
3. Phillips
4. Torx
5. Torx TR
6. Torx Plus
7. XZN
8. Sześciokątny zewnętrzny
9. Sześciokątny wewnętrzny (Inbus)
10. Kwadratowy (Robertson)
11. Torq-Set
12. Tri-Wing
13. Spanner

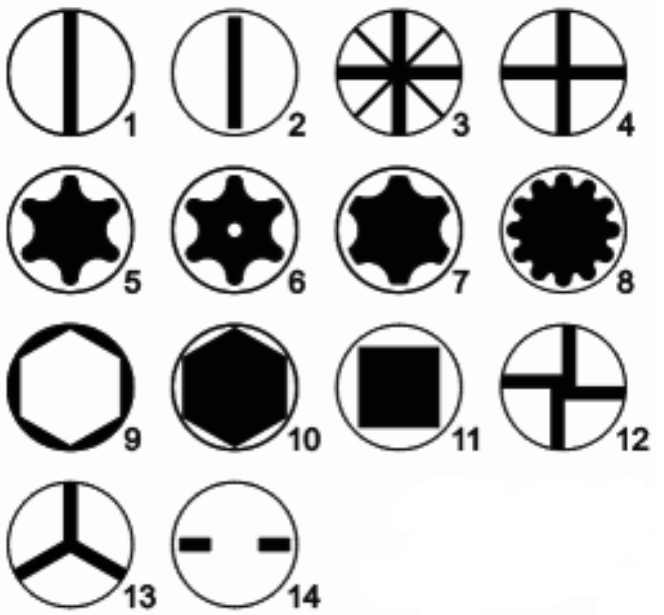

Rys. 1 Podział grotów wkrętaka
Fig.1 Split of the tips of a screwdriver

Powierzchnie zewnętrzne części roboczych wkrętaków powinny być gładkie, bez zadziorów, pęknięć i śladów korozji które mogłyby prowadzić do zmian w materiale, oraz powodować jego szybsze zużycie (Rys. 2) [2].

Rys. 2 Przykładowy wkrętak o grocie płaskim chronionym
Fig. 2 An example of a screwdriver with a flat protected tip

Rękojeść wkrętaków powinny być gładkie, bez wgnieceń, pęknięć i ubytków materiału. Dopuszcza się na rękojeści ślady od krawędzi podziału matrycy wtryskowej oraz dopuszcza się do 4 pęcherzyków powietrza o średnicy do 2mm – dla rękojeści z tworzyw przezroczystych. Rękojeść powinna zapewniać komfort użytkowania narzędzia oraz być wykonana z materiału który nie odkształci się oraz nie zmieni swoich właściwości w czasie wykonywania pracy. [2].

Koszulki elektroizolujące wkrętaków elektrotechnicznych powinny ściśle przylegać do trzpienia, nie marszczyć się, nie przesuwać wzdłuż i nie obracać wokół trzpienia, gdyż w

innym przypadku uniemożliwiało by wykonanie zadania. Długość ostrza i części trzpienia nie osłoniętych koszulką elektroizolacyjną nie powinna być większa niż 15 mm (Rys.3) [2].

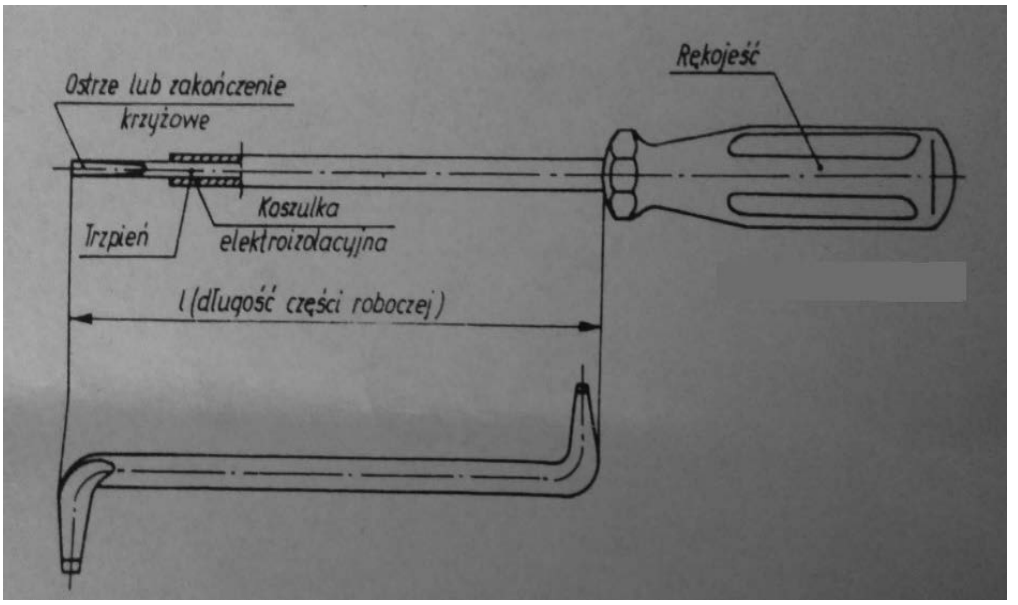

Rys. 2 Budowa wkrętaka płaskiego [1]
Fig. 2 Construction of a flat screwdriver

2. ZAŁOŻENIA MODELOWE

Podczas analizy grot zostł utwierdzony z obu stron dolnej części wkrętaka co ma zasymulować pozycję wkrętaka podczas jego działania. Następnie przyłożono siła skręcająca w górnej pozycji grotu, co odpowiada sile włożonej przez operatora podczas wkręcania wkrętu oraz ma zasymulować rzeczywiste pracę wykonywaną przez śrubokręt.

Symulacje komputerową wykonano dla 2 różnych materiałów: stal stopowa oraz stal węglowa(Tab.1). Wymiary grotu zostały przedstawione na zdjęciu czwartym (rys 4). Siła skręcająca będzie miała wartość: 250 N. Siłą ta odpowiada sile jaką człowiek posiada w dłoni.

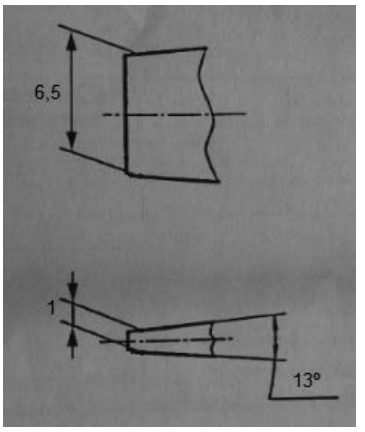

Rys. 3 Wymiary grota wkrętaka oraz kąt pochylenia grota [2]
Fig. 4 Dimensions of the screwdriver tip and tip angle [2]

Tab. 1 Wybrane własności stali stopowej i węglowej [4]
Table 1 Properties of alloy steel [4]

Właściwości	**Stal stopowa**	**Stal węglowa**	**Jednostka**
Współczynnik sprężystości	210000	210000	N/mm^2
Współczynnik Poissona	0.28	0.28	n.d.
Współczynnik naprężenia ścinającego	79000	79000	N/mm^2
Masa właściwa	7700	7800	kg/m^3
Wytrzymałość na rozciąganie	723.83	399.83	N/mm^2
Wytrzymałość na ściskanie			N/mm^2
Granica plastyczności	620.42	220.59	N/mm^2
Współczynnik rozszerzalności cieplnej	1.3e-005	1.3e-005	/K
Współczynnik przewodzenia ciepła	50	43	W/(m·K)
Ciepło właściwe	460	440	J/(kg·K)
Stosunek tłumienia materiału			n.d.

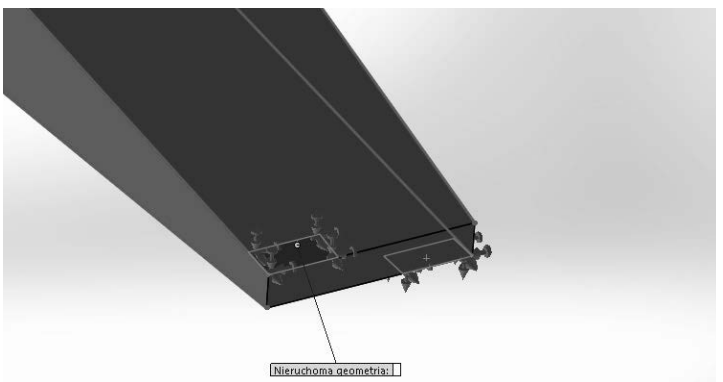

Rys. 4 Miejsca unieruchomienia wkrętaka
Fig 5. Immobilizer location

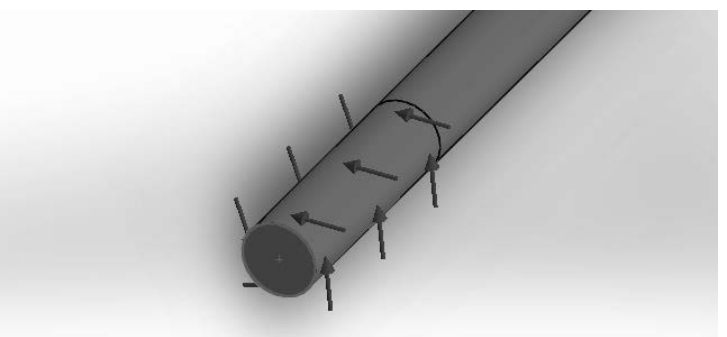

Rys. 5 Górna część wkrętaka obciążona siłą skręcającą o wartości 250 [N]
Fig. 6 The upper part of the screwdriver is loaded with a twisting force of 250 [N]

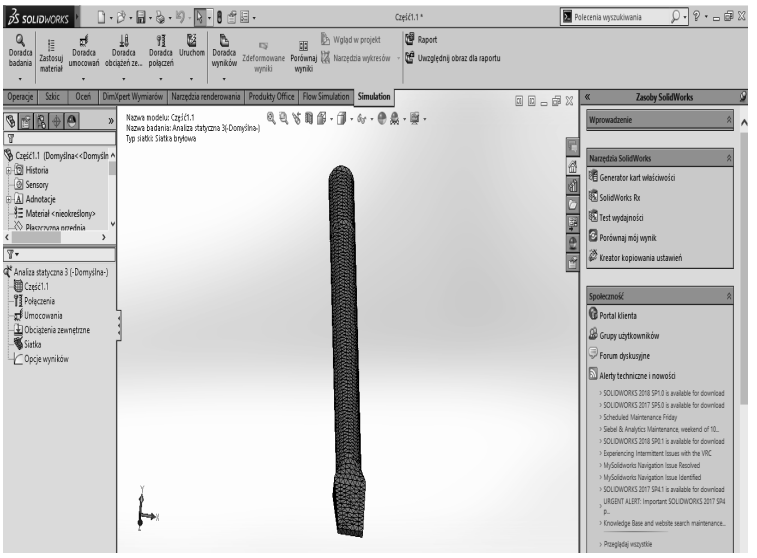

Rys.7 Siatka nałożona na wkrętak.
Fig.7 Mesh imposed on the screwdrive.

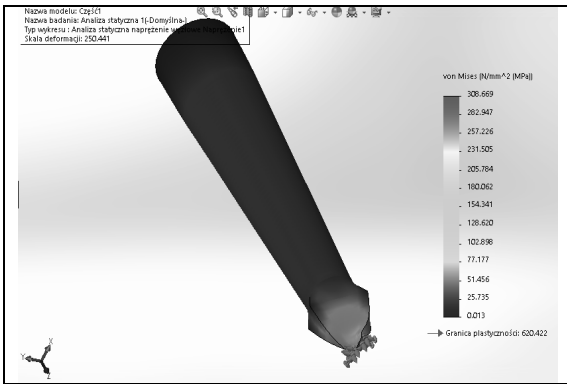

Rys. 8 Naprężenia σ_{red} w stali stopowej
Fig. 8 Stresses von Misses in alloy steel

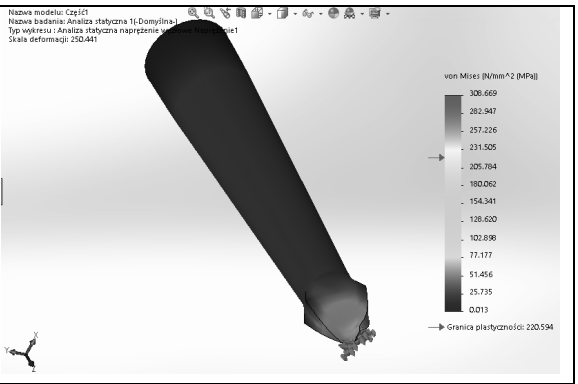

Rys. 9 Naprężenia σ_{red} w stali węglowej
Fig. 9 Stresses von Misses in carbon steel

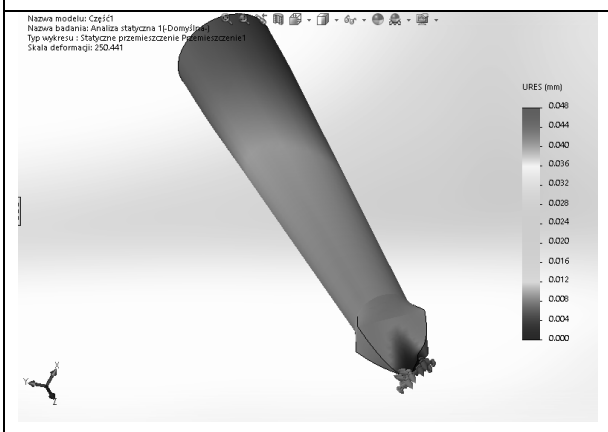

Rys. 10 Przemieszczenie statyczne w stali stopowej
Fig. 10 Static displacement in alloy steel

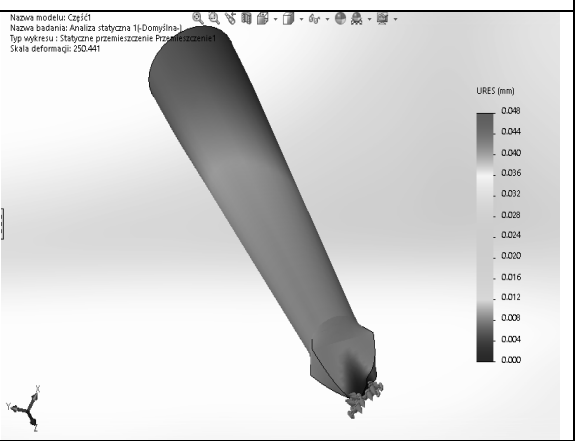

Rys. 11 Przemieszczenie statyczne w stali węglowej
Fig. 11 Static displacement in carbon steel

3. ANALIZA ROZKŁADU NAPRĘŻEŃ

Na rysunkach 8 i 9 przedstawiają rozkład naprężeń zredukowanych (σred) oraz przemieszczenie statyczne powstałe na części roboczej wkrętaka płaskiego podczas działania na niego obciążenia wynoszącego 250N. Badania zostały przeprowadzone dla Sali stopowej oraz stali węglowej.
Dla obu stali możemy zaobserwować, że największe naprężenia powstały w miejscu mocowania wkrętak.
Dla stali stopowej maksymalne σred wynosi 308,7 [MPa], a jej granica plastyczności wynosi 620 [Mpa]. Możemy zaobserwować, że odkształcenie wynikające z naprężenia występuje jedynie w jego dolnej części, co jest przedstawione na rysunek 8. Oprócz naprężenia zaobserwowane przemieszczenie statyczne które swoją najwyższą wartość 0.48[mm] posiada w górnej części, a następnie stopniowo maleje do miejsca mocowania (Rys. 10).
Dla stali węglowej maksymalne σred wynosi 308,7 [MPa], a jej granica plastyczności wynosi 220,9 [Mpa]. Możemy zaobserwować, że odkształcenie wynikające z naprężenia występuje jedynie w jego dolnej części, co jest przedstawione na rysunek 9. Oprócz naprężenia zaobserwowano przemieszczenie statyczne, które swoją najwyższą wartość 0.48[mm] posiada w górnej części, a następnie stopniowo maleje do miejsca mocowania (Rys. 11).

4. PODSUMOWANIE

W pracy przedstawiono analizę metodą elementów skończonych naprężeń powstających podczas wkręcania wkrętu używając wkrętaka. Analizę przeprowadzona dla stali stopowej oraz stali węglowej przy obciążeniu 250N. Otrzymany wynik rozkładu naprężeń dla stali stopowej wynosi σred =308,7 [MPa], granicy plastyczności dla stali stopowej wynosi = 620 [MPa]. Dla stali węglowej rozkład naprężeń wynosi σred =308,7 [MPa], granica plastyczności dla stali węglowej wynosi= 220 [MPa]. Rozkład naprężeń dla stali węglowej przekracza granicę plastyczności. Wartości przemieszczenia statycznego dla stali stopowych i stali węglowych są jednakowe jednak w celu wytworzenia gotowego elementu, zalecane jest wykorzystanie stali stopowej.

PODZIĘKOWANIE

Praca powstała w wyniku projektu PBL zrealizowanego z uczniami szkół ponadpodstawowych w ramach programu Inicjatywa Doskonałości - Uczelnia Badawcza Politechniki Śląskiej.

LITERATURA

1. https://www.castorama.pl/inspiracje-i-porady/narzedzia-i-artykuly/narzedzia-reczne/klucze-i-wkretaki/wkretaki/plaskie/rodzaje-i-zastosowanie-wkretakow.html dostęp dnia:07.01.2017r
2. Norma PN-85/M-64953
3. Norma PN-ISO 2380-1:2001
4. Baza własności materiałów w programie SolidWorks Premium

TalentDetector
9th January 2026
Gliwice, Poland
DEPARTMENT OF ENGINEERING MATERIALS AND BIOMATERIALS
FACULTY OF MECHANICAL ENGINEERING
SILESIAN UNIVERSITY OF TECHNOLOGY
INTERNATIONAL STUDENTS SCIENTIFIC CONFERENCE

Ochronne powłoki fosforanowe na powierzchni stali

Rafał Siemionko[a], Paweł Barański[a], Mateusz Gala[a], Beata Krupińska[b]

[a] Silesian University of Technology, Faculty of Mechanical Engineering, Mechanics and Machine Construction
[b] Silesian University of Technology, Faculty of Mechanical Engineering, Department of Engineering Materials and Biomaterials
email: beata.krupinska@polsl.pl

Streszczenie: Projekt dotyczy zabezpieczenia antykorozyjnego powierzchni stali matowo-szarymi powłokami fosforanów, oceny wpływu parametrów procesu na mikrostrukturę i własności mechaniczne warstwy wierzchniej. W czasie projektu studenci analizują wyniki badań mikrostrukturalnych oraz wybranych własności mechanicznych pokryć w przy zastosowanych parametrach procesu technologicznego.
Abstract: The project involves the anti-corrosion protection of steel surfaces with matte-gray phosphate coatings, assessing the impact of process parameters on the microstructure and mechanical properties of the surface layer. During the project, students analyze the results of microstructural tests and selected mechanical properties of the coatings under the applied technological process parameters.

Keywords: materials, protective coatings, steel coating, phosphate conversion coating

1. WSTĘP

Jednymi z najpowszechniej stosowanych powierzchni konwersyjnych są powłoki fosforanowe. Charakteryzują się wysoką porowatością, kruchością oraz właściwościami antykorozyjnymi i izolacyjnymi. Nie są wykorzystywane jako jedyna i bezpośrednia warstwa ochronna ze względu na swoją porowatość, toteż wzmacnia się je za pomocą olei, lakierów czy farb. [1,2,5]
Proces fosforanowania polega na zanurzeniu przedmiotów w roztworach fosforanu z kwasem fosforowym. Zależnie od fosforanów użytych przy procesie fosforanowania, wyróżniamy powłoki fosforanowe [1,2,5]:

- manganowe (90°C - 95°C),
- cynkowe (35°C - 80°C),
- żelazawą (25°C - 65°C).

Strukturę krystaliczną powłoki fosforanowej możemy kontrolować za pomocą zmiany pH roztworu. Jest to związane z przesuwaniem równowagi dla poniżej przedstawionej reakcji [1,2]:

$$3Me(H_2PO_4)_2 \leftrightarrow Me_3(PO_4)_2 + 4H_3PO_4 \qquad (1)$$

Kąpiel fosforowa powinna posiadać stężenie jonów Me^{2+} i H_2PO_4 w określonej temperaturze, aby przesunąć równowagę reakcji i utworzyć nierozpuszczalne fosforany na metalu (np. fosforany cynku, manganu). Kluczowe jest utrzymanie odpowiedniego pH (lekko kwasowe), temperatury i stężenia, co prowadzi do tworzenia się grubej, drobnoziarnistej i porowatej warstwy fosforanowej, która służy jako doskonała podstawa pod farby lub smary, zwiększając przyczepność i ochronę antykorozyjną. [3]
Metoda ta jest stosowana najczęściej w przemyśle motoryzacyjnym i maszynowym, m.in. przy produkcji karoserii, elementów podwozia i silnika, łożyska czy kół zębatych. [4,5]

2. MATERIAŁY I METODYKA BADAWCZA

Do procesu fosforanowania cynkowego przygotowano profile stalowe wykonane ze stali S235 (Tab. 1) o wymiarach 20x20x2 mm i długości 30 mm (Rys. 1).

Fosforanowanie zostało wykonane przez firmę Elektrocarbon Galwan Sp. z o.o. w Tarnowskich Górach.

Tabela 1. Procentowy skład chemiczny stali S235 według normy PN-EN 10025-2.

C	Mn	P	S	N	Fe
≤ 0,17	**≤ 1,4**	**≤ 0,045**	**≤ 0,045**	**≤ 0,012**	**reszta**

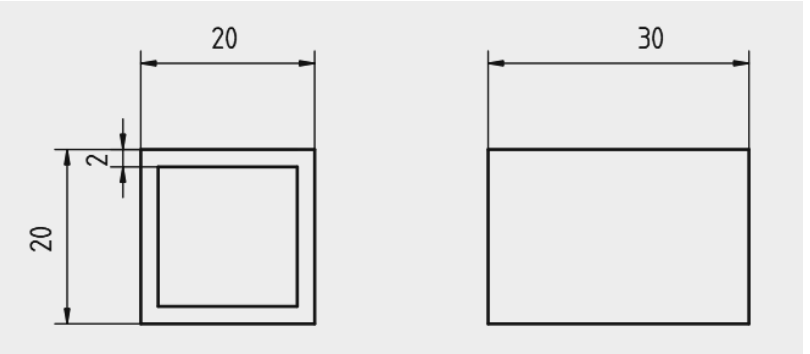

Rysunek 1. Wymiary profili stalowych wykorzystanych

Proces fosforowania wymagał wykonania następujących etapów: odtłuszczania elektrochemicznego w temperaturze około 40-60°C (preferowana temperatura powyżej 50°C) przez 15-30 minut, przy odpowiedniej gęstości prądu (A/dm²), trawienia w kwasie solnym o stężeniu ustalonym przez producenta w czasie 10-30 minut, fosforanowaniu cynkowym wykonanym w temperaturze pomiędzy 50 a 95°C przez 15-30 minut, pokrycia emulsją, suszenia w temperaturze nieprzekraczającej 60 °C.

Otrzymane w ten sposób próbki poddano badaniom mikrostruktury i wybranych własności (Rys.2). Przygotowano zgłady metalograficzne przy użyciu szlifierko-polerki firmy STRUERS.

a) b)

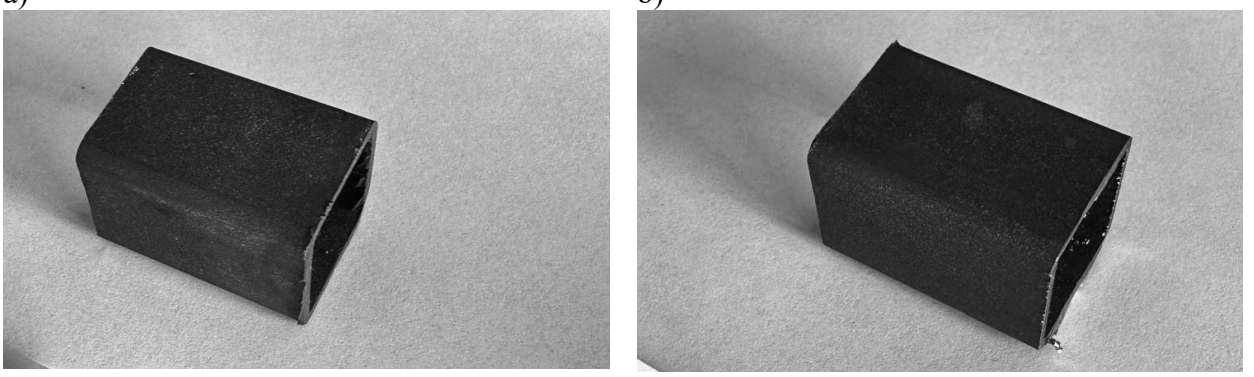

Rysunek 2. a) Profil stalowy z powłoką fosforanową-cynkową; b) Profil stalowy z powłoką fosforanową-cynkową i warstwą antykorozyjną

Następnie wykonano:

a) analizę mikrostruktury za pomocą mikroskopu świetlnego Axio Observer firmy Zeiss wraz z dedykowanym oprogramowaniem do analizy obrazu struktur metalograficznych przy powiększeniach 500X, 2500X i 5000X
b) analizę składu i grubości powłoki elektronowym mikroskopem skaningowym Zeiss Supra 35 z przystawką do analizy składu chemicznego w mikroobszarach EDS,
c) badania mikrotwardości za pomocą twardościomierza Vickers'a - FM-ARS 9000 firmy FUTURE-TECH.

3. WYNIKI BADAŃ

Na rysunku 3a i 3b przedstawiono mikrostrukturę badanych próbek otrzymaną w wyniku badań na mikroskopie świetlnym. Na rysunku 4 przedstawiono mikrostruktury (Rys.4 a-d) i grubości powierzchni uzyskane w wyniku obserwacji na mikroskopie skaningowym (Rys.4b oraz 4d). Na rysunku 5 pokazano analizę składu chemicznego badanych próbek.

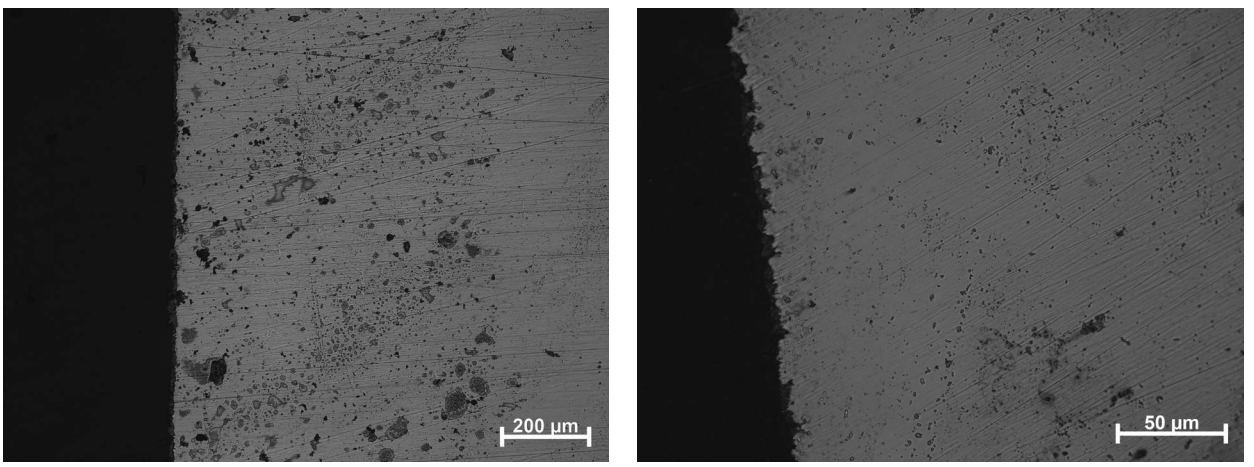

Rysunek 3. a) mikrostruktura próbki stalowej z powłoką fosforanową – cynkową (stan suchy); b) mikrostruktura próbki stalowej z powłoką fosforanową – cynkową z warstwą antykorozyjną

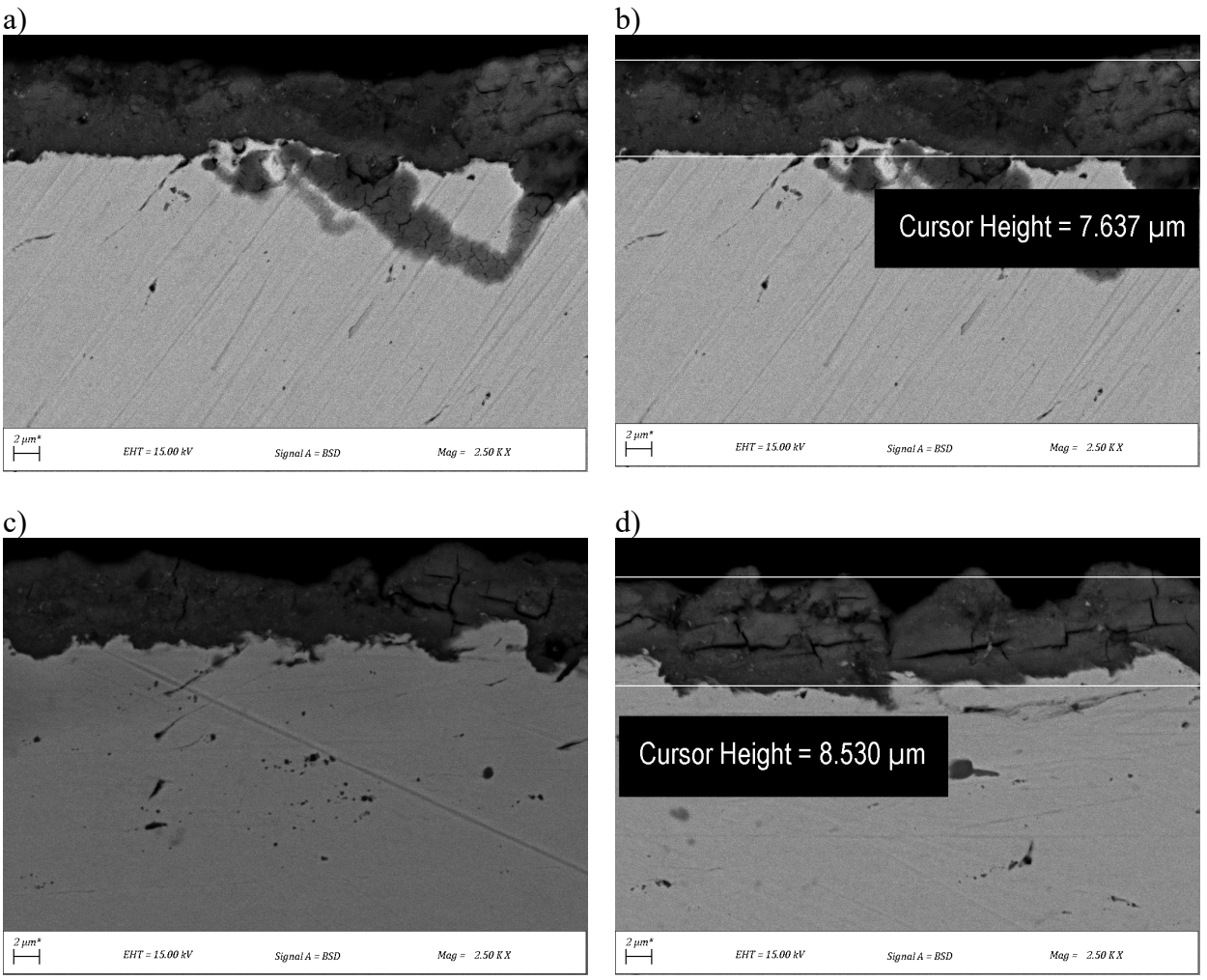

Rysunek 4. a) i b) mikrostruktura próbki stalowej z powłoką fosforanową – cynkową (stan suchy); c) i d) mikrostruktura próbki stalowej z powłoką fosforanową – cynkową z warstwą antykorozyjną

Ocenę jakości powłoki fosforanowej wykonano za pomocą mikroskopu świetlnego i zinterpretowano oprogramowaniem do analizy struktur metalograficznych (program dedykowany danemu mikroskopowi). Średnia grubość powłoki próbki z powłoką antykorozyjnej uzyskana w wyniku obserwacji wynosi 8,04 µm, a dla powłoki próbki suchej grubość wynosi 7,99 µm.

Powierzchnię profili stalowych powłokami fosforanowymi antykorozyjną i suchą zbadano mikrotwardościomierzem pod ciągłym obciążeniem 100 gf (około 1 N) przez 10 sekund. W wyniku pomiarów uzyskano twardości w przedziale 150-200 HV – wynika to z charakterystyki powierzchni i jest zgodne z danymi literaturowymi.

a)

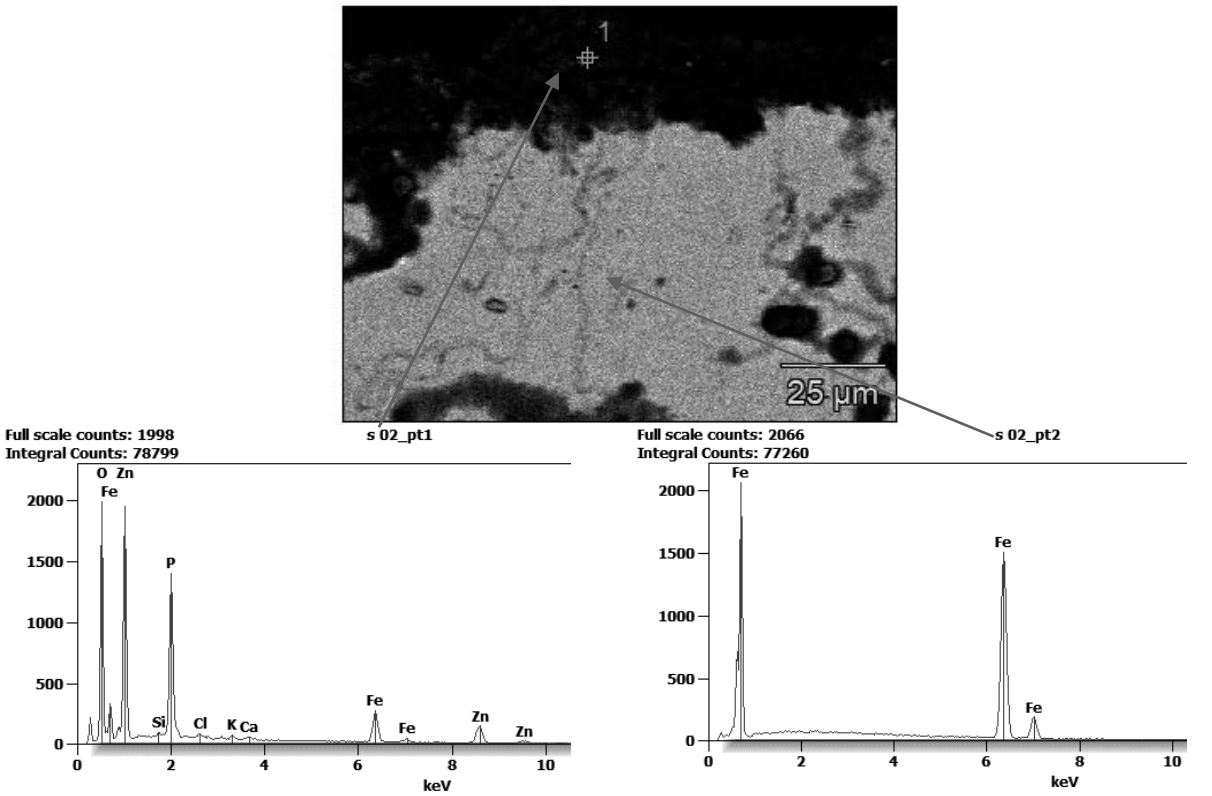

b)

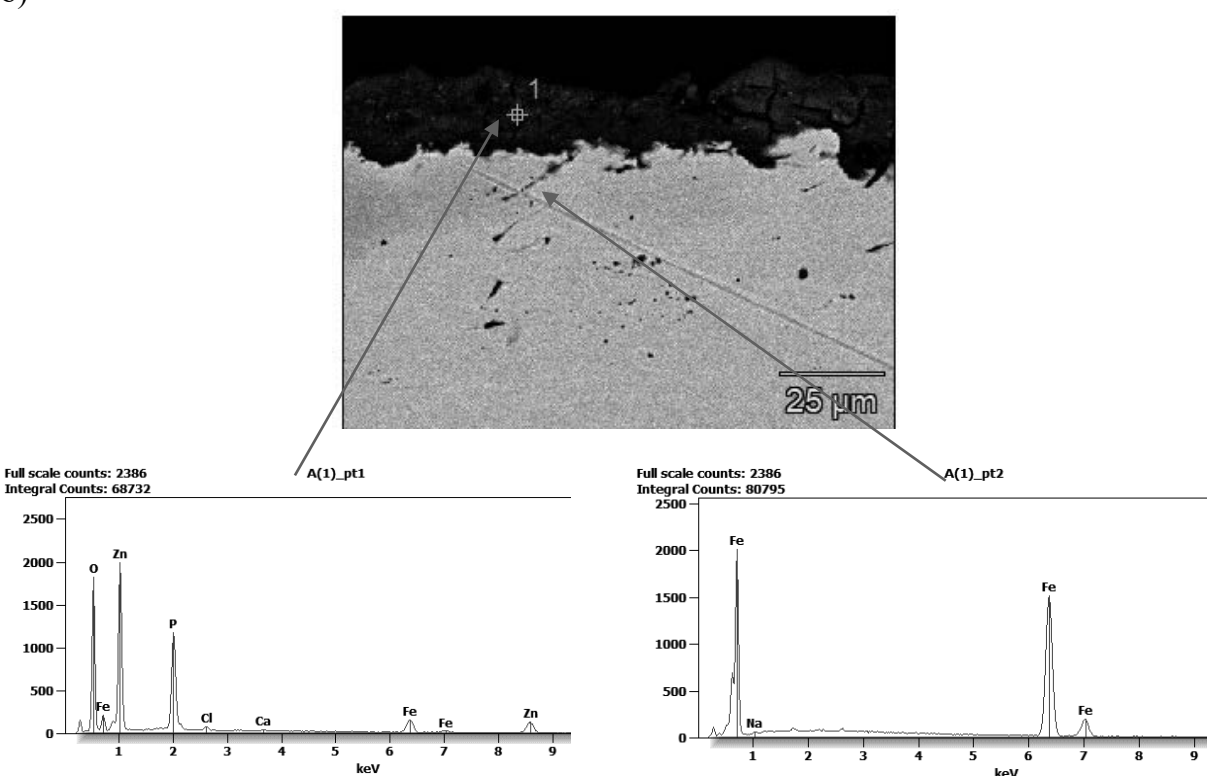

Rysunek 5. a) mikrostruktura próbki stalowej z powłoką fosforanową – cynkową (stan suchy) oraz analiza EDS w punktach 1 i 2; b) mikrostruktura próbki stalowej z powłoką fosforanową – cynkową z warstwą antykorozyjną oraz analiza EDS w punktach 1 i 2;

4. PODSUMOWANIE

Wykonano analizę wyników badań próbek stalowych pokrytych warstwą fosforanowo cynkową w stanie suchym jak i z warstwą antykorozyjną. Średnie grubości warstw ochronnych dla obu próbek (zarówno próbki w stanie suchym jak i pokrytej warstwą antykorozyjną) wykazują różnicę 0,05 μm, co może świadczyć, że warstwa antykorozyjna ma średnią grubość około 0,05 μm. Twardość powłoki fosforanowej w skali Vickersa (HV) nie jest wartością stałą, stąd wyniki wahały się od 100-150 HV. Zależy ona od rodzaju fosforanu (w naszym wypadku cynku), grubości warstwy, struktury krystalicznej, a także parametrów procesu (temperatura, czas, skład kąpieli), przy czym zazwyczaj powłoki te są względnie miękkie, choć twardsze od surowego metalu i stanowią świetny podkład pod farby, zapewniając przyczepność i ochronę przed korozją, ale ich twardość wyraźnie wzrośnie przy smarowaniu.

Nanoszenie powłok fosforanowych na stal (fosforanowanie) ma wiele zalet, zwłaszcza w przemyśle metalowym i maszynowym. Najważniejsze z nich to: ochrona i trwałość. Zwiększona odporność na korozję – warstwa fosforanowa chroni stal przed rdzą, szczególnie jako warstwa podkładowa oraz lepsza przyczepność farb i lakierów – fosforanowanie tworzy chropowatą, aktywną powierzchnię idealną pod malowanie lub lakierowanie.
Właściwości użytkowe tj. zmniejszenie tarcia – powłoki fosforanowe (zwłaszcza manganowe i cynkowe) poprawiają własności ślizgowe, mniejsze zużycie elementów – dzięki redukcji tarcia i mikrouszkodzeń, dobre własności smarne – warstwa dobrze zatrzymuje oleje i smary.
Korzyści technologiczne to przede wszystkim poprawa podatności na obróbkę plastyczną – np. tłoczenie, ciągnienie drutu; jednorodna i kontrolowana powłoka – jest łatwa do powtarzalnego nanoszenia w produkcji seryjnej oraz charakteryzuje się relatywnie niskim kosztem procesu w porównaniu z innymi metodami ochrony powierzchni.

PODZIĘKOWANIA

Praca powstała w wyniku realizacji projektu „*Ochronne powłoki fosforanowe na powierzchni stali*” w ramach kształcenia zorientowanego projektowo – PBL, w XIII konkursie Programu Inicjatywa Doskonałości – Uczelnia Badawcza, Wydział Mechaniczny Technologiczny, Politechnika Śląska.

Podziękowania dla Elektrocarbon Galwan Sp. z o.o. w Tarnowskich Górach za pomoc w wykonaniu próbek fosforanowych.

LITERATURA

1. A. Zalewska, J. Kowalik, Konwersyjne powłoki fosforanowe jako zabezpieczenie antykorozyjne podłoży metalowych, Inż. Ap. Chem. 2016, 55, 5, 212–213, 2016
2. HÄRTHA GROUP. Phosphating processes [link] [dostęp: 13.12.2025]
3. E. Gralak, Technologie chromianowania trójwartościowego stopów odlewniczych aluminium z zastosowaniem związków fluorokompleksowych metali grup przejściowych, praca doktorska, Wrocław 2024
4. Baique Accessories. Co to jest powłoka fosforanowa? [link] [dostęp: 13.12.2025]
5. L.A. Dobrzański, A.D. Dobrzańska-Danikiewicz, Obróbka powierzchni materiałów inżynierskich, Open Access Library, Volume 5, 2011

TalentDetector

9th January 2026
Gliwice, Poland

DEPARTMENT OF ENGINEERING MATERIALS AND BIOMATERIALS
FACULTY OF MECHANICAL ENGINEERING
SILESIAN UNIVERSITY OF TECHNOLOGY

INTERNATIONAL STUDENTS SCIENTIFIC CONFERENCE

A Theoretical Review of Welding Technology for Ultra-High-Strength Steels (UHSS)

Lukáš Šikyňa[a], František Nový [a]

[a] Faculty of Mechanical Engineering, Department of Materials Engineering, University of Žilina, Univerzitná 8215/1, 010 26 Žilina, Slovakia, E-mail: lukas.sikyna@fstroj.uniza.sk, frantisek.novy@fstroj.uniza.sk,

Abstract: This article presents a comprehensive theoretical review of the welding technology applied to Ultra-High-Strength Steels (UHSS), specifically grades such as S960. The review synthesizes information from existing technical publications to establish the fundamental metallurgical and procedural principles governing the successful joining of these high-performance materials. The work focuses on the critical influence of the welding thermal cycle, analyzing how heat input dictates microstructural transformations—namely martensite formation, self-tempering, and potential softening—within the Heat-Affected Zone (HAZ). Additionally, the paper addresses the theoretical mechanism of Hydrogen-Assisted Cracking (HAC), emphasizing procedural control measures. The goal is to consolidate the theoretical knowledge base necessary for optimizing UHSS welding procedures.

Keywords: materials, welding, High-Stengh Stels, hydrogen

1. INTRODUCTION

Ultra-High-Strength Steels (UHSS), represents a class of advanced materials developed to meet the growing need for enhanced performance, load-bearing capacity, safety, and substantial weight saving in various structural applications [1]. The S960 grade, specifically, is defined as an advanced low carbon and low alloy steel with a minimum guaranteed yield strength of 960 MPa [2]. Similarly, the Strenx® product line combines extreme performance with exceptional weldability, allowing for the use of any conventional welding method [3]. The use of these materials is expanding rapidly, including in the automotive sector with Advanced High-Strength Steels (AHSS) [4].

Despite the excellent properties of UHSS, the existing design guidelines for welded UHSS components are often incomplete, especially for applications involving fluctuating operating conditions, which underscores the critical importance of a deep theoretical understanding of the welding process. The fundamental challenge in welding UHSS lies in the fact that the heat input from the welding process inevitably alters the carefully engineered microstructure of the base material, thereby affecting its final mechanical properties [1]. This review provides a theoretical synthesis of the metallurgical and procedural factors governing the successful joining of these high-performance materials.

2. METALLURGICAL TRANSFORMATIONS WIHIN THE WELD ZONE

The weld zone in UHSS structures is fundamentally characterized by three distinct regions: the Weld Metal (WM), the Heat-Affected Zone (HAZ), and the unaffected Base Material (BM). The mechanical properties of the final joint are intimately linked to the microstructural transformations occurring in the HAZ, which are a direct consequence of the thermal cycle experienced during welding.

2.1. Microstructural Constituents

In quenched and tempered UHSS, the base metal typically consists of a fine-grained tempered martensite structure, which is responsible for its high strength. The welding thermal cycle subjects the material to rapid heating and cooling, which dictates the resulting phase transformations. In the case of S960 steel, the microstructure of the WM and the HAZ is primarily composed of martensite and self-tempered martensite [2].

2.2. The Heat-Affected Zone (HAZ)

The HAZ is the most critical area concerning the mechanical integrity of the joint. The local heat exposure leads to potential degradation of properties. Grain Coarsening and Softening: High heat input can result in the formation of a coarser-grained structure, which in turn leads to material softening [2]. Hardness Variation: The hardness profile across the weld is a key indicator of microstructural change. Studies on GMA welded S960QL steel have shown that the hardness in the HAZ can be significantly increased [5]. Conversely, conventional arc welding, which involves a relatively high heat input, can cause softening in the HAZ, leading to reduced joint strength [2]. Martensite Self-Tempering: The rapid cooling following the peak temperature in the HAZ allows for the formation of martensite. The heat retained in the surrounding material, or subsequent weld passes, can cause this martensite to undergo self-tempering [2].

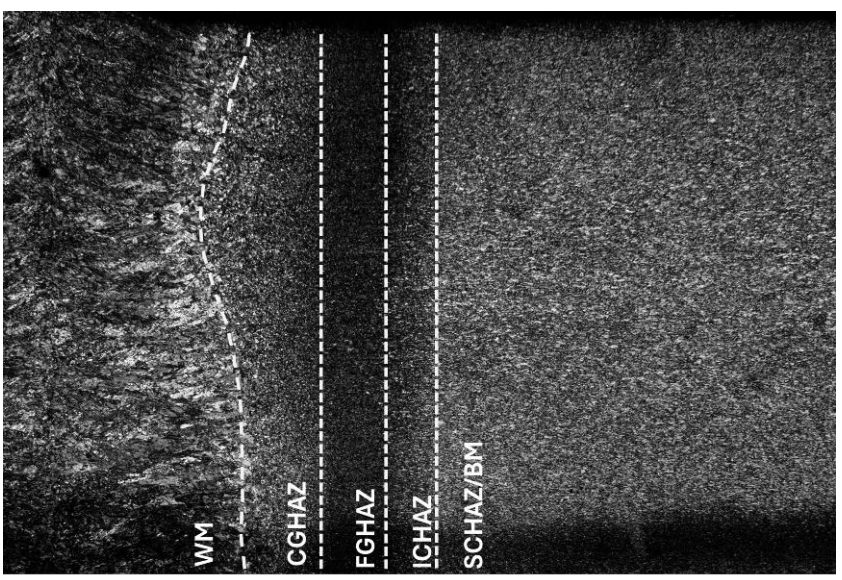

Figure 1. Heat-Affected Zone (HAZ) of laser welded S960MC steel

3. PROCESS CONTROL: HEAT INPUT, COOLING RATE, AND TEMPERATURE MANAGEMENT

Effective control over the welding parameters is paramount for UHSS to maintain the required mechanical performance, as the heat input and the resulting cooling rate have a significant effect on the final microstructure and mechanical properties [1].

3.1. The Role of Heat Input (Q)

The magnitude of the heat input is the primary variable affecting the width of the HAZ and the extent of microstructural change. Property Degradation: A model to predict the strength and microstructure of the weld is required, based on the fundamental welding parameters, because the tensile strength and yield strength are known to decrease with increasing heat input [1].

Low Heat Input Strategy: Utilizing low heat input techniques is essential. Laser welding, for example, is inherently a low heat input process due to its high power density. This low heat input is key to producing a fine-grained structure that maintains high strength and toughness in the joint [2].

3.2. Temperature and Cracking Control

The welding procedure must incorporate strict temperature management, which includes preheat and interpass temperatures. Preheat Temperature: The preheat temperature is applied to reduce the cooling rate, which is a necessary measure to ensure resistance against hydrogen cracking. Due to the generally low carbon and low alloy content in modern UHSS, the Carbon Equivalent (*CEV*) is low, which can help to reduce the need for preheating. Interpass Temperature: Specific maximum interpass temperatures must be observed to prevent the degradation of mechanical properties across the entire welded structure [3].

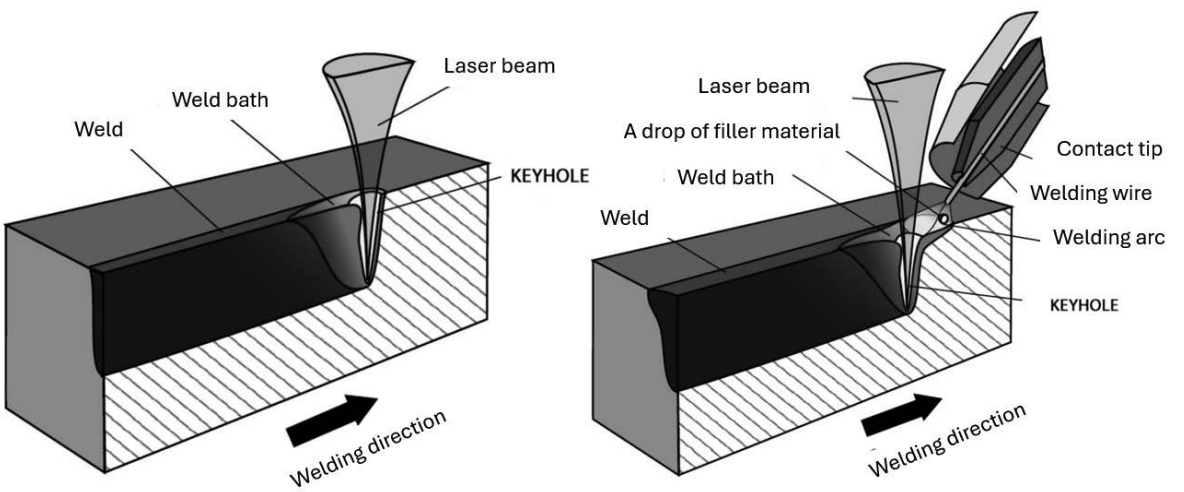

Figure 2. Laser beam welding diagram without and with filler material [6].

4. WELDING TECHNIQUES AND CONSUMABLE SELECTION

The choice of welding technique and the corresponding consumables are integral to controlling the thermal cycle and achieving the desired joint properties.

4.1. Comparison of Welding Methods (MAG vs. Laser)

Both conventional (e.g., MAG/GMAW) and advanced (e.g., Laser) methods are employed for UHSS [1]. Gas Metal Arc Welding (GMAW/MAG): This is a widely used conventional method. However, it typically results in a relatively high heat input compared to laser techniques. This can lead to softening in the HAZ and reduce the strength of the joint [2]. Laser Welding: Utilizing high-power sources, such as a 16 kW fibre laser system, provides high power density and low heat input. Low heat input allows for the retention of a fine-grained microstructure, ensuring the desired strength and toughness characteristics of the joint [2].

4.2. Selection of Welding Consumables and Shielding Gas

The selection of filler material and shielding gas influences both the weld metal chemistry and the degree of hydrogen ingress. For UHSS with very high yield strength, the theoretical recommendation is often to use a filler metal with slightly lower strength than the base material. This strategy is employed to prioritize better toughness in the weld metal.

Shielding Gas: The choice of shielding gas and the gas mixture used for conventional welding methods (such as GMAW/MAG) are critical parameters in the welding procedure. The gas composition is particularly significant for controlling the degree of weld metal hydrogen content, which directly relates to the risk of Hydrogen-Assisted Cracking (HAC) in these high-strength steel joints [3], [7].

5. HYDROGEN-ASSISTED CRACKING (HAC): THE MARGINAL THREAT

The presence of hydrogen during the welding process poses a significant, albeit manageable, risk known as Hydrogen-Assisted Cracking (HAC), also referred to as hydrogen-induced cold cracking (HIC). HAC is a complex phenomenon driven by the coupling of hydrogen transport, accumulation at the fracture process zone, local embrittlement, and subsequent fracture [8].

5.1. Susceptibility and Mitigation

Steels with a martensitic microstructure, are particularly known to be prone to hydrogen-induced cold cracking. Even ultra-high strength steels can exhibit Hydrogen Embrittlement (HE), which manifests as a distinct decrease in ductility and a slight decrease in strength [7], [9].

Microstructural Influence: The base material grade significantly influences HAC resistance. Comparative studies between the quench-and-tempered S960QL and the thermo-mechanically controlled S960MC showed that the HAZ of S960MC has better resistance to HAC compared to the HAZ of S960QL [5]. Fracture Characteristics: The effect of hydrogen on the fracture surface includes the formation of fine pores in the fracture region due to the presence of hydrogen and its displacement by formed stresses and plastic deformation [9]. The fracture topography of resistant grades, such as S960MC, demonstrates a certain degree of degradation depending on exposure [5].

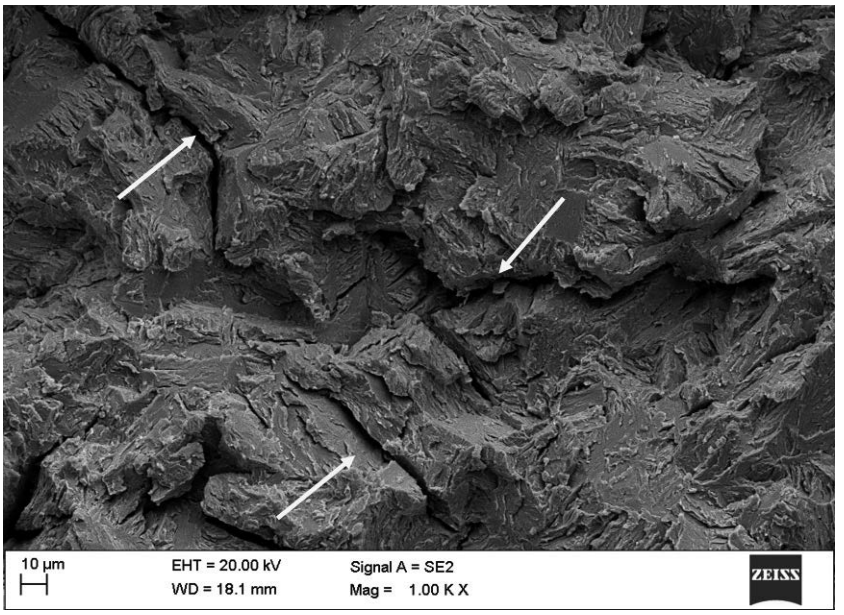

Figure 3. Fracture fractography of hydrogen-saturated steel S960MC welded by TIG method.

Example of fracture surface on (Figure 3.) is completely brittle without any form of ductile fracture. Secondary cracks and mixed transcrystalline and intercrystalline fracture are typical for hydrogen charged steels.

5.2. Analytical and Testing Methods

Controlling the risk of HAC necessitates advanced methods for characterizing and measuring hydrogen content.

Instrumented Confined Cracking Test (IRC Test): This method is used to experimentally assess the susceptibility of materials to hydrogen cracking specifically in the weld metal. IRC test simulates the confined conditions of a weld joint to observe the initiation and propagation of a crack under the influence of hydrogen [7].

Mechanical Degradation Analysis: The effect of hydrogen on welded joints of steels is studied primarily by measuring the resulting loss of properties. This includes performing static tensile tests to reveal a clear decrease in ductility and a slight decrease in strength in hydrogen-induced test specimens [9].

Microscopic examinations: Methods such as macroscopic metallographic examinations and detailed studies using a scanning microscope are used to correlate material degradation with microstructural changes. These techniques help visually confirm the presence of effects and mechanisms such as fine pores in the fracture area caused by hydrogen [9].

6. CONCLUSION AND FUTURE THEORETICAL DIRECTION

The successful welding of UHSS, is based on a rigorous theoretical understanding of the thermal-metallurgical interactions. The primary theoretical imperative is the control of heat input to minimize the detrimental softening and microstructural degradation in the HAZ, as

lower heat input processes, such as laser welding, are shown to be highly effective in retaining the desirable martensitic structure [2].

While the risk of Hydrogen-Assisted Cracking (HAC) is a persistent factor in high-strength materials, proper procedural control, including preheating and the selection of more resistant steel grades (e.g., S960MC over S960QL), is key to mitigation [5]. Future theoretical work should continue to develop predictive models for microstructure and strength based on welding parameters and refine continuum models of HAC to better predict remaining service life [8].

ACKNOWLEDGEMENTS

This paper was prepared within the framework of the joint Slovak-Polish project TalentDetector 2026 as a result of collaboration between the Silesian University of Technology (Poland) and the University of Žilina (Slovakia), and was supported by the project KEGA 033ŽU-4/2026.

BIBLIOGRAPHY

[1]. Keränen, L., Nousiainen, O., Javaheri, V., Kaijalainen, A., Pokka, A. P., Keskitalo, M., Kurvinen, E. (2022). Mechanical properties of welded ultrahigh strength S960 steel at low and elevated temperatures. Journal of Constructional Steel Research, 198, 107517.Volume 198, 2022, 107517. ISSN 0143-974X

[2]. Guo, W., Crowther, D., Francis, J. A., Thompson, A., Liu, Z., Li, L. (2015). Microstructure and mechanical properties of laser welded S960 high strength steel. Materials & Design, Volume 85, 2015, Pages 534-548. ISSN 0264-1275,

[3]. www.damatech.com WELDING OF STRENX. (2021) From: https://www.damatech.com/Portals/0/Dokumenti/EN-Welding Strenx.pdf

[4]. HU, X., FENG, Z. (2021). Advanced high-strength steel-basics and applications in the automotive industry. Oak Ridge National Laboratory (ORNL), Oak Ridge, TN (United States). DOI:https: //doi.org/10.2172/1813170

[5]. Schaupp, T., Ernst, W., Spindler, H., & Kannengiesser, T. (2020). Hydrogen assisted cracking of GMA welded 960 MPa grade high-strength steels. International journal of hydrogen energy, Volume 45, Issue 38, 2020, Pages 20080-20093, ISSN 0360-3199

[6]. www.vaw.sk Ručné laserové zváranie [online]. 2023 Dostupné z: VAW WELDING, s.r.o. https://vaw.sk/rucne-laserove-zvaranie/#

[7]. Aune, R., Fostervoll, H., & Akselsen, O. M. (2003). Hydrogen assisted cracking in welding of 13% Cr supermartensitic stainless steels. International Conference on Offshore Mechanics and Arctic Engineering Volume: 36835, Pages: 177-183. https://doi.org/10.1115/OMAE2003-37282.

[8]. Traidia, A., Chatzidouros, E., & Jouiad, M. (2018). Review of hydrogen assisted cracking models for application to service lifetime prediction and challenges in the oil and gas industry. Corrosion Reviews. Volume: 36 (4). Pages: 323-347. https://doi.org/10.1515/corrrev-2017-0079

[9]. Opiela, M. (2010). Hydrogen embrittlement of welded joints for the heat-treatable XABO 960 steel heavy plates. Journal of Achievements in Materials and Manufacturing Engineering, Volume 38 (1), Pages 41-48.

TalentDetector

9th January 2026
Gliwice, Poland

DEPARTMENT OF ENGINEERING MATERIALS AND BIOMATERIALS
FACULTY OF MECHANICAL ENGINEERING
SILESIAN UNIVERSITY OF TECHNOLOGY

INTERNATIONAL STUDENTS SCIENTIFIC CONFERENCE

Semiconductors as the foundation of the technological revolution

Tymoteusz Skóra[a], Marek Wojnarowski[a], Oskar Górka[b], Jakub Budzynowski[b], Małgorzata Musztyfaga-Staszuk[c], Janusz Wyrwał[d], Aleksandra Drygała[e].

[a] Pupil, Complex of Communication Schools, Warszawska 35, 44-100 Gliwice, Poland
[b] Student, Silesian University of Technology, Faculty of Mechanical Engineering, Konarskiego 18a, 44-100 Gliwice, Poland
[c] Silesian University of Technology, Faculty of Mechanical Engineering, Materials Research Laboratory, Konarskiego 18a, 44-100 Gliwice, Poland
[d] Silesian University of Technology, Faculty of Automatic Control, Electronics and Computer Science, Department of Measurements and Control Systems, Akademicka 16 Str., 44-100 Gliwice, Poland
[e] Silesian University of Technology, Faculty of Mechanical Engineering, Department of Engineering Materials and Biomaterials, Konarskiego 18a, 44-100 Gliwice, Poland email: aleksandra.drygala@polsl.pl

Abstract: Semiconductors constitute the foundation of the modern technological revolution. It is the development of semiconductor technology that has led to the creation of microprocessors, computer memory, and advanced communication systems that shape nearly every aspect of contemporary life. The introduction of semiconductors into electronics enabled the miniaturization of devices, improved their performance and increased their energy efficiency, which in turn has become a driving force behind progress in information technology, telecommunications, and energy sector. Therefore, precise investigation of their electrical properties is essential for the design, optimization, and quality control of modern systems, including electronic and photovoltaic devices. In this study, selected properties of silicon were examined.

Keywords: materials for electronics, semiconductor, silicon, doping, sheet resistance

1. INTRODUCTION

Semiconductors play a key role in the development of modern electronics and information technology. Thanks to their unique physical and chemical properties, they have become the fundamental material used to build components such as transistors, diodes, integrated circuits, and sensors. Among all known semiconductors, silicon plays a particularly important role. Due to its availability, chemical stability, and well-understood physical and chemical properties, which enable precise design and control of technological processes, it has become the primary material in the microelectronics industry [1].

A key feature of semiconductors is their crystalline structure, often based on covalent bonds. Among the crystals with covalent bonding are silicon (Si) and germanium (Ge). Both elements crystallize in the diamond structure. In this structure, each atom is connected by covalent bonds to its four nearest neighbors, forming a spatial, regular, and highly stable lattice [1, 2].

At absolute zero temperature (T = 0 K), the valence band of a semiconductor is completely filled, and the conduction band is empty. As a result, the material behaves like an insulator, as there are no free charge carriers available to conduct electricity. Electrons in the inner shells are strongly bound to the atomic nuclei, while those in the outer shell (the so-called valence band) participate in the formation of interatomic bonds, preventing them from moving freely. Only an increase in temperature provides thermal energy, which allows for partial breaking of the covalent bonds. As a result of excitation, some electrons move to the conduction band, where they can move freely within the crystal. Empty states, or holes, remain in the valence band. These two types of charge carriers —electrons and holes — together enable electrical conduction in the semiconductor. Additionally, the absorption of photons with appropriate energy can cause the excitation of an electron from the interatomic bond, further promoting the conduction of electric current [2, 3].

In semiconductors with covalent bonds, the energy of these bonds is relatively high — for silicon, it is about 4.64 eV — which translates to significant hardness, a high melting point, and a directional character of the material (anisotropy). At the same time, the energy gap between the valence band and the conduction band is much smaller (1.1 eV for silicon, 0.66 eV for germanium), which means that even relatively small amounts of thermal energy or a photon can excite electrons into the conduction band. Although individual chemical bonds are difficult to break, a certain portion of electrons can be easily detached and participate in conduction [2, 3].

Semiconductors can be classified based on their chemical composition into three main groups [3]:

- elemental semiconductors,
- compound semiconductors,
- mixed crystals.

Elemental semiconductors are composed of atoms of a single chemical element. This group primarily includes elements from Group IV of the periodic table, such as diamond (C), silicon (Si), and germanium (Ge). Compound semiconductors are made up of at least two different elements, with the number of atoms in accordance with the stoichiometry rule based on their chemical valency. Depending on the groups of elements in the periodic table, several main types of compound semiconductors are distinguished [4]:

- IV–IV: e.g., silicon carbide (SiC),
- III–V: e.g., gallium arsenide (GaAs), indium phosphide (InP),
- II–VI: e.g., zinc sulfide (ZnS), cadmium selenide (CdSe),
- IV–VI: e.g., lead sulfide (PbS).

In the crystalline structure of semiconductor compounds, the atoms of individual elements form regular sublattices that interpenetrate each other and together create a coherent whole. For example, in gallium arsenide (GaAs) there are two shifted sublattices—one composed of gallium atoms and the other of arsenic atoms—which ensures high structural uniformity and favourably influences the electrical and optical properties of the material. Mixed crystals, built from two or more elements, are not completely homogeneous because the distribution of atoms is partly random, which may slightly modify their properties. Binary III–V semiconductor compounds, such as GaN, GaP, and GaAs, are widely used in light-emitting diodes (LEDs) and semiconductor lasers. Mixed compounds, such as GaAsP or InGaAsP, allow for precise tuning of the optical and electrical properties of the material, which is particularly important in optoelectronic devices. II–VI semiconductors, such as ZnS and CdSe, are used in fluorescent materials and light

detectors.Group IV elements, such as Si and Ge, play a key role in modern electronics. Silicon is the foundation of contemporary integrated circuits, microprocessors, and memory devices, and its dominance results from excellent electrical properties, thermal stability, and well-developed processing technology. It is also the most important material used in photovoltaics, where it is employed to manufacture high-efficiency solar cells, as well as in MEMS technologies and sensors used in measurement systems. Germanium is primarily used in specialized devices, such as ionizing radiation detectors that require exceptionally high energy resolution. In addition, germanium is used in detectors and optical systems operating in the infrared range, where its optical properties are particularly useful [5].

Due to the type of introduced dopant, semiconductors are divided into [2, 3]:

- intrinsic – a pure material without intentionally introduced foreign atoms/dopants. Intrinsic semiconductors are very weak electrical conductors because they have few electrons in the conduction band and few holes in the valence band. The concentration of intrinsic electrons in a semiconductor depends on temperature, because it is the thermal energy received that determines whether an electron gains enough energy to jump into the conduction band.
- doped — a material into which dopant atoms are introduced, affecting the concentration of charge carriers in the conduction band and the valence band. Doping allows control over whether the dominant carriers are electrons or holes. Donors and acceptors are foreign atoms that replace atoms of the original semiconductor in the crystal lattice. The introduction of such atoms is called doping. Doped semiconductors are divided into:
  - p-type, which is created by introducing atoms with fewer valence electrons into the crystal, e.g., by adding trivalent atoms (such as boron, gallium, aluminum) to silicon. Such dopant atoms, called acceptors, have one valence electron fewer than silicon atoms. As a result, more holes than electrons are formed, and the holes become the majority charge carriers.
  - n-type, which is created by adding atoms with more valence electrons to the silicon structure, e.g., by introducing pentavalent atoms (such as phosphorus, arsenic, antimony) into silicon. Such dopant atoms, called donors, have one more valence electron than silicon atoms. Four of these electrons form covalent bonds with neighboring silicon atoms, while the fifth electron is relatively weakly bound and can easily move into the conduction band. As a result, electrons become the majority charge carriers in an n-type material.

Surface resistance measurement is a key step in evaluating the electrical properties of thin semiconductor layers, such as silicon. It allows the determination of the resistance of the layer in the direction parallel to its surface, which is essential for the quality of manufactured emitters and electrical contacts. In practice, this measurement is most often performed using a four-point probe, in which current flows through the two outer electrodes, while the potential difference is measured between the two inner ones. This configuration minimizes the influence of contact resistance on the measurement result, ensuring an accurate assessment of the quality of the surface layer. Thanks to the obtained surface resistance values, it is possible to evaluate conductivity, control the diffusion process, and optimize the production parameters of semiconductor layers [6-8].

An advantage of the four-point probe method is the elimination of many measurement errors that occur in traditional two-wire measurements. By separating the current and voltage paths, the four-point method makes it possible to minimize the influence of the following factors [7-9]:

- the resistance of wires and electrodes,
- the contact resistance between the probe and the material,
- current spreading in the contact area.

An example of an advanced measurement system that uses a four-point probe is the Sherescan device. It is used to measure the surface resistance of thin-film silicon structures, including layers such as emitters in solar cells — thin semiconductor layers forming a p–n junction. In addition, it is possible to identify the type of semiconductor (whether the material is p-type or n-type) and to measure the electrical contact resistance. Sherescan automatically performs the entire measurement process — from the physical contact of the probe with the material, through data acquisition, to their analysis and visualization in the form of point results or resistance maps in a dedicated computer program [6-8]. In this study, the conduction type and surface resistance of a wafer made of monocrystalline silicon were determined.

2. MATERIALS AND METHODS

Monocrystalline silicon wafers of unknown conductivity type, before and after diffusion, with dimensions of 5 cm × 5 cm, were used for the study. Measurements of conductivity type and surface resistance were carried out using a Sherescan device from SunLab equipped with a four-point probe (Fig. 1).

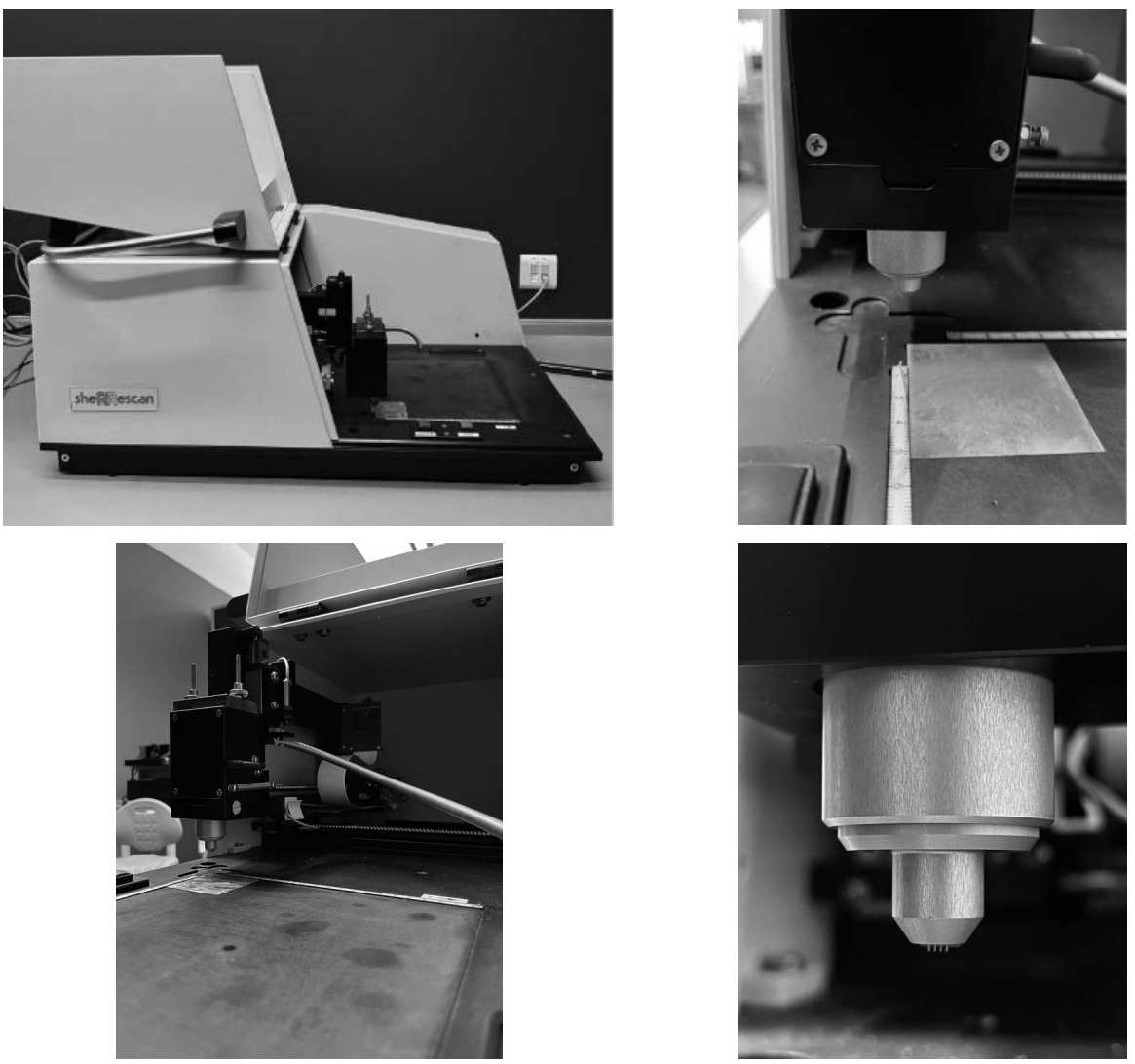

Figure 1. The Sherescan device manufactured by SunLab, equipped with a four-point probe.

3. RESULTS

Figures 2 and 3 present the operating principle of the four-point probe and the measurement results used to identify the conductivity type of monocrystalline silicon wafers, both before and after diffusion. For the wafer before the diffusion process, p-type conductivity was identified, which indicates that the silicon was doped with atoms of an element having three valence electrons, such as boron, gallium, indium, or aluminum. As a result of diffusion, the surface layer of the material changes its conductivity type from p to n. This proves that the majority charge carriers in this type of silicon are electrons, and that the material is doped with an element having five valence electrons, such as phosphorus, arsenic, or antimony.

The results of the sheet resistance measurements of monocrystalline silicon are shown in Figures 4 and 5. For a single wafer, measurements were taken at 16 points. It was found that the average sheet resistance of monocrystalline silicon before diffusion is 100.1 Ω/sq, while the minimum and maximum values are 95.4 Ω/sq and 102.7 Ω/sq, respectively. Monocrystalline silicon after diffusion exhibits a lower sheet resistance, ranging from 56.7 Ω/sq to 61.7 Ω/sq, with an average value of 58.9 Ω/sq. The difference between the extreme sheet resistance values for the silicon wafer before diffusion is 7.3 Ω/sq, whereas after diffusion it is 5 Ω/sq.

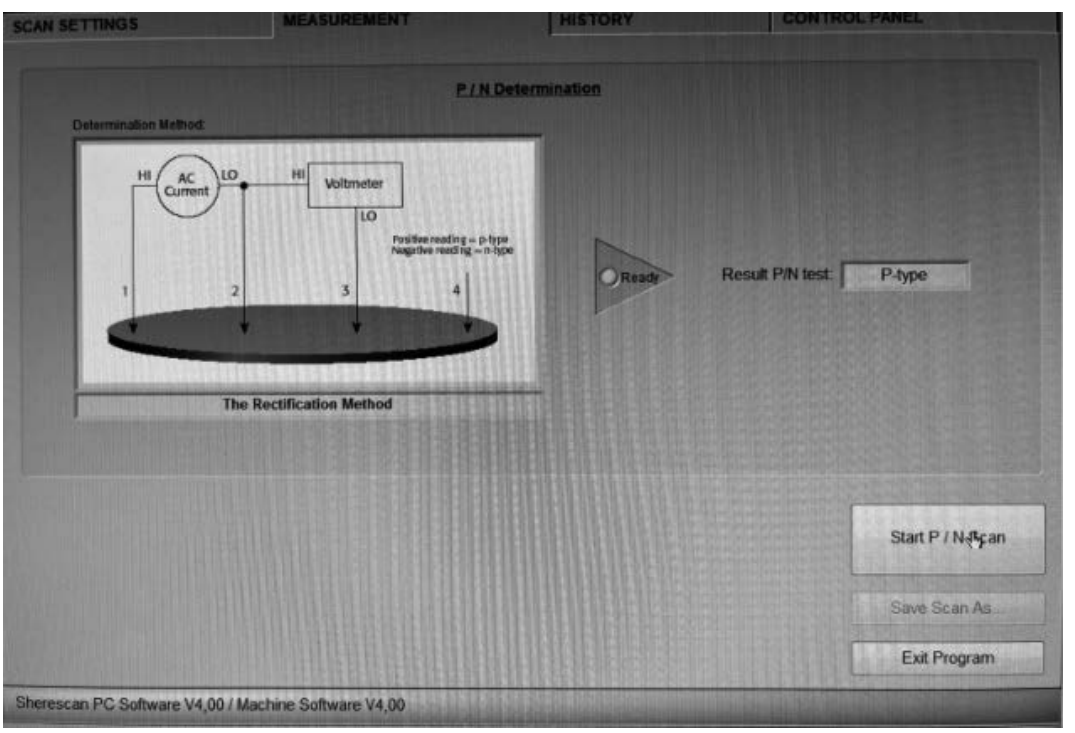

Figure 2. The program window presenting the result of conductivity type determination for monocrystalline silicon before diffusion.

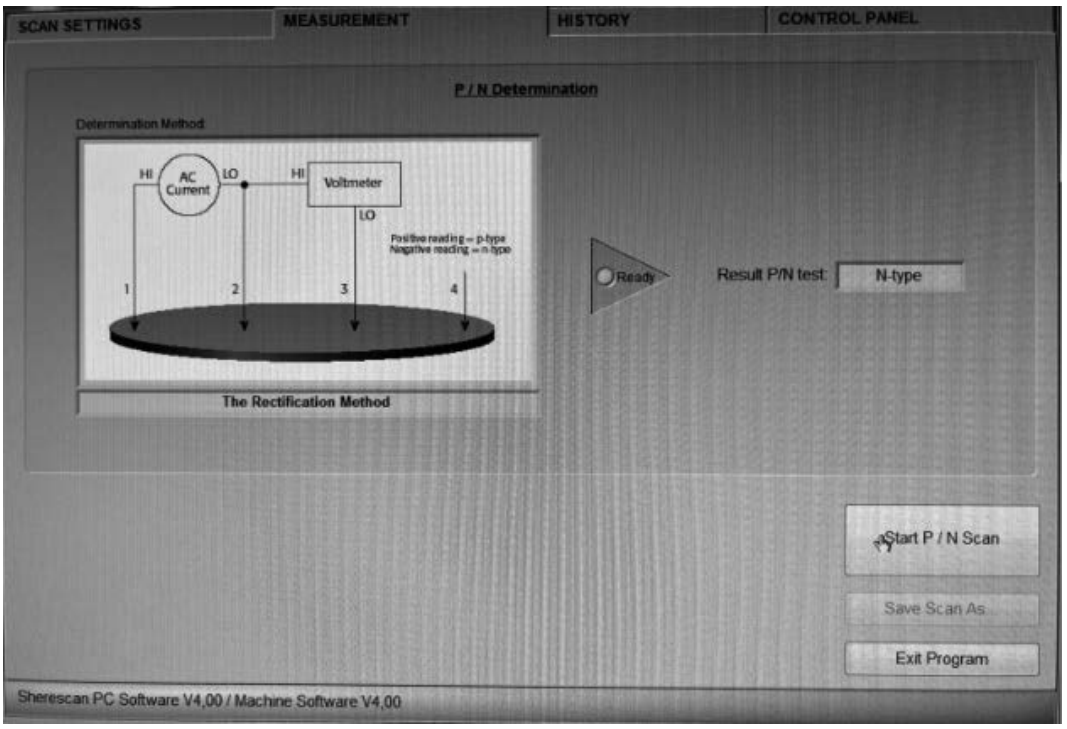

Figure 3. The program window presenting the result of conductivity type determination for monocrystalline silicon after diffusion.

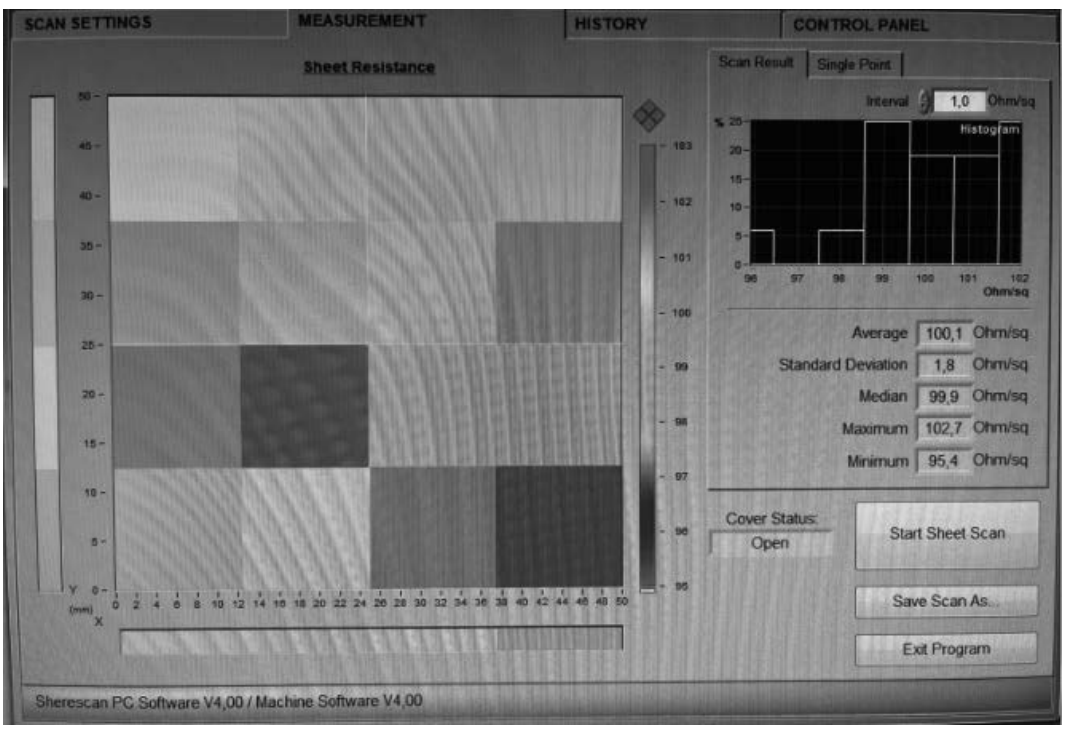

Figure 4. The program window presenting the sheet resistance measurements result for monocrystalline silicon before diffusion

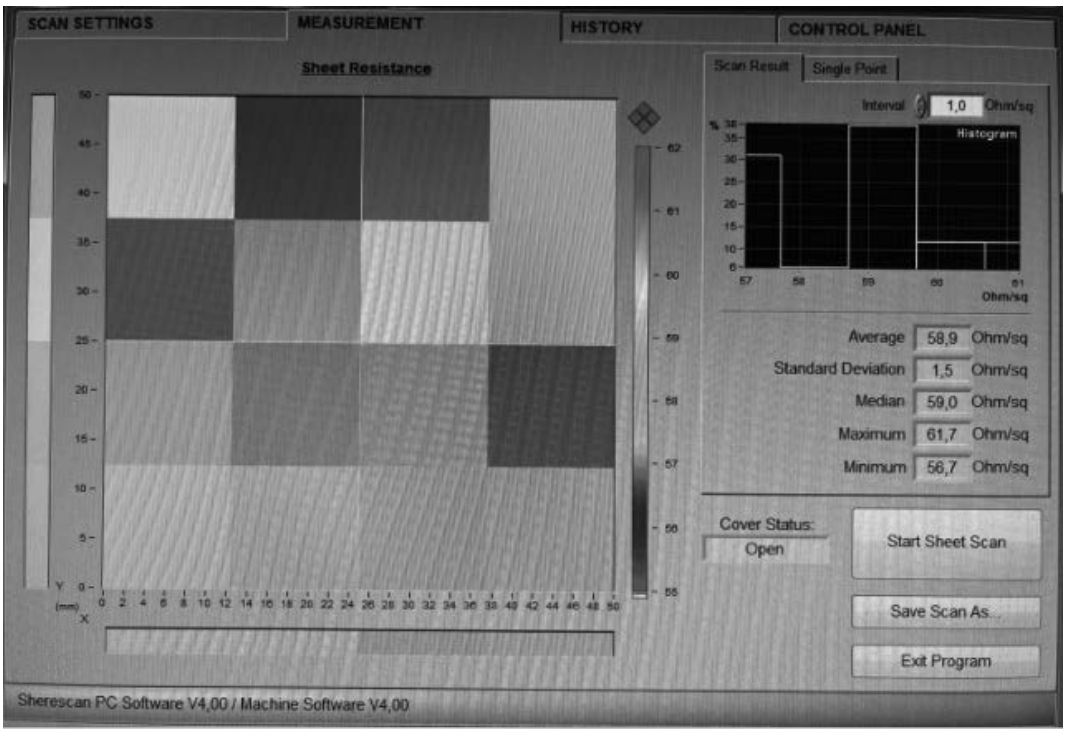

Figure 5. The program window presenting the sheet resistance measurements result for monocrystalline silicon after diffusion

4. CONCLUSIONS

Semiconductors are among the key materials of modern technology. Thanks to their unique properties, they form the basis for the operation of almost all contemporary devices and systems. They are used in electronics (e.g., microprocessors, integrated circuits, LEDs), automotive applications (e.g. ABS systems, engine controllers, sensors), energy engineering (e.g. photovoltaic cells), military and aerospace industries (e.g., radars, advanced sensors), and medicine (e.g., diagnostic equipment and tomography). The research methodology applied in this study allows both the identification of the conductivity type of the surface layer of a semiconductor and the determination of its sheet resistance. It was found that the examined monocrystalline silicon wafer is a p-type semiconductor. As a result of diffusion, the surface layer exhibits electron conductivity, which indicates that the dopant is a pentavalent element, such as phosphorus. It can be assumed that a p–n junction is formed at a certain depth, which is a key component in the operation of many semiconductor devices. Compared to monocrystalline silicon before diffusion, the wafer after diffusion is characterized by a lower average sheet resistance and greater uniformity (smaller variation of values across the measured points), which contributes to stable operation in electronic circuits. Uniform distribution of dopants within the crystal structure reduces local differences in electron scattering, thereby stabilizing conductivity and limiting resistivity fluctuations. An even dopant distribution in silicon is crucial for its use in precision electronic devices such as transistors, semiconductor diodes, and sensors. The stability of sheet resistance and conductivity is essential for the proper operation of devices that require repeatable electrical parameters.

BIBLIOGRAPHY

1. S.M. Sze, K.K. Ng, Physics of Semiconductor Devices, 3rd ed., Wiley-Interscience, Hoboken, 2007.
2. N. Goldsman, C. Darmody, Semiconductor and Device Physics: A Concise Introduction, Cambridge University Press, Cambridge, 2020.
3. J. Hennel, Podstawy elektroniki półprzewodnikowej, Wydawnictwo Naukowe PWN, Warszawa, 1983.
4. B.G. Streetman, S.K. Banerjee, Solid State Electronic Devices, 7th ed., Pearson Education, Boston, 2014.
5. P.Y. Yu, M. Cardona, Fundamentals of Semiconductors: Physics and Materials Properties, Springer, Berlin–Heidelberg, 2010.
6. C.P.C.V. Bernardo, R.A.M. Lameirinhas, J.P. de Melo Cunha, J.P.N. Torres, A revision of the semiconductor theory from history to applications, Dicover Applied Science 6 (2024) 316.
7. Tektronix, Resistivity Measurements of Semiconductor Materials Using the 4200A-SCS Parameter Analyzer and a Four-Point Collinear Probe, Tektronix Application Note, Beaverton, 2025.
8. Inquivix Technologies, How to Test Resistivity of Semiconductor by Four Probe Method, Technical Note, 2023.
9. ITECH, How to Test the Surface Resistivity of Semiconductor Materials, Application Note, 2024.

TalentDetector

9th January 2026
Gliwice, Poland

DEPARTMENT OF ENGINEERING MATERIALS AND BIOMATERIALS
FACULTY OF MECHANICAL ENGINEERING
SILESIAN UNIVERSITY OF TECHNOLOGY

INTERNATIONAL STUDENTS SCIENTIFIC CONFERENCE

Properties and behavior of austenitic steels in biomedical environments

Martin Slezák[a], Peter Palček[a], Melisa Šnircová[a], Milan Uhríčik[a]

[a] University of Žilina, Faculty of Mechanical Engineering, Department of Materials Engineering
email: martin.slezak@fstroj.uniza.sk

Abstract: Austenitic stainless steels are among the most widely used biomaterials due to their biocompatibility and corrosion resistance. Furthermore, their properties are significantly affected by heat treatment and martensitic transformation induced by plastic deformation, which can degrade corrosion behavior. This article briefly summarizes these factors and their importance for the safety and durability of implants.

Keywords: austenitic stainless steel, biomaterials, corrosion, implants

1. INTRODUCTION

Metallic materials form the basis of many biomedical applications, where they are expected to combine high corrosion resistance, biocompatibility, and suitable mechanical properties. In orthopedics and surgery, they serve as load-bearing elements, fixation systems, or functional parts of medical devices, with stainless steels, titanium alloys, and cobalt-chromium alloys dominating. Austenitic stainless steels, which have been used for several decades, occupy an important position, mainly due to the presence of a stable passive layer and a favorable combination of strength, toughness, and chemical stability [1, 2].

Austenitic steels, especially grades AISI 304 and AISI 316L (but also AISI 316Ti), are used in a wide range of implants – from orthopedic and dental systems to cardiovascular applications such as stents and pacemaker components. However, their behavior is significantly influenced by operating conditions and previous technological processing. Heat treatment, especially solution annealing, significantly modifies the corrosion resistance of the material by dissolving carbide precipitates, while mechanical loading can induce martensitic transformation, which changes the microstructure, hardness, and chemical stability of the surface [3,10].

The aim of this article is to provide an overview of the basic principles of the behavior of austenitic steels in a biomedical environment, focusing on their structure, corrosion mechanisms, the influence of plastic deformation, and possibilities for minimizing material degradation. The overview provides a theoretical basis for further study and experiments focused on the long-term functionality of implants .

2. METALLIC MATERIALS IN BIOMEDICINE

Metal materials are often used in biomedical engineering. In clinical practice, they are used as surgical instruments, splints, support structures, and implants. Metals are used in orthopedics, for example, for orthopedic reconstructions (implants for artificial shoulder, elbow, hip and knee joints), fracture fixation (pins, screws, splints), in the maxillofacial and oral areas (dental implants) and cardiovascular interventions (heart valves, stents, pacemakers). Examples of metal implants are shown in Fig. 1 [1].

Figure 1. Examples of metal implants; femoral hip prosthesis (left), acetabular component of the hip joint (center), plate for fracture fixation (right) [1]

Materials used in biomedical environments must have certain specific properties. These metals should be biocompatible (the ability of a material to react with a suitable host response in a specific application [2]), highly resistant to corrosion and wear, and have excellent mechanical properties. One of the key factors contributing to biocompatibility is the passive layer. This layer increases the corrosion resistance of biomaterials. For example, if metal is used to adapt to bone (bone augmentation is a surgical procedure for patients who, for example, have decided to have a dental implant but do not have enough bone to anchor it [1, 3]), the modulus of elasticity of the metal should ideally be the same as the modulus of elasticity of the bone. If these two elasticity models differ and the metal has a higher modulus of elasticity than the bone, a phenomenon known as stress concentration occurs. In many cases, this causes bone remodeling to adapt to lower stress, leading to a loss of bone quality. Another example is coronary stents (a stent is a tubular medical device placed in the body to maintain the patency of a narrowed or closed tubular structure, which are inserted into the coronary arteries – a ring-shaped artery that supplies blood to the heart muscle, which is blocked as a result of atherosclerosis – damage to the arteries caused by the accumulation of fatty substances [1, 4]), for which stainless steel is commonly used due to its suitable mechanical properties.

Stainless steel has a high modulus of elasticity (~ 190 GPa), which contributes to good radial strength, good elasticity, and sufficient flexibility. These properties make it an ideal candidate for stent manufacturing [1, 2]. The bones of the human body vary in size and shape. The four basic types of bones are: long, short, flat, and irregular. Bones that fall into the long category are longer than they are wide. Examples of long bones include the femur and the bones of the forearms [5]. Since the main function of long bones, such as those in the lower body, is to act as

a supporting element, the initial materials introduced to replace joints, such as artificial hips, were metals.

Stainless steels such as AISI 316L, as well as cobalt and chromium alloys, were the first to be used. These metallic materials have relatively good corrosion resistance and adequate fatigue life in the human body. The rigidity and strength of these materials significantly exceed the rigidity of bone. In certain applications, fatigue failures have occurred due to design limitations (e.g., in rods used to straighten the spine in scoliosis). The most commonly used metals in biomedical engineering are stainless steels, titanium alloys, cobalt alloys, and chromium alloys [1, 2].

2.1. Austenitic stainless steel

Currently, there are many types of stainless steel available, but only a few of these steels are used as biomaterials for implants. Stainless steel began to be used in orthopedics in the 1920s. However, it was not until 1943, when ASTM 304 (AISI 304) steel was recommended as a suitable material for the manufacture of reliable implants, that it attracted the most attention from doctors due to its corrosion resistance [2, 6]. The quality of these alloys depends on the processing history and chemical composition of the material. One of the most common steels used in biomedical applications is austenitic steel AISI 316L/316LV. The designation "L" indicates a reduced carbon content in the steel, while "V" defines the vacuum in which the steel was cast. The carbon content must be low to prevent the formation of chromium carbide at the boundaries of austenitic grains [2, 7].

The era of modern disc arthroplasty (arthroplasty is a surgical procedure to restore joint function – either by strengthening the joint or replacing it completely) began in 1982, when the first operation to implant an artificial intervertebral disc was performed at a hospital in Berlin (Fig. 2). The design of the replacement uses the principle of low friction, which had already been used in hip replacement surgery for 20 years at that time. The disc consisted of a sliding core that moved between two end plates made of austenitic steel with multiple serrated projections for fixation to the end plates of the vertebrae [2, 8, 9].

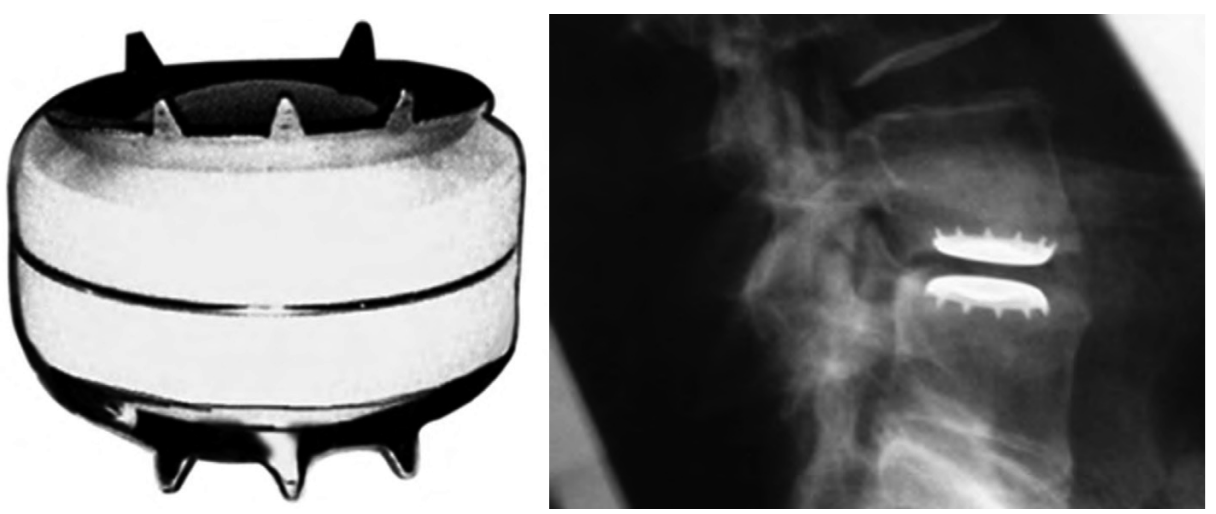

Figure 2. Artificial disc implanted at Berlin Hospital [2]

Currently, austenitic stainless steels are used in the manufacture of medical devices, aids, and implants. These steels are used, for example, in the manufacture of connectors for pacemakers (Fig. 3a) and other medical devices. This type of steel is suitable for this purpose because it has good electrical conductivity and can be welded with a laser. Austenitic stainless steels are popular

in many medical fields. In orthopedics and surgery, they are used for joint replacements (knee, hip, shoulder), bone screws, plates, and pins for fixing fractures. In dental technology, they are used for orthodontic retainers (Fig. 3b), which are used in dental braces. They are also used as stents [2, 6, 13].

a) b)

Figure 3Examples of the use of austenitic steels in biomedical environments; a) pacemaker connector [26]; b) orthodontic retainer [27]

2.2 Characteristics of austenitic steels

Austenitic steels are characterized by a high chromium content, which ensures high corrosion resistance. Other important elements in austenitic steels are nickel, manganese, and possibly nitrogen, which ensure the austenitic structure. Basic steels are alloyed with 18% Cr and 8% Ni with a low C content. The austenitic structure is maintained at normal and very low temperatures. This is ensured by the above-mentioned elements, but mainly by nickel (the Ni content must be at least 8%), which expands the γ region, suppressing the α region to such an extent that the austenite recrystallization region is practically suppressed. It is precisely because of this suppression that the cubic face-centered lattice (FCC) in which austenite crystallizes is also preserved. The absence of phase transformation causes grain coarsening at high temperatures (e.g., during annealing), without the possibility of change through heat treatment. Annealing is a process that ensures equilibrium in alloys. This process is used to eliminate undesirable effects arising as side effects in the manufacture of semi-finished or finished products, which are then ready for direct use. Annealing is used to reduce hardness, modify microstructure, homogenize chemical composition, and for other purposes. Austenitic steels are heat treated to reduce the hardening that has occurred during previous processes, such as forming. The result of this treatment is a homogeneous solid solution that improves corrosion resistance by dissolving carbides and other undesirable phases. The most commonly used heat treatment for austenitic steels is solution annealing [10, 11].

2.3. Corrosion of austenitic stainless steels

As mentioned in the previous chapter, solution annealing is the ideal heat treatment for achieving excellent corrosion resistance. The high chromium content in these steels is primarily for the formation of a protective surface (passive) layer of Cr_2O_3, which protects the base material from the aggressive environments in which austenitic steel is used [2, 12]. Several factors influence the corrosion resistance of austenitic steels. The most important ones include chemical composition, heat treatment method, structural changes due to mechanical stress, and exposure to specific environments such as chloride-containing solutions. Several studies point to the

influence of plastic deformation, which leads to the induction of martensitic transformation. This transformation from austenite (γ) to martensite (α') leads to a reduction in corrosion resistance to pitting and intergranular corrosion [13, 14, 15]. In a study by Solomon 2017 [14], he points to martensitic transformation induced by plastic deformation, which increased the hardness and strength of the experimental material AISI 316, but at the same time led to a deterioration in corrosion resistance in an environment containing chlorides. Similar conclusions were reached in research by Dománková [16], which demonstrate accelerated sensitization after plastic deformation, i.e., precipitation of chromium carbides at the boundaries of austenitic grains, leading to the formation of areas with reduced chromium content and increased susceptibility of austenitic steel to intergranular corrosion. [14, 16].

Pitting corrosion is a common and serious form of corrosion damage to austenitic steels caused by local disruption of the thin passive layer on the steel surface due to the presence of aggressive ions such as chlorides (Fig. 4). These ions react with the surface passive layer and cause its weakening, exposing the unprotected base metal. This unprotected area becomes a site of intense anodic dissolution. During this process, metal cations are formed, which diffuse into the surrounding environment (solution). If the concentration of metal ions and acidity in the damaged area decreases to a certain level, the passive film can reform, leading to repassivation [17, 18, 19]. Abbasi Aghuy [17] found that grain size does not affect pitting potential (corrosion formation), but a fine-grained structure promotes the likelihood that pitting will develop into a stable state, which promotes repassivation. This dynamic is caused by the higher density of grain boundaries, which provide more reactive sites for chemical processes [17]. This corrosion is usually difficult to detect because it involves a relatively small loss of metal. Individual spots may occur in small clusters close to each other or scattered across the steel surface. Anti-corrosion coatings or cathodic protection are used to protect against pitting corrosion [20, 21].

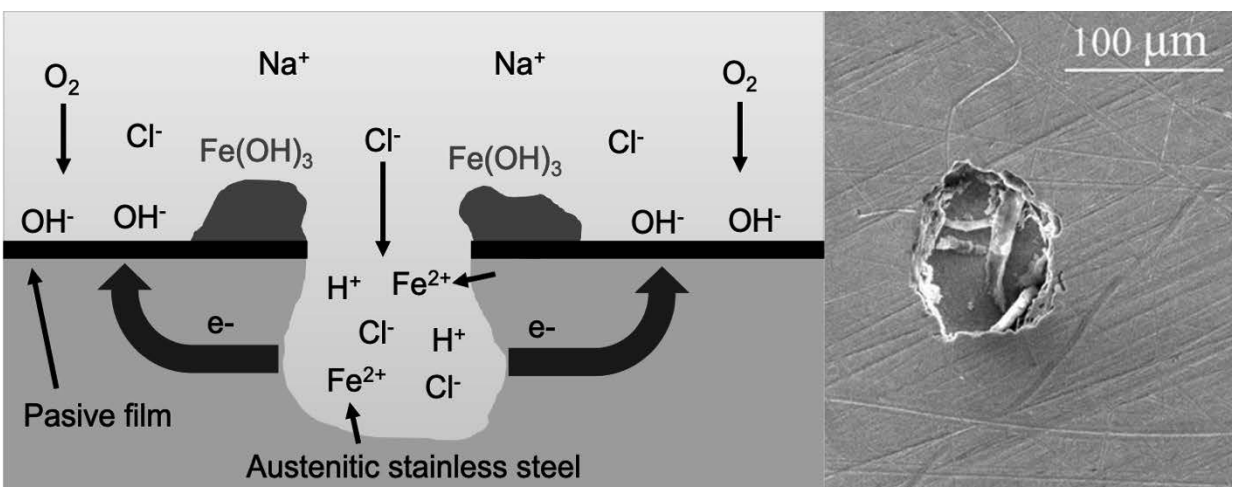

Figure 4. Pitting corrosion [19, 25]

Another form of corrosion to which austenitic steels are susceptible is intergranular corrosion. This type of corrosion occurs at grain boundaries or with minor attack of austenitic grains. In the case of standard grades of austenitic steels (grades 200 and 300), this process is associated with steel sensitization, which occurs during slow cooling from the solution annealing temperature, incorrect heat treatment, in welded joints, in the heat-affected zone of welds, or during hot working of the material [22, 23]. In addition to the heat history, this secondary phase is also related to the chemical composition itself. In the temperature range of 500-800ºC, carbide (most

commonly $M_{23}C_6$) can precipitate at the grain boundaries (Fig. 5). During the formation of chromium-rich carbide, carbon and chromium from the stainless steel matrix combine through diffusion and precipitate at the grain boundaries (which is the most energetically favorable location for carbide nucleation and growth). The precipitation of carbides at the grain boundaries leads to the formation of a chromium-depleted region. If the chromium content falls below 12%, the steel becomes sensitized and, in this state, is susceptible to intergranular corrosion [10, 16]. Materials engineers have several options for minimizing the sensitization process in austenitic steels. One option is to choose steel with a lower carbon content than classic austenitic steels (e.g., 201L, 304L, 316L). This reduced carbon content prolongs the time required for chromium precipitation [10, 24]. This allows hot forming and welding on complex profiles without sensitization. Another option is to use steels that are alloyed with stabilizing elements such as niobium and titanium (at given temperatures, they have a higher affinity for carbon than chromium). In these steels, niobium or titanium carbide is preferentially formed instead of chromium carbide. Thus, chromium remains in solid solution and provides protection against corrosion [10].

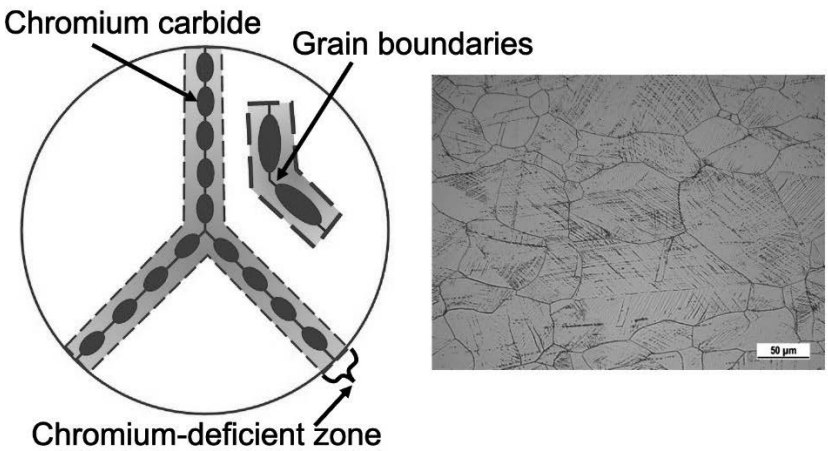

Figure 5. Schematic representation od sensitization and actual microstructure of AISI 304 steel after sensitization (600°C/10 hours) [10]

CONCLUSION

Austenitic stainless steels represent an important group of biomaterials which, thanks to their biocompatibility, mechanical properties, and high corrosion resistance, play a key role in modern orthopedics and medical technology. However, their properties are significantly influenced by chemical composition, heat treatment, and operating conditions. As the theoretical overview shows, solution annealing is essential for maintaining a homogeneous austenitic structure and a stable passive layer, while plastic deformation can induce martensitic transformation, which increases hardness but reduces resistance to pitting and intergranular corrosion.

Corrosion damage, especially sensitization and local attack in chloride-containing environments, are critical factors limiting the service life of implants. Modern material strategies, such as reduced carbon content, alloying with stabilizing elements (Nb, Ti), or controlled forming and welding processes, enable a significant reduction in the risk of degradation.

A comprehensive understanding of the relationships between microstructure, mechanical stress, and corrosion response is therefore essential for the design of safe and reliable biomedical

applications. This review provides a theoretical framework for further research and application development in the field of stainless biomaterials.

ACKNOWLEDGEMENTS

This paper was prepared within the framework of the joint Slovak-Polish project TalentDetector 2026 as a result of collaboration between the Silesian University of Technology (Poland) and the University of Žilina (Slovakia), and was supported by the project KEGA 033ŽU-4/2026.

BIBLIOGRAPHY

1. Agrawal, C. M., Ong, J. L., Appleford, M. R., Mani, G., Introduction to Biomaterials: Basic Theory with Engineering Applications, Cambridge University Press, (2014), ISBN 978-0-521-11690-9
2. Ratner, B. D., Hoffman, A. S., Schoen, F. J., Lemons, L. E., Biomaterials Science: An Introduction to Materials in Medicine, Elsevier, (2013), ISBN 978-0-12-374626-9
3. www.cityclinic.eu. Bone Augmentation, https://cityclinic.eu/bone-augmentation/
4. www.ncbi.nlm.nih.gov, https://www.ncbi.nlm.nih.gov/books/NBK507804/, (2024),
5. www.training.seer.cancer.gov/index.html. Classification of Bones, https://training.seer.cancer.gov/anatomy/skeletal/classification.html.
6. Hermawan, H., Ramdan, D., Djuansjah, J. R. P., Metals for Biomedical Applications, InTech, (2011), ISBN 978-953-307-637-9.
7. Bronzino, J. D., Peterson, D. R., Biomedical engineering Fundamentals, CRC Press, (2015), ISBN 978-1-4398-2519-8.
8. www.hopkinsmedicine.org. Arthroplasty, https://www.hopkinsmedicine.org/health/treatment-tests-and-therapies/arthroplasty.
9. Poittout, D. G., Biomechanics and Biomaterials in Orthopedics: Second Edition. Springer-Verlag London, (2004), ISBN 978-1-84882-664-9
10. Fritz, J., Practical Guidelines for the Fabrication of Austenitic Stainless Steels, International Molybdenum Association, London, UK, (2020), ISBN 978-1-907470-13-4.
11. Padilha, A. F., Plaut, R. L., Rios, P. R., Annealing of Cold-worked Austenitic Stainless Steels, ISIJ International, Vol 43, pp 135-143, (2003), ISSN 1347-5460.
12. Smetana, M., Gombarská, D., Psenakova, Z., Chudáčik V., Non-Destructive Investigation of Intrinsic Magnetic Field of Austenitic Biomaterials by Magnetic Field Sensors, Sensors, pp 1-18, (2022), ISSN 1424-8220.
13. Talonen, J., Aspegren, P., Hänninen, H., Comparison of different methods for measuring strain induced α‘martensite content in austenitic steels, Materials Science and Technology, Vol 20, pp 1506-1512, (2004), ISSN 1743-2847.
14. Solomon, N., Solomon, I., Effect of deformation-induced phase transformation on AISI 316 stainless steel corrosion resistanc, Engineering Failure Analysis, Vol 79, pp 865-875, (2017), ISSN 1350-6307.
15. Srinivasan, N., Kain, V., Birbilis, N., Sunil Kumar, B., Gandhi, M. N., Sivaprasad, P. V., Chai,G., Lohd, A., Ahmedabadi, P. M., Samajdar, I., Plastic deformation and corrosion in

austenitic stainless steel: A novel approach through microtexture and infrared spectroscopy, Corrosion Science, Vol 111, pp 404-413, (2016), ISSN 0010-938X
16. Dománková, M., Kocsisová, E., Pinke, P., Slatkovský, I., Effect od Deformation on sensitisation process in austenitic stainless steel AISI 316, https://www.mtf.stuba.sk/buxus/docs/internetovy_casopis/2013/2/web1_Domank ova.pdf.
17. Aghuy, A. A., Zakeri, M., Moayed. M. H., Mazinani, M., Effect of grain size on pitting corrosion of 304L austenitic stainless steel. Corrosion Science, Vol 94, pp 368-376, (2015), ISNN 0010-938X
18. Tiamiyu, A. A., Eduok, U., Szpunar, J. A., Odeshi, A. G., Corrosion behavior of metastable AISI 321 austenitic stainless steel: Investigating the effect of grain size and prior plastic deformation on its degradation pattern in saline media, Scientific Reports. Vol 9, (2018), ISSN 2045-2322.
19. Tian, W. M., Ai, Y. J., Li, S. M., Du, N., Ye, C., Pitting Kinetics of 304 Stainless Steel Using ESPI Detection Technique. Acta Metallurgica Sinica, Vol 28, pp 430-437, (2015), ISSN 2194-1289.
20. Lu, B. T., Chen, Z. K., Luo, J. L., Patchett, B. M., Xu, Z. H., Pitting and stress corrosion cracking behavior in welded austenitic stainless steel, Electrochimica Acta, Vol 50, pp 1391-1403, (2004), ISSN 1359-6454.
21. Saadawy, M., Kinetics of Pitting Dissolution of Austenitic Stainless Steel 304 in Sodium Chloride Solution, International Scholarly Research Notices. Vol 2012, (2012), ISSN 2356-7872.
22. Haraszti, F., Kovacs, T., Plastic deformation effect of the corrosion resistance in case of austenitic stainless steel, Materials Science and Engineering, Vol 175, (2017), ISSN 0921-5107.
23. Fijii, T., Kawarabayashi, K., Shimamura, Y., Intergranular corrosion in sensitized austenitic stainless steel subjected to tensile loading and unloading in the elastic-plastic region, Corrosion Science, Vol 230, (2024), ISSN 0010-938X
24. Bai, S., Zhang, S., Ma, J., Li, J., Mou, L., Understanding the effect of decreasing C contents and increasing solid-solution time on intergranular corrosion resistance of 304 austenitic stainless steel, Journal of Materials Research and Technology, Vol 30, pp 4750-4761, (2024), ISSN 0884-2914.
25. Shi, X., Fu, L., Sustaible Winter Road Operations, John Wiley & Sons Ltd, (2018), ISBN 9781119185154.
26. www.stainless.eu/en/, SURGICAL STAINLESS STEEL AND HIGH PERFORMANCE METALLIC ALLOYS FOR IMPLANTS AND PROSTHESES,MEDICAL AND SURGICAL DEVICES, INSTRUMENTATION AND ANCILLARIES. https://www.stainless.eu/en/markets/medical/.
27. Kartal, Y., Kaya B., Fixed Orthodontic Retainers: A Review, Turkish Journal of Orthodontics, (2019), ISSN 2148-9505.

TalentDetector

9th January 2026
Gliwice, Poland

DEPARTMENT OF ENGINEERING MATERIALS AND BIOMATERIALS
FACULTY OF MECHANICAL ENGINEERING
SILESIAN UNIVERSITY OF TECHNOLOGY

INTERNATIONAL STUDENTS SCIENTIFIC CONFERENCE

Precision casting of bone plates and their *in vitro* biological evaluation

Mateusz Słonka[a], Igor Szymiczek[b], Maciej Ejfler[c], Magdalena Skonieczna[d], Katarzyna Cesarz-Andraczke[e]

[a] Student of Silesian University of Technology, email: ms309483@student.polsl.pl
[b] Student of Silesian University of Technology, email: is309487@student.polsl.pl
[c] Student of Silesian University of Technology, email: me303753@student.polsl.pl
[d] Silesian University of Technology, Institute of Automation, Department of Systems Engineering and Biology, email: magdalena.skonieczna@polsl.pl
[e] Silesian University of Technology, Faculty of Mechanical Engineering, Department of Engineering Materials and Biomaterials
email: katarzyna.cesarz-andraczke@polsl.pl

Abstract: This paper presents a new concept for prototyping a material and design solution for short-term orthopedic implants in the form of bone plates. The test material was a 1.2% wt ZnMg alloy. Due to their biocompatible chemical composition, zinc alloys can potentially be a new biodegradable or even resorbable implant biomaterial. Both zinc and magnesium are naturally occurring elements in the human body. Hence, the degradation products are likely to be of low toxicity to the human body. The research plan for this work includes degradation studies and an assessment of the impact of implant shape and design on the degradation progression of a zinc alloy with added magnesium. The work also presents preliminary biological studies of the Zn1.2Mg wt% alloy, which was the research material.

Keywords: bone plate, precision casting, degradation process

1. INTRODUCTION

From the point of view of the use of zinc alloys in implantology, it is extremely important to determine the critical points of the implant structure after testing in a simulated operating environment of the implant prototype and then to perform their biological assessment, which is the first step to analyze the materials in terms of possible toxicity. The scientific aim of this work is to find a potential application of precision casting for the assessment of corrosion progression in a simulated body fluid environment and biological evaluation of short-term orthopedic implant prototypes.

Lost wax precision casting is the most common and accurate method of making a precision casting. This method uses wax models that are fired in a furnace and then poured with a liquid alloy. A casting mold is primarily produced by applying successive layers of liquid ceramic material to the model. The material is removed from the model by firing or dissolving it in

water. Finally, a cavity is obtained, ready for pouring molten metal. After the model is poured and the molten metal has solidified, the mold is broken and the model is removed. The main characteristic feature of the casting is, among others, the lack of a mold separation surface and the possibility of obtaining high casting accuracy. This technique allows you to obtain elements with high dimensional accuracy and a smooth casting surface [1].

Zinc alloys are characterized by good castability and a low melting point. However, a disadvantage of these alloys is their tendency to temporary dimensional instability, which is associated with changes in strength due to phase transformation. Most often, precision casting is used for alloys such as ZP16 – a zinc alloy with the addition of copper) or Zn-Al-(Cu) alloys[2].

Zinc alloys are currently used in the automotive industry, as anti-corrosion coatings, and as a cosmetic ingredient. However, recently, biodegradable medical implants have been considered. They are considered, among others, in orthopedic implantology as osteosynthesis elements, such as screws and bone plates. Due to their appropriate mechanical properties and controlled corrosion rate, they can provide mechanical stability in the initial healing phase and then undergo gradual resorption in the body. The biodegradability of zinc and its good biological tolerance make zinc alloys an attractive alternative to traditional, durable implant materials [3].

The concept of biodegradable zinc alloys is a new generation of implant materials that gradually dissolve in the body after fulfilling their mechanical function, eliminating the need for implant removal procedures [4]. Zinc's corrosion rate is moderate. It corrodes slower than magnesium but faster than iron, allowing it to adapt its rate of degradation to the bone healing process. Zinc corrosion products are likely to be biocompatible, and alloying zinc with magnesium, calcium, manganese or aluminum improves strength, hardness and structural stability while maintaining patient safety and the possibility of biodegradation in the human body [3,5].

This paper presents the concept of using precision casting and 3D printing to obtain a prototype of a bone plate for degradation studies and to indicate its critical points as well as to perform a preliminary biological assessment of the ZnMg1.2 wt% alloy.

1.1. Material and concept of manufacturing the bone plate prototype

The first step was to design a mold to obtain a wax model of the bone plate. The mold was designed to produce the wax model required for the lost-wax method. The wax model represents a bone plate intended for medical applications. The mold geometry was carefully crafted to accurately reproduce the shape and dimensions of the bone plate, enabling the dimensions of the final cast to be replicated.

The mold design takes into account the requirements of the wax pattern placement process, including proper cavity filling, ease of removal from the mold, and minimizing defects in the wax pattern. Particular attention was paid to the geometry of the bone plate because it must meet both mechanical and anatomical requirements. The entire design process was conducted using Autodesk Inventor software. This CAD software enabled precise modeling of mold components, assembly verification, and mold design optimization before production. Figure 1 shows the designed CAD mold model.

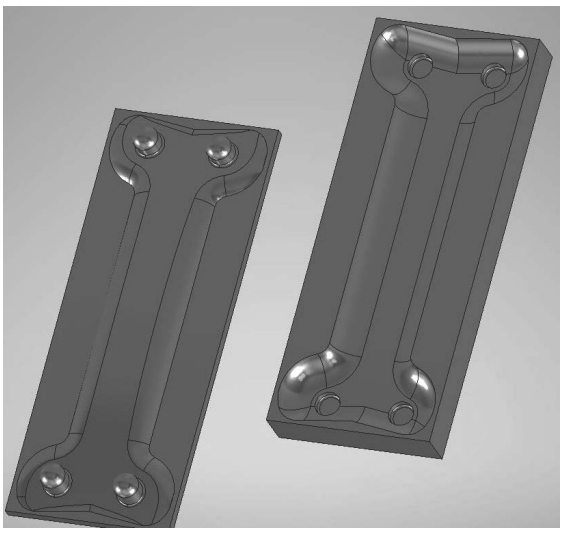

Figure 1. CAD model of the mold for making a wax model.

In the second step, a mold was made according to the design using a Qidi Tech X-Max 3 printer. The designed model from Inventor to G-Code was transferred to the 3D printer software. The mold printing process took approximately one hour. The mold was filled with filament to exactly 15%. The filament material used during printing was green polylactic acid (PLA). The finished form was the final element, for which no auxiliary printing supports were used.

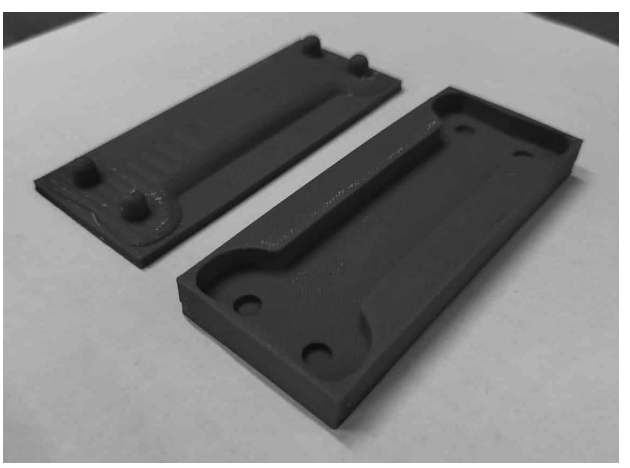

Figure 2. Printed mold for making a wax casting.

The next step was to create a wax model using a printed mold. The model material was modeling wax. In dentistry, modeling wax is used to create models of dentures, crowns, bridges and other elements of dental restorations. It is used for detail modeling, reconstruction planning and tooth positioning. In this work, modeling wax was used as a material to obtain a bone plate model for precision casting using the lost wax method.

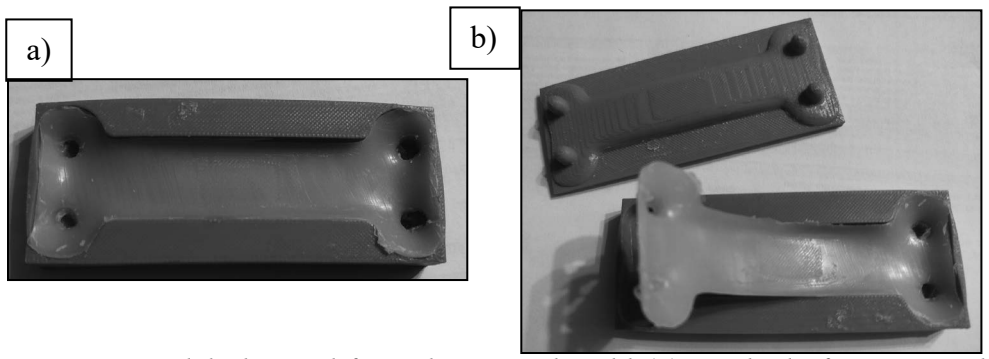

Figure 3. Wax model obtained from the printed mold (a), method of removing the model from the mold (b).

The material was a Zn1.2Mg wt% alloy considered for applications in orthopedic implantology. The production of the pre-alloy involved weighing zinc and magnesium, induction melting the zinc and then the magnesium in molten zinc at a temperature of approximately 520ºC. The alloy was then homogenized by mixing and heating at a temperature of approximately 500ºC. The alloy was allowed to cool. Next, casting molds were prepared and fired in a furnace at 520ºC for approximately 1.5 hours, after which the previously heated liquid Zn1.2Mg wt% alloy was poured into them. Tak uzyskany odlew odtłuszczono w acetonie. Then, immersion tests of the cast were performed in Ringer's solution at 37ºC for 336 hours. The casting surface was observed before and after immersion using a stereoscopic microscope at 10x and 25x magnification. Next, biological tests of the Zn1.2Mg wt% alloy were performed. In vitro biological characterization included cell viability assays and was performed using the reference human osteosarcoma cell line U2OS (ATCC). Cells were cultured in Dulbecco's Modified Eagle Medium/Nutrient Mixture F-12 (DMEM/F12, Merck) supplemented with 10% fetal bovine serum (FBS, Eurx) and 1% penicillin/streptomycin (PS, Merck). Cultures were performed under standard conditions, i.e., at 37°C, in a constant atmosphere with 80% humidity and 5% carbon dioxide (in a Heracell™ 150i incubator, Thermo Fisher Scientific). To assess cell viability on the materials, U2OS cells were seeded at a density of 2 × 105 cells/well, supplemented to 2 ml with medium in 12-well plates (Sarstedt), and cultured for 48 h. After incubation, 200 µl of Alamar blue reagent (Thermo Fisher Scientific) was added to the medium, followed by colorimetric development for another 3 h. Cell viability was assessed using a SYNERGY4 multiwell plate reader (BioTek Instruments, New York, NY, USA) at a wavelength of 570 nm. Survival results were presented as survival fraction (SF) relative to the untreated control growing on the plastic culture plate well. Three biological experiments were performed with 6 technical replicates for each sample; results are presented as the mean value +/- SD; Statistical significance of the change relative to the control was calculated using the T-test at p value ≤ 0.05 (marked with an asterisk).

1.2. Results of in vitro degradation studies of bone plate and biological evaluation of ZnMg1.2 wt%

The degradation process was studied by analyzing surface changes, particularly in the irregular shape and the area around the holes of the bone plate, as well as on the surface connecting both ends of the plate. The observed surface changes are presented in Figure 4. Photos of the surface before immersion (Fig. 4a) show the recreated shape of the wax model with several defects (over- and under-pouring). There are numerous irregularities in the casting surface around the holes and on the connecting surface. Both after 168 hours and after 336

hours of immersion in Ringer's solution, layers of degradation products and salt deposits from the solution are visible in the part around the plate's hole.

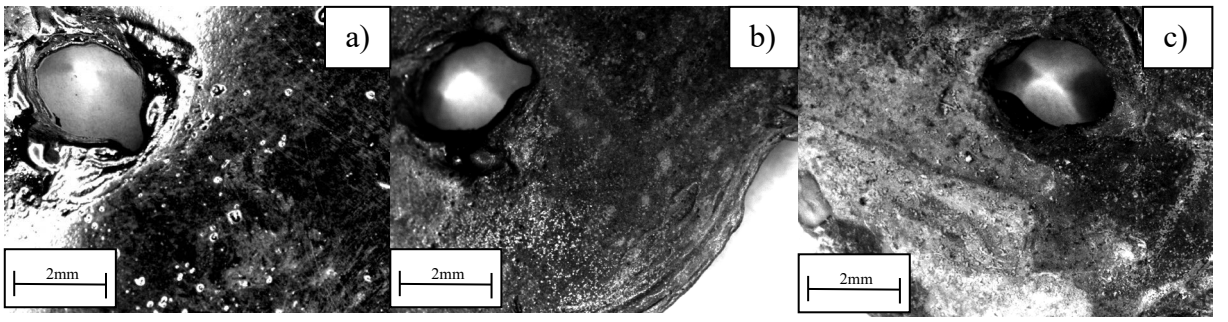

Figure 4. The casting surface: a) before immersion, b) after 168 hours of immersion, c) after 336 hours of immersion in Ringer's solution at 37ºC

Figure 5 shows the surfaces that were characterized by the highest density of the degradation and sediment product layer after 336 hours of immersion in Ringer's solution at 37ºC. The areas around the holes, surfaces with irregularities and deflections of the board prototype turned out to be critical.

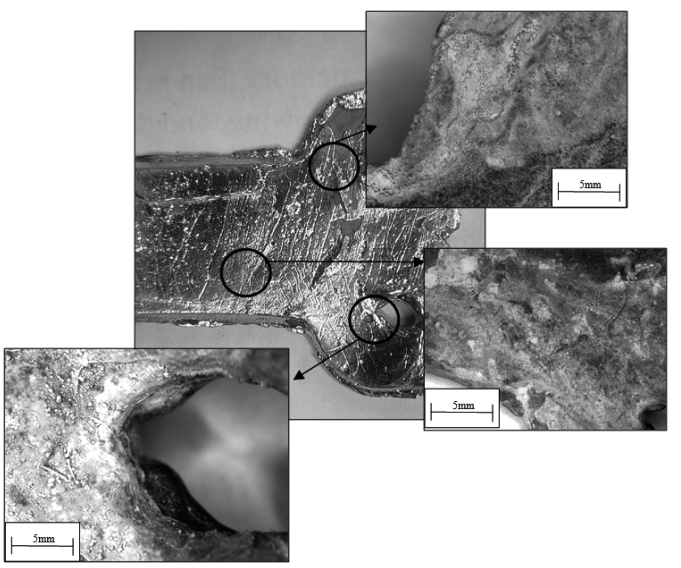

Figure 5. The casting surfaces with the highest density of degradation and sediment products after 336 hours of immersion in Ringer's solution at 37ºC.

U2OS cells, which were used as a model cell line for biocompatibility assessment, showed no negative impact of the presence of the tested material (fig.6). Cells from the tested population responded with survival rates comparable to control cells grown on the plastic culture plate. The change in survival was not significant, as the viability, expressed as a percentage change from the control, was no lower than 99% of the untreated control. It can be clearly stated that the material is non-toxic and, in short-term assessments up to 48 hours, does not cause changes in cell survival in vitro.

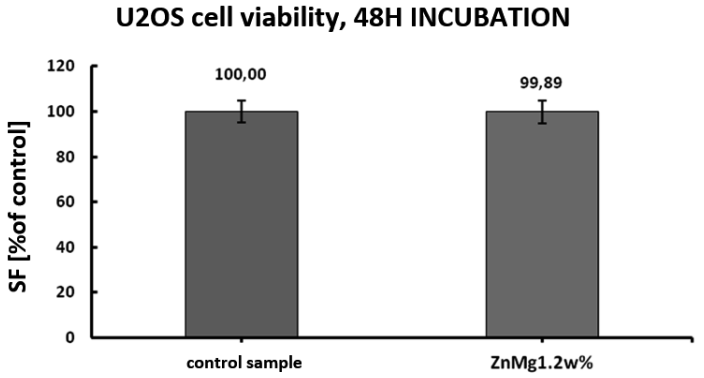

Sample

sample	control	ZnMg1.2w%
p-value	1	0,9668

Figure 6. U2OS cell viability after 48 h of incubation on the materials, Alamar Blue test. The result is presented as the mean surviving fraction (SF) compared to the untreated control. Statistical significance was not demonstrated by the T-test, with p value ≤ 0.05

CONCLUSIONS

The use of the precision casting method in combination with a wax model obtained using a 3D printed mold allows for the production of a prototype bone plate cast for research. The quality of the casting and the number of defects depend on the melt temperature, the gating system and the accuracy of adhesion of the wax pattern to the casting mould. The prototype obtained in this work contained a number of casting irregularities and defects, but it allowed the determination of critical points where the layer of degradation products is deposited to the greatest extent. Any irregularities, deflections and the area around the holes are critical points where the highest amount of degradation products and sediment was observed after immersion of the casting in Ringer's solution. The preliminary assessment of the biocompatibility of the ZnMg1.2 wt% alloy indicates the lack of toxicity of the tested material.

ACKNOWLEGMENTS

The work was carried out thanks to the financing of Project Based Education - PBL (Excellence Initiative - Research University program), in accordance with the Regulations No. 54/2020 and 55/2020 of the Rector of the Silesian University of Technology of March 13, 2020

BIBLIOGRAPHY

1. E. Majchrzak, M. Cholewa, A. Guzierowicz, J. Gawroński, J. Szajnar, Odlewnictwo: Technologia wykonania form i rdzenia, Wydawnictwo Politechnik Śląskiej,1993.
2. S. J. Skrzypek, Karol Przybyłowicz, Inżynieria metali i ich stopów, Wydawnictwo Naukowe PWN, 2019.
3. J. Dutta, The Future of Zinc Implant: Its Revolutionary Effects in Modern Advancements – A Short Overview,In Harmonising Chemical and Biological Sciences for Sustainable Deve lopment, 2025

4. Ch. Ji, A. Ma, J. Jiang, D. Song, H. Liu, S. Guo, Research status and future prospects of biodegradable Zn-Mg alloys, Journal of Alloys and Compounds, 993 (2024) 174669.
5. Y. Qin, A. Liu, H. Guo, Y. Shen, P. Wen, H. Lin, Additive manufacturing of Zn-Mg alloy porous scaffolds with enhanced osseointegration: in vitro and in vivo studies, Acta Biomateralia, 145 (2022) 403-415.

TalentDetector

9th January 2026
Gliwice, Poland

DEPARTMENT OF ENGINEERING MATERIALS AND BIOMATERIALS
FACULTY OF MECHANICAL ENGINEERING
SILESIAN UNIVERSITY OF TECHNOLOGY

INTERNATIONAL STUDENTS SCIENTIFIC CONFERENCE

Investigation of Magnesium and Its Alloys for Biodegradable Implant Applications

Melisa Šnircová[a], Peter Palček[a], Martin Slezák[a], Milan Uhričík[a]

[a]University of Žilina, Faculty of Mechanical Engineering, Department of Materials Engineering, Univerzitná 8215/1, 010 26 Žilina, Slovakia

Abstract: The article presents a comprehensive theoretical investigation of magnesium and its alloys for biodegradable implant applications. The study synthesizes information from existing scientific literature to establish the fundamental material, electrochemical, and biological principles governing the performance of magnesium-based implants in physiological environments. Emphasis is placed on the mechanisms of biodegradation, analysing how alloy composition, microstructural features, and environmental conditions influence corrosion behaviour, degradation kinetics, and mechanical integrity during implantation. Furthermore, the paper addresses the challenges associated with rapid degradation, hydrogen evolution, and localized corrosion, highlighting material design strategies aimed at controlling these effects. The objective of this work is to consolidate the theoretical knowledge necessary for the development and optimization of magnesium-based alloys for temporary, load-bearing biomedical implant applications.

Keywords: magnesium, biodegradation, biodegradable implants

1. INTRODUCTION

Nowadays, degradable materials are becoming an integral part of modern medicine, particularly in the field of orthopaedic implants, stents, and temporary fixation devices. With the increasing number of surgical procedures involving implantations, there is a significantly growing demand for biomaterials that not only provide optimal mechanical support during the healing process but also gradually degrade, thereby reducing the need for subsequent surgical interventions to remove the implant. Among the promising materials in this area are magnesium and its alloys, which, due to their low density, biodegradability, and mechanical properties close to those of bone tissue, represent an attractive alternative to traditional surgical materials. [1]

2. BIOMATERIA

LS - DEFINITION AND THEIR CLASSIFICATION

A biomaterial can be considered any material that is capable of improving bodily functions or repairing, or possibly replacing, damaged tissues. Requirements for biomaterials include biocompatibility, bio inertness, and bioactivity. A new definition of a biomaterial was introduced in 2018: “A material designed to have a form which, through interactions with living systems, directs the course of any therapeutic or diagnostic procedure.” [2]

Materials used for implants can be divided into the following groups based on their type:

- bioceramics
- polymers
- metals
- carbon
- composites [3]

Metals used for medical applications are characterized by their excellent thermal and electrical conductivity. Today, besides fracture fixation, they are used in load-bearing implants such as hip and knee joints. They can also be utilized in artificial heart valves and vascular stents. In all these applications, metals are mainly used thanks to their corrosion resistance and mechanical properties.

In addition to pure metals, metal alloys are widely used. These contain two or more types of elements. Alloys can be produced in several ways, such as alloying, surface treatments, or casting. The dominant metallic biomaterials are pure titanium (Ti), titanium alloys (Ti–6Al–4V), stainless steels, and cobalt–chromium alloys. When choosing a suitable biomedical metal, the following factors play a role:

- appropriate mechanical properties
- reasonable cost
- biocompatibility
- corrosion resistance [3]

The lifespan of an implant is defined as the period during which the implant performs its function in the body without failure, damage, or the need for replacement. Implants can be divided into the following categories based on durability (degradation time):

- permanent implants
- degradable implants

Permanent implants are materials designed to last in the patient’s body for a long time—up to several years—without significant damage. Examples include joint replacements and dental implants. It is important for permanent implants to have good mechanical properties, such as strength and hardness, and to be biocompatible. The expected medium-term lifespan of permanent implants ranges from 10 to 12 years after implantation, unless wear or damage occurs. Factors influencing implant longevity include the patient’s diagnosis, age, weight, and the material used.

Degradable materials are those that gradually break down in the patient’s body and are replaced by new tissue. They are mainly used as temporary implants in stents, screws, and

scaffolds. The main advantage of degradable implants is that there is no need for secondary surgeries to remove or replace the implant. [4]

Biodegradable implants are made from materials such as polymers, metals, and ceramics. The three main biodegradable metals with potential for implant manufacturing are magnesium, zinc, and iron. Magnesium implants release Mg^{2+} during their biodegradation. The amount of magnesium the body can safely absorb is 240–420 mg per day. The estimated lifespan of degradable implants ranges from several weeks to several months. [5]

The main limitation of permanent implants is the difference in elastic modulus compared to human bone. In permanent implants, stress can develop between the bone and the implant, which may lead to damage of both the bone and the implant.

Implants that fail earlier than their intended lifespan manifest as implant movement or persistent pain for the patient. If an implant outlives its expected lifespan, surgery is required to replace it with a new one. In practice, secondary implants never last as long as the first implant placed. This leads to several complications for the patient: the need for repeated surgeries, inflammation, pain, and immune-related issues. [6]

3. PROCESS OF BIODEGRADATION OF METALS

Biodegradation is a process during which compounds with high molecular weight are transformed into compounds with lower molecular weight. The resulting compounds are less complex than the original ones. Through biodegradation processes, organic compounds are converted into simple inorganic molecules, mainly water and carbon dioxide. Biodegradation is sometimes also referred to as biomineralization. The metabolism of microorganisms that use organic substances as substrates for their growth and for enzyme induction is also classified among biodegradation processes. It is important to note that the presence of a growth substrate or another utilizable compound is essential for maintaining biomass and inducing enzymes or cofactors involved in biodegradation. This process is known as cometabolism. [7]

Biodegradable metals are metals and their alloys that are expected to gradually corrode in an *in vivo* environment, while the corrosion products elicit an appropriate host response. After the immune response, the metals are completely dissolved. An important role of biodegradable metals (BMs) is the promotion of tissue healing. Currently, three metals and their alloys appear to be the most promising: magnesium-, iron-, and zinc-based BMs. The concept of biodegradation has been known in medicine for a long time, with degradable polymer sutures being a typical example. Biodegradable metals are a relatively new development in this field; however, their potential benefits for patients are becoming increasingly evident. To date, magnesium alloys are the most extensively studied BMs, mainly due to their low toxicity and weak immune response.

In 2005, Zartner et al. reported the successful implantation of a magnesium-based stent into the left pulmonary artery of a premature infant suffering from a severe congenital heart defect. Postoperative examinations showed that complete degradation of the stent occurred within five months without damage to the surrounding tissue. [8]

Magnesium and its alloys belong to biocompatible materials. In the human body, however, they also have the potential to be biologically resorbable. Magnesium is currently considered a revolutionary bioresorbable material for temporary orthopaedic and cardiovascular applications. It can be used in fracture-fixation devices such as rods, plates, and screws, as well as in temporary cardiovascular stents.

There is a wide range of advantages to using magnesium in temporary biomedical applications compared to, for example, stainless steels or titanium. An important factor is that magnesium has a density and elastic modulus similar to human bone. Therefore, excessive stress at the metal–bone interface does not occur. Furthermore, it is known that magnesium and its alloys do not cause toxicity or allergic reactions in the human body.

Since magnesium alloys completely degrade, the need for secondary surgeries to remove temporary implants can also be eliminated. Thanks to magnesium's osteoconductive character, faster bone regeneration is supported. Magnesium is natural to the body, and therefore its release from biodegradable implants positively influences wound healing, fracture repair, and tissue growth. It is recognized as an element involved in more than 300 enzymatic reactions.

On the other hand, a few disadvantages of magnesium alloys can also be identified. The main issues remain the excessively rapid degradation of implants, hydrogen release, and the deterioration of mechanical properties in simulated human-body environments. [9]

According to some authors, magnesium shows unusual corrosion behaviour compared to materials such as aluminum and iron. In recent years, the idea has emerged that magnesium has a different corrosion mechanism, known as the negative difference effect (NDE). This phenomenon describes a situation where the rate of hydrogen evolution from degrading magnesium alloys increases with increasingly negative anodic polarization of magnesium. In addition to typical electrochemical corrosion, magnesium is also known to undergo fragmentation (the so-called chunk effect). Hydrogen evolution leads to hydrogen embrittlement, which occurs along grain boundaries. [10]

Several factors influence the rate of biodegradation. The most well-known include alloying, precipitation hardening, and grain size. Among alloyed systems, Mg–Al–RE alloys (E alloys) show the lowest biodegradation rate; however, they also do not achieve the required level of mechanical strength. They are followed by Mg–Al–Zn alloys (AZ alloys). In recent decades, it has been shown that lanthanides support the treatment of bone diseases due to their positive effect on bone tissue regeneration and their potential to replace calcium ions with lanthanide ions in osteoporosis therapy. Zinc, as part of alloyed magnesium implants, favourably influences macrophage activity and thus participates in micro-immunological responses in bone disorders.

The properties of magnesium materials can, of course, also be modified using other treatment methods such as shot-peening, extrusion, and protective coatings. [11]

Figure 1 below shows the degradation of various materials implanted into a rat's body over 2, 4, and 12 weeks. The 3D reconstruction of material degradation was created using computed tomography. The rat was implanted with a titanium alloy (TiA), a magnesium alloy (MgA), pure magnesium, and poly-L-lactic acid (PLA). As expected, the titanium alloy did not lose a significant portion of its volume. After 12 weeks, the magnesium alloy showed pitting corrosion and surface deterioration. MgA also experienced a reduction in implant volume. Pure magnesium degraded too quickly and lost a substantial portion of its volume. The Mg implant lost its shape and was therefore unable to fulfil its physiological function. The PLA polymer underwent corrosion and experienced surface degradation, but it retained its shape and volume. [12]

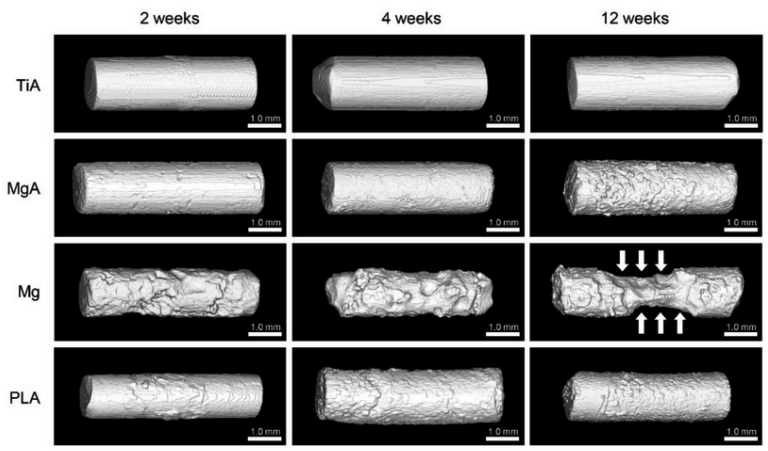

Figure 1. Degradation process of different materials in rat´s body [12]

Magnesium alloys are prone to rapid biodegradation. However, they have the ability to form a layer of corrosion products that creates a kinetic barrier on the material's surface. This prevents the migration of Mg^{2+} cations from the implant into the body. In the presence of water, magnesium undergoes an anodic reaction, leading to the production of Mg^{2+} cations. At the same time, a cathodic reaction occurs, releasing gaseous H_2. However, the human body contains more than just water. As is known, blood plasma contains proteins, water, and ions. The most important plasma ions include Cl^-, Na^+, K^+, HCO_3^-, Mg^{2+}, and PO_4^{3-}.

Chloride ions are quite aggressive and disrupt the surface of magnesium materials. In contrast, PO_4^{3-} ions increase the resistance of implants because they act as a barrier to corrosion. The kinetics of corrosion are influenced not only by inorganic ions but also by organic components such as proteins, cells, and biomolecules. The presence and growth of endothelial cells and osteoblasts on the implant surface slow down degradation and corrosion rates.

The electrochemical degradation process of magnesium in the human-body environment proceeds according to the following reaction (1):

$$Mg + 2\ H_2O \rightarrow Mg(OH)_2 + H_2 \quad (1)$$

This process leads to the formation of magnesium hydroxide $Mg(OH)_2$ and hydrogen gas. The resulting hydroxide forms an effective protective layer on the surface of the material. However, if the corrosive solution contains chlorides, the reaction proceeds differently (2):

$$Mg(OH)_2 + 2\ Cl^- \rightarrow MgCl_2 + 2\ (OH)^- \quad (2)$$

In this reaction, magnesium hydroxide is converted into magnesium chloride ($MgCl_2$). This chloride does not provide as effective a protective layer as the hydroxide. For this reason, the surface — and later the volume — of the implant becomes attacked. The release of hydroxide ions increases local pH. [13]

Another factor affecting degradation and corrosion processes is temperature. The rate of corrosion and degradation increases exponentially with temperature. Human body temperature (37 °C) can increase the corrosion rate. Temperature can also influence the solubility of precipitates on implant surfaces. pH also plays an important role in determining the rate of degradation processes. The hydrodynamic conditions of the human body affect corrosion,

degradation, and the biological behaviour of the material. For example, blood flow around the implant can prevent the growth of corrosion products. Table 1 shows the degradation rates of various magnesium alloys in a simulated human-body environment. [14]

Table 1. Degradation rates of magnesium alloys in various environments [15]

Alloy	Degradation environment	Corrosion rate [mm/year]	Simulation fluid
Mg-Ca	tissue fluid	0.5	Hank´s solution
Mg-Sr	blood	0.3	Hank´s solution
Mg-Zn	subcutaneous tissue	0.7	Phosphate-Buffered Saline
Mg-Y	muscle	0.4	DMEM
Mg-Ca-Zn	bone	0.5	simulated body fluid
Mg-Sr-Zn	muscle	0.55	Phosphate-Buffered Saline
Mg-Zn-Sr-Ca	subcutaneous tissue	0.65	Hank´s solution

In order to model the behaviour of magnesium alloys in the human body environment, solutions that simulate the behaviour and chemical composition of the organism are required. Such simulated solutions include, for example, Hank's solution, simulated body fluid (SBF), Ringer's solution, or synthetic saliva.

A simple and inexpensive option for a simulated solution is a 0.9% NaCl solution. Due to its simplicity, physiological saline mimics the ionic composition of body fluids and is therefore suitable for simulating the degradation of metals in the body. [16]

The degradation rate increases for AZ alloys from AZ31 (2 mm/year) to AZ91 (1.23 mm/year). These results were obtained by immersing AZ alloys in simulated body fluid.

To reduce the degradation rate, extensive research has been conducted focusing on mechanical properties and corrosion behaviour, aiming to improve the biomedical performance of magnesium alloys through alloying elements, technological processes, and other strategies.
The selected alloying material, like magnesium itself, must be non-toxic and easily degradable. Alloying elements intended for use in the human body can be classified according to their mineral composition and related effects, such as toxicity and allergic reactions, as follows:

- Mineral elements: Ca (calcium), Mn (manganese), Zn (zinc), Sn (tin), Sr (strontium)
- Toxic elements: Cd (cadmium), Be (beryllium), Pb (lead), Ba (barium), Th (thorium)
- Allergenic elements: Al (aluminum), Co (cobalt), V (vanadium), Cr (chromium), Ni (nickel), Ce (cerium), La (lanthanum), Cu (copper)

It has been demonstrated that a magnesium-zinc alloy (Mg-Zn) did not cause damage to red blood cells and promoted cell adhesion, confirming its in vitro biocompatibility.
The most commonly used resorbable implants today are made from biodegradable polymers and bioceramics. However, polymers are mechanically weak, and ceramics are relatively brittle. These negative properties limit their potential use in prosthetics. Magnesium alloys, due to their favourable mechanical and corrosion properties, could be used not only as orthopaedic implants, such as bone plates, but also as cardiovascular implants. [13]
Zinc plays an important role in supporting various biological functions, such as protein metabolism, cell growth, and division. As an inorganic element, it promotes the growth of bone tissue around bioimplants. When used as an alloying element in magnesium alloys, it improves

corrosion resistance due to its stable and moderate degradation, which is more favourable than the degradation of pure magnesium.

Furthermore, zinc has the lowest melting point among common alloying elements, allowing casting in an open atmosphere and facilitating the manufacturing process. Due to its low chemical reactivity and good machinability, zinc also contributes to reducing implant production costs. [17]

Currently, degradable magnesium alloy implants are already available on the market, protected with coatings such as MAGNEZIX® and Magmaris®. In modern biomedical practice, not only biocompatible but also biodegradable and bioactive implants are coming to the forefront. These implants may include secondary functions, such as post-operative tissue nourishment. [18]

4. APPLICATIONS OF BIODEGRADABLE MAGNESIUM IMPLANTS

Beyond orthopaedic applications, magnesium alloys could also be used in areas such as cardiovascular, dental, and plastic surgery implants. Magnesium implants for cardiovascular applications are already available on the market. The efficacy of magnesium biliary stents has shown satisfactory results when implanted in rabbits and dogs. The AZ31 alloy retained 94% of its volume one month after implantation into the biliary tract of rabbits. In addition to these experiments, biliary stents were also immersed in human bile. This experiment showed that after approximately 12 weeks, the stent structure was damaged and no longer functional.

In practice, after biliary stent implantation, reflux of intestinal bacteria into the bile ducts may occur, leading to infection. These bacteria could coat the stent and cause sediment buildup, potentially blocking the bile ducts. In 2010, Robinson and colleagues reported that magnesium materials can inhibit the growth of bacteria such as *Staphylococcus aureus* and *Escherichia coli*. As magnesium alloys degrade, they locally increase pH, creating an unfavourable environment for harmful bacteria. In this way, magnesium can act as an antibacterial agent, which, unlike antibiotics, does not easily lead to resistance.

Interestingly, magnesium may also exert anti-tumour effects. Cancerous (malignant) tumour cells rely on anaerobic glycolysis to maintain energy supply, creating an acidic microenvironment. This acidic environment promotes tumour cell proliferation and inhibits the activity of lymphocytes and NK cells, which are responsible for eliminating tumour cells. Moreover, the acidic microenvironment around tumours increases resistance to chemotherapy and radiotherapy. $Mg(OH)_2$, formed during magnesium degradation, alkalizes its surroundings, thereby inhibiting tumour cell growth and division. Hydrogen gas, produced during magnesium degradation, also contributes to anti-tumour activity by inhibiting inflammatory responses. Clinical observations indicate that low levels of Mg^{2+} in oncology patients are associated with faster disease progression and tumour resistance to chemotherapy. Li and colleagues found that magnesium inhibits human carcinoma cell proliferation and induces apoptosis. In animal experiments, magnesium wires were implanted into mice with liver tumours. After 15 days, tumour volumes and masses were significantly reduced compared to the beginning of the experiment.

Following positive animal results, Q3 Medical Equipment Co. recently manufactured a balloon-expandable biodegradable biliary stent, UNITY-B, made from a Mg-Nd-Mn alloy. This stent even received the Conformité Européene (CE) certification for bile duct treatment. This type of stent was tested in a 26-year-old patient who had previously experienced

complications after a plastic stent implantation, specifically biliary duct stricture. Following patient assessment, physicians used two UNITY-B stents, successfully reopening the bile duct. Eight weeks after UNITY-B implantation, the patient reported comfort and exhibited normal biochemical results. Biliary stent UNITY-B and its implantation is showed in Figure 2 below. [19]

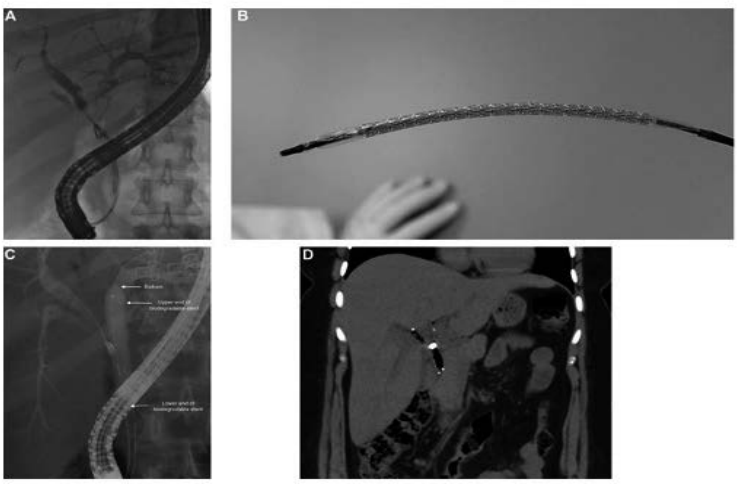

Figure 2. Usage of magnesium biliary stent UNITY-B [19]

BIBLIOGRAPHY

1. K. K. Thomas, M. N. Zafar, W. G. Pitt, G. A. Husseini, Biodegradable magnesium alloys for biomedical implants: properties, challenges, and surface modifications with a focus on orthopaedic fixation repair, Applied Sciences, 14(1), 2023.
2. C. Montoya, Y. Du, A. L. Gianforcaro, S. Orrego, M. Yang, P. I. Lelkes, On the road to smart biomaterials for bone research: Definitions, concepts, advances, and outlook, Bone research, 9(1), 12, 2021.
3. E. T. J. Chong, J. W. Ng, P. C. Lee, Classification and medical applications of biomaterials–a mini review, BIO integration, 4(2), 54, 2023.
4. A. R. Amini, J. S. Wallace, S. P. Nukavarapu, Short-term and long-term effects of orthopedic biodegradable implants, Journal of long-term effects of medical implants, 21(2), 2011.
5. A. K. Nasution, H. Hermawan, Degradable biomaterials for temporary medical implants, Biomaterials and Medical Devices: A Perspective from an Emerging Country, pp. 127-160, Cham: Springer International Publishing, 2016.
6. L. Levin, Dealing with dental implant failures, Journal of applied oral science, 16, pp. 171-175, 2008.
7. N. H. Tran, T. Urase, H. H. Ngo, J. Hu, S. L. Ong, Insight into metabolic and cometabolic activities of autotrophic and heterotrophic microorganisms in the biodegradation of emerging trace organic contaminants, Bioresource technology, 146, pp. 721-731, 2013.
8. H. Li, Y. Zheng, L. Qin, Progress of biodegradable metals, Progress in Natural Science: Materials International, 24(5), pp. 414-422, 2014.
9. Y. Yang, C. He, W. Yang, F. Qi, D. Xie, L. Shen, ... C. Shuai, Mg bone implant: Features, developments and perspectives, Materials & Design, 185, 2020.

10. Y. Yun, Z. Dong, N. Lee, Y. Liu, D. Xue, X. Guo, ... C. Guo, Revolutionizing biodegradable metals, Materials Today, 12(10), pp. 22-32, 2009.
11. K. Wieszczycka, K. Staszak, M. J. Woźniak-Budych, S. Jurga, Lanthanides and tissue engineering strategies for bone regeneration, Coordination Chemistry Reviews, 388, pp. 248-267, 2019.
12. N. Kawamura, Y. Nakao, R. Ishikawa, D. Tsuchida, M. Iijima, Degradation and biocompatibility of AZ31 magnesium alloy implants in vitro and in vivo: a micro-computed tomography study in rats, Materials, 13(2), 2020.
13. S. Kamrani, C. Fleck, Biodegradable magnesium alloys as temporary orthopaedic implants: a review, Biometals, 32(2), pp. 185-193, 2019.
14. S. Amukarimi, M. Mozafari, Biodegradable magnesium-based biomaterials: an overview of challenges and opportunities, MedComm, 2(2), pp. 123-144, 2021.
15. P. Sekar, S. Narendranath, V. Desai, Recent progress in in vivo studies and clinical applications of magnesium based biodegradable implants–a review, Journal of Magnesium and Alloys, 9(4), pp. 1147-1163, 2021.
16. G. Manivasagam, D. Dhinasekaran, A. Rajamanickam, Biomedical implants: corrosion and its prevention-a review, Recent patents on corrosion science, 2010.
17. K. B. NB, N. S. Balaji, A. Saikiran, Effect of Nutrient-Based Alloying Elements on Biodegradable Magnesium Alloys: Evolution, Challenges, and Strategies for Orthopaedic Applications, Biomedical Engineering Advances, 2025.
18. J. Singh, A. W. Hashmi, S. Ahmad, Y. Tian, Critical review on biodegradable and biocompatibility magnesium alloys: Progress and prospects in bio-implant applications, Inorganic Chemistry Communications, 169, 2024.
19. L. Liu, T. E. Liu, T. T. Cheung, A review of biodegradable biliary stents made of magnesium metals: Current progress and future trends, Journal of Magnesium and Alloys, 13(1), pp. 30-40, 2025.

TalentDetector
9th January 2026
Gliwice, Poland
DEPARTMENT OF ENGINEERING MATERIALS AND BIOMATERIALS
FACULTY OF MECHANICAL ENGINEERING
SILESIAN UNIVERSITY OF TECHNOLOGY
INTERNATIONAL STUDENTS SCIENTIFIC CONFERENCE

The influence of external friction on the temperature dependence of internal friction of steel

Yulia Sokolan[a], Kateryna Sokolan[b], Oleh Polishchuk[c], Mirosław Bonek[d]

[a] Khmelnitskyi National University, Faculty of Engineering Mechanics, Khmelnitskyi, Ukraine email: sokolan.julia@gmail.com.
[b] Khmelnitskyi National University, Faculty of Engineering Mechanics, Khmelnitskyi, Ukraine email: sokolan.kateryna @gmail.com .
[c] Khmelnitskyi National University, Faculty of Engineering Mechanics, Khmelnitskyi, Ukraine email: opolishchuk7l@gmail.com.

Abstract: When metal surfaces slide against each other, the contact stresses involved are closely related to inelastic stress relaxation phenomena, which determine the dynamic stress intensity of the frictional contact. Under certain conditions of external friction, stress relaxation processes can develop during dynamic strain aging and stress relief – dynamic aging. Steel 45 was studied in a hardened state, as well as in a low-temperature and high-temperature tempered state. Subsequently, the samples were subjected to external friction and the temperature dependencies of internal friction were studied. It was found that when hardened steel is subjected to friction, dynamic strain aging is accompanied by dynamic stress relief under load, which contributes to additional strengthening stress relaxation, reducing the risk of work hardening with the formation of brittle microcracks and increasing the energy capacity of the metal. The patterns of the influence of the external friction rate on the average temperature dissipation coefficient, taking into account the tempering temperature of steel, were also established.

Keywords: internal friction, external friction, temperature dependence of internal friction, relaxation processes, energy dissipation, temperature coefficient of dissipation, interstitial atoms, stress relaxation.

1. INTRODUCTION

In sliding friction between metal surfaces, the contact stresses are closely related to inelastic stress relaxation phenomena, which determine the dynamic stress intensity of the frictional contact. Under cyclic dynamic loading, stress relaxation processes in metals are interrelated with internal friction (IF), the level of which can serve as a measure of the relaxation capacity of the material and the degree of stress relaxation at a given amplitude of cyclic stresses and deformation temperature.

Under certain conditions of external friction, stress relaxation processes can develop during dynamic strain aging (DSA) and stress relief – dynamic aging (DA). The effectiveness of dynamic aging phenomena depends on the coordination of diffusion processes of interstitial

atoms and dislocation rearrangement, which, in turn, depend on the structure of steel, the deformation rate, and the temperature mode.

The processes of development of strengthening and weakening mechanisms of contact stress relaxation accompanying aging processes during external friction of metals are an important issue in the metallophysics of contact strength.

2. FORMULATION OF THE PROBLEM

The article [1] studied the effect of triboactivation of steel on the hardening and relaxation properties of surface layers, while article [2] studied the effect of external friction on the amplitude dependencies of internal friction. Since parts are subjected not only to friction but also to heating of the surface layer of the material during operation, it is necessary to study the effect of external friction on the temperature dependence of internal friction.

3. PRESENTING MAIN MATERIAL

Steel 45 was studied in a hardened state (hardened in water from a temperature of 850 °C), as well as in a low-temperature (200 °C) and high-temperature (600 °C) tempered state. Substructural changes in steel caused by heat treatment and external friction were studied using the temperature-dependent internal friction method on a torsion pendulum type device (Fig. 1) [3]. The oscillations were recorded by a non-contact capacitive sensor, the signal from which was fed into a recording electronic system with software that determined the initial amplitude A_0, the period of oscillation T, the square of the frequency ν^2, and the logarithmic decrement of oscillation δ, which serves as an indicator of internal friction (dissipative capacity).

To study the temperature dependence of internal friction, samples were heated by passing an electric current through a nichrome element covering the narrow working part of the sample (Fig. 2b), the temperature of which was controlled by a thermocouple. Tribological tests were carried out on a friction machine, the schematic diagram of which is shown in Fig. 3.

The sample 3 (Fig. 2), fixed in the clamp 2 and centering support 8, is driven into rotation at a preset speed by the electric motor 1. Friction is carried out between the narrow working part of the sample and abrasive pad 5 (P500), which is pressed with a controlled force to the cylindrical surface of the sample by the enveloping fixture 4, on which a pressing load is applied from the weights 6 placed on the suspension 7.

The influence of external friction of carbon steel on substructural changes controlling the processes of aging and relaxation of dynamic stresses, which determine the dissipative properties (energy capacity) of frictional contact, was investigated using the method of temperature-dependent internal friction.

4. THE RESULT OF WORK

In addition to volumetric dislocation-shear and diffusion relaxation processes in polycrystals, boundary relaxation plays a significant role, caused by viscous flow along the interfaces of grains, blocks, excess phases, and shear planes. Such viscous flow, like diffusion phenomena, is thermally activated, leading to a change in the leading mechanisms of stress relaxation as the temperature rises.

Temperature dependencies of internal friction (Fig. 4, 5) were studied under cyclic stresses that form the background of internal friction at room temperatures—amplitude-independent

internal friction (AIIF), corresponding mainly to losses caused by vibrations of short dislocation segments located between the nearest impurity atoms that locally fix the dislocations. Energy dissipation is associated with the phase lag of deformations behind the applied stresses during periodic bending of such dislocation segments.

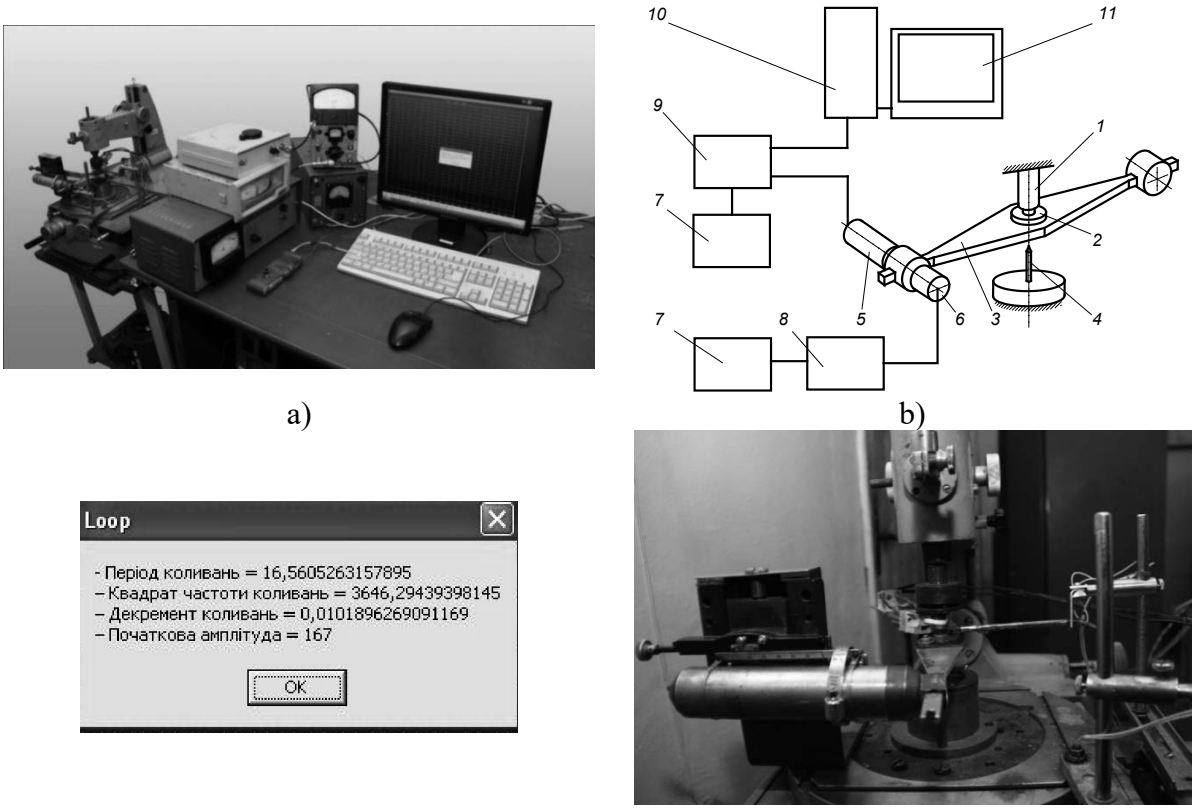

a) b)

c) d)

Figure 1 - General view (a), schematic diagram of the installation (b), measurement results output window (c) and working unit (d):
1 - stationary sample; 2 - moving sample; 3 - pendulum; 4 - support (needle);
5 - displacement sensor; 6 - oscillation excitation coil; 7 - power supply units; 8 - pulse forming unit; 9 - analog-to-digital converter; 10 - computer system unit; 11 - monitor

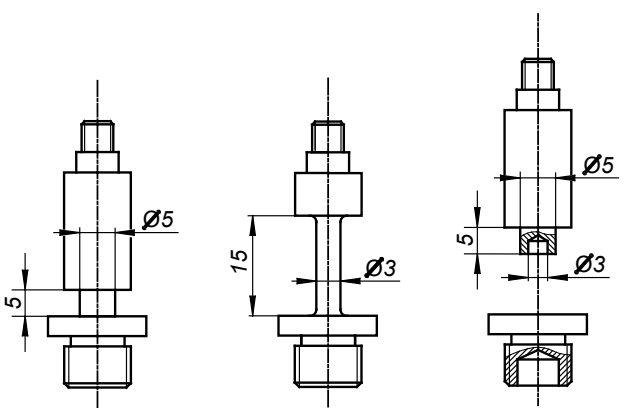

a) b) c)

Figure 2 – Samples for measuring volumetric internal friction (a, b) and frictional contact (c)

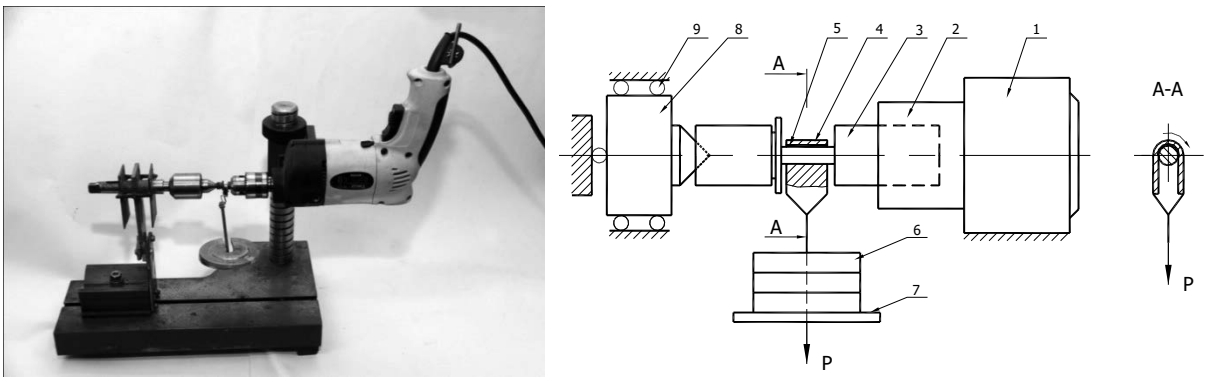

a) b)

Figure 3 – General view (a) and scheme of the friction machine (b): 1 - electric motor; 2 - clamping device (collet); 3 - sample; 4 - counterbody; 5 - abrasive pad; 6 - weights; 7 - suspension base; 8 - movable axial support (centering); 9 - ball bearing supports

The nature of the change and the intensity of the attenuation of vibrations in samples after tribotechnical tests with increasing temperature depend on the structural state of the steel and the friction rate. Relaxation maxima are formed to varying degrees in the temperature dependence of internal friction in the temperature range of 60, 80, and 120 °C. Two maxima correspond to nitrogen (around 60 °C) and carbon (around 80 °C) peaks of IF [4]. The temperatures at which these IF peaks are formed are determined by the frequency of excited freely damped vibrations of the sample (in our experiments, $\nu \sim 60$ Hz). Nitrogen and carbon atoms, as interstitial impurities, are located in octahedral positions, creating tetragonal distortions in the OCC lattice. At a certain temperature and frequency of external periodic loading in the stress field, there is a sharp increase in the migration of interstitial atoms along the interstices of the crystal lattice. As a result of such activation of the diffusion redistribution of impurity atoms, deformation lags behind the change in stresses, which leads to a resonant increase in energy dissipation (mechanical losses) with the formation of relaxation maxima of internal friction (Snoek peaks). The degree of stress relaxation and, consequently, the height of the internal friction peak are proportional to the concentration of interstitial atoms in the crystal lattice of the solid solution, which depends on the tempering temperature of the hardened steel.

In a non-equilibrium system with an increased concentration of vacancies (hardened state), the interstitial atoms partially dissolve into the vacancies. A significant portion of the interstitial atoms will migrate to energetically more favorable positions – to vacancies and dislocations – without contributing to resonant energy scattering. This should manifest itself in a decrease or complete disappearance of the corresponding relaxation peak.

It is known that Snoek relaxation peaks in deformed steel are unstable and can decrease to zero after deformation aging at temperatures of 100–350 °C [4]. At the same time, at around 250 °C, a deformation peak of Kester's internal friction occurs, caused by the interaction of carbon and nitrogen atoms with dislocations. The disappearance of Snoek relaxation indicates the migration of impurity atoms from the solid solution to dislocations. During deformation aging, the mobility of dislocations decreases, which leads to a significant reduction in internal friction. The drop in internal friction can also be caused by large degrees of plastic deformation. For hardened and low-tempered steel, an additional maximum of internal friction may occur in the region of 80 °C, characteristic of deformed residual austenite [4, 5]. According to [5], the occurrence of this peak is associated with the rotation in the stress field of pairs of own atoms of

the crystal lattice, formed as a result of their displacement from normal positions during plastic deformation (Zeger's dumbbell mechanism).

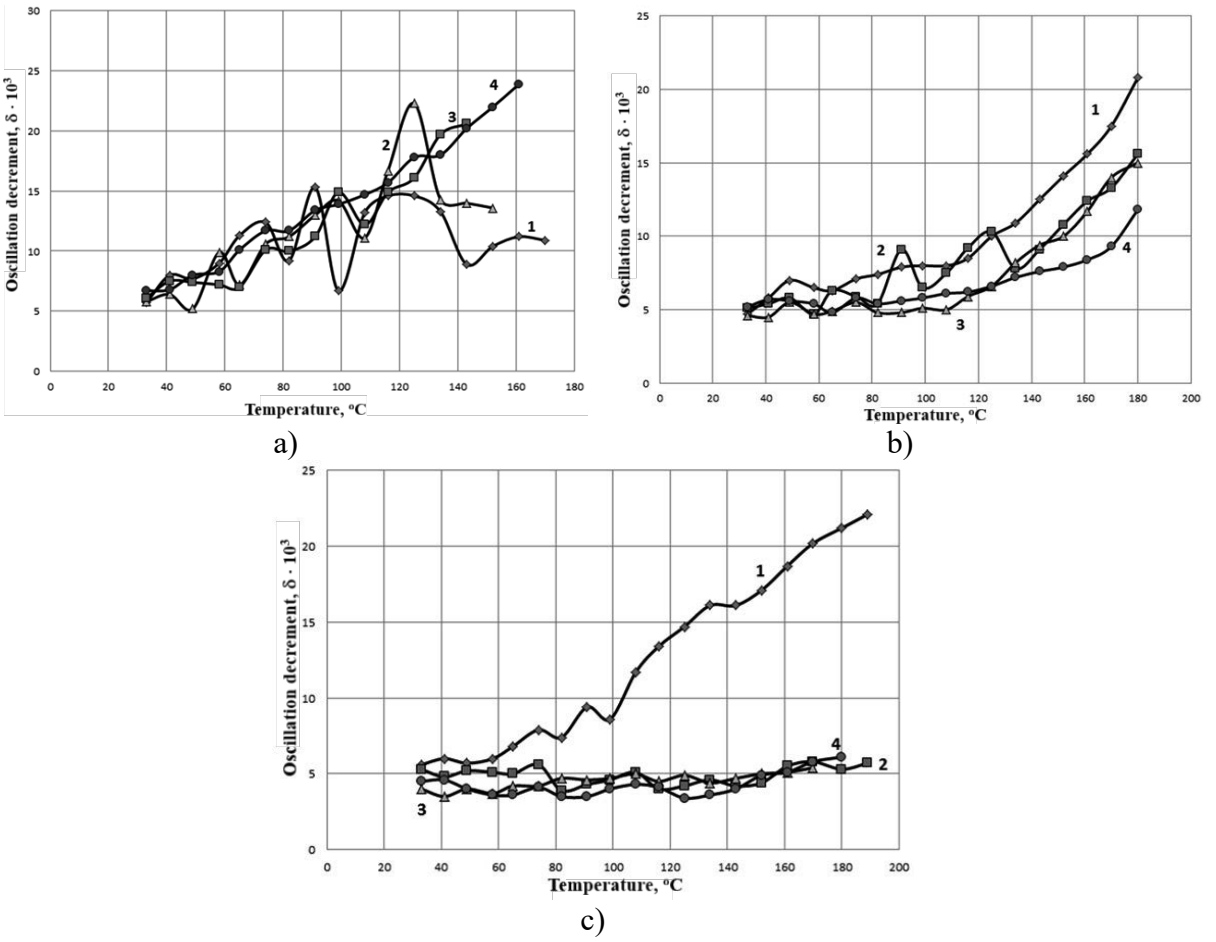

a) b)

c)

Figure 4 – Effect of external friction at P = 5 N on the temperature dependence of the damping coefficient: a – hardening; b – tempering at 200 °C; c – tempering at 600 °C (1 – initial state; 2 – V_1 = 0,08 m/s; 3 – V_2 = 0,21 m/s; 4 – V_3 = 0,34 m/s)

The oscillation of interstitial dumbbells is accompanied by the migration of atoms, leading to the healing of vacancies. With an increase in tempering temperature, the interstitial atoms (C+N) are mainly concentrated in precipitates (carbides, nitrides), and the solid solution becomes depleted of these atoms, which leads to a decrease in the height of the relaxation maxima of internal friction. The appearance of a IF peak in the region of 120 °C is usually associated with ferromagnetism [6]. In [7], it is shown that this peak has a more complex origin, i.e., it is determined not only by ferromagnetism.

The effect of temperature on the relaxation (dissipative) capacity of steel was evaluated by the average temperature coefficient of dissipation: $\alpha_T = \Delta\delta/\Delta T$ (increase in decrement per degree), which characterizes the degree of blocking and mobility of dislocations under conditions of thermomechanical activation. The greater α_T, the easier it is for dislocations to break away from blocking impurity atoms and their precipitates under cyclic loading, and the lower the resistance to viscous flow at the boundaries (Fig. 6).

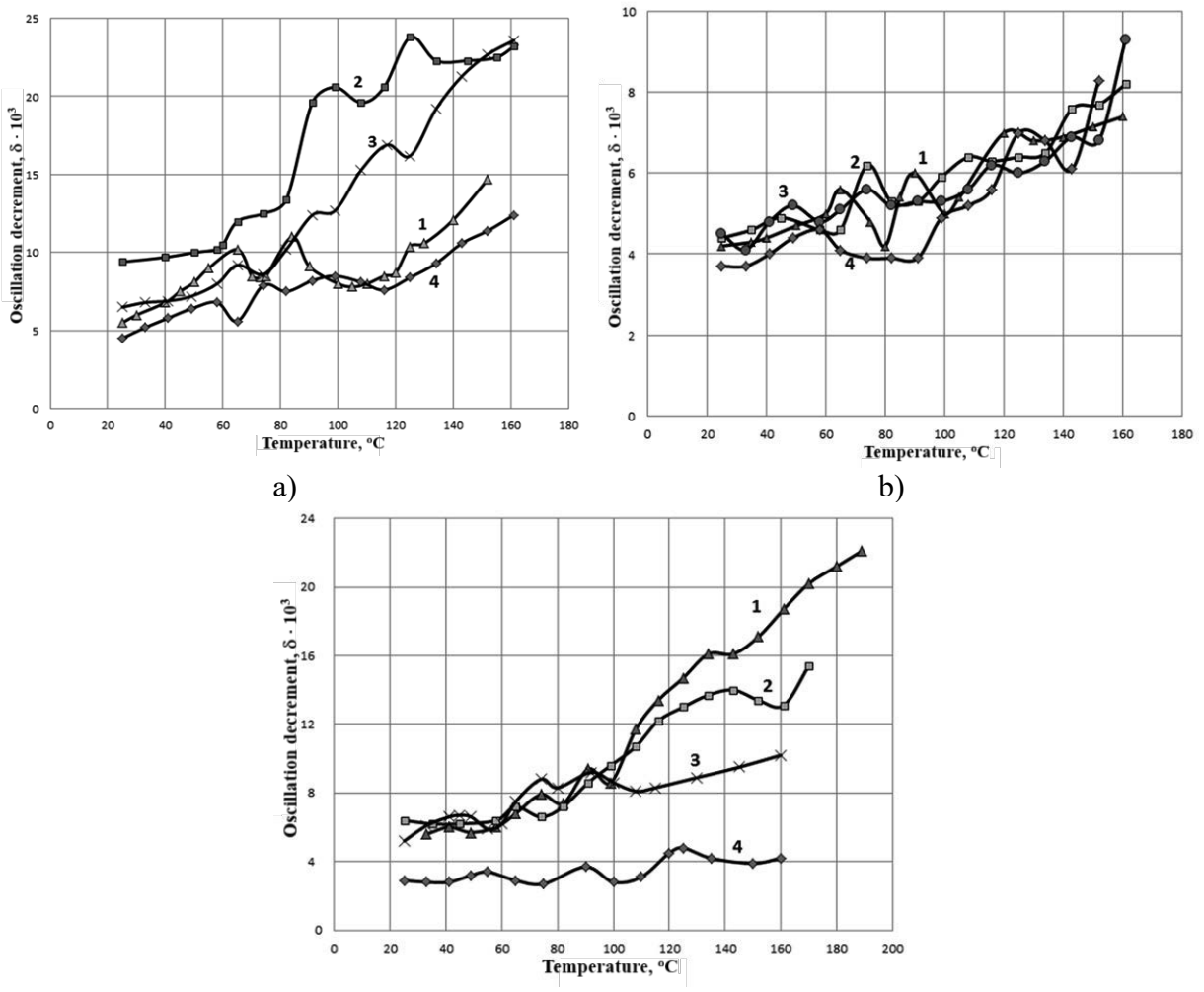

Figure 5 – Effect of external friction at P = 10 N on the temperature dependence of the damping coefficient: a – hardening; b – tempering at 200 °C; c – tempering at 600 °C (1 – initial state; 2 – V_1 = 0,08 m/s; 3 – V_2 = 0,21 m/s; 4 – V_3 = 0,34 m/s)

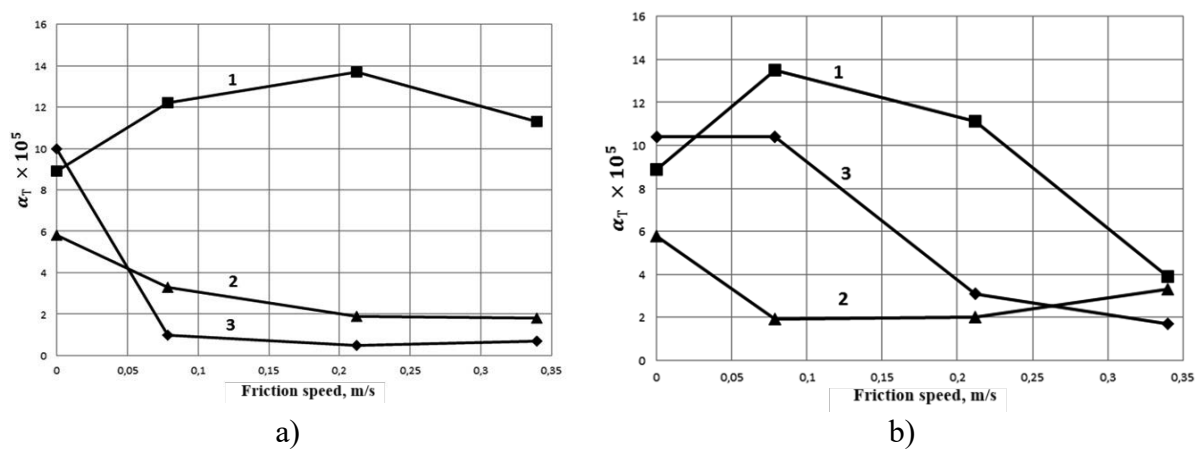

Figure 6 – Dependence of the temperature dissipation coefficient α_T on the friction rate and heat treatment mode of steel: a – P = 5 N; b – P = 10 N (1 – hardening; 2 – tempering at 200 ºC; 3 – tempering at 600 ºC)

Hardened steel is characterized by an initial increase in the αT index after friction at low speeds (Fig. 6, curves 1), which is due to substructure rearrangement processes in the friction contact zone with an increase in the density of mobile dislocations capable of long-range movement. This is apparently facilitated by the migration of impurity atoms along dislocations to pinning sites, which leads to an increase in the size of dislocation segments L_c. The dislocations newly formed under these conditions, with their high density, turn out to be weakly fixed by impurity atoms due to their reduced concentration at the dislocations and thermal instability. Such steel exhibits increased relaxation (dissipative) capacity with increasing temperature. As the slip rate increases, causing an increase in the contact temperature and the velocity of dislocation movement, processes are activated in the friction contact zone, accompanied by an increase in the degree of dislocation pinning by impurity atoms (C+N) and submicroscopic carbide precipitates. The energy and thermal stability of the bond between dislocations and impurity atoms and their atmospheres increases.

After tempering (especially high-temperature tempering), steel typically exhibits a decrease in the α_T index with an increase in slip rate (Fig. 6, curves 2,3). This means that the dissipative capacity of steel decreases significantly and, at a friction rate of $V = 0.34$ m/s, may be lower than the initial value. The observed decrease in the α_T coefficient, which is usually accompanied by metal hardening, occurs due to a decrease in dislocation mobility. This is facilitated by:

— formation of a low-mobility dislocation network during their interaction (upon reaching critical density) with a reduction in the distance between L_N nodes;

— development of dynamic strain aging (DSA) to a greater or lesser extent, as a result of which the generated ("fresh") dislocations are blocked by impurity atoms (C+N) migrating towards them, their atmospheres, and segregations [8].

The dissipative capacity of the structure under DSA decreases due to a reduction in the length of dislocation segments (L_c) and a decrease in the overall mobility of dislocations. Optimal conditions for DSA development are created at friction rates and temperatures where the velocity of dislocation movement becomes comparable to the diffusion rate of impurity atoms. DSA is controlled by diffusion processes, which are significantly accelerated by friction due to an increase in temperature and dislocation density.

The highest values of α_T, as well as its significant decrease with increasing sliding speed and contact load, are characteristic of hardened steel (Fig. 6, curves 1). After hardening, structurally metastable martensite has high residual microstresses and significant microplasticity due to the high density and weak fixation of dislocations formed as a result of phase work hardening. When hardened steel is rubbed at a speed of $V_1 = 0.08$ m/s, in addition to an additional increase in dislocation density, the tetragonal nature of martensite decreases due to a decrease in the concentration of carbon in the solid solution during its decomposition (carbon migrates to dislocations).

Judging by the intensity of the decrease in the α_T index with an increase in the external friction rate, hardened steel is subject to significant strengthening under the conditions studied. Hardening, forming a metastable structure with a high concentration of impurity atoms (C+N) in a solid solution, contributes to the enhancement of the DSA effect during friction. This accelerates the decomposition of martensite and the transformation of residual austenite with the release of highly dispersed carbide particles. This causes the so-called stress relief (dynamic aging), which is the result of structural relaxation caused by the diffusion redistribution of impurity atoms with the formation of new phases [9]. The carbide particles released in this process have high dispersion and increased concentration due to an increase in the number of carbide phase nucleation centers. As a result, the mobility of dislocations is further limited, the

resistance of steel to small plastic deformations increases, and relaxation resistance increases as a result of the relaxation of stresses arising during the martensitic transformation.

Stress relief (dynamic stress relief) contributes to increased hardening efficiency due to the formation of highly dispersed carbides, which create an additional barrier effect for dislocations. On the other hand, carbide particles also have a beneficial effect on the relaxation capacity of the material, as they promote the generation of fresh dislocations and cause a decrease in the concentration of carbon in the matrix, which leads to a reduction in the density of dislocation pinning points. Compared to conventional tempering, dynamic tempering under load results in a more complete decomposition of martensite, which provides an additional increase in the strength of dislocation pinning and a decrease in microplasticity, and the temperature forming the maximum elastic limit is 50-100 °C lower [9]. Consequently, stress relaxation during friction of hardened steel is determined by:

— diffusion redistribution of carbon and nitrogen atoms in a cyclic stress field, as well as the movement of weakly fixed dislocations (weakening factor);

— structural relaxation (physicochemical reactions of decomposition of a supersaturated solid solution – martensite and transformation of residual austenite);

— dynamic strain aging and dynamic tempering, which ultimately cause a decrease in dislocation mobility and hinder viscous flow along the boundaries (strengthening factor).

The relaxation mechanisms described above prevail over conventional work hardening, which is more characteristic of deformation under friction conditions in high-tempered steel. Indeed, in the case of high-tempered steel (T_{temp} = 600 °C), the decrease in the α_T index and, accordingly, in the mobility of dislocations with an increase in the friction rate (Fig. 6b, curve 3) is mainly due to the formation of a low-mobility dislocation structure, accompanied by a decrease in the length of dislocation segments L_c and a reduction in the distance between the fixation points of the dislocation network L_N: with a decrease in L_c and L_N during work hardening of steel, the relaxation (dissipative) capacity of the structure decreases. At reduced contact load (Fig. 6a, curve 3), regardless of the sliding speed, the effect of friction sharply reduces the α_T index, indicating favorable conditions for the development of DSA.

Low-tempered steel (T_{temp} = 200 °C) exhibits the lowest ability to dissipate mechanical energy and the highest temperature stability of relaxation properties under the studied conditions of external friction when the sliding speed and contact load change (Fig. 6, curves 2). Already during low-temperature tempering, there is a significant reduction in internal friction due to the decomposition of martensite with the release of highly dispersed ε-carbide particles coherently bound to the matrix [10].

5. CONCLUSIONS

Depending on the heat treatment of steel and the friction regime, relaxation during dynamic strain aging (DSA) reduces the dissipative capacity of the material to a greater or lesser extent. The result depends on the saturation of the solid solution with impurity atoms, as well as on the number of precipitates and their morphology (dispersibility, shape). By strengthening the steel while maintaining sufficient relaxation capacity of the material, DDA contributes to increased wear resistance.

When hardened steel is subjected to friction, DSA is accompanied by dynamic tempering under load (dynamic aging), which contributes to additional strengthening relaxation of stresses,

reducing the risk of work hardening with the formation of brittle microcracks and increasing the energy capacity of the metal.

The data obtained are of interest in the context of the problem of creating tribotechnical materials with high dissipative (relaxation) capacity while maintaining sufficient strength.

BIBLIOGRAPHY

1. Sokolan Iu. Effect of steel triboactivation on hardening and relaxation properties of surface layers / Iu. Sokolan, K. Sokolan, P. Maidan, S. Matiukh, O. Polishchuk, M. Bonek // International students scientific conference “Talent Detector 2025”. - 31th January, 2025, Gliwice, Poland. - p. 537 - 549
2. Sokolan Iu. Influence of external friction on amplitude dependences of internal friction of steel / Iu. Sokolan, K. Sokolan, O. Polishchuk, M. Bonek // International students scientific conference “Talent Detector 2025. Summer”. - 2025, Gliwice-Brenna, Poland. - p. 583-590
3. Shevelya V.V. Improving the wear resistance of metals by electric arc treatment / V.V. Shevelya, A.S. Trytek, V.P. Oleksandrenko, Iu.S. Sokolan. // V Ukrainian-Polish Scientific Dialogues. – Khmelnytskyi-Yaremche. – 2013. – pp. 80-81.
4. Krystal M.A. Internal friction in metals and alloys / M.A. Krystal, Yu.V. Piguzov, S.A. Golovin. – M: Metallurgy, 1964. – 245 p.
5. Gordienko L. K. Substructural strengthening of metals and alloys / L. K. Gordienko – M: Nauka, 1973. – 223 p.
6. Postnikov V. S. Internal friction in metals / V. S. Postnikov. – M: Metallurgy, 1974. – 352 p.
7. Postnikov V. S., Razumov V. I. University News. Ferrous Metallurgy. – 1957. – No. 11. – pp. 24-31.
8. Babich V. K. Deformation Aging of Steel / V. K. Babich, Yu. P. Gul, I. E. Dolzhenkov. – M: Metallurgy, 1972. – 320 p.
9. Pastukhova Zh. P. Dynamic aging of alloys / Zh. P. Pastukhova, A. G. Rakhstadt, Yu. A. Kaplun. – M: Metallurgy, 1985. – 320 p.
10. hevelya V. V. Influence of heat treatment of steel on the formation of frictional bonds and their dissipative properties / V. V. Shevelya, A. S. Tritek, Iu. S. Sokolon. // Problems of Tribology. – 2012. – No. 3. – P. 6-14.

TalentDetector
9th January 2026
Gliwice, Poland
DEPARTMENT OF ENGINEERING MATERIALS AND BIOMATERIALS
FACULTY OF MECHANICAL ENGINEERING
SILESIAN UNIVERSITY OF TECHNOLOGY
INTERNATIONAL STUDENTS SCIENTIFIC CONFERENCE

Secondary A356 Aluminium Alloys in the Automotive Industry: A review

Zuzana Straková[a]

[a] University of Žilina, Faculty of Mechanical Engineering, Department of Materials Engineering
email: zuzana.strakova@fstroj.uniza.sk

Abstract: The automotive industry is undergoing a significant transformation driven by stringent CO_2 emission regulations and the rapid shift towards electrification. Aluminium alloys, particularly the A356 (AlSi7Mg0.3) cast alloy, have emerged as critical materials for vehicle lightweighting because of their excellent castability, mechanical properties, and corrosion resistance. This review explores the technical profile of A356, its role in safety-critical automotive components, and the transition towards the use of secondary (recycled) aluminium. While recycling offers a 95% reduction in energy consumption and greenhouse gas emissions compared with primary production, managing impurities – especially iron – remains a technical challenge for secondary A356 in high-ductility applications. This review provides an overview of aluminium recycling in the automotive industry, with a focus on the use of A356 alloys in conventional and electric vehicles. The principles of aluminium recycling and its environmental benefits are discussed. Special attention is given to recycling-induced impurities, especially iron, which represents the main metallurgical limitation in secondary A356 alloys.

Keywords: aluminium, A356, recycling, automotive, iron

1. INTRODUCTION – THE DRIVE FOR LIGHTWEIGHTING

The automotive industry is undergoing a significant transformation driven by electrification, resource-efficiency demands, and the shift towards a circular economy. Aluminium alloys play a central role in this transformation due to their advantageous properties, including excellent castability, corrosion resistance, low weight, and high recyclability. These properties make aluminium essential for creating lightweight vehicles, not only in internal combustion engine models but increasingly in electric vehicles. Reducing vehicle weight enhances energy efficiency, driving range, and overall system performance [1-7].
Although the focus has shifted beyond tailpipe emissions with the rise of electrification, reducing vehicle mass remains a key aspect of automotive design. Stricter CO_2 regulations, such as the EU target of 93.6 g CO_2/km, have accelerated the use of lightweight materials, as less mass means lower fuel consumption and emissions. Cutting 100 kg from a car can save

about 8 grams of CO_2 per kilometre, highlighting the correlation between weight and energy use [8-10].
Aluminium is ideal for lightweight parts because of its density of around 2,700 kg/m³, about a third of steel's. It allows significant weight reductions, often up to 50%, in structural and semi-structural parts without sacrificing safety or function [4,11].
In electric vehicles, aluminium's importance is tied to life-cycle considerations, as vehicle mass influences raw-material requirements, battery size, and energy consumption. Using aluminium to reduce structural weight supports longer driving ranges and battery downsizing, lowering the vehicle's environmental footprint over its lifespan. These benefits have led to increased use of aluminium castings in electric cars, especially for battery and motor housings and other structural components [6,12-15].
From a sustainability standpoint, aluminium is notable for its ability to be recycled endlessly without losing its fundamental properties. Recycling aluminium consumes only 5% of the energy required for primary production, making it ideal for reducing greenhouse gas emissions and conserving resources. Consequently, the use of secondary aluminium in the automotive industry has increased, supported by greater end-of-life vehicle volumes and scrap. However, using recycled aluminium presents challenges, including impurity build-up and issues with alloy quality control [16-19].

A356 (AlSi7Mg0.3) is a popular aluminium casting alloy used in automotive manufacturing. It offers excellent castability, corrosion resistance, a good strength-to-weight ratio, and mechanical properties that can be improved through heat treatment. Increasingly, A356 is produced from secondary aluminium to meet economic and sustainability goals. Its significance is most noticeable in high-volume parts, where casting efficiency and recyclability are critical. However, recycling aluminium can lead to higher impurity levels, especially iron and copper, which are difficult to remove during remelting [20-23].

Despite extensive research on aluminium recycling and Fe-rich intermetallics, a detailed overview of how secondary A356 alloy metallurgy connects with electric vehicle requirements remains scarce. Therefore, this review aims to provide a critical overview of the aluminium alloys recycling for automotive applications, with a particular focus on secondary A356 alloys, the recycling-induced impurities on microstructure and performance, and the effectiveness of mitigation strategies such as manganese addition.

2. ALUMINIUM RECYCLING AND CIRCULAR ECONOMY

Aluminium recycling (Figure 1) is a highly effective material loop in industry and a key part of the circular economy in the metal sector. Unlike ceramic or polymer materials, aluminium retains its metallic structure during remelting, enabling it to be recycled into new products without losing key properties. This capacity for repeated circulation makes aluminium and its alloys ideal for sustainable, long-term use in automotive manufacturing [16-18].

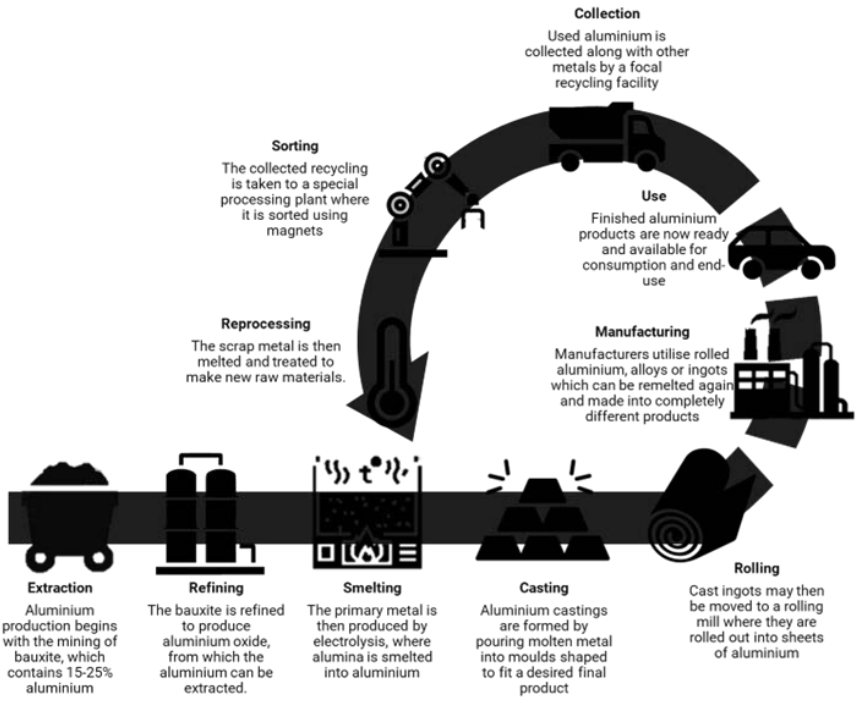

Figure 1 Aluminium life cycle [16,18]

From an energy and environmental standpoint, aluminium offers clear benefits. Producing secondary aluminium uses only about 5-10% of the energy required for primary production, significantly reducing greenhouse gas emissions and environmental impact. Increasing the use of recycled aluminium in products such as vehicles and infrastructure is a key way to lower overall life-cycle impacts, especially important as embodied emissions from materials and batteries contribute more to electric vehicles' total footprint [9,10,12-14,16].

In the automotive sector, aluminium recycling is supported by high collection rates and established infrastructure. End-of-life vehicles are a major source of aluminium scrap, alongside significant pre-consumer scrap from manufacturing that can be directly recycled. In Europe, most aluminium used in cars is already recycled at vehicle end-of-life, and the proportion of recycled aluminium in new casting alloys is steadily growing. Economically, recycled aluminium is attractive because it reduces costs and provides less exposure to fluctuations in the primary aluminium market [16,17,19].

However, recycling aluminium presents metallurgical challenges. Relying on mixed and post-consumer scrap can result in residual elements such as iron, copper, and zinc, which are difficult or uneconomical to remove during remelting. Wrought alloys require strict control of composition and depend heavily on primary aluminium. In contrast, casting alloys, which are more tolerant of compositional variations, are the primary carriers of recycled aluminium, especially Al-Si-Mg systems in the automotive industry [20-23].

Life-cycle assessments show that environmental benefits depend not only on the amount of recycled material but also on effective collection, sorting, and alloy-specific recycling processes. Closed-loop recycling, where scrap is reused within the same or similar alloy types, offers the greatest benefits by reducing processing needs. However, most recycling occurs via open-loop pathways, remelting scrap into generic alloys, which maximises material recovery but also exacerbates impurity issues [18,22,23].

As the automotive industry moves toward electrification and circular economy principles, the use of recycled aluminium is expected to grow. Electric vehicles rely heavily on aluminium castings for structural and functional parts, many of which do not need ultra-pure alloys but must meet strict mechanical standards. Properly engineered secondary alloys can balance sustainability, cost, and performance efficiency, provided that recycling-induced limitations are clearly understood and appropriately managed [6,11,15].

3. SECONDARY A356 ALUMINIUM ALLOYS FOR AUTOMOTIVE AND ELECTRIC VEHICLE APPLICATIONS

Among aluminium casting alloys, A356 (AlSi7Mg0.3) is one of the most widely used in the automotive industry because of its favourable balance of properties, including castability, mechanical and corrosion resistance, and recyclability. From the perspective of aluminium recycling, A356 is particularly significant because Al-Si-Mg casting alloys are the primary source of secondary aluminium from mixed waste streams, pre- and post-consumer [20-23].

The widespread industrial application of A356 is closely linked to its properties and heat-treatable nature. Silicon improves melt fluidity and reduces shrinkage, enabling the production of complex castings with good dimensional accuracy. Magnesium enables precipitation hardening through T6 heat treatment. This combination allows mechanical properties to be tailored directly to application-specific requirements, making A356 suitable for automotive components that require a balance between strength and manufacturing efficiency [20,21].

A356 alloy plays a key role in closing aluminium material loops within the automotive sector. The increasing availability of end-of-life vehicles has led to a growing supply of aluminium scrap, which is predominantly recycled into casting alloys rather than into wrought alloys. As a result, secondary A356 alloys are increasingly used in automotive components where cost efficiency, material availability and sustainability are critical. This trend reflects a broader shift towards maximising recycled content in vehicle structures without altering the established casting routes [16,17,19,22].

The transition towards electric vehicles has further reinforced the relevance of A356 alloys and their recycling. Electric cars use aluminium for battery housings, inverter castings, and underbody structures. These components (Figure 2) require good castability, thermal stability and corrosion resistance. The most suitable alloys for these components are Al-Si-Mg alloys, especially A356 [6,11,15,24].

a) b)

Figure 2 Examples of secondary A356 aluminium alloy application: a) Electric Vehicle Charging Gun Connector; b) Battery housing [25,26]

However, the increased use of recycled aluminium in A356 alloys introduces challenges due to impurities in secondary alloys. Residual elements such as iron and copper are unavoidable in secondary aluminium and strongly influence the microstructure and mechanical properties, thereby affecting performance. These recycling-induced effects impose practical limits on the allowable recycled A356 content in castings and require targeted alloy design and processing strategies to ensure reliable performance in automotive and electric vehicles [22,23].

4. RECYCLING-INDUCED IMPURITIES AND MITIGATION STRATEGIES IN SECONDARY A356 ALLOYS

The increasing use of recycled aluminium in A356 casting alloys inevitably leads to the accumulation of residual elements (impurities). Among these, iron is particularly critical. It primarily originates from mixed pre- and post-consumer scrap streams and cannot be economically removed during remelting. Because aluminium can be repeatedly recycled, the iron content tends to increase, making impurity control a key limitation for the use of secondary A356 alloy in electric vehicle applications[22,23].

In Al-Si-Mg alloys, iron exhibits limited solubility in the aluminium matrix. It tends to form brittle Fe-rich intermetallic phases, such as β-Al_5FeSi, which degrade fatigue resistance and act as stress concentrators that promote cracking. In addition, Fe-rich intermetallic phases can promote microgalvanic couplings with the aluminium matrix, accelerating localised corrosion (particularly in chloride-containing environments). These effects are critical for structural components subjected to cyclic loading and to long service-life requirements [20,26-29].

To mitigate the negative impact of Fe-rich phases, alloying with elements such as manganese has been investigated. Manganese modifies the morphology of Fe-rich intermetallics, favouring the formation of more compact, less harmful α-$Al_{15}(Fe,Mn)_3Si_2$ phases that may exhibit skeleton-like or Chinese-script morphologies. These phases have been proven to reduce stress-concentration effects and be less detrimental to mechanical properties [30-32].

Nonetheless, manganese's effectiveness depends on the Mn/Fe ratio, impurity levels, and solidification conditions. Excessive manganese addition may increase the overall volume of intermetallic phases, negatively affecting castability and toughness. What's more, complete neutralisation of iron during secondary production is not achievable. Industrial practice, therefore, focuses on optimising alloy composition to achieve an acceptable balance between recycled content, microstructural stability and performance requirements [33,34].

Overall, the presence of Fe-rich intermetallic phases in secondary aluminium alloys represents a primary limitation for the use of secondary A356 alloys in demanding automotive and electric vehicle applications. Nevertheless, if recycling-induced impurities are managed through alloy design and process control, A356 alloys remain an economically and environmentally advantageous material for structural components.

4. CONCLUSIONS

The growing emphasis on lightweight design, electrification, and circular-economy principles has underscored the importance of aluminium alloys in the automotive industry. Aluminium recycling plays a critical role in reducing greenhouse gas emissions and energy

consumption, and casting alloys are the primary pathway for incorporating secondary aluminium into vehicle components. A356 alloy is a key alloy in this pathway because of its favourable balance of castability, mechanical properties, and recyclability.

The use of secondary A356 alloys offers economic and environmental benefits, but recycling-induced impurities, particularly iron, limit their performance. The formation of Fe-rich intermetallic phases remains the primary challenge, as they affect fatigue and corrosion resistance in demanding automotive and electric-vehicle applications.

Alloying strategies based on manganese addition provide a limited yet effective means of mitigating the detrimental effects of iron-modifying intermetallic phases on morphology and of partially restoring mechanical properties. However, complete elimination of iron-related limitations is rarely achievable in highly recycled alloys, underscoring the need for a performance-based approach to alloy design.

Overall, secondary A356 aluminium alloys represent a sustainable material solution for a wide range of automotive and electric-vehicle applications, provided recycling-induced limitations are managed.

Continuous development of impurity-tolerant alloy compositions, improved scrap sorting, and application-specific design strategies will be essential for expanding the role of recycled aluminium in next-generation mobility systems.

ACKNOWLEDGEMENTS

This paper was prepared within the framework of the joint Slovak-Polish project TalentDetector 2026 as a result of collaboration between the Silesian University of Technology (Poland) and the University of Žilina (Slovakia), and was supported by the projects VEGA 1/0461/24 and KEGA 033ŽU-4/2026.

BIBLIOGRAPHY

1. Raabe, D., Tasan, C.C., Olivetti, E.A., Strategies for improving the sustainability of structural metals, Nature, 575, 64–74 (2019).
2. Hirsch, J., Recent development in aluminium for automotive applications, Light Metal Age, 78(3), 22–31 (2014).
3. European Aluminium, Sustainability Roadmap for the European Aluminium Industry, European Aluminium Association, Brussels (2018).
4. Miller, W.S., Zhuang, L., Bottema, J., et al., Recent development in aluminium alloys for the automotive industry, Materials Science and Engineering A, 280(1), 37–49 (2000).
5. Kaufman, J.G., Introduction to Aluminum Alloys and Tempers, ASM International, Materials Park, OH, USA (2000).
6. Luo, A., Recent advances in light metals and manufacturing for automotive applications, CIM Journal, 12(11) (2021).
7. Hirsch, J.R., Aluminium in Innovative Light-Weight Car Design, Materials Transactions, 52(5) (2011).
8. Paraskevas, D., Kellens, K., Dewulf, W., Duflou, J.R., Environmental modelling of aluminium recycling: A life cycle assessment approach, Resources, Conservation & Recycling, 77, 46–56 (2013).

9. Ducker Worldwide, Automotive Aluminium Study: Global Aluminium Content in Cars, Ducker Worldwide LLC, Detroit, MI, USA (2016).
10. Das, S., The life-cycle impacts of aluminum body-in-white automotive material, International Journal of Life Cycle Assessment, 16(3), 268–279 (2011).
11. Miller, W.S., Automotive Materials and Manufacturing, SAE International, Warrendale, PA, USA (2014).
12. Ellingsen, L.A.-W., Singh, B., Strømman, A.H., The size and range effect: Life-cycle greenhouse gas emissions of electric vehicles, Journal of Industrial Ecology, 20(1), 76–89 (2014).
13. Kim, H.C., Wallington, T.J., Arsenault, R., Bae, C., Ahn, S., Lee, J., Cradle-to-gate emissions from a commercial electric vehicle lithium-ion battery, Environmental Science & Technology, 50(14), 7715–7722 (2016).
14. Hao, H., Qiao, Q., Liu, Z., Zhao, F., Impact of vehicle electrification and lightweighting on energy use and GHG emissions, Applied Energy, 188, 155–168 (2017).
15. Hirsch, J., Lightweight aluminium for electric vehicles, Light Metals, 2019, 1095–1101 (2019).
16. European Aluminium, Recycling Aluminium – A Pathway to a Sustainable Economy, European Aluminium Association, Brussels (2016).
17. Schlesinger, M.E., Aluminum Recycling, CRC Press, Boca Raton, FL, USA (2013).
18. International Aluminium Institute, Life Cycle Inventory Data for Aluminium Production, IAI, London, UK (2018).
19. Gaustad, G., Olivetti, E., Kirchain, R., Improving aluminum recycling: A material flow analysis, Resources Policy, 58, 166–178 (2018).
20. Taylor, J.A., The effect of iron in Al–Si casting alloys, Progress in Materials Science, 57(4), 701–760 (2004).
21. Campbell, J., Complete Casting Handbook: Metal Casting Processes, Metallurgy, Techniques and Design, 2nd ed., Butterworth-Heinemann, Oxford, UK (2015).
22. Lumley, R., Fundamentals of Aluminium Metallurgy: Production, Processing and Applications, Woodhead Publishing, Cambridge, UK (2010).
23. Makhlouf, M.M., Evolution of a recycled aluminium alloy deformed by the equal channel angular pressing process, Journal of Minerals, Metallurgy and Materials, 19(11), 1016 (2016).
24. Hirsch, J., Recent development in aluminium for automotive applications, Light Metal Age, 78(3), 22–31 (2014).
25. www.made-in-china.com. A356 Aluminium Alloy Metal Casting, Gravity Casting, Die Casting for Electric Vehicle Charging Gun Metal Butt Connector. (2025).
26. www.empcasting.com. Electric Vehicle Battery Housing. (2025).
27. Wang, Q.G., Microstructural effects on the tensile and fatigue properties of A356 alloy, Metallurgical and Materials Transactions A, 34(12), 2887–2899 (2003).
28. Kuchariková, L., Tillová, E. et al., Influence of Fe-rich intermetallics on corrosion behaviour of Al–Si alloys, Metals, 20(2), 65–71 (2013).
29. Šurdová, Z., Tillová, E., Kuchariková, L., Mikolajčík, M., The Study of Porosity in A356 Secondary Aluminium Alloys with Higher Iron Content. System Safety: Human - Technical Facility – Environment. 6(1). pp. 430-438. (2025).
30. Samuel, A.M., Samuel, F.H., Doty, H.W., Observations on the formation of β-Al_5FeSi phase in 319 type Al-Si alloys, Journal of Materials Science**,** 31, 5529-5539 (1996).

31. Taylor, J.A., Iron-containing intermetallic phases in Al–Si based casting alloys, International Journal of Cast Metals Research, 1, 19–33. (2012).
32. Seifeddine, S., Svensson, I. L., The Influence of Fe and Mn Content and Cooling Rate on the Microstructure and Mechanical Properties of A380-die casting alloy. Metallurgical Science and Technology 27(1). pp. 11-20. (2009).
33. Shabestari, S., G., Moemeni, H., Effect of copper and solidification conditions on the microstructure and mechanical properties of Al–Si–Mg alloys. Journal of materials Processing Technology 153-154(10). pp. 193-198. (2004).
34. Šurdová, Z., Tillová, E., Kuchariková, L., Mikolajčík, M., Study of corrosion resistance of secondary AlSi7Mg0.3 alloy in 3.5% NaCl solution. 39th Danubia-Adria Symposium on Advances in Experimental Mechanics. pp. 108.109. (2023).

TalentDetector
9th January 2026
Gliwice, Poland
DEPARTMENT OF ENGINEERING MATERIALS AND BIOMATERIALS
FACULTY OF MECHANICAL ENGINEERING
SILESIAN UNIVERSITY OF TECHNOLOGY
INTERNATIONAL STUDENTS SCIENTIFIC CONFERENCE

Concept of electronic checklists using AR glasses in general aviation

Michał Sujkowski[a], Piotr Pulit[b], Aleksandra Gruszka[c], Michał Szendzielorz[d] , Michał Lach[e], Dariusz Myszor[f], Magdalena Mrozik[g]

[a] Silesian University of Technology, Faculty of Transport and Aviation Engineering, Department of Air Transport
[b] Silesian University of Technology, Faculty of Transport and Aviation Engineering, Department of Air Transport
[c] Silesian University of Technology, Faculty of Transport and Aviation Engineering, Department of Air Transport
[d] Silesian University of Technology, Faculty of Automatic Control, Electronics and Computer Science, Department of Algorithmics and Software
[e] Silesian University of Technology, Faculty of Automatic Control, Electronics and Computer Science, Department of Algorithmics and Software
[f] Silesian University of Technology, Faculty of Automatic Control, Electronics And Computer Science, Department of Algorithmics and Software
[g] Silesian University of Technology, Faculty of Transport and Aviation Engineering, Department of Air Transport, email: ms303388@student.polsl.pl

Abstract: Flight safety in general aviation strongly depends on proper checklist execution and pilot situational awareness, particularly during single-pilot operations. Traditional paper checklists and electronic checklists integrated into avionics systems require head-down attention, increasing the risk of procedural omissions and reduced external visual scanning.
This paper presents a conceptual approach to electronic checklist display using optical see-through augmented reality (AR) glasses in general aviation aircraft. The proposed solution enables checklist items to be presented directly in the pilot's field of view while maintaining continuous observation of the external environment. The concept aims to reduce head-down time and support procedural compliance during critical phases of flight.
The article reviews existing checklist solutions in GA, outlines basic technical characteristics of AR glasses, and discusses potential operational benefits and limitations of AR-based checklist systems. The work provides a foundation for further experimental and human factors research in this area.

Keywords: aviation, safety, checklist, AR technology

1. INTRODUCTION

Aviation operational safety constitutes one of the fundamental areas of research in aviation. The complex nature of flight operations, resulting from the interaction between humans,

technology, and the environment, means that maintaining a high level of safety requires consistent adherence to established rules and operational procedures. Analyses of aviation occurrences indicate that deviations from procedures, their incomplete execution, or improper sequencing of actions are among the significant factors contributing to aviation incidents and accidents, particularly during critical phases of flight. Operational procedures constitute a set of standardized, predefined actions and rules intended to ensure the safe and consistent conduct of flight operations and to reduce the risk of human error [1]. As a core element of risk management in aviation, they support the pilot's decision-making process, especially under conditions of increased cognitive workload, and the omission of even seemingly minor actions may lead to the occurrence of undesired events.

One of the primary tools supporting the correct execution of operational procedures are checklists [2], which constitute an ordered set of control actions assigned to specific stages of flight. Their main function is to ensure the completeness of performed actions and to reduce the pilot's cognitive workload, particularly under conditions of increased stress or time pressure. In aviation, both paper-based and electronic checklists are widely used, available via onboard avionics systems or portable devices. Despite their numerous advantages, these solutions require the pilot to temporarily shift attention to elements located outside the primary field of view, which may result in reduced observation of the external environment and a decrease in situational awareness.

In commercial aviation, this problem has been partially addressed through the implementation of Head-Up Display (HUD) systems. HUDs present critical flight information directly in the pilot's forward field of view and have been shown to improve safety and operational performance by reducing head-down time and supporting situational awareness [3]. This allows continuous observation of the external environment while monitoring flight parameters. This has been shown to reduce head-down time, improve situational awareness, and support safer decision-making during critical phases of flight [3] such as takeoff, approach, and landing. However, due to cost, integration complexity, and certification constraints, HUD systems are rarely available in general aviation aircraft.

In recent years, a dynamic development of technologies supporting operational and training processes in aviation has been observed, including systems based on augmented reality (AR), which have been shown to increase user engagement, attention, and learning effectiveness in procedural training contexts [4]. These solutions enable the presentation of procedures directly within the pilot's field of view while maintaining full observation of the environment and continuous monitoring of flight instruments [3]. The application of optical AR glasses in general aviation opens up the possibility of a new approach to checklist presentation, combining procedural support with continuous control of the external environment. In this context, conducting conceptual research on the use of AR systems as tools supporting the safety of flight operations becomes well justified.

2. CHECKLIST SOLUTIONS CURRENTLY USED IN GENERAL AVIATION

Checklists constitute a fundamental procedural support tool in aviation. Their primary purpose is to support procedural compliance, reduce pilot workload, and improve the consistency and safety of flight operations. They are lists of actions to perform that need to be done to complete a certain task, such as starting up the engines, preparing the plane for takeoff, and they also contain many emergency procedures for situations where there is not much time and all actions

need to be done quickly and correctly. Basic checklists are categorized by their usage, such as Read and Do, and Do-Confirm. In the first one, a pilot needs to read the needed action first, then perform it. He does it throughout a whole list and ends with "xxx checklist complete". This type is used in situations where there is plenty of time, and the procedure needs to be done in a certain order. Do-Confirm does things a little differently. In this situation, there is rarely enough time, so the pilots are expected to complete all the actions by themselves and only then check if all of them were performed with help from this checklist. It is used mostly when landing, doing "memory items" or in emergencies; the order of performing actions usually does not matter.
The other way to categorize checklists is how they are displayed. Most basic checklists are printed on paper, often laminated to preserve them. The other often-used types are the ones programmed into aircraft's avionics.

2.1. Paper-Based Checklists – Characteristics and Operational Limitations

The paper-based checklists have been used in aviation for a long time. They are extremely reliable, as they do not rely on any external power source or any other system. They can be placed whenever the pilot needs them to be, often on the kneepad, which is easily accessible. Unfortunately, some flaws need to be addressed as well, those checklists can be lost mid-flight if not stored properly, a pilot can misplace them and searching for them while flying is no easy task. The other thing is they are susceptible to damage of different types, if not laminated, they can be destroyed by water, or just ripped, which makes it harder to use them. The main operational limitation is their placement relative to the pilot's field of view. As stated previously, if they are on the kneepad, the pilot needs to look away from the horizon and aircraft instruments for a short while, when reading checklists. This is a serious problem, especially for new pilots as the flight parameters must always be maintained, to avoid unintended deviations from the intended flight path.

Despite those, they remain the most used checklists in aviation to this day and are an essential part of any student pilot's career.

2.2. Electronic Checklists Integrated with Avionics Systems

The second most used type is a checklist programmed into avionics. Modern avionics systems from major manufacturers support integrated electronic checklists. They function basically the same, with the only difference being they are displayed on aircraft displays, so they cannot be missed, especially as the pilot has them right in front of their eyes all the time. They are customizable, so that any operator can have their checklists available. Depending on the type of avionics, it can either be a touchscreen or a turning knob, both of them offer different uses of avionics; touchscreen interfaces offer higher interaction efficiency, while physical controls may provide better usability in turbulence or high-vibration environments. Both rely on a power source to function. If it fails, the pilot does not have access to any checklist, which might be a serious safety concern. For this reason, aircraft often have doubled or tripled electrical systems, often backup paper checklists are also present on-board.

This type of checklist is a step-up on the older paper checklists. It offers increased efficiency in performing most checklist-related actions, and is easier to use, it only needs a reliable avionics and power, which in most modern aircraft are guaranteed.

2.3. Human Factors Risks Related to Head-Down Time and Attention Diversion

The use of checklists, both paper-based and electronic, requires pilots to divert visual attention away from the external environment and primary flight instruments. This diversion, commonly referred to as head-down time, introduces specific human factors risks, particularly in general aviation operations characterized by single-pilot workload and dynamic flight conditions.

Head-down time directly reduces the pilot's ability to maintain continuous situational awareness, which depends on uninterrupted perception of external cues, aircraft attitude, and system behavior. During critical phases of flight such as takeoff, approach, landing, and low-altitude maneuvering, even brief interruptions in visual scanning may delay the detection of traffic, terrain, or deviations from the intended flight path.

In single-pilot operations, checklist execution adds an additional attentional and cognitive task to an already high workload environment. This may lead to task saturation and inefficient workload distribution, increasing the likelihood of delayed responses, missed communications, or incomplete monitoring of flight parameters. In abnormal situations, where workload is elevated, the need to locate and interpret checklist information may further slow down decision-making processes.

Similar effects have been empirically observed in other safety-critical transportation domains. A recent simulator-based study in maritime navigation showed that excessive head-down time is associated with reduced situation awareness and that the introduction of an augmented reality interface significantly reduced head-down time (by a factor of 2.67) and head-down occurrences (by 62%) compared to conventional displays. Although conducted outside aviation, these results confirm the general human factors mechanism linking head-down time, attentional tunnelling, and degraded operator awareness in dynamic environments [5].

Moreover, conventional checklist usage requires manual interaction with physical or electronic interfaces, which may interfere with continuous aircraft control, especially in turbulence or during time-critical situations. As a result, while checklists remain essential for procedural compliance, their traditional implementations introduce inherent limitations related to attention management and workload distribution. These limitations motivate the exploration of alternative checklist presentation methods that minimize head-down time and better integrate procedural support into the pilot's visual scan.

3. AUGMENTED REALITY AS A PILOT ASSISTANCE TOOL

Augmented Reality (AR) is a technology that allows the real world to be combined with computer-generated images by placing virtual objects in the field of view in real time. In aviation, this technology allows pilots to read entered data directly in their field of view. The main purpose of this solution is to eliminate the need for pilots to take their eyes off the external environment.

3.1. Technical Specification of AR Glasses

AR glasses, characterized by low weight and high screen resolution, were selected for the task of displaying instructions for pilots. The specifications of the XREAL Air 2 Ultra model used are presented below. The device resembles ordinary glasses in appearance.

The main criterion for selecting the equipment was the resolution of the displayed image. Detailed technical parameters are listed in the table 1.

The selected parameters ensure that checklist text is clearly legible under typical lighting conditions, does not obscure essential cockpit instruments, and does not introduce significant physical discomfort during longer periods of use.

Table 1. Technical specifications of XREAL Air 2 Ultra glasses

Parameter	Value
Display type	Sony Micro-OLED
Resolution	1920 x 1080 pixels per eye
Field of view	52 degrees
Brightness	Up to 500 nits
Weight	83g
Connector	USB-C (DisplayPort Alt Mode)
Refresh rate	Up to 120 Hz

3.2. Visualization of Checklists using AR Glasses

The integration of checklist information is based on the use of AR glasses as a projection display.

Figure 1. Example visualization of an aviation checklist in AR glasses

The key to this solution is the use of an image transmission standard and the specific optical design of glasses. The image display mechanism works as follows:

• Data transmission: The glasses work like a monitor. They are connected to a mobile device via a USB-C port supporting the DisplayPort Alternate Mode standard, mainly supported by Samsung's flagship smartphone models.
• Screen Mirroring: With this connection, the glasses are detected by the phone's operating system as an external screen. Thanks to the screen mirroring function, what is on the phone screen is projected onto the glasses.

The visualization process works as follows:
• Displays located at the top of the frames generate a high-contrast image.
• This image is projected onto a system of prisms or lenses.
• The light from the displays is reflected towards the pilot's eye, while allowing light from the external environment to pass through.

Thanks to the high contrast of OLED panels, black is interpreted as transparency. This allows bright checklist text to be displayed without completely obscuring the pilot's view.

Checklist activation can be performed manually by the pilot or automatically based on predefined triggers such as flight phase selection or specific system parameter thresholds (e.g., abnormal oil pressure). This allows the system to support both routine and abnormal procedures without increasing pilot workload.

In the context of flight procedures, the system allows checklists to be displayed. Pilot interaction with the system has been simplified to a minimum so as not to distract the pilot:
• The pilot manually selects the appropriate checklist on the control device. Also, the checklist can appear automatically, if, for example, the value of oil pressure gets lower than 0.8 bar.
• The checklist appears in the field of view as an AR overlay.
• The pilot verifies the displayed items and can manually hide the view after completing the procedure.
• The entire system acts as a digital equivalent of a paper checklist, always within sight.

4. DISCUSSION AND SUMMARY

The concept of electronic checklist presentation using augmented reality glasses introduces a new class of pilot assistance systems for general aviation. By transferring procedural information directly into the pilot’s forward field of view, the proposed solution addresses one of the fundamental limitations of traditional checklist implementations, namely the requirement for head-down visual attention during checklist execution. This characteristic is particularly relevant in single-pilot operations, where the pilot is simultaneously responsible for aircraft control, navigation, communication, and system monitoring.

From an operational perspective, the primary expected benefit of the AR-based checklist system is the reduction of head-down time during critical phases of flight. By maintaining continuous visual contact with the external environment and primary flight instruments, the pilot can perform procedural tasks while preserving situational awareness. This may contribute to a reduction in omission errors, delayed responses to abnormal situations, and loss of external visual references, especially during low-altitude flight, approach, and departure phases. Furthermore, the constant availability of checklists within the visual field may support better procedural discipline and reduce reliance on memory-based execution under stress.

The proposed solution may also influence pilot workload distribution. Traditional checklist usage often introduces short periods of increased cognitive and visual workload due to attention shifts between the cockpit environment, external references, and checklist media. The AR-based approach has the potential to smooth this workload by integrating procedural information into the existing visual scan pattern. This integration could support more stable cognitive performance and reduce the likelihood of attentional tunneling or task saturation.

Despite these potential advantages, several limitations and challenges must be considered. The introduction of visual overlays into the pilot's field of view carries a risk of information clutter and visual distraction, particularly if checklist content is poorly designed or excessively dense. Ergonomic factors such as display brightness, text size, focal distance, and long-term wearing comfort must be carefully evaluated to prevent visual fatigue or discomfort. Additionally, the system must ensure high reliability and fail-safe behavior, as any malfunction or latency in abnormal situations could negatively affect pilot performance.

From a technical and regulatory perspective, the integration of AR-based systems into certified aviation environments poses challenges related to system qualification, electromagnetic compatibility, and human factors approval. While portable and non-integrated solutions may be used under certain conditions, broader operational deployment would require alignment with aviation authorities and certification frameworks.

This work is conceptual in nature and does not aim to provide a validated operational solution. Its primary purpose is to define a technical and functional framework for the use of AR glasses as a checklist interface in general aviation. Further research should focus on experimental evaluation, including simulator-based studies and in-flight trials, to quantify the impact of AR-based checklist presentation on pilot performance, workload, situational awareness, and error rates. Such studies are necessary to determine whether the theoretical benefits of the proposed concept translate into measurable safety improvements in real operational conditions.

In conclusion, augmented reality glasses represent a promising platform for enhancing procedural support in general aviation. If appropriately designed and validated, AR-based checklist systems may contribute to improved safety, reduced pilot workload, and better situational awareness, particularly in single-pilot operations. The presented concept provides a foundation for further interdisciplinary research combining aviation engineering, human factors, and information technologies.

BIBLIOGRAPHY

1. International Civil Aviation Organization, Safety Management Manual, Doc 9859, Fourth Edition, ICAO, Montréal, 2018.
2. R. Clay-Williams, L. Colligan, "Back to basics: checklists in aviation and healthcare," BMJ Quality & Safety, vol. 24, pp. 428–431, 2015.
3. J. J. Arthur III, R. E. Bailey, S. P. Williams, L. J. Prinzel III, K. J. Shelton, D. R. Jones, V. E. Houston, "Review of head-worn displays for the Next Generation Air Transportation System," Optical Engineering, vol. 56, no. 5, 051405, 2017.
4. T. Gangabissoon, G. Bekaroo, W. Moedeen, "Application of Augmented Reality in Aviation: Improving Engagement of Cabin Crew during Emergency Procedures Training," Proceedings of ICONIC 2020, ACM, 2020.
5. K. P. Houweling, S. C. Mallam, K. van de Merwe, K. Nordby, "The effects of augmented reality on operator situation awareness and head-down time," Applied Ergonomics, vol. 116, 104213, 2024.

TalentDetector

9th January 2026
Gliwice, Poland

DEPARTMENT OF ENGINEERING MATERIALS AND BIOMATERIALS
FACULTY OF MECHANICAL ENGINEERING
SILESIAN UNIVERSITY OF TECHNOLOGY

INTERNATIONAL STUDENTS SCIENTIFIC CONFERENCE

Analiza rozkładu naprężeń i odkształceń szlabanu parkingowego

Michał Szojda[a] , Bianka Wyrobek[a] , Agata Śliwa[b], Marek Sroka[b]

[a] Akademickie Liceum Ogólnokształcące Politechniki Śląskiej w Gliwicach
email: matiszojda@icloud.com, wyrobek.bianka@gmail.com
[b] Silesian University of Technology, Faculty of Mechanical Engineering, Department of Engineering Materials and Biomaterials, email: agata.sliwa@polsl.pl, marek.sroka@polsl.pl

Streszczenie: Celem niniejszej pracy było wykonanie symulacji komputerowej rozkładu naprężeń i odkształcenia szlabanu parkingowego wykonanego ze stopu aluminium PA38. Analiza została wykonana w programie SolidWorks, wykorzystującym metodę elementów skończonych.
Abstract: The aim of this work was to perform a computer simulation of the stress distribution and deformation of a parking barrier made of PA38 aluminum alloy. The analysis was performed using simulation module of SolidWorks, by applying finite element method.

Słowa kluczowe: SolidWorks, naprężenia mechaniczne, szlaban, PA38

1. WPROWADZENIE

Zakupem szlabanów interesują się przede wszystkim osoby, które chcą mieć kontrolę nad dostępem kierowców do określonego terenu. W tej chwili dotyczy to zarówno właścicieli parkingów prywatnych jak i wspólnot mieszkaniowych, szkół, firm czy innych instytucji posiadający własny parking.

Ciągle zwiększająca liczba kierowców, a co za tym idzie zwiększająca się liczba samochodów powoduje duże problemy ze znalezieniem wolnego miejsca parkingowego. Kierowcy zmuszeni są niejednokrotnie do łamania zakazów parkowania, zajmują miejsca parkingowe, które należą do innych użytkowników lub parkują na terenie do tego nieprzystosowanym. Szlaban to takie urządzeniem, dzięki któremu można zautomatyzować kontrolę dostępu na parkingi, obiekty i inne tereny, które powinny być oddzielone od zewnątrz.

Podobną funkcję, co szlaban posiadają automatyczne bariery łańcuchowe i bramy z odpowiednią automatyką. Aczkolwiek zdecydowanie w większości przypadków są one wolniejsze, droższe i umożliwiają mniejszą ilość otwarć dziennie bez przeciążania urządzeń.

Inne rozwiązanie, które można zastosować wymagają obsługi manualnej np. łańcuch, ramię ze wspornikiem lub brama. Są to jednak rozwiązania mało efektywne, przestarzałe i mogą być używane w miejscach, w których ruch występuje w małej intensywności. Większość osób wybiera szlabany ze względu na ich szybkość działania jak i możliwość wykorzystania w warunkach podwyższonego ruchu.

Podstawowymi parametrami decydującymi o doborze szlabanu to:

- ilość cykli dziennie, tzn. ile razy dziennie szlaban będzie otwierany i zamykany. Jeżeli jest to bardzo zmienna ilość to pod uwagę można wziąć okres tygodnia lub miesiąca,
- szerokość drogi, do której dobiera się szlaban,
- czas otwarcia szlabanu. Parametr ten ma największe znaczenie przy dużym natężeniu ruchu, np. na parkingach.

2. WŁASNOŚCI STOPU PA38

Aluminium w czystej postaci jest bardzo miękkim materiałem, dlatego aby polepszyć jego własności mechaniczne wprowadza się odpowiednie składniki stopowe tj., magnez, krzem, miedź, mangan lub cynk [1,2]. Stop użyty do wytworzenia szlabanu parkingowego posiada oznaczenie PA38. Jego skład chemiczny oraz własności fizyczne przedstawiono w tabelach 1 i 2 [3].

Tabela 1. Skład chemiczny stopów aluminium wg PN-EN 573-3[3]

Oznaczenie stopu		**Zawartość składników stopowych, %**						
EN-AW	PN	Si	Fe	Cu	Mn	Mg	Zn	Ti
EN-AW-1070A	A0	0,20	0,25	0,03	0,03	0,03	0,07	0,03
EN-AW-6005A	PA4	0,50÷0,90	0,35	0,50	0,50	0,40÷0,70	0,20	0,10
EN-AW-6060	PA38	0,30÷0,60	0,10÷0,30	0,10	0,10	0,35÷0,60	0,15	0,10
EN-AW-6463	PA38	0,20÷0,60	0,15	0,05	0,05	0,45÷0,90	0,05	-
EN-AW-6063	PA38	0,20÷0,60	0,35	0,10	0,10	0,45÷0,90	0,10	0,10
EN-AW-6082	PA4	0,70÷1,30	0,50	0,10	0,40÷1,0	0,60÷1,20	0,20	0,10

Tabela 2. Własności fizyczne stopu PA38 wg PN-EN 573-3 [3]

Gęstość	g/cm^3	2,7
Temperatura krzepnięcia	°C	610
Temperatura płynięcia	°C	655
Liczba Poissona		0,33
Ciepło właściwe	J/kgK	898
Współczynnik rozszerzalności cieplnej	µm/mK	23,4
Opór właściwy	nWm	34
Przewodność cieplna	W/mK	200
Przewodność elektryczna	%IACS	51
Moduł sprężystości E	MPa	69500
Moduł sprężystości poprzecznej G	MPa	26100

Stop aluminium PA38 cechuje się średnią wytrzymałością na rozciąganie i zmęczenie. Jest podatny do anodowania dekoracyjnego oraz do spawania. Wykorzystuje się go w produkcji prętów i profili aluminiowych. Dzięki wysokiej podatności do tłoczenia pozwala uzyskiwać profile o skomplikowanych kształtach [4].

3. MODEL I SYMULACJA KOMPUTEROWA

W niniejszej pracy analizie z zastosowaniem metody elementów skończonych (MES) poddano szlaban parkingowy przy użyciu programu SolidWorks. Celem analizy było otrzymanie symulacji naprężeń, odkształceń oraz przemieszczeń występujących w elemencie podczas uderzenia samochodu osobowego o masie 1300kg oraz dostawczego o masie 3500kg. MES to matematyczny formalizm, stanowiący podstawę numerycznego algorytmu rozwiązywania układów równań różniczkowych cząstkowych i przybliżony sposób. Głównym zadaniem MES jest taki podział modelu geometrycznego na elementy skończone w wyniku czego powstaje model geometryczny dyskretny łączący się w tzw. węzłach. Podczas obliczeń dyskretyzacji dąży się do maksymalnego przybliżenia postaci dyskretnej i ciągłej przy wykorzystaniu metod aproksymujących. Dyskretyzacji podlegają też inne wielkości fizyczne, np. przemieszczenia, naprężenia czy obciążenia [5].

Modelowanie rozpoczęto od wykonania szkicu ramienia szlabanu parkingowego o długości 3,5m jako najważniejszego elementu złożenia. Zaczęto od naszkicowania powierzchni, nadania jej odpowiednich wymiarów szerokości - 13cm, długości - 3,5m oraz grubości – 8cm. Następnie uwzględniono, że ramie jest profilem, z tego względu wycięto środkową część, zostawiając ściany o grubości 5mm. W miejscu przymocowania ramienia do obudowy, wycięto w materiale otwór o średnicy 10cm, w którym zamocowano element walcowaty ułatwiający przymocowanie ramienia do obudowy. Następnie wykonano rysunek obudowy o wymiarach 0,8x0,3x0,3m oraz podstawy 0,1x0,4x0,4m, na której umieszone będzie ramie szlabanu wraz z otworem na mocowanie ramienia. Na rysunku 1 przedstawiono model geometryczny szlabanu parkingowego a rysunek 2 model numeryczny szlabanu parkingowego dyskretyzowany za pomocą elementów skończonych Kolejnym krokiem był dobór materiałów, dla ramienia jest to stop aluminium EN-AW-6060, natomiast obudowa została zdefiniowana jako żeliwo szare.

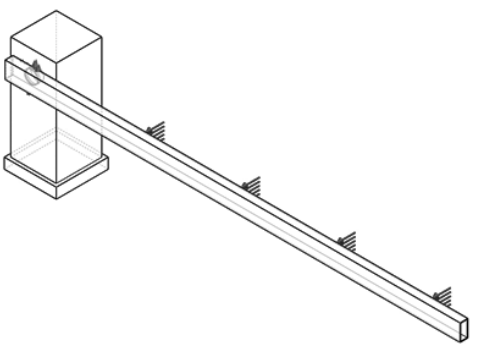

Rysunek 1. Model geometryczny szlabanu parkingowego
Figure 1. Model geometric barrier parking

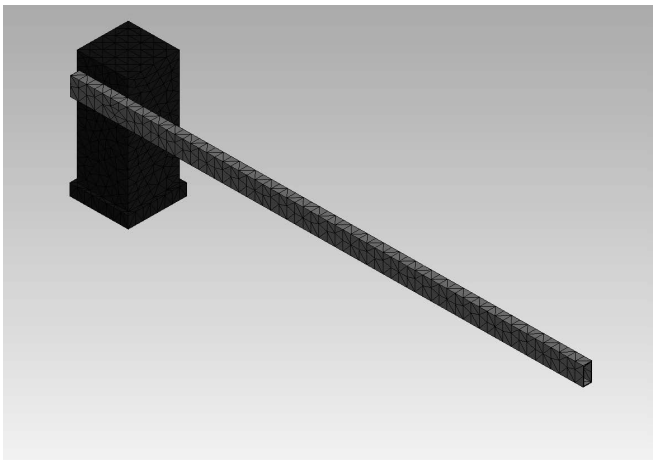

Rysunek 2. Model numeryczny szlabanu parkingowego dyskretyzowany za pomocą elementów skończonych
Figure 2. The numerical model of the barrier Parking discretized using finite elements

4. ANALIZA WYNIKÓW

W pracy przeanalizowano wpływ obciążeń o czterech różnych wartościach, z czego dwa są zdefiniowane dla prędkości 30km/h. W pierwszym przypadku element został obciążony 1,2t, czyli wagą średnią samochodu osobowego, drugi przypadek to również samochód osobowy jadący z prędkością 30km/h gdzie wartość obciążenia wynosi 1,5t, trzeci przypadek rozpatrywany był dla małego samochodu dostawczego o masie 3,5t, a ostatni dla samochodu dostawczego jadącego 30km/h co jest równe obciążeniu 4,1t. Pierwszą przeprowadzoną analizą był rozkład naprężeń von Misesa. Na podstawie analizy można stwierdzić, że największe naprężenia powstają w okolicy umocowania ramienia aluminiowego do obudowy podstawy szlabanu. Na podstawie symulacji można stwierdzić, że dla wybranego stopu aluminium nie dochodzi do uszkodzenia ramienia szlabanu. Została zachowana granica bezpieczeństwa, a wartość granicy plastyczności nie została przekroczona. Wyniki przedstawiono w tabeli 3 oraz na rysunkach 3-6.

Tabela 3. Naprężenia powstałe w materiale

	Obciążenie 1,2t	Obciążenie 1,5t	Obciążenie 3,5t	Obciążenie 4,1t
Naprężenia	9.14291e+008 N/m^2	1.37804e+009 N/m^2	2.38966e+009 N/m^2	2.6578e+009 N/m^2

Druga analiza dotyczyła rozkładu przemieszczeń, we wszystkich przypadkach przemieszczenia rozkładają się w końcowej części ramienia. Wyniki przedstawiono w tabeli 4 oraz na rysunkach 7-10.

Tabela 4. Przemieszczenia powstałe w wyniku działania poszczególnych sił

	Obciążenie 1,2t	Obciążenie 1,5t	Obciążenie 3,5t	Obciążenie 4,1t
Przemieszczenie	809.9 mm	1044.69 mm	1963.9 mm	2191.82 mm

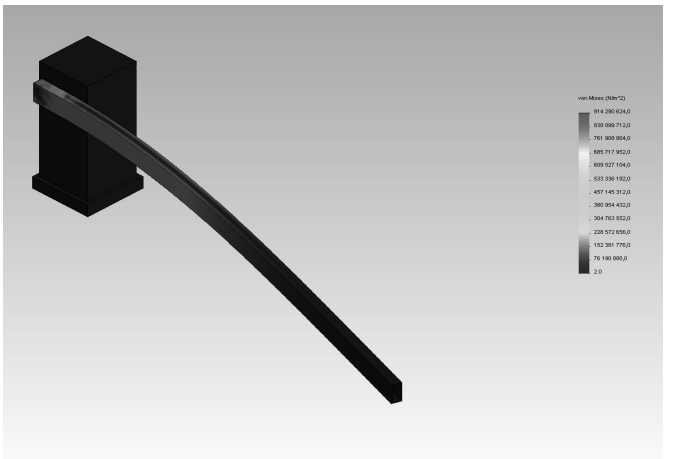

Rysunek 3. Rozkład naprężeń dla szlabanu parkingowego przy obciążeniu 1,2 tony
Figure 3. Stress distribution for barrier parking at a load of 1.2 tons

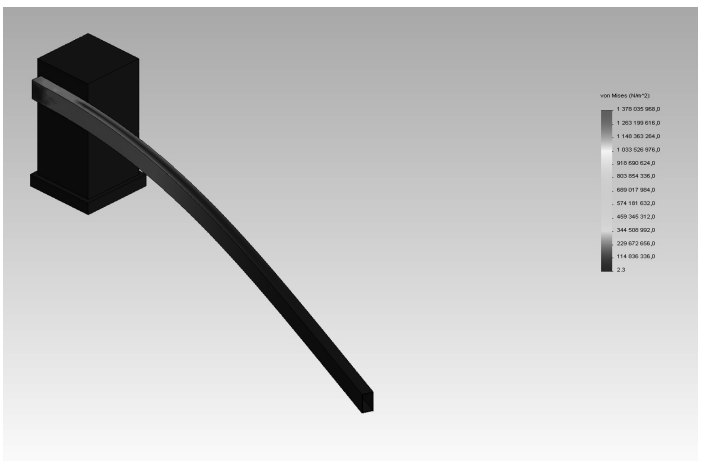

Rysunek 4. Rozkład naprężeń dla szlabanu parkingowego przy obciążeniu 1,5 tony
Figure 4. Stress distribution for barrier parking at a load of 1.5 tons

Rysunek 5. Rozkład naprężeń dla szlabanu parkingowego przy obciążeniu 3,5 tony
Figure 5. Stress distribution for barrier parking at a load of 3,5 tons

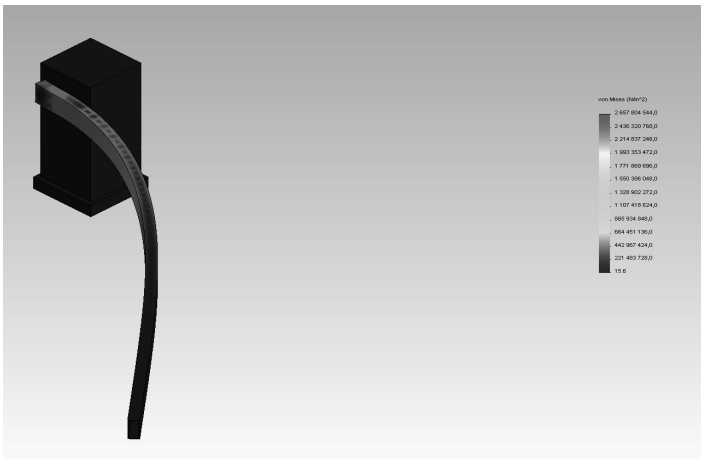

Rysunek 6. Rozkład naprężeń dla szlabanu parkingowego przy obciążeniu 4,1 tony
Figure 6. Stress distribution for barrier parking at a load of 4,1 tons

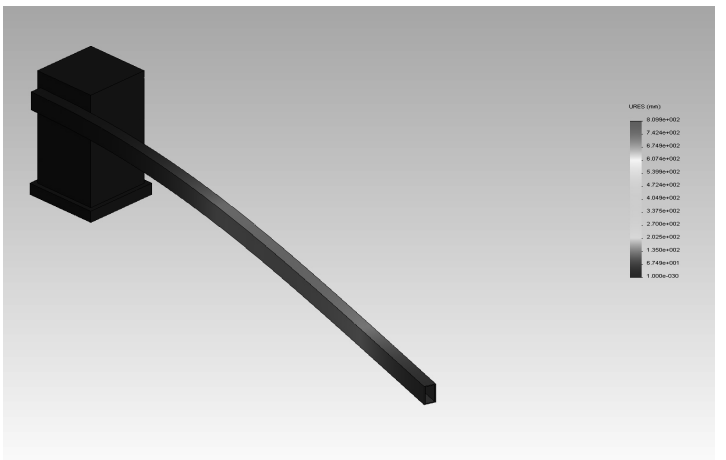

Rysunek 7. Rozkład przemieszczeń dla szlabany parkingowego przy obciążeniu 1,2 tony
Figure 7. Displacement distribution for barrier parking at a load of 1,2 tons

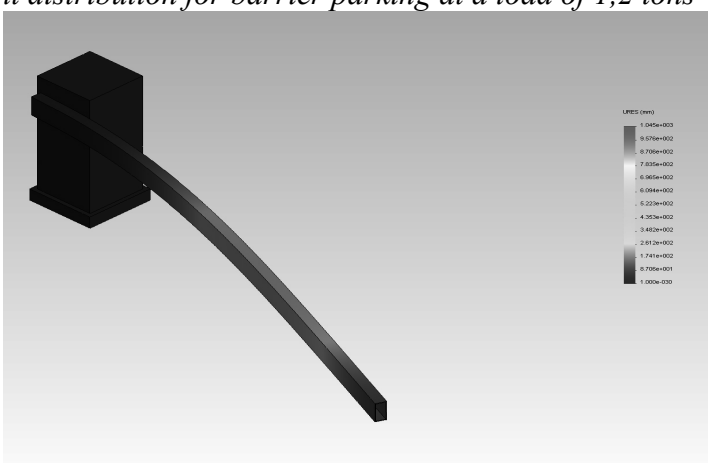

Rysunek 8. Rozkład przemieszczeń dla szlabany parkingowego przy obciążeniu 1,5 tony
Figure 8. Displacement distribution for barrier parking at a load of 1,5 tony

Rysunek 9. Rozkład przemieszczeń dla szlabany parkingowego przy obciążeniu 3,5 tony.
Figure 9. Displacement distribution for barrier parking at a load of 3,5 tons.

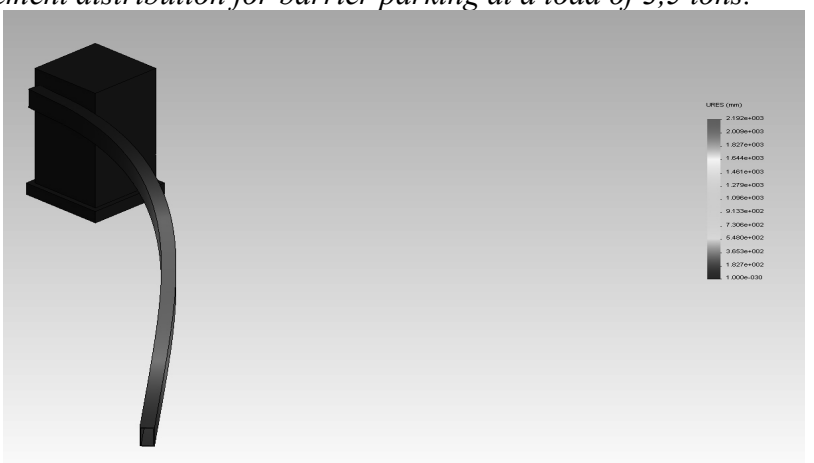

Rysunek 10. Rozkład przemieszczeń dla szlabany parkingowego przy obciążeniu 4,1 tony
Figure 10. Displacement distribution for barrier parking at a load of 4,1 tons

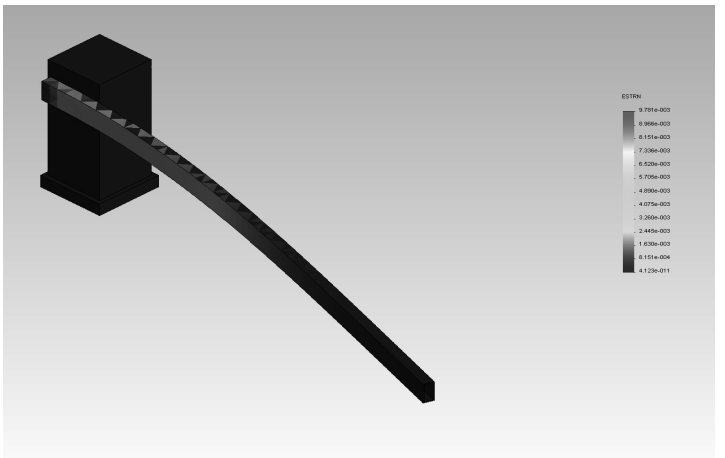

Rysunek 11. Rozkład odkształceń dla szlabanu parkingowego przy obciążeniu 1,2 ton
Figure 11. Deformation distribution for barrier parking at a load of 1,2 tons

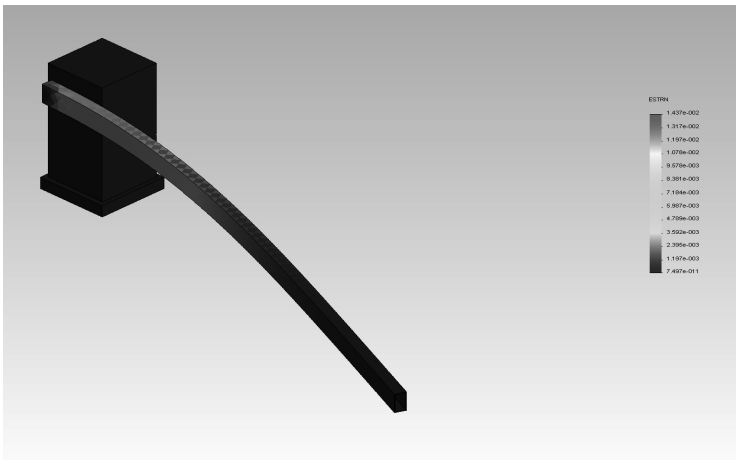

Rysunek 12. Rozkład odkształceń dla szlabanu parkingowego przy obciążeniu 1,5 ton
Figure 12. Deformation distribution for barrier parking at a load of 1,5 tons

Rysunek 13. Rozkład odkształceń dla szlabanu parkingowego przy obciążeniu 3,5 ton
Figure 13. Deformation distribution for barrier parking at a load of 3,5 tons

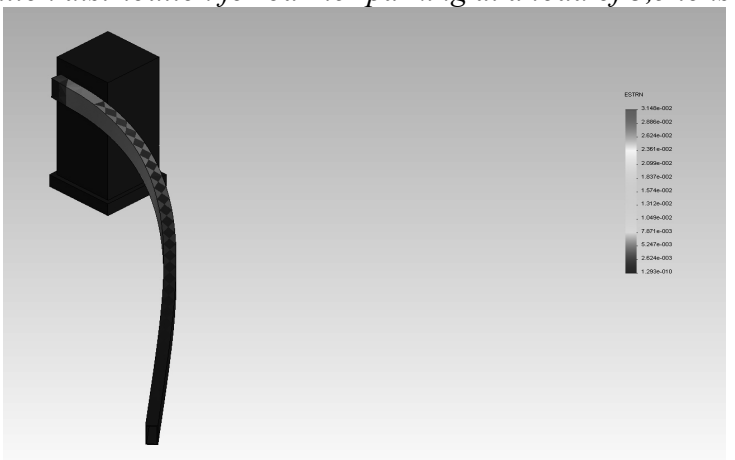

Rysunek 14. Rozkład odkształceń dla szlabanu parkingowego przy obciążeniu 4,1 ton
Figure 14. Deformation distribution for barrier parking at a load of 4,1 tons

Ostatnią przeprowadzoną analizą był rozkład odkształceń We wszystkich przypadkach największe odkształcenie występuje w części łączenia ramienia szlabanu z obudową podstawy. Wyniki przedstawione zostały w tabeli 5 oraz rysunkach 11-14.

Tabela 5. Odkształcenia powstałe w materiale w wyniku działania siły obciążającej

	Obciążenie 1,2t	Obciążenie 1,5t	Obciążenie 3,5t	Obciążenie 4,1t
Odkształcenie	Min. 4.12282e-011 Max. 0.00978067	Min. 7.49692e-011 Max. 0.0143677	Min. 2.47157e-010 Max. 0.0292766	Min. 1.29339e-010 Max. 0.0314848

4. PODSUMOWANIE

W artykule przedstawiono analizę naprężeń mechanicznych, odkształceń oraz przemieszczeń powstałych w szlabanie parkingowym przy uderzeniu samochodu osobowego o masie 1,2t oraz samochodu dostawczego o masie 3,5t przy prędkości 30km/h. Analizowane naprężenia przedstawiono w postaci graficznej, gdzie nadana siła przyłożona na ramię szlabanu określiła stopień odkształcenia sprężystego oraz naprężeń powstałych podczas uderzenia samochodu z daną prędkością. Przemieszczenie występuje na końcowej części ramienia, natomiast na odkształcenia najbardziej narażonym miejscem jest łączenie ramienia z obudową podstawy. Projekt szlabanu parkingowego oraz jego analiza wykonane zostały przy zastosowaniu programu SolidWorks.

PODZIĘKOWANIA

Praca powstała w wyniku projektu PBL zrealizowanego z uczniami szkół ponadpodstawowych w ramach programu Inicjatywa Doskonałości - Uczelnia Badawcza Politechniki Śląskiej.

LITERATURA

1. Kwiatkowski T., Charakterystyka i wykorzystanie stopów aluminium oraz taśm węglowych w budownictwie, Zeszyty Naukowe Politechniki Częstochowskiej – Budownictwo, z.17, nr 167, 2011.
2. Orman M., Orman Z., Technologia aluminium i jego stopów, Wydawnictwo Górniczo-Hutnicze, Katowice 1955.
3. Norma PN-EN 573-3
4. http://metale-kolorowe.eu/aluminium-i-wyroby-hutnicze/
5. Bąk R, Burczyński T. Wytrzymałość materiałów z elementami ujęcia komputerowego, WNT, Warszawa, 2008.

TalentDetector
9th January 2026
Gliwice, Poland
DEPARTMENT OF ENGINEERING MATERIALS AND BIOMATERIALS
FACULTY OF MECHANICAL ENGINEERING
SILESIAN UNIVERSITY OF TECHNOLOGY
INTERNATIONAL STUDENTS SCIENTIFIC CONFERENCE

SMARTGrip - A modular wireless system for interactive motor skills therapy

Daniel Ślusarz, Piotr Kubara, Krzysztof Billik, Julian Czaja, Marcin Śliwiński,
Tomasz Jelonek, Paweł Łój, Małgorzata Muzalewska

Silesian University of Technology, Faculty of Mechanical Engineering, Department of Fundamentals of Machinery Design., email: rmt6@polsl.pl

Abstract: This article describes an interactive prototype system consisting of six wireless smart buttons, a slider board, and a dedicated remote controller. Developed for therapeutic settings and reflex training, the device utilizes the low-latency ESP-NOW protocol to provide real-time sensory feedback. The remote controller acts as a central unit, allowing supervisors to manage gamified activities designed to improve motor coordination, working memory, and physical stamina. All components feature a robust, 3D-printed modular construction, optimized for safety, durability, and ergonomic accessibility for users with limited motor skills.

Keywords: interactive therapeutic tool, psycho-motor rehabilitation, modular design, reflex training, 3D printing, motor skills.

1. INTRODUCTION

The SMARTGrip device focuses on the design and development of an innovative set of light-based interactive devices aimed at supporting the development and further training of reflexes and motor skills. The device responds to physical contact and user interaction, including button presses and slider movements. The device is intended for use in reflex training, occupational therapy, and psycho-motor rehabilitation. It can be used both in preventive training for healthy individuals and in therapeutic settings for users with neurological or developmental disorders. The device also focuses on integrated light-based and auditory feedback mechanisms, enabling the observation and assessment of user reactions and capabilities over time. This model adopts a larger form factor to improve accessibility for users with limited motor skills and a modular set-up that allows the device to be placed in many different combinations at the discretion of the user or supervisor.

2. LITERATURE REVIEW

2.1. Research

Research has demonstrated the effectiveness of play-based therapeutic tools, including toys, in improving motor coordination, reflex responses, and social integration among children with

developmental disorders [1], hospitalized children [2], as well as older individuals dealing with conditions such as Alzheimer's disease [3]. Studies also indicate that reinforcing auditory and visual stimuli, such as sound and light effects, significantly enhances the attractiveness and engagement level of therapeutic toys despite of lack of standardization of its use [4].

2.2. Standards

The design of therapeutic devices necessitates strict adherence to safety standards concerning user protection, structural integrity, and hygiene. To ensure safety in clinical environments, these devices must be free from mechanical hazards including sharp edges or small parts. They must also exhibit resistance to humidity while maintaining securely enclosed power sources. The most important standards are:

• EN 71 – relates to toy safety and provides a general framework of information required for designers and manufacturers. It focuses on mechanical hazards, material properties and the age of the intended user [5];

• EN 62115 – applies to electric toys and in comparison to EN 71 addresses more detailed aspects, particularly protection against electric shock, the use of batteries, and accumulators, resistance to heat and humidity, and requirements for light-emitting optical instruments [6];

• ISO 8124 – is the international counterpart of above standards, covering similar hazards and requirements. It is applicable globally and is especially useful if the product is intended for markets outside the European Union [7].

2.3. Market review

In the current market, the field of therapeutic and sensory toys is rapidly expanding due to increased awareness and reduced stigmatization of mental health and various developmental needs. The market offers many ideas and designs that combine traditional physical play tools with interactive technologies. Examples are shown in Figure 2.1 and Figure 2.2:

Figure 2.1. Wooden Interhemispherical toys manufactured by Tadekmark offered by Empik.com

Figure 2.2. Pop It electronic game manufactured by DymexShop offered by Empik.com

3. PROTOTYPE OVERVIEW

The device consists of two parts. The first one is a set of six separate buttons (example of a button housing shown on figure 3.2), and the second is a board with a slider shown on figure

3.1. It is controlled by a separate remote controller shown on figure 3.4. Each button is enclosed in a dedicated housing and, provided that it remains within communication range, can be placed independently elsewhere in the room, separated from others thanks to wireless technology. Field tests confirmed stable communication at distances of at least 60 m, suggesting the potential for an even greater operational range. Each unit integrates a seven-element RGB LED ring that provides visual cues and sensory stimuli to the user.

The interactive board features a guided path, similar to a gear shift pattern, along which the slider is moved. Integrated LEDs serve as directional indicators, while the slider itself features interchangeable handles to better suit user preferences. The combination of buttons and a slider offers diverse activities for improving motor control. Integrated magnets on the sides allow for a flexible and modular arrangement. This enables the components to be interconnected in various configurations or kept separate depending on the exercise.

The remote controller features a button matrix to select various game modes. Utilizing wireless technology allows the controller to remain independent from the other units, ensuring that access is restricted to supervisors. To enable wireless operation, all components are equipped with internal batteries. Charging is facilitated through connectors located on the bottom of the enclosures. The process is initiated by placing the components into designated docking stations integrated into the case. This approach eliminates the common inconveniences associated with battery-powered devices.

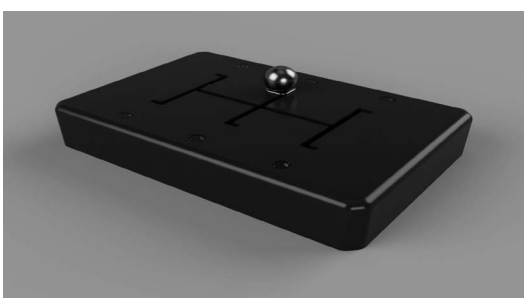

Figure 3.1. Model of a Board with a slider

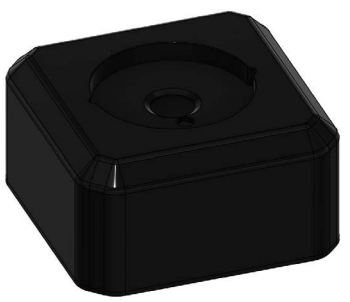

Figure 3.2. Button housing model

3.1 User Accommodations

The device was designed as a training tool for children with disabilities, with particular emphasis on accommodating users with limited motor skills. Compared to similar solutions available on the market, the overall dimensions were increased to improve accessibility and ease of interaction. The buttons were sized to facilitate activation using the entire hand, which, in combination with the modular layout, reduces the risk of unintentional activation of multiple buttons simultaneously. Similarly, the slider was dimensioned to enable a comfortable full-hand grip, eliminating the need for precise finger manipulation.

The housing prevents children from reaching internal electronics while safeguarding critical components against fluid ingress, such as saliva. This design also facilitates efficient cleaning. Given the target audience, the unit is engineered to withstand impacts and accidental drops through a robust, rounded geometry that ensures both user safety and structural durability.

Figure 3.3. Assembled set of 6 smart buttons

Figure 3.4. Remote controller

3.3 Use of 3D printing

All enclosures were manufactured using 3D printing technology and later assembled with bought mechanical and electrical parts. This approach allowed for the easy production of complex shapes to better fit all the different components and offers great adaptability. Making sure that the device does not have any sharp edges and remains lightweight to make it safer for children is also easier with this method. 3D printing makes prototyping and testing various concepts easier and faster, with the low cost of model fabrication being a significant advantage. A limitation of this approach is that, due to the restricted build volume, the board case had to be separated into four distinct parts. [8]

The chosen filament for 3D printing is PETG. It has high tenacity and flexibility that ensures the casings' durability. Another big advantage is its great layer adhesion, which makes the casings water and humidity resistant. PETG also offers high temperature resistance and low thermal expansion, which makes it easy to work with. Along with its water resistance, this allows the device to be used outdoors. Additionally, it is a relatively cheap option. [9]

4. HARDWARE CONFIGURATION

4.1 Smart button system

- Mechanical and Enclosure Construction

Due to functional, safety, and mechanical constraints, each of the six smart buttons was designed to ensure protection of both the end user and the internal electronic components. One of the key requirements was to ensure ergonomic suitability for child users. This requirement was addressed by designing the mechanical actuation surface with adequate dimensions and structural stability to support comfortable and reliable interaction by users with small hands. The enclosure geometry was optimized to enhance durability through smooth contours and reinforced features, providing resistance to repetitive mechanical stress and ensuring suitability for frequent use in interactive and educational environments.

- Electronic Components and Interconnections

Each smart button integrates a large push button with a diameter of 100 mm and a Beetle ESP32-C3 microcontroller, which serves as the primary processing and communication unit. A custom structural insert was developed to secure the LED and optimize light diffusion within the push button. To enhance multimodal user interaction, an acoustic buzzer was incorporated into each smart button. Wiring complexity was minimized to improve system reliability and ease of assembly. All electrical connections between peripheral components and the ESP32-C3 were established using ARK-type screw terminal connectors. This solution ensures stable

electrical contact, mechanical robustness, and simplified maintenance or component replacement.

- Software-Based Signal Integrity

To accurately detect user input and mitigate the effects of mechanical switch bouncing, the internal pull-up resistor of the microcontroller was enabled through software configuration. This approach ensures reliable interpretation of both real-time and planned input signals, thereby improving system responsiveness and operational stability.

4.2 Smart interactive board

The smart interactive board consists of RGB LEDs, an ESP32 WROOM-32D microcontroller, and edge switch sensors. The board provides functionality comparable to that of the smart buttons, enabling interactive input detection and visual feedback. The mechanical design prioritizes accessibility, robustness, and protection of internal components. The electronic architecture employs two parallel power distribution lines. The first power line supplies energy to six edge switch sensors, while the second power line is dedicated to powering six RGB LEDs. Each signal line from the sensors and LEDs is connected individually to a designated input or output pin on the ESP32 microcontroller. This configuration improves signal integrity, simplifies fault isolation, and enables precise control over individual components.

4.3 Remote controller system

The remote controller incorporates a button matrix to facilitate user input and utilizes the ESP-NOW wireless communication protocol for data exchange with the six smart buttons and the smart interactive board. ESP-NOW was selected due to its low latency, low power consumption, and reliable peer-to-peer communication capabilities.

5 SOFTWARE ARCHITECTURE AND GAME LOGIC

While the hardware provides the physical interface, the system's core functionality relies on firmware developed in the Arduino environment for the ESP32-C3 microcontroller. The software is designed to manage near real-time wireless communication, handle game state machines and optimize power consumption utilizing logic-driven sleep cycles.

5.1 Networking and communication protocol

The system utilizes the ESP-NOW [10] protocol in a custom star topology configuration. Unlike standard Wi-Fi, this connectionless protocol allows for immediate transmission of data packets, which is critical for optimizing latency. To make the system easily scalable and reduce maintenance, the software eliminates hardcoded device addresses. Upon startup of the Slave, each Slave node derives a unique ID (in range of 1-100). The ID is made up from the last byte of the MAC address: (ID = fifth byte of MAC % 99 +1) The Controller (Master) does not require
a pre-configured list of devices. It waits for 'ONLINEid' broadcast packets from buttons that are active and dynamically builds a "buttonsOnline" registry. A bidirectional heartbeat mechanism is used to make sure that buttons and the controller remain in sync with each other. The Master broadcasts a global 'Heartbeat' every 5s containing a list of unresponsive Slaves. If a Slave device detects that its own ID is on the "Offline" list, it automatically re-initiates the handshake process, ensuring the network self-heals without user intervention.

5.2 Game modes and algorithms

The Controller acts as a central state machine broadcasting commands that trigger specific behaviour in the Slave nodes. (for example: LED_ON(ID, r , g, b) turns on the Led on a button with a specific colour). The slave nodes operate as an intelligent peripheral that report the user input via BTNid packets. The software implements three distinct therapeutic modes:

I. Reflex Training (Random Button) This mode is designed to improve motor coordination and speed. After pressing '1' on the remote, the system randomly selects one button to light up. As soon as the user presses it, that button turns off and another one immediately activates. This creates a continuous cycle that forces the user to react quickly and move their focus between different points. The game continues until stopped with the '#' key. To ensure smooth gameplay, the system automatically skips any button that does not respond, immediately picking a new target.

II. Memory Training (Simon Says) Inspired by the popular "Memory" game, this mode stimulates working memory and concentration. It is activated by pressing '2' for an infinite session or '3' for a short, three-level game. The device displays a light sequence (pattern) that the user must memorize and repeat in the exact same order. With each successful round, the sequence gets longer and more challenging. If the user makes a mistake by pressing a button out of order, all devices flash red to signal the end of the game, and the session resets.

III. All-Press Game The All-Press mode (activated by key '5') is designed to encourage full physical engagement and movement. Unlike the other modes, all registered buttons light up simultaneously with random colors. The user’s goal is to find and press every single button in the set. The round only ends once the system confirms that every active unit has been pressed, making it an excellent exercise for spatial awareness and general physical activity.

5.3 Software-defined power management

To support the 40-hour battery life goal, the software implements a “Sleep-Listen” cycle:

- Deep Sleep Logic: Upon receiving a “SLEEP_NOW” command (triggered by the key ‘7’ on the Controller) or after a specific inactivity timeout, the Slaves execute the “esp_deep_sleep_start()” function. This disables the Wi-Fi radio and CPU, lowering current consumption from 81mA to 2.6 mA.
- Remote Wake-Up: The ESP32-C3 is configured to wake up via a timer interrupt. Upon waking up, the device enters a “Listening Window” of 8s. If no “Wake” packet is received from the controller during these windows, the device immediately returns to Deep Sleep. This logic allows for the entire system to be remotely activated by the therapist without physical interaction with each button.
- Back-up Wake-Up: If a button doesn’t wake up it’s possible to wake up the button by just simply pressing it.

5.4 Master controller keymap

The controller acts as the “brain” of the system, while the buttons are just acting on the “brains” will. The controller holds the entire state of the game and ensures reliability. It keeps track of online and offline buttons. The buttons do not know the rules of the game they just act on commands sent by their master. A star topology is ideal here because all instructions must originate from a single source of truth.

Table 1. Master device button functions

Key	Function	Description
1	Start Random Game	Initiates the reflex training mode (single active button).
2	Simon Says (Infinite)	Starts the memory game in infinite mode.
3	Simon Says (Short)	Starts the memory game limited to 3 levels.
5	Start All-Press	Activates all buttons simultaneously.
7	Global Sleep	Broadcasts SLEEP_NOW, forcing deep sleep on all nodes. (Off button).
8	Wake Broadcast	Activates the beacon, sending WAKE packets every 3s (Turn on button).
#	Stop Game	Immediately terminates the current session.
0	Reset Stats	Clears the hit counters and timers.

6. TESTING AND VALIDATION

A series of tests was conducted to evaluate the system's performance and reliability:

- Durability test: the device was dropped to the ground to see if the casing can successfully survive the fall
- Wireless connection test: evaluation of the maximum communication range and the influence of physical obstacles on connection stability.
- Battery performance analysis: evaluation of battery endurance across different operational modes, including active use and idle states
- Gameplay test: assessment of all available game modes with respect to suitability for the intended user group.

7. THERAPEUTIC BENEFITS AND ADVANTAGES

The device was developed for therapeutic purposes, primarily for children with disabilities, although it is also suitable for adults with various developmental needs. The main advantages of the device are as follows:

- Hand-Eye Coordination: Children with disabilities often have problems with movement precision and accuracy [11]. The device facilitates motor learning by integrating visual stimuli with physical interaction, helping users to internalize movements and improve coordination through repetitive training.
- Reflex Development: By interacting with the system, users can significantly reduce their reaction times. The "Random Button" mode was specifically designed to evaluate and enhance reflex skills by requiring rapid responses to unpredictable visual cues.

- Adaptation to Unpredictable Situations: The element of randomness across multiple game modes encourages users to adapt to new stimuli. This fosters the ability to react appropriately to unknown situations, which is a critical skill in cognitive development.
- Short-Term Memory Improvement: Individuals with memory deficits often struggle with concentration and following instructions. The "Simon Says" mode addresses these challenges by requiring sequential thinking and sustained focus, which are essential for improving working memory capacity.
- Physical Conditioning: The use of portable buttons encourages gross motor movement. Regular exercise with the device helps build stamina and physical endurance, which has a positive effect on the user's overall health, immunity, and mental state.
- Motivation and Self-Improvement: The gamified nature of the system introduces an element of engagement that motivates users to improve their performance. This allows supervisors to identify highly motivated individuals and provide additional support to those who are less confident.

BIBLIOGRAPHY

1. K. Tseng, S. Tseng and H. Cheng, "Design, development, and clinical validation of therapeutic toys for autistic children," *J Phys Ther Sci,* vol. 28, no. 7, pp. 1972-1980, 2016.
2. L. L. Ciuffo, T. V. Souza, T. M. Freitas, J. R. M. M. Moraes, K. C. O. D. Santos and R. O. J. F. L. D. Santos, "The use of toys by nursing as a therapeutic resource in the care of hospitalized children," *Rev Bras Enferm,* vol. 76, no. 2, p. e20220433, 2023.
3. D. You, S. Hasley Bin Ramli and R. Ibrahim, "A thematic review on therapeutic toys and games for the elderly with Alzheimer's disease," *Disabil Rehabil Assist Technol,* vol. 20, no. 1, pp. 1-13, 2025.
4. M. Lotan and C. Gold, "Meta-analysis of the effectiveness of individual intervention in the controlled multisensory environment (Snoezelen) for individuals with intellectual disability," *J Intellect Dev Disabil,* vol. 34, no. 3, pp. 207-215, 2009.
5. European Committee for Standardization, "EN 71: Safety of toys," CEN, Brussels, Belgium, 2014-2021.
6. European Committee for Standardization, "EN 62115: Electric toys - Safety," CEN, Brussels, Belgium, 2020.
7. International Organization for Standardization, "ISO 8124: Safety of toys," ISO, Geneva, Switzerland, 2023.
8. Y. Xu, "Types and applications of 3D printing," December 2024.
9. Prusa Research, "PETG - Prusa Knowledge Base," [Online]. Available: https://help.prusa3d.com/article/petg_2059. [Accessed 21 December 2025].
10. Espressif Systems, "ESP-NOW API Reference," [Online]. Available: https://docs.espressif.com/projects/esp-idf/en/stable/esp32/api-reference/network/esp_now.html. [Accessed 21 December 2025].
11. D. Goodley and K. Runswick-Cole, "Critical psychologies of disability: boundaries, borders and bodies in the lives of disabled children," *Emotional and Behavioural Difficulties,* December 2014.

TalentDetector
9th January 2026
Gliwice, Poland
DEPARTMENT OF ENGINEERING MATERIALS AND BIOMATERIALS
FACULTY OF MECHANICAL ENGINEERING
SILESIAN UNIVERSITY OF TECHNOLOGY
INTERNATIONAL STUDENTS SCIENTIFIC CONFERENCE

Computational Cooling Bath Design for Energy Cable Extrusion Lines

[a]Bercan Tarhan, [a]Mehmet Oguz Turkoz, [a]Muhammet Beler, [a]Cemal Meran, [b]Erkin Palamutcu, [b]Umutcan Salkam

[a] Pamukkale University, Faculty of Engineering, Department of Mechanical Engineering, Denizli-Turkiye, email: cmeran@pau.edu.tr
[b] Uygar Cable Machinery System, Denizli-Turkiye, email: info@um.com.tr

Abstract: The cable exits the extruder at a high temperature and is then introduced into a cooling bath, where it is cooled in a controlled manner. In this critical process, cooling bath lengths are often determined based on experience, which can lead to unnecessary increases in energy and water consumption, quality control problems, and cost losses. Within the scope of this study, the design of the cooling bath -of critical importance in cable production lines- has been examined, and the parameters affecting the determination of bath length have been identified. Within the study, production lines manufactured by Uygar Makine San. ve Tic. Ltd. Şti., a company that produces extrusion lines for cable manufacturing facilities, were examined.

Keywords: Cable Extruder, Cooling Bath, Cable Cooling Process, PVC, XLPE, HFFR

1. INTRODUCTION

Although extrusion is often regarded as the most critical stage in cable manufacturing, the preparatory processes carried out prior to extrusion and the cooling stage applied after extrusion have an impact on product quality that is at least as significant as the extrusion process itself. Post-extrusion cooling plays a crucial role in ensuring that the cable gains sufficient mechanical strength, internal and external stresses are balanced, electrical conductivity performance is preserved, and the final product complies with relevant standards. The temperature of the copper conductor exiting the extrusion line and the thermal properties of the surrounding molten polymer directly influence the determination of production parameters. For this reason, industrial practices frequently employ methods such as preheating, control of target temperature ranges throughout the process, and stepwise cooling in order to reduce the risk of product deformation.

The basic manufacturing process consists of the conductor entering the extruder, the molten polymer being applied onto the conductor, and the hot cable being conveyed forward by the pulling system. Following these stages, the cable is transferred to the cooling bath in a controlled manner. The sizing of the cooling bath depends on the type of polymer material used, the cable diameter, the production line speed, and the physical conditions of the facility; however, in industrial practice, it is most often determined based on experience and

experimental values. Consequently, selecting a cooling bath length that is shorter or longer than required may lead to deformation of the cable insulation, production of non-standard products, inefficient use of the manufacturing space, and increased energy consumption, Figure 1.

Figure 1: The view of extrusion cooling bath

According to Çengel [1], the flow regime developing along a flat plate exhibits laminar, turbulent, or mixed characteristics depending on the Reynolds number. Boundary layer behavior and flow regime are among the primary factors determining the magnitude of heat transfer. Therefore, the use of dimensionless parameters such as the Reynolds and Prandtl numbers, which are directly related to fluid behavior, is considered appropriate for the quantitative evaluation of heat transfer. The heat transfer coefficient is commonly determined using the Nusselt number, which is defined as a fundamental dimensionless parameter representing the ratio between convection and conduction heat transfer. Çengel [1] also emphasizes that the thermophysical properties of fluids and solid materials—such as density, specific heat capacity, and thermal conductivity—play an important role in heat transfer analyses. It is stated that these properties may vary with temperature, and that selecting experimentally measured values or appropriate literature data for the specific problem is critical to the accuracy of the results. Li et al. [2] the temperature distribution within the insulation layer of a current-carrying PVC-insulated cable was modeled using time-dependent heat conduction equations for cylindrical geometry and numerically validated using ANSYS. The results showed that insulation temperature is strongly dependent on current magnitude, time, and insulation thickness, and that the maximum temperature occurs at the conductor–insulation interface. These findings indicate that temperature control in cable insulation should not be limited to the final temperature, but that the thermal regime throughout the process is a determining factor. Incropera et al. [3] use the flat plate geometry as a reference problem for forced convection analyses and explain that, as the flow progresses along the surface, the hydrodynamic boundary layer develops first, followed by the thermal boundary layer. It is noted that the flow regime is characterized by the Reynolds number, with orderly (laminar) flow observed at low Reynolds numbers, while turbulent flow conditions emerge once critical values are exceeded. In their study, Incropera et al. [3] emphasize that the Nusselt number is a key parameter for the quantitative evaluation of heat transfer, as it represents the influence of the convection mechanism. They demonstrate that the heat transfer coefficient can be calculated using correlations that relate the Nusselt number to the Reynolds and Prandtl numbers. Rosato et al. [4] provide a reliable reference for modeling the cooling process of PVC, XLPE, and HFFR insulation materials used in cable production lines. In particular, the accurate selection of parameters such as density and specific heat capacity is of critical importance for realistic calculation of cooling bath length and cooling time. In another study,

Mitroshin V.N. and Mitroshin Y.V. [5-6] developed a method for the optimal design of water cooling baths used for cooling cable insulation in extrusion lines. The insulation cooling process was treated as a distributed-parameter system, and the spatial distribution of water temperature along the cooling bath was determined using an optimal control approach. The proposed method reduces the cooling bath length while ensuring the desired radial temperature distribution within the insulation, achieves energy savings of approximately 5–10%, and decreases production area requirements. The modular design of the cooling baths also allows rapid adaptation to different cable types.

2. MATERIAL AND METHOD

For the calculations, the flow throughout the entire cooling bath was assumed to be laminar, with heat transfer occurring outward from the insulation, a continuous temperature distribution along the length of the bath, a single-stage cooling configuration, and a single-core cable conductor structure. Within the scope of this study, cable diameters of Ø30 mm, Ø50 mm, and Ø70 mm were considered, with corresponding insulation thicknesses of 1.5 mm, 2.5 mm, and 3 mm, respectively. PVC, HFFR, and XLPE were selected as insulation materials, and separate calculations were performed for each cable diameter and each material. In addition, similar calculations were carried out to determine the production line speed as a function of the cooling bath length. To improve the accuracy of the calculations, forced external convection over a flat plate was assumed, and the corresponding academic constants were adopted accordingly. Based on the flow characteristics, the system was defined using several constant parameters, Table 1.

Table 1. The constant values used calculations

Constants	**Value**
kwater	0.598 W/mK
Pr	7
υ	$1.004 * 10^{-6} m^2/s$
C	0.664

The cooling bath length is influenced by several parameters, including insulation diameter, inlet–outlet temperatures, bath water temperature, and extrusion line speed, Table 2.

Table 2. Diameter and Material dependent Parameters

	Diameter(mm)	**T_{in} (°C)**	**T_{out} (°C)**	**T_∞ (°C)**	**V (m/s)**
PVC	30	185	35	20	1,167
	50				0,833
	70				0,5
XLPE	30	210			1,167
	50				0,833
	70				0,5
HFFR	30	180			1,167
	50				0,833
	70				0,5

Total heat load delivered cooling bath, Eq. 1:

$$\dot{Q}_{given} = \dot{m}c_p dT \tag{1}$$

Heat transferred from the cable to the water by convection, Eq. 2-5:

$$\dot{Q}_{taken} = hA_s(T - T_\infty)dx \tag{2}$$

$$\frac{dT}{T - T_\infty} = -\frac{hA_s}{\dot{m}c_p}dx \tag{3}$$

$$\frac{T_{out} - T_\infty}{T_{in} - T_\infty} = \exp\left(-\frac{hA_sL}{\dot{m}c_p}\right) \tag{4}$$

$$e^{-\left(\frac{Ck\pi DL^{1.5}}{\dot{m}c_p}\right)} = \frac{T_{out} - T_\infty}{T_{in} - T_\infty} \tag{5}$$

The average density and specific heat capacity values of PVC, XLPE, and HFFR insulation materials together with the copper conductor were calculated to improve the accuracy of the analysis, Table 3.

Table 3. Thermophysical Properties of Materials

	D(mm)	ρ(kg/m^3)	cp(J/kg.K)	$c_{p,avarage}$(J/kg.K)	$\rho_{avarage}$(kg/m^3)
PVC	30	1500	900	404,5	7526,4
	50			404,5	7526,4
	70			398,4	7915,1
HFFR	30	1400	1500	424,5	7507,4
	50			424,5	7507,4
	70			418,2	7702,8
XLPE	30	920	2300	430,1	7416,2
	50			430,1	7416,2
	70			422,9	7624,1

3. RESULTS

The calculated cooling bath lengths obtained for different cable diameters, insulation materials, and production line speeds are presented in Table 4.

Table 4. Calculated Cooling Bath Lengths for Different Materials and Diameters

	Diameter(mm)	Velocity(m/s)	Length(m)
PVC	30	1.167	18.26
	50	0.833	22.93
	70	0.5	24.5
XLPE	30	1.167	19.56
	50	0.833	24.58
	70	0.5	26.13
HFFR	30	1.167	18.66
	50	0.833	23.44
	70	0.5	25.11

The calculated cooling bath lengths for PVC, XLPE, and HFFR insulated single-core cables with diameters of Ø30 mm, Ø50 mm, and Ø70 mm are summarized in Table 4. A representative calculation result for a Ø70 mm PVC-insulated cable is illustrated in Table 5.

Table 5. Calculated Cooling Bath Lengths for Different Materials and Diameters

	Production Parameters	
Inlet Temperature (T_{inlet})	180	°C
Cooling Water Temperature (T_{water})	20	°C
Outlet Temperature (T_{outlet})	35	°C
Line Speed (V)	0,5	m/s
Cooling Bath Length (L)	24,9317779	m
	Insulation Material Parameters	
Density (ρ_{ins})	1400	kg/m^3
Specific Heat Capacity ($c_{p\ ins}$)	1500	J/Kg.K
Cable Outer Diamater (D_{ins})	0,07	m
	Condutor(Copper) Parameters	
Density (ρ_{cu})	8940	kg/m^3
Specific Heat Capacity (cp_{cu})	385	J/Kg.K
Copper Conductor Diameter (D_{cu})	0,064	m

4. CONCLUSIONS

In this study, the relationship between production line speed and cooling bath length was theoretically investigated for single-core cables with diameters of Ø30 mm, Ø50 mm, and Ø70 mm using PVC, XLPE, and HFFR insulation materials. The results obtained from the calculations and literature review demonstrate that, in a single-stage cooling bath, the required bath length is directly related to the line pulling speed. In addition, the density and specific heat capacity of the insulation materials were found to have a significant influence on the required cooling bath length.

For cables with identical insulation materials, an increase in cable diameter led to a corresponding increase in the required cooling bath length. The reduction in line speed associated with larger diameters increases the residence time in the cooling bath and enhances total heat transfer. However, the increase in bath length remains reasonable when compared to the increase in production capacity. For instance, production increased from approximately 6.33 kg/h for a Ø30 mm XLPE-insulated cable to about 15.10 kg/h for a Ø70 mm cable.

When only the insulation material was varied under constant conditions, XLPE-insulated cables required the longest cooling bath lengths to reach an outlet temperature of 35 °C, with values of 19.56 m and 26.13 m for Ø30 mm and Ø70 mm cables, respectively. These results indicate that defining a single fixed cooling bath length is not appropriate; instead, the design should consider cable diameter, line speed, and insulation material simultaneously. The findings also show that experience-based sizing approaches commonly used in industry may be insufficient, particularly for XLPE-insulated cables.

In conclusion, a reliable correlation between cooling bath length and production line speed can be established through theoretical calculations. The proposed approach provides a rational engineering basis for cooling bath design, contributing to improved energy efficiency and

consistent product quality. For future studies, experimental validation of the theoretical model and consideration of additional parameters such as water flow velocity, flow direction, and turbulence level are recommended. Moreover, CFD-based analyses are suggested to achieve a more detailed understanding of the cooling process.

BIBLIOGRAPHY

1. Y. A. Çengel, Heat Transfer: A Practical Approach, 2nd ed. New York, NY, USA: McGraw-Hill, 2002.
2. X.-J. Li, J. Yang, B.-Q. Yan, and X. Zheng, "Insulated cable temperature calculation and numerical simulation," MATEC Web of Conferences, vol. 175, Art. no. 03014, 2018, doi: 10.1051/matecconf/201817503014.
3. T. L. Bergman, A. S. Lavine, F. P. Incropera, and D. P. DeWitt, Fundamentals of Heat and Mass Transfer, 8th ed. Hoboken, NJ, USA: John Wiley & Sons, 2017.
4. D. V. Rosato, Extruding Plastics: A Practical Processing Handbook. Boston, MA, USA: Springer, 1998, doi: 10.1007/978-1-4615-5793-
5. V. N. Mitroshin and Y. V. Mitroshin, "Optimal control of cable insulation cooling at extrusion line," in Proc. 2nd Int. Conf. Industrial Engineering, Applications and Manufacturing (ICIEAM), Chelyabinsk, Russia, 2016, pp. 1–4, doi: 10.1109/ICIEAM.2016.7911592.
6. V. N. Mitroshin and Y. V. Mitroshin, "Optimal design of cooling baths of extrusion lines for the imposition of cable insulation," Bulletin of Samara State Technical University, Technical Sciences Series, no. 4(32), pp. 240–243, 2011.

TalentDetector
9th January 2026
Gliwice, Poland
DEPARTMENT OF ENGINEERING MATERIALS AND BIOMATERIALS
FACULTY OF MECHANICAL ENGINEERING
SILESIAN UNIVERSITY OF TECHNOLOGY
INTERNATIONAL STUDENTS SCIENTIFIC CONFERENCE

Additive Manufacturing of Thermoplastic Elastomer Components for Archery Applications

Wojciech Tokarz[a], Błażej Tomiczek[b]

[a] Student of Materials Engineering and Technologies, Silesian University of Technology
[b] Silesian University of Technology, Faculty of Mechanical Engineering, Scientific and Didactic Laboratory of Nanotechnology and Material Technologies, Konarskiego 18A, Gliwice, Poland
email: wt303939@student.polsl.pl

Abstract: This study analyses the properties of thermoplastic polyurethane (TPU) and its application in manufacturing damping elements via Fused Deposition Modelling (FDM). Bending strength tests, hardness measurements, and an analysis of vibration-damping efficiency using an archery vibration sensor were conducted.

Keywords: 3D printing, vibration damping, elastomers, TPU, archery

1. INTRODUCTION

Additive manufacturing, also known as 3D printing, is a rapidly advancing technology that has revolutionised production processes across many industries. Thanks to the capabilities of rapid prototyping and manufacturing complex geometries, additive methods are gaining increasing importance in the automotive, medical, aerospace, and sports industries. One of the most popular additive manufacturing techniques is Fused Deposition Modelling (FDM), which involves the selective deposition of successive layers of plasticised thermoplastic material. The development of this technology has enabled the use of an increasingly wide range of materials, including thermoplastic elastomers, which combine the properties of rubber with the ease of processing typical of thermoplastics [1, 2].

The aim of this article is to investigate the properties of thermoplastic polyurethane (TPU), produce damping elements using the FDM process with commercially available solutions, and compare their performance. To determine the optimal printing parameters for the final product, bending strength tests were conducted on printed samples with different infill types, infill densities, and filament materials. The printed damper was tested during shooting, and its vibration-damping performance was evaluated using the Steady Aim A1 sensor. Hardness measurements were also carried out to assess the influence of damper hardness on its damping capabilities [3, 4].

1.1. Application in Archery

To release an arrow, an archer draws the bowstring, accumulating potential elastic energy in the bow limbs. Releasing the bowstring causes the conversion of this energy into kinetic energy of the arrow. Energy that was not transferred to the arrow is distributed throughout the bow in the form of vibrations, both audible and tactile, which damage the equipment and also distract the archer. Therefore, vibration dampers with weights are used to minimize them [5, 6].

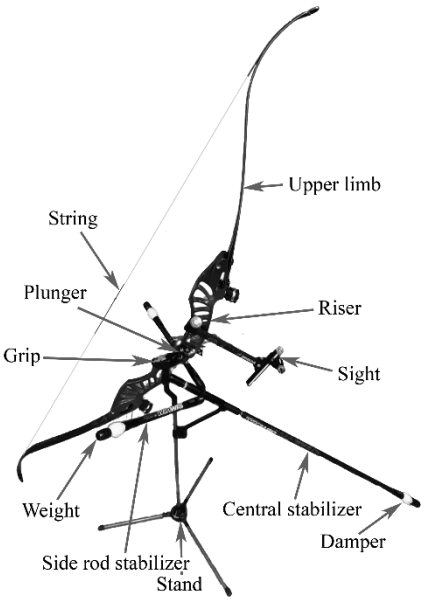

Figure 1. Description of the main components of a professional Olympic bow.

1.2. TPU as a filament

TPU is an elastomer that has found application in 3D printing due to its exceptional mechanical properties. Depending on the brand and type of filament, print properties will vary, but all are flexible, durable, and abrasion-resistant. Despite the difficulties that may occur during printing, it is a filament worth using in many engineering solutions. Among typical applications are seals and shock absorbers, and because it is chemically resistant to oils and fats, it also finds applications in the industrial and automotive spheres [7, 8]. Manufacturers of flexible filaments use an immensely customer-friendly practice: they include the TPU hardness in their names. Thus, knowing the Shore A and D values is enough to assess filament flexibility.

2. PRINTING PARAMETERS

To produce test samples, two types of commercial filaments were selected: ROSA3D TPU Flex 96A and Ultrafuse TPU 64D. To determine the appropriate print settings for the 3D printer, samples measuring 10 x 20 x 15 mm were printed as part of preliminary tests (Fig. 2), varying the temperature and printing speed (Table 1). Paremeters were acquired from the respective websites of manufacturers [9, 10].

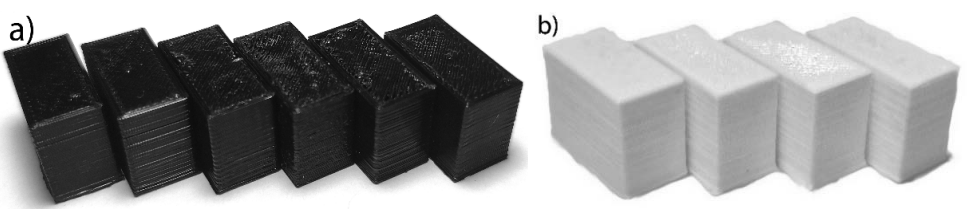

Figure 2. Printed samples from the filaments: a) Flex 96A, b) TPU 64D

Table 1. Print parameter configurations for preliminary samples

Material	Flex 96A						TPU 64D			
Sample number	1	2	3	4	5	6	7	8	9	10
Nozzle temperature, °C	220	235	250	220	235	250	235	250	235	250
Print speed, mm/s	30	30	30	60	60	60	30	30	60	60

Based on the inspection of the printed elements, including their surface roughness and geometry, the optimal printing parameters were determined and are summarized in Table 2.

Table 2. Printing parameters used for the main tests

Material	Flex 96A	TPU 64D
Nozzle diameter, mm	0.4	
Layer height, mm	0.2	
Line width, mm	0.4	
Number of shell layers/walls	2	
Nozzle temperature, °C	235	
Bed temperature, °C	60	
Print speed, mm/s	30	
Cooling	off	

3. DAMPER MANUFACTURING

Based on the commercially available FlexBall damper, a solid model was designed in Autodesk Fusion. Vertical print orientation was selected. Printing in this orientation allows threaded inserts to be placed during printing. In contrast, in the horizontal orientation, the thread would also be printed, thereby reducing the damper's lifespan due to low thread strength.

M6 claw nuts were used as threaded inserts. This is a readily available product, most similar in shape to the insert used in the FlexBall damper, as shown in Figure 3.

a) b)

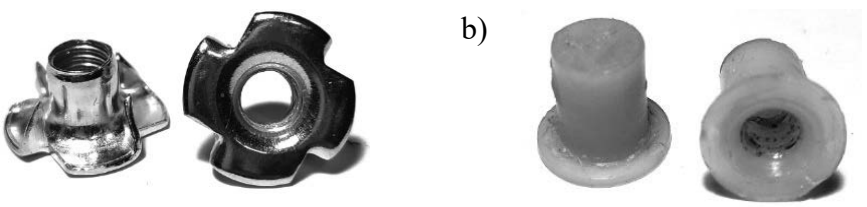

Figure 3. View of a) claw nuts and b) FlexBall threaded inserts

It was decided to print the damper halves separately, allowing the inserts to be placed in an orientation that minimises their weakening of the damper halves' strength. After printing was completed, the halves were welded together using an external heating element, which provided the highest strength among other solutions [11].

a) b)

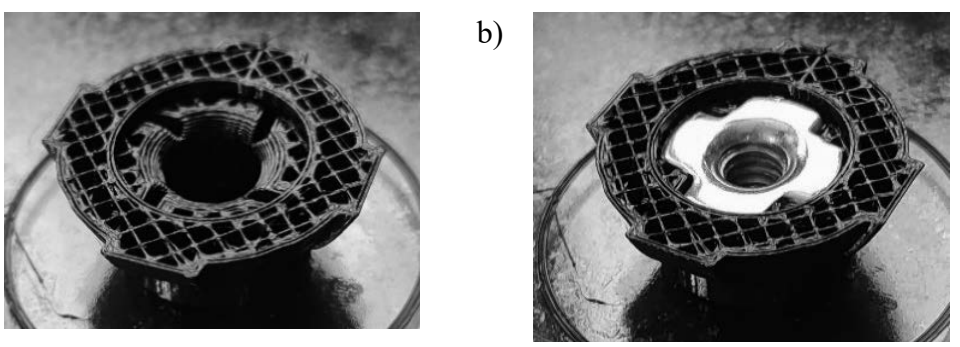

Figure 4. View of the printed damper a) before and b) after mounting the threaded insert

4. CHARACTERIZATION OF PRINTED MATERIALS

4.1. Static bending test

Two types of infill were analysed: grid and cubic, and three infill densities: 40, 60, and 80 per cent. Three rectangular prisms with dimensions of 13 x 20 x 125 mm with six different infills were tested [12, 13]. The bending test was conducted at room temperature on a Zwick Roell Z020 universal testing machine. Samples were bent at 20 mm/min on supports spaced 100 mm apart. The test ended when the deflection reached 36 mm. Each sample was first bent in the same orientation as it was printed, then rotated upside down to check whether bending to such a high degree (approximately 280%) would weaken the sample structure. Three infill structures were selected for printing dampers.

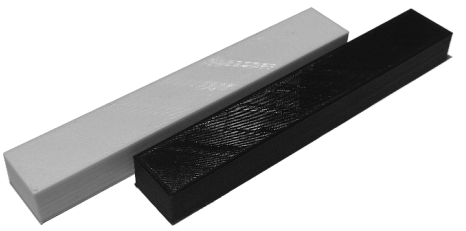

Figure 5. Rectangular prism samples of TPU filaments: 64D (white) and 96A (black)

4.2. Shore hardness

Hardness measurements were performed on finished dampers because this is the only standard geometry of all the tested dampers, both printed and commercially available. Two hardness meters were used for measurement, one on the Shore A scale and the other on the Shore D scale. Ten measurements of each damper material were performed, and the average results and manufacturer-provided values were compiled in Table 3.

4.3. Bow vibrations

Bow vibrations were measured objectively using the Steady Aim A1 device and subjectively through the archer's perception [14]. Steady Aim is an advanced yet very easy-to-use tool that allows the archer to analyse the shot just before and just after it is released. The option used in the study was the "Bow response" tab, which revealed to the user, among other things, the amplitude and frequencies of vibrations along three axes in the range from 0 to 206 Hz. Unfortunately, there is currently no way to import data into a spreadsheet program for in-depth analysis. To collect data, 51 shots were fired: 12 each with four sets of dampers and only three without dampers due to high archer discomfort and concern about equipment damage. After releasing the shot, the application records the bow's vibrations for the following second using angular deviation sensors, which are translated into linear acceleration values along three axes. Based on the data, two graphs are generated: acceleration as a function of time and frequency and four quantities: maximum acceleration value [G], frequency with the highest acceleration value [Hz], vibration decay time [s], sum of all accelerations [G]. Based on the results of static bending tests, three internal damper structures were selected. It was decided to choose the structure with the lowest, highest, and average bending modulus. The selected infills are gathered in Table 3.

Table 3. Parameters of printed damper sets

Parameter	Set 1	Set 2	Set 3
Bending modulus [MPa]	28.9	67.3	106.6
Material	Flex 96A	TPU 64D	TPU 64D
Infill type and density	Grid 40%	Grid 60%	Cubic 80%

5. RESULTS

5.1. Static bending test

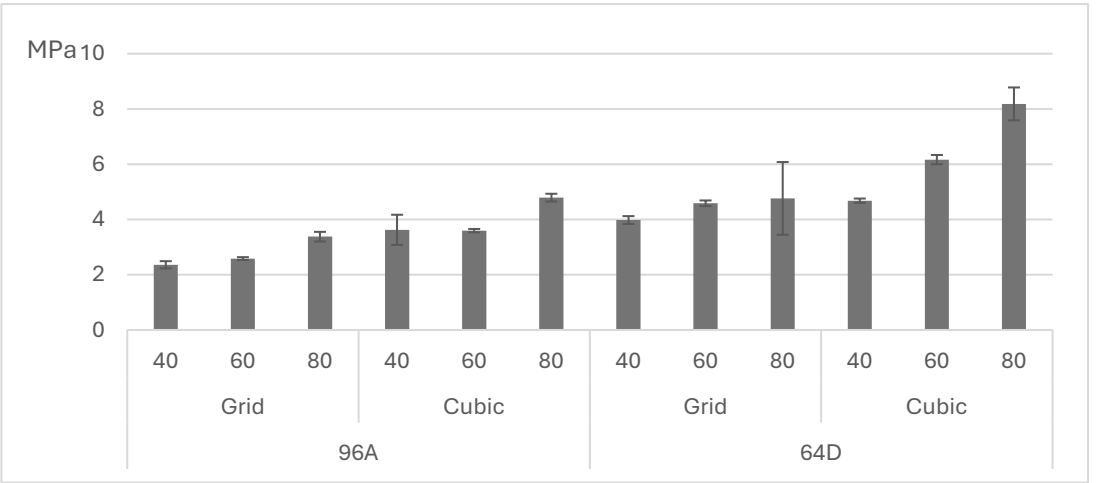

Figure 6. Bending strength s_{fM}

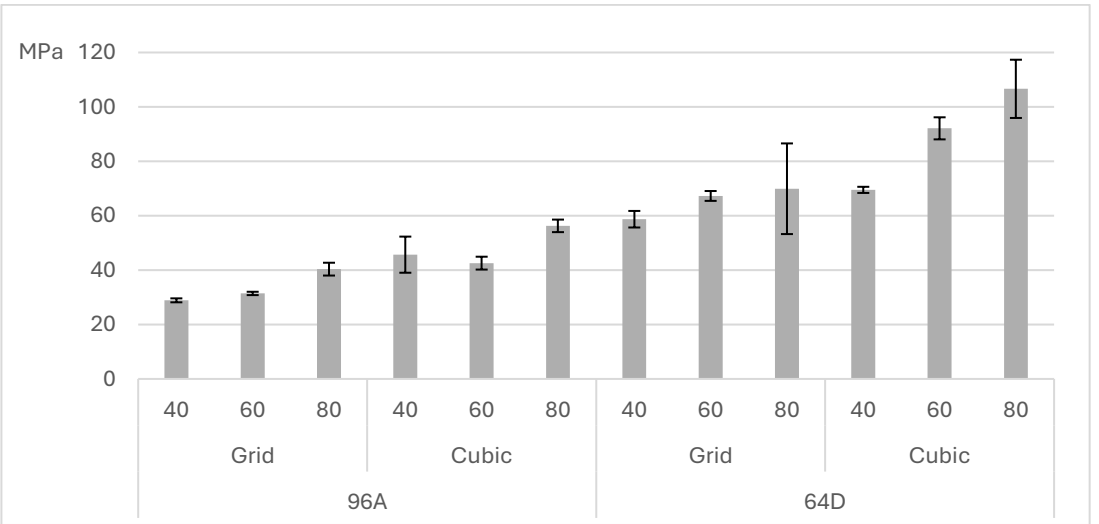

Figure 7. Bending modulus E_f

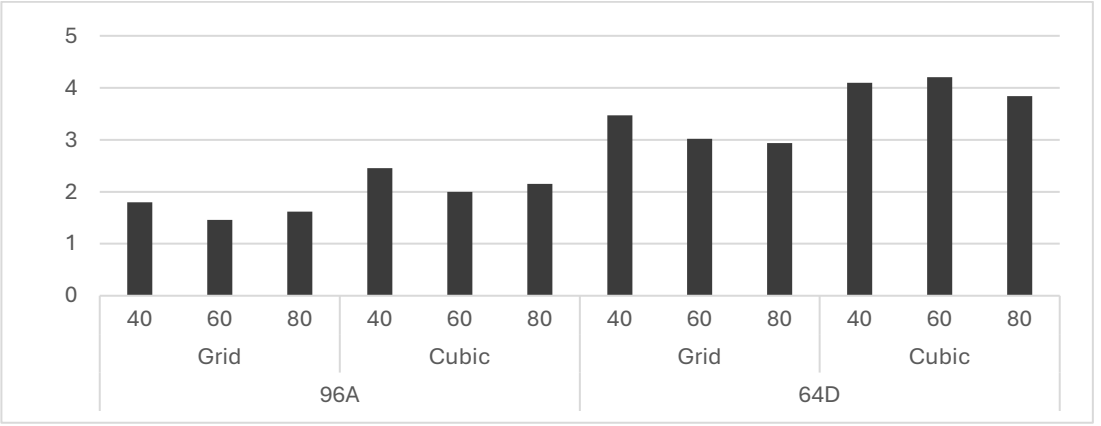

Figure 8. Bending modulus–to–mass ratio

Figures 6 and 7 show that cubic infill results in higher bending strength and bending modulus compared to grid infill. A similar relationship is observed for the materials used: TPU 64D exhibits a higher bending modulus than Flex 96A. The same trend applies to increasing infill density—values closer to 100% lead to higher bending strength and bending modulus. Figure 8 presents the ratio of bending modulus to sample mass. Once again, the results indicate the superiority of cubic infill over grid infill, as well as TPU 64D filament over 96A.

5.2. Hardness measurement

Table 4. Damper hardness

Hardness	FlexBall	UltraFuse TPU	ROSA3D Flex
in material's name	n/a	64D	96A
in material datasheet	n/a	56D ~ 100A*	n/a
measured	63A	50D ~ 97A*	90A

**These are only indicative values. Reliable conversion between Shore A and Shore D scales is not possible.*

5.3. Vibration measurement

Among the acceleration–time plots shown in Figure 10b is the most distinctive, as it represents a shot with FlexBall dampers installed and clearly demonstrates their vibration-damping effectiveness. Using Figure 10b as a reference Figure 10a shows significantly increased vibrations after damper removal, particularly along the Y-axis, where high amplitudes persist throughout the entire one-second recording. Comparing Figure 10c reveals a clear reduction in post-shot vibrations; however, vibrations along the Z-axis remain largely unchanged. Figure 10d provides noticeably better damping of Z-axis vibrations, reaching a stable, low level within 0.4 s. Similarly, Figure 10e rapidly attenuates Z-axis vibrations but shows reduced effectiveness along the Y-axis. The frequency-domain results indicate that all printed damper sets exhibit nearly identical behavior. In the frequency range of 137–205 Hz, their performance is comparable to that of the FlexBall dampers, while Figs 10d and 10e outperform the reference dampers in the 103–137 Hz range. A notable limitation of the printed dampers occurs at low frequencies where their vibration acceleration levels are similar to those observed without dampers.

Table 5. Average values of data read from the Steady Aim application

Parameter	No dampers	FlexBall	Set No. 1	Set No. 2	Set No. 3
Maximum acceleration value [G]	18.17	18.15	17.18	17.54	17.65
Vibration decay time [s]	0.99	0.62	0.98	0.97	0.96
Sum of accelerations over 1s period [G]	2594.5	1810	2085.9	2086.5	2108.6

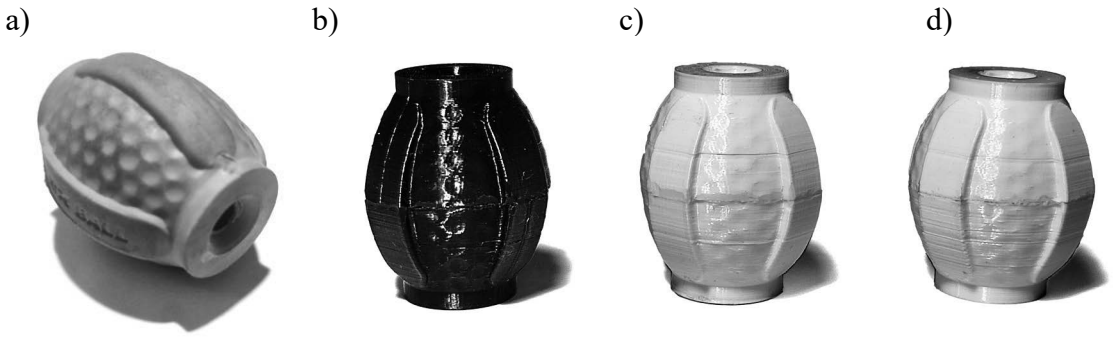

Figure 9. View of FlexBall damper, damper from set 1, damper from set 2, damper from set 3

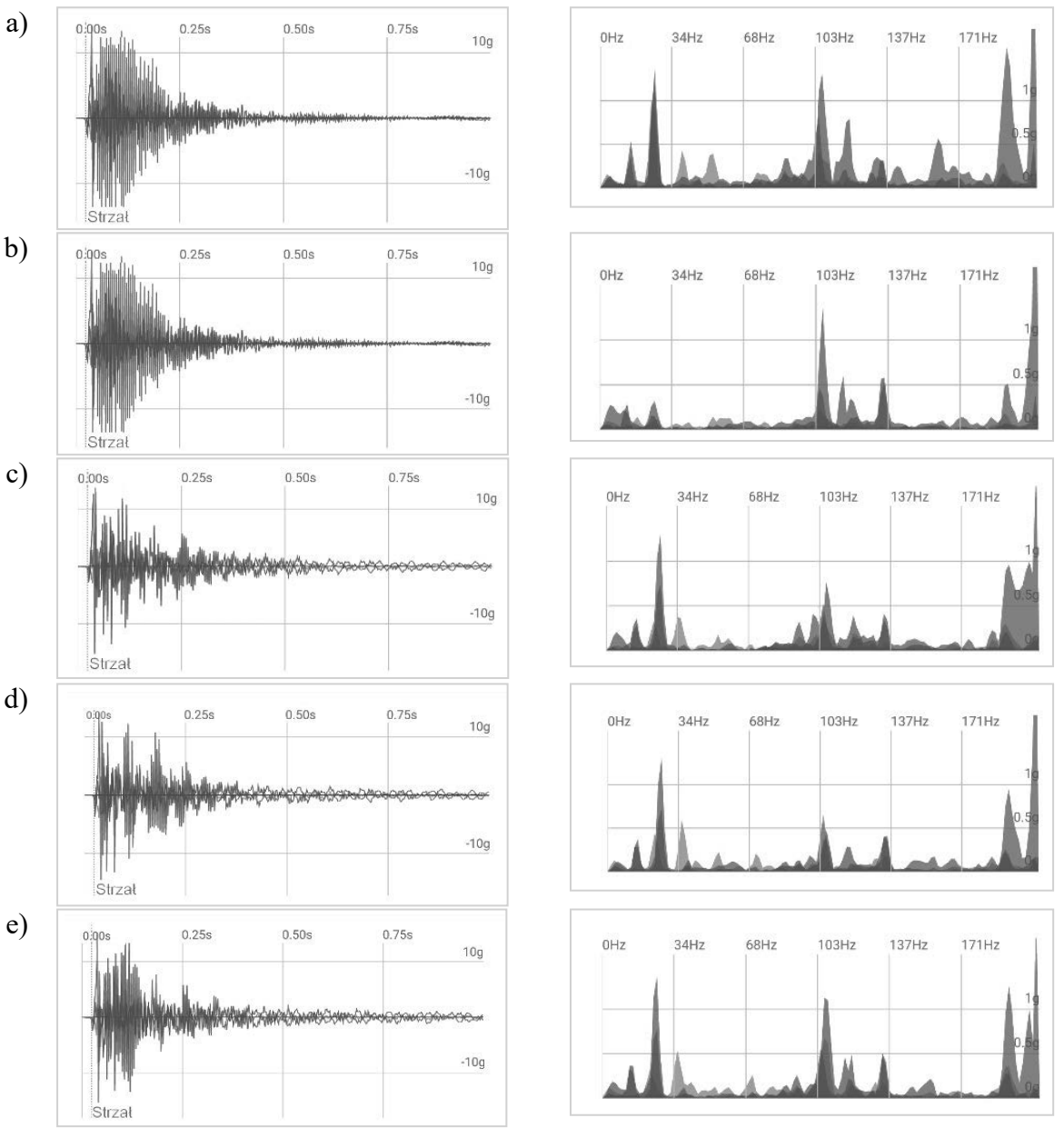

Figure 10. Generated acceleration profiles as a function of time (left) and frequency (right) for one of the shots fired with: a - no dampers, b - FlexBall dampers c - set 1, d - set 2, and e - set 3

6. CONCLUSIONS

The 3D printing process requires precise adjustment of printing parameters and proper filament selection to achieve optimal mechanical properties. Even slight parameter changes can significantly affect the bending modulus, highlighting the potential of 3D printing to tailor the structure and properties of final products. Print quality, particularly on low-budget printers, depends not only on material and parameter selection but also on user experience. Repeatable results require accurate calibration and an understanding of how individual parameters influence mechanical properties. Studies show that the bending modulus is proportional to hardness and infill density, with a higher modulus-to-mass ratio for cubic infill compared to grid structures. The durability of TPU filament was demonstrated, with strength reductions of only 2% after 280% deformation in some cases. Analysis of damper sets confirmed that appropriate infill structure and material selection enable high damping efficiency. The set with the lowest bending modulus performed best, indicating that 3D printing may serve as an alternative to traditional damper, although further research is needed to surpass the performance of existing solutions.

BIBLIOGRAPHY

1. Y. Mohseni, Investigating impacts of FDM printing parameters and geometrical features on void formation in 3D printed automotive components, Materials Today: Proceedings, (2023).
2. W. Hui, Y. Hu, Y. Liu, Q. Cai, W. Zhao, Development of thin-walled polymer glass beads reinforced 3D printed solid rocket motors, Materials Letters 347 (2023) 134558.
3. B. Berman, 3-D printing:The new industrial revolution, Business Horizons 55/2 (2012) 155-162.
4. T. D. Ngo, A. Kashani, G. Imbalzano, K. T. Q. Nguyen, Additive manufacturing: A review of materials, methods, applications and challenges, Composites B: Engineering 143 (2018) 172–196.
5. I. Zaniewski, Recoil and vibration in an archery bow equipped with a multi-rod stabilizer, Shock and Vibration 19 (2012) 235–250.
6. L. Rodríguez-Parada, S. de la Rosa, P. F. Mayuet, Influence of 3D-Printed TPU Properties for the Design of Elastic Products, Polymers 13 (2021) 2519.
7. A. Haryńska, J. Kucińska-Lipka, H. Janik, Thermoplastic elastomer filaments and their application In 3D printig. Elastomery, 20/4, (2016) 109.
8. J. Iwko, M. Robakowska, Badanie wybranych własności polimerów termoplastycznych wykorzystywanych w druku 3D FDM, Tworzywa Sztuczne w Przemyśle 4 (2023) 34-39 (in polish).
9. ROSA3D, Charakterystyka filamentu Flex 96A. Accessed: Oct. 14, 2024. [Online]. https://rosa3d.pl/portfolio-items/rosa-flex-96a (in polish).
10. BASF Ultrafuse, Charakterystyka filamentu TPU 64D. Accessed: Oct. 19, 2024. [Online] https://move.forward-am.com/hubfs/TPU64D/TDS/Ultrafuse_TPU_64D.pdf (in polish).
11. A. Klimpel, Spawanie i zgrzewanie tworzyw termoplastycznych. Gliwice, Wydawnictwo Politechniki Śląskiej, 2000 (in polish).
12. V. Beloshenko, Y. Beygelzimer, V. Chishko, B. Savchenko, N. Sova, D. Verbylo, A. Voznyak, Mechanical Properties of Flexible TPU-Based 3D Printed Lattice Structures: Role of Lattice Cut Direction and Architecture, Polymers 13 (2021) 2986.
13. V. Beloshenko, Y. Beygelzimer, V. Chishko, B. Savchenko, N. Sova, D. Verbylo, I. Vozniak, Mechanical Properties of Thermoplastic Polyurethane-Based Three-Dimensional-Printed Lattice Structures, 3D Print Additive Manufacturing 10/2 (2023) 245-255.
14. F. Pietra, P.W. Loveday, R. Reid, Objective and subjective measurements of the influence of dampers on the shooting experience of barebow archers, Proceedings of the Institution of Mechanical Engineers, Part P: Journal of Sports Engineering and Technology (2024).

TalentDetector

9th January 2026
Gliwice, Poland

DEPARTMENT OF ENGINEERING MATERIALS AND BIOMATERIALS
FACULTY OF MECHANICAL ENGINEERING
SILESIAN UNIVERSITY OF TECHNOLOGY

INTERNATIONAL STUDENTS SCIENTIFIC CONFERENCE

Analysis of the influence of laser cutting parameters on the technological properties of the process

Martyna Urbańska[a], Kinga Stępska[b], Marek Flak[c], Felicjan Glenc[d], Piotr Herian[e], Mirosław Bonek[f], Eva Tillova[g]

[a] Student of Production and Management Engineering, e-mail: mu309689@student.polsl.pl
[b] Student of Production and Management Engineering, e-mail: ks309686@student.polsl.pl
[c] Student of Mechatronics, e-mail: mf310852@student.polsl.pl
[d] Student of Mechanical Engineering, e-mail: fg316671@student.polsl.pl
[e] Student of Electrical Engineering, e-mail: ph305443@student.polsl.pl
[f] Silesian University of Technology, Faculty of Mechanical Engineering, Department of Engineering Materials and Biomaterials, email: miroslaw.bonek@polsl.pl
[g] [a] University of Žilina, Faculty of Mechanical Engineering, Department of Materials Engineering

Abstract: This article presents an analysis of the influence of the fundamental laser cutting process parameters on its technological characteristics and the quality of the produced components. The significance of cutting speed, laser power, assist gas type and pressure, as well as the focal position of the laser beam is discussed. Particular attention is paid to the consequences of improper parameter selection, such as deterioration of edge quality, enlargement of the heat-affected zone, and increased production costs. The study also highlights the economic aspects of process parameter optimization in modern manufacturing systems.

Keywords: laser cutting, technological parameters, cutting speed, laser power, assist gas, edge quality, process optimization

1. INTRODUCTION

Laser cutting is one of the most advanced and widely used material processing methods in modern industry. This technology involves separating material by means of a highly focused laser radiation beam with a high energy density. In the area of interaction between the laser beam and the material, intense heating occurs, leading to melting or vaporization of the material, which enables the production of a precise and narrow cut with high edge quality. [1,3]

Laser cutting is widely applied across many industrial sectors, including the metalworking, automotive, aerospace, and electronics industries. This method allows for the processing of a wide range of materials, such as structural and stainless steels, aluminum, light metal alloys, plastics, as well as wood and composite materials. [2,4]

The most important advantages of laser cutting include high dimensional accuracy, high process repeatability, a small heat-affected zone, and the possibility of full automation of production.

The dynamic development of laser technologies has significantly increased the efficiency and accessibility of this processing method. Compared with traditional mechanical or thermal cutting methods, laser cutting enables a reduction in material losses, shorter process execution times, and improved quality of finished components. For this reason, laser cutting constitutes a key element of modern manufacturing systems and is increasingly widely applied in the industry of the twenty-first century. [1,5]

2. LASER PIERCING PARAMETERS

Laser cutting parameters constitute a set of adjustable and measurable physical quantities entered into the control system, which comprehensively define the conditions of laser beam generation and its interaction with the material. They include key technological settings such as laser power and cutting speed, which determine the energy balance of the process; focal position, affecting power density and kerf geometry; as well as assist gas parameters (type and pressure), which control the thermochemical characteristics of the process and the mechanical removal of molten material (dross).

In addition to the main laser cutting process parameters - such as laser power, cutting speed, focal position, and assist gas pressure - additional parameters can also be distinguished, depending primarily on the type of laser employed. For example, in the case of pulsed lasers, an additional parameter is the pulse frequency, which defines the number of pulses emitted per second. Precise configuration of parameter sets is essential to achieve optimal edge quality, dimensional accuracy, and process efficiency when machining a given material type and thickness. [6,7,8]

3. CUTTING SPEED

Laser cutting speed is one of the key parameters determining both edge quality and the overall duration of the process. In laser cutting technology, the primary criterion for selecting technological conditions is ensuring the highest possible quality of the resulting surfaces. Modern equipment enables precise control of process parameters, including cutting quality and speed, thereby defining optimal ranges for their selection. One of the most important technological parameters is the traverse speed of the laser beam along the cutting path, expressed in mm/s. One of the fundamental advantages of laser cutting is the ability to achieve very high cutting speeds while maintaining high edge quality. The limitations mainly arise from the available laser power and the parameters of the mechatronic system or robotic unit guiding the cutting head.

Cutting speed depends primarily on the power density of the laser beam, the thickness and type of the processed material, as well as the type and pressure of the assist gas. Increasing the cutting speed allows the process execution time to be reduced; however, excessively high speeds may lead to the formation of metal adherences and dross at the lower part of the cut kerf and, in extreme cases, to incomplete material separation. Conversely, excessively low cutting speeds result in excessive heating of the material, an increased risk of deformation, and a

significant deterioration of edge quality. In practice, achievable cutting speeds depend on the applied laser technology, machine design, and the thickness of the cut material. Currently, laser cutting processes are increasingly carried out exclusively in automated or robotic systems, enabling three-dimensional (3D) cutting operations. [9,10]

Below, exemplary cutting speeds for CO_2 gas lasers and Nd:YAG lasers for various materials of different thicknesses are presented in Tables 1 and 2.

Table 1. CO_2 laser cutting parameters including cutting speed for various materials [9]

Material Type	Thickness (mm)	Cutting speed (m/min)	Assist gas type
Carbon steel	1,5	3,8	Oxygen
	3,2	3	Oxygen
	6,4	2	Oxygen
	9,5	1,3	Oxygen
Corrosion-resistant steels (stainless)	1,5	3,8	Nitrogen
	3,2	1	Nitrogen
	6,4	1	Oxygen
	9,5	0,75	Oxygen
Titanium	1,5	3,8	Argon
Glass-polyester	1,5	15,2	Air

Table 2. Nd:YAG laser cutting parameters including cutting speed for various structural materials [9]

Material Type	Thickness (mm)	Cutting speed (m/min)	Assist gas type
Austenitic steel AISI 316L	3,2	0,3	Oxygen
	6,4	0,076	Oxygen
	9,5	0,025	Oxygen
Titanium	1,5	0,636	Argon
Hastelloy X	1,5	0,635	Air

4. CUTTING POWER

The output power of the laser source, expressed in watts (W), is one of the key parameters determining the technological cutting capabilities of a machine. It defines the amount of energy delivered to the material per unit time and thus directly affects the ability to process materials of varying thicknesses and physical properties. An increase in laser power expands the range of effective cutting, enabling the machining of thicker materials as well as those with higher density or hardness, while maintaining adequate edge quality. [11]

The selection of appropriate laser power must therefore be closely matched to the thickness and type of the processed material. As material thickness increases, the energy required for complete melting also rises, necessitating the use of a correspondingly higher laser source power. In the case of thin materials, however, the application of moderate power levels is recommended, as this allows precise process control without the risk of excessive heating and edge damage. [10]

Below, exemplary power requirements for laser cutting using CO_2 gas lasers and Nd:YAG lasers are presented for various materials of different thicknesses.

Table 3. CO_2 laser cutting parameters including beam power for various materials [9]

Material Type	Thickness (mm)	Beam power (W)	Assist gas type
Carbon steel	1,5	400	Oxygen
	3,2	800	Oxygen
	6,4	1200	Oxygen
	9,5	1500	Oxygen
Corrosion-resistant steels (stainless)	1,5	1500	Nitrogen
	3,2	1500	Nitrogen
	6,4	650	Oxygen
	9,5	800	Oxygen
Titanium	1,5	1500	Argon
Glass-polyester	1,5	1000	Air

Table 4. Nd:YAG laser cutting parameters including beam power for various structural materials [9]

Material Type	Thickness (mm)	Beam power (W)	Pulse frequency (Hz)	Assist gas type
Austenitic steel AISI 316L	3,2	0,3	20	Oxygen
	6,4	0,076	25	Oxygen
	9,5	0,025	30	Oxygen
Titanium	1,5	0,636	10	Argon
Hastelloy X	1,5	0,635	12	Air

5. PRESSURE AND TYPE OF ASSIST GAS

Another parameter that has a significant influence on the laser cutting process is the type and pressure of the assist gas. It directly affects the quality, stability, and efficiency of cutting. [12,6]

The primary function of the technological gas is the removal of cutting by-products from the kerf (molten metal, oxides, vapors) and assistance in maintaining process cleanliness. The laser beam causes immediate melting or vaporization of the material, forming a molten metal pool. A high-velocity gas jet penetrates the kerf and blows the material downward and outward. Due to the surface tension and viscosity of the molten material, gas pressures in the range of 5 to even 25 bar are required. Insufficient pressure may result in improper material removal and the formation of dross. [6,13,14,15]

The assist gas also serves a protective and thermal barrier function. Localized heating generates a plume of vapor and particles that could scatter the laser beam, reducing transmission efficiency. The gas creates a clean channel between the nozzle and the cutting zone by flowing concentrically. Its coaxial flow surrounding the beam prevents the ascent of spatter that could damage the focusing lens. This enables immediate evacuation of fumes while maintaining the transparency of the optical path. In the case of reactive gases, it also limits the optical absorption of combustion products, which is critical for maintaining cutting precision. [6,14,15]

In addition, the assist gas cools the heat-affected zone (HAZ). The heat-affected zone is defined as the region of the metal influenced by the thermal input of the laser cutting process

but not melted. In cutting operations, efforts are made to minimize the HAZ, as this reduces changes in material properties such as hardness and strength. Minimization of this zone is therefore essential to preserve the mechanical properties of the material. [15,16]

Surface quality depends on gas pressure and flow stability (absence of turbulence) within the kerf. Smooth, laminar flow is achieved through appropriate selection of the nozzle outlet diameter and its stand-off distance from the workpiece. Both parameters typically fall within the range of 0.5–3.0 mm. The nozzle diameter is selected according to the sheet thickness: the thinner the material, the smaller the nozzle diameter required. An excessively large nozzle leads to increased gas consumption and deterioration of edge quality. The nozzle stand-off distance should be approximately equal to the nozzle diameter; excessive distance reduces the effectiveness of the gas jet in the lower regions of the kerf. [6,8]

Assist gases can be classified into two categories: inert gases and reactive gases. Inert gases include nitrogen and argon, whereas reactive gases include oxygen and air. [8,15]

• Inert gases (nitrogen, argon): Used in fusion cutting. The gas, supplied at very high pressure, mechanically expels the molten material, while all the energy required for cutting is provided by the laser beam. This results in a clean, non-oxidized cut edge.

• Reactive gases (oxygen, air): Actively participate in the cutting process. The gas reacts with the material through oxidation, releasing additional exothermic heat. This increases the cutting speed, particularly for thick sections. These gases are supplied at lower pressure; however, their disadvantage is the formation of an oxidized and rougher cut edge.

Table 5. Comparison of assist gases used in laser cutting

Gas	Type	Application	Max sheet [mm]	Pressure [bar]	Cutting speed	Edge quality	Cost
Oxygen	Reactive	Carbon steel Non-alloy steel Alloy steel Mild steel	30	0,7-6	Very high	Rough surface, slag may occur	Medium
Air	Reactive	Carbon steel Low-alloy steel Aluminum Thermoplastics Mild steel Stainless steel	8-10	6-12	High	Slight oxidation and discoloration	Low
Nitrogen	Inert	Stainless steel Aluminum Copper HSLA steel Corrosion-resistant steel Nickel alloys Aluminum alloys	20-25	8-25	Moderate	Clean, bright, oxidation-free	Very high
Argon	Inert	Reactive metals Hard-to-cut metals	15	5-20	Low	No oxidation or surface damage	High

6. LASER BEAM FOCUSING

Focusing of the laser beam involves setting an appropriate distance between the laser lens and the surface of the material. The selection of this distance is crucial for machining accuracy: an excessively large stand-off distance results in beam divergence and loss of focus, whereas an excessively small distance may lead to damage to the surface of the processed material. The focal distance is selected based on the type of laser used, the characteristics of its focusing lens, and the thickness of the processed material; in practice, distances in the range of 1–3 mm are most commonly applied. [17]

6.1. Laser focusing lens

In laser cutting technology, lenses constitute a critical component of the optical system. They are responsible for shaping and focusing the laser beam; however, they are also among the elements most susceptible to damage caused by molten metal spatter and general wear. The service life of a lens is influenced by factors such as laser power, the quality of optical components, and the cleanliness conditions during laser assembly and maintenance. Lens damage is largely random and difficult to predict; therefore, protective windows are employed to shield the optical components from spatter and contamination.

When a lens becomes contaminated by spatter generated during piercing, a sudden deterioration in cutting quality may occur, accompanied by phenomena such as smoke streaks, poor focus, or uneven cut edges.

Lens replacement and cleaning must be performed under extremely clean conditions, comparable to those in an operating room; consequently, such procedures cannot be carried out directly on the production floor. Typically, the operator removes the damaged cutting head and sends it for the required servicing. To prevent prolonged machine downtime, temporary cutting heads are used, or a completely new, ready-to-operate head is installed, eliminating the need for repeated disassembly and recalibration, which is otherwise necessary when refurbishing the original head. [6,18]

7. PARAMETER SELECTION FOR THE WORKPIECE MATERIAL

Cutting parameters are selected based on the type of processed material and its thickness. Proper selection of the assist gas is particularly important, as it enables the use of a laser source with lower power due to the exothermic reaction between the molten material and the gas. The focusing of the laser beam is of crucial importance for achieving the required cutting quality and accuracy; correct focal adjustment allows complete material separation while maintaining a straight, smooth, and burr-free cut edge.

Appropriate selection of laser power enables fast and precise cutting without material damage or burn-through. In the case of thin sheets (up to 3 mm), a power range of 500–1000 W may be sufficient, whereas for thicker sheets (above 10 mm), laser power exceeding 3 kW and reaching up to 20 kW may be required for materials with thicknesses of up to 50 mm. If there is uncertainty regarding the appropriate parameter values, reference can be made to parameter tables for specific materials provided by the laser manufacturer. [8,10]

8. CONSEQUENCES OF INCORRECT SELECTION OF LASER CUTTING PARAMETERS

Proper selection of laser cutting process parameters is of crucial importance for both the quality of the produced components and the efficiency of the technological process. The basic parameters include cutting speed, laser power, assist gas type and pressure, laser beam focal position, and the properties of the processed material. Incorrect parameter settings may lead to quality defects, increased scrap generation, and higher production costs. [1,3]

One of the most frequently encountered problems is improper selection of cutting speed. Excessively low cutting speeds result in excessive heating of the material, leading to edge burning, widening of the cut kerf, and enlargement of the heat-affected zone. Conversely, excessively high cutting speeds may cause incomplete material separation, rough cut edges, and the presence of uncut sections. [2,4]

The type of assist gas and its pressure also have a significant impact on process quality. Inappropriate gas selection may result in edge oxidation, deterioration of cut surface quality, and changes in material properties. Insufficient gas pressure hinders effective removal of molten material from the kerf, whereas excessive pressure may destabilize the process and cause edge damage. [1,5]

Incorrect settings of laser power and laser beam focal position also negatively affect cutting quality. Excessive laser power leads to intense material melting, component deformation, and edge burning, while insufficient power prevents complete material separation. Improper beam focusing reduces energy concentration in the cutting zone, thereby deteriorating edge quality and process stability. [3,4]

In conclusion, improper selection of laser cutting parameters results in reduced product quality and decreased production efficiency. Therefore, appropriate parameter optimization, tailored to the material type and quality requirements, constitutes an essential element of modern laser processing technologies.

9. ECONOMIC ANALYSIS OF THE INFLUENCE OF TECHNOLOGICAL PARAMETERS ON THE COST OF LASER CUTTING

The economic aspects of industrial laser cutting are largely determined by the unit cost of manufacturing a component. Although total costs also include capital expenditures related to the purchase and commissioning of the machine, in practice the ongoing production costs are primarily driven by operating expenses. Their magnitude depends directly on the technological process parameters, which affect machine operating time, energy consumption, and the use of auxiliary materials. For this reason, proper selection of process parameters is of key importance, as it enables the reduction of operating costs and minimizes the risk of producing defective or non-conforming parts that generate additional losses. [19]

9.1. Cutting Speed and Laser Power – the influence of processing time and electrical Energy consumption

Cutting speed plays a fundamental role in operating costs, as it determines the duration of machine operation required to manufacture a component. Increasing the cutting speed reduces the cutting time per unit length, thereby directly lowering the monetary cost associated with

machine time. However, the risks associated with this approach must be taken into account. Maintaining cutting speeds above the technically optimal range for a given laser power and material leads to deterioration of edge quality, such as excessive dross formation or surface irregularities. This results in higher scrap costs and the need for additional, costly post-processing operations (e.g., grinding), which may offset the time-related savings. [19,20]

Laser power, in turn, determines the maximum achievable cutting speed, particularly in the case of thicker steel sheets. Investment in higher-power machines enables higher cutting speeds and thus increased productivity. Although higher laser power is associated with increased instantaneous electrical energy consumption, economic optimization involves identifying the point at which the reduction in machine operating time due to higher cutting speed outweighs the increase in energy costs. Proper selection of laser power allows minimization of unit costs related to both energy consumption and processing time. [19,20]

9.2. Assist gas parameters and nozzle selection as key raw material cost factors

The cost of assist gas consumption increases proportionally with operating pressure, which is particularly significant in processes requiring the use of expensive gases such as argon or nitrogen. Higher pressure is often necessary to obtain oxide-free cut edges or to ensure stable cutting of thicker materials; however, it simultaneously results in a substantial increase in gas flow rate, thereby raising the unit cutting cost.

The nozzle is responsible for shaping the gas jet, and its orifice diameter directly determines the amount of gas consumed during the process—the larger the nozzle opening, the higher the gas demand. Therefore, the use of the smallest possible nozzle diameter that still ensures stable laser operation is an important means of cost reduction. It should also be noted that the nozzle is a consumable component; damage or improper selection not only increases gas consumption but also generates additional costs associated with more frequent replacement of parts.

The type of assist gas also has a significant impact on process cost, as each medium differs in price, required pressure, and the resulting edge quality. For example, oxygen and air represent lower-cost solutions but may cause increased oxidation or surface roughness. Nitrogen and argon are considerably more expensive but provide higher cutting quality and prevent discoloration. In many cases, high-cost gases can be replaced with less expensive alternatives; however, this is typically achieved at the expense of quality and may require additional post-processing. Consequently, assist gas selection represents a trade-off between unit cost and the required quality standard. [21,22]

9.3. Lens position – impact on consumables and process stability

The laser focal position (adjusted by the lens height) affects costs primarily through process stability and the risk of optical damage. Incorrect focal positioning influences the consumption of expendable components, as it may lead to energy back-reflection or contamination of the protective lens (protective window) by spatter. Frequent replacement of these elements constitutes an additional, measurable cost. Moreover, a non-optimal focal position destabilizes the cutting process (e.g., by causing excessive dross formation), forcing a reduction in cutting speed, which inevitably increases costs associated with machine operating time. [23]

10. SUMMARY

The aim of this study was to present the influence of technological parameters of laser cutting on process performance, edge quality, and manufacturing costs. Based on a literature review, the roles of cutting speed, laser power, assist gas, and laser beam focusing were discussed. It was demonstrated that proper selection of process parameters enables the production of high-quality components while simultaneously reducing energy consumption and the use of auxiliary materials. The importance of process optimization was emphasized as a key factor in achieving efficient and cost-effective laser machining.

ACKNOWLEDGEMENTS

The work was created as part of project based learning - PBL, in the 13th competition under the Initiative of Excellence - Research University, Silesian University of Technology, Gliwice, Poland and as part of project of Students Scientific Circle of Laser Surface Treatment under the Initiative of Excellence - Research University, Silesian University of Technology, Gliwice, Poland.

BIBLIOGRAPHY

1. Steen, W. M., Mazumder, J., Laser Material Processing, Springer, London 2010.
2. Powell, J., CO_2 Laser Cutting, Springer, London 1998.
3. Ion, J. C., Laser Processing of Engineering Materials, Elsevier Butterworth-Heinemann, Oxford 2005.
4. Kalpakjian, S., Schmid, S., Manufacturing Processes for Engineering Materials, Pearson Education, 2014.
5. PN-EN ISO 9013:2017 – Jakość cięcia termicznego — Klasyfikacja geometrycznych właściwości wyrobów ciętych.
6. https://www.acctekgroup.com/pl/does-laser-cutting-use-gases/
7. https://magazynprzemyslowy.pl/artykuly/uwarunkowania-technologiczne-i-dokladnosc-ciecia-laserem
8. A. Klimpel, Technologie laserowe: spawanie, napawanie, stopowanie, obróbka cieplna i cięcie, Gliwice: Wydawnictwo Politechniki Śląskiej, 2012.
9. Dr inż. Andrzej Stanisław Klimpel – Nowoczesne lasery i technologie laserowe w inżynierii spawalnictwa. Wydawnictwo Politechniki Śląskiej, Gliwice, 2023r.
10. https://eckert.com.pl/kompendium/jakie-parametry-decyduja-o-jakosci-ciecia-laserowego.html#sekcja-3
11. https://www.adhmt.com/pl/laser-cutting-machine-specification/
12. https://www.bapromet.com.pl/news.php?newsID=511&lang=pl&action=view
13. https://www.accteklaser.com/pl/parametry-ciecia-laserowego-ostateczny-przewodnik/?srsltid=AfmBOooIrAtuYoQ3O8DCqAc9qqY7ipVV9Uh9JtSK_9pRPTOZhCJ0fpf
14. Czupryński, A., Rzeźnikiewicz, A., Specjalne technologie spawalnicze w ćwiczeniach laboratoryjnych. Część 2. Gliwice: Wydawnictwo Politechniki Śląskiej, 2020.
15. https://yihailasers.com/pl/laser-cutting-gas-pressure/

16. https://pl.liermetal.com/blog/how-does-the-pressure-of-assist-gas-affect-the-laser-cutting-of-metal-parts-1667130.html
17. https://cel-cut.com/jak-poprawnie-ustawi-parametry-ci-cia-laserem-pr-d/
18. https://magazynprzemyslowy.pl/artykuly/soczewki-czyli-wazny-i-wrazliwy-element-optyki-lasera
19. https://laser-adjatech.pl/2025/04/10/ciecie-laserem-technologia-zastosowania-i-parametry-procesu/
20. https://www.accurl.com/blog/laser-cutting-power-consumption/
21. https://centrummaszyncnc.pl/baza-wiedzy/jak-gazy-laserowe-wplywaja-na-koszty-i-jakosc-ciecia-metalu
22. https://magazynprzemyslowy.pl/artykuly/azot-tlen-czy-powietrze-koszty-gazu-w-procesie-ciecia-laserem
23. https://www.hansme.net/knowledgedetail/393

TalentDetector
9th January 2026
Gliwice, Poland
DEPARTMENT OF ENGINEERING MATERIALS AND BIOMATERIALS
FACULTY OF MECHANICAL ENGINEERING
SILESIAN UNIVERSITY OF TECHNOLOGY
INTERNATIONAL STUDENTS SCIENTIFIC CONFERENCE

Charakteristika ocelí s dôrazom na automatové ocele

Jozef Vicena[a], Milan Uhríčik[a]

[a] Žilinská univerzita v Žiline, Strojnícka fakulta, Katedra materiálového inžinierstva, Univerzitná 8215/1, 010 26 Žilina, Slovak Republic

Abstract: Príspevok sa zaoberá charakteristikou ocelí s dôrazom na novú generáciu automatových ocelí (oceľ 11SMnPb30). Teoretická časť poskytuje systematický rozbor danej skupiny materiálov, zahŕňajúci ich triedenie podľa metastabilného diagramu Fe-Fe_3C, štandardizované označovanie podľa systémov STN a EN, ako aj detailné vysvetlenie princípu ich funkcie. Chemické zloženie (so zvýšeným obsahom S, Mn a Pb) a anizotropná mikroštruktúra, charakteristická pretiahnutými inklúziami MnS a časticami olova, sú kľúčové pre ich vynikajúcu obrábateľnosť. Cieľom je teoreticky posúdiť, či a ako môžu chemicky aktívne pracie prostriedky interagovať s touto heterogénnou štruktúrou a iniciovať korózne procesy, čím položiť odborný základ pre následné experimentálne práce.

Keywords: Označovanie ocelí podľa STN a EN , automatová oceľ, MnS fáza.

1. ÚVOD

Základné triedenie zliatin železa je podľa metastabilného diagramu Fe-Fe_3C. Metastabilným stavom kovu alebo zliatiny sa rozumie stav, ktorý nie je za daných teplôt a tlakov termodynamicky stabilný, avšak v dôsledku kinetických bariér (ako je napríklad pomalá difúzia) môže pretrvávať veľmi dlhý čas, prakticky takmer nekonečne. Schematické zobrazenie prechodu kovu do stabilného a metastabilného stavu je uvedené na obr. 1 [2].

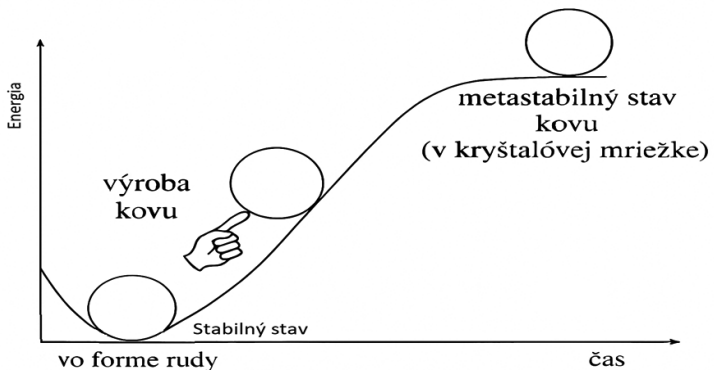

Obr. 1 Schematické znázornenie stabilného a metastabilného stavu kovu [1].
Figure 1. Schematic representation of the stable and metastable states of a metal [1].

Toto členenie sa vzťahuje na ocele a biele liatiny. *Ocele* sú zliatiny s obsahom uhlíka do 2,14 %, čo zodpovedá maximálnej rozpustnosti uhlíka v austenite. Toto zloženie umožňuje pri ohreve ich úplnú premenu na austenit, čo im poskytuje dobrú tvárnosť. (Biele) liatiny obsahujú viac ako 2,14 % uhlíka, čo vedie k tvorbe eutektika a grafitu v ich štruktúre.

Systematika ocelí vychádza z viacerých kritérií:

- *podľa technológie spracovania* sa rozlišujú tvárnené ocele (dodávané hutníctvom ako polotovary pre následné tvarovanie) a ocele na odliatky (určené pre zlievarenské spracovanie).
- *podľa funkčného určenia* sa delia na konštrukčné a nástrojové.
- *podľa kvality a záruky od výrobcu* sa členia na ocele bežnej kvality (kde výrobca nezaručuje alebo len obmedzene garantuje chemické zloženie) a ušľachtilé ocele (s presne garantovaným minimálnym a maximálnym obsahom všetkých legujúcich prvkov).
- *podľa chemického zloženia* sa rozdeľujú na uhlíkové (s definovaným maximálnym obsahom prídavných prvkov podľa STN EN 10020) a zliatinové (s úmyselným prídavkom jedného alebo viacerých legujúcich prvkov).

1.1 Rozdelenie ocelí podľa STN

Norma STN ďalej špecifikuje triedenie ocelí do tried. Pre *ocele bežnej kvality* ide o:

- Trieda 10 - ocele, pri ktorých výrobca negarantuje chemické zloženie.
- Trieda 11 - ocele, kde výrobca zaručuje maximálny obsah uhlíka, fosforu a síry, prípadne aj ďalších vybraných prvkov.
  Ocele bežnej kvality sa vyznačujú nižšou čistotou a nekonzistentnými mechanickými vlastnosťami. Ide väčšinou o uhlíkové ocele so zvýšeným podielom nečistôt (síra, fosfor), prípadne s vyšším obsahom mangánu alebo stopami prvkov ako chróm. Ich hlavnou výhodou je nízka cena, no nie sú vhodné na zušľachťovanie ani chemicko-tepelnú úpravu. Naopak, ušľachtilé ocele vďaka garantovanému zloženiu vykazujú lepšie a stabilnejšie vlastnosti, čo je dôsledkom vyššej čistoty. Sú cenovo náročnejšie a primárne určené na zušľachťovanie alebo chemicko-tepelnú úpravu.

Medzi ušľachtilé patria napríklad ocele:

- Trieda 12 - uhlíkové konštrukčné ocele.
- Trieda 13 - zahŕňa zliatinové konštrukčné ocele legované mangánom, kremíkom, ich kombináciou alebo vanádom.
- Trieda 14 - združuje konštrukčné zliatinové ocele, ktorých legovanie je založené na chróme, samostatne alebo v kombinácii s ľahko dostupnými prvkami (mangán, kremík, hliník).
- Trieda 15 - je určená pre náročnejšie aplikácie a zahŕňa chrómom legované konštrukčné ocele ďalej obohatené o menej bežné legujúce prvky (okrem niklu), typicky molybdén alebo vanád.
- Trieda 16 - zahŕňa všetky konštrukčné zliatinové ocele obsahujúce nikel, vrátane komplexne legovaných typov (napr. kombinácia nikel-mangán-chróm).
- Trieda 17 - je určená pre aplikácie vyžadujúce najvyššie vlastnosti, charakteristická veľmi vysokým obsahom legujúcich prvkov.

- Trieda 19 - zahŕňa všetky nástrojové ocele, vrátane odlievaných nástrojových ocelí [2, 3].

Trieda 18 nie je špecifikovaná. Toto zámerné vynechanie slúžilo ako rezerva pre možnú budúcu špecifikáciu novej, špeciálnej skupiny materiálov, ktorá sa v čase tvorby a platnosti normy nevyskytovala alebo nevyžadovala samostatnú kategóriu. S prechodom na európsky normalizačný systém (STN EN) stratilo toto konkrétne číslovanie tried priamu relevanciu, pretože nový systém používa odlišné princípy označovania [4].

1.2 Označovanie ocelí podľa STN

Systém označovania tvárnených ocelí podľa STN používa päťmiestny číselný kód, ktorý môže byť doplnený o dve ďalšie číslice. Konkrétne pravidlá pre označovanie ocelí tried 10 a 11 sú znázornené na obrázku číslo 2, strana 4 [3]. Pravidlá pre označovanie ocelí vyšších tried, od 12 do 19, sú potom uvedené na obrázku číslo 3, ktorý sa nachádza na strane číslo 5 [5].

1.3 Označovanie ocelí podľa EN

Na zabezpečenie jednotnej identifikácie ocelí v rámci Európskeho hospodárskeho priestoru bola zavedená sústava noriem EN 10027. Tá stanovuje systematické pravidlá pre priraďovanie pomenovaní a číselných kódov materiálom.

Norma pozostáva z dvoch kľúčových častí:

- EN 10027-1 definuje pravidlá pre tvorbu krátkych symbolických názvov ocelí.
- EN 10027-2 určuje pravidlá pre ich číselné označenie.

Tento systém umožňuje jednoznačnú identifikáciu typu ocele na základe jej predpokladaného použitia, mechanických vlastností alebo chemického zloženia, čo je nevyhnutné pre spoľahlivý výber materiálu v priemysle, výskume a vývoji.

Podľa EN 10027-1 sa alfanumerické symboly vytvárajú na základe dvoch hlavných princípov:

- Ocele klasifikované podľa účelu a vlastností (napr. mechanických). Ich označenie začína skratkou aplikačnej oblasti, ako je "S" pre konštrukčné ocele alebo "P" pre ocele pre tlakové nádoby. Následná číselná hodnota typicky vyjadruje minimálnu medzu klzu v MPa. Označenie môže byť doplnené príponami špecifikujúcimi napr. rázovú húževnatosť.
- Ocele klasifikované podľa chemického zloženia. Ich označenie priamo odráža chemické zloženie.

  Pre nelegované ocele sa používa symbol "C" s číslom vyjadrujúcim stonásobok priemerného obsahu uhlíka (napr. C45).

  Pre legované ocele sa používa symbol "X", za ktorým nasleduje údaj o obsahu uhlíka a symboly legujúcich prvkov s ich približnými obsahmi v percentách (napr. X2CrNi18-9).

Podľa EN 10027-2 sa každej oceli priradí unikátny číselný kód v tvare 1.xxxx, kde úvodná číslica "1" identifikuje materiálovú skupinu (oceľ) a číslice za desatinnou čiarkou špecifikujú konkrétny typ. Tento systém je vhodný pre databázové evidovanie a automatizované spracovanie (obr. 2 a obr. 3).

Príklady interpretácie:

- S355J2: "S" - konštrukčná oceľ, "355" - minimálna medza klzu 355 MPa, "J2" - požiadavka na rázovú húževnatosť pri -20 °C.
- X2CrNi18-9: "X" - vysokolegovaná oceľ, "2" - cca 0,02 % uhlíka, "CrNi18-9" - cca 18 % chrómu a 9 % niklu.
- 11SMnPb30 (náš vyšetrovaný materiál): Ide o označenie podľa staršieho systému, kde číslo "11" vyjadruje približný obsah uhlíka (0,11 %), "S" a "Mn" označujú zvýšený obsah síry a mangánu, "Pb" prítomnosť olova a číslo "30" orientačne udáva stonásobok priemerného obsahu síry [3, 6, 7].

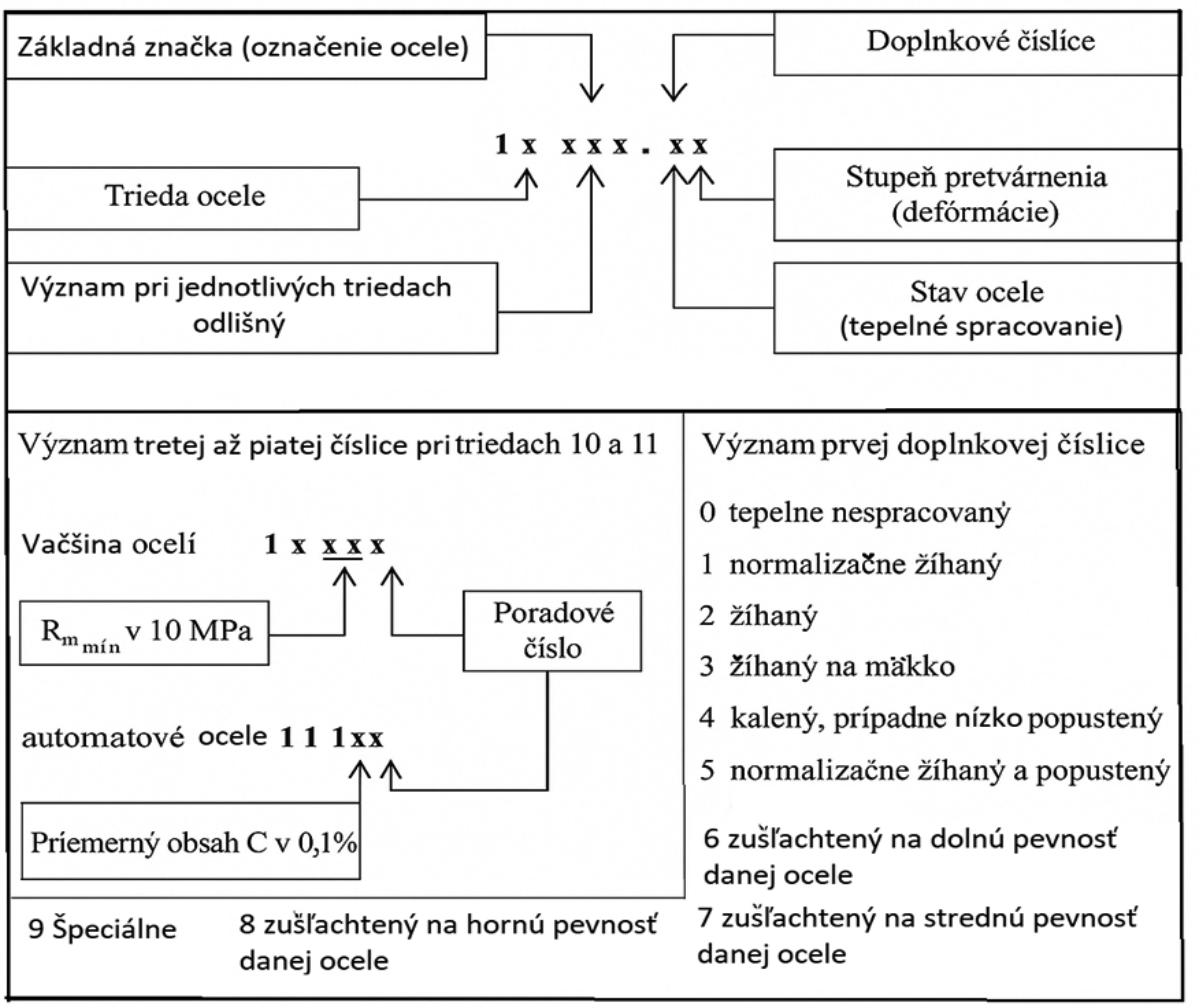

Obr. 2 Pravidlá označovania ocelí triedy 10 a 11 podľa STN [5,10].
Figure 2. Rules for marking steel grades 10 and 11 according to STN [5,10].

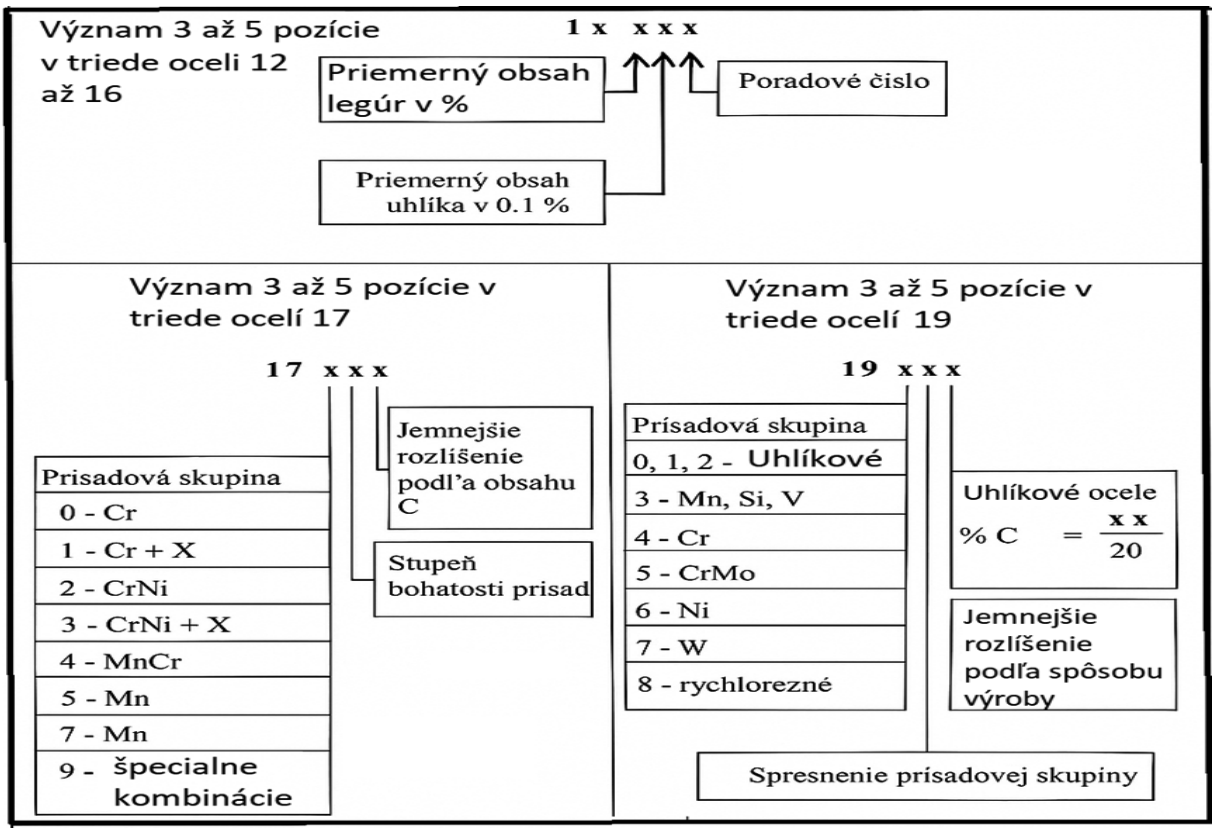

Obr. 3 Pravidlá označovania ocelí triedy 12 až 19 [5,10].
Figure š. Rules for marking steel grades 12 - 19 according to STN [5,10].

2. Automatová oceľ

S rastúcimi nárokmi na produktivitu a presnosť sa v strojárstve uplatňujú špecializované ocele prispôsobené pre automatizované výrobné linky - tzv. automatová oceľ. Automatová oceľ je ideálnym materiálom pre obrábanie na automatizovaných strojoch, napríklad pre sústruženie, frézovanie a vŕtanie.

Sú navrhnuté tak, aby umožňovali rýchle a bezproblémové obrábanie s minimálnymi zásahmi obsluhy, čo je kriticky dôležité pri sériovej a hromadnej výrobe drobných súčiastok, kde každý prestoj znamená straty.

Vyznačujú sa vynikajúcou obrábateľnosťou a kontrolovaným lámaním triesky. Ich chemické zloženie, tepelné spracovanie a mikroštruktúra sú optimalizované na dosiahnutie optimálneho pomeru medzi spracovateľnosťou, stabilitou procesu a kvalitou výsledného povrchu.

Pre komponenty, ktoré sú vystavené vyššiemu namáhaniu, je často optimálnym riešením tepelne upravitelná automatová oceľ. Vysoký obsah uhlíka umožňuje procesy temperovania, s ktorými môžete dosiahnuť veľmi robustné vlastnosti.

Obyčajné nízkouhlíkové ocele na takéto aplikácie nevyhovujú, pretože ich vysoká húževnatosť vedie k tvorbe dlhých, súvislých triesok, ktoré obťažujú proces a môžu poškodiť obrobok alebo nástroj. Naopak, automatové ocele s olovom alebo sírou, špecificky vedú k malým

krehkým inklúziám, kde sa malé kovové triesky môžu ľahšie odlomiť. To umožňuje krátke lámanie triesky, čím sa zabezpečuje hladký povrch aj pri zvýšených rezných rýchlostiach.

Charakteristické prvky zloženia automatových ocelí a ich úloha:

- Síra (S): Kľúčový prvok zlepšujúci obrábateľnosť. Jej obsah okolo 0,25 % znižuje húževnatosť a podporuje krehký typ triesky. Negatívny vplyv síry na tvárnosť je kompenzovaný mangánom.
- Mangán (Mn): Obsahuje sa v množstvách okolo 1,1 %. Jeho hlavnou úlohou je viazať síru do sulfidov mangánu (MnS), čím bráni vzniku krehkej sieťky sulfidov železa na hraniciach zŕn. Tvar a veľkosť týchto vtrúsenín sú kritické - najvhodnejšie sú izometrické (guľovité) častice s priemerom nad 10 µm, ktoré vznikajú pri vyšších teplotách tvárnenia.
- Nízky obsah kremíka (Si): Obsah kremíka je zámerne obmedzený (niekedy pod 0,01 %), pretože oxid kremičitý (SiO_2), vznikajúci pri deoxidácii, zhoršuje opotrebenie nástrojov. Kremík tiež zvyšuje plastickosť sulfidov, čo môže viesť k ich nežiaducemu pretiahnutiu.
- Olovo (Pb): Zahraničné varianty často obsahujú 0,1-0,3 % olova. Keďže je olovo v oceli nerozpustné, vytvára v štruktúre jemné izolované častice, ktoré pôsobia ako vnútorné mazivo. Toto znižuje trenie medzi trieskou a nástrojom, zlepšuje lámavosť triesky a zvyšuje životnosť nástroja. Pri vysokých rezných rýchlostiach (nad 115 m/min) sa však olovo môže odparovať, čím stráca svoj účinok. Výroba týchto ocelí si vyžaduje špeciálne opatrenia proti vyparovaniu olova a exhaláciám.

Ako ekologickejšia alternatíva k oceliam s vysokým obsahom olova sa vyvinuli materiály s nízkym obsahom síry (0,02-0,04 %) a olova (0,04-0,06 %), deoxidované *silikokalciom* (zliatina obsahujúca cca 30-35 % Ca a 60-65 % Si).

Silikokalcium účinne odstraňuje kyslík z taveniny, pričom vznikajú kremičitany vápenaté, ktoré prechádzajú do trosky.

Chemické zloženie podporuje modifikáciu vtrúsenín - jeho najdôležitejšou úlohou je zmena morfológie sulfidov. Namiesto pretiahnutých vrstiev MnS podporuje tvorbu guľovitých (globulárnych) sulfidov a oxosulfidov vápenatých, čo výrazne zlepšuje obrábateľnosť, tvárnosť a húževnatosť. Zvyškové množstvá vápnika v oceli môžu mierne zvýšiť jej pevnosť a tvrdosť.

Obrábateľnosť nového typu automatových ocelí je možné vylepšiť aj prídavkom selénu (Se), telúra (Te) alebo bizmutu (Bi), ktoré podobne ako síra zlepšujú lámavosť triesky. Ich praktické využitie je však kvôli vysokej toxicite a nákladom obmedzené.

Vzhľadom na zníženú húževnatosť a tvárnosť (spôsobenú sírou a sulfidmi) sa automatové ocele používajú výhradne na výrobu súčiastok, ktoré nie sú namáhané dynamickým alebo rázovým zaťažením. Ide typicky o menšie komponenty vyrábané vo veľkých sériách, ako sú napríklad skrutky, podložky, puzdrá alebo elektrotechnické súčiastky [8].

2.1 Mikroštruktúra automatovej ocele

Mikroštruktúra automatovej ocele pozostáva z hlavných fáz, ktoré sú výrazne orientované v smere valcovania, čo materiálu udeľuje anizotropný charakter.

Tieto fázy sú:

- *Feritická matrica*: Predstavuje kontinuálnu základnú fázu svetlejšieho vzhľadu.

- *Perlit:* Tretiu významnú zložku predstavuje perlit, ktorý sa v materiáli vyskytuje ako tmavšie, rovnako orientované oblasti.
- *Sulfidové inklúzie*: V matrici sú výrazne pretiahnuté inklúzie sulfidov mangánu (MnS) s preferenčnou orientáciou v smere plastického preformovania (valcovania). Ich charakteristický tvar je znázornený na obr. 4.
- *Častice elementárneho olova*: V mikroštruktúre sú prítomné častice elementárneho olova (Pb), ktoré majú tendenciu kumulovať sa najmä v oblasti koncových častí sulfidových inklúzií.

Všetky tieto štrukturálne zložky sú výsledkom výrobného procesu a vykazujú výraznú preferenčnú orientáciu v smere valcovania. Tento anizotropný charakter mikroštruktúry je dobre viditeľný na obr. 4 a tak sú na obrázku označené miesta ktoré obsahujú vyššie spomenuté štruktúrne elementy. [9].

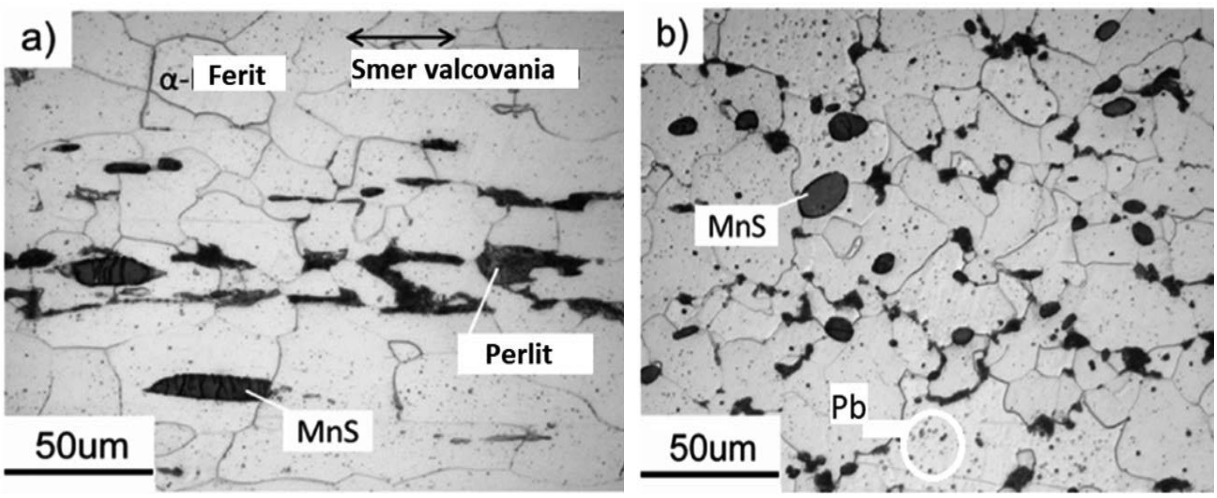

Obr. 4 Mikroštruktúra automatovej ocele: a) v smere valcovania; b) v priečnom smere [9].
Figure 4. Microstructure of free-cutting steel: a) in the rolling direction; b) in the transverse direction [9].

POĎAKOVANIE

Príspevok vznikol v rámci riešenia spoločného slovensko-poľského projektu TalentDetector 2026 ako výsledok spolupráce medzi Politechnikou Slaskou, Gliwice a Žilinskou univerzitou v Žiline a projektu KEGA č. 033ŽU-4/2026.

BIBLIOGRAPHY

1. Centrum vedecko-technických informácií. Stabilný a metastabilný stav kovu. Dostupné na internete: https://vedanadosah.cvtisr.sk/technika/materialy/kto-co-zerie-kovy/. Cit. 2.11.2025

2. CALLISTER W. D., JR. Materials Science and Engineering. USA 2018. ISBN-13: 9781119321590. Dostupné na internete: https://ftp.idu.ac.id/wp-content/uploads/ebook/tdg/TEKNOLOGI%20REKAYASA%20MATERIAL%20PERTAHANAN/Materials%20Science%20and%20Engineering%20An%20Introduction%20by%20William%20D.%20Callister,%20Jr.,%20David%20G.%20Rethwish%20(z-lib.org).pdf Cit.29.10.2025
3. Skočovský P., Bokůvka O., Konečná R., Tillová E.. Náuka o materiáli. EDIS- vydavateľstvo Žilinskej univerzity. Žilina 2014 ISBN 978-80-554-0871-2
4. Nový F.. Prednášky KMI UNIZA z predmetu Degradačné procesy 2024.
5. Trpčevská J., Rafinácia a príprava zliatin FMM TUKE. 2017. Dostupné na internete:https://iret.fmmr.tuke.sk/files/RaPZ.pdf Cit. 30.11.2025
6. SteelNumber. Steel Numbers Steel Classification according to EN 10027-2. Designation systems for steels. Dostupné na internete: https://www.steelnumber.com/en/number_en10027_eu.php . Cit. 9.11.2025
7. Standars.iteh.ai. EN 10027-1:2016 (Main) Designation systems for steels - Part 1: Steel names. Dostupné na internete: https://standards.iteh.ai/catalog/standards/cen/8b108662-8742-45e3-a9ba-2f0534ac0ce7/en-10027-1-2016 Cit. 10.11.2025
8. Houdek O.. Studium dezoxidace oceli na odlitky a její vliv na konečnou kvalitu výrobku. (Diplomová práca). Dostupné na internete: https://dspace.vsb.cz/items/df5140eb-f768-406c-a66a-2894d56ab48a Cit. 6.11.2025
9. D. Seo, H. Toda, M. Kobayashi, K. Uesugi, A. Takeuchi, Y. Suzuki. In Situ Observation of Void Nucleation and Growth in a Steel using X-ray Tomography. 2014Japan. Dostupné na internete: https://www.researchgate.net/publication/282824162_In_Situ_Observation_of_Void_Nucleation_and_Growth_in_a_Steel_using_X-ray_Tomography
10. Bokůvka O.. Prednášky KMI UNIZA z predmetu Materiáli I a II v rokoch 2022-2023. Cit. 23.10.2025

TalentDetector

9th January 2026
Gliwice, Poland

DEPARTMENT OF ENGINEERING MATERIALS AND BIOMATERIALS
FACULTY OF MECHANICAL ENGINEERING
SILESIAN UNIVERSITY OF TECHNOLOGY

INTERNATIONAL STUDENTS SCIENTIFIC CONFERENCE

Design and Development of an Experimental Setup for Corrosion–Erosion Testing under Continuous Liquid Flow

Julia Wawrzynek[a], Błażej Tomiczek[b], Marek Kremzer[b]

[a] Student of General Engineering, Silesian University of Technology
[b] Silesian University of Technology, Faculty of Mechanical Engineering, Scientific and Didactic Laboratory of Nanotechnology and Material Technologies, Konarskiego 18A, Gliwice, Poland
email: jw305636@polsl.pl

Abstract: The article presents the concept and preliminary design of a laboratory experimental setup for corrosion–erosion testing in continuous liquid flow. The main idea is to define the measurement concept and overall layout of the stand, including the selection and functional arrangement of key subsystems such as flow generation, control and monitoring. CAD tools are used to model the proposed solution, verify basic design assumptions and outline possibilities for further optimization and future construction of the test stand.

Keywords: erosion–corrosion, continuous liquid flow, laboratory experimental setup, CAD design, material degradation, optimization

1. INTRODUCTION

Safe operation of industrial installations depends on the durability of materials used in components such as pipelines, valves, pumps and turbine parts. During long-term service these elements are exposed to variable flow and pressure, temperature changes, dissolved gases and aggressive ions, and often to suspended solid particles [1]. In flowing liquid environments, these factors act simultaneously: reactive species are continuously transported to the surface, protective films may form and be removed, and the surface is repeatedly affected by mechanical interactions with the medium [1]. Such conditions gradually reduce mechanical and functional properties, lowering efficiency and increasing operating as well as maintenance costs in severe cases they lead to failures and shutdowns [2]. Because the most severe damage is usually localized, laboratory tests should focus on reproducing the critical conditions that drive it, not just the average operating state [2]. Because real environments are complex, laboratory testing should reproduce the key degradation conditions in a controlled and repeatable way. In many flowing-liquid systems the most important coupled processes are corrosion and particle erosion, which can accelerate each other [1,2]. In practice, this means defining boundary conditions that can be set and reproduced between tests (e.g., flow velocity or impingement conditions, medium chemistry and solids content), so that material ranking and parameter effects can be compared reliably [1,2].

Corrosion is the spontaneous degradation of a metal due to chemical or electrochemical interaction with the environment [3]. Chemical (dry) corrosion is mainly related to gases and elevated temperatures, whereas electrochemical (wet) corrosion dominates in aqueous and other conductive media. In wet conditions the corrosion response depends strongly on the electrolyte composition and its ability to sustain electrochemical reactions, which is why controlled solution chemistry is essential for repeatable laboratory exposure. [4] For safety, corrosion form is critical: uniform corrosion causes more even wall thinning, while localized corrosion (pitting, crevice or intergranular) may result in rapid perforation or local loss of load capacity even when average metal loss is small. Localized forms are especially critical during exploatation because they can develop into through-wall defects without a proportional increase in the average material loss, making early detection and proper test reproduction important. Stress corrosion and corrosion fatigue may additionally cause brittle cracking under combined environmental and mechanical loading [5]. Corrosion behaviour is commonly assessed using electrochemical methods such as polarization and impedance, supported by microstructural observations and corrosion-product analysis [6]. The findings support mitigation through alloy selection, coatings and inhibitors. These mitigation routes are typically evaluated comparatively under standardized or well-defined exposure conditions to confirm performance in the intended medium [7]. To define repeatable wet exposure conditions, the Japanese standard JIS D 0203 provides standardized moisture and water resistance procedures (including rain/splash/spray or immersion-type exposure) for components and assemblies, enabling comparison of results between tests. Such standardized water/spray exposures are useful for screening and for defining comparable wet-contact conditions, especially when the goal is to compare resistance of different materials or surface protections under the same procedure [8].

Erosive wear occurs when solid particles carried by a fluid impact the surface, as in slurry transport and contaminated flow passages of pumps and turbines [9]. Repeated impacts cause plastic deformation, micro-cutting and crack initiation, producing grooves and craters and increasing roughness [10]. The erosion rate depends on impact velocity and angle, particle properties (size, shape, hardness, concentration) and the target material's hardness and microstructure. Because impact angle governs whether abrasion (low angles) or crater-type impact damage (near-normal angles) dominates, test rigs that allow defined impingement conditions are useful for separating and comparing these wear modes [11]. In practice, erosion and corrosion often act together: particle impacts remove protective films and expose fresh metal, while corrosion roughens the surface and can intensify particle attack. Consequently, erosion–corrosion may be more damaging than the two processes considered separately. This coupled behaviour motivates laboratory systems that can run a corrosive liquid together with controlled solids content, so that depassivation by impacts and electrochemical dissolution occur under the same, repeatable conditions [12]. Resistance can be improved using surface engineering solutions such as hard coatings (e.g., HVOF) or laser-cladded layers, provided they adhere well and remain stable under loading. In such solutions, effectiveness depends not only on hardness but also on coating integrity and stability in the working medium, because cracking, poor adhesion or chemical instability can negate the expected benefit under combined mechanical and chemical action [13,14]. Because real installations show spatially varying conditions, combined-flow laboratory rigs are needed to reproduce continuous flow, controlled chemistry and particle-laden media in a repeatable manner, for example using closed-loop flow systems and jet/impingement methods. Closed-loop systems support long-duration circulation with adjustable flow and medium parameters, while jet or impingement methods provide a localized, well-defined attack

zone. Together these approaches cover a broad range of service-relevant conditions and enable systematic parameter studies [15].

Overall, degradation in flowing liquids results mainly from the combined action of electrochemical corrosion and particle-impact wear. In regions where pressure fluctuates, flow-related effects can further accelerate surface damage. For this reason, a pressurized erosion test stand must allow precise control of flow rate and pressure conditions. It should also enable adjustment of the working medium (chemistry and solids content) while keeping exposure conditions repeatable to compare materials and protective surface solutions reliably.

2. CONCEPT OF THE CORROSION-EROSION EXPERIMENTAL SETUP

2.1. Conceptual variants of the flow and test system

For the analysis of conceptual variants of the flow and test system, a common set of operating parameters was first defined based on literature data and relevant standards for liquid impact and water-spray testing. Some recommended values were slightly adjusted to suit a compact, low-pressure laboratory setup while still enabling simulation of typical corrosion–erosion conditions. The final parameter set working medium, test duration, pressure range and jet impact angle are summarised in Table 1.

Table 1. Experimental setup parameters

Parameter	Value	Impact on the process
Working medium	Brine with sand particles	Allows simulation of a corrosion–erosion environment typical of industrial practice.
Working temperature	20-25°C	Most erosion tests are carried out at room temperature.
Test duration	30 min	Typical exposure times reported in the literature range from several minutes to 24 hours, which makes it possible to reproduce long-term erosive action.
Pressure	1-5 bar	This range corresponds to low-pressure operating conditions.
Jet impact angle	45 or 90 °	These angles produce the most severe damage to the material.

Apart from selecting the operating parameters, several design considerations are equally important at the conceptual stage of the experimental setup. The hydraulic circuit must ensure reliable leak tightness through the appropriate selection of seals, connections, and assembly techniques, as any leakage may disturb the flow conditions or compromise operational safety. All components in direct contact with the working medium should be made of materials that are chemically resistant and mutually compatible in order to prevent corrosion, material degradation, or contamination of the test fluid. In addition, the test stand should provide rigid and stable specimen mounting to ensure repeatable loading conditions during testing. The design should allow for precise adjustment of the nozzle-to-specimen distance and the jet impact angle,

enabling systematic investigation of their influence on erosion–corrosion behavior. Equally important is easy access to the test section, which facilitates visual inspection, cleaning, maintenance, and rapid replacement of specimens and key components, thereby improving both usability and experimental efficiency.

2.2. Variant solutions of the experimental setup

All proposed Experimental Setups share a similar structural concept based on the adopted operating principle. Regardless of the specific configuration, the stand consists of a flow and delivery subsystem that generates and guides the liquid jet onto the specimen, and a supporting structure that provides accurate positioning and overall stability. The flow subsystem comprises the pump, nozzle, measurement section with the specimen, hoses and fittings, along with instrumentation for monitoring parameters such as pressure and flow rate, while the frame, covers and mountings ensure the required rigidity and safe operation of the setup.

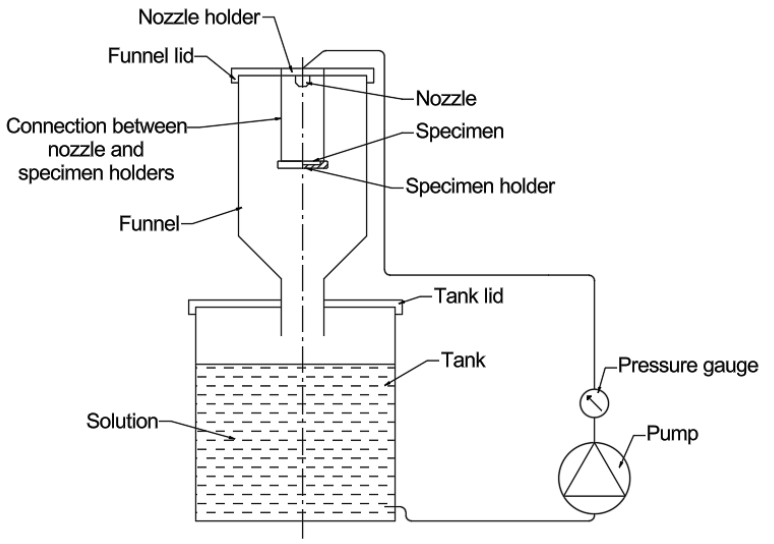

Figure 1. Experimental setup scheme - variation 1

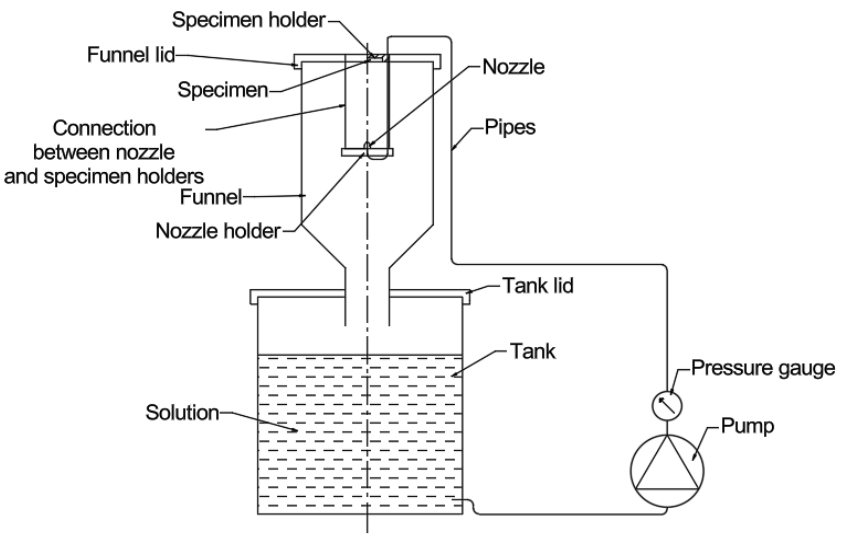

Figure 2. Experimental setup scheme - variation 2

Table 2. Comparison between proposed setup 1 and 2

Feature	Experimental Setup 1	Experimental Setup 2
Layout and assembly	The setup is vertical and has few parts. It is easy to assemble and has fewer connections that may leak.	The nozzle goes through the chamber wall. This needs an extra hole and an extra seal.
Sealing and leak risk	Good sealing is needed at the funnel–tank joint and at the covers. A leak causes liquid loss and may pull air into the loop.	There is no high-pressure line in the funnel lid. The top is easier to seal, but the side nozzle seal becomes very important.
Jet uniformity	The jet has a short distance before it hits the specimen. It may be less stable and less even.	The jet travels a longer distance inside the chamber before impact, becoming more stable and more uniform upon reaching the specimen.
Alignment sensitivity	The nozzle and specimen positions are fixed. After assembly the setup is usually repeatable.	Small misalignment changes the impact area more. The nozzle position must be set very accurately.
Particle build-up	Particles may settle in the tank and lower funnel, leading to changes in particle concentration during the test.	The piping path is shorter and has fewer sharp bends. Particles are less likely to get trapped in the piping.
Chamber wall exposure	The funnel catches splash and returns liquid to the tank. Less liquid escapes outside the setup.	Splashes may strike the chamber walls before draining, potentially increasing local wear and corrosion of the chamber.
Maintenance	Access to the specimen is limited by the narrow chamber. Changing the specimen may require partial disassembly.	Nozzle service is less convenient. The side connection must be loosened to reach the nozzle.
Aerosol and shielding	The jet can create mist. A transparent shield is recommended for safety.	The nozzle and specimen are closer to the centre. A transparent shield is easier to install.
Vibration transfer	The setup needs a stiff support. Pump vibration can shift the chamber and funnel and affect alignment.	Vibration can enter through the feed pipe at the nozzle inlet. Vibration isolation may be needed.

2.3. Selection of the preferred layout and justification

Based on the qualitative comparison presented in Table 2, Variant 1 was selected for further design. The table indicates that this concept features a simple vertical layout with fewer components and joints, which simplifies fabrication and assembly while reducing the number of potential leak points. It also eliminates the additional side-wall nozzle penetration required in Variant 2, thereby avoiding an extra critical sealing location. Furthermore, Table 2 shows that Variant 1 offers better repeatability, as the nozzle–specimen geometry is fixed and less sensitive to minor misalignment. The integrated funnel returns the liquid directly to the tank and limits splashing around the setup. Overall, the comparison in Table 2 supports Variant 1 as the optimal balance between simplicity, sealing reliability, and repeatable loading conditions.

2.4. Liquid circulation and control system of the experimental setup

The hydraulic circuit of the experimental setup is presented in Fig. 3. The working liquid is withdrawn from the tank by the pump and delivered via the piping system with tee/cross fittings and valves to the nozzle mounted in the upper part of the funnel. After impinging on the specimen, the liquid flows along the funnel wall and returns to the tank, forming a closed-loop circulation. Reconfiguration of the valves enables several operating modes within the same circuit, including the standard test mode with the full flow directed to the nozzle, as well as rinsing/flushing, drainage from the lowest point, and venting or refilling of the loop without auxiliary lines.

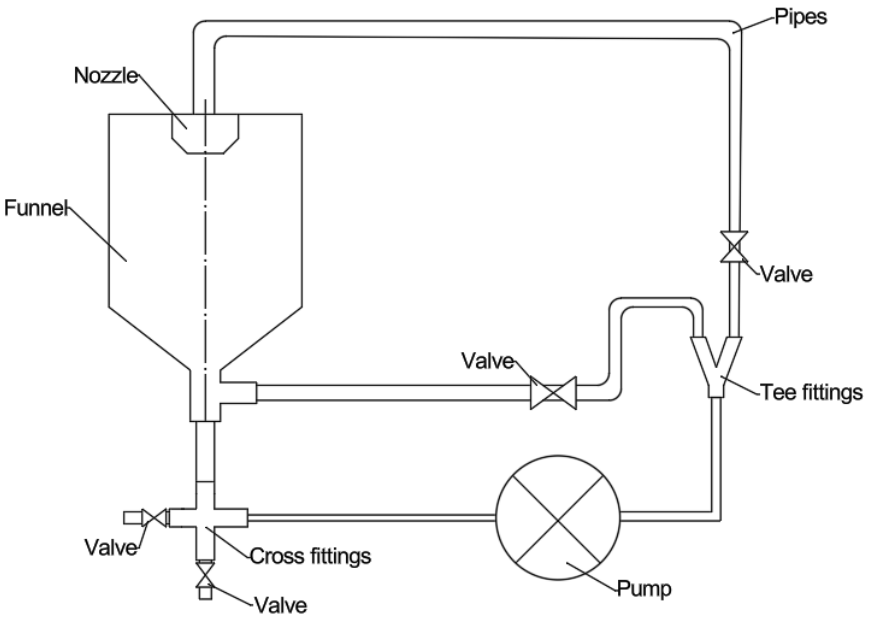

Figure 3. Schematic diagram of the liquid circulation system in the erosion experimental setup under continuous flow conditions

An additional inlet to the funnel (Fig. 3) allows tangential feeding of the liquid and generation of a swirling flow. This promotes particle suspension and limits sedimentation at the bottom of the system, which is particularly important for erosion–corrosion testing with solid-laden media. Overall, the hydraulic layout combines stable test conditions at the specimen with operational flexibility and improved maintainability (Fig. 3).

2.5. Model CAD

The experimental setup consists of a funnel-shaped base and a transparent plexiglass tube closed with a 3D-printed polypropylene top cover. The cover incorporates the spray nozzle with a protective shroud, while a specimen holder mounted underneath positions flat samples (10 × 10 × 2 mm) in the jet axis. The system operates in a closed loop: the liquid is collected in the funnel, pumped to the nozzle and directed onto the specimen surface.

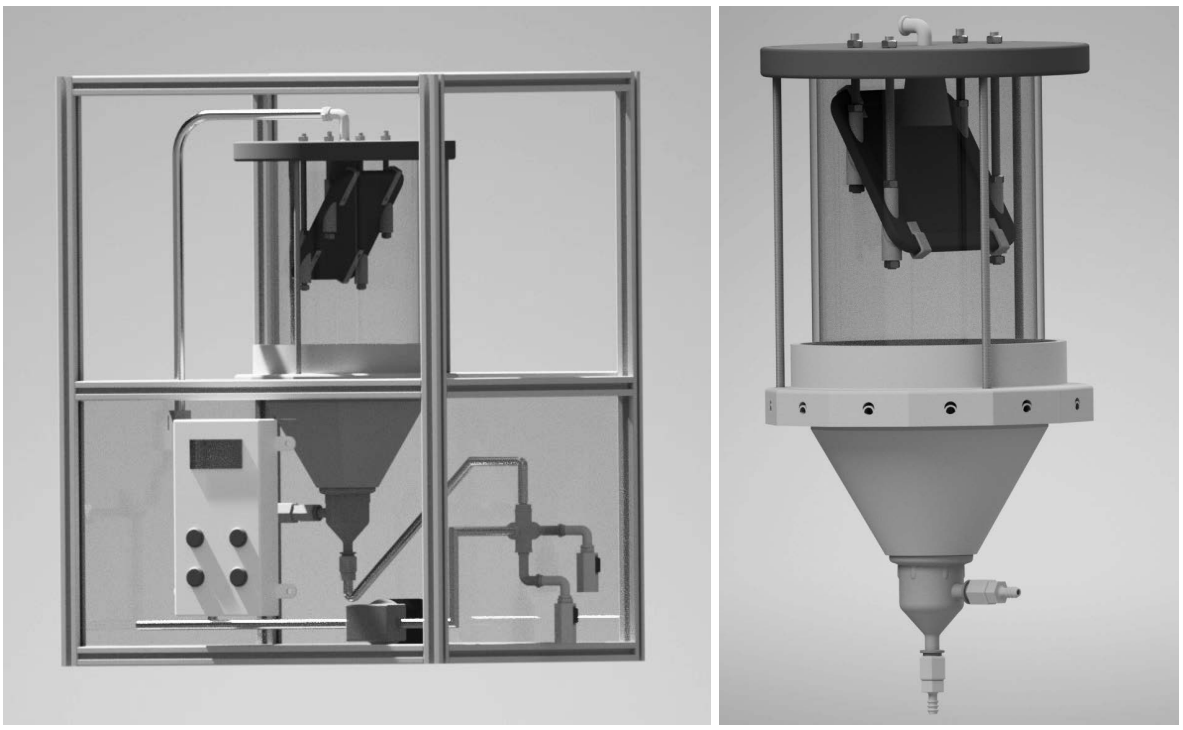

Figure 4. 3D model of the enclosure of the experimental setup for erosion investigations under continuous liquid flow

The assembled test section (Fig. 4) includes the pump, fittings and flexible hoses, with all additively manufactured parts made of polypropylene to ensure chemical resistance. The transparent tube and side panels provide visual access to the test zone for monitoring the jet and specimen surface, while the external frame and enclosure ensure mechanical stiffness and safe operation.

3. CONCLUSIONS

This work presents the concept of a laboratory experimental setup for investigating corrosion–erosion processes in materials operating under liquid flow with suspended solid particles, as commonly encountered in industrial installations. Particular emphasis is placed on the need to reproduce the coupled effects of corrosion and erosion under controlled, well-defined, and repeatable laboratory conditions, which is essential for meaningful comparison of material performance. Based on an analysis of literature data and relevant international standards, the key operating parameters of the setup were defined to reflect typical service conditions while remaining suitable for a compact laboratory-scale system. Two conceptual layout variants of the experimental setup were proposed and evaluated using qualitative design criteria. The comparison demonstrated the superiority of Variant 1, which features a simple vertical configuration, improved sealing reliability, and greater repeatability of specimen loading conditions due to fixed nozzle–specimen geometry. The system operates in a closed-loop configuration, enabling stable flow conditions and efficient use of the working medium, and includes the option of generating a swirling flow to minimize particle sedimentation during testing. In addition, a detailed CAD model of the setup is presented, illustrating a design that

ensures chemical resistance, operational safety, visual access to the test zone, and flexibility for a wide range of erosion–corrosion experiments.

BIBLIOGRAPHY

1. M. Kutz, Handbook of Environmental Degradation of Materials, Elsevier, 2013.
2. M. Bijak-Żochowski, M. Dietrich, T. Kacperski, J. Stupnicki, J. Szala, J. Witkowski, Podstawy konstrukcji maszyn, Wydawnictwo Naukowo-Techniczne, Warszawa, 1999 (in polish).
3. H. H. Uhlig, Uhlig's Corrosion Handbook, London, 1948.
4. Praca zbiorowa, Poradnik inżyniera – mechanika, vol. I, Wydawnictwo Naukowo-Techniczne, Warszawa, 1968 (in polish).
5. H. Woźnica, Podstawy materiałoznawstwa, Wydawnictwo Politechniki Śląskiej, Gliwice, 2002 (in polish).
6. L. A. Dobrzański, Materiały inżynierskie z podstawami projektowania materiałowego, Wydawnictwo Naukowo-Techniczne, Gliwice–Warszawa, 2002 (in polish).
7. M. Bichlarski, Inżynieria powierzchni, WNT, Warszawa, 2012 (in polish).
8. Japanese Industrial Standard, JIS D 0203-1994: Method of Moisture, Rain and Spray Test for Automobile Parts, Japan, 1994.
9. T. Deng, Erosive Wear Mechanisms of Materials—A Review of Understanding and Progresses, Materials 18 (2025) 2–28.
10. A. Alghurabi, A. Abduljabbar, M. A. Maoinser, A. Alqushaibi, H. Hagar, M. E. Mohyaldinn, A Systematic Review of Material Erosion Prediction Techniques: Incorporating Model Parameters Variability and the Lack of Field-Scale Representation, Results in Engineering 28 (2025) 107194
11. A. Krella, Erozja elementów maszyn przepływowych, Wydawnictwo Monograficzne Maszyny Przepływowe, IMP PAN, Gdańsk, 2019 (in polish).
12. J. Ć. M. Kućma, Metody badań odporności materiałów na zużycie ścierne i erozyjne, Instytut Materiałów Inżynierskich i Biomedycznych, Gliwice, 2017 (in polish).
13. Y. Korobov, M. Antonov, V. Astafiev, I. Brodova, V. Kutaev, S. Estemirova, M. Devyatyarov, A. Okulov, Erosion Wear Behavior of HVAF-Sprayed WC/Cr_3C_2-Based Cermet and Martensitic Stainless Steel Coatings on AlSi7Mg0.3 Alloy: A Comparative Study, Manufacturing and Materials Processing, 2024.
14. D. E. Zakrzewska, A. Krella, Cavitation Erosion Resistance: Influence of Material Properties, Sciendo, Gdańsk, 2019.
15. E. Adnane, C. Abdelouahed, S. Nawal, B. Hassan, N. Sanae, Design and Performance of a Novel Closed-Loop Erosion–Corrosion Tester, Tribology International, 2023.

TalentDetector
9th January 2026
Gliwice, Poland
DEPARTMENT OF ENGINEERING MATERIALS AND BIOMATERIALS
FACULTY OF MECHANICAL ENGINEERING
SILESIAN UNIVERSITY OF TECHNOLOGY
INTERNATIONAL STUDENTS SCIENTIFIC CONFERENCE

Assessment of applicability of continuous-wave Nd:YAG laser for heat treatment of Fe–Co–Nb–B amorphous ribbons

Oskar Węgrzyn[a], Kacper Górski[a], Jakub Otyński[a], Inez Kredowska[b], Wirginia Pilarczyk[b]

[a] Students of Silesian University of Technology, Faculty of Mechanical Engineering
email: ow303958@student.polsl.pl
[b] Silesian University of Technology, Faculty of Mechanical Engineering, Department of Engineering Materials and Biomaterials
email: inez.kredowska@polsl.pl

Abstract: In this study, the applicability of continuous-wave Nd:YAG laser processing for heat treatment of thin melt-spun Fe–Co–Nb–B amorphous ribbons was evaluated. The amorphous ribbons were produced by the melt-spinning technique and subsequently subjected to laser irradiation at different scanning speeds while maintaining constant laser power and beam diameter. Surface morphology before and after laser treatment was examined using stereoscopic microscopy. The results revealed that continuous-wave Nd:YAG laser irradiation led to excessive thermal input, causing overheating, burning, and material degradation of the ribbons rather than controlled remelting or heat treatment. For all investigated scanning speeds, no stable remelted or heat-affected zone could be obtained. The low thermal mass of the thin amorphous ribbons combined with continuous energy delivery resulted in heat accumulation exceeding the thermal stability limits of the material.

Keywords: amorphous alloys, Fe-based alloy, heat treatment, laser heat treatment, melt-spinning

1. INTRODUCTION

Amorphous materials are a special group of engineering materials that have been developed since the 1960s. The first amorphous ribbons, designed by accident by Duwez et al. [1] from an Au-Si alloy, exhibited a disordered atomic structure but underwent spontaneous crystallization overnight. Since then, research in this field has grown rapidly, expanding the range of possible elemental bases for producing metallic glasses. These materials, also known as metallic glasses, possess unique physical and mechanical properties such as high strength, excellent corrosion resistance, and superior magnetic behaviour, which make them attractive for both structural and functional applications.. From the technological point of view, to produce alloys with such amorphous structures, very high cooling rates must be applied in order to prevent crystallization [2]. Only some advanced processing technologies, such as melt spinning, splat quenching, and laser surface melting, are able to achieve the required high cooling rates on the

order of around 10^6 K/s [3]. More recently, techniques such as additive manufacturing [4] and physical vapor deposition [5] have also been explored to fabricate amorphous materials with controlled geometries and microstructures. Comparison of the most common methods were listed in Table 1. As it can be seen, though amorphous alloys can be obtained by a few different techniques, melt-spinning is the best one, especially for preliminary tests, due to its low cost and good cooling rates [6]. Though methods like thermal spraying [7] allows to have an amorphous coatings on a big surfaces, they biggest limitations are relatively high initial cost (in the term of equipment) and high volume need of input material. Porosity or oxidation problems may be solved by using proper method or applied heat treatment post-processing.

Table 1. Comparison of most common methods of obtaining metallic glasses.

Method	Typical Cooling Rates [K/s]	Typical form of product obtained	Advantages	Limitations	Lit.
Melt-spinning	10^5–10^6	Metallic ribbons, flakes, amorphous foils	Very high cooling rates; low cost; good thickness control; most researched method	Limited to thin ribbons; alloy restrictions	[6]
Thermal Spraying	10^3–10^5 (for APS) 10^3–10^6 (for HVOF)	Coatings, splats, lamellar structures	Large-area coatings; wide material flexibility	Porosity; oxidation; residual stresses; high-volume of input material (>1 kg of powder)	[7]
PVD	10^3–10^6	Thin films, multilayers, nanocoatings	High purity; precise thickness; dense films	Line-of-sight; slow for large areas; costly equipment	[5]
AM	10^3–10^5	Near-net-shape 3D components	Complex geometries; microstructure control	Residual stress; porosity; alloy limitations	[4]
APS – atmospheric plasma spraying, HVOF – high velocity oxygen fuel, PVD – physical vapour deposition, AM – additive manufacturing					

In terms of thermodynamics every alloy has a parameter called the glass-forming ability (GFA), which expresses the tendency of a material to form a non-crystalline structure during rapid cooling [8]. For every alloy, the GFA value is different, mostly because each element and each binary or multicomponent combination of elements has its own intrinsic effect on glass formation. High GFA is often associated with factors such as large atomic size mismatch, negative heat of mixing between constituent elements, and complex multicomponent systems that hinder atomic rearrangement and delay crystallization. Among the various classes of metallic glasses, Fe-based amorphous alloys have attracted particular attention due to their favourable combination of magnetic, mechanical, and economic advantages [9].

Heat treatment strongly influences the structure and performance of Fe-based amorphous alloys, and the choice between furnace annealing and laser processing leads to distinct outcomes. Furnace annealing heats the alloy uniformly at slow rates, enabling controlled structural relaxation or nanocrystallization that improves soft-magnetic properties by reducing

internal stress and coercivity [10]. However, its long thermal cycles can also cause unwanted grain growth and bulk crystallization if not carefully controlled.
Laser heat treatment, by contrast, delivers extremely rapid, localized heating with very high cooling rates [11]. This allows selective surface modification, such as mild relaxation or controlled surface nanocrystallization, while largely preserving the amorphous bulk. It is well suited for thin films and components requiring precise surface property tuning. The trade-off is that steep thermal gradients can introduce residual stresses or localized crystallization if parameters are not optimized. Comparison of both approaches are listed in Table 2.

Table 2. Comparison of heat treatment types of amorphous alloys

	Conventional Heat Treatment (Furnace Annealing)	**Laser Remelting (Laser Heat Treatment)**
Heating Rate	Slow (1–20 K/min)	Extremely high (10^5–10^8 K/s)
Temperature Distribution	Uniform throughout the sample	Highly localized to the laser interaction zone
Cooling Rate	Slow and uniform	Very rapid due to steep thermal gradients
Typical Effects on Structure	Structural relaxation or bulk nanocrystallization depending on temperature	Surface remelting, rapid solidification, minimal crystallization in the bulk
Control Over Crystallization	High risk of bulk crystallization if overheated	Crystallization limited to surface; amorphous bulk often preserved
Residual Stress Development	Low if heating is uniform	Higher risk of localized residual stresses due to thermal gradients
Suitability for Bulk vs Surface	Best for bulk treatments and overall property improvement	Best for surface modification, coatings, and thin sections
Precision/ Spatial Selectivity	Low; entire sample is heated	Very high; micrometre-scale control possible
Risk Factors	Uncontrolled crystallization, grain growth	Local cracking or stress if parameters are poorly chosen
Typical Applications	Bulk relaxation, nanocrystalline soft magnets, structural improvement	Surface hardening, surface amorphization, magnetic micro-patterning, thin-film processing

2. RESEARCH METHODOLOGY

For the research a $Fe_{66.54}Co_{16.85}Nb_{10.86}B_{5.75}$ (at. %) has been chosen. Alloy used for this article was obtained by alloying pure chemical elements: Fe (>99.9%), Co (>99.9%), Nb (>99.9%), B (>99.9%). Table 2. presented precise chemical composition for atomic and weight percentage for 100 g of material.

Table 2. Chemical composition of Fe-Co-Nb-B alloy.

	Fe	**Co**	**Nb**	**B**
% at.	66.54	16.85	10.86	5.75
% wg.	64.29	17.18	17.45	1.07

In the first stage of the process, the required elements were carefully weighed and placed into a corundum crucible, as illustrated in section (a) of Figure 1. The mixture was then melted using an induction heater under a protective atmosphere to prevent oxidation and ensure the purity of the alloy. After complete melting, the molten alloy was allowed to cool, forming solid ingots, which are shown in section (b) of the figure. Subsequently, the cooled ingots were mechanically crushed into smaller fragments, as depicted in section (c), and these fragments were then processed using the melt-spinning technique to produce thin ribbons (section (d)). During the melt-spinning process, the linear velocity of the spinner was precisely set at 30 m/s to achieve uniform ribbon formation. Finally, the ribbons were cut and prepared as test specimens with a standardized length of 50 mm, ready for subsequent experimental evaluation.

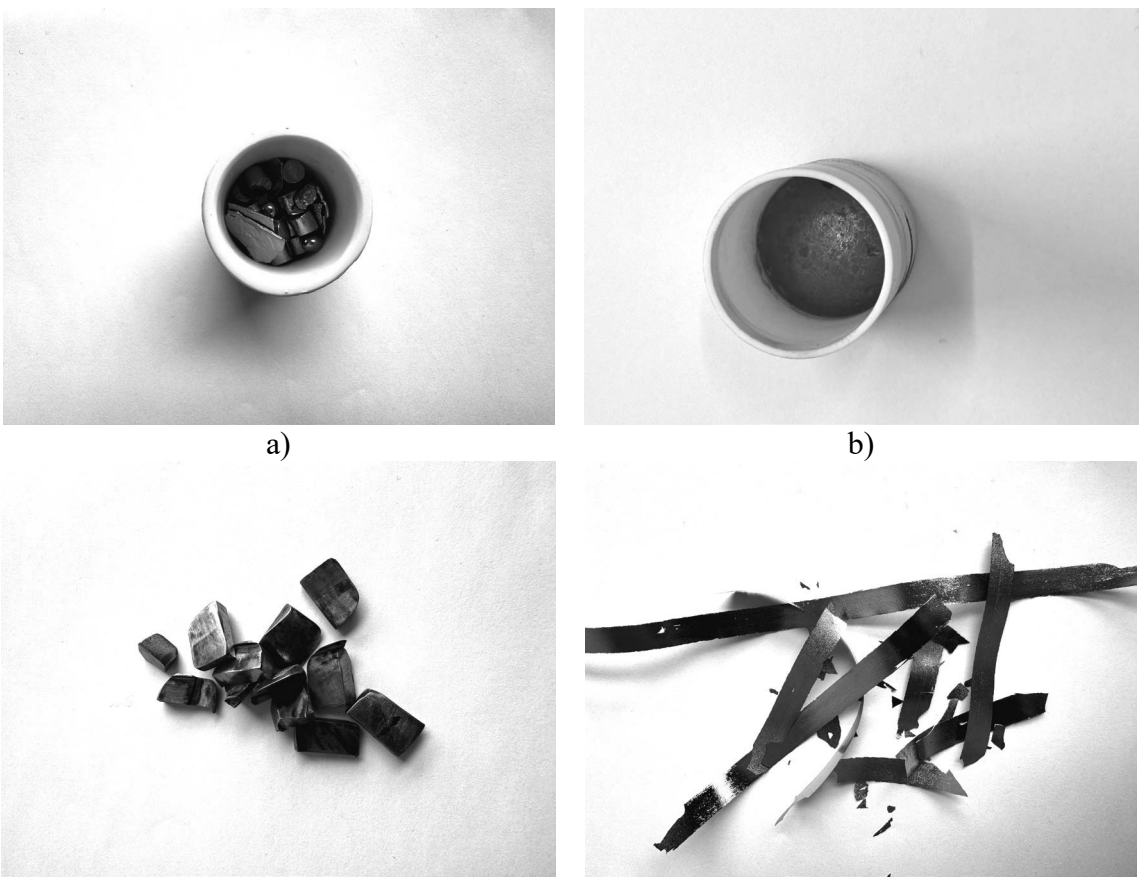

a) b) c) d)

Figure 1. Stages of ribbons preparation: a) weighted elements, b) melted ingot, c) crushed ingot, d) as-cast ribbons.

The alloy was subsequently subjected to heat treatment through laser remelting. This process was carried out using a continuous-wave Nd:YAG laser with a wavelength of 1064 nm, maintaining a constant beam diameter of 5 mm and a laser power of 400 W. The primary variable parameter was the scanning speed, which was varied in large increments to evaluate its effect on the process: V_{s1} = 5 mm/s, V_{s2} = 25 mm/s, and V_{s3} = 200 mm/s. To assess the quality of the material following laser treatment, the samples were examined using a stereoscopic microscope (SteREO Discovery, ZEISS) at magnifications of ×10, ×50, and ×100.

3. RESULTS WITH DISCUSSION

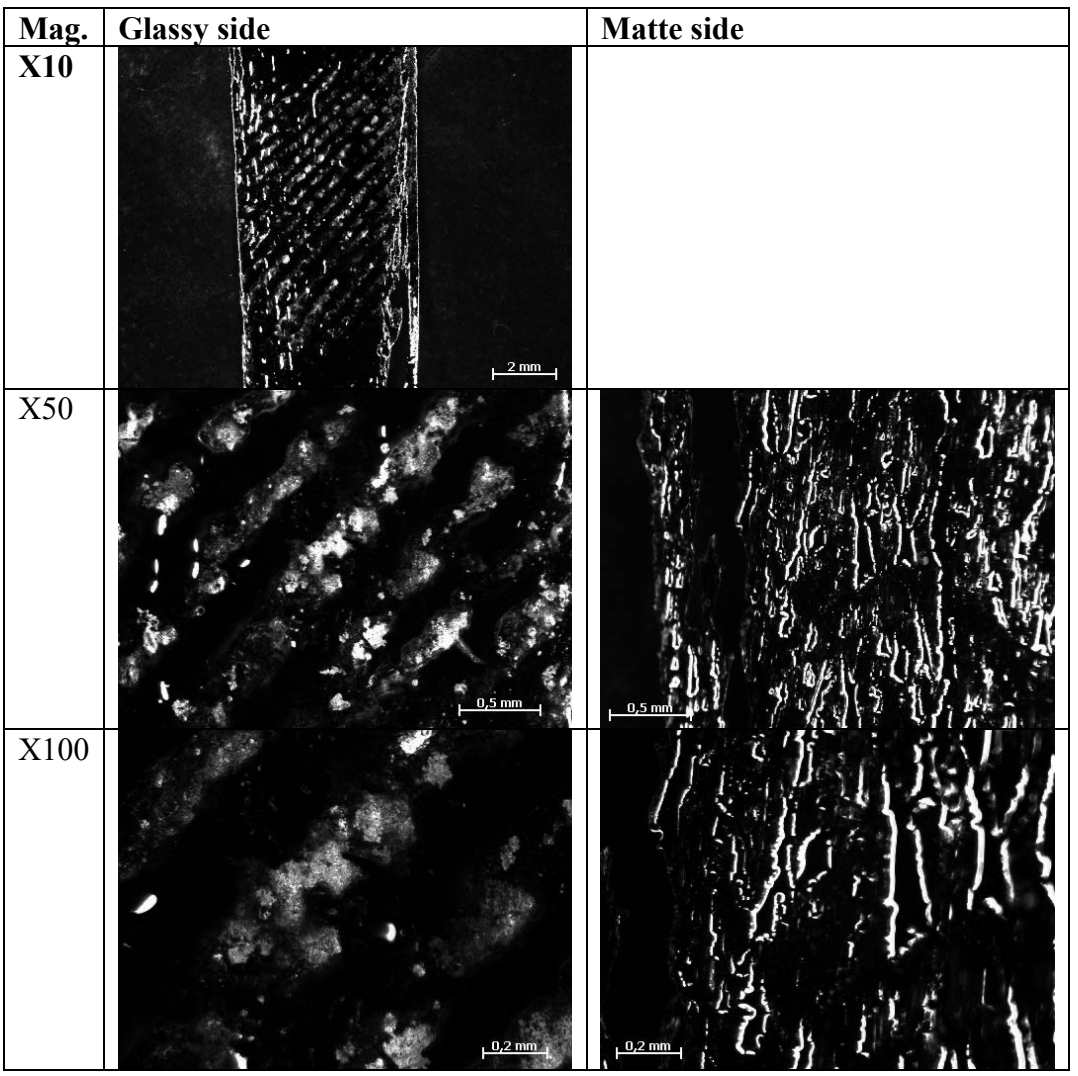

Figure 2. Stereoscopic images of as-cast ribbons.

The surface morphology of the amorphous ribbon was examined using a stereoscopic microscope at magnifications of ×10, ×50, and ×100 and showed in Figure 2. At low magnification (×10), the ribbon exhibits a clear asymmetry between its two surfaces, reflecting the different solidification conditions during melt spinning. With increasing magnification, the differences in surface topography become more pronounced. One side of the ribbon shows a relatively smooth, uniform surface with elongated, parallel features oriented along the ribbon length and strong specular reflections. This surface is identified as the glassy side, which was in direct contact with the rotating cooling wheel during rapid solidification. In contrast, the opposite side displays a significantly rougher and more heterogeneous morphology, characterized by irregular, granular features and locally varying reflectivity, which become especially evident at ×50 and ×100 magnifications. Due to the features of this side of ribbon, x10 magnification was unreadable. This surface is identified as the matte side, formed on the free surface of the melt exposed to the ambient environment. The observed morphological

differences between the glassy and matte sides are typical for melt-spun amorphous ribbons and confirm the influence of cooling conditions on surface structure.

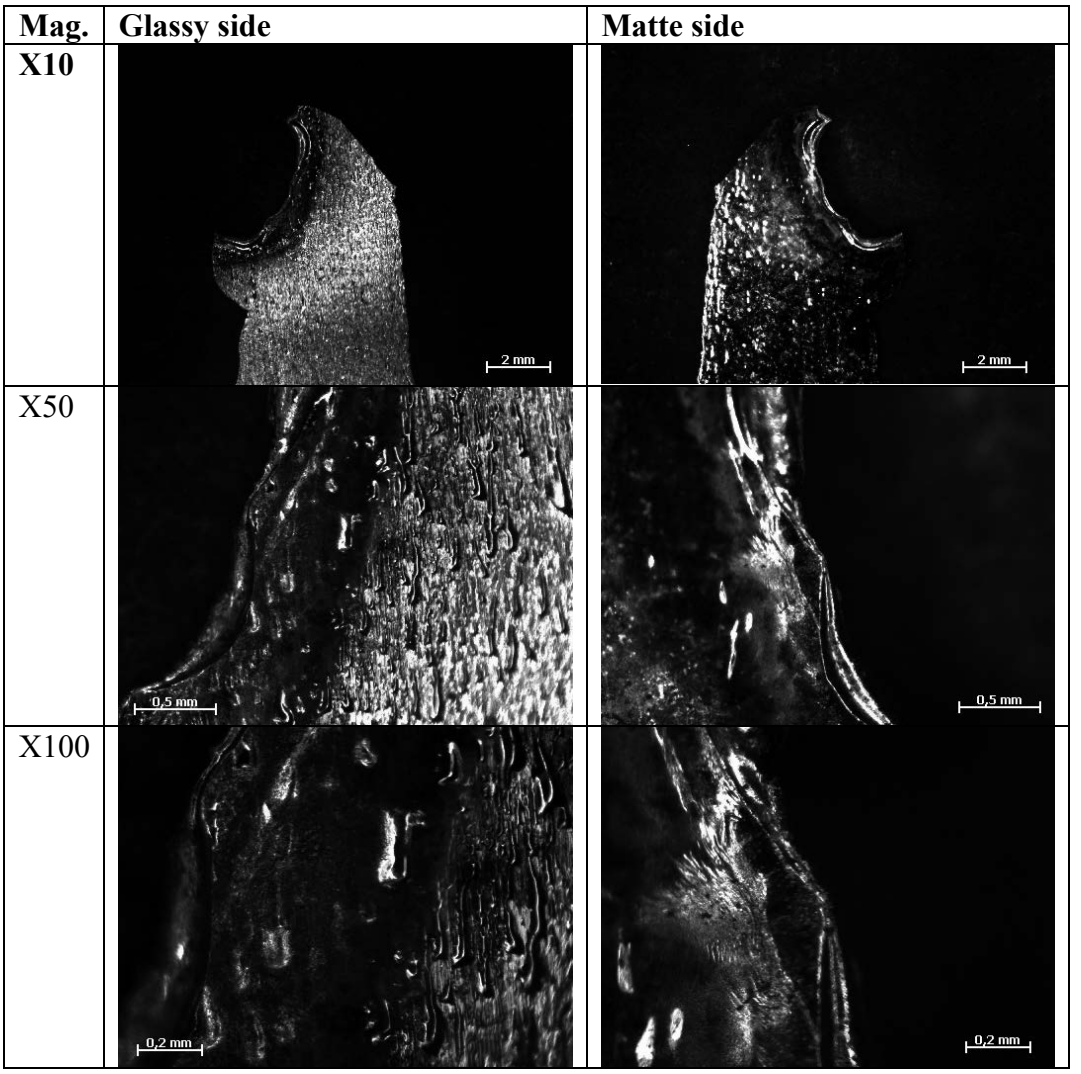

Figure 3. Stereoscopic images of ribbons after laser remelting for scanning speed of 200 mm/s.

At laser scanning speeds of 5 mm/s and 25 mm/s, the amorphous ribbon was almost completely destroyed due to excessive thermal input. Under these conditions, intense laser–material interaction led to severe overheating, burning, and material loss, preventing the formation of any stable or continuous remelted layer. The ribbon surface exhibited extensive degradation, and these processing parameters were therefore considered unsuccessful. The micrographs shown in Figure 3. correspond to the sample processed at a higher scanning speed of 200 mm/s; however, even at this scanning speed, the laser treatment did not result in proper remelting of the ribbon. Stereoscopic microscope observations reveal that the upper edge of the ribbon is characterized by irregular morphology, darkened regions, and signs of local material removal, indicating burning rather than melting. At higher magnifications, the surface remains highly heterogeneous, with sharp features and uneven resolidified areas, further confirming that the applied laser parameters led to thermal damage instead of controlled laser remelting.

Consequently, the laser processing conditions used in this study were not suitable for effective remelting of the amorphous ribbon.
In contrast, satisfactory results of laser-based heat treatment of Fe-based amorphous ribbons have been reported in the literature when pulsed laser systems were employed. In literature [12], the authors successfully induced controlled structural modifications in Fe-based amorphous ribbons using pulsed laser irradiation, which enabled precise temporal control of energy delivery and limited heat diffusion into the material. This allowed localized heating and rapid cooling, preventing extensive crystallization and thermal damage while preserving the amorphous matrix.
Similar observations were reported in different study [13], where pulsed laser heat treatment of Fe-based amorphous ribbons resulted in effective structural relaxation or partial nanocrystallization without loss of ribbon integrity. While pulsed lasers provide short, high-intensity energy input followed by rapid cooling, continuous-wave lasers deliver sustained thermal energy that accumulates in thin ribbons and exceeds the thermal stability limits of the amorphous structure. As a result, continuous-wave laser processing lacks the level of thermal control required for effective remelting or heat treatment of thin melt-spun Fe-based amorphous ribbons.

4. CONCLUSIONS

Based on experimental observations and literature analysis, it can be concluded that melt-spun Fe–Co–Nb–B ribbons exhibited the typical surface morphology of amorphous materials, confirming the correctness of the fabrication process. However, continuous-wave Nd:YAG laser irradiation led to excessive heating, resulting in burning and material loss rather than controlled remelting or heat treatment of the amorphous ribbons. Increasing the scanning speed did not prevent thermal degradation, indicating that continuous energy delivery is unsuitable for thin ribbons with low thermal mass. These results demonstrate that continuous-wave laser systems lack sufficient thermal control for effective processing of Fe-based amorphous ribbons. To achieve controlled heat treatment or surface modification, a change in laser type is necessary, with pulsed laser systems being more appropriate due to their short interaction times and limited heat diffusion.

BIBLIOGRAPHY

1. W. Klement, R. Willens, P. Duwez, Non-crystalline Structure in Solidified Gold–Silicon Alloys, *Nature* 187, 869–870, 1960. https://doi.org/10.1038/187869b0
2. D. Turnbull, Under what conditions can a glass be formed?, *Contemporary Physics*, 10(5), 473–488, 1969. https://doi.org/10.1080/00107516908204405
3. H.H. Liebermann, Rapidly solidified alloys made by chill block melt-spinning processes, *Journal of Crystal Growth*, 70(1), 497–506, 1984. https://doi.org/10.1016/0022-0248(84)90308-7
4. N. Sohrabi, J. Jhabvala, G. Kurtuldu, et al., Additive manufacturing of a precious bulk metallic glass, *Applied Materials Today*, 24, 101080, 2021. https://doi.org/10.1016/j.apmt.2021.101080

5. Q. Yang, B.Y. Wang, Z.H. Zhao, et al., Vapor-Deposited High-Entropy Metallic Glasses, *J. Phys. Chem. B*, 129(1), 456–464, 2025. https://doi.org/10.1021/acs.jpcb.4c04677
6. R. Hasegawa, Present status of amorphous soft magnetic alloys, *Journal of Magnetism and Magnetic Materials*, 215–216, 240–245, 2000. https://doi.org/10.1016/S0304-8853(00)00126-8
7. G.S. Ham, K.W. Kim, G.S. Cho, C.P. Kim, K.A. Lee, Fabrication, microstructure and wear properties of novel Fe-Mo-Cr-C-B metallic glass coating layers manufactured by various thermal spray processes, *Materials & Design*, 195, 109043, 2020. https://doi.org/10.1016/j.matdes.2020.109043
8. C. Tang, H. Zhou, Thermodynamics and the Glass Forming Ability of Alloys, *InTech*, 2011. https://doi.org/10.5772/20803
9. C. Pan, R. Zhang, D. Wang, Y. Li, T. Yamaguchi, X. Fan, D. Zhao, W. Wang, Preparation of High Performance Fe-Based Amorphous Coating by Resistance Seam Welding, *Surface & Coatings Technology*, 408, 126813, 2021. https://doi.org/10.1016/j.surfcoat.2020.126813
10. D.M. Minić, Structural transformations of $Fe_{81}B_{13}Si_4C_2$ amorphous alloy induced by heating, *Journal of Magnetism and Magnetic Materials*, 323, 400–404, 2011.
11. O. Kapustynskyi, N. Višniakov, The Influence of Heat Treatment and Laser Alternative Surface Treatment Methods of Non-Alloy Steels: Review, *Photonics*, 12, 207, 2025. https://doi.org/10.3390/photonics12030207
12. A. Radziszewska, O. Czyż, Influence of Pulsed Interference Laser Heating on Crystallisation of Amorphous Fe77Cu1Si13B9 Ribbons, *Materials*, 17(9), 2060, 2024. https://doi.org/10.3390/ma17092060
13. J. Kusinski, O. Czyż, A. Radziszewska, et al., Local crystallization in amorphous Fe80Si11B9 ribbon by pulsed laser interference heating, *Materials Characterization*, 193, 112262, 2022. https://doi.org/10.1016/j.matchar.2022.112262

TalentDetector

9th January 2026
Gliwice, Poland

DEPARTMENT OF ENGINEERING MATERIALS AND BIOMATERIALS
FACULTY OF MECHANICAL ENGINEERING
SILESIAN UNIVERSITY OF TECHNOLOGY

INTERNATIONAL STUDENTS SCIENTIFIC CONFERENCE

Generating Binary Segmentation Masks for Neural Networks using COCO Annotation Format

Jagoda Więcek[a], Julian Koterba[a], Michał Sujkowski[b], Eugeniusz Piechoczek[c]

[a] Silesian University of Technology, Faculty of Automatic Control, Electronics and Computer Science, Student Research Club vFly
[b] Silesian University of Technology, Faculty of Transport and Aviation Engineering, Student Research Club vFly
[c] Silesian University of Technology, Faculty of Transport and Aviation Engineering, Department of Air Transport, email: jw300503@student.polsl.pl

Abstract: The automation of power line and infrastructure inspection via Unmanned Aerial Vehicles generates vast amounts of data that require efficient computer vision processing. A significant bottleneck in training Neural Networks Model is the discrepancy between vector-based polygonal annotations (such as the COCO format) and the rasterized binary masks required for pixel-level computation. This paper details a methodology for converting vector COCO annotations into binary segmentation masks optimized for the YOLOv8 architecture. By implementing a pipeline that preserves the geometric integrity of high-frequency spatial details—such as thin high-voltage wires—we demonstrate effective model convergence.

Keywords: Computer Vision, Binary Masks, COCO

1. INTRODUCTION

The deployment of Unmanned Aerial Vehicles has significantly advanced the inspection of critical energy infrastructure. UAVs enable the acquisition of high-resolution imagery capturing power lines and pylons from multiple perspectives. The substantial volume of collected data renders manual analysis inefficient and necessitates automated solutions based on computer vision.

A primary challenge in training Convolutional Neural Networks for this application is data preparation. Annotators typically generate vector-based polygonal annotations using formats such as COCO (Common Objects in Context). However, neural networks require rasterized binary masks to perform pixel-level computations. This discrepancy creates a need for accurate vector-to-raster conversion. This process is particularly critical for high-frequency spatial details like thin high-voltage wires, where improper rasterization leads to aliasing or information loss.

This paper addresses the methodology of processing vector COCO annotations into binary segmentation masks for the YOLOv8 architecture. We present a pipeline that converts

polygonal coordinates into tensor inputs and validate this approach by training a model on a multi-class dataset. The objective is to demonstrate that the proposed rasterization strategy preserves geometric integrity and enables effective model convergence.

2. DATABASE

The database consists of two complementary parts: a collection of RGB images and corresponding JSON files. The images contain high-voltage power lines captured from multiple perspectives and against various backgrounds. The JSON files store detailed pixel-level information describing the location of objects, their assigned classes, and the colors associated with each class. When all this information is combined to generate a segmentation mask, the resulting image contains multiple colored regions corresponding to different object classes (see Figure 2.1).

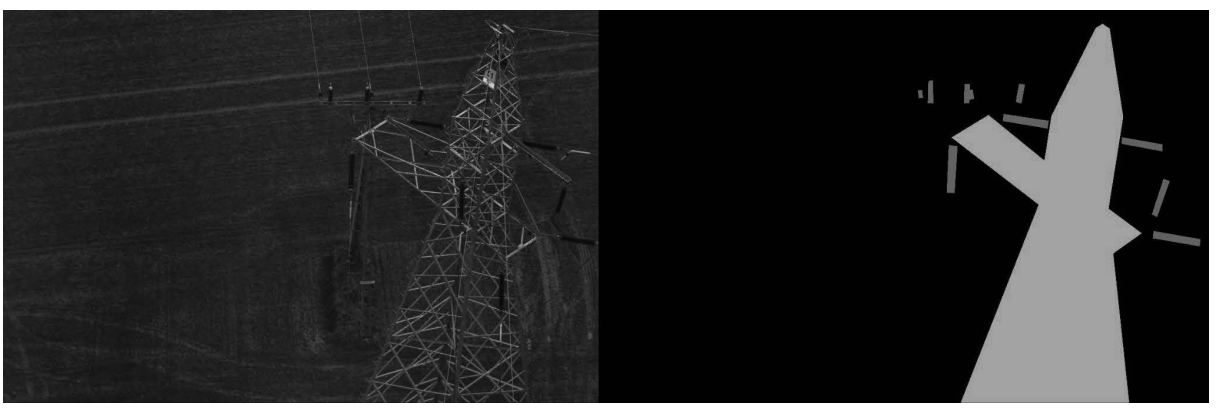

Figure 2.1 Comparison of the photo with its mask

However, for more effective learning, artificial neural network models require separate binary masks that distinguish only between the background and the object of interest. Therefore, the multi-class mask must be converted into individual binary masks, each representing a single object class.

3. COCO METHOD

Creating data in COCO (Common Objects in Context) format requires the operator to define a set of annotations for each image and save them in a single JSON file. Each annotation refers to a specific image via an identifier and provides a precise geometric description of the object. Unlike the rectangular area approach, the COCO method allows objects to be described as polygons, with their vertices stored as a sequence of coordinates in the image's pixel grid. This notation enables the object's shape to be mapped with great precision, in accordance with its actual boundaries as seen in the image. The process of creating such data typically starts with a visual analysis of the image and the manual selection of the object's contours using an annotation tool. The tool then records the user's successive clicks as points of a polygon. When the polygon is closed, it defines the area of the object. In the COCO format, these polygons are stored as a flat list of numbers, where each pair corresponds to the coordinates of a point. A

single annotation can contain several such lists, enabling the description of objects with complex shapes or holes.

4. RESULTS

To validate the effectiveness of the proposed data preparation pipeline, we conducted experiments using the YOLOv8 architecture. The model was trained on the described dataset containing 13 distinct classes of infrastructure elements. Since the generated binary masks serve as the direct supervision signal for the artificial neural network, the evaluation focuses on the model's ability to converge and generalize based on this input.
The correctness of the vector-to-raster conversion was initially validated by analyzing the training loss functions. Figure 4.1 illustrates the Segmentation Loss curve over 100 epochs.

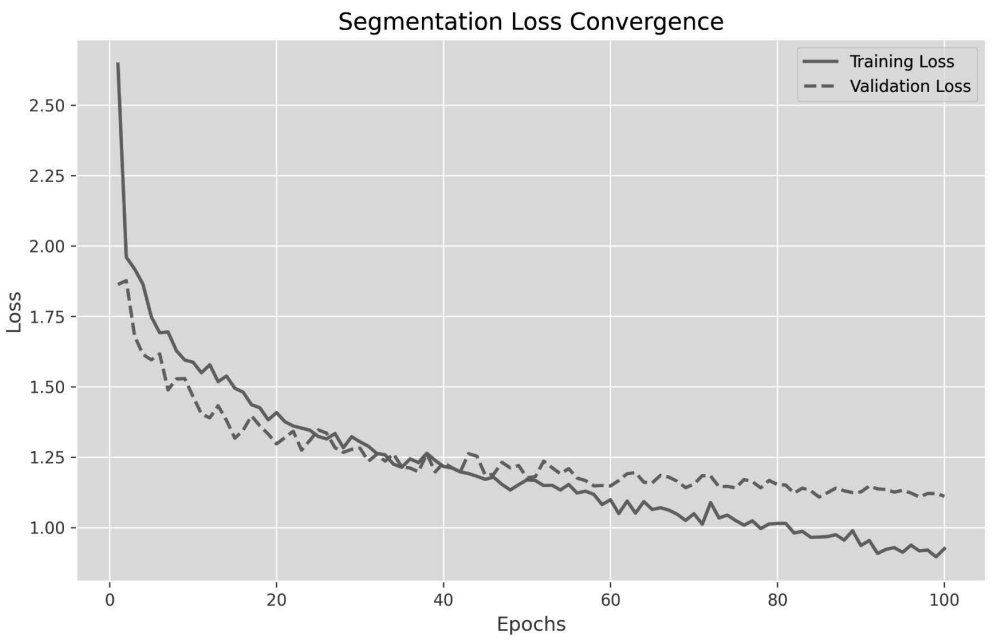

Figure 4.1 Segmentation loss convergence during training.

The segmentation loss exhibited a consistent downward trend, stabilizing around epoch 60. This convergence serves as quantitative proof that the generated masks were mathematically consistent and correctly aligned with the input images. The quality of the generated training data was further evaluated using the Mean Average Precision metric as presented in Figure 4.2.

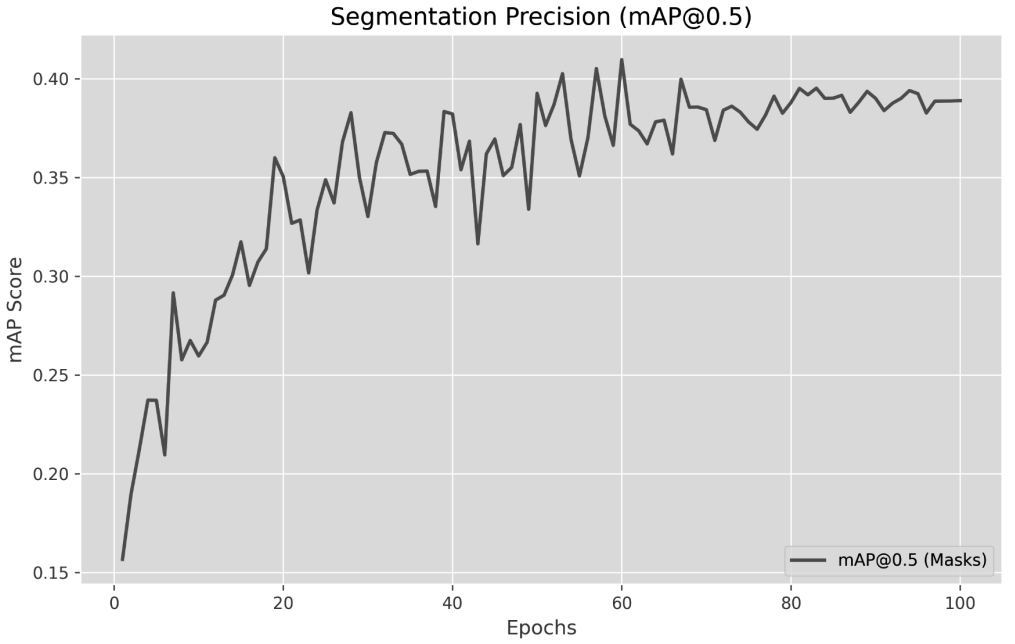

Figure 4.2 Mean Average Precision at 0.5 for segmentation masks.

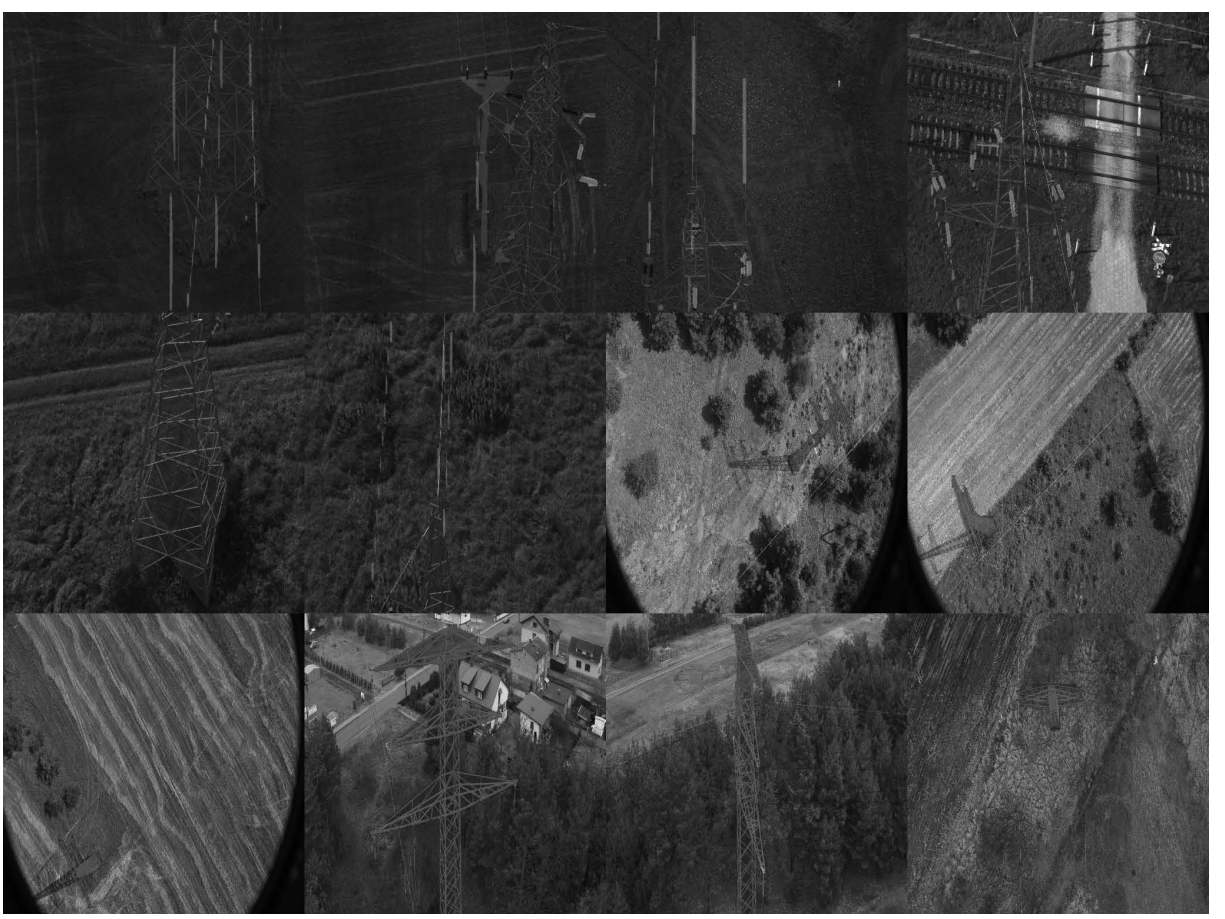

Figure 4.3 Qualitative results of the trained YOLOv8 model on the test set.

The model achieved a peak mAP score of 0.4097 (see Figure 4.2). Considering the complexity of the dataset and the presence of fine-grained wire structures, this result confirms that the bit masks generated using the COCO method are semantically correct. A high precision score would not be attainable if the input rasterization process had introduced significant artifacts. To visually confirm the utility of the approach, the trained model was tested on unseen data. Figure 4.3 displays the inference results on selected test samples.
The network successfully detects and segments multiple object classes, including thin power lines and pylons. The model's ability to accurately predict shapes on new images demonstrates that the training pipeline based on COCO vector conversion was effective.

BIBLIOGRAPHY

1. Lin, TY. et al. (2014). Microsoft COCO: Common Objects in Context. In: Fleet, D., Pajdla, T., Schiele, B., Tuytelaars, T. (eds) Computer Vision – ECCV 2014. ECCV 2014. Lecture Notes in Computer Science, vol 8693. Springer, Cham. https://doi.org/10.1007/978-3-319-10602-1_48
2. Bonechi, S., Andreini, P., Bianchini, M., Scarselli, F. (2019). COCO_TS Dataset: Pixel–Level Annotations Based on Weak Supervision for Scene Text Segmentation. In: Tetko, I., Kůrková, V., Karpov, P., Theis, F. (eds) Artificial Neural Networks and Machine Learning – ICANN 2019: Image Processing. ICANN 2019. Lecture Notes in Computer Science(), vol 11729. Springer, Cham. https://doi.org/10.1007/978-3-030-30508-6_20
3. G. Jocher, J. Qiu, and A. Chaurasia, "Ultralytics YOLO," version 8.0.0, Jan. 2023. [Online]. Available: https://github.com/ultralytics/ultralytics
4. Roverso, Davide & Nguyen, Van & Jenssen, Robert. (2018). Automatic autonomous vision-based power line inspection: A review of current status and the potential role of deep learning. International Journal of Electrical Power & Energy Systems. 99. https://doi.org/10.1016/j.ijepes.2017.12.016

TalentDetector

9th January 2026
Gliwice, Poland

DEPARTMENT OF ENGINEERING MATERIALS AND BIOMATERIALS
FACULTY OF MECHANICAL ENGINEERING
SILESIAN UNIVERSITY OF TECHNOLOGY

INTERNATIONAL STUDENTS SCIENTIFIC CONFERENCE

Analysis of the Influence of Measurement Technique on the Determination of the Critical Micelle Concentration of Ionic Surfactants with Varying Molecular Weights

Zofia Witkowska[a], Anna Mielańczyk[b], Oliwia Chojecka[b], Natalia Swoboda[b], Adrianna Hadyk[c], Szymon Siedlaczek[d], Artur Bal[e]

[a] Silesian University of Technology, Faculty of Chemistry, Department of Inorganic Chemistry, Analytical Chemistry and Electrochemistry.
email: zw301276@student.polsl.pl
[b] Silesian University of Technology, Faculty of Chemistry, Department of Physical Chemistry and Technology of Polymers
[c] Silesian University of Technology, Faculty of Energy and Environmental Engineering, Department of Environmental Biotechnology.
[d] Silesian University of Technology, Faculty of Automatic Control, Electronics and Computer Science, Department of Automatic Control and Robotics.
[e] Silesian University of Technology, Faculty of Automatic Control, Electronics and Computer Science, Department of Data Science and Engineering.

Abstract: This article presents ionic surfactants and methods for determining their critical micelle concentration (CMC). Applications of polymeric ionic surfactants are discussed, along with the advantages and limitations of direct and indirect methods for CMC determination. Particular emphasis is placed on the use of tensiometry and conductometry for CMC evaluation. In addition, factors influencing the CMC of low-molecular-weight ionic surfactants are highlighted.

Keywords: ionic polymers, ionic surfactants, surface tension, Critical Micelle Concentration, conductometry

1. INTRODUCTION

1.1 Ionic Surfactants – Definition, Classification, and Applications

Ionic surfactants are classified as amphiphilic compounds which means that they consist of hydrophilic and hydrophobic part[1]. Typically, the hydrophobic part – called a „tail" is a long hydrocarbon chain and hydrophilic part – called a „head" contain chemical individuum which can be ionized. Figure 1 shows the structure of ionic surfactants using sodium dodecyl sulfate (SDS) as an example.

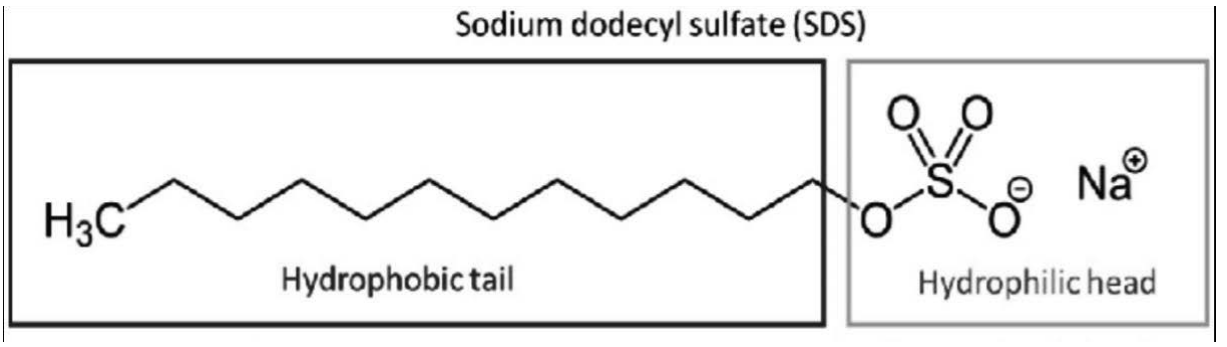

Figure 1. Example of the structure of ionic surfactant.

Ionic surfactants can be divided, among others by means of molecular mass, into two groups: low – molecular – mass (LMM) and high – molecular – mass surfactants (HMM)[2]. In Figure 2 there are a few examples of this two groups. LMM surfactants have the molecular weight between 300 and 1500 Da, while HMM surfactants (polymers) have molecular masses of up to several thousand Da[3]. This difference affects properties such as: stability, CMC or wetting values. It is worth to notice that ionic polymers are more stable and harder to remove from phase boundaries (interfaces) due to their typically multipoint and essentially irreversible adsorption. On the other hand they reduce the surface tension slower than LMM[4].

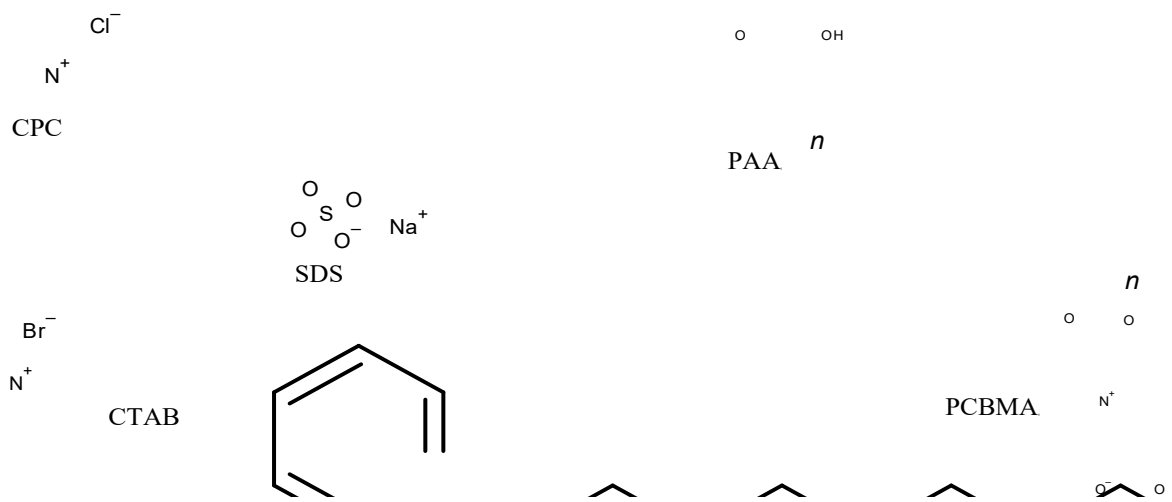

Figure 2. Examples of LMM surfactants (on the left): Cetylpyridinium chloride (CPC), Sodium Dodecyl Sulfate (SDS), Hexadecyltrimethylammonium bromide (CTAB); and HMM surfactants (on the right): Poli(acrylic acid) (PAA) and Poly(carboxybetaine methacrylate) (PCBMA).

Ionic polymers can be divided into three different classes: zwitterionic polymers, ionomers, and ionens. Examples of substances mentioned above are presented in Figure 3. Zwitterionic surfactants (inner salts) consist of main chain and the side chain where there are two groups which can be ionized. Meaning they can carry both positive and negative charge at the same time[5]. The next group, called ionomers, contains up to 8% of ionic functional groups[6]. The last mentioned are ionens. Their structure could be compared to cationic surfactants, because they are carrier of positive charge in their main chain. In most cases, the ionic groups are quaternary ammonium nitrogen groups[7].

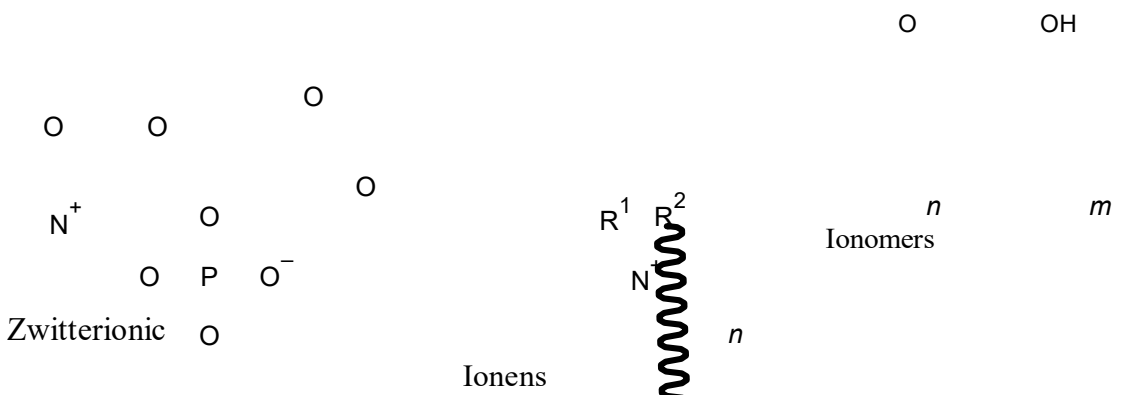

Figure 3. Structures of the ionic polymers. Zwitterionic polymers – example of phospholipids (the wavy line indicates the alkyl chain). Ionens where R^1 and R^2 indicates the alkyl chain. Ionomers – example of copolymer poly(ethylene –co–acrylic acid) (EAA).

HMM ionic surfactants are used in the food and cosmetics industry as emulsion stabilizers and viscosity modifiers[8]. Moreover, they found applications in many innovative fields such as energetic systems, environmental protection and biomedicine, shown in Figure 4. In case of energetic systems (batteries, fuel cells) they are used as a selective membranes, because they provide selective charge exchange[9]. Moreover, due to their stability, they are used as solid electrolytes in batteries, increasing the safety of the batteries. [10,11]. Electrodes also can be made from ionic surfactants. Second branch, where ionic surfactants have found their applications, is environmental protection. As it was said before, due to ability to exchange ions, ionic surfactants can be used as selective membranes. They can be used to: filter the pollution[12], desalination[13], and to treat the sewage[14,15]. The most innovative application of ionic polymers is biomedicine. Due to the ability to form a micelles, polymers bearing for example cyclodextrins can be used as a drug delivery system. They provide the controlled release of the drug in the desired place, allow to precise distribution of the medicine by increasing its bioavailability and at the same time decrease the influence of external factors[16]. Another paper describes utilization of polyelectrolytes in construction of biohybrid muscle tendon units. As a result the obtained artificial tissue allowed effective force transfer without damage to muscles. Moreover the newly engineered tissue successfully passed mechanical endurance testing, withstanding more than 7,000 contraction cycles without loss of structural integrity or functional performance [17]. Another research reports on polymers of quaternary ammonium chlorides exhibiting strong bactericidal activity while maintaining low hemo- and cytotoxicity. They are applied in dental implants and dental cements.[18].

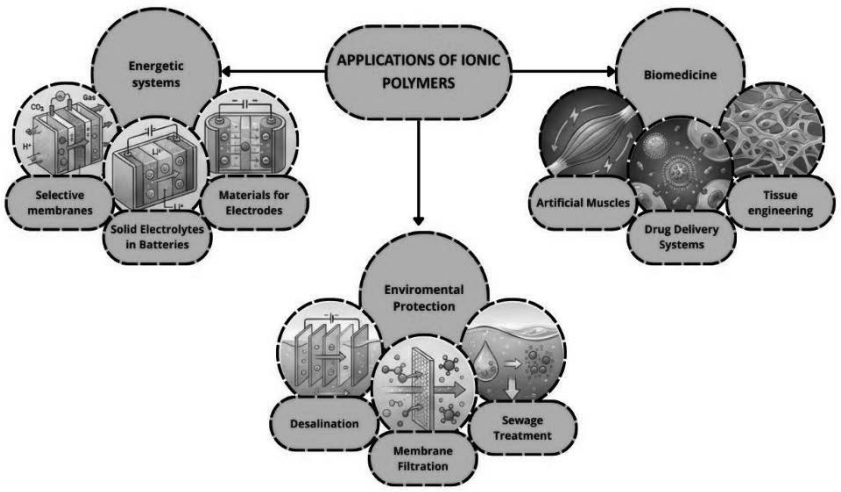

Figure 4. Applications of ionic polymers.

1.2 Critical Micelle Concentration – Direct and Indirect Methods of Determination

CMC is a concentration of a surfactant above which molecules start to organize themselves into a micelles. Near this concentration the surface tension of ionic surfactant stops decreasing, whereas the electrical conductivity stops increasing, and becomes a nearly constant line[19]. There are many methods for determining the CMC value. General path of determining the CMC value is showed in Figure 5. Three main ways of determination of CMC values for ionic surfactants were highlighted: spectroscopy (including absorbance and fluorescence measurements), conductivity and surface tension measurements. Indirect methods, such as UV–Vis spectroscopy, have limitations because they require the presence of chromophores; therefore, the addition of an low molecular weight fluorescence probe like pyrene is necessary. On the other hand there are direct methods like surface tension and conductivity which are strictly connected with observation of changes in physical properties. Another advantages of direct methods are the high reproducibility, low cost of the measurement and relatively easy procedures of sample preparation[20].

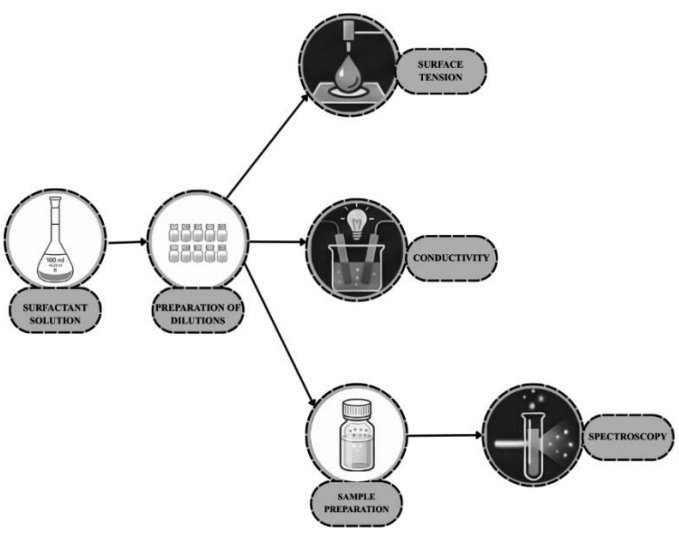

Figure 5. Possible path to determine the CMC of an ionic surfactant solution.

The self-assembly of ionic surfactants into micelles is accompanied by changes in surface tension of their solution. Typically, surface tension (or its base-10 logarithm) is plotted versus surfactant concentration. With the increasing concentration of the surfactant in aqueous solution the characteristic shape of the curve is observed (Figure 6a). The point of the intersection of the two curves determines the CMC value[19].

Another direct method for CMC determination involves monitoring changes in the electrical conductivity of an ionic surfactant solution. As depicted in Figure 6b, at first conductivity curve is linear due to the fact that monomers have the character of simple electrolytes. Further the curve takes non – linear shape due to micelle formation[19].

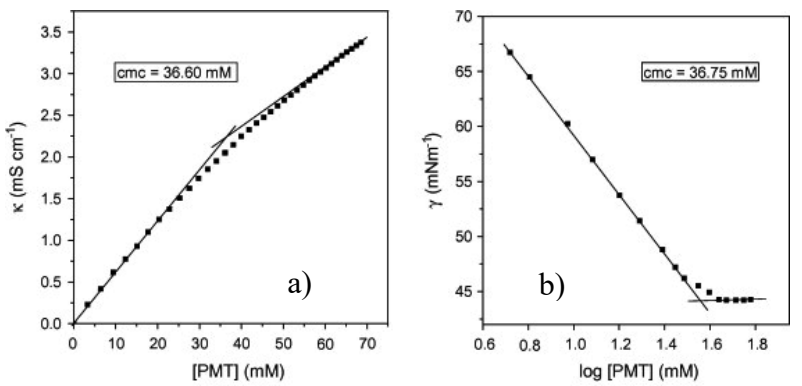

Figure 6. CMC curves determined by a) conductometer and b) tensiometer. Intersection of two lines determine the CMC values. CMC was determined on Promethazine hydrochloride (PMT)[21]

2. CHARACTERISATION OF IONIC SURFACTANTS

Table 1 presents a comparison of selected methods used for the determination of the CMC of an exemplary ionic surfactants. In addition to the applied method and the determined CMC values, the table also includes the molecular weight of the surfactants and examples of their practical applications. This comparison highlights the diversity of analytical approaches and the influence of surfactant structure on both CMC values and application areas.

Table 1. Popular surfactants with molecular masses and their CMC

Compound	CMC Value (mM)	Determination Method	Molecular Weight (g/mol)	Applications
NaC (Sodium Cholate)	14.02 [22]	Tensiometry	430.6	Solubilization and absorption of fats, drug delivery systems, protein purification.
NaDC (Sodium Deoxycholate)	5.53 [22]	Tensiometry,	414.6	Enhancing drug transport across biological barriers, pharmaceutical formulations, chromatographic separation.

Table 1. Popular surfactants with molecular masses and their CMC

Compound	CMC Value (mM)	Determination Method	Molecular Weight (g/mol)	Applications
DTAB (Dodecyltrimethyl-ammonium Bromide)	~16.0 [23]	Tensiometry	308	Cationic surfactant used in fragrances, personal care, and cosmetic products.
SDS (Sodium Dodecyl Sulphate)	~8.0 [23] 8.0 [24] 8.4 [25]	Tensiometry	288	Detergents, cosmetics.
	8,18[26] 8.1 [24] 8.4 [25]	Conductivity		
DDS (Sodium-N-dodecanoyl sarcosinate)	6.19 [27]	Tensiometry	293.38	Toothpaste component (dental caries control), low toxicity emulsions, and biodegradable detergents.
SDBS (Sodium Dodecyl Benzenesulfonate)	0.77 [27]	Tensiometry	348.48	Detergents, model lipid systems, and research on protein fibrillation (e.g., insulin).
CTAB (Cetyltrimethyl -ammonium Bromide)	0,99 [28]	Tensiometry	364.45	DNA extraction, anti – static.
	0.93 [26] 1.00 [28]	Conductivity		
CHAPS (3-((3-cholamidopropyl) dimethylammonio)-1-propanesulfonate)	5.80 [26]	Conductivity	614.88	Detergent for the solubilization of receptor-binding sites.
TTAB (Tetradecyltrimethylammonium Bromide)	3.7 [28]	Tensiometry	336.39	Nano – building blocks in polymers synthesis.
	3.8 [28]	Conductivity		
CPC (Cetylpyridinium Chloride)	0.99 [28]	Tensiometry	339.99	Used in oral hygiene products.
	1.2 [28]	Conductivity		
CPB (Cetylpyridinium Bromide)	0.9 [28]	Tensiometry	384.44	Used as disinfectant in mouthwashes.
	0.9 [28]	Conductivity		

As presented in Table 1, surfactants may differ in their CMC values. The main factors influencing these differences include::

- hydrophobic alkyl chain length;
- nature and structure of the polar head group;
- position of the polar group;

- type of counterion;
- addition of salts;
- presence of organic impurities;
- temperature;
- pressure [5,19]

3. CONCLUSIONS

CMC is a very important factor in context of describing a surfactant. It indicates where the surfactant can find its application. Sources describes also usage of HMM surfactants in innovative medicine, environmental protection and electrical sources. Yet there are not many examples of CMC determination for HMM surfactants. Direct methods for determining the CMC of ionic surfactants, such as conductivity measurements and surface tension measurements, are gaining importance due to their simplicity, low cost, and broad applicability. Unlike certain spectroscopic methods, these techniques do not require the addition of a low molecular weight fluorescent probe, making them universal and suitable for a wide range of ionic surfactants The CMC values differ, which is associated with the applied measurement method and the influence of external factors such as temperature or presence of organic impurities. Determination of CMC for ionic surfactants is effectively achieved through conductivity, which provides a clear breakpoint at the intersection of two linear segments on equivalent conductivity plots. In contrast, the surface tension method acts as an exceptionally sensitive tool for assessing sample purity, as the presence of organic contaminants typically induces a characteristic minimum on the concentration-dependent curve. It is necessary to continue the research of determining the CMC in polymeric ionic surfactants due to indications of their applications.

ACKNOWLEDGMENTS

The research was financially supported by the PBL „Analiza wpływu techniki pomiarowej na wyznaczanie krytycznego stężenia micelizacji jonowych surfaktantów o zróżnicowanej masie cząsteczkowej''.

LITERATURE

[1] P. Matějíček, *Curr. Opin. Colloid Interface Sci.* **2020**, *45*, 97.
[2] E. Rosenberg, E. Z. Ron, *Appl. Microbiol. Biotechnol.* **1999**, *52*, 154.
[3] Natural Surfactants and Biosurfactants, In *Surfactant Science and Technology*, John Wiley & Sons, Ltd, **2020**, pp. 75–91.
[4] Special Topics in Surfactant Applications, In *Surfactant Science and Technology*, John Wiley & Sons, Ltd, **2020**, pp. 323–367.
[5] The Classification of Surfactants, In *Surfactant Science and Technology*, John Wiley & Sons, Ltd, **2020**, pp. 17–59.
[6] EMAC - Jonomer E/MA [EMAC] - Baza Tworzyw - Wiedzopedia - Tworzywa Sztuczne – Vortal TWORZYWA.PL, .
[7] Polimery jonowe: wybrane aspekty budowy i właściwości, .

[8] Polymeric Surfactants and Surfactant–Polymer Interactions, In *Surfactant Science and Technology*, John Wiley & Sons, Ltd, **2020**, pp. 205–224.
[9] S. Lee, Y. E. Choi, J. Y. Lee, T. Yang, J. Y. Jho, J. H. Park, *J. Ind. Eng. Chem.* **2023**, *122*, 79.
[10] Q. Zhao, S. Stalin, C.-Z. Zhao, L. A. Archer, *Nat. Rev. Mater.* **2020**, *5*, 229.
[11] P. C. Dhanush, **2026**.
[12] E. Richard, K. Fatyeyeva, S. Marais, *Chem. Eng. J.* **2025**, *505*, 158916.
[13] J. H. Park, E. Fontananova, F. Galiano, A. Figoli, R. Mancuso, B. Gabriele, T. K. Lee, C. H. Park, E. Tocci, S. Y. Nam, *Desalination* **2026**, *617*, 119434.
[14] S. Basri, D. Shee, T. K. Panda, D. Bhattacharyya, *J. Environ. Chem. Eng.* **2025**, *13*, 118634.
[15] H. Ben Hamed, M. Mainardis, A. Moretti, D. Toye, A. Léonard, *J. Environ. Manage.* **2025**, *376*, 124407.
[16] E. Kashani, S. Maghsoudi, H. Rezania, M. Yarazavi, M. Hajiabbas, G. Benkovics, E. Bilensoy, I. Lacík, A. Heydari, *Mater. Today Chem.* **2024**, *39*, 102186.
[17] N. Castro, R. Heisser, M. Bawa, B. Aymon, S. Wu, A. Marschner, S. Kohli, A. Bu, L. Rosado, M. Culpepper, X. Zhao, R. Raman, *Adv. Sci. n/a*, e12680.
[18] N. Kula, E. Mazurkiewicz, E. Obłąk, *Postępy Hig. Med. Dośw.* **2020**, *74*, 556.
[19] R. Zieliński, *Surfaktanty. Budowa, właściwości, zastosowania*, Wydawnictwo Uniwersytetu Ekonomicznego w Poznaniu, Poznań, **2000**.
[20] K. Nesměrák, I. Němcová, *Anal. Lett.* **2006**, *39*, 1023.
[21] M. A. Rub, A. M. Asiri, J. M. Khan, R. H. Khan, Kabir-ud Din, *J. Mol. Struct.* **2013**, *1050*, 35.
[22] R. Sharma, S. Chauhan, K. Kumar, *J. Mol. Liq.* **2025**, *419*, 126825.
[23] O. A. Soboleva, E. A. Gryzunova, L. A. Tsarkova, *Colloids Surf. Physicochem. Eng. Asp.* **2023**, *676*, 132119.
[24] M. K. Mandal, M. Barai, H. Sultana, E. Manna, D. Musib, D. K. Maiti, A. K. Panda, *J. Oleo Sci.* **2021**, *70*, 185.
[25] D. Das, K. Ismail, *J. Colloid Interface Sci.* **2008**, *327*, 198.
[26] Y. Chenyakin, D. D. Y. Chen, *ELECTROPHORESIS* **2025**, *46*, 990.
[27] S. Das, P. Roy, P. S. Sardar, S. Ghosh, *Int. J. Biol. Macromol.* **2024**, *271*, 132368.
[28] R. K. Banjare, M. K. Banjare, S. Panda, *J. Solut. Chem.* **2020**, *49*, 34.

TalentDetector

9th January 2026
Gliwice, Poland

DEPARTMENT OF ENGINEERING MATERIALS AND BIOMATERIALS
FACULTY OF MECHANICAL ENGINEERING
SILESIAN UNIVERSITY OF TECHNOLOGY

INTERNATIONAL STUDENTS SCIENTIFIC CONFERENCE

Surface Modification of Advanced Bainitic Steels: A Comprehensive Review

Frederico Murilo Wlassak[a*], Mario Wolfart Júnior[b], Thiago Marques Ivaniski[a], João Vitor P. Dalla Nora[a], Felipe Canal[a], Morvan Silva Franco[a], Alexandre da Silva Rocha[a]

[a] Universidade Federal do Rio Grande do Sul (UFRGS), Laboratório de Transformação Mecânica (LdTM)
[b] Instituto Federal de Educação, Ciência e Tecnologia Catarinense *campus* Luzerna (IFC – Luzerna), *e-mail: frederico.wlassak@ufrgs.br

Abstract: This review examines the effects of combined shot peening, plasma nitriding and post-oxidation on the mechanical, tribological and corrosion performance of advanced continuously cooled bainitic steels. These steels can achieve high strength and toughness without the need for subsequent heat treatments after hot deformation, representing an energy-efficient alternative for industrial applications. The hybrid treatment route integrates the benefits of each individual process: near-surface work hardening and compressive residual stresses induced by shot peening; nitrogen diffusion and compound-layer formation provided by plasma nitriding, followed by the development of a compact magnetite film through controlled post-oxidation. Literature analysis shows that this combined approach had a synergistic effect: significantly improve wear resistance, fatigue performance and corrosion protection compared to isolated treatments.

Keywords: shot-peening, plasma-nitriding, post-oxidation.

1. INTRODUCTION

Modern manufacturing increasingly demands techniques capable of meeting strict requirements for productivity, quality, and durability, as components across numerous industrial sectors are routinely exposed to severe thermal and mechanical loads that promote accelerated wear. As performance expectations rise, materials with high strength, thermal stability, and reliable in-service behavior have become essential, since inadequate material performance shortens component lifespan and leads to unplanned downtime, higher maintenance costs, and reduced production efficiency. At the same time, growing concerns regarding energy consumption and environmental impact have driven interest in more sustainable processing routes. In this context, continuously cooled bainitic steels emerge as an attractive alternative, eliminating the need for energy-intensive reheating and quenching and tempering cycles after forging while still providing excellent mechanical properties and microstructural homogeneity. This simplified processing route not only improves the energy efficiency of the manufacturing chain

but also may reduces CO_2 emissions and resource consumption, aligning with modern sustainability goals [1].

Despite the favorable bulk properties of bainitic steels, many engineering applications still require improved surface performance, particularly regarding wear resistance. Plasma nitriding has been successfully applied to these alloys [2], showing no significant reduction in core hardness for treatments carried at temperatures below 500 °C [3]. Plasma nitriding is a thermochemical diffusion process in which nitrogen is incorporated into the surface of the material, forming hard, wear-resistant layers. It is widely recognized as one of the most effective treatments for enhancing fatigue strength and wear resistance in steels [4].

Nevertheless, the characteristics of the nitrided layer, such as thickness, phase composition, ductility, and load-bearing capacity, may still fall short of the requirements for highly demanding applications. To overcome these limitations and further extend the performance of nitrided components, complementary pre- and post-treatments have increasingly been explored [5]. Among these, shot peening is a well-established mechanical surface treatment that introduces beneficial compressive residual stresses and promotes near-surface work hardening, resulting in substantial improvements in fatigue life and fretting-fatigue resistance [6].

Completing the combined treatment sequence, a controlled post-oxidation step performed immediately after plasma nitriding constitutes the final stage of the process. This step produces a thin oxide layer composed predominantly of magnetite (Fe_3O_4) and, to a lesser extent, hematite (Fe_2O_3), depending on the temperature, duration, and redox conditions applied. The preferential formation of magnetite is particularly desirable because it enhances the tribological and anticorrosive performance of the surface. A thin magnetite-rich layer on nitrided parts can enhance surface properties by providing a lower coefficient of friction, self-lubricating behavior, higher chemical stability, and substantially improved corrosion resistance in humid, saline, or mildly acidic environments [7].

2. MATERIAL AND SURFACE TREATMENT PROCESSES

In recent years, combined surface treatments have emerged as an effective strategy to enhance the performance of high-strength steels. Strategies integrating mechanical processes such as shot peening with thermochemical diffusion techniques like plasma nitriding, followed by controlled post-oxidation, have shown synergistic improvements in fatigue, tribological behavior, and corrosion protection. These hybrid routes exploit the individual advantages of each process, near-surface work hardening and compressive residual stresses from shot peening, hardness gradient from nitrogen diffusion, and the development of protective magnetite layers through post-oxidation [8, 9].

2.1. Material selection

Advances in steel production, particularly through microalloying additions and strict control of heating, rolling, and cooling parameters, have enabled the development of microstructures capable of achieving excellent mechanical properties without the need for post-deformation heat treatment, provided that strength and thickness requirements fall within appropriate limits [10]. This approach, known as thermomechanical processing, integrates deformation and heat treatment into a single controlled processing route, allowing precise manipulation of the microstructure and significant improvement of mechanical performance during hot deformation [11]. Within this context, the new generation of bainitic steels formed during continuous

cooling can develop diverse bainitic morphologies, such as granular bainite, upper bainite with lath structures, and lower bainite, while also potentially containing retained austenite and ferrite [12]. Unlike Q&T steels, which require additional heat treatment to achieve service-ready properties, continuously cooled bainitic steels exhibit high strength and toughness directly after hot rolling or forging, eliminating the need for further thermal processing. This results in a shorter manufacturing cycle and lower production costs, making these steels promising candidates for efficient industrial production [13].

2.2. Shot Peening prior to nitriding

Shot peening relies on the material's ability to undergo localized plastic deformation caused by the impact of small steel spheres (shots). During the process, the surface is repeatedly impacted, which increases surface hardness, roughness, and the magnitude of compressive residual stresses. In addition, the successive impacts promote grain refinement in the surface and subsurface regions of the material [14].

Building on these deformation-induced effects, previous studies have shown that radio-frequency plasma nitriding of stainless steel combined with a high-pressure torsion pre-treatment significantly increases the nitrided layer thickness and surface hardness due to the transformation of coarse grains into an ultra fine structure [15]. A comparable improvement was observed when shot peening was applied prior to plasma nitriding [16], where the combined effects of increased dislocation density and the strain-induced transformation of austenite into martensite enhanced nitrogen diffusion. In AISI 304 stainless steel, shot peening produced severe near-surface deformation, resulting in nitrided layers up to twice as thick and with deeper hardness penetration compared to untreated specimens under the same conditions [17]. Similar benefits were also reported for 316L steel, in which shot peening prior to gas nitriding improved both wear resistance and corrosion behavior [6].

Taken together, these studies generally focused on enhancing the nitrogen diffusion rate and reported that nitriding efficiency was improved by a shot peening pre-treatment. In addition to diffusion-related effects, several investigations examined the combined influence of shot peening and nitriding on the fatigue properties of materials. Their findings indicated that fatigue strength was increased by the shot peening plus plasma nitriding treatment, primarily due to the formation of a deeper hardened case, higher compressive residual stresses, and increased surface hardness. However, despite the extensive literature addressing the tribological properties of plasma-nitrided materials alone, the effects of shot peening and combined shot peening and plasma nitriding on tribological behavior have been examined in only a limited number of works [18].

2.3. Plasma nitriding

Plasma nitriding is a diffusional process in which nitrogen is introduced to enhance wear resistance and component lifespan, forming modified surface layers without dimensional changes. Surface hardening results mainly from precipitation hardening, since the solid-solution effect of interstitial nitrogen is relatively small. After nitrogen saturation, high-hardness compounds form through reactions with iron or alloying elements. In commercial applications, the modified layer typically reaches 200–300 μm [19].

During plasma nitriding, a compound layer of ε($Fe_{2–3}N$) and/or γ'(Fe_4N) forms at the surface, followed by a thicker diffusion zone beneath it. The temperature and nitriding time strongly influence nitrided layer characteristics, as well as by the chemical composition, initial

microestructure, and core hardness of the treated part. Depending on the gas mixture, the compound layer may form or be intentionally suppressed [20].
Both the compound layer and the diffusion zone are governed by process parameters and by nitrogen diffusivity, which is strongly affected by the steel's grain structure and composition. While the compound layer mainly improves tribological and anticorrosive properties, the diffusion zone dictates mechanical performance through its hardness and depth [20]. Podgornik et al. [21] emphasize that the extent of improvement also depends on microstructure and residual stress distribution, making residual stress analysis essential for optimizing surface treatments.
The hardness of the compound layer is unaffected by carbide-forming elements because it consists of ε($Fe_{2-3}N$) and/or γ'(Fe_4N) iron nitrides. Low nitrogen concentrations (≈30 wt.% or lower) favor the formation of the γ' phase, which exhibits lower hardness and wear resistance but greater toughness, making it suitable for impact-loaded components. In contrast, nitrogen-rich atmospheres (above 60 wt.%) promote the formation of the ε phase,which offers higher hardness and improved wear and fatigue resistance, at the cost of reduced impact resistance [20].

2.4. Post Oxidation

Nitriding treatments are traditionally employed as a solution for reducing wear due to the significant increase in surface hardness they provide. However, there are applications that demand exceptionally high performance, in which nitriding alone is not sufficient [22]. Moreover, nitriding by itself does not significantly improve other properties, such as the corrosion resistance of low-alloy steels, and may even depending on the process conditions, reduce performance by accelerating localized corrosion [22].
Oxidized surfaces can be used as solid lubricants to promote friction reduction and as passivating layers with excellent anticorrosive properties. However, materials that exhibit only an oxidized surface layer do not show effective resistance to abrasive wear [23].
The combination of nitriding with post-oxidation merges the wear resistance provided by nitriding with the enhanced anticorrosive and friction-reducing properties resulting from oxidation. Several references have reported that performing post-oxidation treatments on nitrided samples is a critical factor for achieving adequate corrosion resistance. Owing to its low friction coefficient and good chemical stability, the formation of a magnetite (Fe_3O_4) layer is particularly desirable for improving the tribological and anticorrosive performance of oxidized surfaces. Therefore, treatment parameters must be carefully selected to favor the formation of this phase [24].

3. COMBINED SURFACE TREATMENTS

In modern manufacturing chains involving multiple thermal and mechanical stages, the careful selection and combination of surface modification techniques is essential to ensure high fatigue and wear performance while avoiding the introduction of undesirable characteristics [25]. The use of multi phase microstructures in advanced steels further expands the range of achievable mechanical properties, enabling tailored combinations of strength and ductility, while forging routes based on continuous-cooling bainitic steels present an energy-efficient alternative to conventional quenching and tempering by eliminating reheating steps [26]. Within this context, the present study highlights the significant potential of applying shot peening prior to plasma

nitriding. This combined approach enhances microstructural refinement and creates more effective diffusion pathways, thereby improving the formation and performance of nitrided layers, increasing resistance to wear, corrosion and fatigue, and extending component lifespan. Previous studies have shown that the initial surface state strongly influences nitrided layer development, reinforcing that integrating shot peening before nitriding can be more effective than plasma nitriding alone [20].

Table 1 presents the surface residual stresses of plasma-nitrided samples and of samples treated by combined shot peening and plasma nitriding. As expected, plasma nitriding alone generates compressive residual stresses on the surface, with values of approximately −380 MPa for 500 °C–1 h and −430 MPa for 500 °C–4 h treatments [18]. When shot peening is applied prior to nitriding, these stresses increase further due to the combined effects of near-surface plastic deformation and nitrogen diffusion. While plasma nitriding contributes to compressive stress through nitride formation, shot peening induces lattice distortion to a certain depth, generating additional compressive stress. The synergy of both processes therefore enhances the residual stress profile more effectively than either treatment alone [18].

Studies have shown that shot peening induces surface defects, increases dislocation density, and generates new grains/sub-grains, which create additional diffusion pathways for nitrogen and lower the activation energy for its diffusion, thereby enhancing nitriding kinetics [27]. This effect is more significant than increasing the nitriding temperature, which may cause stress relaxation even during high-temperature plasma nitriding [28].

Specimens	Surface hardness ($HV_{0.1}$)	Compound layer (μm)	Diffusion zone (μm)	Surface residual stress (MPa)	Friction coefficient (μ)	Wear Rate × 10^5 (mm^3/Nm)
AR	200–220	–	–	−190 ± 15	0.33	9.5
16A	350–370	–	–	−270 ± 25	0.42	5.7
20A	400–420	–	–	−320 ± 30	0.45	4.7
24A	480–500	–	–	−410 ± 40	0.48	2.2
500 °C-1 h	530–550	18–20	150	−380 ± 40	0.40	6.4
16A + 500 °C-1 h	540–560	14–16	180	−340 ± 30	0.41	0.25
20A + 500 °C-1 h	550–570	10–12	250	−370 ± 35	0.43	0.068
24A + 500 °C-1 h	530–550	14–16	300	−420 ± 45	0.44	0.049
500 °C-4 h	660–680	21–23	225	−430 ± 45	0.42	3.6
16A + 500 °C-4 h	660–680	22–24	300	−450 ± 40	0.43	0.13
20A + 500 °C-4 h	650–670	14–16	325	−460 ± 50	0.44	0.033
24A + 500 °C-4 h	650–670	16–18	350	−480 ± 45	0.46	0.011

Figure 1 illustrates the relationship among wear rate, surface roughness, and surface hardness for untreated, plasma-nitrided, shot-peened, and shot-peened plus plasma-nitrided samples. As shown in Figure 1 and Table 1, the untreated sample exhibits the highest wear rate despite its low surface roughness, which is attributed to its insufficient surface hardness.[18].

As shown in Figure 1 and Table 1, the combination of shot peening and plasma nitriding leads to a marked reduction in wear rate compared with the untreated condition. Despite the initially low roughness, the untreated material exhibits a significantly higher wear rate due to its limited surface hardness and absence of a hardened layer. In contrast, shot peening introduces near-surface plastic deformation, increasing hardness and favoring nitrogen uptake during subsequent plasma nitriding. This synergistic effect results in a deeper and more mechanically robust modified layer, directly reflected in the lower wear rates obtained [18].

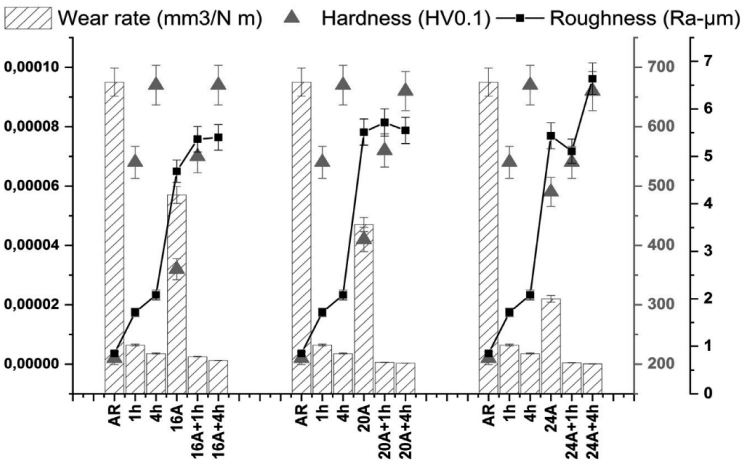

Figure 1: Changes on the surface properties. From [18]

While the synergistic effects of shot peening and plasma nitriding provide clear improvements in wear behavior, another widely explored route for enhancing surface performance is the combination of plasma nitriding followed by post-oxidation. Although the simultaneous application of all three treatments were examined in a limited number of studies, the nitriding and post-oxidation sequence is well documented and offers important insights into the formation of protective oxide layers.

Mahboubi and Fattah [29] reported that plasma nitriding followed by post-oxidation results in the formation of nitride phases such as γ' (Fe_4N) and ε ($Fe_{2–3}N$) during nitriding, and oxide phases such as hematite (Fe_2O_3) and magnetite (Fe_3O_4) during post-oxidation. Similarly, Mirjani et al. [30] presented X-ray diffraction results for treated AISI 4140 steel samples, showing that post-oxidation led to the formation of oxide layers composed mainly of magnetite and hematite.

Naeem and Díaz-Guillén [31] reported that the consolidation of the oxidized layer prevents the detachment of abrasive particles from the nitrided surface. This feature produces a smoother surface and reduces the coefficient of friction. The improvement is mainly attributed to the ceramic nature of the oxide phases formed, which inherently exhibit low friction coefficients and low adhesion tendencies. As a result, the presence of the oxide layer can modify the prevailing tribological mechanisms, shifting from predominantly abrasive and oxidative wear to primarily adhesive wear.

The duplex treatment resulted in an oxidized layer with a markedly reduced friction coefficient, approximately 40% lower than that measured for nitrided or untreated samples. Consistent with the morphology observed in the wear tracks, this reduction is primarily associated with a shift in the dominant wear mechanisms, in which plastic yielding becomes more evident. Moreover, the high hematite content within the oxidized layer appears to play a decisive role in enhancing wear performance, contributing to more stable sliding conditions and improved overall tribological behavior [31].

CONCLUSION

Surface engineering treatments such as plasma nitriding and subsequent post-oxidation play a crucial role in enhancing the mechanical, tribological, and chemical performance of steel components. This combined approach increases surface hardness, wear and oxidation resistance, and provides improved protection under demanding service conditions. The duplex sequence of nitriding followed by post-oxidation promotes the formation of a hardened diffusion zone and a stable oxide layer, which together offer superior load-bearing capacity and reduced friction compared with the treatments applied individually. Moreover, when integrated with surface deformation processes such as shot peening, this methodology can further optimize the surface morphology and support the formation of more efficient protective layers, contributing to improved durability and functional performance of the treated components.

ACKNOWLEDGMENTS

This work was carried out with the support of National Council for Scientific and Technological Development (CNPq) in Brazil, through the Universal call process number 407185/2023-2. Frederico Murilo Wlassak acknowledges CAPES (process number 88887.007108/2024-00), Alexandre da Silva Rocha acknowledges CNPq/MCTI N° 10/2023 (Grant 308773/2018-7), Morvan Silva Franco acknowledges CAPES (Process no. 88887.842729/2023-00), Felipe Canal acknowledges CAPES (Process no. 88887.988547/2024-00).

BIBLIOGRAPHY

1. R.L. Dalcin, *et al*, Response of a Din 18MnCrSiMo6-4 continuous cooling bainitic steel to different plasma nitriding gas mixtures, Mater. Res. 23 (2020).
2. R.L. Dalcin, *et al*, Microstructure and wear properties of a low carbon bainitic steel on plasma nitriding at different N2-H2 gas mixtures, Mater. Res. 25 (2022).
3. R.L. Dalcin, *et al*, Response of a din 18mncrsimo6-4 continuous cooling bainitic steel to plasma nitriding with a nitrogen rich gas composition, Mater. Res. 23 (2020) 1–9.
4. H. Kovacı, *et al*, Fatigue crack growth analysis of plasma nitrided AISI 4140 low-alloy steel: part 1-constant amplitude loading, Mater. Sci. Eng. A 672 (2016) 257–264.
5. J. Wu, *et al*, Enhancement of corrosion resistance for plasma nitrided AISI 4140 steel by plain air plasma post-oxidizing, J. Alloys Compd. 632 (2015) 397–401.
6. B. Hashemi, M.R. Yazdi, V. Azar, The wear and corrosion resistance of shot pee- ned–nitrided 316L austenitic stainless steel, Mater. Des. 32 (2011) 3287–3292.
7. N. Mandkarian, F. Mahboubi, Effect of gas mixture of plasma post-oxidation on corrosion properties of plasma nitrocarburised AISI 4130 steel. Vacuum, v. 83, n. 7, p. 1036-1042, 2009.
8. J. Ni, et al, Novel Effect of Post-Oxidation on the Comprehensive Performance of Plasma Nitriding Layer. Coatings 2024, 14, 86.
9. Z. Bai, X. Wu, Improving stress corrosion and wear resistance of austenitic hot-stamping die steels via synergistic effects of shot peening and plasma nitriding. Surface and Coatings Technology, 2024, v. 48.

10. C. J. Leitão, P. R. Mei, R. Libardi, Efeitos da cementação e da nitretação no custo e na qualidade de engrenagens produzidas com aços ABNT 4140 e 8620. Tecnologia em Metalurgia, Materiais e Mineração. 2012, 9, 257–263. (in Portuguese)
11. F. G. Caballero, *et al*, Design of novel high strength bainitic steels: Part 2. Mater. Sci. Technol. 2001, 17, 517–522.
12. E. A. Ochao, *et al*, Microstructure and properties of the compound layer obtained by pulsed plasma nitriding in steel gears. Surf. Coat. Technol. 2009, 203, 1457–1461.
13. E. Rolinski, Deep nitriding for gear applications and their partial treatments: plasma/ion nitriding meets demanding gear applications by increase load capacity of gears and increased fatigue strength of components as well as less complicated masking treatments. In Gears Solutions, 2016.
14. S. Bagherifard, et al, Nanoscale surface modification of AISI 316L stainless steel by severe shot peening, Mater. Des. 102 (2016) 68–77.
15. H. Ferkel, M. Glatzer, Y. Estrin, R. Z. Valiev, RF plasma nitriding of a severely deformed high alloyed steel. Scr Mater 2002;46:623–8.
16. S. J. Ji, L. Wang, J. C. Sun, Z. K. Hei, The effects of severe surface deformation on plasma nitriding of austenitic stainless steel. Surf Coat Technol 2005;195: 81–4.
17. L. Shen, L. Wang, Y. Wang, C. Wang, Plasma nitriding of AISI 304 austenitic stainless steel with pre-shot peening. Surf Coat Technol 2010;204:3222–7.
18. H. Kovaci, I. Hacisalihoglu, A. F. Yetim, A. Çelik, Effects of Shot Peening pre-treatment and plasma nitriding parameters on the structural and tribological properties of AISI 4140 low-alloy steel. Surface and Coatings, Nov. 2018, 0257-8972.
19. F. Czerwinski, Thermochemical Treatment of Metals. In Heat Treatment - Conventional and Novel Applications. Intech: Canada, 2012. pp. 73–112.
20. R. L. Dalcin, et al, Surface Processing to improve the fatigue strength of bainitic steels – An overview, International Journal of Engineering & Technology, 8 (3), (2019) 324-332.
21. B. Podgornk, V. Leskovsek, M. Kovacic, J. Vizintin, Analysis and prediction of residual stresses in nitrided tool steel. Mater. Sci. Forum, 2011, 681, 352–357.
22. A. Alsaran, et al, Effects of post-aging on wear and corrosion properties of nitreded AISI 4140 steel. Surface and Coatings Technology, v. 176, n. 3, p. 344-348, 2004.
23. H. R. Abedi, M. Salehi, M. Yazdkahsti, Novel plasma nitriding – oxidizing duplex treatment of AISI 316L austenitic stainless steel. Materials Letters, v. 64, n. 6, p. 698-701, 2010.
24. M. Zlatanovic, et al, Formation of magnetite overlayer on nitrocarburized low-alloy steel by plasma post oxidation. Surface and Coatings Tachnology, v. 188-189, n. 1-3 SPEC.ISS., p.307-313, 2004.
25. D. K. Matlock, et al, Surface processing to improve the fatigue resistance of advanced bar steels for auto- motive applications. Materials Research. 2005, 453-459.
26. S. Zajac, et al, Quantitative structure–property relationship for complex bainitic microstructures. In Technical Steel Research report no. EUR 21245EN. European Commission, Luxembourg, 2005.
27. S. Kikuchi, J. Komotori, Effect of fine particle peening treatment prior to nitriding on fatigue properties of AISI 4135 steel, J. Solid Mech. Mater. Eng. 2 (2008) 1444–1450.
28. P. Ranaware, M. Rathod, Combined effect of shot peening, subcritical austenitic nitriding, and cryo-treatment on surface modification of AISI 4140 steel, Mater. Manuf. Process. 32 (2017) 349–354.

29. F. Mahboubi, M. Fattah, Duplex treatment of plasma nitriding and plasma oxidation of plain carbon steel. Vacuum, v. 79, n. 1-2, p. 1-6, 2005.
30. M. Mirjani, et al, Investigation of the effects of time and temperature of oxidation on corrosion behavior of plasma nitrided AISI 4140 steel. Surface and Coatings Technology, v. 206, n. 21, p. 4389-4393, 2012.
31. M. Naeem, et al, Improved wear resistance of AISI 1045 steel by hybrid treatment of plasma nitriding and post oxidation. TRIBOLOGY International, August, 2022.

TalentDetector

9th January 2026
Gliwice, Poland

DEPARTMENT OF ENGINEERING MATERIALS AND BIOMATERIALS
FACULTY OF MECHANICAL ENGINEERING
SILESIAN UNIVERSITY OF TECHNOLOGY

INTERNATIONAL STUDENTS SCIENTIFIC CONFERENCE

Synergy of CAD/CAM systems and modern automation in laser cutter control processes

Jan Wypiór[a], Kinga Stępska[a], Katarzyna Ptasznik[a], Martyna Urbańska[a], Marek Flak[b], Mirosław Bonek[c], Eva Tillova[d]

[a] Silesian University of Technology, Faculty of Mechanical Engineering, Student of Production and Management Engineering
email: jw309692@student.polsl.pl
[a] Silesian University of Technology, Faculty of Mechanical Engineering, Student of Production and Management Engineering
email: ks309686@student.polsl.p
[a] Silesian University of Technology, Faculty of Mechanical Engineering, Student of Production and Management Engineering
email: kp309682@student.polsl.pl
[a] Silesian University of Technology, Faculty of Mechanical Engineering, Student of Production and Management Engineering
email: mu309689@student.polsl.pl
[b] Silesian University of Technology, Faculty of Electrical Engineering, Student of Mechatronics
mf310852@student.polsl.pl
[c] Silesian University of Technology, Faculty of Mechanical Engineering
[d] Faculty of Mechanical Engineering, Department of Materials Engineering, University of Žilina

Abstract: The paper discusses the development of NC numerical control systems and their importance for the automation of production processes. It presents the construction of laser cutting machines in the context of robotics, with particular emphasis on gantry structures and drive systems. It describes the role of CAD/CAM and nesting systems in the preparation and optimisation of the cutting process. Attention is drawn to the limitations of classic G-code-based control systems and the importance of modern solutions enabling the effective use of fibre lasers.

Keywords: production automation, NC/CNC numerical control, laser cutting, G-code (ISO 6983), CAD/CAM systems, industrial robot, Industry 4.0

1. INTRODUCTION

The dynamic development of manufacturing technology in recent decades has led to a significant increase in the importance of automation and digitisation of production processes.

Numerically controlled machine tools and modern laser cutting machines, which are the basic equipment of modern industrial plants, play a special role in this area. These solutions enable high precision, repeatability and efficiency, responding to the growing quality
and economic requirements of production.

The aim of this study is to present the development and stages of NC system automation, as well as to discuss the construction of laser cutting machines in the context of robotics. Particular attention is paid to the role of CAD/CAM systems and methods of preparing and optimising the cutting process, including issues related to nesting. The rest of the paper also presents the issue of laser machine control using G-code and the limitations of classic control systems in comparison with the high dynamics of modern fibre lasers.

The scope of work includes an analysis of both historical aspects and contemporary technological solutions, with particular emphasis on their impact on the efficiency, precision and stability of the laser cutting process.

2. DEVELOPMENT AND STAGES OF NC SYSTEM AUTOMATION

The history of machine tool development combines concepts ranging from rigid mechanics to advanced data analytics, forming the foundation of the modern Industry 4.0 concept. The origins of this history date back to the 1940s, when the first NC systems were developed. Numerical Control systems were designed by American engineer John Parsons on behalf of the United States Army Air Forces [1][5].

Numerically controlled machines were used in factories producing American fighter planes. These were large, expensive devices that required specialist operation [1][2].

In the early 1950s, these solutions were commercialised. At that time, control was based on so-called hard-wired logic. Machines were not equipped with computers or memory as we understand them today. Movement instructions were recorded on cards or punched tapes, which were interpreted by the machine's reader line by line. This process was labour-intensive and inflexible [1][2].

The 1970s brought significant changes in numerical control technology with the introduction of microprocessors. This change completely revolutionised the way machines were controlled. Thanks to modern electronic systems, CNC machine tools gained the ability to store, edit and reproduce programmes without the need for physical data carriers. The integration of machine tools with computers enabled the full automation of technological processes and significantly increased the precision and repeatability of machining [2].

With the development of CAD (Computer-Aided Design) and CAM (Computer-Aided Manufacturing) software, technology has entered a new era of production. The use of specialised software has enabled the creation of complex three-dimensional models and their verification in a virtual environment. These solutions allow errors to be detected even before actual machining begins, which reduces production costs and increases the safety of the technological process [4].

Today, we are witnessing the next stage of development, in which classic CNC systems are evolving towards intelligent solutions integrated with the Internet of Things (IoT). Machine tools are becoming active elements of the production network, equipped with advanced sensor systems. Modern machines continuously collect and analyse data on operating parameters such as temperature, vibrations and energy consumption. This enables the implementation of predictive maintenance strategies and dynamic adjustment of machining parameters [3].

These processes are often mapped in the form of a Digital Twin, which enables simulation and real-time data exchange.

3. MACHINE CONSTRUCTION FOR CUTTING IN THE CONTEXT OF ROBOTS

A laser cutting machine can be considered a robot because it is a device that automatically moves a working tool, i.e. a laser head, within a specific space. From an automation perspective, such a machine meets the definition of a manipulator – it has a mechanical structure, drives and a control system that enable precise positioning of the laser during the cutting process [6][8].

Most laser cutters used in industry are so-called Cartesian robots, moving along three perpendicular linear axes: X, Y and Z. The most common design is a gantry structure, in which the machine portal moves in one axis, the laser head in another, and the third axis is used to adjust the height of the head above the material. This arrangement is characterised by its simple design and ease of control, while at the same time ensuring high accuracy and repeatability of movement, which is important in the laser cutting process [7] [9].

In some applications, industrial robots with a six-axis arm are used instead of classic gantry cutters. These solutions enable the cutting of spatial elements in 3D technology, where tool movements at different angles are required. The advantage of this type of robot is its high freedom of movement, while its disadvantage is its lower structural rigidity and positioning accuracy compared to gantry machines. For this reason, six-axis robots are less commonly used for precision cutting of flat sheets [6][8].

An important component of a laser cutting machine is the axis drives. Servo drives are most commonly used, which set the machine axes in motion via ball screws or rack and pinion gears, ensuring precise control of position and speed. More modern designs use linear motors, which enable direct axis drive without intermediate elements. This solution allows for higher speeds and greater accuracy, but it is associated with higher costs and the need for a very rigid support structure [9].

The rigidity of the machine structure has a direct impact on the quality of the laser cutting process. Excessive flexibility of the structure can lead to vibrations that negatively affect the quality of the cut edges. For this reason, gantry cutters, characterised by their massive and stable construction, are better suited to precision laser cutting than arm robots. For this reason, laser cutting machines can be considered specialised robots, designed primarily for high accuracy and stability of operation [6][8].

4. THE ROLE OF CAD/CAM SYSTEMS

In the process of laser cutting steel, the proper preparation of documentation and production data, based on the integrated use of CAD, CAM and nesting systems, plays a key role. These technologies form the basis of modern digitisation and automation of manufacturing, performing complementary functions in the areas of design, process preparation and material consumption optimisation. [10,11,12]

4.1 Geometry design in CAD systems

The CAD (Computer-Aided Design) stage is the starting point for the entire manufacturing process. CAD systems are computer tools that enable the creation of precise geometric models – both two-dimensional and three-dimensional – which define the shape, dimensions and tolerances of the designed parts. Their functionality includes, among other things, contour sketching, dimensioning, geometry analysis, technical documentation generation and integration with other engineering environments. The CAD system thus creates a geometric definition of the element, which then forms the basis for further technological operations. Proper preparation of the CAD file has a direct impact on the quality and efficiency of subsequent cutting. It is important to maintain minimum design dimensions, such as minimum gap width or hole diameter, and to avoid overly complex or delicate geometry that may be deformed by the thermal energy of the laser beam. Well-prepared CAD documentation reduces the number of potential errors in production and allows the full potential of laser technology to be exploited. [10,11]

4.2 Planning cutting operations in CAM

The next stage is the processing of model data in CAM (Computer-Aided Manufacturing) systems, which are responsible for generating the cutting path and creating the code that controls the laser machine. CAM systems bridge the gap between the digital model and the actual production process, automating calculations related to head movement, laser operating parameters and the sequence of operations. Their operation includes, among other things, the translation of geometry into tool paths, process simulation, collision control and the selection of technological parameters in accordance with the type of material, sheet thickness and type of machine. In the CAM phase, all process parameters are determined, including cutting speed, laser power, type and pressure of technical gas, as well as the location of piercing points and the sequence of individual contours. Of particular importance here is the optimisation of the cutting sequence, which affects the thermal stability of the sheet. An improperly planned sequence can cause local stresses and deformations, which reduce the dimensional accuracy of the components. The CAM system also enables the design of micro-joints that prevent the cut parts from moving during machine operation. The appropriate configuration of these parameters guarantees a stable, repeatable cutting process and high edge quality. [13,14]

4.3 Optimal placement of components using nesting

An integral part of the CAM stage is nesting, i.e. the optimal arrangement of elements on a steel sheet. Nesting is not only a software functionality, but a fully-fledged calculation method based on optimisation algorithms, such as evolutionary algorithms, geometric heuristics or methods based on cutting and packing problems. The nesting system analyses the shapes of individual details and the geometry of the available material, and then arranges the elements in such a way as to maximise the use of the sheet surface and minimise waste. This type of software often also takes into account technological factors, such as minimum spacing between elements, surface directionality, the possibility of reorienting parts or areas excluded from cutting. Effective placement of details not only reduces material consumption, but also shortens the total cutting time by reducing the length of the laser head's travel path. In the case of serial production, where the number of details is large, the use of nesting translates into measurable savings in both material costs and machine operating time. Nesting also allows the use of remnants from previous cuts, which further increases the efficiency of the process. [12,15]

5. MACHINE CONTROL – G CODE

The introduction of fibre lasers after 2010 was a significant breakthrough in metal cutting technology. This solution made it possible to cut thin sheets at speeds up to five times higher than with the older CO_2 technology. Despite the significant increase in the capabilities of the laser sources themselves, the actual increase in production efficiency in many plants was limited to around 30%.

Analysis of this phenomenon indicates that the main limiting factor is the architecture of control systems. In many cases, solutions directly adapted from slow-speed cutting machine tools, such as lathes or milling machines, are used, whose dynamic characteristics do not meet the requirements of modern fibre lasers. These systems are based on concepts developed in the 1950s, when technological limitations forced the use of offset control.

The essence of the error system is to determine the speed of the servo drive based on the delay of the axis relative to the position set by the interpolator. The interpolator calculates the theoretical position of the head at a given moment in time, while the difference between this position and the actual position of the axis is defined as the tracking error. This error is not a random error, but an essential element of the operation of a classic controller, and it increases proportionally to the feed speed.

In practice, this means that during operation, the cutting head constantly 'keeps up' with the interpolator. While delays of fractions of a millimetre were negligible in slow cutting machines, in fibre lasers operating at speeds of 1 m/s, the deviation can reach values of up to 1 cm. This leads to deformation of the cutting trajectory, especially at critical points such as corners or small-radius arcs. When there is a sudden change in direction, the physical drive axis, burdened by the deviation, is unable to react immediately, resulting in rounded corners.

In order to maintain the required dimensional accuracy, manufacturers using classic control systems are forced to implement algorithms that limit machine dynamics, such as speed reduction on curves or stopping the interpolator at the vertices of the trajectory. This leads to a reduction in the average efficiency of the process, despite the use of an efficient laser source.

An additional limitation in process optimisation remains the ISO 6983 (G-code) trajectory recording standard, developed in the era of perforated media. This format is based on the approximation of geometric curves using a large number of short linear segments. At high feed rates, this generates a significant computational load on the control unit, leading to dynamic instability of the system, resonance vibrations and deterioration in the quality of the cutting edge.

The answer to these limitations came in the form of new-generation control systems designed for high-dynamic kinematics. This approach was pioneered in the late 1990s with solutions developed for high-speed plotters and milling machines, which had to meet speed requirements far exceeding the standards of classic CNC machine tools. With the widespread use of fibre lasers after 2010, it became apparent that these types of systems are fully compatible with the drive characteristics of modern laser cutters.

The foundation of modern control architecture is the use of high-performance signal processors (DSP) and a change in the structure of the feedback loop. A key element is the decentralisation of control, which involves transferring position, speed and current loops directly to the servo drive controllers. This eliminates communication delays between the interpolator and the drives. Unlike classic solutions, a modern interpolator simultaneously transmits position, speed and acceleration information to the drives, which allows for a significant increase in sampling frequency and almost complete elimination of tracking error.

The hardware layer is complemented by advanced control algorithms, such as Dynamic Vector Analysis (DVA), which take into account the physical model of the machine and the permissible centrifugal accelerations for complex curves. This allows for smooth speed modulation on curves without sudden changes in the motion vector. The use of error-free control systems with high sampling frequencies is a prerequisite for fully exploiting the potential of fibre lasers, enabling high precision and maximum process efficiency to be maintained simultaneously.

6. CONCLUSIONS

Based on the analysis, it can be concluded that the development of numerical control systems has played a key role in the evolution of modern manufacturing processes. The transition from simple, rigidly wired NC systems to advanced CNC systems integrated with CAD/CAM technologies and the Internet of Things has enabled a significant increase in precision, repeatability and the degree of production automation.

It has been demonstrated that laser cutting machines, due to their design, control method and nature of operation, can be treated as specialised industrial robots. The gantry structures, which are predominant in laser cutting machines, ensure high rigidity and positioning accuracy, which is crucial for edge quality and cutting process stability.

CAD/CAM and nesting systems play an important role in the preparation and implementation of the cutting process, enabling correct geometry design, tool path optimisation and efficient use of material. The proper use of these tools translates directly into reduced production costs and shorter machine operating times.

At the same time, it was pointed out that classic control systems based on G-code and offset control are a significant limitation in the case of high-dynamic fibre lasers. The use of modern, error-free control systems and advanced motion analysis algorithms allows for fuller utilisation of the potential of laser technology, combining high operating speed with the required precision.

ACKNOWLEDGEMENTS

The work was created as part of project based learning - PBL, in the 13th competition under the Initiative of Excellence - Research University, Silesian University of Technology, Gliwice, Poland and as part of project of Students Scientific Circle of Laser Surface Treatment under the Initiative of Excellence - Research University, Silesian University of Technology, Gliwice, Poland.

BIBLIOGRAPHY

1. https://www.cms.it/en/news-events/news/history-of-cnc-machining-how-the-cnc-concept-was-born.n68710.html [dostęp: 19.12.2025]
2. https://vorster.pl/historia-obrobki-cnc-od-pierwszych-obrabiarek-do-wspolczesnych-maszyn/ [dostęp: 19.12.2025]

3. https://www.siemens.com/pl/pl/o-firmie/aktualnosci/2025/iot-w-przemysle-inteligentne-rozwiazania-dla-produkcji.html [dostęp: 19.12.2025]
4. https://eurostal.tech/pl/integracja-technologii-ciecia-laserowego-z-systemami-cad-cam-w-nowoczesnej-produkcji/ [dostęp: 19.12.2025]
5. https://en.wikipedia.org/wiki/John_T._Parsons [dostęp: 19.12.2025]
6. Steen, W. M., Mazumder, J., Laser Material Processing, Springer, London 2010
7. Powell, J., CO_2 Laser Cutting, Springer, London 1998
8. Ion, J. C., Laser Processing of Engineering Materials, Elsevier Butterworth-Heinemann, Oxford 2005
9. Kalpakjian, S., Schmid, S., Manufacturing Processes for Engineering Materials, Pearson Education, 2014
10. https://www.smx.com.pl/jak-przygotowac-projekt-cad-pod-laser/ [dostęp: 19.12.2025]
11. https://www.adhmt.com/pl/laser-cutting-machine-components/ [dostęp: 19.12.2025]
12. https://techweek.pl/nesting.html [dostęp: 19.12.2025]
13. https://www.hypertherm.com/pl/solutions/technology/cam-software/laser-nesting-software/ [dostęp: 19.12.2025]
14. https://rauhut.com.pl/aktualnosci/89-nesting-i-minimalizacja-odpadu-jak-obnizyc-koszt-detalu-przy-cieciu-laserem [dostęp: 19.12.2025]
15. https://verashape.com/pl/nesting/ [dostęp: 19.12.2025]

TalentDetector

9th January 2026
Gliwice, Poland

DEPARTMENT OF ENGINEERING MATERIALS AND BIOMATERIALS
FACULTY OF MECHANICAL ENGINEERING
SILESIAN UNIVERSITY OF TECHNOLOGY

INTERNATIONAL STUDENTS SCIENTIFIC CONFERENCE

Formation of a fine-grained microstructure in metals by laser treatment

Jan Wypiór[a], Katarzyna Ptasznik[a], Piotr Konieczny [b], Bartosz Dziki [b], Natalia Rupala [c], Mirosław Bonek [d], Oleh Polishchuk [e]

[a] Silesian University of Technology, Faculty of Mechanical Engineering, Student of Production and Management Engineering, email: jw309692@student.polsl.pl
[a] Silesian University of Technology, Faculty of Mechanical Engineering, Student of Production and Management Engineering, email: kp309682student.polsl.pl
[b] Silesian University of Technology, Faculty of Electrical Engineering, Student of Electrical engineering, email: pk308597@student.polsl.pl
[b] Silesian University of Technology, Faculty of Electrical Engineering, Student of Mechatronics email: bd310822@student.polsl.pl
[c] Silesian University of Technology, Faculty of Automatic Control, Electronics and Computer Science, Student of Teleinformatics, email: nr310520@student.polsl.pl
[d] Silesian University of Technology, Faculty of Mechanical Engineering
[e] Khmelnytskyi National University, Faculty of Mechanical Engineering, Transport and Architecture

Abstract: The text discusses the importance of the surface layer of the material and modern methods of shaping it using laser technologies. Particular attention is paid to processes such as selective laser melting, ablation and remelting, which enable precise modification of the structure without affecting the entire body of the detail. Studies on HS6-5-3-8 high-speed steel have shown that an increase in laser power increases the hardness and homogeneity of the surface layer, which highlights the potential of this method in materials engineering.

Keywords: laser surface modification, selective laser melting, laser ablation, laser remelting, HS6-5-3-8 steel, hardness

1. INTRODUCTION

The surface layer of a material has a significant impact on its behaviour during everyday use. It determines its anti-corrosion properties, abrasion resistance and strength. For many years, the main methods of shaping the surface of a material were mechanical, thermal or thermochemical treatments. However, technological advances have increased the number of methods available. With the emergence and development of high-power lasers, it has become possible to quickly and precisely shape selected areas of the material. Controlling process parameters such as beam power, scanning speed and type of protective atmosphere has enabled precise planning of the entire procedure, resulting in high repeatability. Unlike traditional methods, laser technology has

allowed for very rapid heating and cooling of the treated surfaces, leading to the formation of a fine-crystalline structure. These changes increase the homogeneity and uniformity of the surface layer, significantly improving the material's parameters. During operation, the laser affects only a small section of the material, while the rest of the component is protected from thermal deformation, creating a centre with a gradient of properties – the surface character is changed while the interior of the centre remains unchanged.

2. DESCRIPTION OF LASER MODIFICATION METHODS – DEVELOPMENT, ADVANTAGES AND DISADVANTAGES

Laser surface modification is one of the most important tools in materials engineering today — it allows local changes to be made to the composition, microstructure and properties of the working layer without the need for large-scale heating of the entire workpiece. Below is an overview of these methods, their evolution, advantages, disadvantages and a brief comparison [1].

2.1. Main Methods of Laser Surface Modification

• Selective Laser Melting/Reconstruction

The first of the methods described is selective laser melting. Selective laser melting (SLM) is an innovative technology that has revolutionised the production process of metal components. Thanks to the precise sintering of layers of fine metal particles, SLM enables the creation of advanced shapes with excellent properties. The process begins with the application of a thin layer of metal powder onto a working platform. A laser then heats selected areas of the powder, forming durable structures. After each layer is formed, the platform descends slightly to apply the next layer of powder. This process is repeated until the finished product is obtained. Selective laser melting (SLM) technology uses a variety of metal materials, such as:

- stainless steel,
- aluminium alloys,
- titanium alloys,
- precious metals. [1],[2]

The right choice of material has a significant impact on the characteristics of the final product, including its strength, resistance to high temperatures and protection against corrosion. In the field of medicine, this technology is gaining popularity as it enables the creation of biocompatible implants and prostheses.

The SLM process involves layer-by-layer sintering and melting of metal powder only in those areas where the finished part is to be created. This ensures that the principle of minimal raw material consumption is fully implemented – most of the unused powder can be recovered and reused in the next production cycle. This closed material cycle radically reduces waste generation and translates into high cost efficiency. The design aspect of SLM technology, namely rapid prototyping, allows for smooth and quick concept validation. There are also disadvantages – selective laser melting machines are highly complex technically – they require a controlled atmosphere of inert gases (e.g. argon). High entry threshold and continuous monitoring of laser parameters. [2]

• Laser ablation

This technology uses a laser beam to precisely remove material. It is used both in industry (cleaning, metalworking, micro-drilling, engraving) and in medicine. When the laser beam hits

the surface of the material, its top layer absorbs the energy of the photons. This leads to a rapid increase in temperature. Depending on the intensity of the laser and the properties of the material, the following phenomena occur:
- change in the state of the material to liquid,
- sometimes sublimation occurs (change from solid to gas),
- formation of plasma. [3]

The most important aspect of this process is that it is possible to select the laser material in such a way that, for example, dirt or rust can be removed without damaging the material underneath. This allows the method to be used for cleaning, marking or removing coatings.
• Laser remelting
Laser remelting involves the rapid remelting of a thin surface layer of the substrate material, followed by crystallisation or amorphisation. During the process, evaporation may occur, producing plasma. This plasma protects the material from overheating. [3]

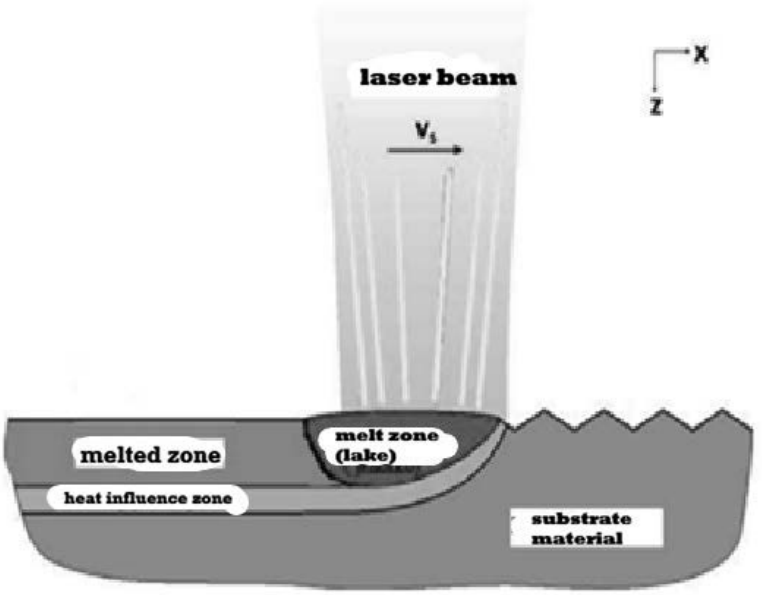

Figure 1 - Laser remelting diagram

• Laser brazing
• Laser heat treatment

2.2 Explanation of the word 'laser' and how it works in steps

The word LASER stands for: Light Amplification by Stimulated Emission of Radiation [10].
1. The laser medium is placed between two mirrors forming an optical resonator.
2. Spontaneous radiation, which is parallel to the resonator axis, is repeatedly reflected, passing through the medium with population inversion.
3. The process of stimulated emission increases exponentially, resulting in the production of an intense, coherent beam of laser light.

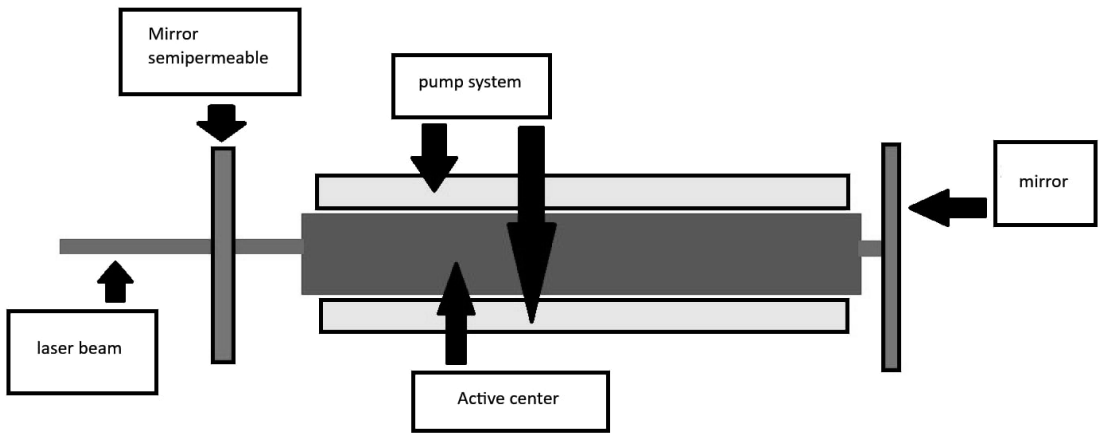

Figure 2 - Diagram of an optical resonator [9]

2.3. Key properties of laser radiation

• **Coherence:** Radiation is coherent in time and space (phases, frequencies, polarizations are identical).
• **Monochromaticity**: Very narrow wavelength range.
• **Directivity:** The beam is emitted in one specific direction, with a very small divergence angle.
• **Focusability:** A spot with a small diameter (10-300) and high power density can be obtained.
• **High Power Density**: Pulse or continuous operation is possible. [11]

3. DESCRIPTION OF RESEARCH INTO THE STRUCTURAL TRANSFORMATION OF THE SURFACE LAYER OF HS6-5-3-8 HIGH-SPEED STEEL

3.1 Zone structure of the surface layer

As a result of the impact of a high-power diode laser (HPDL) beam, a clearly differentiated layered structure is formed in the material, consisting of three main areas [1]:
- Melted zone (SP): The outermost part, which has been completely melted and then rapidly solidified [2].
- Heat-affected zone (HAZ): The area below the remelted zone where the temperature was high enough to cause structural changes (e.g., solid-state phase transformations) but too low to melt the material [3].
- Native material (substrate): The original structure of the steel that has not been altered by the laser heat [4].

3.2 The mechanism of structural change

Structural transformation is based on rapid heating and cooling, which leads to the following processes:
- Dissolution of carbides: When heated to very high temperatures (above the solidus line in the remelted zone), carbides (such as M_{23}C_6, M_6C_ and less soluble MC rich in vanadium) dissolve in the austenite matrix [5].

- Matrix saturation: Alloying elements (tungsten, molybdenum, vanadium, chromium) pass into the solid solution, which increases the hardenability of the steel and affects the secondary hardness [6].
- Martensitic transformation: Very rapid cooling after the laser beam passes causes a non-diffusive transformation of austenite into lamellar martensite [7]. Approximately 20% of residual austenite and fine, undissolved carbides also remain in the final structure [8].

3.3 The influence of process parameters on structure

The depth and nature of structural changes are closely related to the laser power used [9]:
- Depth of melting: As the laser power increases, so does the depth of the melted zone. At a power of 0.7 kW, this depth is approx. 0.4 mm, while at a power of 2.1 kW it increases to approx. 1.1 mm [10].
- Substrate contribution: Higher beam power density results in deeper heat penetration and a greater contribution of melted native material to the newly formed layer [11].

3.4 The purpose and effects of transformation

The main objective of these structural changes in HS6-5-3-8 steel is to increase the hardness and wear resistance of the surface layer [12]. Thanks to the refinement of the structure and saturation of the matrix with alloying elements, the steel obtains better performance properties compared to conventional heat treatment [13].

4. CONCLUSIONS

One way to give the top layer of the material the desired parameters is laser processing. Rapid phase changes significantly break down the internal structure of the remelted layer of material, leading to an increase in its strength.

The parameters of the laser used have a significant impact on the result of the process. When testing a sample of HS6-5-3-8 steel, the final hardness of the sample increases with the increase in laser power and, consequently, the depth of the remelted layer. For the tested powers – 0.7kW and 2.1kW, the hardness of the sample reached 1300HV0.1 and 1400HV0.1. These results indicate an increase in hardness of approx. 30% compared to the native material for the procedure with a stronger laser. The laser power also affects the smoothness of the path and the formation of rough areas. With stronger laser beams, the path was smoother, but this was associated with the occurrence of areas with greater roughness. A significant increase in the hardness of the material surface with high precision of the method indicates great potential for further development of this method.

ACKNOWLEDGEMENTS

The work was created as part of project based learning - PBL, in the 13th competition under the Initiative of Excellence - Research University, Silesian University of Technology, Gliwice, Poland.

BIBLIOGRAPHY

1. https://dlaprodukcji.pl/technologia-przetapiania-laserowego/ [dostęp: 18.12.2025]
2. https://www.openaccesslibrary.com/2009/warstwy.pdf [dostęp: 18.12.2025]
3. https://pimib.polsl.pl/pdf/31/313.pdf [dostęp: 18.12.2025]
4. A. Pindor, W. Gorzkowski, A. Szymacha : Feymana wykłady z fizyki. Tłumaczenie z j. ang. Książki p.t. „ The Feyman Lectures on Physics, Volume III, Massachusetts, U.S.A., 1965.
5. H. Klejman : Lasery, PWN, Warszawa, 1974.
6. J. Kusiński : Lasery i ich zastosowanie w inżynierii materiałowej, Wydawnictwo Naukowe Akapit, Kraków, 2000.
7. W. Woliński : Laser – właściwości promieniowania, parametry, Materiały VIII Krajowej Szkoły Optoelektroniki n.t. Laserowe technologie Obróbki materiałów, Gdańsk – Wyspa Sobieszewska, 1994.
8. U. Habich, D. Ehrlichmann, U. Jarosch : Development of an Industrial CO_2 Laser witch More Than 40-kW Output Power : Recent Results, 10^{th} International Symposium on Gas Flow and Chemical Lasers, SPIE 1994.
9. http://naukamlodego.blogspot.com/2015/03/wszystko-o-laserach.html [dostęp: 18.12.2025]
10. B. Ziętek : Lasery, Wydawnictwo Naukowe UMK, Toruń 2008
11. Z. Płochnicki : Co to jest laser, Wiedza Powszechna, Omega, Warszawa, 1984
12. A. Kujawski, P. Szczepański : Lasery. Podstawy fizyczne.Oficyna wydawnicza Politechniki Warszawskiej, Warszawa, 1999
13. http://www.w12.pwr.wroc.pl/swiatlowody/pdf/laser.pdf [dostęp: 18.12.2025]

TalentDetector

9th January 2026
Gliwice, Poland

DEPARTMENT OF ENGINEERING MATERIALS AND BIOMATERIALS
FACULTY OF MECHANICAL ENGINEERING
SILESIAN UNIVERSITY OF TECHNOLOGY

INTERNATIONAL STUDENTS SCIENTIFIC CONFERENCE

The role of metrology and roughness analysis in the laser cutting of steel

Jan Wypiór[a], Kinga Stępska[a] , Katarzyna Ptasznik[a], Martyna Urbańska[a],
Mirosław Bonek [a], Eva Tillova [b]

[a] Silesian University of Technology, Faculty of Mechanical Engineering, Student of Production and Management Engineering, email: jw309692@student.polsl.pl
[a] Silesian University of Technology, Faculty of Mechanical Engineering, Student of Production and Management Engineering, email: ks309686@student.polsl.p
[a] Silesian University of Technology, Faculty of Mechanical Engineering, Student of Production and Management Engineering, email: kp309682@student.polsl.pl
[a] Silesian University of Technology, Faculty of Mechanical Engineering, Student of Production and Management Engineering , email: mu309689@student.polsl.pl
[b] Faculty of Mechanical Engineering, Department of Materials Engineering, University of Žilina

Abstract: Metrology in laser cutting is crucial for ensuring repeatability and high product quality. Measuring and controlling cutting parameters such as laser power, speed and focus location minimises deformation and burrs. Assessing surface roughness, both in 2D and 3D, provides a complete characterisation of edge quality. The use of ISO standards allows for standardised assessment and documentation of product compliance, and the selection of the appropriate measurement method increases the efficiency and precision of the process.

Keywords: laser cutting, industrial metrology, surface roughness, 3D analysis, contact and non-contact measurements

1. INTRODUCTION

Metrology is the foundation of modern laser cutting, guaranteeing not only quality but also efficiency and repeatability of production. Despite the high technological advancement of the machines, measurements are necessary due to the physics of the process: the laser introduces a large amount of heat into the material, causing thermal deformation, and without dimensional control, there is no certainty that the cooled element will retain its specified shape. In addition, wear and tear on consumables such as nozzles and lenses can alter the geometry of the gas stream and cause edge beveling. The heterogeneity of the material, which may bend under the influence of stress release, and the dynamics of the machine, which generates vibrations affecting the head path at high cutting speeds, must also be taken into account. [1, 2]

2. THE ROLE OF METROLOGY IN THE CUTTING PROCESS

The measurements enable verification and optimisation of key cutting parameters, such as the focus location (affecting the gap width and edge shape), cutting speed and laser power (affecting burrs and scorching), and the selection of the exhaust gas. Analysis of the results allows these parameters to be adjusted, ensuring stable production quality and eliminating deviations. [3, 4, 5]

The use of systematic metrology translates directly into business and operational benefits: it reduces the number of defects and the need for corrections, which is crucial for waste reduction. Increased process repeatability enables compliance with stringent requirements based on commonly used standards such as ISO 9013 (classification of thermal cutting quality, including perpendicularity and roughness) and ISO 2768 (general tolerances for linear and angular dimensions). Although the detailed characteristics of these standards will be presented later in this paper, it is worth noting that they form the basis for documenting product compliance with customer requirements in industries such as aerospace and automotive. Furthermore, surface roughness control, often integrated with vision systems, allows for a quality that eliminates the need for further grinding, which significantly reduces production costs. [1, 2, 6]

Advanced control includes minimising roughness, which avoids post-processing, and integration with CMM systems for real-time parameter correction. The process is divided into three stages: preliminary metrology (machine calibration and laser interferometry), in-process control (capacitive measurements maintaining a constant focus and gap monitoring) and post-process control (dimensional verification and edge analysis). This approach ensures that each of the thousands of cut parts is identical, which is essential for production automation. [1, 7, 8].

3. CHARACTERISTICS OF SURFACE ROUGHNESS

The characteristics of edge roughness after laser cutting boil down to a description of the height and arrangement of micro-irregularities (striations) on the cut surface and their numerical parameters, mainly Ra, Rz, Rq, and Rt. [9] [10]

3.1. General description of roughness after laser cutting

Vertical or diagonal lines (grains/grooves) form on the surface of the edges, and their depth and uniformity determine the perceived roughness: the deeper and more irregular the lines, the poorer the surface quality. Roughness affects not only the appearance (matt/“ragged” vs shiny/smooth), but also tribological properties – friction, wear, compatibility with seals or coatings. [11][12][13]

3.2. Typical roughness parameters

The following parameters are most commonly used to evaluate edges after laser cutting: Ra (arithmetic mean deviation of the profile), Rq (root mean square deviation), Rz (mean height of peak-to-valley roughness) and Rt (total profile height). In laser steel cutting studies, the Ra, Rq, Rz, Rt/Rt set is often analysed, as well as functional parameters from the Rk (profile core) group, in order to better describe the load-bearing capacity and nature of the unevenness distribution. [14][15]

3.3. Features of the edge profile after laser cutting

The roughness profile of edges after laser cutting can be positively asymmetrical (skewness > 0), which means that there are more 'sharp' peaks than deep valleys; for laser-cut steel, typical Rq/Ra ratios of ≈ 1.2 have been demonstrated. The Ra and Rz parameters vary along the height of the edge – the upper part (at the beam entry point) tends to be smoother, while the lower part, where it is more difficult to remove liquid metal, has higher Ra, Rz and more pronounced striations. [10][16]

3.4. Dependence of roughness on process conditions

Increasing the cutting speed in many studies leads to a decrease in Ra and Rz, as long as the stability of the melting front is maintained, while too low a speed or too high a gas pressure increases roughness through deeper grooves and stronger 'carving' of the surface by the gas stream. Increasing the laser power may initially improve quality (more stable melt), but further increasing the power at the same speed causes overheating, thicker striations and an increase in roughness parameters. [9][10][11]

4. ROUGHNESS PARAMETERS

The quality of the side surface of laser-cut steel elements is an important parameter for assessing the effectiveness of the thermal processing. In order to determine it in an unambiguous and comparable manner, a set of standards describing both the macrogeometry of edges and the micro- and mesogeometry of surfaces is used. For this purpose, three complementary standards are used: PN-EN ISO 9013, specifying quality requirements for thermally cut products, ISO 4287, defining 2D profile roughness parameters, and ISO 25178-2, describing surface texture parameters in 3D spatial terms. The combined application of these standards enables a comprehensive characterisation of the surface after laser cutting, including both an assessment of geometric quality and a detailed analysis of the roughness structure. [1,2,3]

4.1 ISO 9013 standard

The PN-EN ISO 9013 standard classifies the quality of a cut edge based on parameters describing its geometric accuracy and characteristic features arising during the cutting process. The three basic quality parameters are: perpendicularity or slope tolerance of the cut surface u, average height of the cut surface profile Rz_5, and dimension of the upper edge overmelt zone Δa. [1]

The parameter u defines the deviation of the side surface from ideal perpendicularity and is important for maintaining dimensional accuracy and correct further processing of the element. The Rz_5 value refers to the characteristic grooving of the surface, which is the result of pulsating removal of liquid metal during the process. This parameter is defined as the sum of the average values of the five highest peaks and the five lowest valleys of the roughness profile. The Δa dimension, on the other hand, describes the extent of overmelting in the upper zone, which is an indicator of local overheating of the material and the correctness of the selection of technological parameters. [4,5]

4.2 ISO 4287 standard

The normative approach contained in ISO 9013 allows for the assessment of the macrogeometry of a surface, but does not provide detailed information about the roughness structure. For this purpose, ISO 4287 is used, which defines parameters describing the 2D profile of a surface, such as Ra, Rz, Rt, Rp, Rv, Rsk and Rku. [2,5,6]

The Ra parameter (which is the arithmetic mean of profile deviations) is commonly used, but on laser-cut surfaces it does not accurately reflect the structure of the grooves, as it averages the depth and shape of the irregularities. Rz is more representative, as it is the average difference between the five highest peaks and the deepest valleys averaged over five measurement sections. Rt determines the maximum profile height and allows local defects to be detected. The parameters Rp and Rv define the extreme values of the profile, indicating its asymmetry, while the statistical Rsk (skewness) and Rku (kurtosis) characterise the distribution of irregularities. Laser-cut surfaces often have a negative Rsk, resulting from the predominance of valleys formed during the removal of liquid metal. [6,8,9]

4.3 ISO 25178-2 standard

In addition to classic profile parameters, the importance of spatial roughness analysis in accordance with ISO 25178-2, which allows the surface structure to be described in 3D, is also growing. Parameters such as Sa (average areal height), Sq (standard deviation of height), Sp and Sv (highest peak and deepest valley), Sz (maximum height difference) and statistical Ssk and Sku (skewness and kurtosis) enable the topography to be assessed across the entire surface, rather than just along a single profile. 3D analysis provides more comprehensive information about the distribution of irregularities and is particularly useful in studying surfaces with irregular grooves or variable structures, typical of laser cutting. [3,9]

5. METHODS OF MEASURING ROUGHNESS

5.1. Roughness measurement

Roughness measurement is a metrological process involving the quantitative determination of micro-irregularities on the surface of a material. It is a test of deviations of the actual shape of a surface from its ideal shape (e.g. perfectly flat) [26]. In engineering and materials science, roughness is a key element of the so-called Surface Geometric Structure (SGP) [27]. It refers to minor irregularities, i.e. depressions and elevations in the material.

In many cases, surface geometric structure (SGS) is an important factor determining product quality, which is why numerous rules for measuring surface roughness parameters have been developed. Some of them have been introduced into industrial practice and used as a basis for the design of measuring instruments. [26,28]

Among the many, the following can be distinguished:

- Contact instruments in which the measuring tip moves across the surface being tested. These include profilographs and profilometers.
- Optical and optoelectronic instruments (non-contact) [26].

Roughness standards (which are usually grouped into sets) can also be used to check surface roughness. Before each surface roughness measurement, a preliminary (visual) check should be carried out, using roughness standards to outline the directionality of the profile structure for different types of surface treatments. The preliminary check may indicate that accurate methods of control are not necessary. In order to determine whether accurate

measurement is necessary, roughness standards should be used to compare the visual or tactile assessment of the surface. [28]

5.2. Measurement with a profilometer

Contact profilometry (also known as contact measurement) is a method of measuring surface irregularities by moving a very thin stylus over the measured surface, which records vertical movements resulting from the topography of the material, converting them into a measurement signal, which allows for the analysis of roughness, coating thickness or defects. This is a precise method, but it can damage delicate surfaces. Of course, modern devices are capable of measuring very soft materials with minimal pressure, which allows the structure of the material to be preserved. In this method, potential sources of error include the skills of the person performing the measurement and the software used. [26,29]

5.3 Optical methods

Currently, various optical methods are becoming increasingly popular, characterised by fast and contactless evaluation of elements. The instruments used do not damage the surface cross-section (because they use a light beam). The Linnik microscope and the Schmaltz double microscope are instruments that operate on the principle of light section. Both have a common measurement principle, whereby a flat beam of light from the illuminating microscope falls on the measured surface at an angle of 45°. We then see the light section through the eyepiece. [29]

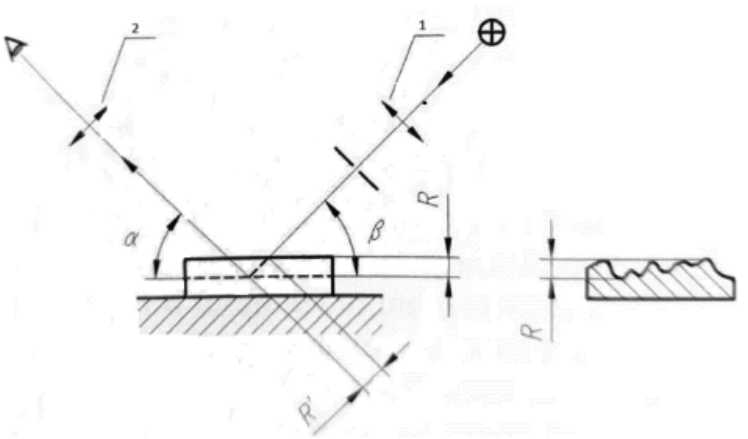

Figure 1 - Principle of measurement using the light section method: 1) lens, 2) eyepiece; α, β) 45°

Optical measurements have both advantages and disadvantages. The main advantages include: no impact on the measured surface, low intrinsic noise (Rq) at 80 pm, speed and simplicity of measurement. The most common disadvantages are: poor penetration of the measured surface, false results when measuring structures with sharp edges. It should be mentioned that an interferometer is required for optical measurements. White light interferometry is currently one of the most commonly used optical methods for non-contact, three-dimensional measurement of surface roughness and topography
with high vertical resolution. [30]

5.4. Laser methods

The laser scanning method involves moving a laser beam across a surface and recording the reflected signal — most often using triangulation or confocal laser scanning — resulting in a line profile or point cloud/height grid from which parameters such as Ra and Rq are calculated. The method is non-contact and fast, making it attractive for online inspection and large surface area measurements. Its limitations include lower vertical resolution compared to white light interferometry. Another serious problem is its sensitivity to the optical properties of the material, such as strong scattering and high specular reflectance. [31]

5.5. When should you use 3D instead of 2D?

The reliability of the analysis of machined surfaces depends mainly on the selection of the appropriate device and measurement procedure. In many cases, 2D analysis is insufficient to fully describe the surface structure. Three-dimensional scanning comes to the rescue. Nowadays, machined surfaces increasingly have a stochastic structure (containing random elements) instead of a directional structure, which cannot be properly assessed using a 2D section. The parameters for quantitative assessment of surface topography (3D) and their operators are described in the PN-EN ISO 25178 standard. On the other hand, 2D measurements still make sense when fast, cheap and simpler quality control is needed for homogeneous and hard materials, where a single cross-section well represents the surface condition. [30,32,33]

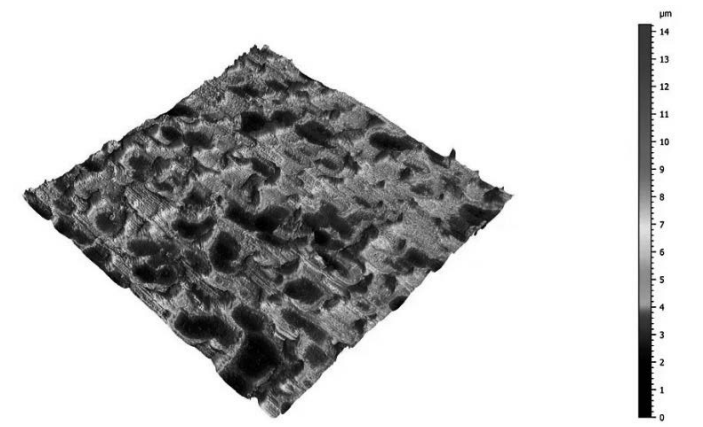

Figure 3 - 3D topography of a steel sheet Surface

6. CONCLUSIONS

Metrology plays a key role in the laser cutting process, ensuring repeatability, dimensional accuracy and high product quality. Precise control of cutting parameters – such as laser power, speed, focus location and gas selection – minimises thermal deformation, burrs and scorching, thereby reducing the number of defects and the need for corrections. Analysis of edge and surface roughness, both in 2D and 3D, enables the evaluation of the micro- and mesogeometry of components, which is important for their tribological properties and further processing.

The use of ISO standards, such as ISO 9013, ISO 4287 and ISO 25178-2, allows for standardised quality assessment and documentation of product compliance with industry requirements. The choice of the appropriate measurement method – contact, optical or laser –

should be adapted to the type of material, surface structure and accuracy requirements. As a result, the systematic use of metrology in laser cutting not only improves production quality, but also increases the efficiency of industrial processes and reduces production costs.

ACKNOWLEDGEMENTS

The work was created as part of project based learning - PBL, in the 13th competition under the Initiative of Excellence - Research University, Silesian University of Technology, Gliwice, Poland and as part of project of Students Scientific Circle of Laser Surface Treatment under the Initiative of Excellence - Research University, Silesian University of Technology, Gliwice, Poland.

BIBLIOGRAPHY

1. https://www.bapro-met.com.pl/news.php?newsID=511&lang=pl&action=view [dostęp: 19.12.2025]
2. https://centrummaszyncnc.pl/baza-wiedzy/na-czym-polega-ciecie-laserowe-zalety-materialy-i-zastosowanie-wycinania-laserem [dostęp: 19.12.2025]
3. https://centrummaszyncnc.pl/baza-wiedzy/na-czym-polega-ciecie-laserowe-zalety-materialy-i-zastosowanie-wycinania-laserem [dostęp: 19.12.2025]
4. https://www.accteklaser.com/pl/parametry-ciecia-laserowego-ostateczny-przewodnik/ [dostęp: 19.12.2025]
5. https://www.trumpf.com/pl_PL/rozwiazania/zastosowania/ciecie-laserowe/ [dostęp: 19.12.2025]
6. https://www.koenigstahl.pl/pl/blog/aktualnosci/ciecie-laserowe-3d-stali-czym-jest-i-jakie-sa-jego-zalety/ [dostęp: 19.12.2025]
7. https://virmer.com/pl/metal-laser-cutting-operating-principles/ [dostęp: 19.12.2025]
8. https://www.koenigstahl.pl/pl/blog/aktualnosci/ciecie-laserowe-3d-stali-czym-jest-i-jakie-sa-jego-zalety/ [dostęp: 19.12.2025]
9. http://jamme.acmsse.h2.pl/papers_vol54_1/54114.pdf [dostęp: 15.12.2025]
10. Zaleski, K., Skoczylas, A., 2014. Studies on selected properties of surface layer of C45 steel objects after laser cutting and milling. Advances in Science and Technology Research Journal, Volume 8.
11. https://jest.journals.ekb.eg/article_231180.html [dostęp: 15.12.2025]
12. https://www.harsle.com/checking-quality-of-laser-cutting/ [dostęp: 15.12.2025]
13. https://www.jrpanel.com/engineerhome/keyword/JRPanel_Cutting_Quality_Assessment_of_Laser_Cutting_Machin.html [dostęp: 15.12.2025]
14. https://richconn.com/surface-roughness/ [dostęp: 15.12.2025]
15. Jasiński, M., 2025. Optimization of Steel Laser Cutting Processes Using the Roughness Parameter Sq and Response Surface Methodology (RSM). Periodica Polytechnica Mechanical Engineering, pp. 340-346.
16. https://re.public.polimi.it/bitstream/11311/973057/1/On%20the%20use%20of%20Areal%20Roughness%20Parameters%20to%20Assess%20Surface%20Quality%20in%20Laser%20Cutting

%20of%20Stainless%20Steel%20with%20CO2%20and%20Fiber%20Sources.pdf [dostęp: 15.12.2025]
17. A. Klimpel, *Technologie laserowe: spawanie, napawanie, stopowanie, obróbka cieplna i cięcie*, Gliwice: Wydawnictwo Politechniki Śląskiej, 2012.
18. https://www.hoffmann-group.com/media/media/pl/downloads_25/Pomiar-chropowato-ci-powierzchni.pdf [dostęp: 15.12.2025]
19. Krajewski S., Nowacki J., *Assessment of the parameters of the cutting edge of massive and porous metal alloys*, Metale & Nowe Technologie, „Technologie cięcia", maj–czerwiec 2020, s. 40–44.
20. https://www.laserspechub.com/guides/edge-quality-standards [dostęp: 15.12.2025]
21. https://www.sms-group.com/sn-200-3-przepisy-produkcyjne-ciecie-i-giecie-termiczne-817/download [dostęp: 15.12.2025]
22. Krajewski S., Nowacki J., *Assessment of the parameters of the cutting edge of massive and porous metal alloys*, Metale & Nowe Technologie, „Technologie cięcia", maj–czerwiec 2020, s. 40–44.
23. J. Kosmol (red.), *Laboratorium z metrologii warsztatowej*, Gliwice: Wydawnictwo Politechniki Śląskiej, 1997
24. https://www.mitutoyo.com/educational-resource/surface-roughness-measurement/ [dostęp: 15.12.2025]
25. https://cdn.standards.iteh.ai/samples/42785/043e77b9088d449fb2c328b8c6db329c/ISO-25178-2-2012.pdf [dostęp: 15.12.2025]
26. Adamczak S. (2023), Metrologia geometryczna powierzchni technologicznych, Wydawnictwo Naukowe PWN, Warszawa.
27. PN-EN ISO 4287:1999. Specyfikacje geometrii wyrobów – Struktura geometryczna powierzchni: metoda profilowa – Terminy, definicje i parametry struktury geometrycznej powierzchni.
28. https://www.sandvik.coromant.com/pl-pl/knowledge/materials/workpiece-surface-measurement
29. Buchenau T. i in., Comparison of Optical and Stylus Methods for Surface Texture
30. https://www.mechanik.media.pl/artykuly/optyczne-pomiary-3d-powierzchni.html
31. https://www.qualitymag.com/articles/95593-how-to-make-the-right-choice-between-2d-vs-3d-in-surface-metrology?
32. https://www.sciencedirect.com/science/article/pii/S0950061825022639?
33. https://www.mechanik.media.pl/artykuly/optyczne-pomiary-3d-powierzchni.html

TalentDetector

9th January 2026
Gliwice, Poland

DEPARTMENT OF ENGINEERING MATERIALS AND BIOMATERIALS
FACULTY OF MECHANICAL ENGINEERING
SILESIAN UNIVERSITY OF TECHNOLOGY

INTERNATIONAL STUDENTS SCIENTIFIC CONFERENCE

Comparison of Weldability Characteristics of Different Welding Methods in Armor Steel

[a]Ahmet Yılmaz, [a]Efe Atılgan, [a]Beytullah Keklik, [a]Cemal Meran, [a]Emre Korkmaz, [b]Kazım Bilgin,

[a] Pamukkale University, Faculty of Engineering, Department of Mechanical Engineering, Denizli-Turkiye, email: cmeran@pau.edu.tr
[b] Askon Mechanics San. ve Tic. A.Ş., Denizli-Turkiye, email: info@askondemir.com

Abstract: In this study, 6,35 mm thick armor steel plates were joined using Gas Metal Arc Welding (GMAW) and Gas Tungsten Arc Welding (GTAW). Tensile, impact, bending, and hardness tests were carried out to evaluate the mechanical performance of the welded joints produced by each welding technique. Subsequently, macrostructural and microstructural examinations were performed to investigate weld integrity and heat-affected zone (HAZ) characteristics. The experimental results indicate that welding method and heat input play a crucial role in determining the mechanical properties and microstructural evolution of armor steel joints. Among the applied methods, GTAW provided the highest tensile strength, while GMAW exhibited competitive mechanical performance together with superior applicability for industrial production.

Keywords: GMAW, GTAW, Armor steel, weldability

1. INTRODUCTION

Armor steels, which belong to the class of high-strength low-alloy (HSLA) steels, are widely used in military and civilian applications such as tanks, armored personnel carriers, and VIP vehicles due to their superior ballistic protection capabilities. Owing to the complex geometries of these structures, welding is the primary joining method employed during fabrication. Consequently, armor steels are manufactured and qualified according to strict military standards, including MIL-A-46100 and MIL-A-12560 (RHA).

The material investigated in this study complies with Class 1 Rolled Homogeneous Armor (RHA) specifications, which prioritize weldability and impact toughness. The metallurgical design of armor steels is based on a carefully controlled chemical composition to achieve an optimal balance between hardness, toughness, and weldability. Carbon content is maintained below 0.30% to minimize the risk of cold cracking in the heat-affected zone (HAZ). Alloying elements such as manganese, chromium, and molybdenum are added to enhance hardenability, while nickel is incorporated to improve low-temperature impact toughness. Conversely, impurity

elements such as sulphur and phosphorus are kept at minimal levels to prevent embrittlement and degradation of ballistic performance.

The mechanical performance of armor steels depends on a delicate balance between high hardness, which is necessary to resist projectile penetration, and sufficient toughness to absorb impact energy without catastrophic failure. The armor steel examined in this study exhibits superior ballistic properties compared to conventional armor steels, with a hardness range of 420–480 HBW, yield strength exceeding 1200 MPa, and maintained impact toughness even at temperatures as low as −40 °C.

2. MATERIALS AND METHOD

In this study, nine armor steel plates with dimensions of 6,35 × 100 × 350 mm and a hardness range of 420–480 HB were welded using three different welding methods in accordance with relevant standards. The mechanical properties of the base material are presented in Table 1, while its chemical composition is given in Table 2.

Table 1. Typical mechanical properties of armor steel

Thickness (mm)	Tensile Strength (Rm) (N/mm^2)	Elongation (%)	Impact Charpy	Hardness Ranges (HBW)	C_{eq}
4,00-20,00	1300-1500	10	30	420-480	0,74

Table 2. The Chemical Composition of Armor Steel

C (max%)	Si (max%)	Mn (max%)	P (max%)	S (max%)	Cr (max%)	Ni (max%)	Mo (max%)	B (max%)
0.25	0.5	1.2	0.015	0.005	1	2	0.6	0.003

For the GMAW process, a shielding gas mixture consisting of 80% Ar, 18% CO_2, and 2% O_2 was employed. A 1,2 mm diameter austenitic stainless steel filler wire (ESAB OK Autrod 16.95), conforming to EN ISO 14343-A and classified as ER307, was used as the filler material. The chemical composition of the filler metal is provided in Table 3.

Table 3. Chemical Composition (%) of Filler Metal used GMAW and GTAW [5]

C	Mn	Si	S	P	Ni	Cr	Mo	Cu	N
0,06	6,2	0,8	0,009	0,022	8,0	18,4	0,2	0,2	0,05

GTAW samples were prepared using a Kolarc TX400 welding machine. Pure argon (100% Ar) was utilized as the shielding gas. An ESAB 307 austenitic stainless-steel electrode with a diameter of 2,4 mm, conforming to ISO 14343-A-W 18 8 Mn, was employed as the filler metal.

3. RESULTS

The welding parameters for GMAW, and GTAW given in Table 4. A series of mechanical tests were performed on the samples according to the parameters given in Table 5. The heat inputs were calculated using the Eq. (1).

$$q = \eta IU60 / \nu \quad (1)$$

where q, U, I, ν and η are the heat input (kJ/mm), welding arc voltage (V), welding current (A), ν welding speed (mm/min) and the arc efficiency (η =0.7 GTAW, η =0.8 GMAW), respectively.

Table 4. The welding parameters used GMAW, and GTAW

Method	Pass No.	Current (A)	Voltage (V)	Duration (s)	Welding Speed (mm/s)	Arc Efficiency (η)	Heat Input (Q) (kJ/mm)
GMAW 1	1	220	24	73	4,79	0,8	0,88
	2	220	24	110	3,18		1,33
GMAW 2	1	220	24	56	6,25	0,8	0,68
	2	220	24	102	3,43		1,23
GMAW 3	1	220	24	144	2,43	0,8	1,74
TIG 1	1	155	13	150	2,33	0,6	0,52
	2	200	18	277	1,26		1,71
TIG 2	1	155	13	177	1,98	0,6	0,61
	2	200	18	260	1,35		1,60
TIG 3	1	155	13	150	2,33	0,6	0,52
	2	200	18	85	4,12		0,52
	3	200	18	210	1,67		1,30

As presented in Table 5, the GTAW method yielded the highest average tensile strength of 1073 MPa, while GMAW exhibited a tensile strength of 811 MPa. Bending tests revealed that the maximum bending force was 11,2 kN for GMAW and 10,6 kN for GTAW.

Table 5. The average tensile, hardness, impact, and bending test results of welded joints

Welding Method	**Yield Strength, Re, (MPa)**	**Tensile Strength, Rm, (MPa)**	**Elongation, A (%)**	**Charpy Impact Energy (J)**	**Hardness (HRA)**	**Bending Force (kN)**
GMAW	-	811	-	50	48	11,2
GTAW	1063	1073	7	36	50	10,6

The samples were immersed in a 2% Nital solution and etched for micro and macro images. The images were then captured. Vickers microhardness test was used under 10 s dwell time and 200 g load to measure the hardness of WZ, HAZ and BM regions of the welded sample. Measurements were made at 1 mm intervals.

Macrostructural examinations (Figure 1) demonstrated that full penetration was achieved in both GMAW and GTAW joints, with no visible defects such as cracks or discontinuities.

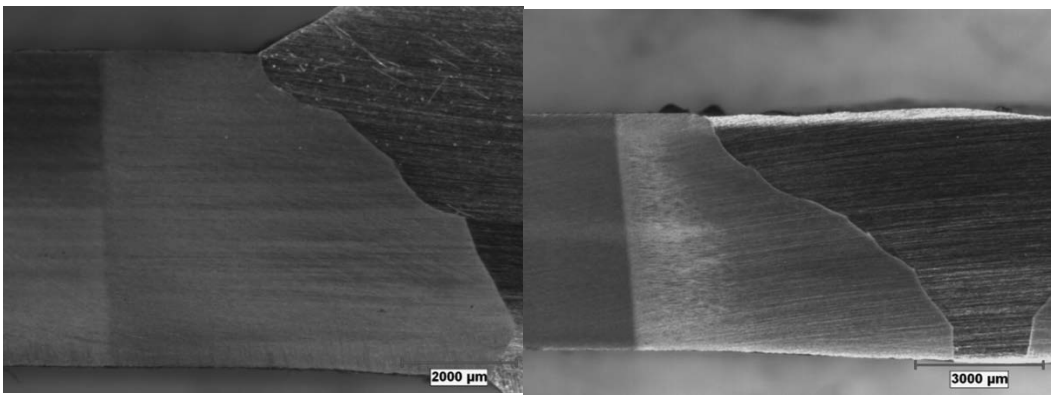

Figure 1. Macro images of GMAW (left), and GTAW (right)

The base metal microstructure (Figure 2) consists predominantly of needle-like tempered martensite, which is responsible for the high hardness of the material. This structure is obtained through rapid quenching followed by low-temperature tempering, which slightly reduces hardness while significantly improving toughness and ductility.

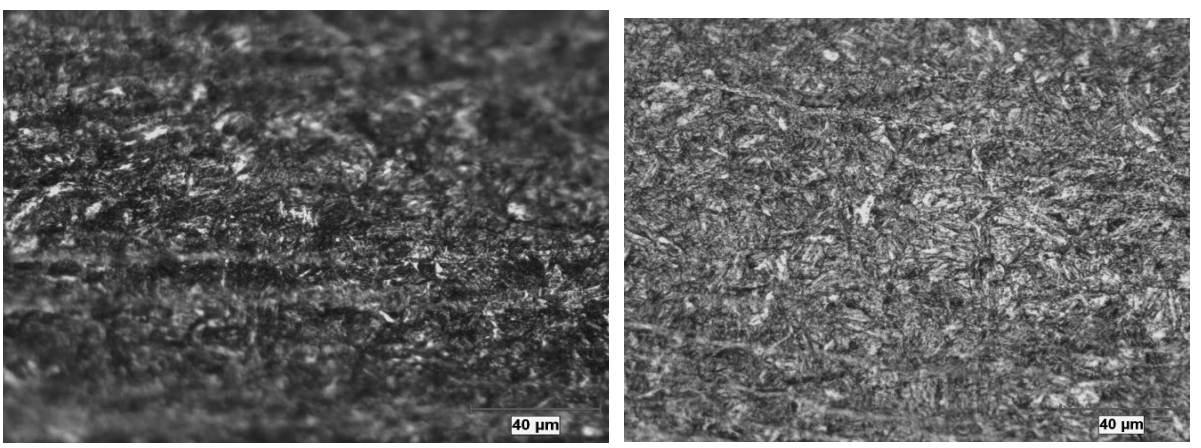

Figure 2. Microstructural images of the base metal of GMAW, and GTAW welded specimens (500x)

The coarse-grained heat-affected zone (CGHAZ) microstructure is shown in Figure 3. Due to high heat input, grain coarsening occurred, and tempered martensitic structures with carbide precipitation were observed. As confirmed by microhardness measurements, this region exhibited lower hardness compared to other HAZ regions due to matrix softening caused by carbide formation.

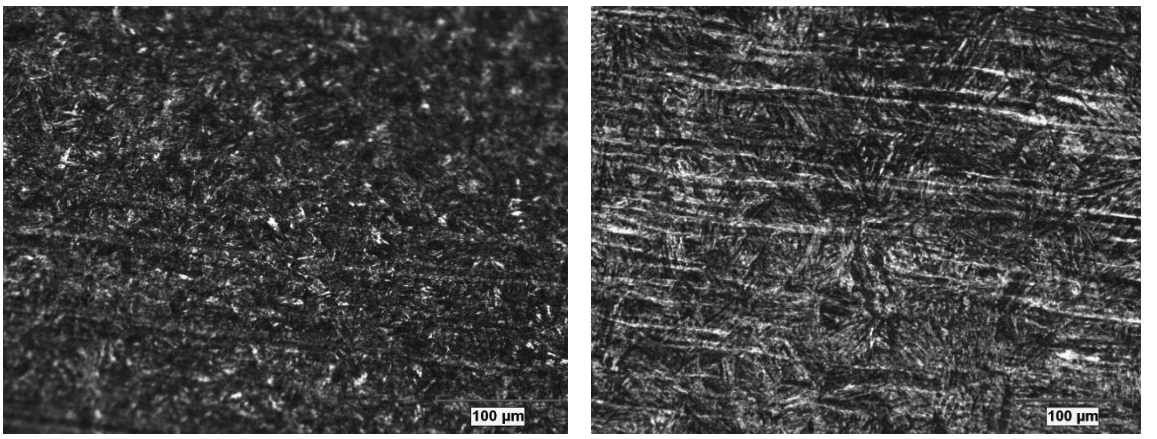

Figure 3. Micrographs of coarse grains in the CGHAZ region of GMAW and GTAW welded specimens (200x)

Figure 4 illustrates the fine-grained heat-affected zone (FGHAZ), where the heat input was insufficient to cause grain coarsening. Partial transformation of ferrite and pearlite into austenite occurred, followed by refinement during cooling. This fine-grained structure restricted dislocation movement, resulting in higher hardness values compared to the CGHAZ.

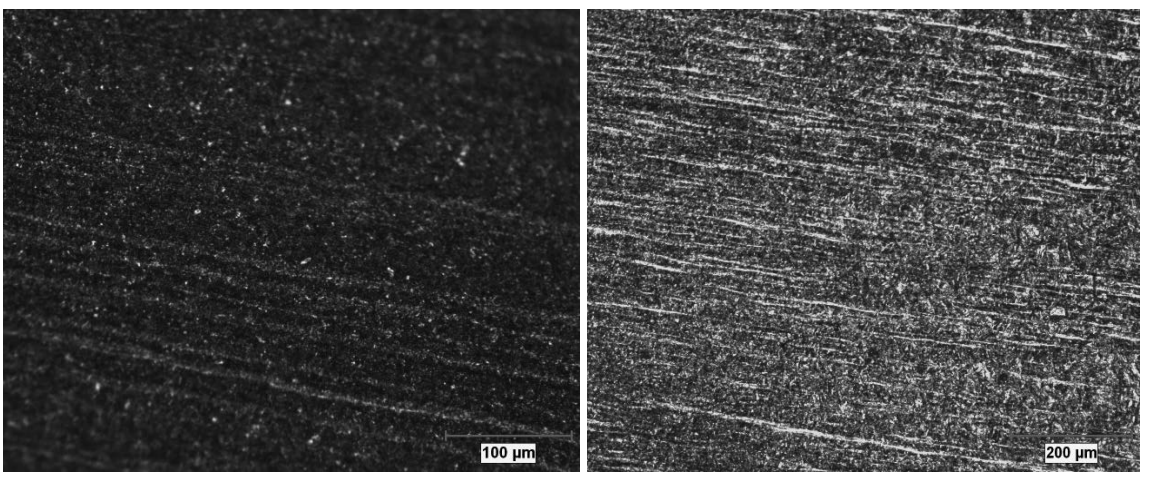

Figure 4. Micrographs of fine grains in the FGHAZ region of GMAW and GTAW welded specimens (200x)

The weld metal microstructure (Figure 5) consisted of delta-ferrite dispersed within an austenitic matrix. The hardness of the weld metal was considerably lower than that of the base metal. The use of austenitic filler metal reduced the risk of hydrogen-induced cracking, improved notch toughness, and helped redistribute residual stresses due to its higher ductility.

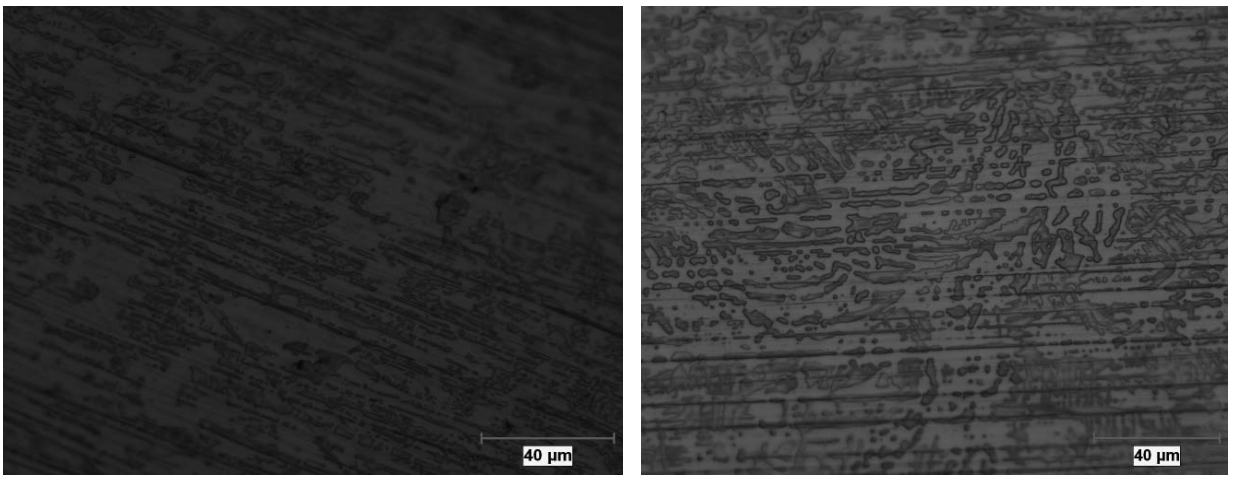

Figure 5. Microstructure of the weld zone of GMAW and GTAW welded specimens (500x)

Microhardness profiles (Figure 6) showed that hardness values in the weld metal increased toward the HAZ but did not reach base metal hardness in the CGHAZ. In the FGHAZ, hardness exceeded that of the base metal due to grain refinement. GTAW joints exhibited higher hardness values, attributed to higher heat input.

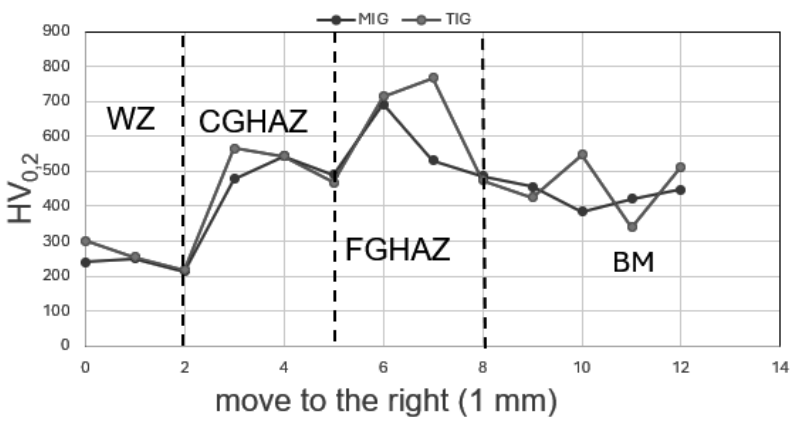

Figure 6. Microhardness Test Results

During tensile testing, all specimens except three GTAW samples fractured in the weld metal without noticeable elongation. This behaviour is attributed to the significantly higher strength of the base metal compared to the weld metal. Specimens exhibiting elongation fractured in the HAZ, indicating improved weld penetration and fusion.

In bending tests, all specimens cracked or fractured. GMAW and GTAW joints cracked in the HAZ, demonstrating improved ductility due to effective bonding with the austenitic filler metal.

Impact test results indicated that GTAW and GMAW joints exhibited high impact toughness, primarily due to the austenitic weld metal microstructure, which suppressed brittle fracture mechanisms.

4. CONCLUSIONS

The use of austenitic filler metal in welding armor steel eliminates the need for preheating due to its high hydrogen absorption capability, provided that the material thickness does not exceed 25 mm. Among the investigated welding methods, GTAW produced the highest mechanical strength; however, its time-consuming and labour-intensive nature limits its industrial applicability. GMAW emerged as the most suitable welding method for mass production, offering a favourable balance between cost, productivity, and mechanical performance comparable to GTAW.

Heat input was found to be a critical parameter influencing mechanical properties. Excessive heat input adversely affected the martensitic structure of the armor steel, leading to reduced mechanical performance. An optimal heat input range of 0,6–1,2 kJ/mm was identified. Multi-pass welding significantly increased heat input and should be avoided whenever possible. To achieve superior mechanical properties, adequate weld penetration is essential; however, this is difficult to consistently achieve using manual welding methods. Therefore, the use of robotic welding systems is recommended. Future studies will focus on minimizing penetration defects and HAZ degradation to further enhance joint performance.

BIBLIOGRAPHY

1. Çelik, C., Göçmen, M., Çoban, O., Baykal, H., Gürol, U. ve Koçak, M. (2023). Yüksek mukavemetli balistik zırh çeliklerinin kaynaklanabilirliği. Uludağ Üniversitesi Mühendislik Fakültesi Dergisi, 28(3), 1010-1028. https://doi.org/10.17482/uumfd.1333002
2. Örenler, A. (2018). Zırh çeliklerinin kaynak kabiliyetinin incelenmesi [Yüksek lisans tezi]. Sakarya Üniversitesi.
3. Skowrońska, B., Szulc, J., Bober, M., Baranowski, M. ve , T. C. (2022). Selected properties of ramor 500 steel welded joints by hybrid pta-mag. Journal Of Advanced Joining Processes, 5, 1-11. https://doi.org/10.1016/j.jajp.2022.1001117
4. Magudeeswaran, G., Balasubramanian, V. ve Reddy, G. M. (2018). Metallurgical characteristics of armour steel welded joints used for combat vehicle construction. Defence Technology, 14(5), 590-606. https://doi.org/10.1016/j.dt.2018.07.021
5. https://esab.com/us/nam_en/products-solutions/product/filler-metals/stainless-steel/mig-wires-tig-rods-gmaw-gtaw/ok-autrod-16-95/
6. Korkmaz, E., & Meran, C. Gas metal arc welding of XPF800 steel for automotive industry: Microstructural evaluation and mechanical properties investigation. Proceedings of the Institution of Mechanical Engineers, Part L: Journal of Materials: Design and Applications, 236(4), 747-756, (2022).
7. Korkmaz, E., and Meran, C., “Mechanical properties and microstructure characterization of GTAW of micro-alloyed hot rolled ferritic XPF800 steel”, Engineering Science and Technology, an International Journal 24, 503-513,DOI: 10.1016/j.jestch.2020.04.006, (2021).

TalentDetector

9th January 2026
Gliwice, Poland

DEPARTMENT OF ENGINEERING MATERIALS AND BIOMATERIALS
FACULTY OF MECHANICAL ENGINEERING
SILESIAN UNIVERSITY OF TECHNOLOGY

INTERNATIONAL STUDENTS SCIENTIFIC CONFERENCE

Numerical analysis of the wear of the cutting edge of mulcher tool

Zuzanna Zielińska[a], Wiktoria Borowiec[a], Dominik Boho[a], Łukasz Lomania[b], Michał Szojda[c], Wojciech Mikołejko[d], Agata Śliwa[d], Marek Sroka[d], David Varholík[e], Peter Očovský[e], Miroslava Tavodova[e]

[a] Silesian University of Technology, Faculty of Materials Science and Industrial Digitalization
email: zz304779@student.polsl.pl, wiktbor155@student.polsl.pl, db301763@student.polsl.pl,
[b] Silesian University of Technology, Faculty of Electrical Engineering
email: lukalom979@student.polsl.pl
[c] Silesian University of Technology, Faculty of Architecture
email: ms303646@student.polsl.pl
[d] Silesian University of Technology, Faculty of Mechanical Engineering, Department of Engineering Materials and Biomaterials
email: wojciech.mikolejko@plsl.pl, agata.sliwa@polsl.pl, marek.sroka@polsl.pl
[e] Technical University in Zvolen, Faculty of Technology, Department of Manufacturing Technology and Quality Management
email: xvarholik@is.tuzvo.sk, xocovsky@is.tuzvo.sk, tavodova@tuzvo.sk

Abstract: Forest cutters, crushers (mulchers) are an essential part of modern forestry technology, where they are used mainly for stand maintenance, processing of post-harvest residues, and preparing sites for new planting. These machines can shred woody material—such as shrubs, invasive tree species, branches, or stumps—directly in the field, which increases work efficiency and reduces environmental burden. Technological progress has resulted in a diverse range of forest cutter types, from smaller attachment-based models to powerful tracked machines built for challenging conditions. Selecting the right machine depends on the characteristics of the site and the needs of forest management. As efficiency demands grow, increasing focus is being placed on the cutting tools themselves. Their design, material composition, and arrangement significantly affect both performance and environmental impact. Studying these tools provides important insights for improving and sustainably applying forestry machinery in the future.

Keywords: forest cutter, mulcher tools, tool geometry, tool material

1. FOREST MULCHERS

Mulchers of undesired woody regeneration (fig. 1) are auxiliary work attachments – adaptors - designed to effectively expand the technological capabilities of universal mobile work machines and to increase their operational utilization. They are commonly used in silvicultural operations for the removal of unwanted woody growth on multi-year clear-cut areas or other sites designated for afforestation, for the preparation of forest soil prior to new planting, for eliminating undesirable vegetation along roadsides and forest edges, as well as for other forest stand tending activities [1].

Figure 1. Forestry mulcher: Fecon 3-Point PTO Bull Hog [2]

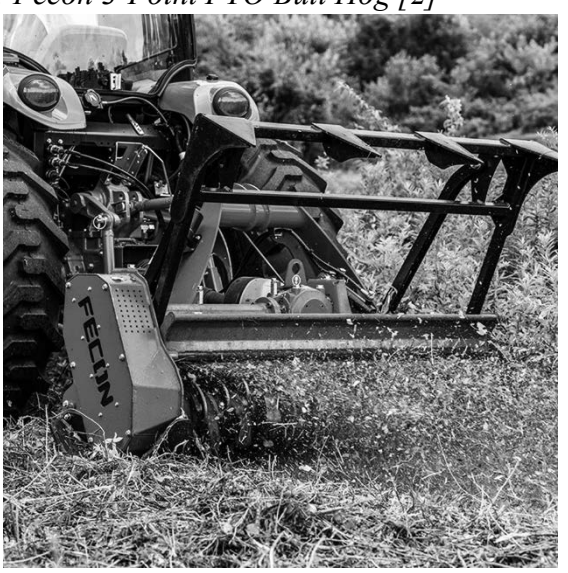

They are designed as auxiliary attachments of the base machine, such as LKT or UKT skidders, or as adaptors mounted on various specialized machines, including those installed on hydraulic manipulators. The parameters of the base machine influence the structural design of these adaptors, particularly in terms of power transmission. The drive system of the adaptors can be implemented in several ways. Torque transfer from the base machine to the adaptor is provided either via the power take-off (PTO) using a universal joint shaft, or by directly connecting the adaptor to the machine's external hydraulic circuit [1].

2. TOOLS OF MULCHERS

Mulchers play a significant role in environmental management**.** By converting vegetation into mulch, they improve soil health, enhance fertility, and help the soil retain moisture. They support habitat restoration by removing invasive species with minimal soil disturbance, which promotes biodiversity. By clearing underbrush and dead vegetation, mulchers reduce wildfire risks. They also recycle plant material on-site, eliminating the need for burning or transporting debris, and support water conservation by reducing runoff and maintaining soil moisture. In disaster recovery, mulchers are valuable for processing large amounts of organic waste after hurricanes, floods, or wildfires. They speed clean-up efforts, reduce erosion, and support faster regrowth of vegetation. By recycling organic debris into mulch, they help restore damaged areas more efficiently and sustainably.

Maintenance of mulchers includes regular cleaning, lubrication of moving parts, inspection and replacement of blades, and routine changes of fluids and filters. Structural checks for cracks or other damage are also important to ensure safe operation and extend the machine's lifespan. Common issues include blade wear, clogging from wet or fibrous material, mechanical failures of components such as bearings or belts, engine overheating, and the risk of debris ejection, which can be hazardous [3].

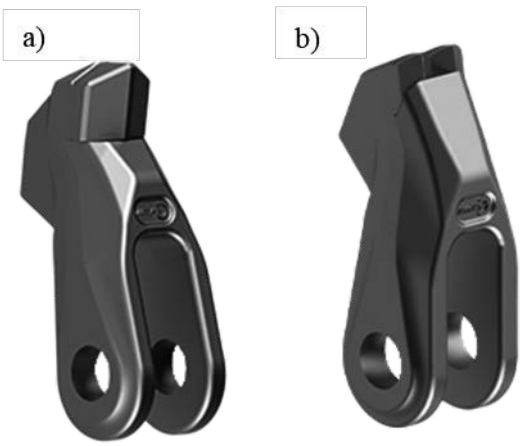

Figure 2. Types of tools a) Tool with a single WC tip [4], b) Tool with two WC tips [4]

2.1 MATERIALS OF TOOLS FOR MULCHERS

The tools (fig. 2) are manufactured by hot forming, free or drop forging. Materials suitable for these tools are steels suitable for heat treatment (carburization) such as 37Cr4, 16MnCr5, or 32CrMo12, 42CrV6, 14NiCr14 etc.

According to information in the product catalog of King Kong Tools, it is possible to significantly increase the tool's service life and wear resistance - and thus also productivity during use - by applying a so-called "armor" (fig. 3). This is presented as a hard carbide cutting edge with homogeneous grain size, offering high resistance to abrasion and impact. The steel body is reinforced, either fully or partially, achieving very high wear resistance [5,6].

Figure 3. Tool with an "armored" layer [7]

In addition to WC carbide tips, some manufacturers also offer the placement of WC plates onto the tool body to further increase protection against rapid wear (fig. 4). However, such modifications naturally also significantly increase the tool's price.

Figure 4. Example of WC plates insertion onto the tool body [8]

3. MODELS USED IN COMPUTER SIMULATION

In this study, numerical simulations were performed using the SOLIDWORKS 2025 software package with the Simulation module. The aim of the study was to develop a numerical model representing the behavior of a mulching tool under operating load conditions.

As a first step of the analysis, geometrical model was developed. In the next step the material commonly used for the mulching flails was applied. Before the analysis the finite element mesh was generated using Jacobian criterion evaluated at 16 integration points. This criterion is a measure of finite element distortion and is commonly used to evaluate mesh quality and reliability of numerical results. Geometrical model of the tool and applied mesh is shown in fig. 5a. The next important step in the simulation was the placement of the applied force and the definition of its direction on the model, which is marked in blue on fig. 5b.

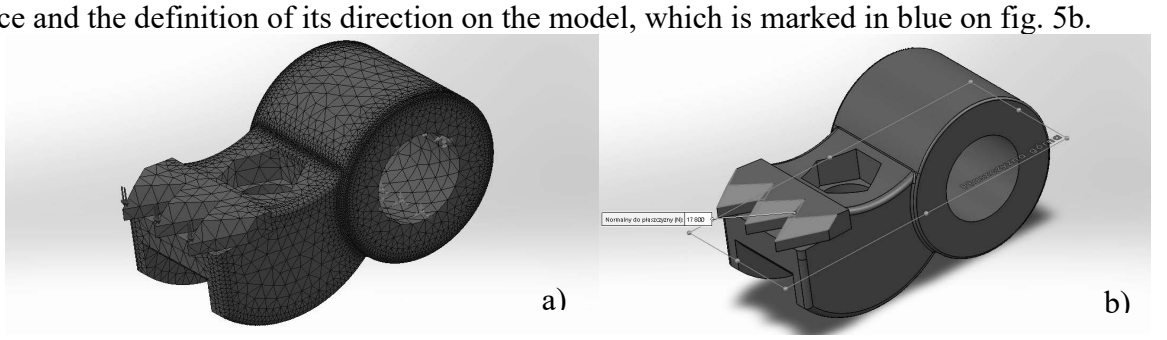

Figure 5. Example of WC plates insertion onto the tool body [8]

In the next step, a stress analysis was performed under applied load of 17,800 N. The obtained stress distribution on both sides of the model are shown in fig. 6. It is necessary to identify critical stress regions and asses the structural response of the mode under operating conditions.

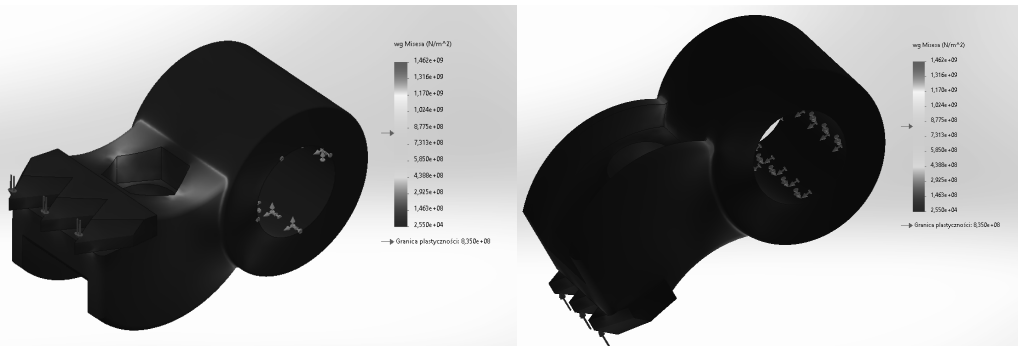

Figure 6. Distribution of the stress on the upper and lower side of the analyzed model of tool

The next analysis focused on the displacement of the model. Red represents high displacement and blue represents low displacement. The results are shown in fig. 7. This simulation allows the identification of regions with the highest displacement.

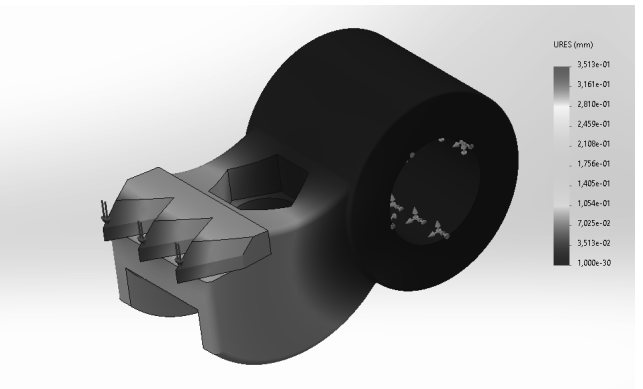

Figure 7. Force application point marked in red

Last analysis focused on the deformation of the model. Higher deformation values are indicated in red, an lower deformation values are shown in blue. The results are presented in fig. 8. This simulation helps identify critical regions where deformation may occur.

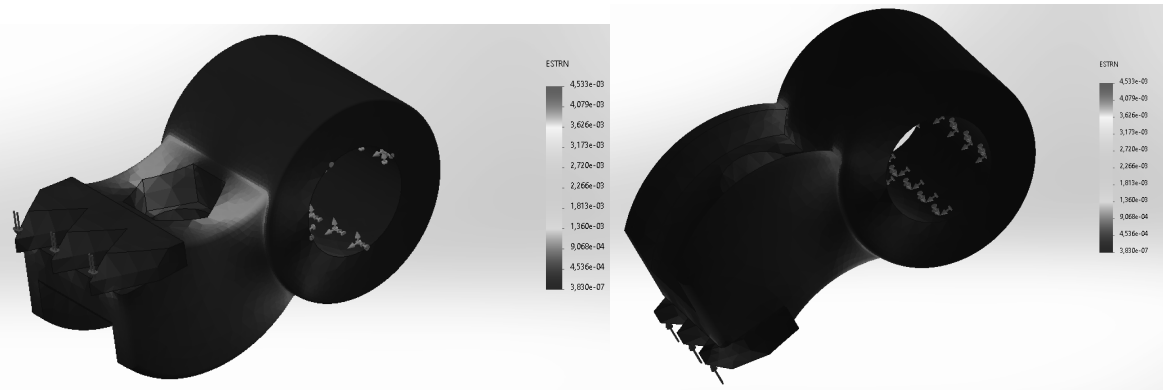

Figure 8. Areas of deformation on the upper and lower side of the analyzed model of tool

4. CONCLUSIONS

The finite element analysis carried out using SOLIDWORKS 2025 and the simulations module allowed the determination of displacement, stress, and strain distributions. The obtained stress distribution results enabled the identification of regions with increased stress concentration in the model, which under operating conditions may constitute potential sites for damage initiation or accelerated wear. This provides a basis for further development studies aimed at improving geometry and force distribution.

The displacement analysis illustrated at the structural response of the model under applied loads, when the strain analyze revealed the deformation behavior and identified critical regions susceptible to damage or excessive wear.

The application of tungsten carbides (WC) offers significant advantages in terms of very high resistance to abrasive wear. However, the WC exhibit limited plastic deformability which may lead to sudden failure of the plates. Simulation module also enables material selection, which directly influences the strength properties of the analyze component. The cooperation of good material selection and numerical simulations helps to properly construct a tool.

ACKNOWLEDGEMENT

This study was conducted as part of the project-oriented education - PBL, in the XIII competition within the Excellence Initiative - Research University program.

This work was supported by Scientific Grant Agency of the Ministry of Education, science, research and sport of the Slovak Republic and the Slovak Academy of Sciences under the grant number VEGA 1/0073/24 „Experimental analysis of shapes and materials of working tools of additional equipment of forestry mechanization technology “.

LITERATURE

1. MARKET RESEARCH INTELLECT, 2024, Available at: https://www.marketresearchintellect.com/blog/the-digital-forest-advances-in-mulching-technology-and-software-integration/
2. SIPSK, 2025, Available at: https://www.sipsk.com/lesne-frezy-forst-ino
3. Ján KOVÁČ, Jozef KRILEK, Ján JOBBÁGY a Jiří DVOŘÁK. *Technika a mechanizácia v lesníctve: vysokoškolská učebnica*. Zvolen: Technická univerzita vo Zvolene, 2017. ISBN 978-80-228-3021-8.
4. Jaroslav JECH, Tepelné zpracování oceli: Metalografická příručka. 4. přeprac. dopl. vyd. Praha: SNTL, 1983, 391 s.
5. Miroslava ŤAVODOVÁ, Daniela KALINCOVÁ, Martin KOTUS, Ľubomír PAVLÍK, The Possibility of Increasing the Wearing Resistance of Mulcher Tools, from Journal: Acta Technologica Agriculturae Volume 21 (2018): Issue 2 (June 2018) (pages: 87-93), Available at: https://www.researchgate.net/publication/326401109_The_Possibility_of_Increasing_the_Wearing_Resistance_of_Mulcher_Tools
6. FECON, 2025, Available at: https://fecon.com/product/bull-hog-mulching-teeth/
7. FECON, 2025, Available at: https://fecon.com/product/bull-hog-rotors/
8. KONECARBIDE, 2023, Available at: https://konecarbide.com/mulcher-teeth-steel-or-carbide/
9. SKID STEER SOLUTIONS, 2025, Available at: https://www.skidsteersolutions.com/double-carbide-mulching-tooth-adapter-promac/

TalentDetector
9th January 2026
Gliwice, Poland
DEPARTMENT OF ENGINEERING MATERIALS AND BIOMATERIALS
FACULTY OF MECHANICAL ENGINEERING
SILESIAN UNIVERSITY OF TECHNOLOGY
INTERNATIONAL STUDENTS SCIENTIFIC CONFERENCE

Metallic Implant Used for Temporary Fracture Fixation

Jakub Živor[a], Viera Zatkalíková[a]

[a] Žilinská univerzita v Žiline, Strojnícka fakulta, Katedra materiálového inžinierstva, Univerzitná 8215/1, 010 26 Žilina, Slovak Republic
email: zivor@stud.uniza.sk viera.zatkalikova@fstroj.uniza.sk

Abstract: This article summarizes theoretical knowledge on biomaterials used in medicine, with a focus on metallic materials intended for temporary fracture fixation. Attention is given to the classification of biomaterials, properties of metallic implants, the structure and behaviour of commonly used materials - stainless steels, titanium, and cobalt alloys. The article also describes corrosion mechanisms that influence implant lifetime.

Keywords: biomaterials, metallic implants, titanium, stainless steel, corrosion

1. INTRODUCTION

Biomaterials are a fundamental component of modern medical applications. Their task is to replace, support, or regenerate damaged human tissue. Metallic biomaterials play a crucial role especially in orthopedics, where materials are exposed to high mechanical loads, chemically aggressive environments, such as long-term contact with body fluids.

A key requirement for any biomaterial is biocompatibility, ensuring that the implant does not cause toxic, allergic, or inflammatory reactions. Equally important is biofunctionality and the ability to withstand long-term mechanical and corrosion stress [1].

2. BIOMATERIALS

A biomaterial is defined as a material intended to interact with a biological system. It may be of natural or synthetic origin. When assessing suitability, chemical stability, mechanical strength, and biological response must be considered.

Biomaterials serve several key roles:

- replacement of damaged tissue (dental implants, joint replacements),
- support of healing (temporary fracture fixation),
- correction of functional abnormalities (pacemakers, intraocular lenses),
- assistance in diagnosis and treatment (medical probes, catheters) [1].

2.1. Biocompatibility and biofunctionality

Biocompatibility is the ability of a material to function in a living system without causing harmful reactions such as inflammation, allergies, or toxicity. It depends on the intended application and is assessed through evaluation of cytotoxicity, carcinogenicity, mutagenicity, corrosion resistance, and interactions with host tissue.

A biofunctional material must perform its intended mechanical or physiological role. Depending on the device, this may involve transferring loads and providing mechanical support, transmitting light or sound, filling or stabilizing space, enabling joint movement, or regulating blood and fluid flow [1, 2].

2.2. Classification of biomaterials by interaction with tissue

Biomaterials can be divided into four main groups based on their interaction with surrounding tissue (Figure 1.):

- *Bioinert materials* - Cause minimal reaction when implanted and remain stable in the body. Examples include titanium, aluminium, and certain polymers.
- *Biotolerant materials* - Form a thin fibrous tissue layer at the interface due to mild ion release or degradation products, typical for most synthetic polymers and metals.
- *Bioactive materials* - Interact with surrounding tissue and support osteogenesis, forming a biologically active hydroxyapatite (HA) layer that enables strong bonding with bone. Examples include HA and bioactive glasses.
- *Biodegradable materials* - Gradually dissolve in the body, with degradation products safely removed. These are used for sutures, temporary scaffolds, and drug delivery, with common examples including polylactic acid (PLA), polyglycolic acid (PGA), calcium phosphates, and magnesium alloys [2].

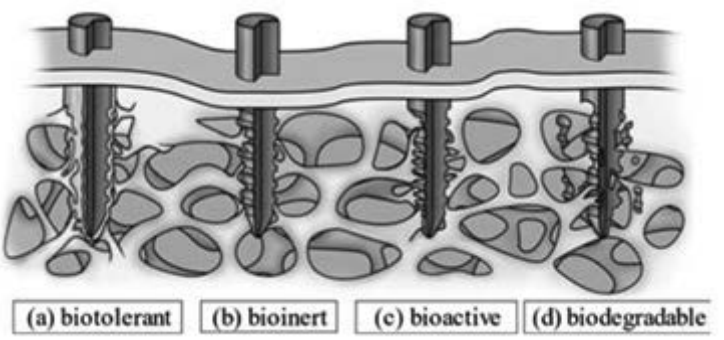

Figure 1. Schematic representation of the classification of biomaterials on a bone screw [2]

2.3. Classification by material type

Biomaterials may be divided into:

- metals and alloys,
- ceramics,
- polymers,
- composites.

Metal alloys are commonly used where high mechanical strength and toughness are needed, such as in load-bearing orthopedic implants [3].

3. METALLIC BIOMATERIALS

Metallic biomaterials are metals and alloys used in implants for bone repair, dental work, and joint replacements, prized for their high strength, toughness, and wear resistance, with common types including titanium alloys, stainless steels, and cobalt-chromium alloys, though challenges like corrosion and poor integration persist, leading to ongoing research in modifications and additive manufacturing.

3.1. Stainless steels

Stainless steels are widely employed in medical applications due to their corrosion resistance, ensured by a passive chromium oxide layer often enhanced by molybdenum. To qualify as stainless, the steel must have at least 10.5 % chromium. They are primarily used for fixation devices, plates, screws, and joint replacements. Stainless steels are categorized into austenitic, ferritic, martensitic, and duplex types.

- *Austenitic stainless steels* - especially AISI 316L, are widely used for bone implants and surgical instruments. Their face-centered-cubic structure provides high toughness and corrosion resistance. Chromium provides passivation, nickel stabilizes austenite, and molybdenum improves pitting resistance, while low carbon content prevents intergranular corrosion.
- *Ferritic stainless steels* - are Fe-Cr alloys with low carbon content. They are magnetic and less tough, which limits their use in medical applications, particularly due to MRI incompatibility.
- *Martensitic stainless steels* - contain higher carbon, making them heat-treatable and hard but more brittle. AISI 420 is commonly used for surgical instruments where high hardness and wear resistance are required.
- *Duplex stainless steels* - contain roughly equal proportions of austenitic and ferritic phases. They offer high strength, good corrosion resistance, and lower nickel content. Their combination of properties is being explored for biomedical applications [3].

3.2. Titanium alloys

People made efforts to utilize titanium as a biomaterial from 1930 onwards and nearly 1000 ton of titanium-based alloys are used as biomaterials in patients worldwide every year. For orthopedic applications the focus over the past few decades has been to find a suitable metallic implant that forms an extremely firm passive layer of TiO_2 on its surface. Ti is biocompatible and often shows direct bone apposition. Further an advanced behaviour of Ti is the low elastic modulus (two times lower compared to stainless steel and Co Cr), which in turn exhibits less stress shielding and linked bone resorption around Ti- orthopedic and dental implants. Moreover, Ti has lighter weight than other surgical biometals and shows some artifacts on magnetic resonance imaging and computer tomography. Ti has outstanding corrosion resistance. It forms a stable TiO_2 passive layer that protects against corrosion.

Titanium alloys are classified as α, β, or α+β depending on the stabilizing elements added. Ti-6Al-4V is the most widely used alloy for joint replacements and fracture fixation due to its favourable combination of strength, toughness, and biocompatibility. The most helpful group of Ti alloys in clinical applications are Ni-Ti alloys, known as Nitinol which contains 54 - 60 wt.% Ni. Nitinol demonstrates the unique properties of superelasticity and shape memory which is used in guide wires, stents, peripheral vascular devices, and embolic protection filters.

3.3. Cobalt alloys

Cobalt-based alloys (Co-Cr-Mo) are used in applications requiring high strength and wear resistance. They typically contain cobalt, chromium, molybdenum, and sometimes nickel. These alloys have a higher elastic modulus but lower toughness than stainless steels. Excellent corrosion resistance is provided by a Cr_2O_3 passive film. Their superior tribological performance makes them suitable for articulating components exposed to repetitive motion and high contact stresses. Co-Cr-Mo alloys are commonly used in knee implants, hip prostheses, and dental prosthetics where wear resistance is critical [3, 4].

Examples of common orthopedic implants made from metallic biomaterials are shown in Figure 2., including *(a)* stainless steel fixation plates, *(b)* titanium alloy endoprostheses, and *(c)* cobalt alloy knee endoprosthesis.

a) Fixation plates made of stainless steel

b) Endoprostheses made of a titanium alloy

c) Knee endoprosthesis made of a cobalt alloy

Figure 2. Representative metallic implants used in orthopedics

4. CORROSION MECHANISMS OF METALLIC IMPLANTS

Corrosion involves chemical and electrochemical reactions between a metal surface and its environment (ISO 8044:2015). In the human body, rich in ions, proteins, and with variable pH, corrosion can release harmful products, reduce implant lifetime, and compromise mechanical integrity. Understanding corrosion mechanisms is essential for material selection, implant design, and ensuring long-term biocompatibility. Degradation may result from electrochemical

dissolution phenomena, wear or a synergis-tic combination of the two. Electrochemical processes may include generalized corrosion, uniformly affecting the entire surface of the implant, and localized corrosion, affecting either regions of the device that are shielded from the tissue fluids (crevice corrosion) or seemingly random sites on the surface (pitting corrosion). Electrochemical and mechanical processes (e.g. stress corrosion cracking (SCC), corrosion fatigue and fretting corrosion) may interact, causing premature structural failure and accelerated release of metal particles and ions.

The following sections describe the most common corrosion mechanisms observed in metallic biomaterials:

- **Pitting corrosion** - arises from localized breakdown of the passive layer, often induced by chloride ions. It produces deep, narrow pits (Figure 3) that act as stress concentrators, weakening the material and potentially initiating fracture.

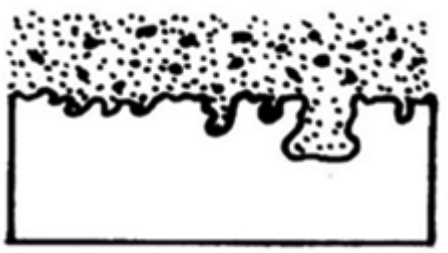

Figure 3. Pitting corrosion [5]

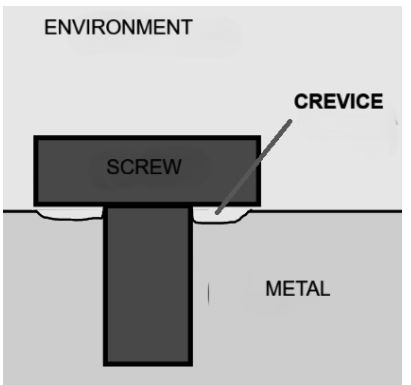

Figure 4. Crevice corrosion

- **Crevice corrosion** - occurs in narrow gaps with limited oxygen access, such as screw threads or between implant components (Figure 4). This leads to localized acidification, pit formation, and microcracks, which can compromise the structural stability of the implant.
- **Galvanic corrosion** - develops when dissimilar metals are in contact within an electrolyte, such as body fluids (Figure 5). The less noble metal corrodes preferentially, which can accelerate degradation in mixed-metal implant systems.

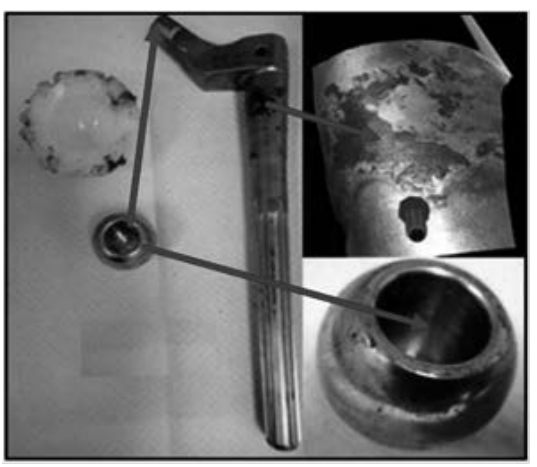

Figure 5. Galvanic corrosion and debris on an implant [5]

- **Intergranular corrosion** - attacks the grain boundaries of metals due to carbide precipitation also called sensitization. It is particularly critical in austenitic steels exposed to 400 - 850 °C during processing. Using low-carbon grades (AISI 316L) or stabilizing elements prevents this type of corrosion.
- **Stress corrosion cracking (SCC) -** is caused by the combined effect of tensile stress and a corrosive environment. It leads to crack growth without significant plastic deformation, representing a dangerous and often sudden failure mode in load-bearing implants [6] (Figure 6).

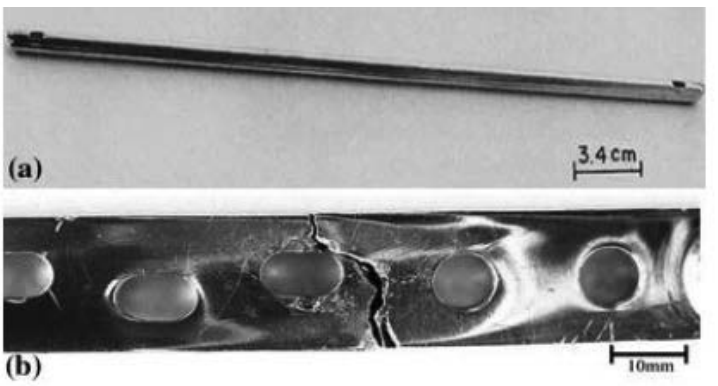

Figure 6. Examples of in vivo corrosion-assisted fractures: (a) SCC failure of 316L stainless steel nail implant (cracks emanated from the edges at the end of nail), (b) SCC failure of a femoral stainless steel implant [7]

ACKNOWLEDGEMENTS

The article was created as part of the joint Slovak-Polish project TalentDetector 2026 as a result of cooperation between the Silesian University of Technology, Gliwice and the Faculty of Mechanical Engineering, University of Žilina and project KEGA č. 033ŽU-4/2026.

BIBLIOGRAPHY

1. Q. Chen, G. Thouas. Biomaterials: A Basic Introduction [online]. 2015, Available at: https://books.google.co.uk/books?id=v9PMBQAAQBAJ&pg=PA3&dq=biomaterials
2. Y. Oshida, T. Miyazaki. Chapter 2: Biofunctionality and biomaterials. Biomaterials and Engineering for Implantology. Berlin: De Gruyter, 2022, pp. 28-44.
3. P. Palček, L. Markovičová, V. Zatkaliková. Materiály pre biomedicínske inžinierstvo. Žilina: EDIS, 2015. ISBN 978-80-554-0988-7.
4. K. S. Ødegaard, J. Torgersen, C. W. Elverum. Structural and biomedical properties of common additively manufactured biomaterials: A concise review. Metals, 2020, 10.
5. Istanbullu, O. B., Akdogan, G. A Simulation Study of Galvanic Corrosion Potential on the Surface of Implantable Biometallic Couples. J Bio Tribo Corros 7, 25 (2021).
6. P. Palček. Poškodzovanie biomateriálov koróziou [online]. Žilina: Katedra materiálového inžinierstva, Žilinská univerzita, Available at: http://kmi2.uniza.sk/wp-content/uploads/2010/12/Prezent%C3%A1cia-korozia-podklad.pdf
7. Jafari, S., Harandi, S. E. & Singh Raman, R. K. A Review of Stress-Corrosion Cracking and Corrosion Fatigue of Magnesium Alloys for Biodegradable Implant Applications. JOM 67, 1143-1153 (2015).

WYDAWNICTWO POLITECHNIKI ŚLĄSKIEJ
ul. Akademicka 5, 44-100 Gliwice
tel. (32) 237-13-81
wydawnictwo@polsl.pl
www.wydawnictwopolitechniki.pl

UIW 48600

Sprzedaż i Marketing
tel. (32) 237-18-48
wydawnictwo_mark@polsl.pl

Nakł. 130 + 22 Tom 2: 24,5 arkusze wydawnicze (21,375 arkusza drukarskiego)

Monografia 1098